LOMA LINDA UNIVERSITY
School of Medicine
in conjunction with the
Faculty of Graduate Studies

Episodic Continental Arc Magmatism in Peru: An Analysis of Flare-ups

by

Lance R. Pompe

A Dissertation submitted in partial satisfaction of
the requirements for the degree
Doctor of Philosophy in Earth Science

June 2023

Each person whose signature appears below certifies that this thesis in his/her opinion is adequate, in scope and quality, as a thesis for the degree Doctor of Philosophy in Earth Science.

_____, Chairperson
Benjamin L. Clausen, Adjunct Associate Professor of Earth Science

_____
William K. Hayes, Professor of Biology

_____
Ana M. Martinez Ardila, Assistant Professor of Earth Science

_____
Ronald Nalin, Adjunct Assistant Professor of Earth Science

_____
Kevin E. Nick, Associate Professor of Geology

_____
Scott R. Paterson, Professor of Earth Science (ret.), University of Southern California

ACKNOWLEDGEMENTS

I am especially grateful to God for not only creating a beautiful world and empowering me with the curiosity and resources to study it, but also for His patient and loving guidance throughout my life.

This research project would not have been possible without the help and positive vibes of the people around me. First and foremost, my deepest gratitude goes to my wife Mogi, she has patiently supported me on the long road and endured the uncertainty that this research presented. Special thanks goes to my parents, my sister and her husband for their support and encouragement. My advisor, Dr. Ben Clausen has now guided me through two graduate research degree programs. His scientific knowledge, insight and patience made this project possible. Thank you for bringing me into the world of geochronology and geochemistry and making it possible to travel to different conferences, perform fieldwork in the mountains of Peru and work with experts in the field. More importantly, I am impressed with the high value you place in treating people with kindness, in a Christlike manner. I am very grateful for the friendship and mentoring of Dr. Seth Wiafe at the LLU Health Geoinformatics Lab where I worked part time, thank you so much for always being available to help with anything.

I would like to express my appreciation to my committee members for their advice and input, Dr. Scott Paterson for your insightful discussions, expert guidance and advice, and notably for suggesting we collect samples for detrital zircon analysis while doing fieldwork in Peru; Dr. Ana Martinez for always being available to answer my questions, and for friendship and encouragement; Dr. Kevin Nick for help with defining the goals and aims, Dr. Ronny Nalin for great discussions and insightful questions; and

Dr. Bill Hayes for keeping an eye on the quantitative and statistical aspects of the project and asking intriguing questions at meetings.

I appreciate the friendship and help from the other members of the “hard rock” team, Mateo Ospino, Luiz Santos, Alex Voos, Raquel Bendita, Felipe Pichinual, and Dan O’Hare. Ed Santos was always available to lend his technical expertise on data analysis and has been a great friend, thank you so much. I really appreciate the many discussions, friendship and support of Sarah Maithel and Caleb LePore. Thank you to Muhammad Saleem for friendship and assisting in organizing and analyzing GIS data when I was too busy.

I am grateful to Elieze Strydom for her friendly and helpful presence as the EBS departmental admin assistant for most of my study program. Sarah Maithel’s more recent admin help has been much appreciated. My academic success was made possible by the financial support facilitated by Dr. Leonard Brand and Dr. Paul Buchheim, thank you so much for having confidence in me. I am grateful to Dr. Tim Standish for introducing me to the EBS geology program after I attended a talk he gave on a visit to Loma Linda.

My two bearded dragons Gilly and Tiger seemed to never get tired of hanging out on my shoulder and keeping me company and entertained during countless hours of data analysis and writing. If I have forgotten anyone, this one is for you: Thank you!

This PhD thesis was supported by funding from the Geoscience Research Institute and Loma Linda University Department of Earth and Biological Sciences. We acknowledge support from NSF-EAR 1649254 for the Arizona LaserChron Center and NSF EAR-0929777 for image acquisitions at the Arizona LaserChron SEM Facility.

CONTENT

Appendices

FIGURES

TABLES

ABBREVIATIONS

AFC	Assimilation fractional crystallization
AOC	Altered oceanic crust
BA	Bedrock age
BSE	Back scatter electron
CL	Cathodoluminescence
CNS	Cretaceous normal superchron
CS	Central segment
DZ	Detrital zircon
EC	Eastern Cordillera
GIS	Geographic information system
ICP-AES	Inductively coupled plasma atomic emission spectroscopy
KDE	Kernel density estimation
LA-ICP-MS	Laser ablation inductively coupled plasma mass spectrometer
LIP	Large igneous province
LOESS	Locally weighted least squares regression
LST	Lithium heteropolytungstate
LNS	Lower north segment
Ma	Million years ago
MAR	Magma addition rate
MC_P	mantle-derived crust preserved

MC_R	mantle-derived crust removed
MASH	Melting, assimilation storage and hybridization
MMA	Mantle magma addition
My	Million years
PCB	Peruvian Coastal Batholith
ppm	Parts per million
SEM	Scanning electron microscope
SIMS	Secondary-ion mass spectrometry
Sr_i	Initial strontium = $^{87}Sr/^{86}Sr\|_i$
SS	South segment
TGA	Thermogravimetric analysis
TIMS	Thermal ionization mass spectrometry
XRF	X-ray fluorescence

ABSTRACT OF THE DISSERTATION

Episodic Continental Arc Magmatism in Peru: An Analysis of Flare-ups

by

Lance R. Pompe

Doctor of Philosophy, Graduate Program in Earth Sciences
Loma Linda University, June 2023
Dr. Benjamin L. Clausen, Chairperson

The Peruvian arc forms part of the American Cordillera, Earth's longest continental margin subduction system. This Phanerozoic continental arc provides an excellent opportunity to study processes contributing to the creation of continental crust. The intensity of magmatic activity and therefore rate of magma emplacement into the arc over time is not steady but composed of a series of "flare-ups" against a low level of background magmatism termed "lulls". In this study, new U-Pb zircon geochronological and geochemical data are added to existing data to give a picture of the Phanerozoic magmatic history of the Peruvian Coastal Batholith and Eastern Cordillera of the Peruvian arc. Flare-ups are variable with no regular cycles (periodicity) evident. Magma volume is calculated for each flare-up from GIS area data and crustal thickness estimates. Changes in the geochemistry proxies for extent of differentiation, crustal thickness and mantle vs crust are compared between flare-ups and lulls and the rising and falling parts of flare-ups. No systematic differences are found for any of these proxies, leading to the assumption that upper plate arc-internal cyclic feedback models are not likely operating as flare-up triggers at least at the regional arc scale considered here in Peru. Geochemical data do not show consistent patterns during flare-up initiations nor between flare-ups in

different arc segments. Spatial and temporal variability of arc flare-ups, as well as basement types, tectonic regimes, crustal thicknesses and geochemistry imply that an equivalent temporal-spatial variability is needed for flare-up triggers. Much of the geochemical data point to the importance of mantle sources in producing the greatest volume of magmatism during flare-ups, suggesting that episodic mantle processes likely dominate in triggering flare-ups.

CO-AUTHORSHIP STATEMENT

This dissertation consists of three manuscripts which have been prepared for publication in scientific journals.

For both chapters two and three I am the first author and my co-authors are Ana María Martínez Ardila, Benjamin L. Clausen, Scott R. Paterson, and Orlando Poma. I was responsible for fieldwork, assembling some of the data, developing ideas and solutions, all data analysis, writing of both manuscripts, and all maps and plots. Ana Martínez was responsible for assisting with fieldwork, assembling some of the data, contributing ideas and strategies and editing. Benjamin Clausen was instrumental in advising, contributing and checking ideas and strategies, assisting with fieldwork and laboratory analysis, assembling some of the data, editing, and procuring funding. Scott Paterson contributed to overall ideas and strategies, detailed analysis of issues, fieldwork, editing and ultimately drove the direction of the research. Orlando Poma provided crucial assistance and logistics with fieldwork in Peru and assisted at scientific meetings where the research was presented.

In chapter four I am the second author for an invited review paper published in *Lithos*. I provided most figures and maps and contributed to discussions and ideas. I also assisted with fieldwork, laboratory analysis, data assembly and analysis, and some writing and editing of the manuscript.

CHAPTER ONE

INTRODUCTION

> "My religion consists of a humble admiration of the illimitable superior spirit who reveals himself in the slight details we are able to perceive with our frail and feeble mind."
>
> ~ Albert Einstein

Continental subduction-related magmatic arcs are thought to be instrumental in the production of new continental crust (Condie and Aster, 2010; Condie and Kröner, 2013; Voice et al., 2011). Magmatic processes in these arcs vary in both space and time as shown by studies using large geochronological datasets. In particular, magmatism tends to be episodic rather than continuous in nature, being characterized by a "steady state" baseline that is punctuated by a number of "flare-ups" (E.g. Cao et al., 2017; De Silva et al., 2015; Kirsch et al., 2016; Paterson and Ducea, 2015). Identifying the mechanisms driving magmatic addition and flare-ups is a key issue in magmatic and tectonic studies (E.g. Ducea et al., 2015; Kirsch et al., 2016; Martínez et al., 2019; Paterson and Ducea, 2015)

This research impacts society in various ways. Continental arcs create much thicker crust than oceanic arcs, often building high mountains and creating volcanic emissions that are important climate modifiers. They provide valuable sources of raw materials through ore deposits and water resources. An improved understanding of continental arc processes could provide predictive power in understanding geochemical distributions and therefore improve the management of key mineral resources associated with arcs such as copper, gold and rare earth elements. A better understanding of the

spatial and temporal history of continental arcs would improve our ability to predict and respond to geologic hazards such as earthquakes, tsunamis, volcanic eruptions, landslides and floods. They also serve as an excellent teaching resource about the Earth's dynamically evolving geologic system, for example, the importance of understanding crust/mantle interactions for plate tectonics and the timing of physical processes such as magma emplacement and cooling (Cao et al., 2017; Paterson and Ducea, 2015).

Research Goal and Specific Aims

Goal: To constrain the controls on episodic continental arc magmatism by testing specific models on the Eastern Cordillera and Peruvian Coastal Batholith of the Peruvian segment of the Cordilleran continental arc (Peruvian arc).

Aim 1: Describe and calibrate episodic continental arc magmatism in the Peruvian arc (paper 1).

Aim 2: Evaluate models of continental arc magmatic episodicity to identify potential triggers of magmatic flare-ups in the Peruvian Coastal Batholith and Eastern Cordillera of Peru (paper 2).

Structure of the Dissertation

This dissertation is divided into five chapters and nine appendices. The current chapter presents the methods used in this research project in terms of fulfilling the aims and providing details about fieldwork and analytical techniques. Chapters two and three focus on the scientific objectives as outlined above and on the specific aims. Chapter two

presents a paper that focuses on establishing the geochronology framework of the Peruvian Coastal Batholith and Eastern Cordillera. Chapter three presents a paper that analyzes the compilation of geochemical data for Peru to compare models of flare-up triggers. Chapter four is an invited review paper on the Peruvian Coastal Batholith published in *Lithos* in which I am a coauthor. The paper reviews work that has been done on the Peruvian Coastal Batholith and gives an updated analysis and interpretation using the data currently available, including over two-hundred and fifty new geochronology and geochemical samples. Finally, chapter five summarizes the research project and presents considerations for future work.

Geological Setting

The American Cordillera is a chain of mountain ranges from Alaska to the Antarctic that extends the length of the western continental margins of North and South America and represents a continuous ~15000 km long record of subduction magmatism at the boundary between oceanic and continental plates.

The Central Andes (~5–37° S) is an interesting segment of the American Cordillera for several reasons (Mamani et al., 2010; Mišković et al., 2009). It contains the thickest continental crust of any subduction zone worldwide, and the greatest orogenic volume along the Cordillera within the Central Andean orocline (currently at ~13–28° S). It has been built by a variety of processes that have changed along and across strike in nature, time and intensity. In parts of the Peruvian segment of the Cordilleran arc, flat-slab subduction of the Nazca ridge during the Neogene has created a break in ubiquitous Cenozoic volcanic cover, conveniently exposing older arcs. The Peruvian arc provides a

long record of subduction-related magmatism from initiation in the Early Paleozoic and earlier (for some parts of the arc) up until the present. Batholiths in the Eastern Cordillera of the Peruvian Andes straddle the western margin of Amazonia, recording over 1000 Ma of intermittent magmatism on part of the Earth's oldest continuously active continental margin (Mišković et al., 2009).

The Andean margin of Peru has been characterized by both extensional and compressional tectonic regimes throughout the Paleozoic and Mesozoic. The NW-SE trending ~1600 km long Peruvian segment (5–18° S) extends from the Huancabamba deflection in the north to the Arica bend in the south. It has also been subdivided into six along-strike longitudinal geological zones. From west to east, they are the Coastal Forearc, Western Cordillera, Altiplano, Eastern Cordillera, Sub-Andean fold and thrust belt, and foreland basin (Jaillard et al., 2000).

The basement of the Peruvian arc is characterised by several distinct blocks. The eastern belt is on the Gondwana protomargin which developed along the western margin of the Amazonia craton and is represented by the plutonic, metamorphic and metasedimentary rocks of the Eastern Cordillera (Ramos, 2009). The Proterozoic parautochthonous Arequipa basement is found in the southwest broadly underlying the altiplano south of Paracas (near Ica) (Mamani et al., 2008; Ramos, 2009). The parautochthonous Paracas terrane, composed of high grade metamorphic rocks including ophiolites, collided with the Gondwana margin during the Early Ordovician, forming the basement that underlies the Coastal Forearc and Western Cordillera from northern Peru down to Paracas (Ramos et al., 2012; Ramos, 2008).

Previous Work

In likely the most significant work to date on episodic continental magmatism in the American Cordillera, Kirsch et al. (2016) looked at the extent to which episodic magmatism is governed by external factors, such as plate motions, or internal factors, such as feedback processes in the upper plate. Large datasets of geochronological, geochemical, and plate kinematic data were integrated to analyze the Paleozoic to Mesozoic development of the Cordilleran orogen in eight transects from British Columbia to Patagonia, **Figure 1**. They found a periodicity of 50-80 My for some age patterns, which suggests a cyclic controlling mechanism. Other magmatic lulls and flare-ups were not correlated in adjacent sectors, indicating an influence of either discrete events or variable lag times. Comparing these results to plate kinematic data showed variable patterns that seemed to reflect different combinations of processes.

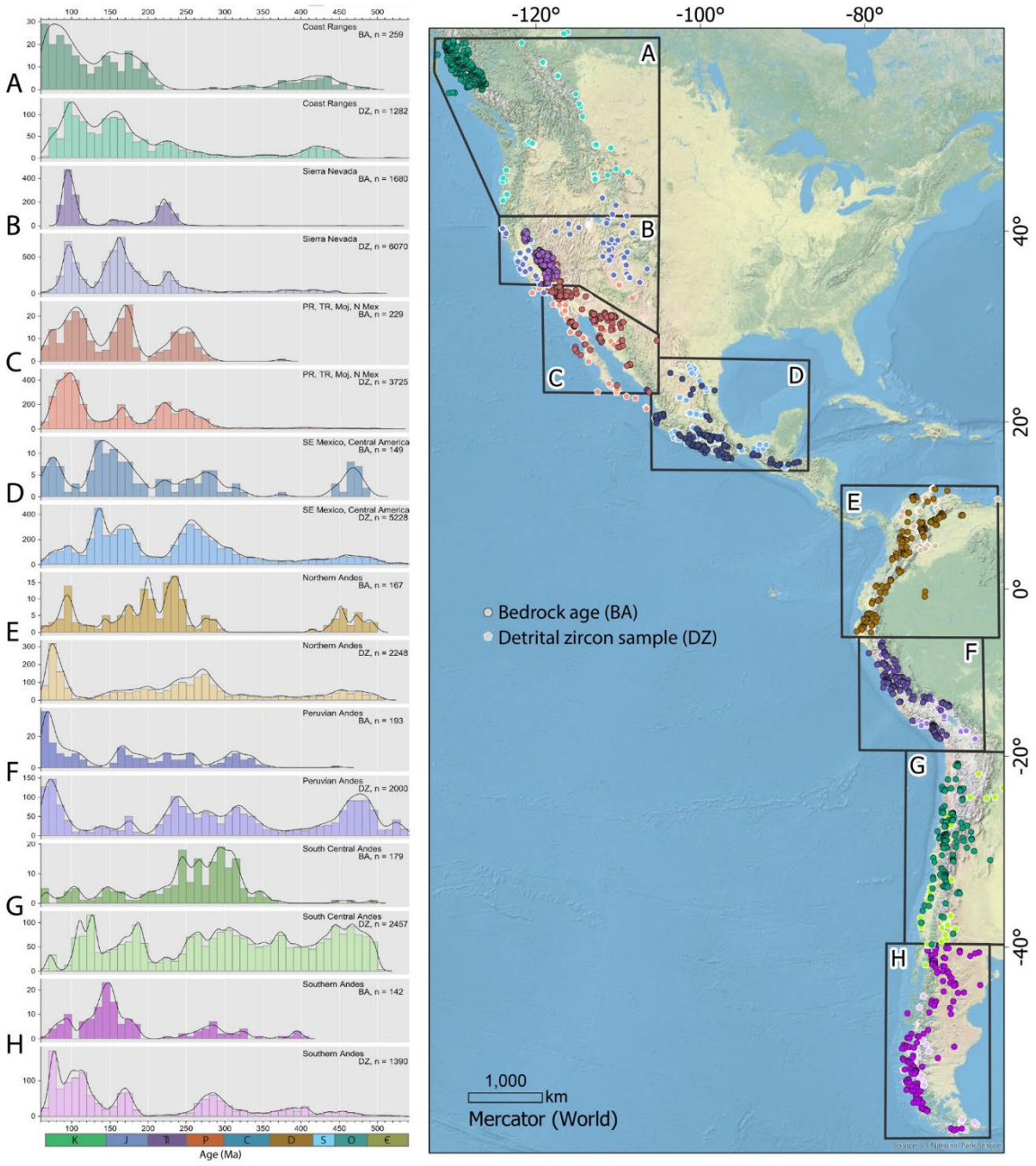

Figure 1. Bedrock and detrital zircon ages along Paleozoic and Mesozoic arcs of the American Cordillera, showing flare-ups. Based on Paterson and Ducea (2015) and Kirsch et al. (2016).

Specific Aims

Aim 1: Describe ages and volumes of episodic continental arc magmatism in the Peruvian arc (paper 1).

- Compile a database of all existing U-Pb zircon igneous bedrock and detrital zircon data for Peru.
- Collect appropriate samples from sedimentary units with at the earliest a Cretaceous age for an across-arc U-Pb detrital zircon study, separate zircons and perform laser ablation inductively coupled plasma mass spectrometer (LA-ICP-MS) analysis.
- Collect samples for U-Pb zircon igneous bedrock geochronology and geochemistry analysis from major intrusive and extrusive units in under-represented areas of the Peruvian Coastal Batholith and Eastern Cordillera, separate zircons and perform LA-ICP-MS analysis.
- Plot age spectra for the detrital zircon samples using histograms and kernel density estimation (KDE) to give an across-arc spatiotemporal view of arc magmatism.
- Add the new detrital zircon and igneous bedrock ages to existing detrital zircon and igneous bedrock age data.
- Plot age spectra for all age data together (detrital zircon and igneous bedrock) for the Peruvian arc and try to relate flare-ups to major tectonic and orogenic events from the literature.
- Plot age spectra for U-Pb zircon ages for segments of the Peruvian Coastal Batholith and for the Eastern Cordillera and identify flare-ups.

- Estimate average crustal thickness for each flare-up.
- Compile a GIS database of igneous geological units for the Peruvian Coastal Batholith and Eastern Cordillera.
- Find the best age for each GIS geological unit using sample ages and unit age designations.
- Estimate magmatic volume for each flareup in each segment of the Peruvian Coastal Batholith and Eastern Cordillera using the GIS geological unit area data and crustal thickness estimates.
- Present spatiotemporal data for flare-ups interactively using an online GIS dashboard application.

Aim 2: Evaluate models of continental arc magmatic episodicity to identify potential triggers of flare-ups in the Peruvian Coastal Batholith and Eastern Cordillera of Peru (paper 2).

- Select samples from those that were newly collected and dated in Aim 1 and conduct laboratory analysis of whole rock major and trace elemental geochemistry, as well as whole rock Sr, Nd and Pb radiogenic isotope analysis.
- Assemble a compilation of regional data:
    - εHf: analyze zircons from sedimentary and bedrock samples already dated to give a large dataset over which to evaluate the mantle contribution with respect to age spectra on a regional scale.
    - Tectonic data:
        - Convergence rate data (cm/yr)

- Dip angle data (degrees)

- Examine elemental and isotopic geochemistry to test models of flare-up triggers for segments of the Peruvian Coastal Batholith and Eastern Cordillera.
  - From elemental geochemistry and radiogenic isotope results, check whether each of the following varies systematically between flare-ups vs lulls and rising vs falling parts of flare-ups:
    - **Extent of differentiation** using SiO_2 as a proxy.
    - **Crustal thickness** using the following proxies:
      - Sr/Y ratio, which is related to the fractionation of garnet at depth and shallower fractionation of plagioclase in subduction zones (Morton et al., 2014; Profeta et al., 2015).
      - La/Yb ratio, the lightest and heaviest rare-earth elements.
    - C**rust vs mantle** source using:
      - Initial strontium ($^{87}Sr/^{86}Sr\ |_i$ or Sr_i) - estimate the relative influence of continental crust versus mantle (Faure and Powell, 2012) ($Sr_i > 0.706$ suggests a predominantly continental crust magma source; $Sr_i < 0.706$ suggest a mainly mantle source (Kistler et al., 2003)).

- εNd - estimate the relative influence of continental crust versus mantle (inversely proportional to Sr_i) (Faure and Powell, 2012).

- Interpret results using lower plate arc external and upper plate arc internal models suggested for controlling continental arc magmatism.

Field Data Collection

Fieldwork took place over three separate field seasons in Peru: August 2015 (prior to this project), March 2017, and June 2018, during which sedimentary samples for detrital zircon analysis and igneous bedrock samples for dating and geochemical analysis were collected, see **Figure 2** (the "LP" prefix was dropped from sample names later after analyzing the laboratory analysis results). Planning for the last two field trips included creating a GIS map showing geological units of interest, a road network with planned route to allow sampling of units of interest, and places to stay each night. A tiled version of the map was created and loaded into an app (Paper Maps) running on a tablet that allowed the current location with respect to the GIS map to be viewed offline in the field. This facilitated more accurately picking units of interest and then finding outcrops to sample, usually roadcuts.

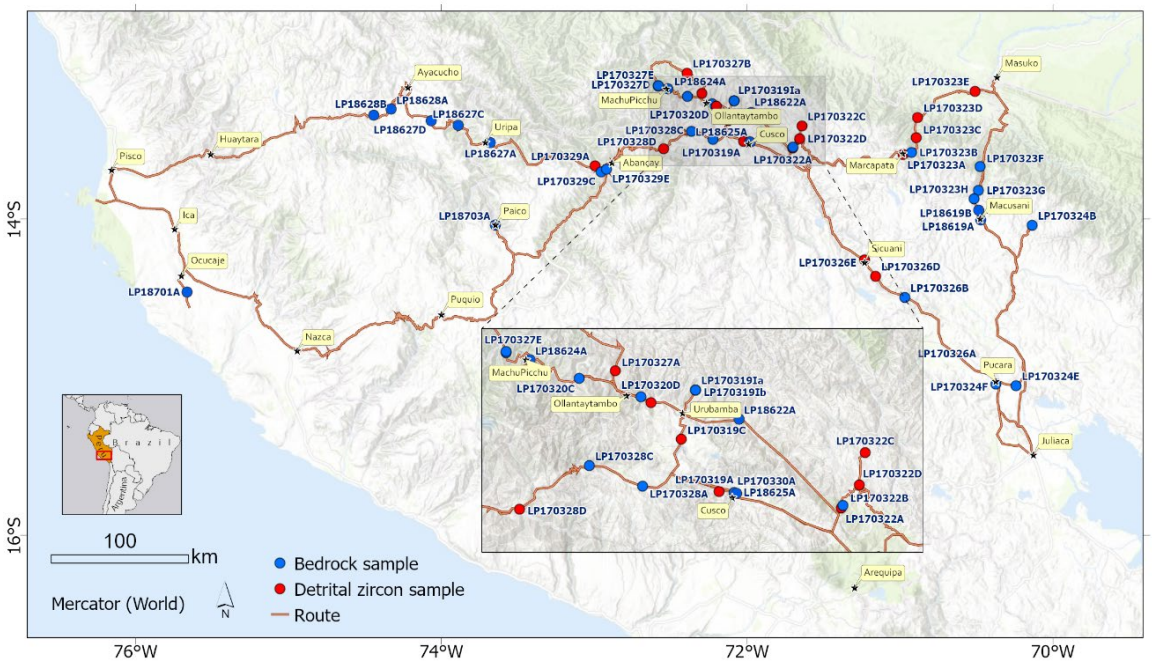

Figure 2. Map of locations and route travelled during 2017 and 2018 fieldwork for igneous bedrock samples and sedimentary samples collected for potential detrital zircon analysis, showing sample label and cities and towns along the route.

August 2015

At the time, the purpose of this field trip was to assist with other research projects and took place before this project started; however, the samples collected have turned out to be useful for this research project with most collected samples being used. Fieldwork took place over thirty days in August 2015. A total of thirty-six igneous bedrock samples were collected.

March 2017

The focus of this fieldtrip was collecting samples in the Eastern Cordillera to augment areas that had sparse existing data. Sampling took place over 18 days and covered approximately 3000 km through the Eastern Cordillera and down to the Amazon

basin in the sub-Andean fold and thrust belt for a sedimentary sample for detrital zircon analysis. A total of twenty-five igneous bedrock samples and thirteen sedimentary samples for possible detrital zircon analysis were collected.

June 2018

This fieldtrip focused on collecting additional samples in the Eastern Cordillera as well as in the Peruvian Coastal Batholith. An additional objective was to conduct a field conference to educate a group of students and educators from various South American countries on field geology. The trip took place over 22 days and covered approximately 5000 km. A total of twelve igneous bedrock samples were collected.

Igneous Bedrock Sampling

Our sampling strategy was to target large intrusive and extrusive units reachable from the road network. We attempted to collect samples from all reasonably accessible units, targeting the most representative and homogenous areas and avoiding xenoliths and dikes. Samples that were representative of major units of interest distributed across the study area were preferred, with the objective of having a reliable age for samples that would later undergo elemental and isotope geochemical analysis. A total of 28 intrusive and 9 volcanic samples were collected, with approximately 1 - 2 kg of fresh rock taken at each location. In addition, thirty-six plutonic and volcanic samples were collected from the Peruvian Coastal Batholith in 2015. See **Table 7** in **Appendix E** for the list of samples personally collected during fieldwork.

Sampling for Detrital Zircons

Thirteen samples were collected from sedimentary units in locations across the study area, with sandstones no older than Cretaceous age being preferred. Samples weighed approximately 0.5 kg each. Of these, a Cretaceous sandstone from Cusco and a quartzite sample from the Amazon basin east of the arc were selected for U-Pb detrital zircon geochronology analysis. A sandstone sample previously collected from a Miocene sandstone near Ica was also selected for U-Pb detrital zircon geochronology analysis. These samples were selected as the best examples for an across-arc detrital zircon study based on their locations and depositional ages.

Analytical Methods

Geochronology Analysis

Sample Preparation

Most samples selected for geochronology analysis were sent to the Arizona LaserChron Center at the University of Arizona in Tucson (www.laserchron.org) for zircon separation. Four igneous bedrock (170320C, 15810E, 15811A, 15811C) and three detrital zircon samples (170319A, 170323E and A11-118A) had zircons separated at California State University, Fullerton. Zircons were extracted using standard crushing, density separation and Frantz magnetic separation techniques.

At the Arizona LaserChron Center, zircon crystals were individually mounted together with SL (Sri Lanka) and FC (Forest Center) standards on 2.5 cm epoxy mounts. These were then ground down to expose fresh zircon surfaces and polished by 1 μm. Prior to analysis, grains were imaged at the Arizona LaserChron SEM (scanning electron

microscope) facility (www.geoarizonasem.org). Both back scatter electron (BSE) and cathodoluminescence (CL) imaging were done. BSE images were used to aid in distinguishing between zircon grains and others, such as apatite. CL imaging provided a guide for locating laser beam spots in optimal locations by avoiding inclusions and other crystal imperfections. CL images were also used for observing elemental zoning in zircon crystals. Zoning patterns are useful for detecting pre-magmatic inherited cores, metamorphic overgrowths and hydrothermal replacement zones (Kirsch et al., 2016). Both BSE and CL images were made for igneous mounts, but only BSE images for detrital zircon mounts. See **Appendix A** for more details on zircon separation and imaging techniques.

Zircon U-Pb Geochronology

The mineral zircon ($ZrSiO_4$) is widely considered to be a reliable geochronometer due to its relatively high retention temperature and resulting good precision and accuracy when used as an accessory mineral for U-Pb isotope geochronology (Condie and Kröner, 2013; Roberts and Spencer, 2015). In addition, zircon is abundant in most igneous, sedimentary and metamorphic rocks and dating can be performed with reasonable efficiency. Consequently, high-precision U-Pb zircon geochronology has become the standard to which all other geochronologic methods are compared (Schoene, 2014).

Although the basic U-Pb analytical methods have been in use for some time, issues can arise when geological processes disturb the zircon crystal in a way that affects the U/Th-Pb system. For zircon to be a reliable geochronometer, it needs to have remained a closed system with little Pb loss since crystalizing. The U/Th-Pb system

includes three chronometers, $^{238}U \rightarrow {}^{206}Pb$, $^{235}U \rightarrow {}^{207}Pb$, and $^{232}Th \rightarrow {}^{208}Pb$. Having these three decay systems available enhances the power of the U/Th-Pb system by allowing for the use of an internal check for closed system behavior over long timescales. For example, if the $^{206}Pb/^{238}U$ and $^{207}Pb/^{235}U$ pairs do not plot along the curve on which they would be in agreement for a given age (the concordia), they are considered discordant, thus suggesting open system behavior and yielding an unreliable age. (Gehrels, 2014; Gehrels et al., 2006; Schoene, 2014)

Recent technical advances have made it possible to not only target individual zircon grains but also certain regions of grains, greatly improving U-Pb dating accuracy. Whole-rock U-Pb ages analyzed before this capability are composed of an average of many zircon grains in a sample, meaning the presence of older inherited grains will bias the age to be older than the true crystallization age of the rock. If Pb loss has occurred in the rock, the age will be biased younger, but this should, in theory, be detectable as discordance.

Before the development of zircon TIMS (thermal ionization mass spectrometry) analysis and geochronological studies by SIMS (secondary-ion mass spectrometry), the assumption that a zircon date is the time of crystallization of a pluton was reasonable since absolute age uncertainties were large enough to include assembly and solidification. Miller et al. (2007) showed that assigning pluton crystallization ages based on zircon dating is complicated by the tendency of zircon to survive multiple intrusive events culminating in a large pluton. They categorize zircons into four groups. *Magmatic zircons* nucleate and grow directly from a melt or grow on an inherited zircon crystal. *Xenocrysts* are zircon crystals that are incorporated from the surrounding host rocks during transit

and emplacement. *Antecrysts* are zircon crystals that crystallized from an earlier pulse of magma and are incorporated in a later pulse(s). *Autocrysts* are zircon crystals that are associated exclusively with a distinct magma pulse. These relatively common complexities introduce uncertainties in determining the age of a sample, often requiring an informed interpretation of the data in arriving at a reliable age. Imaging techniques that show internal zircon crystal structure, such as cathodoluminescence, are valuable in revealing a zircon crystal's history.

Age analysis of samples (some were collected by others) was done entirely using zircon U-Pb analysis at the Arizona LaserChron Center at the University of Arizona in Tucson, applying methods described in Gehrels et al. (2006) and Gehrels et al. (2008). Visits to the Arizona LaserChron Center were made between July 2017 and March 2020 with a remote analysis session in September 2020. See **Appendix B** for more details on the methods used.

Igneous Bedrock Dating

Dating of igneous bedrock is used to establish accurate ages of intrusive and extrusive igneous units to help form a picture of regional magmatic history and constrain a geochemical sample to a particular geological period. Bedrock ages are also important in interpreting the source of zircons in detrital zircon age data. From the igneous samples collected during fieldwork (**Table 7)**, a total of 19 samples were dated. An additional 65 samples from previous and subsequent trips by others were also dated, bringing the total to 84 samples. Igneous bedrock U-Pb ages range from 16.03 – 1132 Ma.

Detrital Zircon Dating

The ability to target individual zircon grains has led to the development of detrital zircon geochronology, providing a valuable source of information about a wide range of geological processes, such as the history of regional magmatism and historical drainage patterns. Detrital zircons are considered to constitute the record of bedrock that has been eroded away, in particular the eruptive volcanic cover of an arc and part of the plutonic roots in older arcs (Ducea et al., 2015).

The first paper reporting on the use of LA-ICP-MS for detrital zircon analysis was published by Machado and Gauthier (1996), leading to a surge of interest in detrital zircon studies in the following two decades (Gehrels, 2014). Detrital zircons from sedimentary fore arc and back arc basins provide a very important complementary record of the temporal history of an arc. However, detrital zircon data by itself does not provide quantitative information about the volume of igneous rocks (Ducea et al., 2015).

Two detrital zircon samples from this collection, 170319A (Cretaceous sandstone near Cusco), and 170323E (Cretaceous quartzite in the Amazon basin just east of the Eastern Cordillera) as well as a detrital zircon sample from the Ica-Pisco region, A11-118A (Miocene sandstone) were analyzed. This resulted in 269 zircon grains being dated for the Cusco Cretaceous sample, 126 for the Amazon Cretaceous sample, and 192 for the Ica-Pisco Miocene sandstone sample. **Figure 3** shows locations and U-Pb zircon ages obtained from a number of the samples collected.

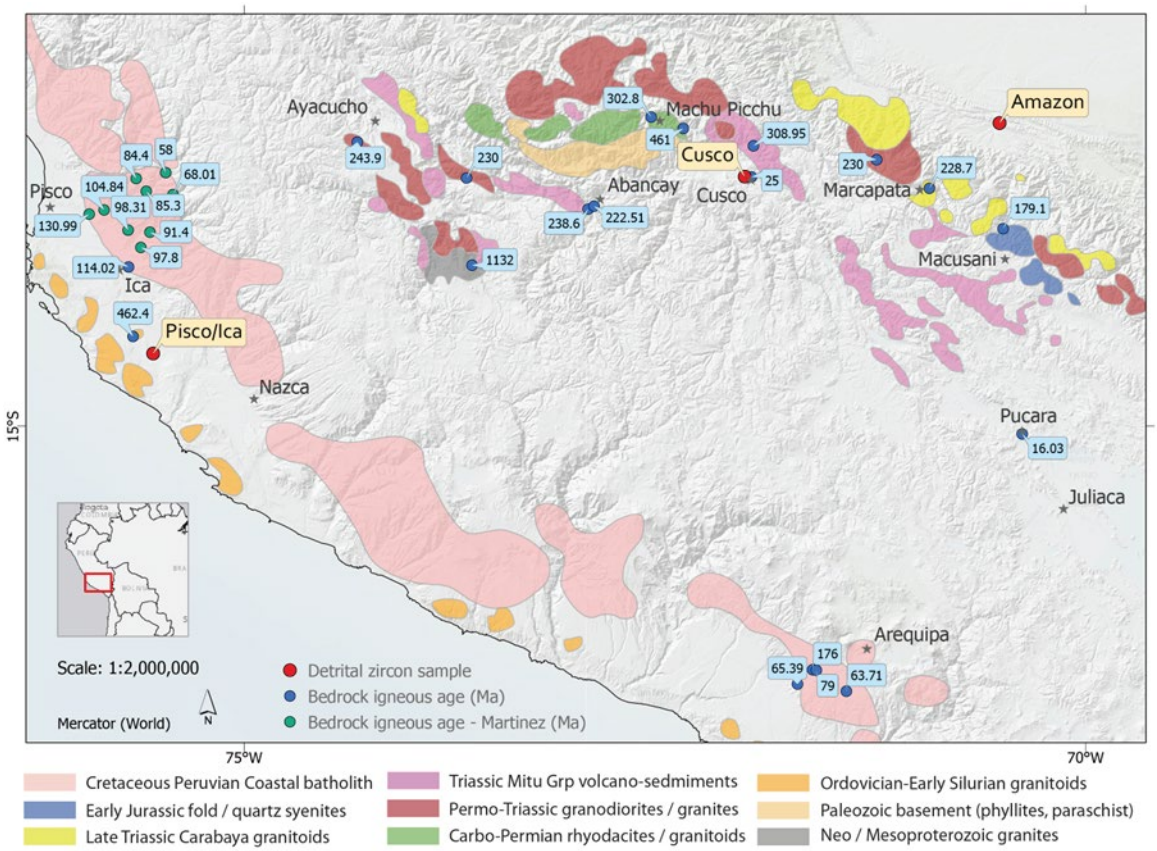

Figure 3. New U-Pb detrital zircon and igneous bedrock ages (Ma) from 2017 and 2018 sampling, also showing 9 igneous bedrock ages from the Peruvian Coastal Batholith near Ica from Martinez (2016) and four samples from the Arequipa area sampled in 2015. Three sedimentary samples were analyzed for detrital zircons from locations across the arc, near Ica, Cusco, and the Amazon. Peruvian Coastal Batholith outline is from Pitcher and Cobbing (1985), Eastern Cordilleran units are from Mišković et al. (2009) and were used to guide sampling in this region.

Geochemical Analysis

Sample Preparation

Eleven samples were prepared for XRF (X-ray fluorescence) analysis at Cal Poly Pomona. Samples were first crushed in a jaw crusher, then pulverized in a shatterbox to create the powders. Next, the powders were fused in a furnace using a flux to lower the melting temperature. After cooling, the beads were etched and polished. The remaining

major and trace element geochemical analysis was done by ALS Minerals in Tucson, Arizona, at their lab facility in Vancouver, Canada. Samples were prepared for analysis using the PREP-31Y procedure. A crusher/rotary splitter was used to crush samples to 70% less than 2 mm, then rotary split off 250g before pulverizing the split to better than 85% passing 75 microns.

Major Element Analysis

Whole rock major elements were primarily analyzed by ALS Minerals using the ME-ICP06 method. This involves using a combination of XRF with fused bead and acid digestion as well as inductively coupled plasma atomic emission spectroscopy (ICP-AES) finishes. Eleven samples were analyzed using XRF at Cal Poly Pomona but later re-analyzed by ALS Minerals since results excluded rare earth elements.

Trace and Rare Earth Element Analysis

Whole rock trace element data were obtained using the ME-MS81 analysis by ALS Minerals. A lithium borate fusion was applied prior to acid dissolution and inductively coupled plasma mass spectrometry (ICP-MS) analysis.

Radiogenic Isotope Analysis

Whole rock radiogenic Rb-Sr, Sm-Nd, and U-Th-Pb isotopic analyses were performed for 16 selected samples by Mihai Ducea at the Geochronology and Thermochronology Lab of the University of Arizona in Tucson, Arizona. Radiogenic isotopes were measured using multicollector ICP-MS.

Zircon Hafnium Isotope Analysis

Hafnium isotope data were obtained on previously dated zircon grains from both igneous bedrock and detrital zircon samples using LA-ICP-MS at the Arizona LaserChron Center on a Nu Instruments multi-collector mass spectrometer coupled with a Photon Machines Analyte G2 excimer laser system. See Gehrels and Pecha (2014) for details on the analytical procedures and interference corrections. Care was taken to only use zircons that had concordant ages. A total of 206 zircons were analyzed from the three across-arc detrital zircon samples (Ica-Pisco, Cusco and Amazon) and 212 zircons from 21 igneous bedrock samples. To ensure Hf isotope results are coupled as closely as possible to the zircon age, Hf analysis was performed on the previously dated U-Pb ablation pit.

Data Compilation

An extensive regional geochronological and geochemical database for Peru was compiled from published literature, with some detrital zircon data extending slightly into southern Ecuador (Witt et al., 2017) and northern Bolivia (Leier et al., 2010; Reimann et al., 2010). The new geochronological and geochemical data sampled and anlyzed here were added to these data to form the basis for data analysis for this project. Dated bedrock igneous samples added 84 ages to the existing age data for a total of 421 samples with U-Pb zircon ages, each determined from approximately 30 individual zircon grains. The three across-arc detrital zircon samples analyzed added a total of 587 zircon ages to the existing detrital zircon data for a total of 3290 detrital zircon ages for Peru.

Geological unit data covering the surface of Peru was obtained from INGEMMET for use in GIS software to select arc-related igneous units (both plutonic and volcanic).

Software used in Data Analysis, Plots and Maps

All data analysis and plotting was done using the R statistical package version 4.2.2. (R-Core-Team, 2023). Spatial data analysis and mapping was done using Esri ArcGIS Pro 3.1. The online operations dashboard for interactive exploration of flare-up data was implemented using ArcGIS Online (Esri, 2023). The R-ArcGIS Bridge package in R was used to facilitate data analysis and transfer between R and ArcGIS.

References

Cao, W., Lee, C.-T. A., and Lackey, J. S., 2017, Episodic nature of continental arc activity since 750 Ma: A global compilation: Earth and Planetary Science Letters, v. 461, p. 85-95.

Condie, K. C., and Aster, R. C., 2010, Episodic zircon age spectra of orogenic granitoids: the supercontinent connection and continental growth: Precambrian Research, v. 180, no. 3, p. 227-236.

Condie, K. C., and Kröner, A., 2013, The building blocks of continental crust: evidence for a major change in the tectonic setting of continental growth at the end of the Archean: Gondwana Research, v. 23, no. 2, p. 394-402.

De Silva, S. L., Riggs, N. R., and Barth, A. P., 2015, Quickening the pulse: Fractal tempos in continental arc magmatism: Elements, v. 11, no. 2, p. 113-118.

Ducea, M. N., Paterson, S. R., and DeCelles, P. G., 2015, High-volume magmatic events in subduction systems: Elements, v. 11, no. 2, p. 99-104.

Esri, 2023, ArcGIS for Desktop: https://www.arcgis.com: Redlands, CA.

Faure, G., and Powell, J. L., 2012, Strontium isotope geology, Springer Science & Business Media.

Gehrels, G., 2014, Detrital zircon U-Pb geochronology applied to tectonics: Annual Review of Earth and Planetary Sciences, v. 42, p. 127-149.

Gehrels, G., and Pecha, M., 2014, Detrital zircon U-Pb geochronology and Hf isotope geochemistry of Paleozoic and Triassic passive margin strata of western North America: Geosphere, v. 10, no. 1, p. 49-65.

Gehrels, G., Valencia, V., and Pullen, A., 2006, Detrital zircon geochronology by laser-ablation multicollector ICPMS at the Arizona LaserChron Center: The Paleontological Society Papers, v. 12, p. 67-76.

Gehrels, G. E., Valencia, V. A., and Ruiz, J., 2008, Enhanced precision, accuracy, efficiency, and spatial resolution of U-Pb ages by laser ablation–multicollector–inductively coupled plasma–mass spectrometry: Geochemistry, Geophysics, Geosystems, v. 9, no. 3.

Jaillard, E., Hérail, G., Monfret, T., Díaz-Martínez, E., Baby, P., Lavenu, A., and Dumont, J., 2000, Tectonic evolution of the Andes of Ecuador, Peru, Bolivia and

northernmost Chile, *in* U.G. Cordani, E. J. M., A. Thomaz Filho, D.A. Campos, ed., Tectonic Evolution of South America, Volume 31, p. 481-559.

Kirsch, M., Paterson, S. R., Wobbe, F., Martínez, A. M., Clausen, B. L., and Alasino, P. H., 2016, Temporal histories of Cordilleran continental arcs: Testing models for magmatic episodicity: American Mineralogist, v. 101, no. 10, p. 2133-2154.

Kistler, R. W., Wooden, J. L., and Morton, D. M., 2003, Isotopes and ages in the northern Peninsular Ranges batholith, southern California.: U. S. Geological Survey Open-File Report, v. 03, p. 45.

Leier, A. L., McQuarrie, N., Horton, B. K., and Gehrels, G. E., 2010, Upper Oligocene conglomerates of the Altiplano, central Andes: the record of deposition and deformation along the margin of a hinterland basin: Journal of Sedimentary Research, v. 80, no. 8, p. 750-762.

Machado, N., and Gauthier, G., 1996, Determination of $^{207}Pb/^{206}Pb$ ages on zircon and monazite by laser-ablation ICPMS and application to a study of sedimentary provenance and metamorphism in southeastern Brazil: Geochimica et Cosmochimica Acta, v. 60, no. 24, p. 5063-5073.

Mamani, M., Tassara, A., and Wörner, G., 2008, Composition and structural control of crustal domains in the central Andes: Geochemistry, Geophysics, Geosystems, v. 9, no. 3.

Mamani, M., Wörner, G., and Sempere, T., 2010, Geochemical variations in igneous rocks of the Central Andean orocline (13 S to 18 S): Tracing crustal thickening and magma generation through time and space: Geological Society of America Bulletin, v. 122, no. 1-2, p. 162-182.

Martinez, A. M. A., 2016, Compositional Diversity in Arcs: A Record of Magmatic Processes in the Peru Coastal Batholith, Ica [PhD dissertation: Loma Linda University, 410 p.]

Martínez, A. M. A., Paterson, S. R., Memeti, V., Parada, M. A., and Molina, P. G., 2019, Mantle driven cretaceous flare-ups in Cordilleran arcs: Lithos, v. 326, p. 19-27.

Miller, J. S., Matzel, J. E., Miller, C. F., Burgess, S. D., and Miller, R. B., 2007, Zircon growth and recycling during the assembly of large, composite arc plutons: Journal of Volcanology and Geothermal Research, v. 167, no. 1-4, p. 282-299.

Mišković, A., Spikings, R. A., Chew, D. M., Košler, J., Ulianov, A., and Schaltegger, U., 2009, Tectonomagmatic evolution of Western Amazonia: Geochemical

characterization and zircon U-Pb geochronologic constraints from the Peruvian Eastern Cordilleran granitoids: Geological Society of America Bulletin, v. 121, no. 9-10, p. 1298-1324.

Morton, D. M., Miller, F. K., Kistler, R. W., Premo, W. R., Lee, C.-T. A., Langenheim, V. E., Wooden, J. L., Snee, L. W., Clausen, B. L., and Cossette, P., 2014, Framework and petrogenesis of the northern Peninsular Ranges batholith, southern California: Geological Society of America Memoir, v. 211, p. 61-143.

Paterson, S. R., and Ducea, M. N., 2015, Arc magmatic tempos: gathering the evidence: Elements, v. 11, no. 2, p. 91-98.

Pitcher, W. S., and Cobbing, E. J., 1985, Phanerozoic Plutonism in the Peruvian Andes, *in* Pitcher, W. S., Atherton, M. P., Cobbing, E. J., Beckinsale, R. D., ed., Magmatism at a plate edge: the Peruvian Andes, Springer, p. 152-167.

Profeta, L., Ducea, M. N., Chapman, J. B., Paterson, S. R., Gonzales, S. M. H., Kirsch, M., Petrescu, L., and DeCelles, P. G., 2015, Quantifying crustal thickness over time in magmatic arcs: Scientific reports, v. 5.

R-Core-Team, 2023, R: A language and environment for statistical computing: Vienna, http://www.r-project.org.

Ramos, V., Valencia, K., and Romero, D., 2012, The Paracas Terrane (central-northern Perú): A Greenville age sialic basement accreted to the western Gondwana margin during the Famatinian orogeny. 13° Congreso Geológico Chileno, Antofagasta: Actas, v. 1, no. T2, p. 141-143.

Ramos, V. A., 2008, The basement of the Central Andes: the Arequipa and related terranes: Annu. Rev. Earth Planet. Sci., v. 36, p. 289-324.

Ramos, V. A., 2009, Anatomy and global context of the Andes: Main geologic features and the Andean orogenic cycle: Backbone of the Americas: Shallow subduction, plateau uplift, and ridge and terrane collision, v. 204, p. 31-65.

Reimann, C., Bahlburg, H., Kooijman, E., Berndt, J., Gerdes, A., Carlotto, V., and Lopez, S., 2010, Geodynamic evolution of the early Paleozoic Western Gondwana margin 14°–17° S reflected by the detritus of the Devonian and Ordovician basins of southern Peru and northern Bolivia: Gondwana Research, v. 18, no. 2-3, p. 370-384.

Roberts, N. M., and Spencer, C. J. J. G. S., London, Special Publications, 2015, The zircon archive of continent formation through time, v. 389, no. 1, p. 197-225.

Schoene, B., 2014, 4.10-U–Th–Pb Geochronology: Treatise on geochemistry, v. 4, p. 341-378.

Voice, P. J., Kowalewski, M., and Eriksson, K. A., 2011, Quantifying the timing and rate of crustal evolution: global compilation of radiometrically dated detrital zircon grains: The Journal of Geology, v. 119, no. 2, p. 109-126.

Witt, C., Rivadeneira, M., Poujol, M., Barba, D., Beida, D., Beseme, G., and Montenegro, G., 2017, Tracking ancient magmatism and Cenozoic topographic growth within the Northern Andes forearc: Constraints from detrital U-Pb zircon ages: Geological Society of America Bulletin, v. 129, no. 3-4, p. 415-428.

CHAPTER 2

EPISODIC CONTINENTAL ARC MAGMATISM:

TEMPOS OF THE PERUVIAN ARC

Lance R. Pompe[1], Ana María Martínez Ardila[1], Benjamin L. Clausen[1,2], Scott R. Paterson[3], and Orlando Poma[4]

[1] Department of Earth and Biological Sciences, Loma Linda University, Loma Linda, CA 92350, USA
[2] Geoscience Research Institute, Loma Linda, CA 92350, USA
[3] Claremont, CA 91711, USA
[4] Universidad Peruana Unión, Carretera Central, km. 19, Ñaña, Lima, Peru

Corresponding author: Lance Pompe (lpompe@llu.edu)

Abstract

The Phanerozoic American Cordillera provides an excellent opportunity to study processes contributing to the creation of continental crust. In this study we characterize and quantify the magmatic history of the Peruvian segment of this continental subduction system. The intensity of magmatism and therefore rate of magma emplacement into the arc over time is non-steady, being composed of a series of high magma addition "flare-ups" against an intermittent and variable lower level of background magmatism. We add new U-Pb ages for igneous bedrock samples and detrital zircons from sedimentary rocks to existing geochronological data to give a picture of the magmatic history of the Peruvian arc. Detrital zircons from three sedimentary samples collected from locations in the west, center and east of the arc show magmatism younging to the west. Flare-ups in magmatism from segments of the Peruvian Coastal Batholith (PCB) and Eastern

Cordillera (EC) are analyzed to estimate the volume and rate of mantle magma addition (MMA) to the crust. Average flare-up duration is longer for the EC than for the PCB at ~80 vs 50 My. Flare-ups are found to have variable durations from ~10 to ~100 My with variable periodicity, thus being episodic in nature rather than cyclic. Magma volumes are calculated from areas of igneous map units using GIS, crustal thickness estimates based on element ratios, and a published calculation method based on tilted crustal sections. Total MMA volume added to the arc crust is estimated at 1070k km^3 and 1148k km^3 for the PCB and EC respectively, assuming a mantle/crust ratio of 80/20. This contributes ~6900 km^3 per My or ~1% of Permian-Paleogene global continental crust growth. We have created a web-based dashboard to facilitate interactive exploration of the mapped flare-ups.

Key words: geochronology, flare-up, Peruvian Coastal Batholith, Eastern Cordillera, mantle magma addition

Introduction

Overview

An understanding of the Earth's subduction-related magmatic arcs is essential for developing models of the nature and formation of continental crust and for the processes of plate tectonics, particularly where volcanic hazards and earthquakes are of concern. Continental arcs are formed when oceanic plates continuously subduct beneath continental plates, generating magma via flux melting – the process in which volatiles lower the melting temperature enough to cause rocks to melt. Since they are sensitive recorders of tectonomagmatic changes through time in Cordilleran orogenic systems, studying spatiotemporal processes in these arcs can yield valuable insights. Studies using large geochronological datasets have shown that continental arc magmatism is not continuous in nature, but episodic in both space and time, being characterized by periods of high-volume magmatic activity, or *flare-ups* against a background of lower-volume and variable activity, or *lulls*. See for example, Paterson and Ducea (2015), Kirsch et al. (2016), Cao et al. (2017), and Ducea et al. (2015). It has been suggested that lulls correspond to times of low mantle power (i.e. supply of thermal energy and volatiles to the base of the crust by basalt intrusion from the mantle) (De Silva et al., 2015). The question of what processes drive flare-ups is as yet unresolved, with suggestions being an increase in mantle power, a change in subduction zone geodynamics or lithospheric processes, see for example De Silva et al. (2015), DeCelles et al. (2009), and Paterson and Ducea (2015). Being much longer lived than oceanic arcs, continental arcs record multiple high magma addition rate events, averaging tens of millions of years each. The mostly granodioritic Cordilleran batholiths as well as their andesitic eruptive equivalents

were primarily created during these flare-up periods, and are considered to be the main continental crust building factories on Earth (Stern and Scholl, 2010).

Extensive regional geochronologic databases have been compiled for the Peruvian arc from published literature, e.g. by Mirian Mamani (Mamani, 2022) and Kirsch et al. (2016), with some data extending into southern Ecuador (Witt et al., 2017) and northern Bolivia (Leier et al., 2010; Reimann et al., 2010). Our new geochronology data are added to these data to give a picture of the magmatic history of this region. Zircon age peaks are interpreted to represent periods of increased rates of magma addition and termed *flare-ups* while troughs are interpreted to represent background magmatism and termed *lulls*.

This study aims to establish the magmatic tempo framework for the Peruvian arc, facilitating further study to better understand the mechanisms that trigger flare-ups.

Geological Setting

The NW-SE trending ~2000 km long Peruvian segment (5° S – 18° S) of the American Cordillera extends from the Huancabamba deflection in the north to the Arica bend in the south. The Peruvian arc is distinguished by three main geomorphic features: two cordilleras, the Western and Eastern Cordillera that run north-west to south-east parallel to the coast, separated by a central highland plateau, the Altiplano that pinches out in the north-west and widens in the south-east. Other along-strike longitudinal geomorphic features are the Sub-Andean fold and thrust belt and foreland basin in the east (Jaillard et al., 2000; Pfiffner and Gonzalez, 2013), see **Figure 4**.

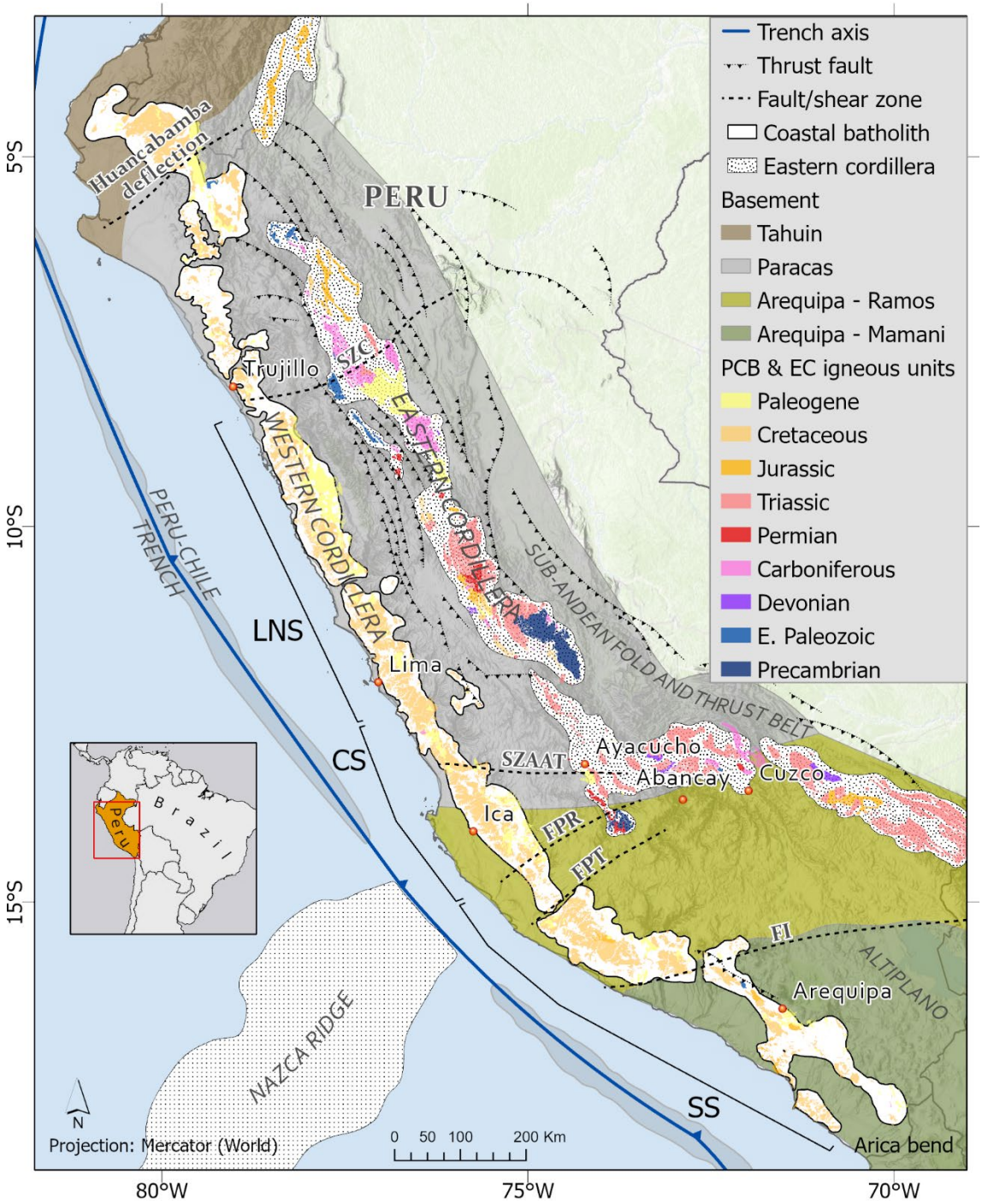

Figure 4. Map of the Peruvian arc showing the along-strike geophysical and geological provinces, in particular the Peruvian Coastal Batholith and Eastern Cordillera. The Coastal batholith is divided into North, Central and South segments. Modified from Martínez et al. (2019). SZC = Contaya shear zone, SZAAT = Abancay-Andahuaylas-Tambuco shear zone, FPR = Puyentimari fault, FPT = Patacancha Tambuco fault, FI = Iquipi fault system. Plutonic and volcanic igneous rock units in the PCB and EC are from the Peruvian Instituto Geológico Minero y Metalúrgico (INGEMMET, 2021).

The Central Andes of Peru (~5° S–28° S) is an interesting part of the American Cordillera for several reasons (Mamani et al., 2010; Mišković et al., 2009). It contains the thickest continental crust of any modern active arc, and the greatest orogenic volume along the American Cordillera within the Central Andean orocline (currently at ~13° S–28° S). It has been built by a variety of processes that have changed along and across strike in nature, time, and intensity. Flat-slab subduction due to subduction of the Nazca ridge during the Neogene has created a break in Cenozoic volcanic cover, conveniently exposing older arcs. In general, the Peruvian Coastal Batholith (PCB) in the west represents the Mesozoic magmatic history and the Eastern Cordillera (EC) the Paleozoic magmatic history of the region.

Basement

The basement of the Peruvian arc is characterized by several distinct blocks. Whether they were accreted or are an integral part of South America has been long debated, especially since the Andes would seem to be the type example of an ocean-continent tectonic setting (the Andean type margin). Earlier studies concluded that subduction of oceanic crust alone is insufficient to explain the deformation patterns of the Central Andes, raising the question of the collision of suspect terranes being involved, e.g. Pitcher (1985) and Nur and Ben-Avraham (1983).

The eastern belt defines the autochthonous Gondwana proto-margin which developed along the western margin of the Amazonia craton and is represented by the plutonic, metamorphic and metasedimentary rocks of the Eastern Cordillera (Ramos, 2008).

The Arequipa Massif is a metamorphic Paleoproterozoic basement inlier in south-western Peru described by Casquet et al. (2010). Rocks of the Arequipa Massif are mostly metasedimentary, ranging from amphibolite to granulite facies. This terrane is offset to the south-west along the western margin of the parautochthonous Arequipa terrane (also known as the Arequipa-Antofalla basement), a Proterozoic crustal block that is exposed along the central Andean margin and broadly underlies the altiplano south of Arequipa (Loewy et al., 2004; Mamani et al., 2008; Ramos, 2009). This crustal block was interpreted by Loewy et al. (2004) as being accreted onto Amazonia during the Sunsás orogeny at about 1.0 Ga. The parautochthonous Paracas terrane collided with the Gondwana margin during the Early Ordovician, coeval with the Famatinian orogeny, forming the basement that underlies the Coastal Forearc and Western Cordillera from northern Peru down to Paracas (Ramos, 2008). In general, Ramos (2008) concludes that accretionary tectonics in this part of the Andes were controlled by changes in plate dynamics at a continental scale related mainly to supercontinent reorganizations and also required oceanic plate subduction.

The Tahuín terrane in the northwest is not as well understood as the Arequipa and Paracas terranes since it lacks the required geophysical, geochronological and geochemical studies to adequately characterize its tectonic evolution. However, some suggestions have been made. Feininger (1987) and Mpodozis and Ramos (1990) used paleomagnetic data and comparison with the Paleozoic sequences exposed in southern Ecuador to suggest the Tahuin terrane is an allochthonous Paleozoic terrane accreted during the Cretaceous. An interpretation based on the dating of metamorphic rocks suggests the Tahuín terrane was possibly a part of Laurentia that collided with the

Gondwana margin during the Alleghanian orogeny, and became detached from Laurentia, remaining on the Gondwana margin (Cardona et al., 2005; Ramos, 2009). Witt et al. (2017) used a detrital zircon study to suggest the Tahuín terrane docked with the Paracas terrane and subsequently collided with the Gondwana margin in the Early Permian.

Eastern Cordillera (EC)

The Eastern Cordillera or *Cordillera Oriental* of Peru is a ~1400 km long composite and complex belt with northern and southern parts. Batholiths in the Eastern Cordillera straddle the western margin of Amazonia, recording over 1000 Ma of intermittent magmatism on part of the Earth's oldest continuously active continental margin (Mišković et al., 2009). Magmatism in the Eastern Cordillera was periodic in nature with highly variable mantle and crustal sources (Kontak et al., 1984). Within the Central Andes of Peru, Paleozoic or older pre-Andean cycle plutonic and sedimentary units are mostly confined to the Eastern Cordillera (Cardona et al., 2006).

Cobbing (1985) (and references therein) provides an overview of the tectonic structure of the Eastern Cordillera. The Marañón Massif in the north is composed of medium to high grade meta-sediments and volcanics, with regional metamorphism documented at about 600 Ma. Cardona et al. (2006) documented an Early to Middle Ordovician magmatic arc in the Eastern Cordillera which forms part of the Marañón Massif. The southern part is a Paleozoic composite belt of meta-sediments and plutons deposited in a curvilinear trough from central Peru to northern Argentina. Source regions for these sediments are both the Amazonian Craton to the north-east and the Arequipa Massif to the south-west. Middle Permian folding of the sedimentary rocks was followed

by two episodes in the late Permian to Early Triassic that define the structure of the Eastern Cordillera. The first episode formed the Mitu Group, a post-tectonic molasse sequence composed of continental deposits and rifting volcanism from the final phase of the Paleozoic pre-Andean orogeny and initial phase of the subsequent Mesozoic Andean orogeny. These deposits settled in elongate horst and graben structures formed during a period of extensional tectonics. The emplacement of large granitic plutons in the Permo-Triassic composed predominantly of true granites with rare tonalites and granodiorites marked the second episode and ended magmatic activity in this belt. Older rocks found in the Eastern Cordillera occur as plutonic remnants belonging to the Early Paleozoic Famatinian arc as well as reworked Mesoproterozoic crust.

Peruvian Coastal Batholith (PCB)

The Western Cordillera consists of plutonic and volcanic rocks on the western side of the Andean arc. The Peruvian Coastal Batholith is a belt of plutons and volcanic rocks running over ~2000 km parallel to the coast along the western flank of the Western Cordillera, and is up to 65 km across. The most detailed studies of this batholith culminated in the impressive volume *Magmatism at a plate edge: The Peruvian Andes* by Pitcher et al. (1985).

The recent rapid uplift of the Andes has allowed deep canyons to be carved in bedrock by westward flowing rivers at relatively regular intervals throughout the length of the batholith. Well-maintained roads follow these canyons from the coast into the interior, providing convenient access to researchers. These fortuitous features in addition to an arid climate along the Peruvian coast means the Coastal Batholith has particularly

good bedrock exposure in three dimensions, creating one of the best opportunities on Earth to study continental arc processes (Pitcher, 1985).

The Coastal Batholith is intruded into the volcaniclastics of the Early Cretaceous Casma and Quilmana volcanic arcs which were deposited within the interconnected and subsiding linear basins of the Huarmey Cañete Trough. The Huarmey Cañete Trough is in turn the western part of the West Peruvian Trough, a larger marginal basin that developed on the western side of the Marañon basement block that to the east contains the Late Jurassic to Late Cretaceous sedimentary Marañon fold-and-thrust belt (Cardona et al., 2009; Hildebrand and Whalen, 2014; Pitcher et al., 1985).

Several longitudinal divisions have been proposed for the batholith based on geochemistry observations, 5 segments (Piura, Trujillo, Lima, Arequipa and Toquepala) by Pitcher et al. (1985) and more recently, 3 segments (Piura, Lima and Arequipa) by Ccallo Morocco et al. (2021). The current division proposal is lower north (8-12.5° S), central (12.5-15° S), and south (15-18° S) segments by Martinez et al. (2023). The geometry of the Coastal Batholith was suggested by Haederle and Atherton (2002), using geophysical observations, to be a flat slab with varying thickness. They estimated the batholith is made up of approximately 1000 individual plutons.

Methods

Previous Geochronology Data

Historically, much of the geochronology in the Peruvian arc used whole rock Rb-Sr and K-Ar dating methods. These ages need to be used with caution since K-Ar ages are often cooling or reheating ages, while Rb-Sr ages may be due to mixing isochrons of

different magmas or reset mineral ages. For these reasons, U-Pb zircon ages are preferred in this study. Existing geochronological data for the Peruvian arc include 393 in-situ U-Pb igneous bedrock sample ages and 2703 U-Pb detrital zircon ages from individual zircon grains; most notably with 46 Peruvian Coastal Batholith whole rock igneous bedrock sample ages by Mukasa and Tilton (1985) and 57 igneous bedrock sample ages by Mišković et al. (2009) in the Eastern Cordillera.

Noting the above concerns regarding a potential young bias, we have included K-Ar, ^{40}Ar-^{39}Ar and Rb-Sr age data only in the more geographically focused analyses with the caution that these data may reduce the average values for flare-ups. In this case, adding some non-U-Pb age data is justified since flare-up parameters are not appreciably affected as can be seen by comparing age spectra including these data with age spectra using only U-Pb data (compare **Figure 10** with **Figure 42**).

Sampling

Sampling between the latitudes of 10° S and 16° S was conducted between 2010 and 2019. The study area spanned the Andean orogenic belt from Rio Fortaleza in the north to Arequipa in the south, and from along the coast in the west to the fold and thrust belt bordering the Amazon in the east. This region was selected for the reasons noted above, namely having a long history of subduction conveniently exposed by a break in Cenozoic volcanic cover. Existing maps provided by the Peruvian geological survey, Instituto Geológico Minero y Metalúrgico (INGEMMET, 2017) both paper and web-based, were used to guide sampling.

Igneous Bedrock Sampling

Our sampling strategy was to target large intrusive and some extrusive units reachable from the road network. We attempted to collect samples from all reasonably accessible units, targeting the most representative and homogenous areas and avoiding xenoliths and dikes. Samples that were representative of major units of interest distributed across the study area were preferred, with the objective of having a reliable age for samples that would later undergo elemental and isotope geochemical analysis. A total of 84 collected samples were selected for analysis, 77 intrusive and 7 volcanic, with approximately 0.5 - 2 kg with an average of about 1 kg of fresh rock taken at each location. These include 12 samples from the Eastern Cordillera and 72 from the Peruvian Coastal Batholith.

Sedimentary Detrital Zircon Sampling

Thirteen samples were collected from sedimentary units in locations across the study area, with sandstones no older than Cretaceous age being preferred. Samples weighed approximately 0.5 kg each. A Cretaceous sandstone sample from Cusco and a Cretaceous quartzite sample from the Amazon basin east of the arc were selected to represent the central and eastern part of the Peruvian arc. A Miocene sandstone sample from the Ica area represents the western part of the arc. These samples were selected as our best examples for an across-arc U-Pb detrital zircon study based on their locations and depositional ages.

Sample Preparation

Samples selected for geochronology analysis were sent to the Arizona LaserChron Center at the University of Arizona in Tucson (www.laserchron.org) for zircon separation.

Prior to analysis, grains were imaged at the Arizona LaserChron SEM facility (www.geoarizonasem.org). Both back scatter electron (BSE) imaging and cathodoluminescence (CL) imaging were done. BSE images were used to aid in distinguishing between zircon grains and other minerals, such as apatite. CL imaging provided a guide for locating laser beam spots in optimal locations by avoiding inclusions and other crystal imperfections. CL images were also used for observing textures and elemental zoning in zircon crystals, aiding in detection of pre-magmatic inherited cores, metamorphic overgrowths and hydrothermal replacement zones, as described by Ducea et al. (2015). Both BSE and CL images were made for igneous mounts, but only BSE images for detrital zircon mounts. See **Appendix A - Zircon Separation and Imaging** for more details on these techniques.

Geochronology Analysis

U-Pb zircon geochronology analysis was conducted using LA-ICP-MS at the Arizona LaserChron Center, applying methods described in Gehrels et al. (2006) and Gehrels et al. (2008). See **Appendix B - Geochronology Analysis Methods** for more details on the methods used.

Age Spectra and Maps

Age spectra were constructed using a combination of histograms with an appropriate bin width and kernel density estimation (KDE) to visualize flare-ups as curves, using a manually adjusted bandwidth. Kernel density estimation is a technique to visualize the shape of data by fitting a smooth curve to the data. The "smoothness" of the curve is controlled by a bandwidth parameter; see Chen (2017) for more details. Flare-up durations were subjectively estimated by measuring the time intervals between the approximate point at which the probability density curve starts increasing from a lower baseline level to the point at which it drops back down and levels out at the baseline level again. The compilation of existing ages was augmented with our new igneous bedrock and detrital zircon ages and plots were made extending back to the Proterozoic, with a focus on the Phanerozoic interval.

Mantle magma addition volume data for the Peruvian Coastal Batholith and Eastern Cordillera were plotted by adding all geological unit volume data binned into 5 My bins, and plotted with a smooth curve using a spline function.

Age spectra and volume plots were made using the R statistical package version 4.2.2 (R-Core-Team, 2023). Spatial data analysis and mapping was done using Esri ArcGIS Pro 3.1 and ArcGIS Online (Esri, 2023).

Quantifying Magmatic Volumes

Once flare-ups and lulls have been characterized using available geochronology data, we consider the question of estimating magma volumes and addition rates. Arriving at reasonable estimates depends on resolving a number of issues. Age controlled maps of

compositionally distinct plutonic and volcanic units are needed to determine the spatial footprint of arc flare-ups. Deformation during and after arc activity may have modified the areal extent, complicating the area estimates. An indication of the vertical extent of the units is also needed. A further complication is estimating the amount of crustal contamination in the arc (Ducea et al., 2015).

Ratschbacher et al. (2019) outline a protocol to estimate the volume of igneous material added to the arc crust based on volume additions at different depths. They apply this protocol to three well-studied and exposed continental arc crustal sections to arrive at estimated magma volumes and addition rates. Volumetric addition to the continental arc crust is determined by the volume of magma originating from the mantle, which they define as mantle-derived magma addition (MMA), calculated as:

MMA = mantle-derived crust preserved (MC_P) + mantle-derived crust removed (MC_R)

where:

MC_P = volume addition to arc crust − recycled crust

and

MC_R = rifted igneous arc crust + igneous material eroded from surface

+ igneous material eroded by subduction erosion + volcanic air fall outside the arc

As noted in Ratschbacher et al. (2019) and references therein, magma volume addition is high in the main arc compared to the fore and back arc regions and also tends to increase with increasing crustal depth. Arc width and thickness can change during its active period, in response to changes in deformational stresses and tectonic regimes. Tectonic effects on igneous units can be accounted for by retro-deforming to determine

pre-deformation 2-D surface areas; however, this is only necessary for volcanic areas since plutonic areas are not significantly affected. Since plutonic volume additions are thought to be more than an order of magnitude greater than volcanic volume additions, errors related to volcanic volume estimations will only have a small effect on the total magma addition rate. See Ratschbacher (2017) for a discussion on dealing with MC_R.

Estimating mantle versus crust contributions in arc magmas is complicated by several factors. Ratschbacher et al. (2019) use two end-member scenarios, 80:20 and 50:50 mantle:crust input to constrain the upper and lower bounds of MMA estimates. The Central Andes was noted to have roughly equal contributions of mantle and crust by Freymuth et al. (2015), while Martínez et al. (2019) found the mantle component of rocks in the Ica-Pisco region of the Peruvian Coastal Batholith to be 65-70% using assimilation and fractional crystallization (AFC) calculations.

The following steps were used to estimate magma volume addition for the Peruvian arc: (1) estimate the surface area covered by age-controlled igneous arc rocks; (2) estimate the vertical thickness of these rocks using paleo-crustal thickness; (3) use carefully calculated MMA estimates from a tilted arc section of a similar arc setting and adjust by vertical thickness estimates to obtain MMA estimates (km^3 per km^2 of arc area); (4) use this result to calculate MMA volume per geological unit from the area data.

Although MMA quantities are commonly normalized to arc length (km), we agree with Ratschbacher et al. (2019) that normalizing to arc area (km^3/km^2) makes more sense since arcs vary so much in width along strike and throughout the active period. Similarly, MMA rates are reported as volume/area/time ($km^3/km^2/My$). Of the three arc sections studied by Ratschbacher et al. (2019), the Famatinian arc section in Argentina is most

applicable to the Peruvian Andes, with the Famatinian arc spanning from Colombia to Patagonia and forming part of the Eastern Cordillera in Peru. The average percentage of igneous rocks exposed for the Peruvian Coastal Batholith as a whole is 24%, based on calculations using GIS controlled area data. Mantle magma addition to the crust for the Famatinian arc section was calculated at 21 km^3/km^2 for flare-ups assuming a mantle to crust ratio of 50:50 and factoring in the varying contributions of the fore-, main and back-arc regions. Assuming a mantle to crust ratio of 80:20, MMA was calculated at 31 km^3/km^2. Total crustal thickness in the Ordovician arc at time of emplacement was estimated to be ~63 km based on isostatic mass balance modeling by Ratschbacher (2017).

Estimating Exposed Areal Extent of Arc-Related Igneous Rocks

Estimating the surface area of igneous rocks involved using GIS software to select igneous units (both plutonic and volcanic) from INGEMMET geological unit data covering the whole land surface of Peru. Arc-related igneous units that contained at least one U-Pb sample age (a point in polygon GIS operation) were given the average of all sample ages they contained. Since each geological unit is typically made up of many individual polygons with the same unit name, all polygons of a particular unit were given the same averaged age calculated from all U-Pb age samples contained within their areas. If no sample ages were found for a particular unit (unfortunately the case for most units), the age was given an estimated average numerical value based on the geological period assigned to the unit by INGEMMET. The resolution of these age data required using the variable duration geological periods of Carboniferous, Permian, Triassic, Jurassic,

Cretaceous and Cenozoic. Since these periods need to be quantified to facilitate calculations, fixed average values were given where no measured ages were available. This introduced data spikes at these average age values that skew age distributions in plots, requiring a smoothing function to be applied. This was achieved by randomizing age values throughout a relatively narrow range centered on the original age value.

Estimating Arc Crustal Thickness from Geochemical Data

Studies on modern volcanic rocks have shown that the thickness of crust at convergent plate margins has an influence on the chemistry of magmas generated through differentiation processes (e.g. Hildreth and Moorbath, 1988; Kay and Mahlburg-Kay, 1991; Profeta et al., 2015). Using information gathered from these studies, the chemistry of arc rocks formed in the geologic past can be used to infer the thickness of the crust at that time by functioning as a *mohometer* or measure of the depth to the Moho – the seismically defined boundary between the crust and mantle. Reconstructing crustal thickness using chemical and isotopic proxies is called *chemical mohometry* (Luffi and Ducea, 2022). Most applications of this method have previously focused on the two element ratios, La/Yb and Sr/Y, as described in Profeta et al. (2015).

Luffi and Ducea (2022) present 41 whole-rock mohometer models that they base on the composition of subalkaline volcanic rocks found in modern arcs. They calibrated these models using elevation as a proxy for Moho depth and accounted for magma differentiation degree using MgO, since many mohometers have been found to be sensitive to the extent of differentiation of the magma. Elements and elemental ratios that correlate with crustal thickness were calibrated to serve as mohometers, or quantitative

proxies of paleo-Moho depths. For example, a number of incompatible elements (preferentially partitioned into the liquid phase) such as K_2O, P_2O_5, Sr, Ba, Ce, Zr, and elemental ratios such as Dy/Yb, and La/Yb, correlate with crustal thickness; whereas some compatible elements (preferentially partitioned into minerals) such as CaO, Sc, and V display negative correlation with crustal thickness. Our geochemical dataset was analyzed using their MATLAB® mohometer application to find paleo-crustal thicknesses of flare-ups as seen in the geochemical data. See Luffi and Ducea (2022) for more details on the method used.

Sources of Bias and Uncertainty in Geochronology and Geochemistry Data

The use of large U-Pb zircon databases to quantify magmatism over geological time is a generally accepted and reliable technique, forming the basis of many studies. However, Kirsch et al. (2016) and others noted the following issues that can affect the observed distributions in age spectra, especially in a subduction-zone context.

Preservation Bias

Preservation bias arises due to relative changes in the rates of subduction-related arc processes. Peaks in zircon age spectra might be measuring times of reduced destruction by subduction instead of increased magma addition rates. A combination of igneous bedrock ages and detrital zircon samples from units with different depositional ages helps to compensate for uneven preservation of arc magmatism.

Detrital zircon data may provide a record of magmatic activity from igneous rocks that have been completely eroded, biased by intrinsic factors such as erodibility and

zircon abundance of the parent rock, and extrinsic factors such as erosion and transport processes. Since the observed zircon abundance is likely biased relative to the true abundance of the source region, age spectra should only be used as a general, qualitative indicator of magmatic activity and not quantitatively, such as for mass balance modelling (Condie et al., 2011; Kirsch et al., 2016).

Tectonic Setting Bias

In addition to subduction processes, igneous zircons can be generated by continental collision or rifting. Mišković et al. (2009) have documented the effects of collisional processes due to Pangea assembly as well as episodes of extension in the Permo-Triassic for the Eastern Cordillera. This is likely not a significant bias as magma due to rifting tends to be mafic and therefore has a low zircon yield and low volumes of non-subduction magma are typically generated during continental collision, being dominated by granite derived from partial melting of the pre-existing crust (Cawood et al., 2012; Hawkesworth et al., 2010; Kirsch et al., 2016; Storey, 1995).

Sampling Bias

Igneous bedrock samples can be concentrated in areas that are more accessible while areas that are difficult to reach tend to be under-represented. This can result in clusters of samples in small geographic areas with large areas having no samples. This is an issue in Peru with rough and steep terrain being difficult to access, apart from roads following river valleys. Arc parallel displacement of crustal blocks and fragments by strike-slip faults can shift external material into the study area. Detrital zircon

distributions are subject to drainage and wind patterns and can be moved over significant distances (Kirsch et al., 2016).

Methodological Bias

The complex nature and longevity of magmatic systems can result in complex patterns in the growth of zircons and obscure true crystallization ages. Zircons can contain older, inherited cores that need to be identified and analyzed correctly during geochronology analysis to avoid a positive bias in crystallization age. Failure to adequately treat zircon grains with chemical abrasion can lead to a negative age bias due to lead loss (Crowley et al., 2015).

A small number of zircon grains in detrital zircon samples can result in inadequate statistical power and the failure of peaks to be detected or spurious peaks in age spectra. Sample preparation for detrital zircon samples can also introduce a bias (Kirsch et al., 2016; Vermeesch, 2004).

Completeness of Zircon Record

De Silva et al. (2015) note an important consideration relating to zircon in the context of a melt. Depending on conditions in a magmatic chamber, history as recorded by zircons can be preserved or lost. Zircons readily crystallize when Zr saturation is reached in a melt; however, in a Zr-undersaturated melt, zircons will dissolve. In addition, larger zircons are more likely to survive than smaller ones and may record complex histories by providing nucleation sites for additional zircon growth in multiple magmatic events or cycles.

Results

New U-Pb Ages

Zircon U-Pb dating was performed on a subset of our collected samples – 84 igneous bedrock samples and three detrital zircon samples. Igneous bedrock U-Pb ages range from 16.03 to 1132 Ma. **Figure 5** gives an overview of all igneous units in the Peruvian arc displayed by geological age and locations of samples with bedrock U-Pb ages.

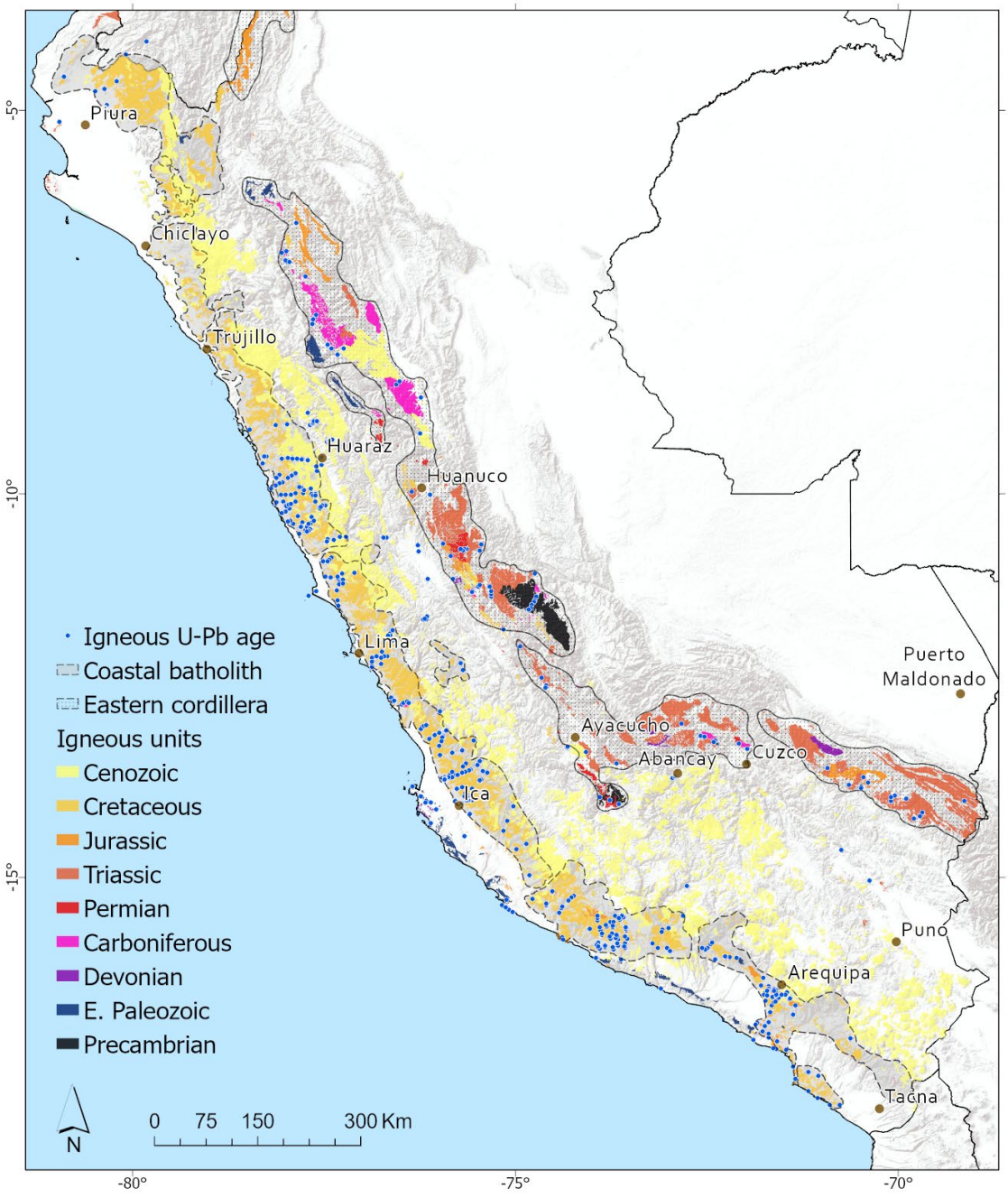

Figure 5. All Peruvian arc igneous units (both plutonic and volcanic) plotted by geological age, showing igneous bedrock sample U-Pb age locations. Plutonic and volcanic igneous rock unit names are from the Peruvian Instituto Geológico Minero y Metalúrgico (INGEMMET, 2021).

Figure 6 displays the ages and locations of the igneous bedrock samples and locations of the detrital zircon samples. For data see **Appendix F Geochronology Data**.

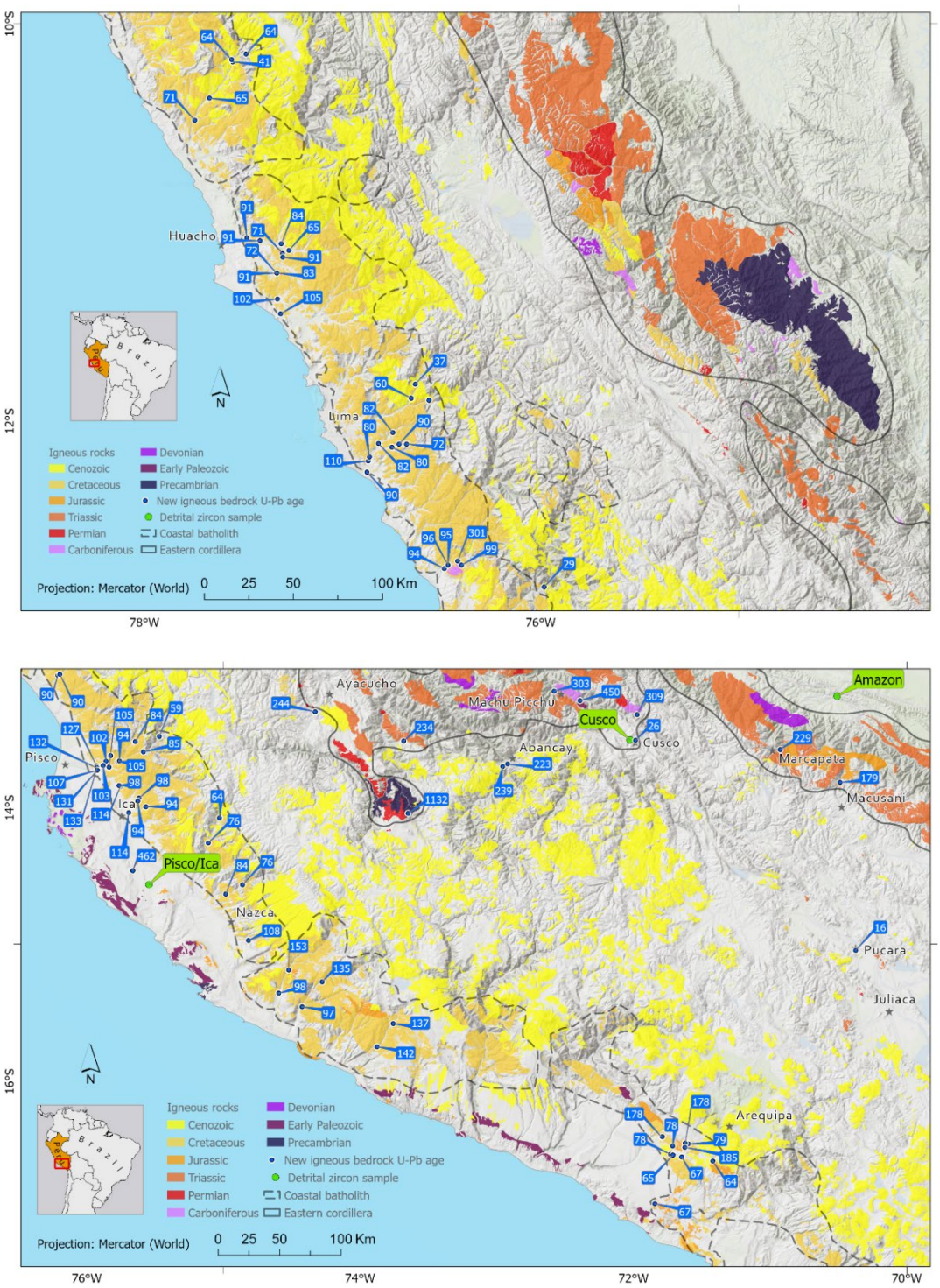

Figure 6. New U-Pb detrital zircon and igneous bedrock ages (Ma) in the Peruvian arc. Detrital zircon samples are from three locations across the arc, near Ica, Cusco, and the Amazon. Ages rounded to the nearest whole digit. Plutonic and volcanic igneous rock unit names are from the Peruvian Instituto Geológico Minero y Metalúrgico (INGEMMET, 2021).

Age Spectra: All Peruvian Geochronology Data

Augmenting the existing igneous bedrock geochronology data compilation for Peru with our new igneous bedrock ages yields a total of 421 igneous bedrock ages, each determined from approximately 30 individual zircons. Adding the 587 new detrital zircon ages to existing detrital zircon data yields a total of 3290 individual detrital zircon ages. Limiting the time interval to <2000 Ma results in 3547 combined igneous bedrock and detrital zircon ages plotted in **Figure 7**, and 2856 when including only the Phanerozoic.

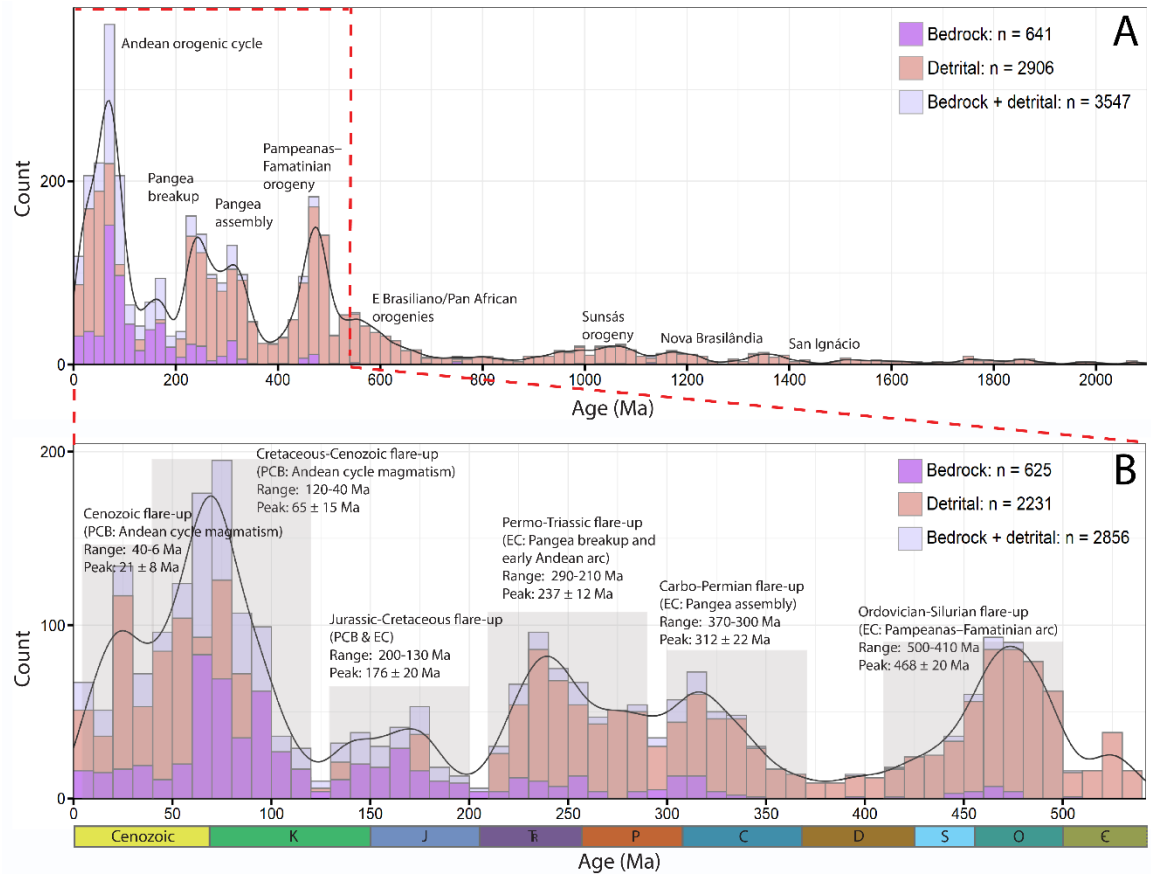

Figure 7. Igneous bedrock zircon and detrital zircon U-Pb age spectra providing a history of arc magmatism in (A) the entire Peruvian arc with (B) an expanded view of the Phanerozoic. Peak height does not indicate magma volume and the voluminous Neogene volcanism of some areas is excluded. Data are compiled from existing sources and augmented with our new igneous bedrock and detrital zircon data. Detrital zircon data are individual zircon grains and igneous bedrock ages are sample ages. Orogenies and supercontinent events are as suggested by Miškovic et al. (2009).

The following flare-ups can be associated with interpreted orogenies and supercontinent events for the EC from Mišković et al. (2009). Several volumetrically minor earlier peaks are related to earlier orogenies, namely Sunsás, Nova Brasilândia and San Ignácio. The earliest major peak is in the Ordovician-Silurian, interpreted to be related to the Pampeanas-Famatinian arc (range 500-410 Ma, peak 468 ± 20 Ma). A broad period of increased magmatism is found in the Carbo-Permian (range 370-300 Ma, peak 312 ± 22 Ma) and Permo-Triassic (range 290-210 Ma, peak 237 ± 12 Ma) age spectra peaks. The Jurassic to Early Cretaceous period corresponds to a minor peak (range 200-130 Ma, peak 176 ± 20 Ma). We interpret the Cretaceous-Cenozoic flare-up (range 120-40 Ma, peak 65 ± 15 Ma) and Cenozoic flare-up (range 40-6 Ma, peak 21 ± 8 Ma) to be related to the current Andean orogeny. A notable feature of **Figure 7** is the significance of the Phanerozoic period compared to the volumetrically minor contribution of the Precambrian. The greatest volume of zircons is found in the Late Cretaceous-Cenozoic, a period dominated by Andean orogenic cycle magmatism of the Western Cordillera.

Age Spectra: Across Arc Detrital Zircon Geochronology Data

The three across-arc detrital zircon samples yielded a total of 587 zircons, 192 for the Ica-Pisco (A11-118A, Miocene sandstone of currently unknown formation in the Laguna Seca area with location 75.54297 W, 14.56564 S), 269 for the Cusco Cretaceous sandstone (17319A Saegarara Fm) and 126 for the Amazon Cretaceous quartzite (17323E, Oriente Group). Age spectra are plotted for each of these samples in **Figure 8**.

A number of peaks corresponding to broadly coeval orogenic events are noted, with orogenies from Mišković et al. (2009).

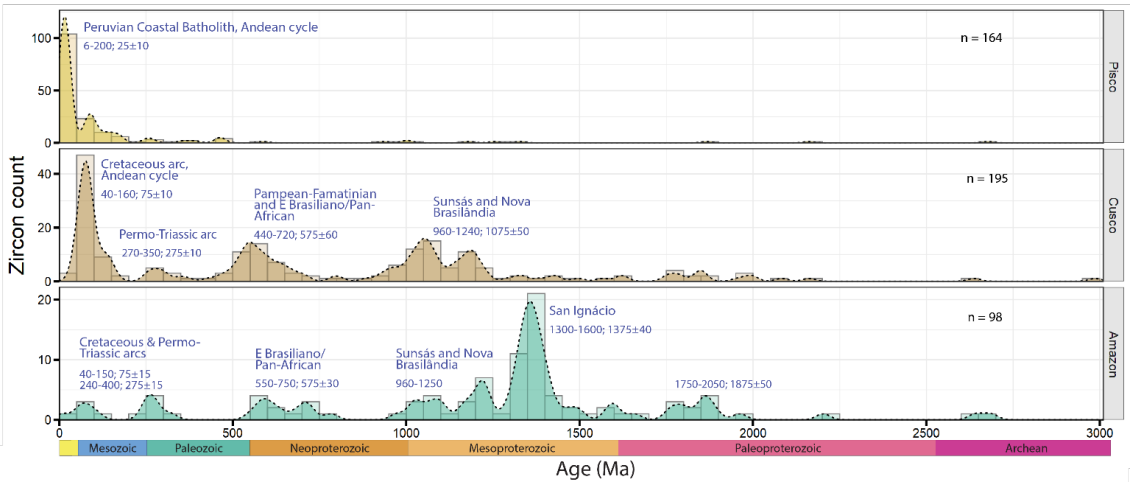

Figure 8. Across-arc detrital zircon U-Pb age spectra for samples taken from near Ica-Pisco (Miocene sandstone), Cusco (Cretaceous sandstone) and the Amazon just east of the arc (Cretaceous quartzite). Ranges and peaks of flare-ups are in Ma. Orogenies are from Mišković et al. (2009).

The three across-arc detrital zircon samples give a picture of variation in magmatism over time and space: (1) In the western Ica-Pisco area, peaks are found especially corresponding to Cenozoic volcanism and Cretaceous magmatism of the Peruvian Coastal Batholith. (2) Further east in the Cusco area, a strong Cretaceous and smaller Permo-Triassic peak are found in the Phanerozoic along with several Precambrian peaks. (3) Just east of the arc in the Amazon basin, the same two small peaks are found in the Phanerozoic as well as significant Precambrian input.

For the Cusco sample, the most significant zircon peak is found in the Cretaceous-Cenozoic (range 160-40 Ma, peak 75 ± 10 Ma), related to the Andean cycle. A Permo-Triassic peak (range 350-270 Ma, peak 275 ± 10 Ma) is related to a Permo-Triassic arc.

A Neoproterozoic-Paleozoic peak (range 720-440 Ma, peak 575 ± 60 Ma) is related to the Pampean-Famatinian and E Braziliano/Pan African orogenies. Finally, a Mesoproterozoic-Neoproterozoic composite peak (range 1240-960 Ma, peak 1075 ± 50 Ma) is related to the Sunsás and Nova Brasilândia orogenies.

The easternmost Amazon sample has volumetrically minor peaks younger than 1000 Ma, in the Cretaceous (range 150-40 Ma, peak 75 ± 15 Ma) related to the Andean, the Permo-Triassic (range 400-240 Ma, peak 275 ± 15 Ma) related to the Permo-Triassic arc, the Neoproterozoic (range 750-550 Ma, peak 575 ± 30 Ma) related to the E Braziliano/Pan African orogenies. The majority of zircons are found in the Mesoproterozoic with two smaller peaks ranging from 1250-960 Ma related to the Sunsás and Nova Brasilândia orogenies, and the biggest peak related to the San Ignácio orogeny (1600-1300 Ma, peak 1375 ± 40 Ma).

Age Spectra: Local Scale Peruvian Coastal Batholith Geochronology Data

Figure 9 displays U-Pb zircon ages plotted as the 248 individual zircons that make up 9 igneous bedrock samples averaging about 25 zircons each, collected from the Peruvian Coastal Batholith near Ica by Martinez (2016). This study shows the order of crystallization of major units of the Peruvian Coastal Batholith starting with gabbro-diorite plutons in the Early Cretaceous (130.99 Ma), followed by Linga Auquish (104.84), Linga Rinconada (98.31 Ma), Pampahuasi (97.8 and 91.4 Ma), Tiabaya (85.3 and 84.4 Ma) and finally Incahuasi (68 and 58 Ma) in the Early Paleogene.

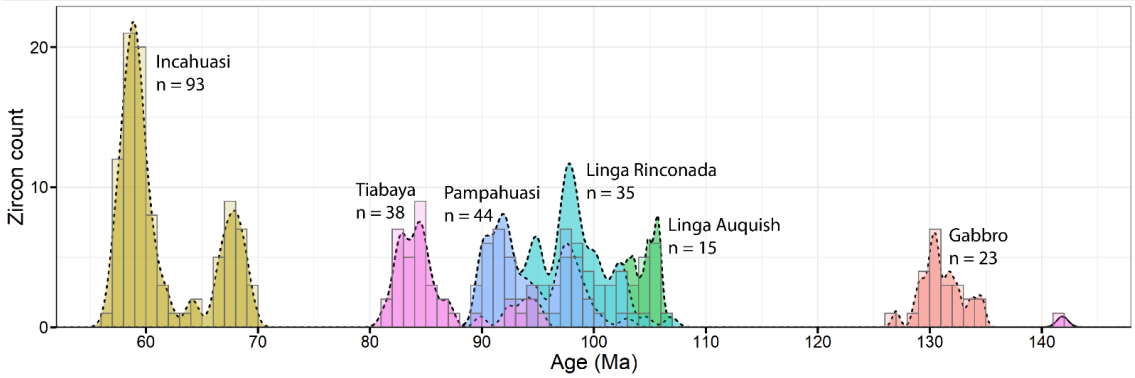

Figure 9. Igneous bedrock U-Pb age spectra of individual zircons from 9 samples collected from the Peruvian Coastal Batholith near Ica, adapted from Martínez et al. (2019).

Age Spectra: PCB and EC Flare-ups

Using the bedrock age data (U-Pb, K-Ar, Ar-Ar and Rb-Sr) for the PCB and EC produces the flare-ups visualized in **Figure 10**. Detrital zircon data is not used in these plots since location is poorly constrained. Flare-ups were visually determined for each PCB segment and the EC. Four flare-ups were found in the PCB north segment (NS-1, NS-2, NS-3, NS-4), three in the central segment (CS-1, CS-2, CS-3); four in the south segment (SS-1, SS-2, SS-3, SS-4) and two in the EC (EC-1, EC-2).

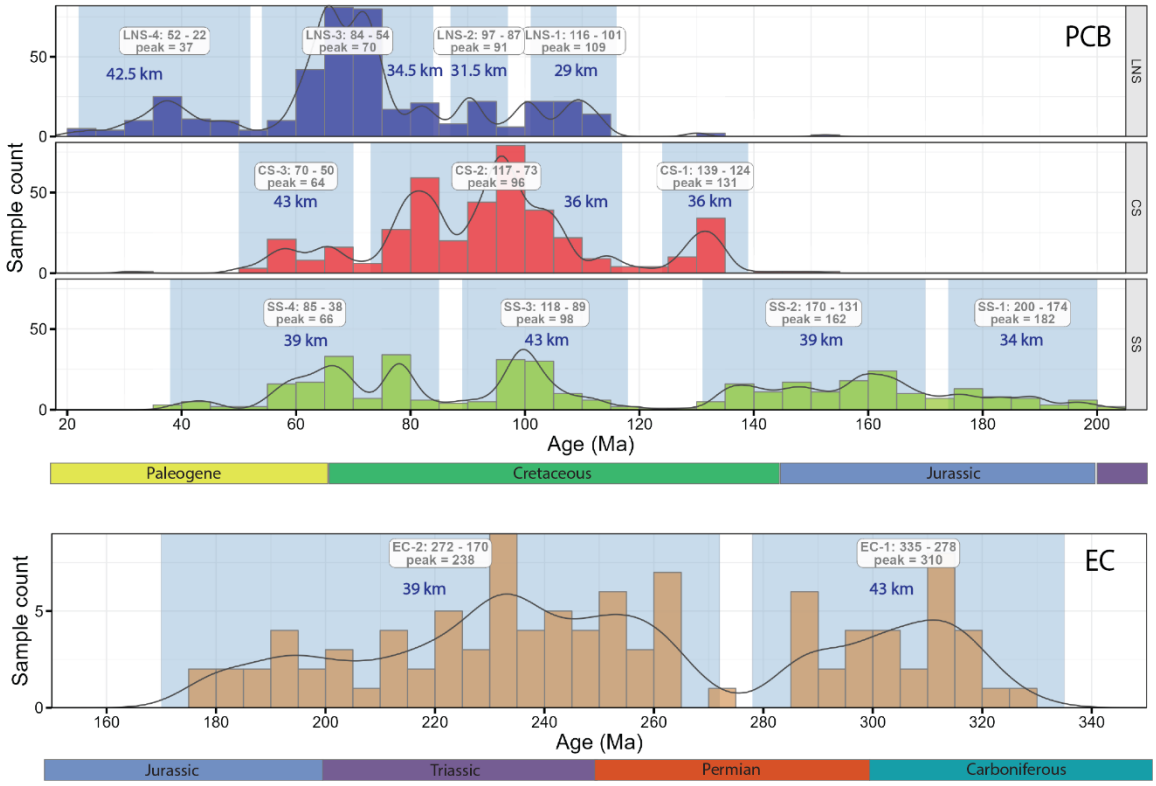

Figure 10. U-Pb bedrock age spectra for the three PCB segments and the EC showing flare-up range and peak. Peak height is not an indication of magma volume. Data are from published and unpublished sources including the compilation by Kirsch et al. (2016), augmented with new igneous bedrock age data. Data total 1022 samples with dating techniques including U-Pb (744), K-Ar (208), Ar-Ar (231) and Rb-Sr (47). Bin width is 5 My. Crustal thickness estimates (in km) are from the mohometer approach of Luffi and Ducea (2022). LNS = lower north segment, CS = central segment, SS = south segment.

Crustal Thickness Estimation

The chemical "mohometer" approach of Luffi and Ducea (2022) was used to estimate the paleo-thickness of the arc crust in both the PCB and EC corresponding to flare-ups. Geochemical data was analyzed by Peter Luffi using the mohometer algorithm, resulting in a number of *sensors* or paleo-crustal thickness proxies defining a number of clusters in the geochemical data, corresponding to flare-up intervals; see **Figure 43** in **Appendix C - Supporting figures**. Some of the geochronology data do not include

geochemistry but are used in determining flare-up parameters, thus flare-ups seen in geochemical data do not always align exactly with flare-ups in geochronology data. Assigning paleo-crustal depths to flare-ups in geochronology data using the paleo-crustal depths determined with geochemical data is done as accurately as possible considering these slight offsets.

The PCB north segment has paleo-Moho depths estimated at between 32 and 43 km, the central segment between 35 and 43 km and the south segment between 34 and 43 km. The north and central segments show an increasing thickness trend over time for each flare-up while the south increases for the first three flare-ups then decreases for the Late Cretaceous flare-up. Depth for the EC is fairly constant at between 39 and 43 km, therefore never as shallow as the PCB.

Flare-up Mantle Magma Addition Volume Estimation

We estimate mantle magma addition (MMA) volumes and rates for each of the flare-ups determined in **Figure 10** by calculating adjusted MMA values using areas, crustal thickness and durations.

Both the PCB and EC magmatic belts are presumed to represent main arc crustal columns and do not include forearc and backarc magmatism. Volumes of MMA to the arc crust are calculated using volumes from Ratschbacher et al. (2019) for the main arc of the Famatinian arc exposed in their studied tilted crustal column in Argentina, using their estimated Ordovician crust thickness of 63 km. Values are adjusted for estimated Moho depth for each flare-up for the two mantle/crust ratio end-members, using 3.73 km^3/km^2 for the volcanic section and factoring in a volcanic to plutonic ratio of 1/20, 4.61

km^3/km^2 for the upper crust (0 – 10 km), 9.32 km^3/km^2 for the mid crust (10 – 20 km), 8.3 km^3/km^2 for the deep crust (20 – 30 km) and 24.89 km^3/km^2 for the unexposed crust. See Ratschbacher et al. (2019) for more details on the technique and assumptions. Areal data is available for only the upper crust for both the PCB and EC and is used to calculate total magma volumes.

Table 1 gives the total exposed areas of arc-related igneous rocks (in units of 1000 km^2) and total mantle magma addition volumes (in units of 1000 km^3) for each flare-up. Volume data is listed for the 80/20 and 50/50 mantle vs crust ratios. Various attributes are listed for flare-ups.

Table 1. Flare-up parameters for the three PCB segments and the EC. Mantle magma addition volume has been adjusted from estimates for the Famatinian arc in Ratschbacher et al. (2019) by factoring in estimated Moho depth for each flare-up. Mantle magma addition rate is mantle magma volume normalized by flare-up duration. End member mantle/crust ratios of 80/20 and 50/50 are given to constrain upper and lower limits on mantle magma addition.

Flare-up	Range (Ma)	Duration (My)	Peak (Ma)	Moho Depth (km)	Area (1000 km^2)	MMA (km^3/km^2)		MMA rate (km^3/km^2/My)		MMA volume (1000 km^3)	
						80/20	50/50	80/20	50/50	80/20	50/50
LNS-1	116-101	15	109	29	4.1	20.4	13.7	1.36	0.91	83.7	56.0
LNS-2	97-87	10	91	29	3.9	20.4	13.7	2.04	1.37	79.6	53.3
LNS-3	84-54	30	70	34.5	3	25.8	17.3	0.86	0.58	77.5	51.9
LNS-4	52-22	30	37	42.5	3.8	34.1	22.8	1.14	0.76	129.5	86.7
CS-1	139-124	15	131	36	0.32	27.4	18.3	1.83	1.22	8.8	5.9
CS-2	117-73	44	96	36	7.6	27.4	18.3	0.62	0.42	208.1	139.4
CS-3	70-50	20	64	43	0.11	34.6	23.2	1.73	1.16	3.8	2.5
SS-1	200-174	26	182	34	0.6	25.3	17.0	0.97	0.65	15.2	10.2
SS-2	170-131	39	162	39	1.3	30.5	20.4	0.78	0.52	39.6	26.5
SS-3	118-89	29	98	43	8.6	34.6	23.2	1.19	0.80	297.6	199.3
SS-4	85-38	47	66	39	0.78	30.5	20.4	0.65	0.43	23.8	15.9
EC-1	335-278	57	310	39	5	30.5	20.4	0.53	0.36	152.4	102.0
EC-2	272-170	102	238	43	25.4	34.6	23.2	0.34	0.23	879.0	588.6

Mantle magma addition volume data for the PCB and EC summarized in **Table 1** are plotted against time in **Figure 11**. For the PCB, total MMA volume added to the crust during flare-ups is estimated at 967k km^3 for the 80/20 mantle vs crust ratio and 648k km^3 for the 50/50 mantle vs crust ratio. For the EC, flare-up MMA volume is slightly higher, estimated at 1030k km^3 and 690k km^3 for 80/20 and 50/50 mantle vs crust ratios respectively.

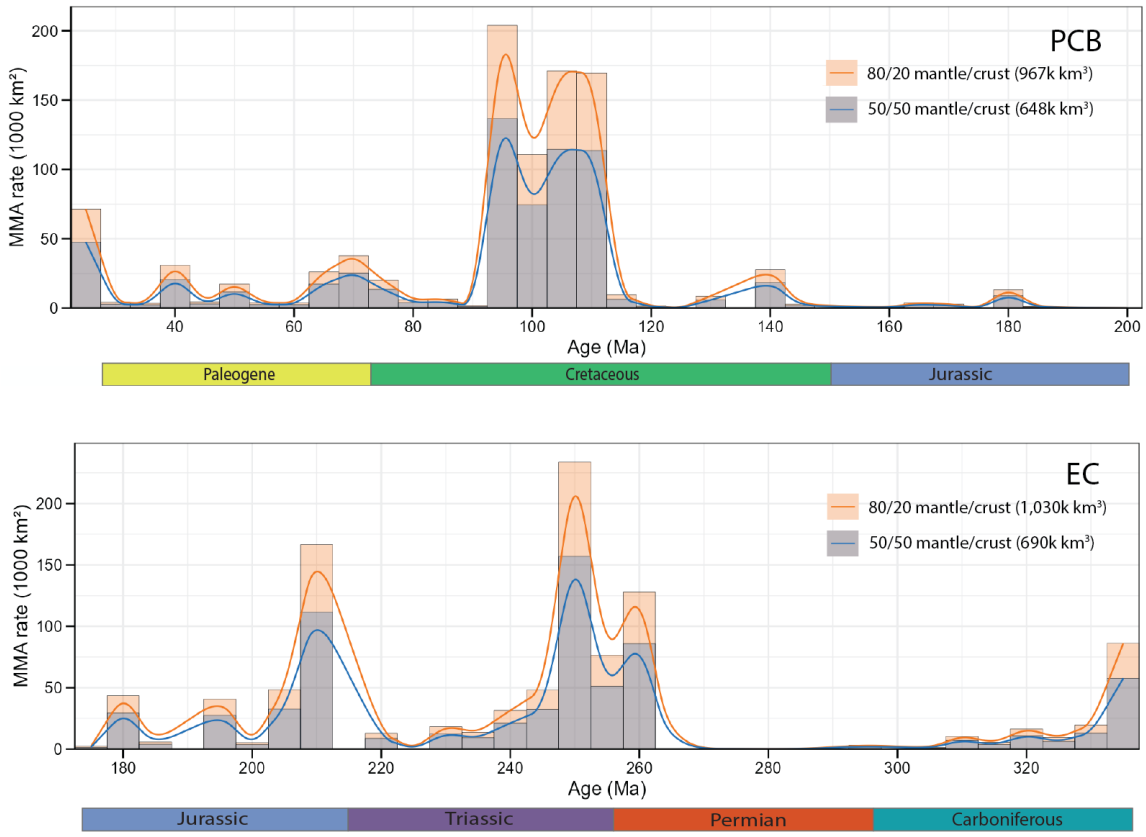

Figure 11. Calculated mantle magma addition (MMA) rates and implied volumes (area under curves) for 5 My age bins over geological time for flare-ups of the Peruvian Coastal Batholith and the Eastern Cordillera using 80/20 and 50/50 mantle/crust ratios.

Spatiotemporal Patterns of Flare-ups

The evolution of flare-ups in the Peruvian PCB and EC is displayed spatially and temporally in **Figures 12** through **15**. These patterns can be explored interactively using the Peruvian Flare-up Explorer interactive dashboard (**Figure 16**).

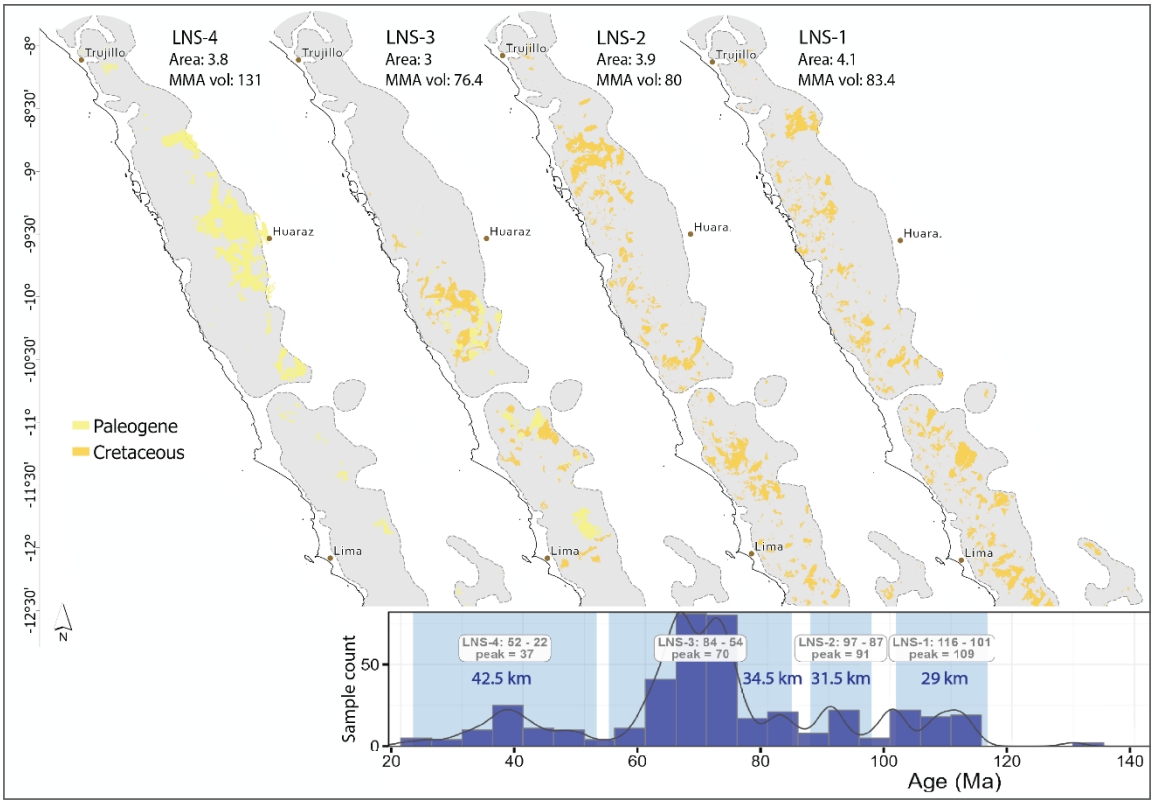

Figure 12. Spatiotemporal evolution of flare-ups in the lower north segment of the Peruvian Coastal Batholith. Geological unit area values are in units of 1000 km^2 and MMA volume values are in units of 1000 km^3. The histogram and kernel density plot consists of U-Pb, K-Ar, Ar-Ar and Rb-Sr bedrock sample geochronology data. Values in blue refer to estimated Moho depth.

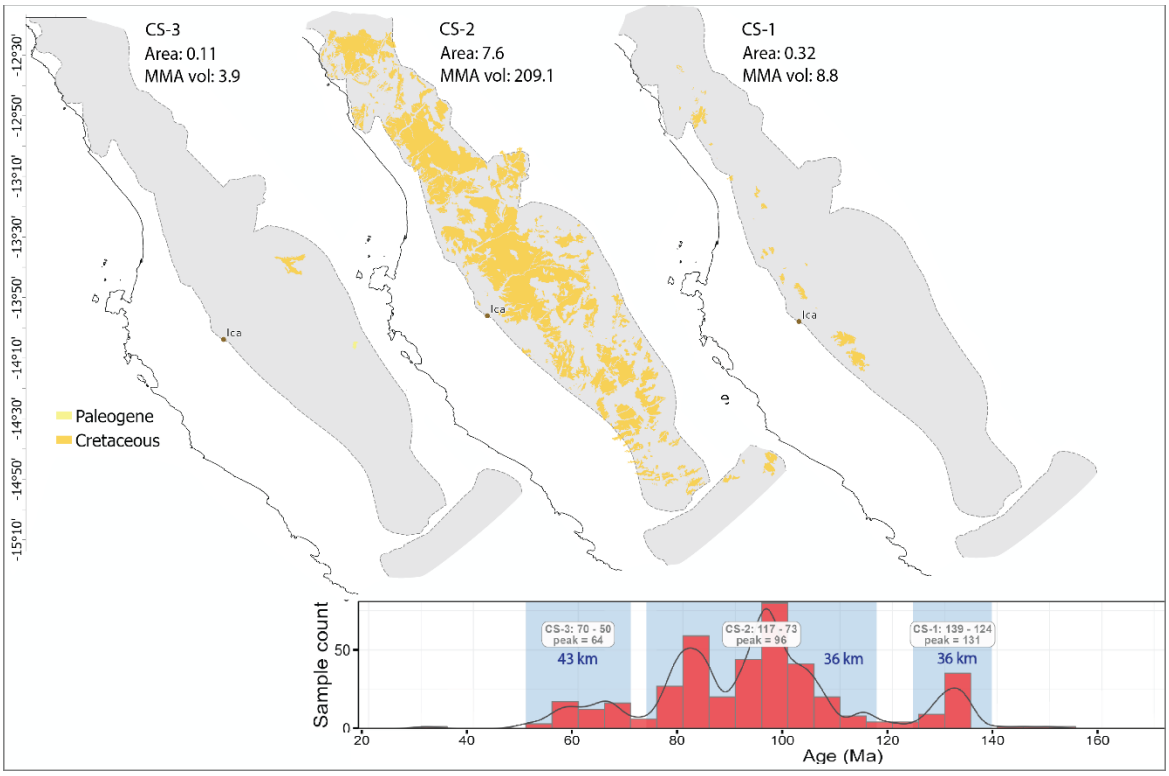

Figure 13. Spatiotemporal evolution of flare-ups in the central segment of the Peruvian Coastal Batholith. Description as in **Figure 12**.

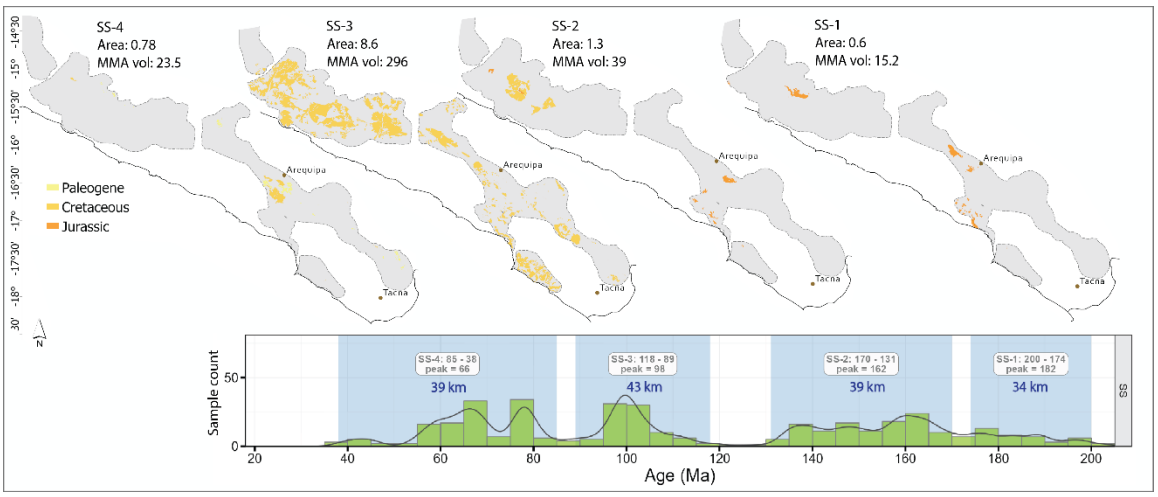

Figure 14. Spatiotemporal evolution of flare-ups in the south segment of the Peruvian Coastal Batholith. Description as in **Figure 12**.

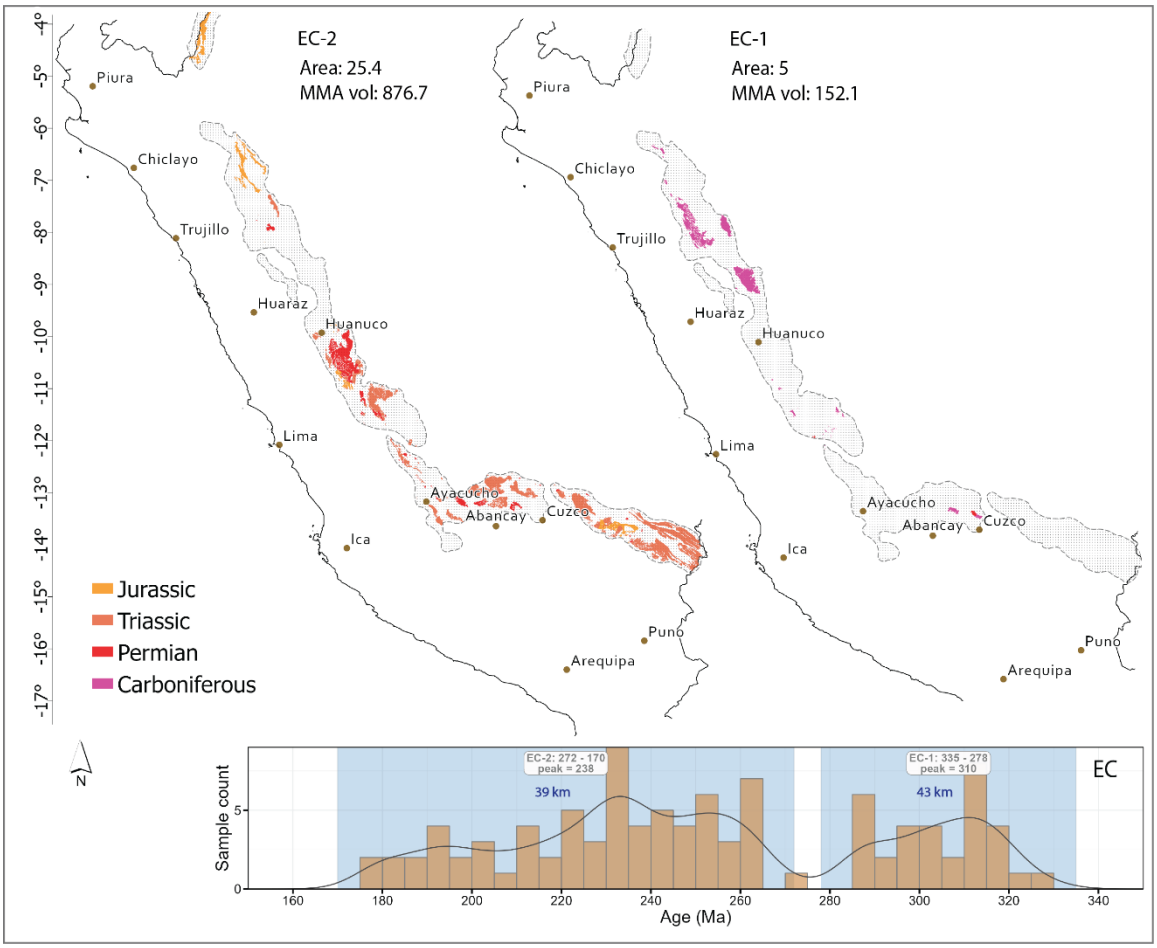

Figure 15. Spatiotemporal evolution of flare-ups in the Eastern Cordillera Description as in **Figure 12**.

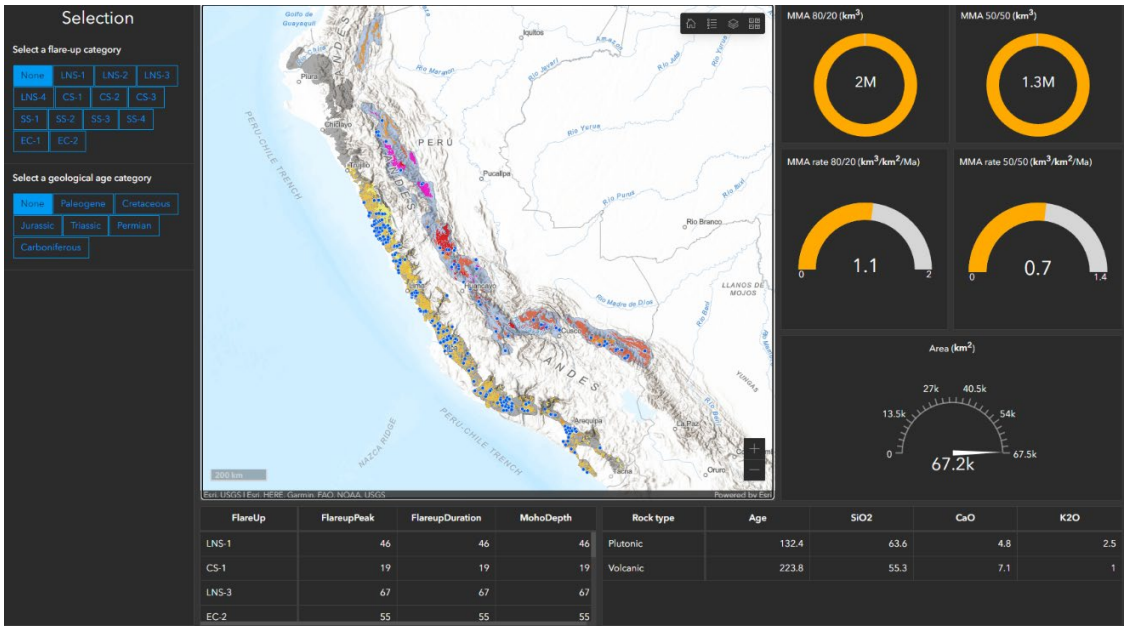

Figure 16. Peruvian Flare-up Explorer – interactive dashboard for exploring spatiotemporal patterns in flare-ups in the Peruvian Coastal Batholith and Eastern Cordillera. Selections can be made for flare-up and geological age categories, causing the map to zoom to the selected features and the gauges to adjust. Gauges display mantle magma addition volumes and rates for 80/20 and 50/50 mantle/crust ratio and area covered by igneous rocks. Tables show parameters for flare-ups and U-Pb age samples.

Discussion

Data Considerations, Limitations and Implications

We have attempted to display a picture of magmatic tempos for the Peruvian arc by assembling all available geochronology data augmented with our own U-Pb zircon geochronology data, both bedrock igneous and detrital zircon. It is important to keep in mind the differences between these types of data. Bedrock ages are derived from a number of zircons, typically about 30 per sample, representing substantially more dated zircons than appear in age spectra, whereas detrital zircon data are depicted as individual zircons, so can appear to be relatively greater in volume than the bedrock data. We have

considered 4 different spatial and temporal scales, from the entire Peruvian arc, to segments of the Peruvian Coastal Batholith and the Eastern Cordillera, across the arc and the local pluton scale in the Ica-Pisco area.

The age range from the start to the end of a flare-up is manually and subjectively determined from age spectra in this study. Although it is possible to mathematically determine these parameters, we argue that the uncertainty due to potential biases suggests that using a precise method is not warranted. In addition, a manual approach may be preferable due to complex patterns often being present in age spectra that may be better resolved manually.

Quantifying magmatic addition rates for continental arcs is as difficult as it is important for understanding arc magmatism and the growth of the continental crust. Although it is tempting to interpret flare-ups with higher counts as being more significant than those with lower counts, they provide only indirect information about volumes, as can be seen in the spatiotemporal plots (**Figures 12 – 15**) where the size of flare-ups often does not match the magma addition volumes. Flare-ups in age spectra give an indication of the range of ages to use when estimating magma addition volumes; however, igneous geological unit area data coupled with crustal thickness estimates and additional parameters are needed for magma addition volume to be estimated (Ducea et al., 2015).

A caveat with the INGEMMET provided igneous geology unit data is that in most cases, ages are poorly constrained, usually from just the age designation from the igneous unit name, such as Jurassic, etc. This creates uncertainty about which igneous units should be included in a particular flare-up. Where dated samples are found within a rock

unit, all polygons with the same unit name are given the accurately dated age, otherwise an average value is given, such as 100 Ma for Cretaceous. Smoothing is then applied to the estimated unit ages to remove spikes from the estimated ages.

Few Cenozoic rocks are seen in the central and south segments whereas Cenozoic grains show a spike in the Ica-Pisco detrital zircon sample. The detrital zircon samples include zircons from Neogene volcanics that we are not considering in the bedrock data.

Working with incomplete datasets has challenges, so results need to be interpreted with this in mind. Estimating MMA volumes adds another level of uncertainty as it is necessary to make a number of assumptions. We lay out a procedure for doing so here using the best currently available data and techniques. Since we are including only igneous bedrock samples in these calculations and ignoring previously eroded rocks as depicted in the detrital zircon record, the results of these calculations should be considered lower bounds on mantle magma addition volumes.

Flare-ups determined by U-Pb bedrock geochronology data do not necessarily match flare-ups determined when calculating mohometers, since while the geochronology and geochemistry datasets have many samples in common, some dated samples do not have geochemistry data. This requires interpolation in some cases to apply paleo crustal thickness to flare-ups determined by age spectra.

In spite of these limitations, we believe that these datasets give reasonable estimates of the size and duration of magmatic flare-ups. Detrital zircon data represent rocks that have eroded away and are otherwise lost to the historical record while igneous bedrock data represent currently exposed rocks. Combining bedrock and detrital zircon data in one figure (**Figure 7**) allows cross-checking between these two different datasets.

Visually, peaks in the igneous bedrock data correspond reasonably well to peaks in the detrital zircon data, lending some confidence to the assumption that age spectra depict fluctuations in rates of magmatism in spite of potential biases in both of these datasets (i.e. preservation bias, tectonic setting bias, sampling bias, methodological bias, and completeness of zircon record). It should be noted that disagreement between these datasets would not necessarily imply that this assumption is incorrect, since lack of correspondence between the datasets may be due to missing data in either one of the datasets. As more data become available, age spectra parameters may change; however periods represented by flare-ups should in theory still stand out in age spectra as peaks. Adding additional high quality geochronology data would have a similar effect to increasing the sample size in a statistical study, so that the margin of error and bias would decrease, increasing confidence in the resulting age spectra.

Flare-up Characteristics

At the entire arc scale (**Figure 7**), age spectra composed of both detrital zircon and igneous bedrock data have a variable wavelength with no obvious periodic cycles. At the arc segment scale (**Figure 10**), age spectra composed of U-Pb, K-Ar, Ar-Ar and Rb-Sr bedrock data also have a variable wavelength with no cyclicity being evident. Flare-ups vary in duration from ~10 My to ~100 My. PCB flare-ups have an average duration of ~21 My for the LNS, ~26 My for the CS and ~35 My for the SS. Average flare-up duration is longer for the EC at ~80 My. Comparing the three PCB segments, flare-ups coincide somewhat during the Cretaceous-Early Paleogene but otherwise do not correlate

between segments. The south segment has two unique flare-ups in the Jurassic while the lower north segment displays a unique mid-Paleogene flare-up.

Comparing our results with findings for the entire American Cordillera, Kirsch et al. (2016) found that flare-ups have a wavelength of 60-80 My in the Cordillera as a whole with a high degree of variability between sectors. Others have found flare-up wavelengths of 20 – 50 My in the Central Andes and North American Cordillera (DeCelles and Graham, 2015; Gehrels et al., 2009; Haschke et al., 2006; Paterson et al., 2011). Some sectors of the Cordillera have synchronous flare-up patterns along thousands of kilometers while others are synchronous after a shift of up to 30 My. The adjacent LNS and CS segments of the PCB exhibit approximately synchronous patterns with a shift of ~20 My, while the SS is synchronous for the Cretaceous and Paleogene but also has two flare-ups extending back to the Jurassic.

Tectonomagmatic Context

Eastern Cordillera

At a large temporal and spatial scale, peaks in our age spectra have been related to orogenies and supercontinent assembly and breakup (**Figures 7, 8**). Interpreting the age spectra of the Eastern Cordillera (Jurassic and older) in a tectonic context, the following observations can be made from the literature. Subduction of oceanic crust along the western margin of Amazonia began soon after the break-up of Rodinia in the Late Proterozoic and has remained intermittently active since that time up to the present, forming the current Pacific margin (Ramos, 2009). This composite continental proto-margin of Gondwana shows evidence of the Late Proterozoic to Early Phanerozoic

Braziliano-Pan African and Pampean-Famatinian orogenies with subduction-related magmatism forming Ordovician-Silurian arcs along the western margins of Amazonia and the Arequipa-Antofalla block (Ramos, 2009). According to Mišković et al. (2009), granitoids in the Eastern Cordillera of Peru record magmatism related to the assembly and break-up of Pangea during the Paleozoic-Mesozoic transition, seen in **Figure 7**. Very few Cenozoic rocks are found in the EC.

Some of the non-mainstream proposals and suggestions related to arcs and the especially large magmatic volumes of the Cretaceous are presented in **Appendix D - Additional and Unconventional Ideas.**

Peruvian Coastal Batholith

The onset of Andean phase subduction of the Pacific oceanic plate in the Late Jurassic coincided with the opening of the Atlantic ocean and the commencement of a period marked by significantly increased magmatism through the Cretaceous and into the Cenozoic (Pitcher and Cobbing, 1985). This is especially seen in the Cretaceous Peruvian Coastal Batholith, but also throughout the Western Cordillera and parts of the Eastern Cordillera. Voluminous Neogene volcanism is found mostly east of the PCB as the arc migrated eastward during the Cenozoic, as can be seen in **Figure 5**. A zone in the central Peruvian arc east of Lima contains relatively fewer Cenozoic rocks, interpreted to be where flat slab subduction of the Nazca ridge shut off subduction in the Cenozoic.

The Jurassic to Early Cretaceous is a period of lower magmatic activity. Charrier et al. (2007) noted that the first phase of Andean evolution was marked by rifting and

extensional tectonics during the Middle to Late Jurassic and Early Cretaceous, coinciding with a period of subdued subduction.

Across Arc

An important observation of the across-arc detrital zircon age spectra is the significant differences between the three samples (**Figure 8**). This shows that regional/local factors are important considerations. The bulk of the zircons in the westernmost Ica-Pisco detrital zircon sample are Cretaceous or younger; this can be related to western magmatism during the emplacement of the Peruvian Coastal Batholith and Cenozoic volcanism of the recent Andean phase. A large number of Neogene zircon grains with few older than Cretaceous indicate the Andes likely became a zircon barrier by the Cretaceous.

The Cusco and Amazon samples sourced zircons from along the central proto-Andean western margin of the Amazonian craton. The Amazon sample is dominated by recycled zircons from the Mesoproterozoic, showing the much older cratonic source. Similar to the implications for the low number of older zircons in the west, the very low number of Cretaceous or younger zircons in the east also shows that the Andes became a detrital zircon barrier by the Cretaceous at the latest (Giambiagi et al., 2016).

Continental Crust Growth Rates

Continents are often considered to be built from the accretion of oceanic arcs (Condie and Kröner, 2013); however this is just the movement of existing crustal blocks from one place to another, or crustal reworking. Subduction-related magmatism along

continental arcs is the main factory of new continental crust on Earth. This is a process that builds continental crust of average thickness (30-40 km) over as much as 100 My or as little as 4 My (Ducea et al., 2017; Ducea et al., 2015). Continental arcs are longitudinal zones where continental crust is being both created and recycled. Growth of the continental crust is quantified as the volume of new crust generated from mantle magma addition through time less the amount that gets recycled into the mantle. Volumes and amounts of crustal growth have been difficult to quantify, usually by using radiogenic isotopes and evidence of complementary depletion of the upper mantle (Cawood et al., 2013; Hawkesworth et al., 2010; Kemp and Hawkesworth, 2014).

An estimated 65-70% of the volume of the present continental crust was generated before 3 Ga, after which crustal growth rates slowed. This slowing is attributed to the period in which plate tectonics became the dominant mechanism for creating continental crust, but also accounts for continental crust being destroyed by being recycled back into the mantle (Hawkesworth et al., 2019). The lower rates of growth of the continental crust since ~3 Ga are estimated by Hawkesworth et al. (2019) to be 0.6 – 0.9 km^3 per annum or 600k – 900k km^3/My.

We provide a first order approximation of mantle magma addition volume over time for the PCB and EC (**Figure 11**). Areas under MMA volume curves can be interpreted as total volumes since the values include surface area and crustal thickness data in addition to flare-up parameters. For the PCB flare-ups using a mantle/crust composition of 80/20, a volume of 967k km^3 is added to the arc crust over 160 My, giving an average addition rate of 6044 km^3/My. For the EC flare-ups using an 80/20

mantle/crust ratio, 1030k km^3 is added to the arc crust over 160 My, giving a similar average addition rate of 6438 km^3/My.

Recycling of the crust takes place via subduction erosion and sediment subduction (Stern, 2011) and this needs to be estimated to quantify continental crust growth rates. We include the recycled component of magma by quantifying mantle to crust ratios (80/20 and 50/50 mantle/crust). To fully account for magma production in the Peruvian arc, magma generated during lulls as well as magmatism outside the boundaries of the PCB and EC needs to be considered; however, lulls are expected to be relatively minor contributions and most magmatism outside the PCB and EC is Late Cenozoic volcanism. These estimated volumes should therefore be considered lower bounds. **Table 2** gives estimated total mantle magma addition volumes for the PCB and EC for both flare-ups and lulls. On average, flare-ups represent 6x more MMA volume than do lulls for the PCB and 5.4x more for the EC.

As would be expected from age spectra patterns, MMA is not continuous, but episodic in nature. Mantle magma addition for the PCB was dominated by a Cretaceous pulse with most of the volume added in this interval, while a Permo-Triassic pulse dominates the EC with relatively minor episodes in the Carboniferous, Late Triassic, and Jurassic.

Table 2. Estimated total MMA during the Phanerozoic for the PCB and EC for flare-ups and lulls. Moho depth values used for calculating lull volumes are averages of all the flare-up Moho depth values for the PCB and EC respectively.

	Total flare-up MMA (km^3, 80/20 crust/mantle)	Total lull MMA (km^3, 80/20 crust/mantle)	Total MMA (km^3, 80/20 rust/mantle)
PCB	967k	103k	1070k
EC	1030k	118k	1148k

Assuming a mantle/crust ratio of 80/20, the PCB and EC account for a combined MMA volume (flare-ups and lulls) of ~2218k km^3 during the Permian-Paleogene which averages ~6688 km^3/My for the PCB and ~7175 km^3/My for the EC, a contribution of ~0.8 – 1.2 % of global continental crustal growth, using the estimates of Hawkesworth et al. (2019).

Scale Considerations

Geochronological data from the Peruvian arc clearly show the episodic nature of Cordilleran arc magmatism, whether we look at the big picture of all igneous bedrock and detrital zircon U-Pb data at the scale of the entire Peruvian arc or down to the regional scale (PCB segments, EC) or local scale (Ica-Pisco plutons). In other words, at the smaller spatial and temporal scale (**Figure 9**) we see a pattern of flare-ups and lulls similar to the arc-scale pattern over a much greater area and longer period of time. This fractal nature of magmatism was noted by De Silva et al. (2015). The availability of additional high-quality U-Pb zircon geochronology data would facilitate an increase in both spatial and temporal resolution, allowing the question of scale-dependent arc processes to be further investigated.

Magmatic Arcs, Mountain Building and Climate

Continental magmatic arcs are large-scale geomorphic features that can have dramatic effects on society. Subduction zones pose a number of dangers to nearby communities as well as benefits. Earthquakes, volcanoes and landslides are some of the hazards, while benefits include ore deposits, water resources and fertile new soils from

volcanic eruptions (Paterson and Ducea, 2015). High mountains above subduction zones have a huge impact on local as well as more distant climates, by acting as watersheds and creating rain shadows. Continental arcs are major contributors to mountain building, creating a number of present and past orogenic systems.

In addition to these short-term effects on climate, continental arcs may play an important role in long term climate cycles. The dominant control on long term climate variation is the amount of greenhouse gases in the atmosphere, mainly CO_2. As arc magmas interact with carbonates on continents, volcanic and metamorphic fluxes can move large volumes of CO_2 from the crust and mantle into the carbon system in the atmosphere, hydrosphere, and biosphere. These effects are insignificant on short timescales (< 100k years), but over long timescales (> 1 My), these effects are thought to act as an external forcing on Earth's climate. The greenhouse conditions during the Cretaceous may have been related to CO_2 fluxing from a big increase in flare-ups along magmatic arcs globally during this period of Earth's history (Cao et al., 2017; Lee and Lackey, 2015).

Conclusions

We have attempted to characterize the magmatic history of the Peruvian segment of the Cordilleran arc using existing data augmented with new data. Peaks in zircon U-Pb geochronology data are assumed to represent periods of increased magmatism, or flare-ups. Flare-up wavelength varies for the Peruvian Coastal Batholith and Eastern Cordillera, with no periodic cycles being evident. In spite of potential biases, peaks in igneous bedrock data correspond reasonably well to peaks in detrital zircon data, lending

some confidence to the assumption that age spectra depict fluctuations in rates of magmatism. We use GIS spatial analysis methods and age spectra plots to form a spatiotemporal picture of magmatic history. We have attempted to provide an estimate of mantle magma addition to the Peruvian arc crust using area data for geological units and estimates of arc mantle magma addition volumes adjusted for crustal thickness estimates calculated using chemical mohometry. This was done for flare-ups found in each of the PCB segments and for the EC. From our calculations, the Peruvian arc contributed at least 0.8 – 1.2% to global crustal growth during the Phanerozoic. A web-based dashboard (Peruvian Arc Explorer) was built using these datasets to allow flare-ups to be explored interactively along the Peruvian arc.

It is noteworthy that magmatic episodicity occurs at all scales, ranging from entire arc systems and arc segments to single volcanoes and plutons. An important feature of Peruvian arc age spectra and mantle magma addition volumes is the significance of the Cretaceous.

An improved understanding of continental arc processes furthers our understanding of continental crust growth rates, mountain building processes, societal hazards and benefits as well as both short-term and long-term effects of continental arcs on climate.

Future Work

Age spectra depicting magmatic arc tempos are sensitive to the quantity and quality of data. As additional high-quality geochronology datasets become available in the future, we hope the techniques used here will lead to new insights. Although we have

not attempted to speculate on triggering mechanisms of flare-ups here, having a solid geochonologic framework is the basis for any work in this respect.

Acknowledgements

We would like to thank the Geoscience Research Institute and the Loma Linda University Department of Earth and Biological Sciences for funding this research. We gratefully acknowledge support from NSF grants EAR 1649254 and EAR-1624854 for the Arizona LaserChron Center, and EAR-0929777 for image acquisitions at the Arizona LaserChron SEM Facility. We also thank Peter Luffi for running a chemical Mohometry analysis on our data to provide paleo-crustal thickness estimates.

Data Availability

The following data and appendices associated with this paper are uploaded to an online supplementary dataset: all geochronological and isotopic data including analyses of LA-ICP-MS zircons as well as cathodoluminescence images of dated zircons; information regarding analytical procedures used for separating zircons; information regarding analytical procedures used for LA-ICP-MS dating.

References

Cao, W., Lee, C.-T. A., and Lackey, J. S., 2017, Episodic nature of continental arc activity since 750 Ma: A global compilation: Earth and Planetary Science Letters, v. 461, p. 85-95.

Cardona, A., Cordani, U., Nutman, A., Zimmermann, U., and Sánchez, A., 2005, Tectonic setting and geochronology of Pre-Llanvirnian metamorphic rocks of the Marañon Complex (E. Peru): From rifting to collision to form the Rheic Ocean: Gondwana 12 Abstracts: Academia Nacional de Ciencias, Mendoza, Argentina, p. 87.

Cardona, A., Cordani, U. G., Ruiz, J., Valencia, V., Armstrong, R., Chew, D., Nutman, A., and Sanchez, A., 2009, U-Pb zircon geochronology and Nd isotopic signatures of the pre-Mesozoic metamorphic basement of the eastern Peruvian Andes: Growth and provenance of a late Neoproterozoic to Carboniferous accretionary orogen on the northwest margin of Gondwana: Journal of Geology, v. 117, no. 3, p. 285-305.

Cardona, A., Cordani, U. G., Ruiz, J., Valencia, V., Nutman, A., and Sánchez, A., 2006, U/Pb detrital zircon geochronology and Nd isotopes from Paleozoic metasedimentary rocks of the Maranon Complex: insights on the proto-Andean tectonic evolution of the Eastern Peruvian Andes: Journal of Geology, v. 117, p. 285-305.

Casquet, C., Fanning, C. M., Galindo, C., Pankhurst, R. J., Rapela, C. W., and Torres, P., 2010, The Arequipa Massif of Peru: New SHRIMP and isotope constraints on a Paleoproterozoic inlier in the Grenvillian orogen: Journal of South American Earth Sciences, v. 29, no. 1, p. 128-142.

Cawood, P. A., Hawkesworth, C., and Dhuime, B., 2013, The continental record and the generation of continental crust: Geological Society of America Bulletin, v. 125, no. 1-2, p. 14-32.

Cawood, P. A., Hawkesworth, C., and Dhuime, B. J. G., 2012, Detrital zircon record and tectonic setting: Geology, v. 40, no. 10, p. 875-878.

Ccallo Morocco, W. E., López Aguilar, Y. P., Guo, W., Liu, J., Chen, S., and Duan, Z., 2021, Características litogeoquímicas y petrográficas en los bordes norte y sur del segmento Lima-Batolito de la Costa, comparada con el sureste de China-[SGP Boletín D 35].

Charrier, R., Pinto, L., and Rodríguez, M. P., 2007, Tectonostratigraphic evolution of the Andean Orogen in Chile, The geology of Chile, Geological Society of London.

Chen, Y.-C., 2017, A tutorial on kernel density estimation and recent advances: Biostatistics & Epidemiology, v. 1, no. 1, p. 161-187.

Cobbing, E., 1985, The tectonic setting of the Peruvian Andes, *in* Pitcher, W. S., Atherton, M. P., Cobbing, E. J., Beckinsale, R. D., ed., Magmatism at a plate edge: The Peruvian Andes, Glasgow, UK, Blackie, p. 3-12.

Condie, K. C., Bickford, M., Aster, R. C., Belousova, E., and Scholl, D. W. J. B., 2011, Episodic zircon ages, Hf isotopic composition, and the preservation rate of continental crust: Bulletin, v. 123, no. 5-6, p. 951-957.

Condie, K. C., and Kröner, A., 2013, The building blocks of continental crust: evidence for a major change in the tectonic setting of continental growth at the end of the Archean: Gondwana Research, v. 23, no. 2, p. 394-402.

Crowley, Q., Key, R., and Noble, S. J. G. R., 2015, High-precision U–Pb dating of complex zircon from the Lewisian Gneiss Complex of Scotland using an incremental CA-ID-TIMS approach: Gondwana Research, v. 27, no. 4, p. 1381-1391.

De Silva, S. L., Riggs, N. R., and Barth, A. P., 2015, Quickening the pulse: Fractal tempos in continental arc magmatism: Elements, v. 11, no. 2, p. 113-118.

DeCelles, P. G., Ducea, M. N., Kapp, P., and Zandt, G., 2009, Cyclicity in Cordilleran orogenic systems: Nature Geoscience, v. 2, no. 4, p. 251-257.

DeCelles, P. G., and Graham, S., 2015, Cyclical processes in the North American Cordilleran orogenic system: Geology, v. 43, no. 6, p. 499-502.

Ducea, M. N., Bergantz, G. W., Crowley, J. L., and Otamendi, J., 2017, Ultrafast magmatic buildup and diversification to produce continental crust during subduction: Geology, v. 45, no. 3, p. 235-238.

Ducea, M. N., Paterson, S. R., and DeCelles, P. G., 2015, High-volume magmatic events in subduction systems: Elements, v. 11, no. 2, p. 99-104.

Esri, 2023, ArcGIS for Desktop: https://www.arcgis.com: Redlands, CA.

Feininger, T., 1987, Allochthonous terranes in the Andes of Ecuador and northwestern Peru: Canadian Journal of Earth Sciences, v. 24, no. 2, p. 266-278.

Freymuth, H., Brandmeier, M., and Wörner, G., 2015, The origin and crust/mantle mass balance of Central Andean ignimbrite magmatism constrained by oxygen and

strontium isotopes and erupted volumes: Contributions to Mineralogy and Petrology, v. 169, no. 6, p. 1-24.

Gehrels, G., Rusmore, M., Woodsworth, G., Crawford, M., Andronicos, C., Hollister, L., Patchett, J., Ducea, M., Butler, R., and Klepeis, K., 2009, U-Th-Pb geochronology of the Coast Mountains batholith in north-coastal British Columbia: Constraints on age and tectonic evolution: Geological Society of America Bulletin, v. 121, no. 9-10, p. 1341-1361.

Gehrels, G., Valencia, V., and Pullen, A., 2006, Detrital zircon geochronology by laser-ablation multicollector ICPMS at the Arizona LaserChron Center: The Paleontological Society Papers, v. 12, p. 67-76.

Gehrels, G. E., Valencia, V. A., and Ruiz, J., 2008, Enhanced precision, accuracy, efficiency, and spatial resolution of U-Pb ages by laser ablation–multicollector–inductively coupled plasma–mass spectrometry: Geochemistry, Geophysics, Geosystems, v. 9, no. 3.

Giambiagi, L., Mescua, J., Bechis, F., Hoke, G., Suriano, J., Spagnotto, S., Moreiras, S. M., Lossada, A., Mazzitelli, M., and Dapoza, R. T., 2016, Cenozoic orogenic evolution of the southern central Andes (32–36 S), Growth of the Southern Andes, Springer, p. 63-98.

Haederle, M., and Atherton, M. P., 2002, Shape and intrusion style of the Coastal Batholith, Peru: Tectonophysics, v. 345, no. 1-4, p. 17-28.

Haschke, M., Günther, A., Melnick, D., Echtler, H., Reutter, K.-J., Scheuber, E., and Oncken, O., 2006, Central and southern Andean tectonic evolution inferred from arc magmatism, *in* Franz, G., Chong, G., Götze, H., Strecker, M.R., Oncken, O., Giese, P., Wigger, P., Ramos, V., ed., The Andes: Active Subduction Orogeny, Springer-Verlag, Berlin, p. 337-353.

Hawkesworth, C., Cawood, P. A., and Dhuime, B., 2019, Rates of generation and growth of the continental crust: Geoscience Frontiers, v. 10, no. 1, p. 165-173.

Hawkesworth, C. J., Dhuime, B., Pietranik, A., Cawood, P., Kemp, A. I., and Storey, C., 2010, The generation and evolution of the continental crust: Journal of the Geological Society, v. 167, no. 2, p. 229-248.

Hildebrand, R., and Whalen, J., 2014, Arc and Slab-Failure Magmatism in Cordilleran Batholiths I: The Cretaceous Coastal Batholith of Peru and its Role in South American Orogenesis and Hemispheric Subduction Flip: Geoscience Canada: Journal of the Geological Association of Canada/Geoscience Canada: journal de l'Association Géologique du Canada, v. 41, no. 3, p. 255-282.

Hildreth, W., and Moorbath, S., 1988, Crustal contributions to Arc Magmatism in the Andes of Central Chile: Contributions to Mineralogy and Petrology, v. 98, no. 4, p. 455-489.

INGEMMET, 2017, http://www.ingemmet.gob.pe/.

-, 2021, http://www.ingemmet.gob.pe/.

Jaillard, E., Hérail, G., Monfret, T., Díaz-Martínez, E., Baby, P., Lavenu, A., Dumont, J.-F., Cordani, U., Milani, E., and Campos, D., 2000, Tectonic evolution of the Andes of Ecuador, Peru, Bolivia and northern Chile, *in* Cordani, U. G., Milani, E. J., Thomaz Filho, A., and Campos, D.A, ed., Tectonic evolution of South America, edited by: Cordani, UG, Milani, E. J., Thomaz Filho, A., and Campos, DA, Rio de Janeiro, Brazil, p. 481-559.

Kay, R. W., and Mahlburg-Kay, S., 1991, Creation and destruction of lower continental crust: Geologische Rundschau, v. 80, no. 2, p. 259-278.

Kemp, A., and Hawkesworth, C., 2014, Growth and differentiation of the continental crust from isotope studies of accessory minerals, *in* Turekian, K. K., Holland, H.D., ed., Treatise on Geochemistry: Second Edition, Elsevier, p. 379-421.

Kirsch, M., Paterson, S. R., Wobbe, F., Martínez, A. M., Clausen, B. L., and Alasino, P. H., 2016, Temporal histories of Cordilleran continental arcs: Testing models for magmatic episodicity: American Mineralogist, v. 101, no. 10, p. 2133-2154.

Kontak, D., Clark, A., and Farrar, E., 1984, The magmatic evolution of the Cordillera Oriental, southeastern Peru, *in* Harmon, R. S., Barreiro, B.A, ed., Andean Magmatism: Chemical and Isotopic Constraints, Springer, p. 203-219.

Lee, C.-T. A., and Lackey, J. S., 2015, Global continental arc flare-ups and their relation to long-term greenhouse conditions: Elements, v. 11, no. 2, p. 125-130.

Leier, A. L., McQuarrie, N., Horton, B. K., and Gehrels, G. E., 2010, Upper Oligocene conglomerates of the Altiplano, central Andes: the record of deposition and deformation along the margin of a hinterland basin: Journal of Sedimentary Research, v. 80, no. 8, p. 750-762.

Loewy, S. L., Connelly, J. N., and Dalziel, I. W., 2004, An orphaned basement block: The Arequipa-Antofalla Basement of the central Andean margin of South America: Geological Society of America Bulletin, v. 116, no. 1-2, p. 171-187.

Luffi, P., and Ducea, M., 2022, Chemical Mohometry: Assessing Crustal Thickness of Ancient Orogens Using Geochemical and Isotopic Data: Reviews of Geophysics, v. 60, no. 2.

Mamani, M., 2022, Repositorio Institucional INGEMMET.

Mamani, M., Tassara, A., and Wörner, G., 2008, Composition and structural control of crustal domains in the central Andes: Geochemistry, Geophysics, Geosystems, v. 9, no. 3.

Mamani, M., Wörner, G., and Sempere, T., 2010, Geochemical variations in igneous rocks of the Central Andean orocline (13 S to 18 S): Tracing crustal thickening and magma generation through time and space: Geological Society of America Bulletin, v. 122, no. 1-2, p. 162-182.

Martinez, A. M. A., 2016, Compositional Diversity in Arcs: A Record of Magmatic Processes in the Peru Coastal Batholith, Ica [PhD dissertation: Loma Linda University, 410 p.]

Martínez, A. M. A., Clausen, B. L., Memeti, V., and Paterson, S. R., 2019, Source contamination, crustal assimilation, and magmatic recycling during three flare-up events in the Cretaceous Peruvian Coastal Batholith: An example from the Ica-Pisco plutons: Journal of South American Earth Sciences, v. 95, p. 102300.

Martínez, A. M. A., Pompe, L., Clausen, B. L., Paterson, S. R., Holk, G. J., & Luffi, P. (2023). A synthesis of the Peruvian Coastal Batholith: An exploration of temporal histories, causes of compositional diversity, and tectonomagmatic links in arcs. Lithos, 107298.

Mišković, A., Spikings, R. A., Chew, D. M., Košler, J., Ulianov, A., and Schaltegger, U., 2009, Tectonomagmatic evolution of Western Amazonia: Geochemical characterization and zircon U-Pb geochronologic constraints from the Peruvian Eastern Cordilleran granitoids: Geological Society of America Bulletin, v. 121, no. 9-10, p. 1298-1324.

Mpodozis, C., and Ramos, V., 1990, The Andes of Chile and Argentina: Circum-Pacific Council for Energy and Mineral Resources Earth Science Series, v. 11.

Mukasa, S., and Tilton, G., 1985, Zircon U-Pb ages of super-units in the Coastal batholith, Peru: Unknown Journal, p. 203-207.

Nur, A., and Ben-Avraham, Z., 1983, Volcanic gaps due to oblique consumption of aseismic ridges: Tectonophysics, v. 99, no. 2-4, p. 355-362.

Paterson, S. R., and Ducea, M. N., 2015, Arc magmatic tempos: gathering the evidence: Elements, v. 11, no. 2, p. 91-98.

Paterson, S. R., Okaya, D., Memeti, V., Economos, R., and Miller, R. B., 2011, Magma addition and flux calculations of incrementally constructed magma chambers in continental margin arcs: Combined field, geochronologic, and thermal modeling studies: Geosphere, v. 7, no. 6, p. 1439-1468.

Pfiffner, O. A., and Gonzalez, L., 2013, Mesozoic–Cenozoic evolution of the western margin of South America: Case study of the Peruvian Andes: Geosciences, v. 3, no. 2, p. 262-310.

Pitcher, W., 1985, A Multiple and Composite Batholith, *in* Pitcher, W. S., Atherton, M. P., Cobbing, E. J., Beckinsale, R. D., ed., Magmatism at a plate edge. The Peruvian Andes, p. 93-101.

Pitcher, W. S., Atherton, M. P., Cobbing, E. J., and Beckinsale, R., 1985, Magmatism at a plate edge: the Peruvian Andes, Wiley.

Pitcher, W. S., and Cobbing, E. J., 1985, Phanerozoic Plutonism in the Peruvian Andes, *in* Pitcher, W. S., Atherton, M. P., Cobbing, E. J., Beckinsale, R. D., ed., Magmatism at a plate edge: the Peruvian Andes, Springer, p. 152-167.

Profeta, L., Ducea, M. N., Chapman, J. B., Paterson, S. R., Gonzales, S. M. H., Kirsch, M., Petrescu, L., and DeCelles, P. G., 2015, Quantifying crustal thickness over time in magmatic arcs: Scientific reports, v. 5, no. 1.

R-Core-Team, 2023, R: A language and environment for statistical computing: Vienna, http://www.r-project.org.

Ramos, V. A., 2008, The basement of the Central Andes: the Arequipa and related terranes: Annu. Rev. Earth Planet. Sci., v. 36, p. 289-324.

Ramos, V. A., 2009, Anatomy and global context of the Andes: Main geologic features and the Andean orogenic cycle: Backbone of the Americas: Shallow subduction, plateau uplift, and ridge and terrane collision, v. 204, p. 31-65.

Ratschbacher, B. C., 2017, Depth-dependent physical, chemical and temporal evolution of crustal differentiation in magmatic arcs [PhD dissertation: University of Southern California, 331 p.]

Ratschbacher, B. C., Paterson, S. R., and Fischer, T. P., 2019, Spatial and depth-dependent variations in magma volume addition and addition rates to continental

arcs: Application to global CO2 fluxes since 750 Ma: Geochemistry, Geophysics, Geosystems, v. 20, no. 6, p. 2997-3018.

Reimann, C., Bahlburg, H., Kooijman, E., Berndt, J., Gerdes, A., Carlotto, V., and Lopez, S., 2010, Geodynamic evolution of the early Paleozoic Western Gondwana margin 14°–17° S reflected by the detritus of the Devonian and Ordovician basins of southern Peru and northern Bolivia: Gondwana Research, v. 18, no. 2-3, p. 370-384.

Stern, C. R., 2011, Subduction erosion: rates, mechanisms, and its role in arc magmatism and the evolution of the continental crust and mantle: Gondwana Research, v. 20, no. 2-3, p. 284-308.

Stern, R. J., and Scholl, D. W., 2010, Yin and yang of continental crust creation and destruction by plate tectonic processes: International Geology Review, v. 52, no. 1, p. 1-31.

Storey, B. C., 1995, The role of mantle plumes in continental breakup: case histories from Gondwanaland: Nature, v. 377, no. 6547, p. 301-308.

Vermeesch, P., 2004, How many grains are needed for a provenance study?: Earth and Planetary Science Letters, v. 224, no. 3-4, p. 441-451.

Witt, C., Rivadeneira, M., Poujol, M., Barba, D., Beida, D., Beseme, G., and Montenegro, G., 2017, Tracking ancient magmatism and Cenozoic topographic growth within the Northern Andes forearc: Constraints from detrital U-Pb zircon ages: Geological Society of America Bulletin, v. 129, no. 3-4, p. 415-428.

CHAPTER 3

EPISODIC CONTINENTAL ARC MAGMATISM: GEOCHEMISTRY OF FLARE-UPS IN THE PERUVIAN ARC

Lance R. Pompe[1], Ana María Martínez Ardila[1], Benjamin L. Clausen[1,2], Scott R. Paterson[3], and Orlando Poma[4]

[1] Department of Earth and Biological Sciences, Loma Linda University, Loma Linda, CA 92350, USA
[2] Geoscience Research Institute, Loma Linda, CA 92350, USA
[3] Claremont, CA 91711, USA
[4] Universidad Peruana Unión, Carretera Central, km. 19, Ñaña, Lima, Peru

Corresponding author: Lance Pompe (lpompe@llu.edu)

Abstract

Cordilleran continental arcs are known to exhibit episodic magmatism characterized by sequences of flare-ups and lulls. The controls on this episodic behavior have not been adequately resolved at this time, but model types can be classified as either cyclic feedback processes operating internal to the arc system related to the upper plate, or external forcing processes acting on the arc related to the lower plate, such as an increase in mantle power or plate dynamics. This study analyzes a geochronology and geochemical dataset from the Peruvian segment of the American Cordillera in an attempt to determine likely triggering mechanisms, with a focus on testing upper plate internal feedback models. A sequence of stacked time series plots is created for segments of the

Peruvian Coastal Batholith and for the Eastern Cordillera to compare both flare-ups and lulls as well as rising and falling parts of flare-ups. Results show very limited support for upper plate internal feedback models at the arc segment scale. No conclusive links are found between tectonic data and magmatic episodicity. Although variable geochemical data suggests a combination of processes operating as triggers of flare-ups, it appears the mantle plays an important role. Episodic mantle processes possibly dominate as driving mechanisms of flare-ups.

Key words: Cordillera, Peruvian arc, geochronology, geochemistry, flare-up, lull

Introduction

Continental magmatic arcs formed over subduction zones are considered to be the primary means for creation of new continental crust. Magmatic histories, as revealed by geochronological records, reveal episodicity in both intrusive and extrusive Cordilleran arc rocks. A large volume of igneous rocks formed in Cordilleran magmatic arcs are the result of a series of magmatic pulses termed *flare-ups*. These high magma addition rate (MAR) events mostly produce dacitic and andesitic ignimbrites and their intrusive equivalents, granodioritic batholiths. Flare-ups punctuate a background of much lower-volume activity, termed *lulls*, during which the arc is gradually built with tonalitic plutons and their andesitic eruptive equivalents (Ducea et al., 2015). Magma production from the mantle wedge during flare-ups is several times higher than during lulls (DeCelles et al., 2009). Patterns of flare-ups and lulls are seen in both bedrock and detrital zircon geochronologic data for all Cordilleran arc segments and are evident at all resolvable scales from continental arcs to individual plutons and volcanoes (De Silva et al., 2015; Kirsch et al., 2016).

Several mechanisms have been suggested for triggering these high MAR events, but no consensus has yet emerged to adequately settle this debate. The goal of this paper is to review models of triggers for high MAR events in the context of geochronological and geochemical data from the Peruvian segment of the American Cordilleran arc.

Geological Setting

The ~2000 km long Peruvian arc is part the larger Andean orogenic system, trending NW-SE from the Huancabamba deflection in the north (5° S) to the Arica bend

in the south (18° S). The Peruvian arc is dominated by three main geomorphic features: two igneous belts that parallel the coast, the Western and Eastern Cordillera separated by a central highland plateau, the Altiplano, that pinches out in the northwest and widens to the southeast. Other major along-strike longitudinal geomorphic features are the Sub-Andean fold and thrust belt and the foreland basin in the east (Jaillard et al., 2000; Pfiffner and Gonzalez, 2013), see **Figure 17**.

In general, the Eastern Cordillera (EC) in the east represents the Paleozoic magmatic history and the Peruvian Coastal Batholith (PCB) in the west, the Mesozoic magmatic history of the Peruvian arc.

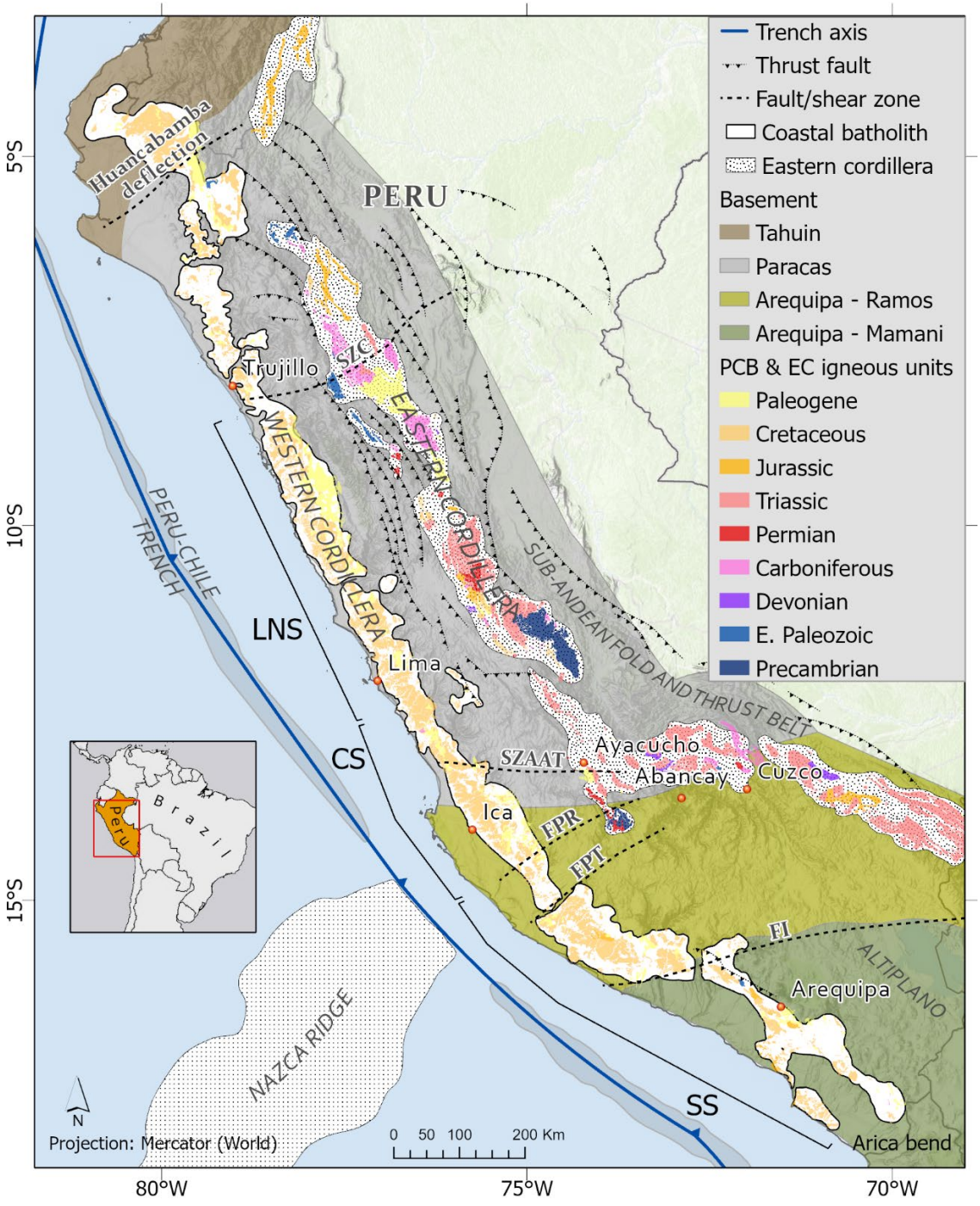

Figure 17. Map of the Peruvian arc showing the geophysical and geological provinces, in particular the Coastal batholith and Eastern Cordillera. The Coastal batholith is divided into north, central and south segments. Modified from Martínez et al. (2019a). SZC - Contaya shear zone, SZAAT - Abancay-Andahuaylas-Tambuco shear zone, FPR - Puyentimari fault, FPT - Patacancha Tambuco fault, FI - Iquipi fault system. Plutonic and volcanic igneous rock units in the PCB and EC are from the Peruvian Instituto Geológico Minero y Metalúrgico (INGEMMET, 2021). From (Pompe et al., 2023)

Basement

Several distinct blocks make up the basement of the Peruvian Andes. The autochthonous Gondwana proto-margin forms the eastern belt which developed along the western margin of the Amazonia craton. Today, the plutonic, metamorphic and metasedimentary rocks of the Eastern Cordillera are found in this region (Ramos, 2009).

The Arequipa Massif is a metamorphic Paleoproterozoic basement inlier in southwestern Peru, described by Casquet et al. (2010) and forms part of the Arequipa terrane. The parautochthonous Arequipa terrane is a Proterozoic crustal block that is exposed along the central Andean margin and broadly underlies the Altiplano south of Arequipa. This crustal block was interpreted by Loewy et al. (2004) as being first accreted onto Amazonia during the Sunsás orogeny in the late Mesoproterozoic during the assembly of Rodinia (Reimann et al., 2010). It was reactivated during the Ordovician, forming a back-arc basin along the old Mesoproterozoic suture (Díaz-Martínez et al., 2001; Sempere et al., 2002).

According to Ramos (2008) the parautochthonous Paracas terrane collided with the Gondwana margin during the Early Ordovician, coeval with the Famatinian orogeny, forming the basement that underlies the Coastal Forearc and Western Cordillera from northern Peru down to Paracas. The Paracas terrane was reactivated during Early Paleozoic extension, reopening the old suture and forming oceanic crust between Amazonia and Paracas. In general, Ramos (2008) concludes that accretionary tectonics for the Paracas terrane were controlled by changes in plate dynamics at a continental scale related mainly to supercontinent reorganizations and also required oceanic plate subduction.

The northwest of Peru is underlain by the Tahuín terrane, a basement block that is not as well understood as the Arequipa and Paracas due to fewer geophysical, geochronological and geochemical studies. However, several suggestions have been made regarding the tectonic evolution of this terrane. In one of the first studies of this basement block, Feininger (1987) and Mpodozis and Ramos (1990) used paleomagnetic data and comparison with the Paleozoic sequences exposed in southern Ecuador to suggest the Tahuin was accreted during the Cretaceous as an allochthonous Paleozoic terrane. An interpretation based on the dating of metamorphic rocks suggests the Tahuín terrane was likely a part of Laurentia that collided with the Gondwana margin during the Alleghanian orogeny, and became detached from Laurentia, while remaining on the Gondwana margin (Cardona et al., 2005; Ramos, 2009). In a more recent detrital zircon study, Witt et al. (2017) suggested the Tahuín terrane docked with the Paracas terrane and subsequently collided with the Gondwana margin in the Early Permian.

Eastern Cordillera (EC)

The Eastern Cordillera forms a major part of the proto-Andean orogenic belt, extending over 1400 km from north to south with a long history of magmatic episodes. Batholiths in this belt mark active lithospheric boundaries between western Gondwana and Paleozoic crustal terranes during the final assembly and break-up of Pangea (Mišković et al., 2005). Magmatism in the Eastern Cordillera was episodic in nature with highly variable mantle and crustal sources (Kontak et al., 1984). Paleozoic or older pre-Andean cycle plutonic and sedimentary and meta-sedimentary units are mostly confined to the Eastern Cordillera within the Central Andes of Peru. Igneous rocks in the EC are

mainly composed of plutonic rocks with ages of most ranging from the Early Carboniferous to the Early Triassic (Cardona et al., 2006).

Cobbing (1985) (and references therein) provides an overview of the tectonic structure of the Eastern Cordillera. The Marañón Massif in the north is composed of medium to high grade meta-sediments and volcanics, with regional metamorphism documented at about 600 Ma. Cardona et al. (2006) documented an Early to Middle Ordovician magmatic arc in the Eastern Cordillera which forms part of the Marañón Massif. The southern part is a Paleozoic composite belt of meta-sediments and plutons deposited in a curvilinear trough from central Peru to northern Argentina. Source regions for these sediments are both the Amazonian Craton to the north-east and the Arequipa Massif to the south-west. Middle Permian folding of the sedimentary rocks was followed by two episodes in the late Permian to Early Triassic that define the structure of the Eastern Cordillera. The first episode formed the Mitu Group, a post-tectonic molasse sequence composed of continental deposits and rifting volcanism from the final phase of the Paleozoic pre-Andean orogeny and initial phase of the subsequent Mesozoic Andean orogeny. These deposits settled in elongate horst and graben structures formed during a period of extensional tectonics. The emplacement of large granitic plutons in the Permo-Triassic composed predominantly of true granites with rare tonalites and granodiorites marked the second episode and ended magmatic activity in this belt. Older rocks found in the Eastern Cordillera occur as plutonic remnants belonging to the Early Paleozoic Famatinian arc as well as reworked Mesoproterozoic crust.

Peruvian Coastal Batholith (PCB)

The Peruvian Coastal Batholith, forming part of the Western Cordillera, primarily developed during the Late Cretaceous to Paleogene period through multiple episodes of magmatism associated with subduction-related processes (Martinez et al., 2023; Pitcher et al., 1985). The PCB is a belt of plutons and volcanic rocks extending over ~2000 km parallel to the coast along the western flank of the Western Cordillera. The batholith's genesis involved the interaction of mantle-derived magmas with the continental crust, resulting in the emplacement of large-scale intrusive bodies. The book *Magmatism at a plate edge: The Peruvian Andes* by Pitcher et al. (1985) contributed significantly to the understanding of this batholith. Convenient access is made possible to researchers studying the PCB by deep canyons carved in bedrock by westward flowing rivers at relatively regular intervals throughout the length of the batholith, traversed by well maintained roads. These fortuitous features in addition to an arid climate along the Peruvian coast give the PCB superior bedrock exposure in three dimensions, resulting in one of the best locations on Earth to study continental arc processes (Pitcher, 1985).

The Peruvian Coastal Batholith is intruded into the volcaniclastics of the Early Cretaceous Casma and Quilmana volcanic arcs which were deposited within the interconnected and subsiding linear basins of the Huarmey Cañete Trough. This trough is the western part of the West Peruvian Trough, a larger marginal basin that developed on the western side of the Marañon basement block that to the east contains the Late Jurassic to Late Cretaceous sedimentary Marañon fold-and-thrust belt (Cardona et al., 2009; Hildebrand and Whalen, 2014; Pitcher and Cobbing, 1985).

Historically, several longitudinal divisions have been proposed for the batholith with a current suggestion being lower north (8 - 12.5° S), central (12.5 - 15° S), and south (15 - 18° S) segments by Martinez et al. (2023). The central segment is transitional in nature between the north and south segments.

Episodic Continental Arc Magmatism

The episodic nature of magmatism in continental arcs was recognized decades ago by Armstrong (1988). Ducea et al. (2015) note that magmatic flare-ups appear to reflect some fundamental mechanism in subduction systems rather than simply being due to sampling bias.

In a recent finding for the entire 15,000 km long American Cordillera, Kirsch et al. (2016) looked at the extent that episodic magmatism is governed by external factors, such as plate motions, or internal factors, such as feedback processes in the upper plate. They found a periodicity of 50-80 Ma for some age patterns, which suggests a cyclic controlling mechanism. However, other magmatic lulls and flare-ups were not correlated in adjacent sectors, indicating an influence of either discrete events or variable lag times. Comparing these results to plate kinematic data showed variable patterns that seemed to reflect different combinations of processes.

Cao et al. (2017) used a global compilation of geological maps and associated literature to determine the addition rates and changes in continental arcs over time. They found most arc magmatism occurred during two periods, the Proterozoic-Cambrian (670 – 480 Ma) and the Mesozoic-Paleogene (250 – 50 Ma). They determined that plate

tectonics and subduction zones fluctuate in a non-steady manner, related to the assembly and breakup of continents.

Arc Magmatic Tempo Models

Models to explain the observed episodicity in continental arc magmatism can be broadly divided into (1) processes external to the arc system related to the lower plate, also known as external forcing models, such as plate motions or mantle power; or (2) internal feedback processes related to the upper plate driven by intra-arc cycles that are fairly independent of external controls.

Lower plate external forcing models involve processes external to the arc, often associated with the lower plate and mantle (e.g., Chapman et al., 2013; De Silva et al., 2015; Hughes and Mahood, 2008; Matthews et al., 2012; Paterson and Ducea, 2015). These models involve processes such as plate reconfigurations, changes in the subduction angle and convergence rate, or mantle processes like changes in flow, plumes, increased mantle melting, mantle wedge volatile fluxing and thick continental crust modulating magma ascent.

Upper plate internal feedback models involve upper continental plate processes driven by internal feedback that create cycles in magmatism (e.g., DeCelles, 2017; DeCelles et al., 2014; DeCelles et al., 2009; DeCelles and Graham, 2015; Ducea, 2001). In a magmatic arc, convergence of the two plates induces shortening of the continental upper plate. The cycle starts with retroarc foreland underthrusting of melt-fertile continental crust by the retroarc thrust belt in response to an increased convergence rate or slab shallowing. This pushes the lowermost continental lithosphere beneath the arc,

fueling episodic high-flux magmatism and simultaneously creating dense eclogitic melt residues. When a critical mass is reached, the residues delaminate and sink into the mantle, creating uplift and space for renewed retroarc underthusting and renewal of the cycle. Thus, in this model flare-ups are periodic events controlled by arc-internal processes superimposed on the background magmatism from the mantle wedge which is tectonically controlled (DeCelles et al., 2009).

Methods and Data

Geochronology Data

We use a geochronology data compilation composed of past bedrock sample and detrital zircon ages from published and unpublished literature, including Kirsch et al. (2016), augmented with 84 new U-Pb zircon bedrock sample ages and 587 new detrital zircon ages, described in Pompe et al. (2023). The compilation includes a total of 641 U-Pb igneous bedrock ages, each determined from up to 30 individual zircons and 2906 individual detrital zircon ages. Zircon is a reliable recorder of age due to its relatively high closure temperature, making U-Pb ages preferred in constructing age spectra. This in contrast to the potential for a young-bias in the case of K-Ar, ^{40}Ar-^{39}Ar and Rb-Sr ages if reheating events affected the plutonic or volcanic rocks post emplacement. Age data for U-Pb were analyzed predominantly using laser ablation-inductively coupled plasma-mass spectrometry (LA-ICP-MS), but also secondary ion mass spectrometry (SIMS), thermal ionization mass spectrometry (TIMS), and sensitive high-resolution ion microprobe (SHRIMP) analyses. Some older age data were analyzed using whole rock U-Pb dating methods. All new data were analyzed using LA-ICP-MS. All sample ages and detrital

zircon samples have location coordinates. Since geochemical data used here need to be age constrained, and U-Pb ages are not available for all geochemical samples, we have included K-Ar, ^{40}Ar-^{39}Ar and Rb-Sr age data in the more geographically focused histograms with the caution that these data may be young-biased and so reduce the average values for flare-ups. In this case, adding some non-U-Pb age data is justified since flare-up parameters are not appreciably affected as can be seen by comparing age spectra including these data with age spectra using only U-Pb data (compare **Figure 20** with **Figure 42**).

Geochemical Data

Geochemical data have been selected with the goal of investigating the degree to which changes in the composition of igneous rocks in the Peruvian arc are related to variations in magmatism over time. All geochemical data used are associated with rocks that have well-constrained ages. Since most of the available Peruvian geochemical data have ages that are too poorly constrained for the purpose of this study, they were unfortunately excluded. We have selected SiO_2 as a proxy for differentiation extent and Sr/Y, La/Yb and Sm/Yb as proxies for crustal thickness and magma source depth. The isotopes εNd_i, εHf and $^{87}Sr/^{86}Sr_i$ are selected to evaluate the ratio of mantle to crust in the igneous arc rocks. The εHf values are largely regional (from detrital zircons) while all other geochemical values relate to the particular arc segment being plotted. Examples of more recent geochemical data include 127 igneous bedrock samples from Mišković et al. (2009) in the Eastern Cordillera and our samples from the Peruvian Coastal Batholith and

Eastern Cordillera described in Pompe et al. (2023), totalling 202 igneous bedrock samples.

Geochemical data were plotted as individual points fitted with a smoothed curve using locally weighted least squares regression (LOESS); for details see Gijbels and Prosdocimi (2010). Standard error bands of ±1σ indicate the confidence interval. Mean values for geochemical data within flare-ups and lulls and rising and falling intervals are shown using colored triangle symbols.

Isotopic analyses of Sr and Nd was performed by the Geochronology and Thermochronology Lab of the University of Arizona on a VG Sector TIMS instrument using the techniques described by Ducea (1998) and Otamendi et al. (2009). Thermal ionization mass spectrometry was used to measure the trace element concentrations of Rb, Sr, Sm, and Nd and isotopic ratios of $^{87}Sr/^{86}Sr$ and $^{143}Nd/^{144}Nd$. Extraction of lead was done using an anion exchange procedure modified after Chen and Wasserburg (1981). Common isotopes of lead were analyzed on separate batches of dissolved samples.

Tectonic Data

Tectonic data include Moho depth, plate parameters including dip angle and convergence rate. Moho depth is determined using the chemical mohometer approach of Luffi and Ducea (2022) to estimate the paleo thickness of the arc crust in both the PCB and EC for each of the flare-ups. This method is the best currently available for this purpose, however only one data point is available for each of the flare-ups. Convergence rate data (cm/yr) are from Jaillard and Soler (1996). Dip angle data is from Jaillard et al.

(1990) and Ramos (1999). Pre-Jurassic plate parameters are not available due to the lack of a reliable plate model (Kirsch et al., 2016).

Data Biases and Limitations

Biases affecting geological data are discussed in Kirsch et al. (2016) and (Pompe et al., 2023) and involve preservation, tectonic setting, sampling, the methodology used, and issues regarding the completeness of the zircon record. Since these biases can have significant effects on bedrock age data, detrital zircon age data, and geochemical data, they need to be considered when making interpretations based on these data.

Age Spectra and Maps

Age spectra were constructed as described in Pompe et al. (2023) using a combination of histograms with an appropriate bin width and kernel density estimation (KDE) to visualize flare-ups as curves. Flare-up intervals were visually delineated with the objective of capturing the peaks.

To facilitate identifying possible geochemical changes related to magmatic pulses, two approaches were followed. In the first approach, flare-ups were compared to lulls using a relatively narrow range to capture just the peaks, leaving a relatively large lull between peaks. In the second approach, a wider range was used for flare-ups by starting at the approximate point at which the probability density curve turns up from near base level to the point at which it drops back down and starts leveling out near base level. This allows for a comparison between the rising and falling parts of each flare-up. For the PCB we considered a sample age range of between 200 and 20 Ma only, since this is

considered the active period of this batholith, see Martinez et al. (2023). Cenozoic magmatism younger than 20 Ma tends to be concentrated east of the PCB. Magmatism in the EC predominantly occurs from the Early Paleozoic through the Mid Mesozoic and we have selected an age range of between 400 and 150 Ma to capture the active period.

Age spectra plots were made using the R statistical package version 4.2.2 (R-Core-Team, 2023). Spatial data analysis and mapping was implemented using Esri ArcGIS Pro 3.1 and ArcGIS Online (Esri, 2023).

Results

Geochronology Data

The locations of igneous U-Pb dated samples and igneous rock units are mapped in **Figure 18**. All relevant arc-related igneous rock units falling within the estimated outlines of the PCB and EC are included with ages given as accurately as the available data allows. Igneous rock units are given the average age value calculated from all U-Pb dated samples falling within the unit, otherwise the unit is given a poorly constrained value from the INGEMMET age designation such as 175 Ma for Jurassic, 100 for Cretaceous etc.

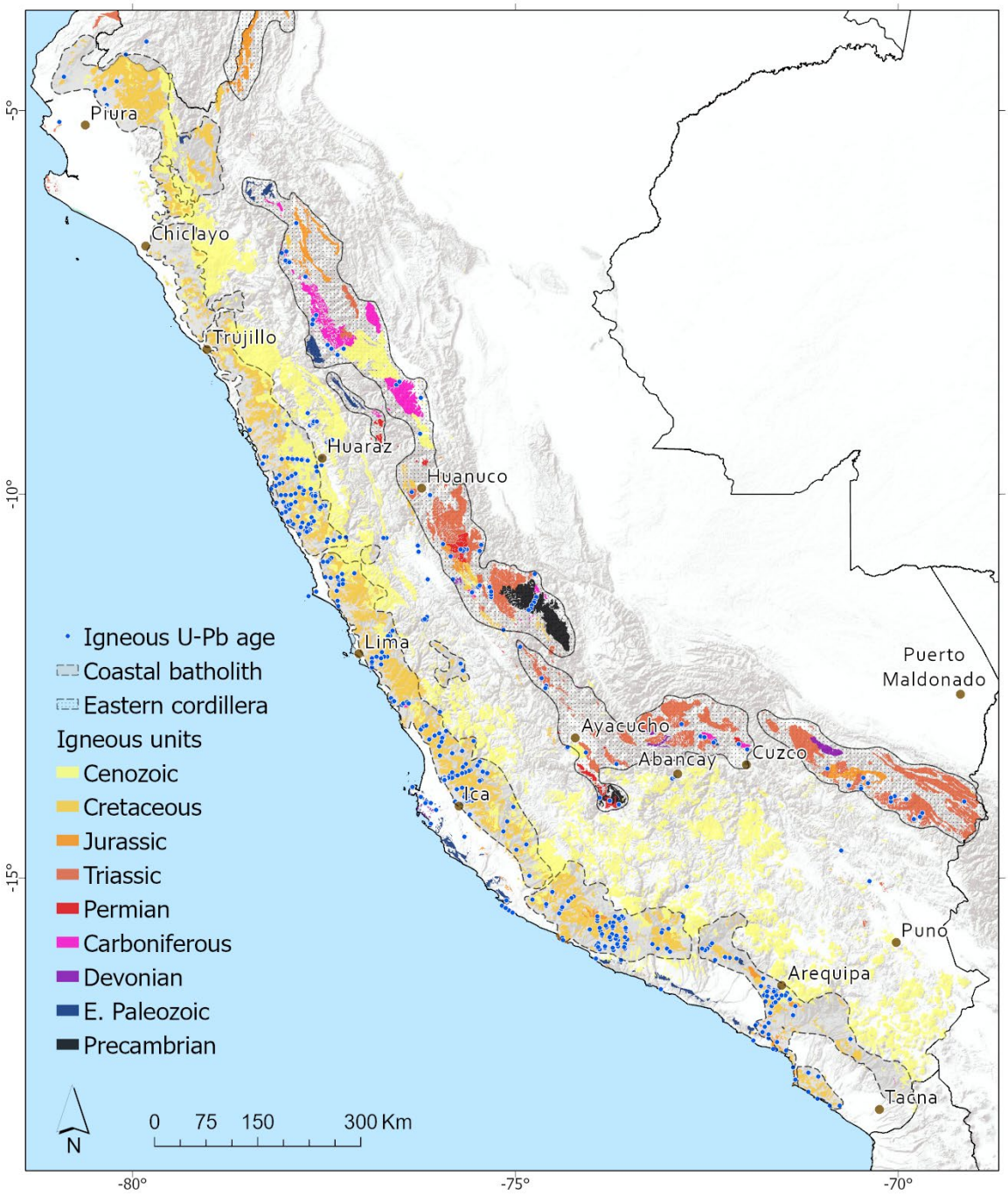

Figure 18. Map of all Peruvian arc igneous units (both plutonic and volcanic) plotted by geological age, showing igneous bedrock sample U-Pb age locations. Approximate outlines for the PCB and EC are given. Igneous rock units are from the Peruvian Instituto Geológico Minero y Metalúrgico (INGEMMET, 2021) with ages from dated samples where available, otherwise given relatively poorly constrained ages estimated from INGEMMET unit age category designations. From Pompe et al. (2023)

All available U-Pb bedrock and detrital zircon ages for the Peruvian segment of the Cordilleran arc from the Paleoproterozoic to the present are plotted in **Figure 19**, giving a picture of the magmatic history of this part of the Cordilleran arc as a whole.

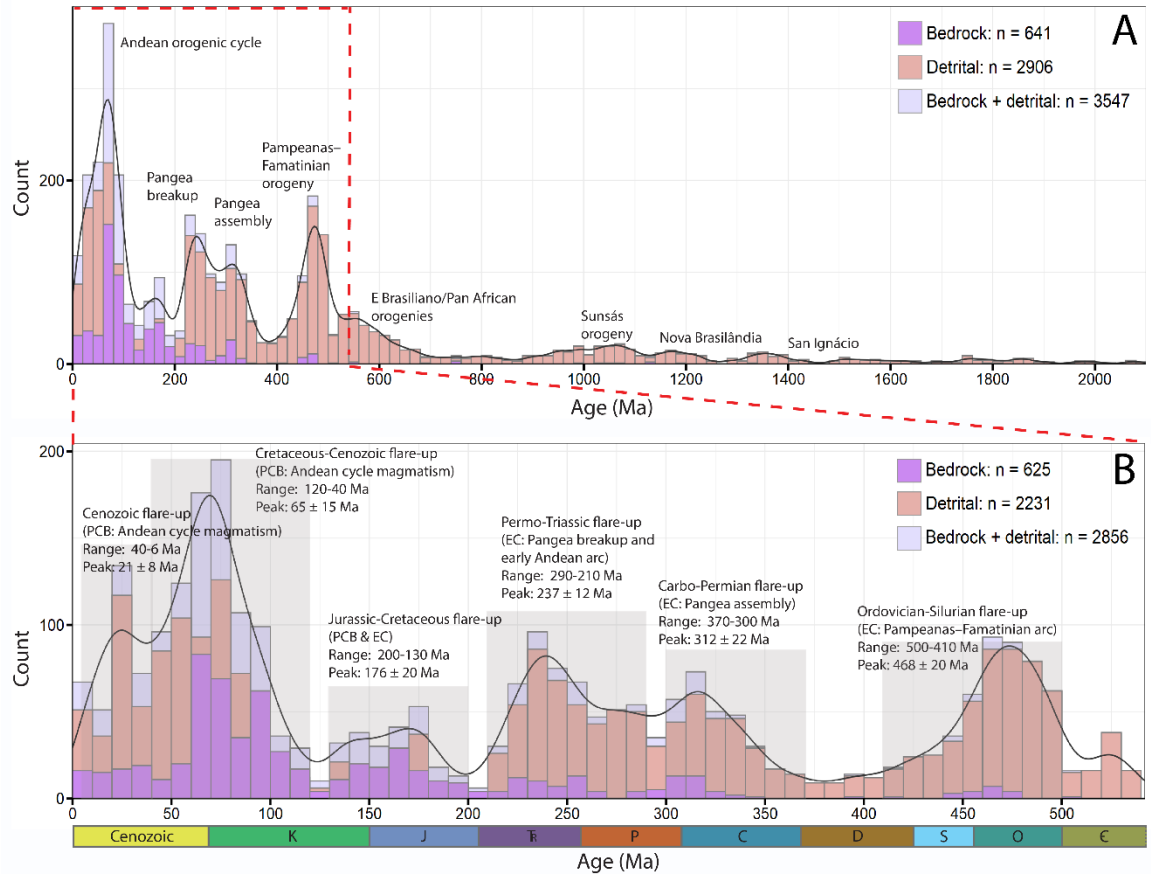

Figure 19. Igneous bedrock zircon and detrital zircon U-Pb age spectra providing a history of arc magmatism in the Peruvian arc with an expanded view of the Phanerozoic. Data are from published and unpublished sources including the compilation by Kirsch et al. (2016), augmented with new igneous bedrock and detrital zircon ages. Bedrock age data represents dated samples with each comprising a number of zircon grains, detrital zircon data is made up of individual zircon grains. From Pompe et al. (2023).

A number of volumetrically minor flare-ups are found in the Precambrian, however magmatic activity increases markedly from the Paleozoic onwards. Flare-ups

have been linked to suggested supercontinent events and orogenies, see Pompe et al. (2023).

Narrowing down the data to the more geographically focused PCB belt in the west and EC belt in the east, but expanding age data to include K-Ar, Ar-Ar and Rb-Sr ages in addition to U-Pb ages, age spectra and flare-ups are plotted in **Figure 20**. These bedrock igneous sample age data comprise a total of 744 U-Pb, 208 K-Ar, 231 Ar-Ar, and 47 Rb-Sr ages.

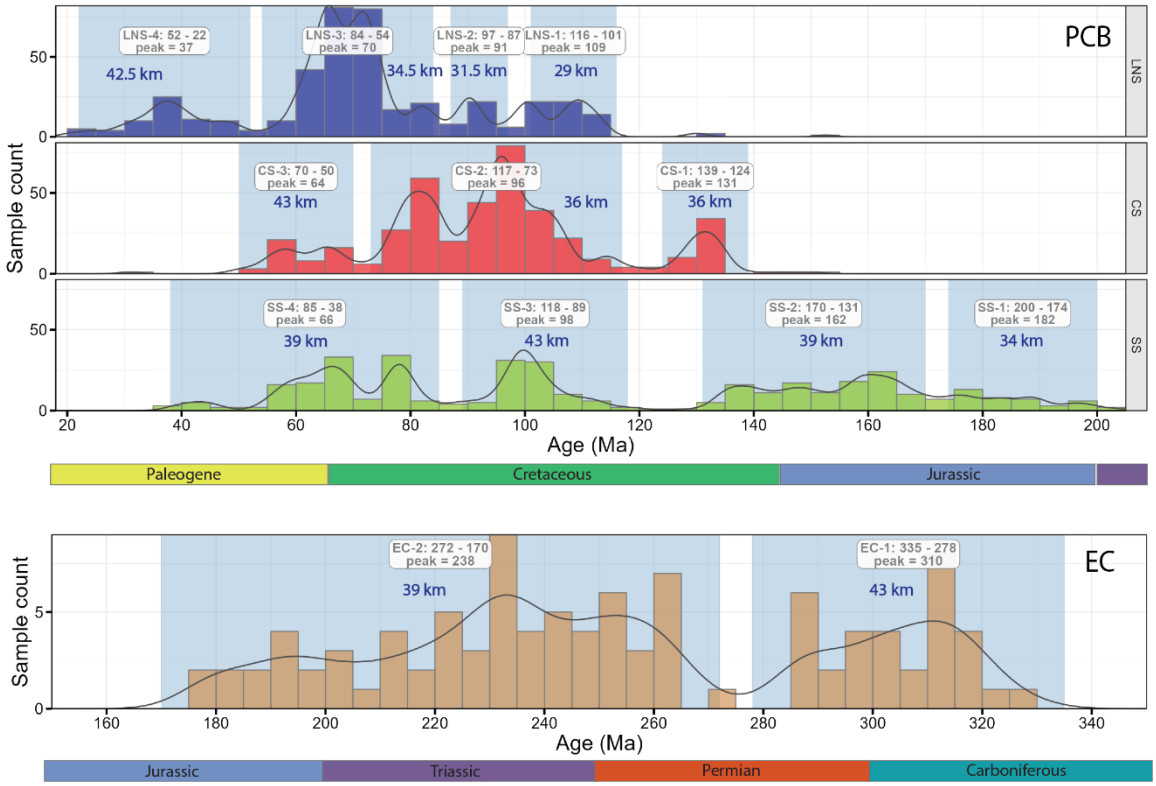

Figure 20. U-Pb bedrock age spectra for the three PCB segments and the EC showing flare-up range and peak. Data are from published and unpublished sources including the compilation by Kirsch et al. (2016), augmented with new igneous bedrock age data. Data total 1022 samples with dating techniques including U-Pb, K-Ar, Ar-Ar and Rb-Sr. Binwidth is 5 Ma. Crustal thickness estimates in blue are from the mohometer approach of Luffi and Ducea (2022). LNS = lower north segment, CS = central segment, SS = south segment. From Pompe et al. (2023).

Tectonic Data

Geochemical and tectonic data are plotted against age using stacked time series plots for the PCB and EC in **Figures 21– 24** and **26 – 29**.

For the PCB, the north segment has paleo-Moho depths estimated at between 32 and 43 km, the central segment between 35 and 43 km and the south segment between 34 and 43 km; see **Figure 20**. The north and central segments show an increasing crustal thickness trend over time for each flare-up while the south increases for the first three flare-ups, then decreases for the Late Cretaceous flare-up. Depth for the EC is fairly constant at between 39 and 43 km.

Tectonic data are available only for the more recent part of the Mesozoic and the Cenozoic. Regional tectonic data for the period 180 Ma through 20 Ma includes dip angle, convergence rate and εHf data. Dip angle transitions from steep (> 50°) in the Early Cretaceous to relatively flat (~30°) in the Paleogene. Convergence rate (cm/yr) varies between slow in the Early Cretaceous to fast in the Mid Cretaceous, slowing down in the Late Cretaceous before speeding up again in the Paleogene.

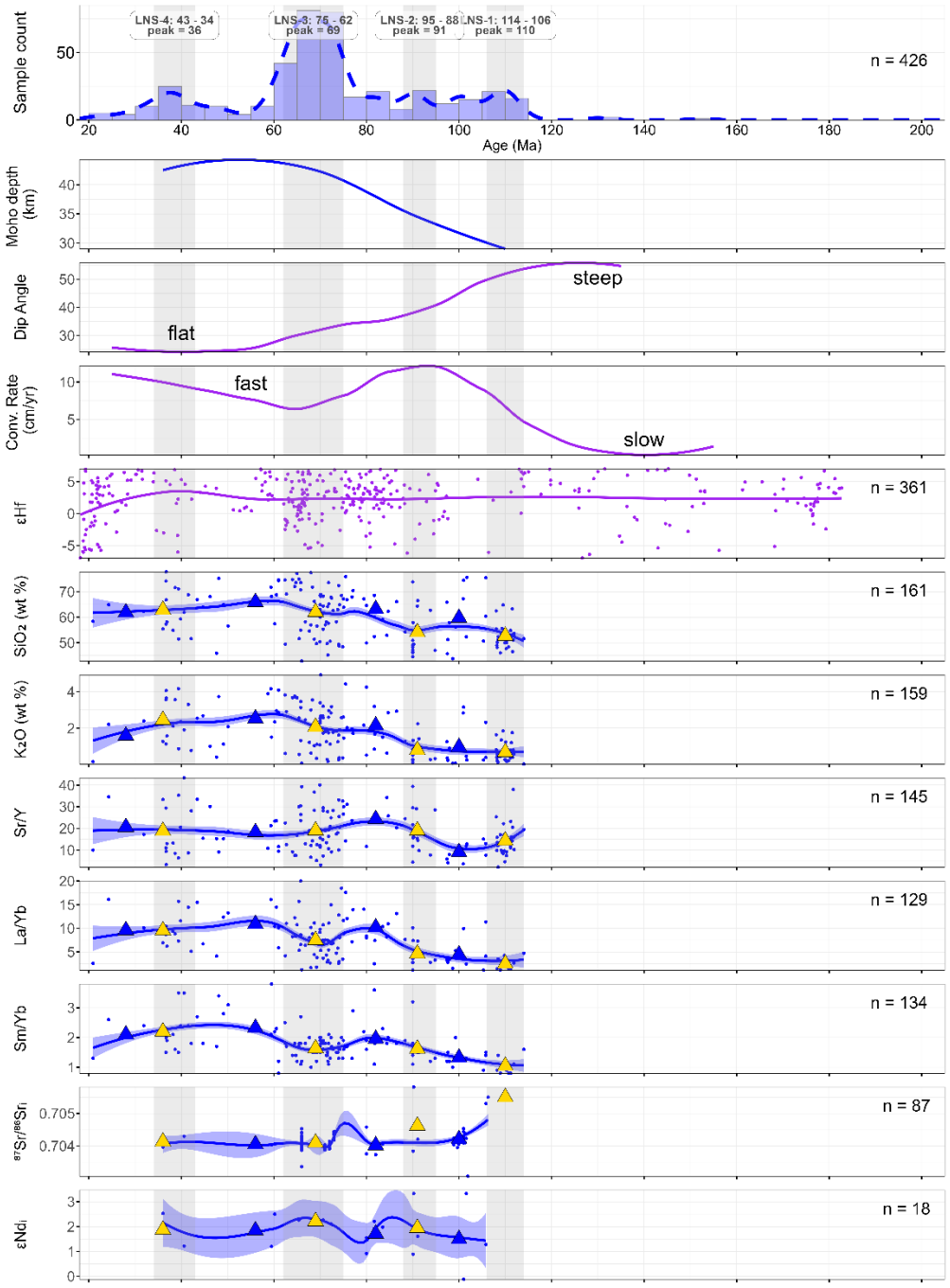

Figure 21. Flare-up/lull stacked time series plot for the PCB lower north segment. with panels comparing geochronology, tectonic and chemistry data. Dip angle, convergence rates and εHf data are mostly regional. Flare-ups are indicated by shading with range and peak labeled in the age spectra panel. Moho depth data is calculated using the mohometer approach of Luffi and Ducea (2022) with one data point per flare-up. Individual data points are plotted for geochemical data and fitted with regression curves showing standard error bands of ± 1σ. Mean values for geochemical data falling within flare-ups and lulls and rising and falling intervals are depicted with colored triangles. Sources for the other tectonic data are given in the methods section.

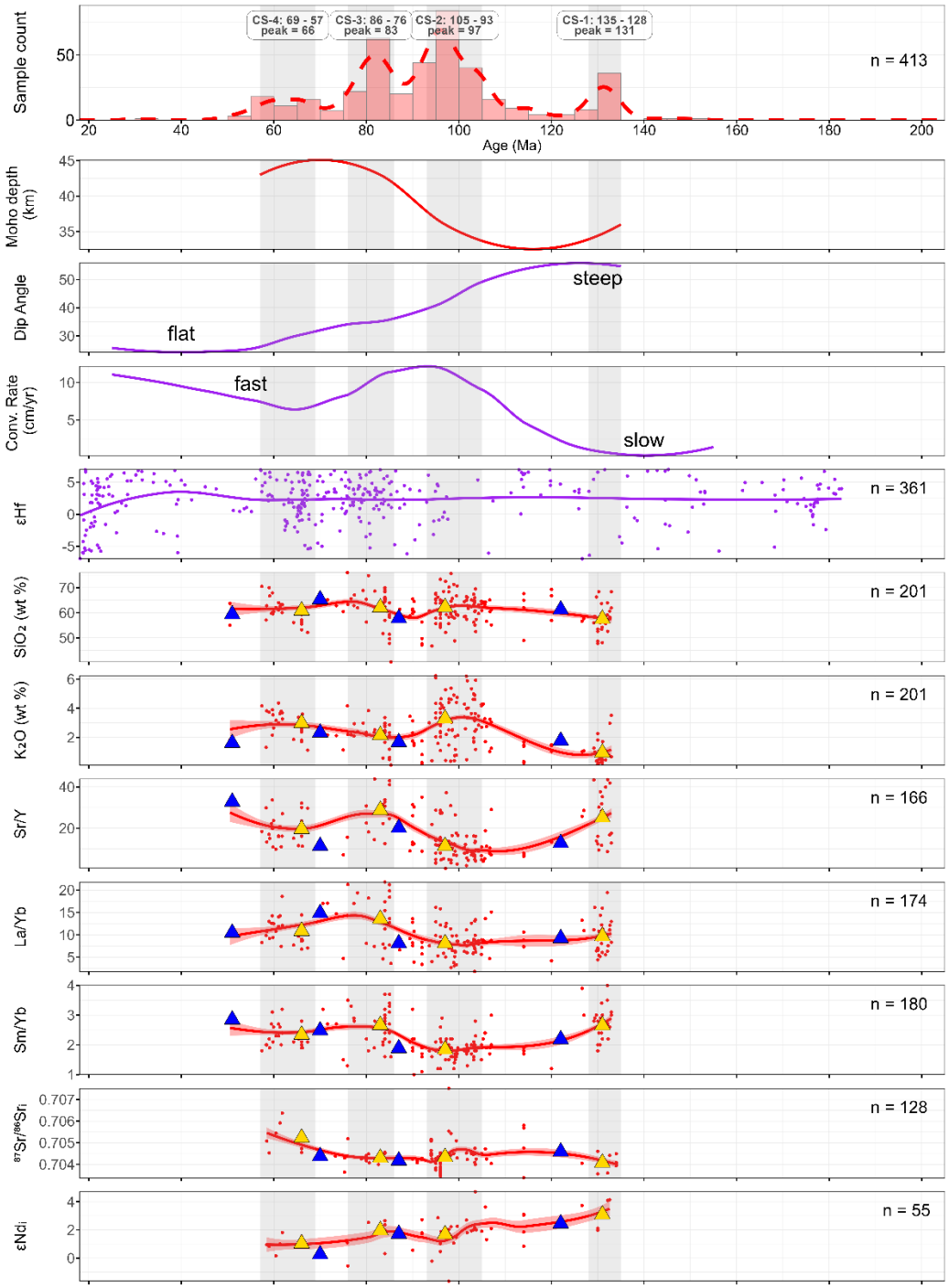

Figure 22. Flare-up/lull stacked time series plot for the PCB central segment. Description as in **Figure 21.**

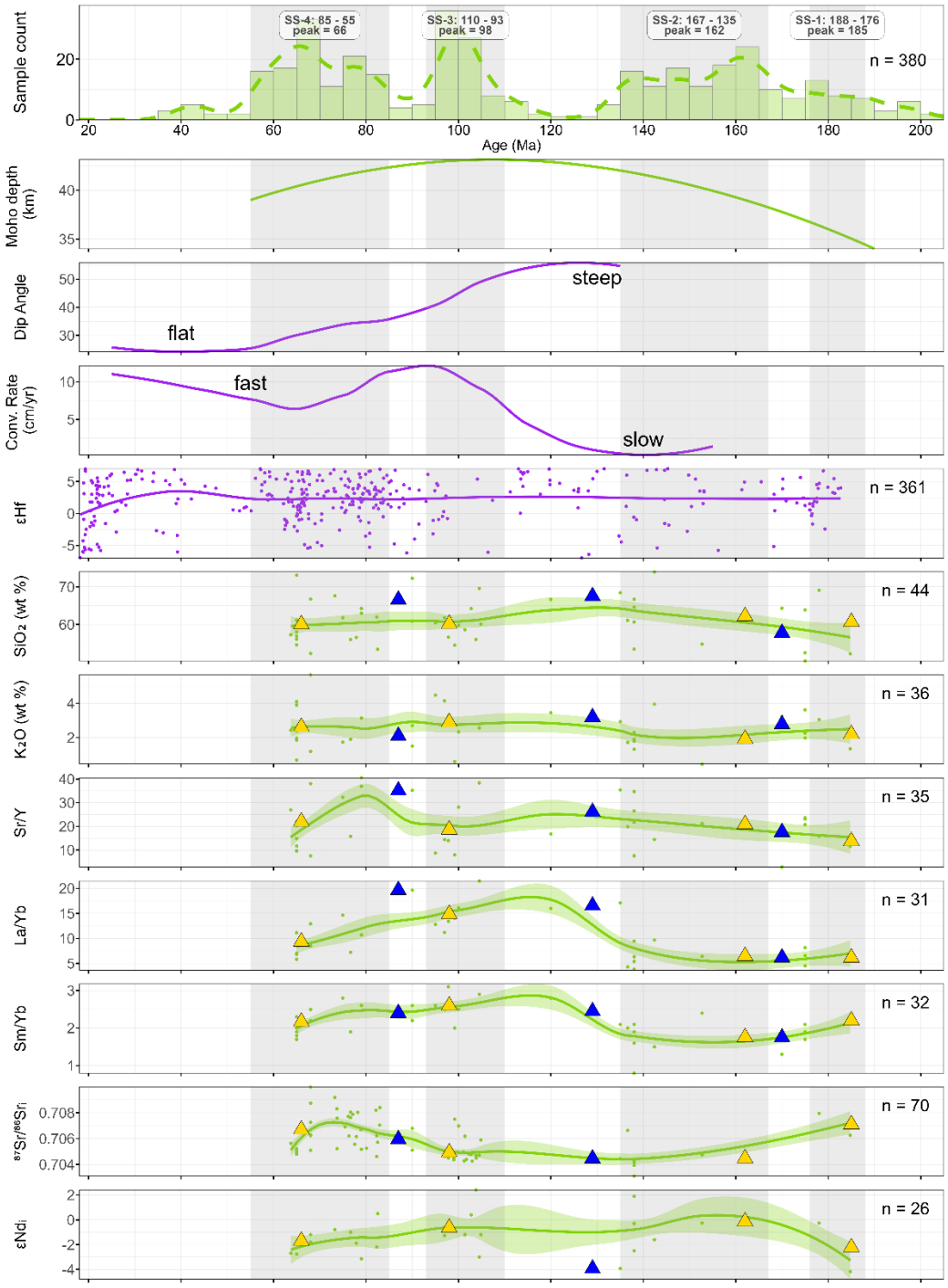

Figure 23. Flare-up/lull stacked time series plot for the PCB south segment. Description as in **Figure 21.**

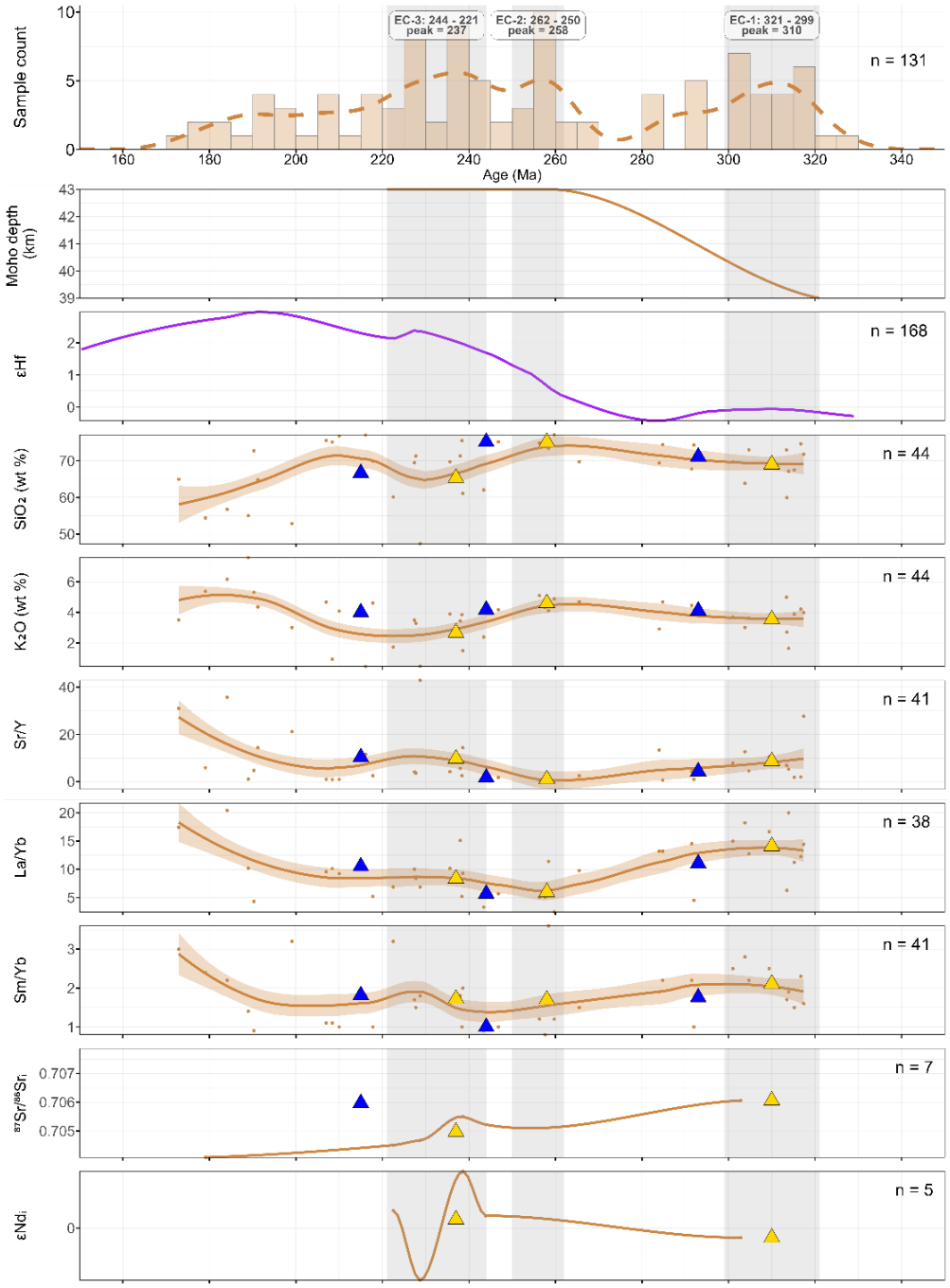

Figure 24. Flare-up/lull stacked time series plot for the EC. Description as in **Figure 21.**

Geochemical Data

For the three segments of the PCB, age spectra are composed of relatively similar amounts of data, between 318 and 357 samples each while the EC is less at 131 samples. A greater amount of age constrained geochemistry data is available for the north and central segments of the PCB than for the south segment and EC.

Figures 21 through **24** focus on comparing flare-ups to lulls with a relatively narrow range selected for flare-ups, capturing the peak. Grey shading marks the flare-up episodes. For flare-ups and lulls, mean values for geochemical data are summarized for comparison in **Figure 25**. **Figures 26** through **29** compare the rising to falling parts of flare-ups using a relatively wide range for flare-ups. The rising part of a flare-up episode is shaded in light orange while the falling part is shaded in olive green. In the time series plots, tectonic and εHf data are not constrained to the segments being plotted but are regional in extent, and colored purple to indicate this. The value of εHf fluctuates between 0 and 5 with a notable decrease in the Late Paleogene.

The following broad relationships between geochemical data can be observed. Regression curves in **Figures 21 – 24** and **26 – 29** for SiO_2 and K_2O show positively correlated patterns for the PCB north and central segments but are inversely correlated for the Cretaceous part of the south segment and for the EC from 230 to 170 Ma. In all PCB segments and the EC, the proxies for crustal thickness, Sr/Y, La/Yb and Sm/Yb are approximately positively correlated with each other, as expected. In all segments with data, the proxies for crust/mantle contribution, εNd_i and $^{87}Sr/^{86}Sr_i$ are approximately

inversely correlated with each other, as expected. In most plots, SiO_2 and K_2O are negatively correlated with the crustal thickness proxies, Sr/Y, La/Yb and Sm/Yb.

Flare-ups vs Lulls

The following geochemical observations can be made from **Figures 21 – 24**, comparisons between flare-ups and lulls summarized by *flare-up* in **Figure 25** and comparisons between flare-ups and lulls summarized by *segment* in **Figure 31**. Note that no geochemical data is available for the lulls following flare-ups SS-1 and SS-4.

SiO_2 and K_2O

For the PCB north segment, SiO_2 shows an increasing trend over time from the low 50 wt% range in LNS-1 and LNS-2 to around 63 wt% in LNS-3 and LNS-4 while K_2O increases from under 1 wt% to around 3 wt%. In every flare-up except LNS-4, SiO_2 exhibits lower mean values compared to the following lull, likewise for K_2O; see **Figure 25**. For the central and south segments, SiO_2 fluctuates around a mean value of just above 60 wt% and K_2O shows a slightly increasing trend over time with flare-ups and lulls not showing any notable difference. For the EC, SiO_2 increases and then decreases slightly over time from 70 to 60 wt% with K_2O following a similar pattern. Similar to the PCB north segment, EC flare-ups have slightly lower values for SiO_2 and K_2O compared to lulls. **Figure 31** summarizes the comparisons by segment, showing SiO_2 values to be slightly lower for flare-ups than for lulls except for the central segment, while K_2O is lower for flare-ups in the PCB north segment and EC and higher for flare-ups in the PCB central and south segments.

Sr/Y, La/Yb and Sm/Yb

The crustal thickness proxies increase slightly over time for the PCB north segment. For the EC, Sr/Y, La/Yb and Sm/Yb decrease slightly from EC-1 before fluctuating higher from EC-2. No notable systematic pattern is found for the comparison between flare-ups and lulls in **Figure 25** and **Figure 31**.

εNd_i and $^{87}Sr/^{86}Sr_i$

For the central segment a slightly increasing trend over time is evident for $^{87}Sr/^{86}Sr_i$ with the inverse for εNd_i. No notable pattern can be seen from **Figure 25**. In **Figure 31** flare-ups have slightly lower values for $^{87}Sr/^{86}Sr_i$ than lulls for the EC and slightly higher values for the PCB in each segment, while εNd_i values are slightly higher for all PCB segments.

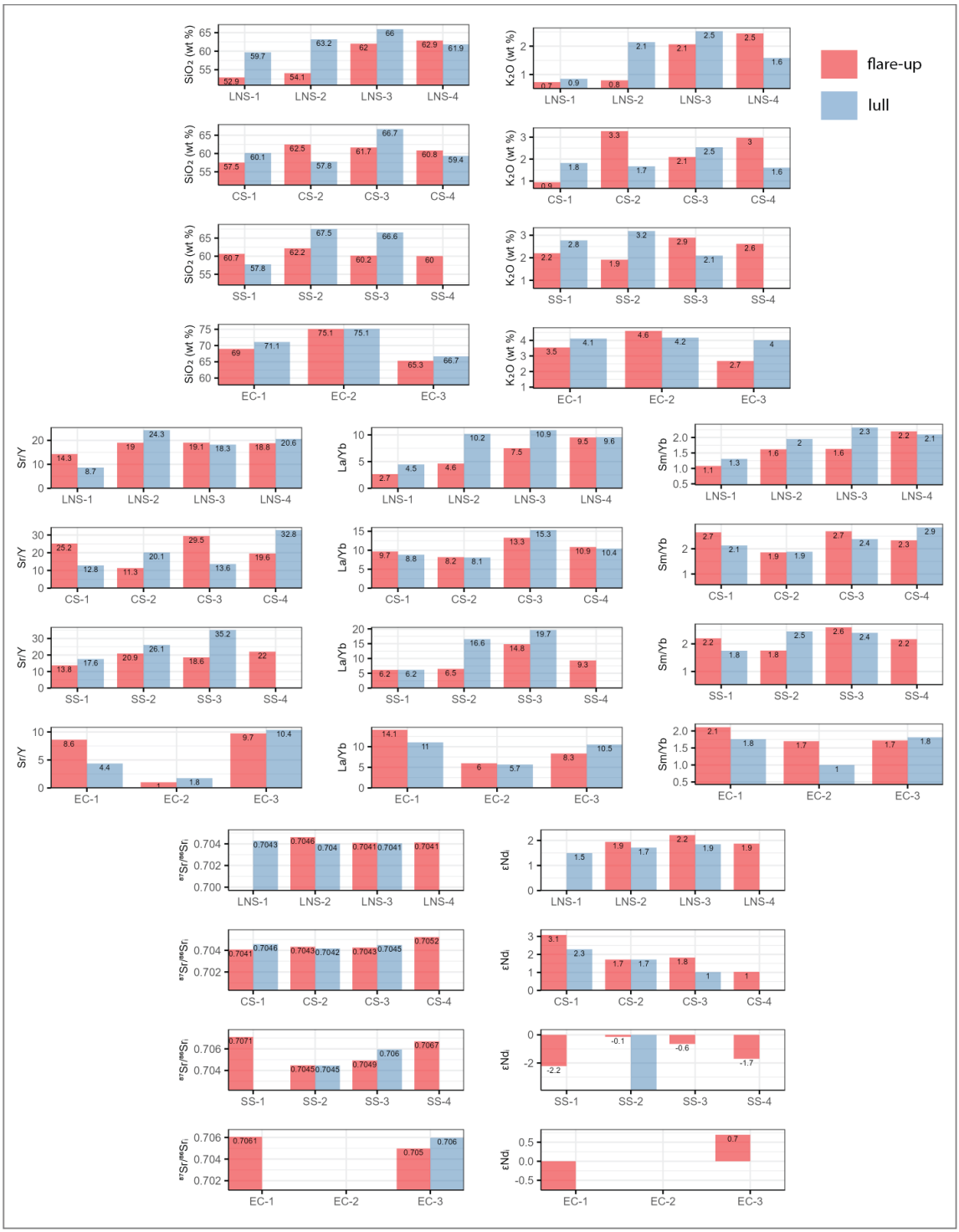

Figure 25. Comparative summary of mean values of geochemical data for flare-ups and lulls for the north, central and south segments of the PCB and for the EC.

Rising/falling parts of Flare-ups

The following geochemical observations can be made from **Figures 26 – 30**, comparisons between rising and falling parts of flare-ups summarized by *flare-up* in **Figure 30** and comparisons between rising and falling parts of flare-ups summarized by *segment* in **Figure 31**.

SiO_2 and K_2O

For each flare-up in the PCB north segment, except for LNS-2, both SiO_2 and K_2O exhibit lower values for the rising part compared to the falling part, see **Figure 30**. For the central and south PCB segments as well as for the EC, SiO_2 and K_2O fluctuate between higher and lower values for rising and falling parts of flare-ups with no notable pattern. Likewise, no notable pattern can be seen in the segment summary, **Figure 31**.

Sr/Y, La/Yb and Sm/Yb

The crustal thickness proxies don't display any notable systematic differences between rising and falling values for the PCB, but do indicate relatively lower rising values for flare-ups in many cases.

εNd_i and $^{87}Sr/^{86}Sr_i$

No significant difference is evident in the $^{87}Sr/^{86}Sr_i$ results. εNd_i values are lower for rising compared to falling parts of flare-ups for the LNS and higher for the CS.

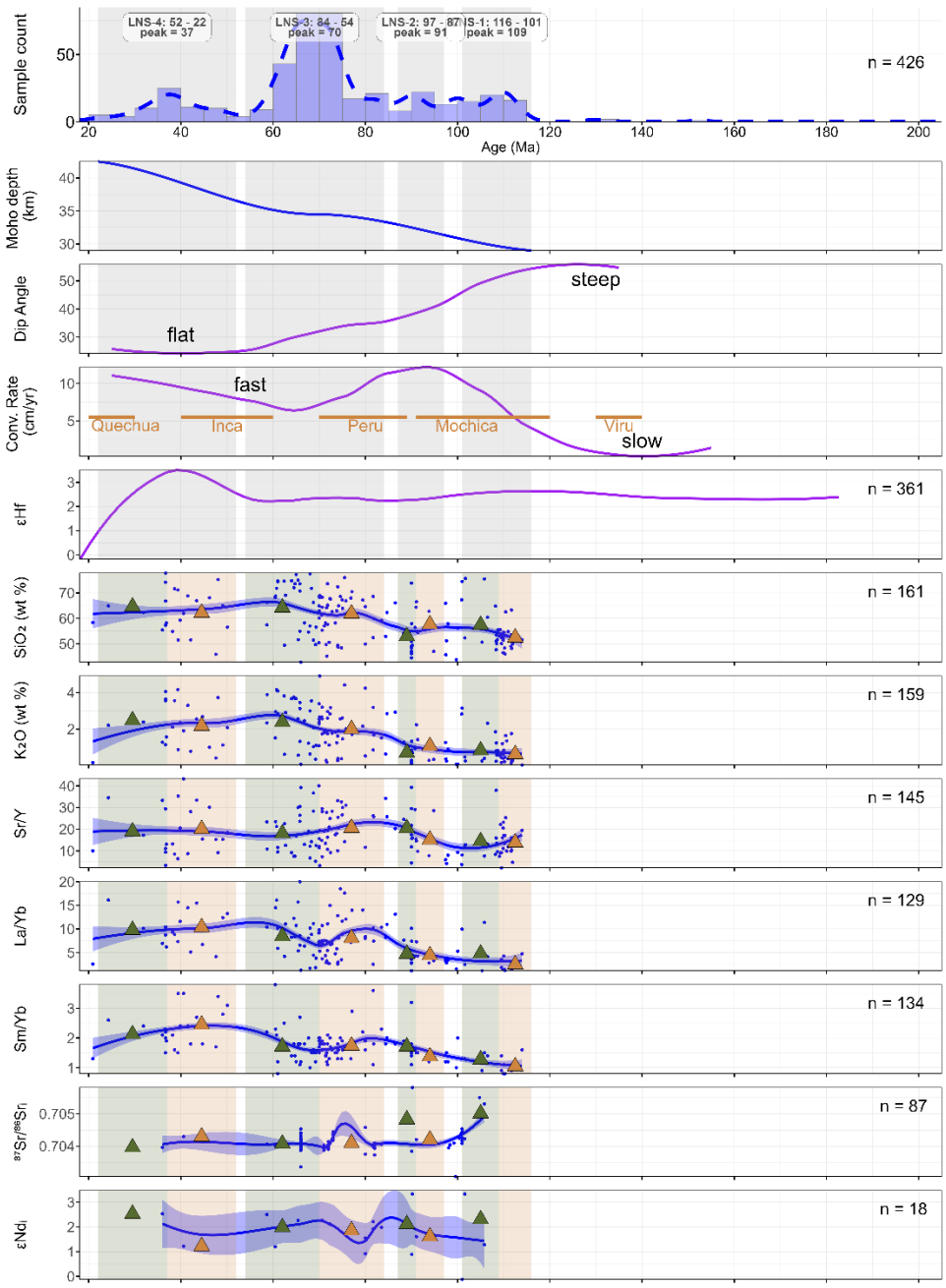

Figure 26. Rising/falling stacked time series plot for the PCB north segment with panels comparing geochronology, tectonic and chemistry data. Dip angle, convergence rates and εHf data are regional. Flare-ups are indicated by shading with range and peak labeled in the age spectra panel. Moho depth data is calculated using the mohometer approach of Luffi and Ducea (2022) with one data point per flare-up. Individual data points are plotted for geochemical data and fitted with regression curves showing standard error bands of ± 1σ. Rising parts of flare-up episodes are shaded in light orange while falling parts are shaded in olive green. Mean values for geochemical data falling within rising and falling intervals are depicted with colored triangles. Sources for the other tectonic data are given in the methods section.

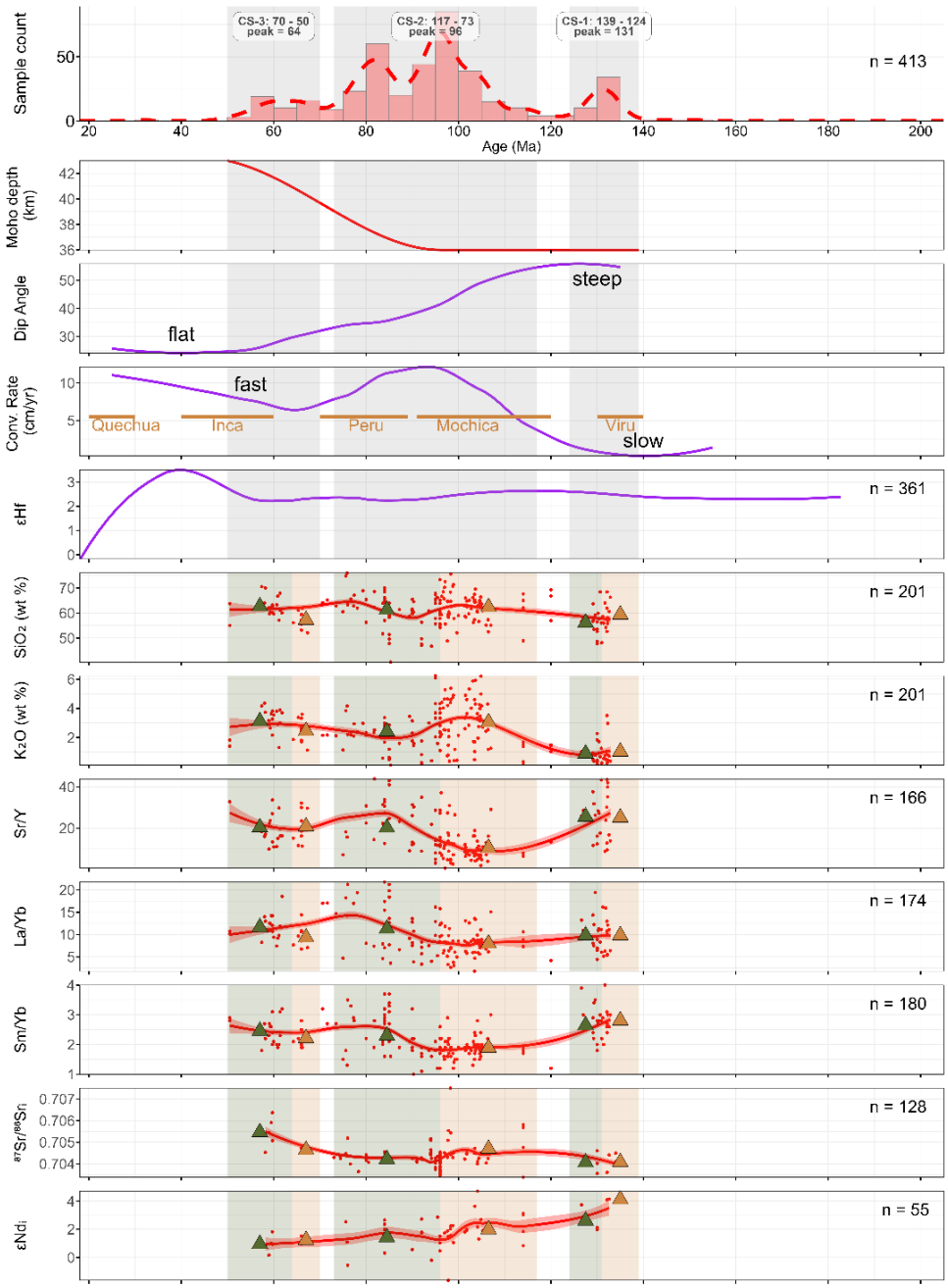

Figure 27. Rising/falling stacked time series plot for the PCB central segment. Description as in **Figure 26.**

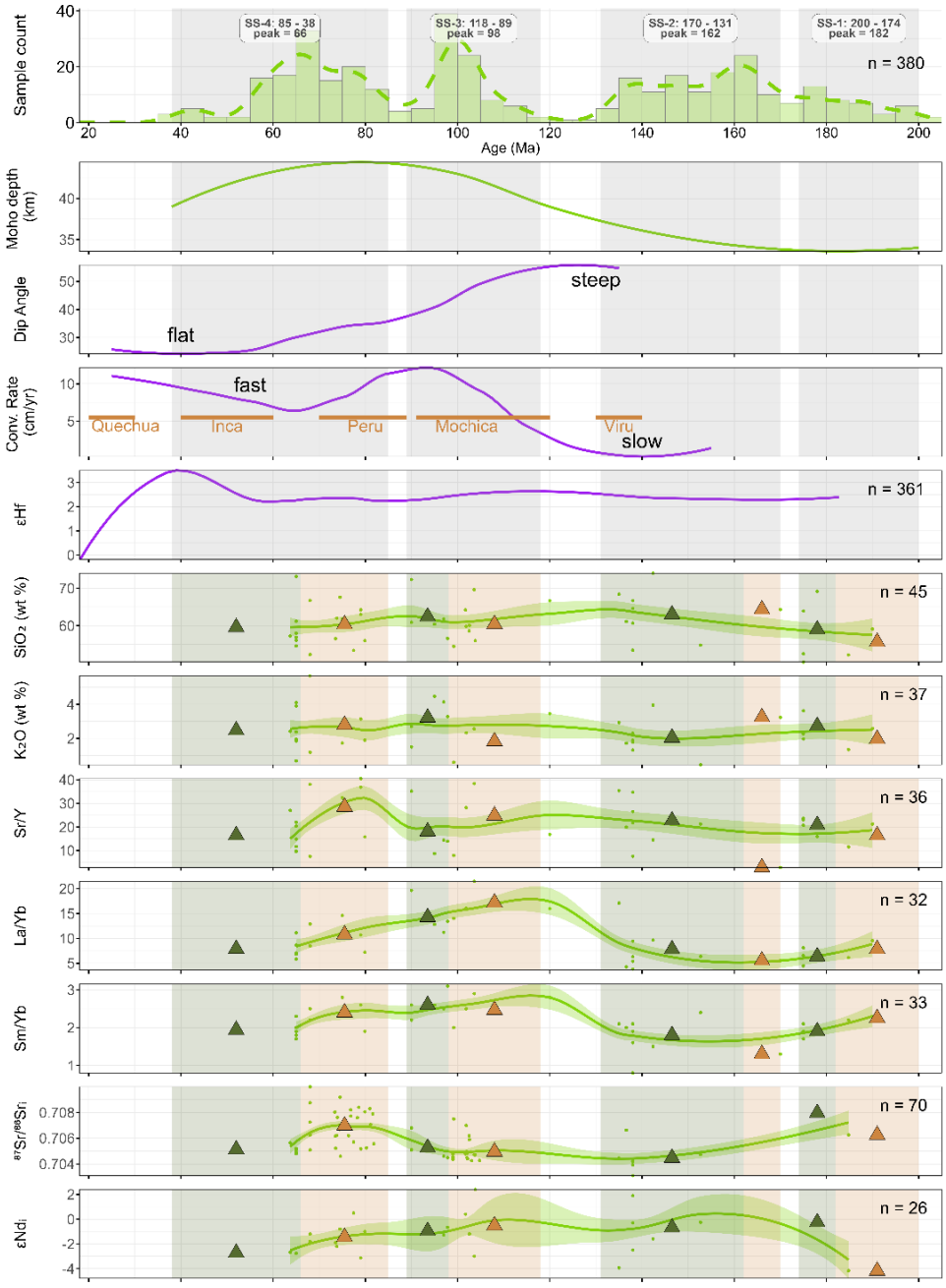

Figure 28. Rising/falling stacked time series plot for the PCB south segment. Description as in **Figure 26.**

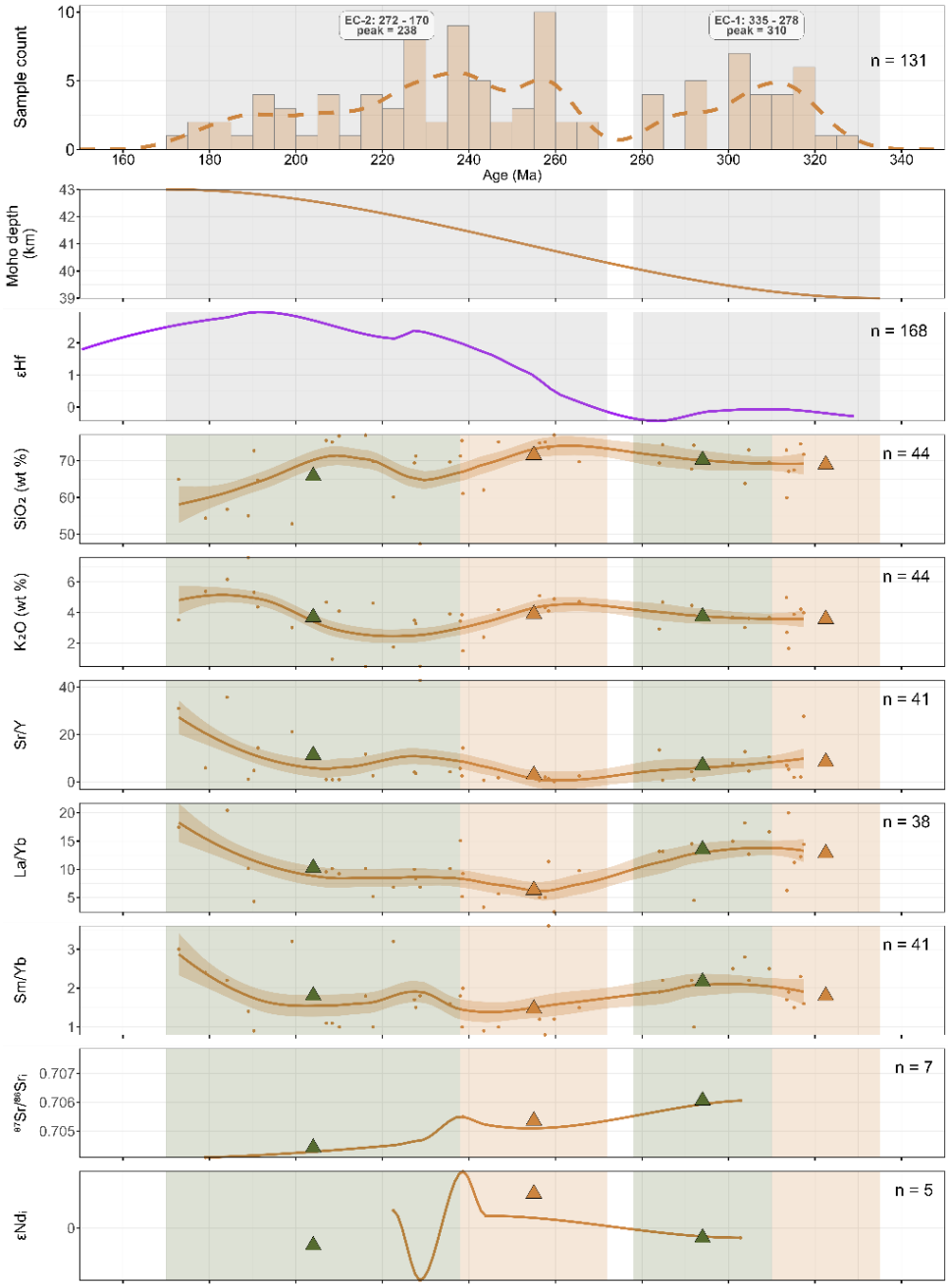

Figure 29. Rising/falling stacked time series plot for the EC. Description as in **Figure 26** with no convergence rate and dip angle data for this time period.

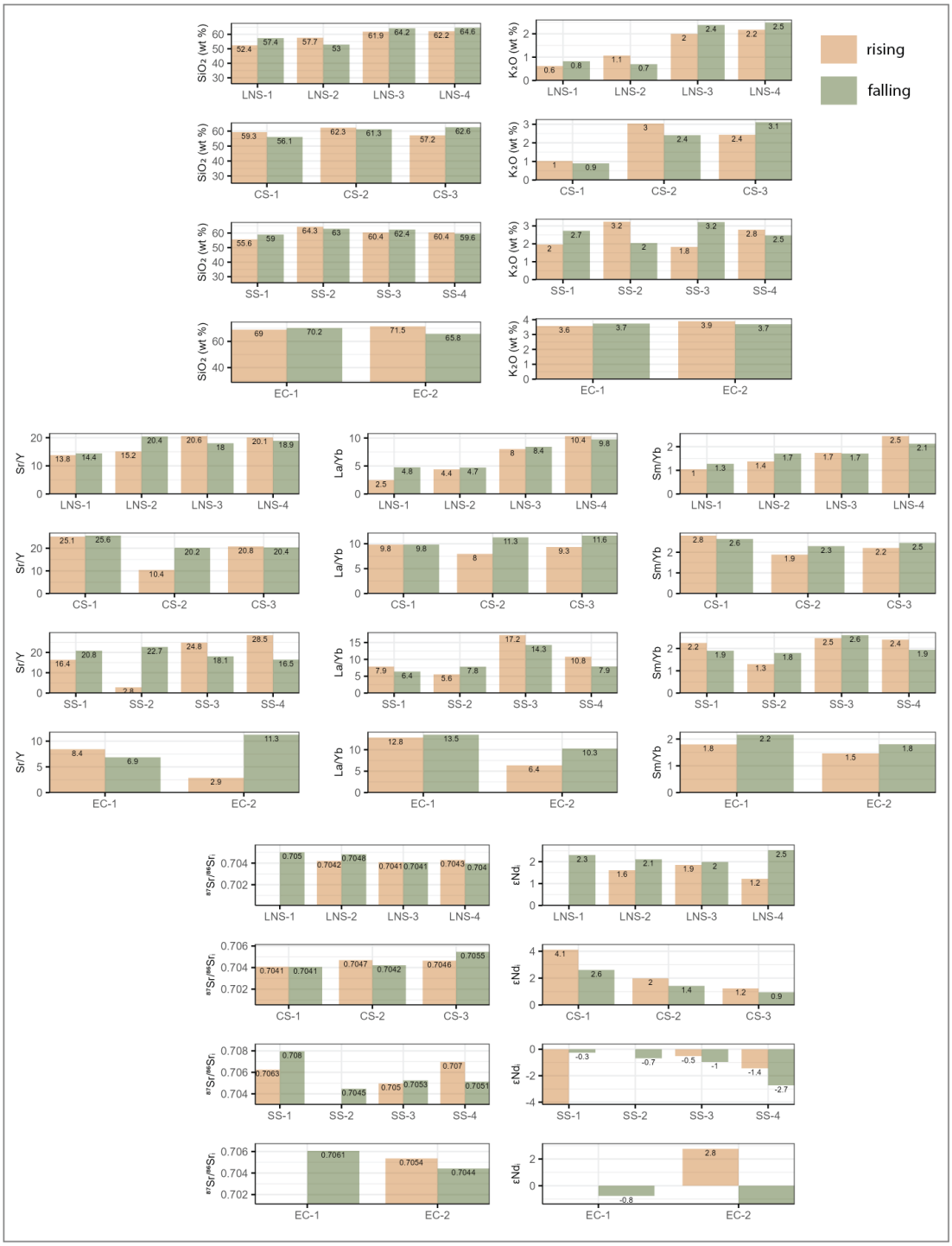

Figure 30. Comparative summary of mean values for geochemical data for rising/falling parts of flare-ups for the north, central and south segments of the PCB and for the EC, summarized by flare-up.

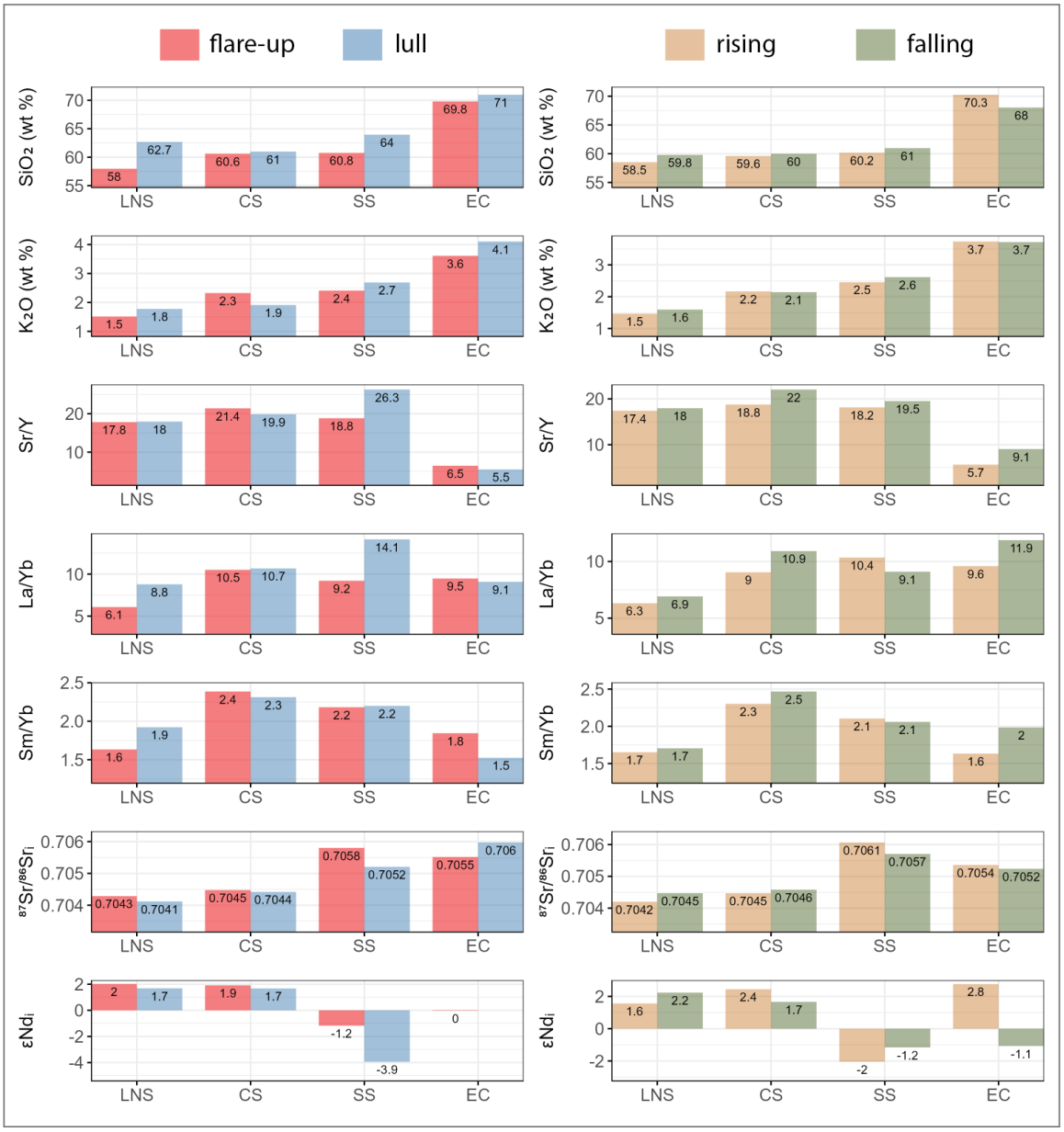

Figure 31. Comparative summary of mean values for geochemical data for flare-ups and lulls and rising and falling parts of flare-ups for the north, central and south segments of the PCB and for the EC, summarized by area.

Discussion

Lower plate external forcing and upper plate internal feedback models have both been proposed to explain the driving force behind pulses in magmatic activity in continental arcs. These models involve geological processes that predict differences in

crustal thickness and geochemical composition of arc rocks associated with magmatic pulses. In both cases, data have shown that arcs don't respond to triggers instantaneously, but in a fashion decoupled from continuous subduction, displaying gradual increases and decreases in magmatism, chemistry and tectonism (Paterson and Ducea, 2015). In the internal feedback model of DeCelles et al. (2009), cycles in magmatic pulses occur as the arc undergoes internal processes that cycle at regular intervals.

Age Spectra and Flare-up Controls

Considering the timing of age spectra in the Peruvian arc, flare-up durations and periods between flare-ups appear to be somewhat variable with no obvious cycles evident for each of the PCB segments or for the EC. Internal feedback models would be implied if cycles in magmatism are found, suggesting internal feedback processes are at work. External tectonic controls would be implied if magmatic episodes coincided over distance along strike as well as with large scale tectonic processes like plate motion changes. The effect of lower plate external controls on magma composition is theoretically not clear, but in general, no particular relationship to magmatic composition would be expected (Kirsch et al., 2016).

For the American Cordillera as a whole, Kirsch et al. (2016) found that flare-ups have a wavelength of 60-80 My with a high degree of variability between sectors. Others have found flare-up wavelengths of between 20 – 50 My in the Central Andes and North American Cordillera (DeCelles and Graham, 2015; Gehrels et al., 2009; Haschke et al., 2006; Paterson et al., 2011). Some sectors of the Cordillera have synchronous flare-up

patterns along thousands of kilometers while others are synchronous after a shift of up to 30 My.

In the Peruvian arc, the adjacent LNS and CS segments of the PCB exhibit approximately synchronous patterns for the Cretaceous and Paleogene after accounting for a shift of ~20 My, while the SS is also approximately synchronous for this interval but with differing durations and two earlier Jurassic flare-ups. These patterns suggest the possibility of an external control operating on the arc segments during the Cretaceous-Paleogene, possibly with a lag of ~20 My for the LNS and earlier Jurassic episodes for the SS.

Geochemistry and Flare-up Controls

Changes in arc chemistry related to variations in magmatic activity would be expected if cycles of crustal thickening and delamination are taking place. In particular, the following would be expected if an internal feedback model was operating in the arc (DeCelles et al., 2014; DeCelles et al., 2009; DeCelles and Graham, 2015; Kirsch et al., 2016): 1) Increased arc magma production would generate more silicic magma compared to magma generated as background magmatism during lulls. 2) Geochemical proxies for crustal thickness, such as Sr/Y, La/Yb and Sm/Yb, would be expected to increase during flare-ups. 3) Isotopes reflecting relative mantle and crust contributions, such as εNd_i, εHf and $^{87}Sr/^{86}Sr_i$ would be expected to vary between flare-ups and lulls with εNd_i and εHf decreasing and $^{87}Sr/^{86}Sr_i$ increasing during flare-ups (DeCelles et al., 2009; Kirsch et al., 2016).

Interpreting geochemistry in arcs is complicated by the fact that arcs tend to migrate. As arcs move across basement terranes of varying composition, the rising mantle-derived magma assimilates some of the basement material producing a composition intermediate between the two (Kirsch et al., 2016). Considering that the Peruvian Coastal Batholith overlies the Arequipa and Paracas terranes with the Eastern Cordillera also straddling the western margin of Amazonia, variations in composition due to basement contamination is a possibility.

Flare-up/Lull Comparisons

Slightly lower SiO_2 values are found for flare-ups compared to lulls for all four arc segments. Upper plate internal feedback models predict an increase in SiO_2 during flare-ups. With the exception of the CS, K_2O is also lower for flare-ups, indicating more mafic compositions. The crustal thickness proxies (Sr/Y, La/Yb and Sm/Yb) indicate a slightly thinner crust for the LNS and SS for flare-ups vs. lulls, with little difference for the CS and a thicker crust for EC flare-ups. Therefore the EC crustal thickness data fits with a crustal thickening upper plate model, but the PCB data does not. Values of $^{87}Sr/^{86}Sr_i$ for the LNS and CS are similar between flare-ups and lulls, higher for flare-ups for the SS and lower for the EC. Only the SS $^{87}Sr/^{86}Sr_i$ data fit an upper plate model, however all $^{87}Sr/^{86}Sr_i$ values for both flare-ups and lulls for the PCB segments are low (< 0.706), indicating a predominantly mantle source, while EC lulls are slightly higher at 0.706 showing relatively greater crustal assimilation. Values of εNd_i increase during flare-ups compared to lulls for each of the PCB segments, which is not what would be expected for an upper plate internal feedback model. Too little εNd_i data are available to

make any conclusions for the EC, but it would likely be the inverse of the Sr_i data. In summary, geochemical data analysis results for PCB age spectra show SiO_2, K_2O, crustal thickness proxies (Sr/Y, La/Yb, Sm/Yb) and $^{87}Sr/^{86}Sr_i$ to be inversely proportional and εNd_i directly proportional to an increase in arc magma production, and thus do not correspond well with expectations for upper plate cyclic internal models. Only $^{87}Sr/^{86}Sr_i$ values are moderately supportive of upper plate models for the PCB. For the EC, SiO_2, K_2O and $^{87}Sr/^{86}Sr_i$ data do not support upper plate models while the crustal thickness proxies do on average.

Table 3 summarizes the results of flare-up to lull comparisons and considers upper plate internal feedback models to be a likely control if two out of the three criteria, differentiation extent, crustal thickness and mantle/crust ratio are supported. Only the CS-2 flare-up seems to support upper plate models and more flare-ups have a relatively greater mantle composition compared to the following lull.

Table 3. Summary of flare-up comparisons to lulls for differentiation extent, crustal thickness and mantle vs crust composition. Upper plate arc processes are considered to be involved if two out of the three parameters of higher SiO_2, thicker crust and a predominantly crustal composition are found for a flare-up. Only CS-2 displays a crustal signature in flare-ups and indicates upper plate arc processes are likely involved.

Flare-up	Flare-up SiO_2 higher	Flare-up crust thicker	Flare-up more crust	Flare-up more mantle	Upper plate arc internal likely
LNS-1					
LNS-2					
LNS-3					
LNS-4	x				
				x	
CS-1		x			
CS-2	x		x		x
CS-3		x		x	
CS-4	x				
SS-1	x				
SS-2				x	
SS-3					
SS-4					
EC-1		x			
EC-2		x			
EC-3				x	

Rising/Falling Comparisons

The rising part of a flare-up can be considered to be the acceleration phase and the falling part the deceleration phase of a flare-up. We use a longer duration than that used for flare-up vs lull comparisons to allow chemistry changes to be adequately investigated. Comparing rising and falling parts of flare-ups from approximately the initiation of the flare-up to the return to background magmatism might give insights into processes that may be operating during the accelerating phase compared to after the magmatic pulse peaks and starts decelerating.

We find rising part SiO_2 values to be slightly lower for the LNS, CS and SS than for falling part values in the PCB but higher for rising in the EC. The crustal thickness proxies are slightly lower for rising parts of flare-ups but don't display any strong systematic difference compared to falling parts. The same is found for εNd_i and $^{87}Sr/^{86}Sr_i$ values.

A Combination of Processes

Only one flare-up (CS-2) seems to be adequately linked to upper plate internal feedback models, although many flare-ups show some degree of support for these models. Do lower plate external forcing models explain the rest of the data or are there other possibilities? Local tectonic data of high enough spatial and temporal resolution are lacking to adequately test the lower plate models; however, we can consider the impact of large-scale plate reconfigurations driven by supercontinent assembly and breakup. Pangea assembled in the Carboniferous and broke up in the Triassic (Santosh et al., 2009). Kontak et al. (1985) attributes all Permo-Triassic magmatism of the Eastern Cordillera to a period of extensional tectonics. Emplacement of the Permo-Triassic plutons occurred soon after Mitu Group volcanism and represent relatively high temperature dry melts, possibly in response to partial fusion of the lower crust due to a high thermal input from the Mitu volcanics. The Eastern Cordilleran Carbo-Permian and Permo-Triassic flare-ups coincide with a period of major plate reorganization during the assembly and breakup of Pangea (see **Figure 19**) (Mišković et al., 2009). It is conceivable that these major arc-external tectonic events would be related to magmatic episodicity for the Eastern Cordillera.

As DeCelles et al. (2009) note, correlations between magmatic pulses and rates of plate convergence or plate geometry are not obvious from the available data. This in general also seems to be the case for the Peruvian arc data examined here. However, the stacked time series plots presented here indicate that from the Early Cretaceous through the Paleogene, dip angle transitions from steep to flat, convergence rate speeds up, slows slightly then speeds up again, and Moho depth increases showing a trend of thickening crust with time. These factors correlate roughly with the large increase in magmatism in the Cretaceous to Cenozoic flare-up, especially when detrital zircon data are included as seen in **Figure 19**, indicating possible arc-external triggers for the Peruvian Coastal Batholith (Martínez et al., 2019).

In general, geochemical data do not show any consistent patterns between flare-ups and lulls, between rising and falling parts of flare-ups or between flare-ups in different arc segments. However, much of our geochemical data do point towards the importance of mantle sources in producing the greatest volume of magmatism during flare-ups, suggesting that episodic mantle processes likely play an important role in triggering flare-ups. Episodic mantle processes can be both external to the arc or internal (in the mantle wedge). An interplay of linked processes involving the mantle needs to be investigated, for example, plate motion, such as convergence rate, might have an effect on the behavior of the mantle (Turner and Langmuir, 2015). Higher convergence rates can increase the temperature of the mantle wedge corner as well as increase mantle wedge hydration (Plank et al., 2009), resulting in an increase in mantle melting, as suggested in Martinez et al. (2023). In a study of episodic magmatism in three Cretaceous Cordilleran arc segments (the western Peninsular Ranges batholith, the Peruvian Coastal

Batholith and the Chilean Coastal batholith), Martínez et al. (2019) used geochronology and geochemical data to show that magmas in these arc segments generally have a depleted mantle source. This finding was supported by assimilation and fractional crystallization (AFC) modeling which indicated that the magmas experienced fractional crystallization with only minor crustal assimilation, therefore being primarily mantle derived. However, it was unclear whether the episodic mantle processes reflected internal feedback or external tectonically driven processes.

Some ideas suggest an interplay between external forcing and processes internal to the arc system. For example, mantle wedge decompression melting suggested by Lee and Lackey (2015) being driven by changes in thickness of the upper plate (internal to the arc) which are in turn controlled by magmatic thickening and tectonic thinning cycles (external to the arc).

Scale Considerations

Considering geochronological and geochemical data for each of the three segments of the Peruvian Coastal Batholith and for the Eastern Cordillera allows location and scale-related differences to be examined. We do not find cyclicity operating at the scale of any of the segments studied or at the regional scale of the entire Peruvian arc. Kirsch et al. (2016) did find good correlation between geochemistry and arc magma production in some regional scale Cordilleran segments, but not for the Sierra Nevada segment, the Peninsular Ranges and northern Mexico sectors, or the Southeastern Mexico or Central America segment.

De Silva et al. (2015) categorize flare-ups into a hierarchy of pulses with successively coupled space/time scales related to specific scales of continental-arc magmatic processes. The primary pulse is the high volume mantle signal with a large footprint over space and time, for example, the 50-60 Ma flare-up in the Sierra Nevada batholith in the California arc. In the California case, DeCelles et al. (2009) found flare-ups to be driven by delamination events or triggered by a regional change in plate parameters from low-angle plate convergence to an increasingly extensional regime and where peak volcanism largely preceded the bulk of the extension. Secondary pulses occur at a smaller scale than the primary pulse as magmatism gets localized into regional nodes. Thus, the primary pulse may be modulated by processes of melting, segregation, and transfer through the crust, along with local upper-plate tectonics to produce secondary pulses with a smaller reach in space and time, on the order of 10 – 20 My. These secondary pulses reflect the timescale of melt production and delivery from the melting, assimilation storage and hybridization (MASH) zone at or near the mantle/lower crust boundary and its interaction with upper-plate tectonics over the area of each component. At the scale of individual volcano-plutonic systems, magmatic histories can often be characterized by a timescale on the order of 10 My (Grunder et al., 2008) which suggests that this is a fundamental signal in continental arc magmatism.

Conclusions

Peaks in the amount of geochronology data are assumed to represent periods of increased magmatism. Lower plate external forcing models and upper plate internal feedback models each predict differences in the timing of magmatic activity and in the

relationship between magmatic activity and magma composition. A detailed examination of flare-ups for the Peruvian segment of the Cordilleran arc has shown there is no strong support for internal feedback models for either the PCB or the EC. Very weak support for internal feedback models is found from a slightly higher crust composition for flare-ups for the PCB and slightly thicker crust during flare-ups for the EC.

Although we don't find strong evidence of upper plate arc internal cyclic magmatic processes, this does not mean these processes are ruled out, since they may simply be overprinted by external tectonic events such as supercontinent reorganizations or increased mantle power (i.e. the supply of thermal energy and volatiles to the base of the crust by basalt intrusion from the mantle), especially at a larger spatial and temporal scale. Cycles corresponding to internal feedback models may be operating at smaller spatial scales with timings that vary along the arc and become obscured at larger scales. Arc magmatism is fractal in nature both in time and space with a number of scale-dependent processes acting at different scales to modulate magmatic activity (De Silva et al., 2015). It is conceivable that magmatic episodicity in the Peruvian arc is governed by an interplay between external forcing and processes internal to the arc system, as suggested by Lee and Lackey (2015), with scale being the distinguishing factor.

This kind of study relies heavily on the availability of preferably U-Pb zircon dated geochemical data that include isotopes as well as tectonic data with adequate temporal and spatial resolution over the same age range. High quality tectonic data especially for the Paleozoic and earlier would be very helpful in establishing links between geochemical findings and tectonics to further elucidate magmatic triggers. Therefore, future work on this question will benefit greatly from a larger and higher

quality dataset. With enough data, processes operating at much smaller spatial and temporal scales can be effectively investigated. These types of data are difficult to collect effectively and can be expensive to analyze. However, with increasing interest in understanding continental arc subduction zones, locations like Peru will no doubt continue to produce valuable data. Being able to explore a broad range of resolvable scales would undoubtably lead to new insights in processes that govern arc magmatism.

References

Armstrong, R. L., 1988, Mesozoic and early Cenozoic magmatic evolution of the Canadian Cordillera: Geological Society of America Special Papers, v. 218, p. 55-92.

Cao, W., Lee, C.-T. A., and Lackey, J. S., 2017, Episodic nature of continental arc activity since 750 Ma: A global compilation: Earth and Planetary Science Letters, v. 461, p. 85-95.

Cardona, A., Cordani, U., Nutman, A., Zimmermann, U., and Sánchez, A., 2005, Tectonic setting and geochronology of Pre-Llanvirnian metamorphic rocks of the Marañon Complex (E. Peru): From rifting to collision to form the Rheic Ocean: Gondwana 12 Abstracts: Academia Nacional de Ciencias, Mendoza, Argentina, p. 87.

Cardona, A., Cordani, U. G., Ruiz, J., Valencia, V., Armstrong, R., Chew, D., Nutman, A., and Sanchez, A., 2009, U-Pb zircon geochronology and Nd isotopic signatures of the pre-Mesozoic metamorphic basement of the eastern Peruvian Andes: Growth and provenance of a late Neoproterozoic to Carboniferous accretionary orogen on the northwest margin of Gondwana: Journal of Geology, v. 117, no. 3, p. 285-305.

Cardona, A., Cordani, U. G., Ruiz, J., Valencia, V., Nutman, A., and Sánchez, A., 2006, U/Pb detrital zircon geochronology and Nd isotopes from Paleozoic metasedimentary rocks of the Maranon Complex: insights on the proto-Andean tectonic evolution of the Eastern Peruvian Andes: Journal of Geology, v. 117, p. 285-305.

Casquet, C., Fanning, C. M., Galindo, C., Pankhurst, R. J., Rapela, C. W., and Torres, P., 2010, The Arequipa Massif of Peru: New SHRIMP and isotope constraints on a Paleoproterozoic inlier in the Grenvillian orogen: Journal of South American Earth Sciences, v. 29, no. 1, p. 128-142.

Chapman, A. D., Saleeby, J. B., and Eiler, J., 2013, Slab flattening trigger for isotopic disturbance and magmatic flare-up in the southernmost Sierra Nevada batholith, California: Geology, v. 41, no. 9, p. 1007-1010.

Chen, J., and Wasserburg, G., 1981, Isotopic determination of uranium in picomole and subpicomole quantities: Anal. Chem.;(United States), v. 53, no. 13.

Cobbing, E., 1985, The tectonic setting of the Peruvian Andes, *in* Pitcher, W. S., Atherton, M. P., Cobbing, E. J., Beckinsale, R. D., ed., Magmatism at a plate edge: The Peruvian Andes, Glasgow, UK, Blackie, p. 3-12.

De Silva, S. L., Riggs, N. R., and Barth, A. P., 2015, Quickening the pulse: Fractal tempos in continental arc magmatism: Elements, v. 11, no. 2, p. 113-118.

DeCelles, P., 2017, Periodic activity in continental magmatic arcs: American Mineralogist, v. 102, no. 1, p. 1-2.

DeCelles, P., Zandt, G., Beck, S., Currie, C., Ducea, M., Kapp, P., Gehrels, G., Carrapa, B., Quade, J., and Schoenbohm, L., 2014, Cyclical orogenic processes in the Cenozoic central Andes: Geological Society of America Memoirs, v. 212, p. MWR212-222.

DeCelles, P. G., Ducea, M. N., Kapp, P., and Zandt, G., 2009, Cyclicity in Cordilleran orogenic systems: Nature Geoscience, v. 2, no. 4, p. 251-257.

DeCelles, P. G., and Graham, S., 2015, Cyclical processes in the North American Cordilleran orogenic system: Geology, v. 43, no. 6, p. 499-502.

Díaz-Martínez, E., Acosta, H., Cardenas, J., Carlotto, V. c., and Rodríguez, R., 2001, Paleozoic diamictites in the Peruvian Altiplano: evidence and tectonic implications: Journal of South American Earth Sciences, v. 14, no. 6, p. 587-592.

Ducea, M., 2001, The California arc: Thick granitic batholiths, eclogitic residues, lithospheric-scale thrusting, and magmatic flare-ups: GSA today, v. 11, no. 11, p. 4-10.

Ducea, M. N., 1998, A petrologic investigation of deep-crustal and upper-mantle xenoliths from the Sierra Nevada, California: Constraints on lithospheric composition beneath continental arcs and the origin of Cordilleran batholiths, California Institute of Technology.

Ducea, M. N., Paterson, S. R., and DeCelles, P. G., 2015, High-volume magmatic events in subduction systems: Elements, v. 11, no. 2, p. 99-104.

Esri, 2023, ArcGIS for Desktop: https://www.arcgis.com: Redlands, CA.

Feininger, T., 1987, Allochthonous terranes in the Andes of Ecuador and northwestern Peru: Canadian Journal of Earth Sciences, v. 24, no. 2, p. 266-278.

Gehrels, G., Rusmore, M., Woodsworth, G., Crawford, M., Andronicos, C., Hollister, L., Patchett, J., Ducea, M., Butler, R., and Klepeis, K., 2009, U-Th-Pb geochronology of the Coast Mountains batholith in north-coastal British Columbia: Constraints on age and tectonic evolution: Geological Society of America Bulletin, v. 121, no. 9-10, p. 1341-1361.

Gijbels, I., and Prosdocimi, I., 2010, Loess: Wiley Interdisciplinary Reviews: Computational Statistics, v. 2, no. 5, p. 590-599.

Grunder, A. L., Klemetti, E. W., Feeley, T. C., and McKee, C. M., 2008, Eleven million years of arc volcanism at the Aucanquilcha Volcanic Cluster, northern Chilean Andes: implications for the life span and emplacement of plutons: Earth and Environmental Science Transactions of the Royal Society of Edinburgh, v. 97, no. 4, p. 415-436.

Haschke, M., Günther, A., Melnick, D., Echtler, H., Reutter, K.-J., Scheuber, E., and Oncken, O., 2006, Central and southern Andean tectonic evolution inferred from arc magmatism, *in* Franz, G., Chong, G., Götze, H., Strecker, M.R., Oncken, O., Giese, P., Wigger, P., Ramos, V., ed., The Andes: Active Subduction Orogeny, Springer-Verlag, Berlin, p. 337-353.

Hildebrand, R. S., and Whalen, J. B., 2014, Arc and slab-failure magmatism in Cordilleran batholiths II–The Cretaceous Peninsular Ranges batholith of southern and Baja California: Geoscience Canada, v. 41, no. 4, p. 399-458.

Hughes, G. R., and Mahood, G. A., 2008, Tectonic controls on the nature of large silicic calderas in volcanic arcs: Geology, v. 36, no. 8, p. 627-630.

INGEMMET, 2021, http://www.ingemmet.gob.pe/.

Jaillard, E., Hérail, G., Monfret, T., Díaz-Martínez, E., Baby, P., Lavenu, A., Dumont, J.-F., Cordani, U., Milani, E., and Campos, D., 2000, Tectonic evolution of the Andes of Ecuador, Peru, Bolivia and northern Chile, *in* Cordani, U. G., Milani, E. J., Thomaz Filho, A., and Campos, D.A, ed., Tectonic evolution of South America, edited by: Cordani, UG, Milani, E. J., Thomaz Filho, A., and Campos, DA, Rio de Janeiro, Brazil, p. 481-559.

Jaillard, E., and Soler, P., 1996, Cretaceous to early Paleogene tectonic evolution of the northern Central Andes (0–18 S) and its relations to geodynamics: Tectonophysics, v. 259, no. 1-3, p. 41-53.

Jaillard, E., Soler, P., Carlier, G., and Mourier, T., 1990, Geodynamic evolution of the northern and central Andes during early to middle Mesozoic times: a Tethyan model: Journal of the Geological Society, v. 147, no. 6, p. 1009-1022.

Kirsch, M., Paterson, S. R., Wobbe, F., Martínez, A. M., Clausen, B. L., and Alasino, P. H., 2016, Temporal histories of Cordilleran continental arcs: Testing models for magmatic episodicity: American Mineralogist, v. 101, no. 10, p. 2133-2154.

Kontak, D., Clark, A., and Farrar, E., 1984, The magmatic evolution of the Cordillera Oriental, southeastern Peru, *in* Harmon, R. S., Barreiro, B.A, ed., Andean Magmatism: Chemical and Isotopic Constraints, Springer, p. 203-219.

Kontak, D., Clark, A., Farrar, E., and Strong, D., 1985, The rift associated Permo-Triassic magmatism of the Eastern Cordillera: A precursor to the Andean orogeny: Magmatism at a plate edge: The Peruvian Andes: London, Blackie and Son, p. 36-44.

Lee, C.-T. A., and Lackey, J. S., 2015, Global continental arc flare-ups and their relation to long-term greenhouse conditions: Elements, v. 11, no. 2, p. 125-130.

Loewy, S. L., Connelly, J. N., and Dalziel, I. W., 2004, An orphaned basement block: The Arequipa-Antofalla Basement of the central Andean margin of South America: Geological Society of America Bulletin, v. 116, no. 1-2, p. 171-187.

Luffi, P., and Ducea, M., 2022, Chemical Mohometry: Assessing Crustal Thickness of Ancient Orogens Using Geochemical and Isotopic Data: Reviews of Geophysics, v. 60, no. 2.

Martínez, A. M. A., Paterson, S. R., Memeti, V., Parada, M. A., and Molina, P. G., 2019, Mantle driven cretaceous flare-ups in Cordilleran arcs: Lithos, v. 326, p. 19-27.

Martínez, A. M. A., Pompe, L., Clausen, B. L., Paterson, S. R., Holk, G. J., & Luffi, P. (2023). A synthesis of the Peruvian Coastal Batholith: An exploration of temporal histories, causes of compositional diversity, and tectonomagmatic links in arcs. Lithos, 107298.

Matthews, K. J., Seton, M., and Müller, R. D., 2012, A global-scale plate reorganization event at 105− 100 Ma: Earth and Planetary Science Letters, v. 355, p. 283-298.

Mišković, A., Schaltegger, U., and Chew, D., Carboniferous plutonism along the Eastern Peruvian Cordillera: Implications for the late Paleozoic to early Mesozoic Gondwanan tectonics, *in* Proceedings Proceedings of the 6th International Symposium on Andean Geodynamics, Barcelona, Spain, Institut de recherche pour le développement2005, p. 508-511.

Mišković, A., Spikings, R. A., Chew, D. M., Košler, J., Ulianov, A., and Schaltegger, U., 2009, Tectonomagmatic evolution of Western Amazonia: Geochemical characterization and zircon U-Pb geochronologic constraints from the Peruvian Eastern Cordilleran granitoids: Geological Society of America Bulletin, v. 121, no. 9-10, p. 1298-1324.

Mpodozis, C., and Ramos, V., 1990, The Andes of Chile and Argentina: Circum-Pacific Council for Energy and Mineral Resources Earth Science Series, v. 11.

Otamendi, J. E., Ducea, M. N., Tibaldi, A. M., Bergantz, G. W., de la Rosa, J. D., and Vujovich, G. I., 2009, Generation of tonalitic and dioritic magmas by coupled partial melting of gabbroic and metasedimentary rocks within the deep crust of the Famatinian magmatic arc, Argentina: Journal of Petrology, v. 50, no. 5, p. 841-873.

Paterson, S. R., and Ducea, M. N., 2015, Arc magmatic tempos: gathering the evidence: Elements, v. 11, no. 2, p. 91-98.

Paterson, S. R., Okaya, D., Memeti, V., Economos, R., and Miller, R. B., 2011, Magma addition and flux calculations of incrementally constructed magma chambers in continental margin arcs: Combined field, geochronologic, and thermal modeling studies: Geosphere, v. 7, no. 6, p. 1439-1468.

Pfiffner, O. A., and Gonzalez, L., 2013, Mesozoic–Cenozoic evolution of the western margin of South America: Case study of the Peruvian Andes: Geosciences, v. 3, no. 2, p. 262-310.

Pitcher, W., 1985, A Multiple and Composite Batholith, *in* Pitcher, W. S., Atherton, M. P., Cobbing, E. J., Beckinsale, R. D., ed., Magmatism at a plate edge. The Peruvian Andes, p. 93-101.

Pitcher, W. S., Atherton, M. P., Cobbing, E. J., and Beckinsale, R., 1985, Magmatism at a plate edge: the Peruvian Andes, Wiley.

Pitcher, W. S., and Cobbing, E. J., 1985, Phanerozoic Plutonism in the Peruvian Andes, *in* Pitcher, W. S., Atherton, M. P., Cobbing, E. J., Beckinsale, R. D., ed., Magmatism at a plate edge: the Peruvian Andes, Springer, p. 152-167.

Plank, T., Cooper, L. B., and Manning, C. E., 2009, Emerging geothermometers for estimating slab surface temperatures: Nature Geoscience, v. 2, no. 9, p. 611-615.

Pompe, L. R., María Martínez Ardila, A., CLause, B. L., Paterson, S. R., and Poma, O., 2023, Episodic continental arc magmatism:
magmatic tempos of the Peruvian arc: In development.

R-Core-Team, 2023, R: A language and environment for statistical computing: Vienna, http://www.r-project.org.

Ramos, V. A., 1999, Plate tectonic setting of the Andean Cordillera: Episodes Journal of International Geoscience, v. 22, no. 3, p. 183-190.

-, 2008, The basement of the Central Andes: the Arequipa and related terranes: Annu. Rev. Earth Planet. Sci., v. 36, p. 289-324.

Ramos, V. A., 2009, Anatomy and global context of the Andes: Main geologic features and the Andean orogenic cycle: Backbone of the Americas: Shallow subduction, plateau uplift, and ridge and terrane collision, v. 204, p. 31-65.

Reimann, C., Bahlburg, H., Kooijman, E., Berndt, J., Gerdes, A., Carlotto, V., and Lopez, S., 2010, Geodynamic evolution of the early Paleozoic Western Gondwana margin 14°–17° S reflected by the detritus of the Devonian and Ordovician basins of southern Peru and northern Bolivia: Gondwana Research, v. 18, no. 2-3, p. 370-384.

Santosh, M., Maruyama, S., and Yamamoto, S. J. G. R., 2009, The making and breaking of supercontinents: some speculations based on superplumes, super downwelling and the role of tectosphere: Gondwana Research, v. 15, no. 3-4, p. 324-341.

Sempere, T., Carlier, G., Soler, P., Fornari, M., Carlotto, V. c., Jacay, J., Arispe, O., Néraudeau, D., Cárdenas, J., and Rosas, S., 2002, Late Permian–Middle Jurassic lithospheric thinning in Peru and Bolivia, and its bearing on Andean-age tectonics: Tectonophysics, v. 345, no. 1-4, p. 153-181.

Turner, S. J., and Langmuir, C. H., 2015, The global chemical systematics of arc front stratovolcanoes: Evaluating the role of crustal processes: Earth and Planetary Science Letters, v. 422, p. 182-193.

Witt, C., Rivadeneira, M., Poujol, M., Barba, D., Beida, D., Beseme, G., and Montenegro, G., 2017, Tracking ancient magmatism and Cenozoic topographic growth within the Northern Andes forearc: Constraints from detrital U-Pb zircon ages: Geological Society of America Bulletin, v. 129, no. 3-4, p. 415-428.

CHAPTER 4

A SYNTHESIS OF THE PERUVIAN COASTAL BATHOLITH: AN EXPLORATION OF TEMPORAL HISTORIES, CAUSES OF COMPOSITIONAL DIVERSITY, AND TECTONO-MAGMATIC LINKS IN ARCS

Ana María Martínez Ardila [1], Lance Pompe[1], Benjamin L. Clausen [1,2], Scott R. Paterson [3], Gregory J. Holk [4], and Peter Luffi [5,6]

[1] Department of Earth and Biological Sciences, Loma Linda University, Loma Linda, California 92350, USA
[2] Geoscience Research Institute, Loma Linda, CA 92350, USA
[3] Claremont, CA 91711, USA
[4] Department of Geological Sciences, California State University, Long Beach, California 90840-3902, USA
[5] Sabba Stefanescu Institute of Geodynamics, Bucharest, Romania
[6] Geological Institute of Romania, Bucharest, Romania

Corresponding author: A.M. Martínez-Ardila (anmartinez@llu.edu)

Abstract

The causes for spatial geochemical trends in the central Andes of Peru have been studied since the early 1970s. Along-arc chemical changes observed in the Peruvian Coastal Batholith (PCB) were fundamental to developing models for the evolution of the Pacific margin of South America. However, explanations for these trends and the processes that control magmatic compositional diversity along this arc are not fully understood. In this contribution we use an up-to-date database of high quality geochemical and geochronological data to: 1) assess the evidence for the previously proposed chemical trends, 2) document patterns of episodic magmatism to examine

spatial and temporal changes covering a timespan of >170 million years along the PCB segments, 3) investigate PCB-wide variation of the parameters previously studied in the Ica-Pisco plutons, and 4) relate these to the tectonic setting, subduction parameters, magma sources, and crustal assimilation processes. Our results show that the PCB has a clear non-steady-state pattern over variable temporal and spatial scales and that arc magma chemistry covaries with arc magmatic activity. We conclude that the identified diversity in magma chemistry both along- and across-arc is the result of the extent of differentiation, types of assimilated materials, different types of basement, changes in crustal thickness, arc migration, changes in mantle input, and transitioning from depleted to lithospheric mantle resulting from changes in slab dip angle. In order to explain the causes of flare-ups and arc chemical diversity in the PCB we suggest that coupling of external (lower plate) and internal (upper plate) processes in complex ways at different spatial and temporal scales form the final arc diversity.

Introduction

The Peruvian Coastal Batholith (PCB) and associated volcanic rocks are the dominant features of Mesozoic arc magmatism in the Andes of Peru. It is located at the western margin of the Peruvian Andes and results from the Nazca plate subduction beneath the South American plate between 4° S at the Huancabamba deflection and 18° S (**Figure 32**). The PCB is composed of >1000 plutonic bodies, cropping out over a 1600 km- long and 60 km-wide array. Along strike petrological trends in the PCB have been studied since the early 1970s and five distinct segments have been proposed from north to south: Piura, Trujillo, Lima, Arequipa, and Toquepala (**Figure 32**).

Along-arc chemical changes observed in the PCB were fundamental for developing models describing the evolution of the Pacific margin of South America (Castroviejo Bolibar et al., 2009; Dalmayrac et al., 1977; Fanlo et al., 2009; Rodrigues et al., 2010). Explanations for these trends initially included modification of the subduction style and parameters, changes in crustal thickness (Beckinsale et al., 1985; Boily et al., 1989; Cobbing and Pitcher, 1972; Mukasa, 1986), and pluton emplacement in different crustal domains (Mamani et al., 2010). The early understanding of the PCB has been extended by recent studies on structural style and orogenic evolution (Henrique-Pinto et al., 2021; Hildebrand and Whalen, 2014; Pfiffner and Gonzalez, 2013; Ramos, 2018), emplacement mechanisms and heat flow modeling (Gonzalez et al., 2020; Moore, 1984; Myers, 1975), and magma diversity as a result of the addition of subduction-related components to the mantle source, crustal assimilation, and magmatic recycling (Martínez Ardila et al., 2019a, 2019b). However, the timing of the magmatic events, the causes of

the magmatic compositional diversity along the arc, and the precise geological history of the subduction-related magmatism are some of the questions that remain unanswered.

In this contribution we: 1) assess the evidence for the previously proposed along- and across-strike trends and evaluate magmatic processes by using an up-to-date database of high quality geochemical and geochronological data, 2) document patterns of episodic magmatism to examine spatial and temporal changes covering a timespan of >170 million years along the PCB segments, 3) compare PCB-wide variation of the same parameters previously studied in the Ica-Pisco plutons (Martínez Ardila et al., 2019a, 2019b), and 4) focus on the tectonic setting, subduction parameters, magma sources, and crustal assimilation processes to explain the chemical and geochronological trends of the PCB. In addition, we use our geochemical and geochronological data to discuss some older concepts such as the superunit classification system, the relationships among plutons, the boundaries proposed for the mineralogical and chemical differences between segments, types of basement and accreted terrains, and problems associated with the scarcity of isotopic and radiometric data, especially in the northern segment, needed to establish its petrogenetic history.

Outstanding Issues About the Evolution of Arcs

To understand better continental arcs and their evolution we must consider several topics such as the magma sources and mechanisms of compositional diversity, causes of flare-ups and lulls, spatial and temporal variations, and tectonic processes driving arc evolution.

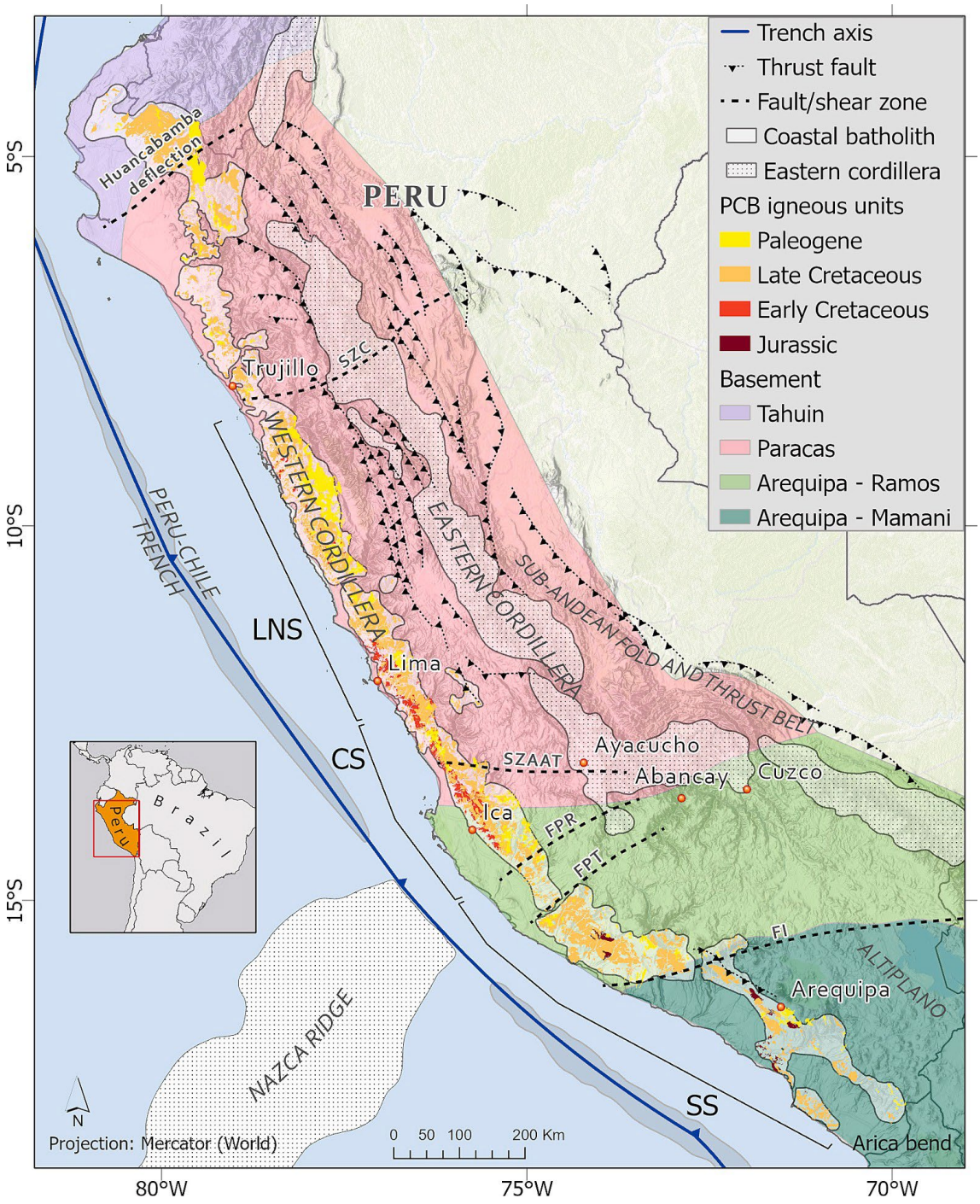

Figure 32. Simplified geologic map of the Peruvian Coastal Batholith (PCB), crustal domains, and suggested segments. Lower North Segment (LNS), Central Transitional Segment (CS), and South Segment (SS). Patacancha-Tambuco Fault (FPT), Puyentimary Fault (FPR), Iquipi Fault (FI), Contaya Shear Zone (CSZ), Shear Zone Abancay-Andahuaylas (SZAAT).

Geochemists and petrologists agree that magmatic rocks generated in subduction-related settings represent the end-product of a complex petrogenetic evolution involving multiple processes (e.g., partial melting, source contamination, crustal assimilation, magmatic mingling, mixing and recycling, and fractional crystallization) and variable contributions from depleted asthenospheric mantle, deep lithosphere, including the mantle lithosphere and lower crust, and a sedimentary component (Arndt and Goldstein, 1989; Ducea, 2001; Hildreth and Moorbath, 1988). The sedimentary component may be assimilated during magmatic differentiation and emplacement, may originate from subducted sediments or sedimentary rocks, or may be transported to the lower crust during shortening (Chapman et al., 2017). Also, changes in magma source compositions have been correlated with changes in tectonic processes which are necessary to drag crustal materials into the mantle (Castro et al., 2021; Castro et al., 2013). However, distinguishing and determining the exact proportions and mechanisms by which mantle- and crustal-derived components are involved in generating the compositional diversity of arc magmas remains challenging.

Continental arcs in the American Cordillera are characterized by patterns of episodic magmatism (de Silva et al., 2015; Kirsch et al., 2016; Paterson and Ducea, 2015). Episodicity may reflect a combination of internal feedback processes in the upper plate, mantle, or crust within the arc (Cao et al., 2016; Chin et al., 2015; DeCelles et al., 2009; DeCelles et al., 2015; Ducea, 2001), and/or external forcing by tectonic events outside the arc (de Silva et al., 2015; Hughes and Mahood, 2008; Zellmer, 2008). Linked geochemical, geochronological, and kinematic datasets from Cretaceous continental arcs suggest uncertain and variable correlations between flare-up events and convergence

rates as well as with global events of plate tectonic reorganization (Kirsch et al., 2016). These observations support the idea that episodic mantle processes play the major role for triggering and driving continental arc flare-ups (Attia et al., 2020; Martínez Ardila et al., 2019a, 2019b; Schwartz et al., 2017).

Episodic arc magmatism and spatial and temporal variations (e.g., chemical trends, arc migration, and magmatic focusing) need further study to resolve or highlight the significance of chemical and isotopic changes related to different orogenic processes (de Silva and Gosnold, 2007; Hildreth and Moorbath, 1988; Lipman, 2007). A well-studied spatial trend is exemplified by the $^{87}Sr/^{86}Sr|_i$, εNd, and εHf isotopic trends in which the radiogenic isotopic composition of magmatism becomes increasingly evolved landward of the trench. A common interpretation of this isotopic variation indicates that the spatial isotopic trends may reflect crustal assimilation or mixing between depleted asthenospheric mantle and isotopically evolved continental lithospheric mantle and/or be associated with arc migration and/or changes in crustal thickness (Chapman et al., 2017; Kirsch et al., 2016).

Review of Previous Studies

Seventy years ago, Jenks and Harris (1953) published one of the first papers referring to the Peruvian Coastal Batholith, which provided the basis for understanding the nature and origin of the PCB. This preliminary work was followed by contributions from Harrison (1960), Bellido Bravo (1969), and Stewart and Garcia (1968) who studied the central zone of the batholith near Lima.

In 1965 a geological survey was begun by British and Peruvian geologists. It resulted in a number of outstanding papers focusing on the chronology, petrology, tectonic setting and structural complexity of the PCB, and it introduced the idea of dividing the batholith into five segments. In 1975 Myers published a paper presenting the cauldron subsidence model as an important emplacement mechanism and suggested a volcanic-plutonic link for the batholith. Bussell et al. (1976) supported Myers' ideas with data from four ring complexes he studied north of Lima. Cobbing et al. (1977) explained the segmentation of the PCB as the consequence of discontinuities in the subduction zone, with magmatism in each segment possessing its own unique emplacement and spatial distribution. The same year, Dalmayrac et al. (1977) determined the first U–Pb ages from the Precambrian rocks of the southern Arequipa massif and distinguished it from the Paleozoic basement exposed in north and central Peru. He recognized the different basement rocks from north to south Peru and suggested that the Sr_i values and petrological changes along the length of the batholith were the result of magmas interacting with different types of basement.

A general summary of the segmented PCB and its geochemical character along with the associated volcanic rocks became available in 1979 when Atherton and Tarney edited a book, Origin of Granite Batholiths: Geochemical Evidence. The advance in understanding the PCB was complemented with new K–Ar, Rb–Sr, and U–Pb ages indicating that the igneous activity took place from Cretaceous to Paleocene (Beckinsale et al., 1985; Moore, 1984; Mukasa, 1984; Noble et al., 1978; Sanchez-Fernandez, 1982).

The 1965 survey, involving more than thirty British and Peruvian geologists, culminated in 1985 with the publication of the book Magmatism at a Plate Edge: The

Peruvian Andes edited by Pitcher, Atherton, Cobbing and Beckinsale. This publication included a comprehensive review of the geological setting and pre-Mesozoic history of the Peruvian Andes, addressed the concept of units and superunits, emplacement mechanisms, structure and shape of the batholith, and origin of mineral deposits, and discussed the importance of the geochronology and geochemical characteristics in identifying the magma sources.

Motivated by ideas from Pitcher's book, new researchers became interested in studying the petrological changes along the PCB. Boily et al. (1989) presented a study of the chemical and isotopic evolution of the southern PCB indicating that the parental mafic magma(s) were derived from an isotopically depleted mantle wedge above the subduction zone and that magmas experienced crustal assimilation during ascent. In order to better explore the along-arc geochemical changes and their relationship to crustal changes, Atherton and Aguirre (1992) addressed the thermal and geotectonic setting of Cretaceous volcanic rocks in relation to Andean crustal thinning. They concluded that the source of the southern volcanic rocks was old enriched mantle beneath the Precambrian Arequipa Massif, in contrast to the mantle beneath central Peru which they considered to be much younger and less enriched.

Several models were suggested to explain the mineralogical and chemical differences between the PCB segments, but it was not until after 2000 that evidence supporting the accretion of parautochthonous Paracas and allochthonous Arequipa continental terrains was linked to the geochemical changes observed in the PCB (Mamani et al., 2008; Ramos, 2018; Rodrigues et al., 2010 and Willner et al., 2014). The chemistry of the northern segment was explained as resulting from accreted terrains and the

development of a rift zone with back arc basins and volcanic arcs (Rodríguez Morante and Huanacuni Mamani, 2011). Plutons emplaced in the central segment intruded an oceanic crust of Permian-Triassic age developed by attenuation of the preexisting continental crust (Bahlburg et al., 2006; De Haller et al., 2006; Polliand et al., 2005; Ramos and Alemán, 2000). Carlotto et al. (2009) suggested that the emplacement mechanisms in the central segment were associated with the Ica, Tapacocha-Conchao-Cocachacra fault systems and plutons in this area interacted with Jurassic and Lower Cretaceous volcano-sedimentary units. On the other hand, the southern segment is influenced by the rise of magmas through thicker Precambrian and Paleozoic basement with evidence of higher crustal contamination than the other segments (Moore and Agar, 1985; Boily et al., 1989).

The most recent publications dealing with the magmatic history of the PCB include the studies developed by Martínez Ardila et al. (2019a, 2019b) and Ccallo Morocco et al. (2021). The first study included field, petrographic, geochronological, and geochemical data to unravel magma sources. It concluded that the PCB composition in the Ica-Pisco area was derived from magmas made up of approximately 65–70% mantle, 20–25% mantle source contamination from an isotopically evolved subduction component dominated by Pacific Ocean sediments, and 5–10% assimilated and recycled crustal materials. The second publication reported new geochemistry and U–Pb ages from plutons in the central segment. It was conducted within the framework of a geological survey developed by the Geological Mining and Metallurgical Institute (INGEMMET) of Peru and the China Geological Survey (CGS) between the years 2017 and 2018.

Geologic Overview

The Peruvian Andes (**Figure 32**), located between 4° S (the Huancabamba deflection) and 18° S (the Arica deflection, or Bolivian orocline), are made up of six linear geological provinces parallel to the Pacific coast (Dunbar et al., 1990; Jaillard et al., 2000; Sébrier et al., 1988; Wipf, 2006). From west to east, these are (1) Coastal Forearc, (2) Western Cordillera, (3) Altiplano, (4) Eastern Cordillera, (5) Sub-Andean Fold and Thrust Belt, and (6) Foreland Basin.

The Coastal Batholith, which is the focus of this paper, dominates the Western Cordillera. It represents a linear belt of calc-alkaline granitoids ranging from Lower Jurassic to Upper Eocene (Hildebrand and Whalen, 2014; Mukasa, 1986; Pitcher et al., 1985). In the Western Cordillera, stratigraphically and structurally continuous basins are considered to be part of a marginal basin that encompassed all of the West Peruvian Trough (Atherton et al., 1985; Cobbing, 1978). The major interconnected basins are Huarmey in the north and Rio Cañete to the south, both of which were filled with 5–9 km of Cretaceous, Tithonian-Albian, submarine basaltic, andesitic, and dacitic volcanic rocks, referred to as the Casma Group (Cobbing, 1978, 1985). It is assumed that the rocks of the Huarmey-Cañete basins were intruded by the early plutons of the Coastal batholith (Atherton et al., 1983; Atherton et al., 1985; Cobbing et al., 1977; De Haller et al., 2006; Myers, 1975). The basement for the Huarmey-Cañete Trough and the Coastal batholith in the south is the Mesoproterozoic Arequipa terrane (Casquet et al., 2010; Loewy et al., 2004; Shackleton et al., 1979). To the north, there are no exposures of the Neoproterozoic to Paleozoic basement of the Arequipa-Paracas terrane on land; however, recent exploration wells and studies of offshore islands identified Precambrian basement

underlying the Paracas terrane (Romero et al., 2013). The youngest units in the Western Cordillera correspond to remnants of several units of Cenozoic volcanic and volcanoclastic rocks that cap the Western Cordillera. These rocks range in age from at least Eocene to Quaternary and the older units show the effects of contractional deformation (Wipf, 2006).

Old Paradigms of the Architecture and Structural Framework

The PCB is made up of more than a thousand plutons in a belt that runs subparallel to the coast, extends for 1600 km, and is up to 80 km across (**Figure 32**). The batholith is described as a series of Mesozoic-Tertiary plutons, mostly classified as diorite, tonalite, granodiorite, and monzogranite. These plutons were emplaced at high crustal levels through a combination of roof-lifting and cauldron subsidence forming nested plutons and dike swarms (Haederle and Atherton, 2002; Mukasa, 1986; Myers, 1975; Pitcher et al., 1985). This area is one of the first places where cauldron subsidence was considered an important emplacement mechanism (Myers, 1975). Their interpretation was based on apparent weak, structural and thermal pluton aureoles, the lack of physical disruption of the volcanic host rock, the geometry of the typically tabular plutons with Andean-trending, assumed fault-controlled contacts, and ring dikes and nested plutons with steeply dipping sides and flat roofs (Bussell et al., 1976; Agar, 1978; Moore, 1979; Pitcher et al., 1985). Bussell and Pitcher (1985) suggested the dike swarm and nested pluton (with younger ages towards the center) shapes as evidence of batholith-normal extension during emplacement and that the magmas rose everywhere to a similarly high subvolcanic level in the crust independent of the time of emplacement.

Haederle and Atherton (2002) also suggested that the melts ascended up dike-like conduits to within 2 to 3 km of the surface, then spread laterally to form tabular plutons. Other authors like Wise (2002) and Polliand et al. (2005) favored several emplacement mechanisms including strike-slip control developed by contractional stresses and suggested a correlation between magmatism and strike-slip faulting.

Tectonic Evolution of Western Peru

The tectonic history of Peru over the Phanerozoic was one of continuous eastward subduction of the Nazca and precursor Farallon oceanic plate beneath the continental South American plate (Mišković et al. Ramos, 2009). Jaillard and Soler (1996) concluded that over the past ~200 Ma the tectonic evolution of the central and southern PCB is defined by short-lived contractional and extensional tectonic events controlled by changes in convergence rate and/or direction. Jaillard and Soler (1996) also suggested that major periods of shortening correspond to times of relatively fast convergence rates, while periods of extension are marked by relatively slow convergence rates. They based the convergence rates on global spreading rates and the contraction/extension and subsidence on stratigraphic analysis of two W-E transects in the north and south of Peru. Over time, the magmatic arc migrates towards the east. This has been explained by a decrease in dip angle, which would result in subduction erosion and subsidence of the forearc (Jaillard and Soler, 1996).

The tectono-magmatic history of the PCB as discussed by several authors (Espurt et al., 2008; Jaillard and Soler, 1996; Pardo-Casas and Molnar, 1987; Sdrolias and

Müller, 2006; Soler and Bonhomme, 1990) has been divided into four main stages illustrated in **Figure 33** and summarized below.

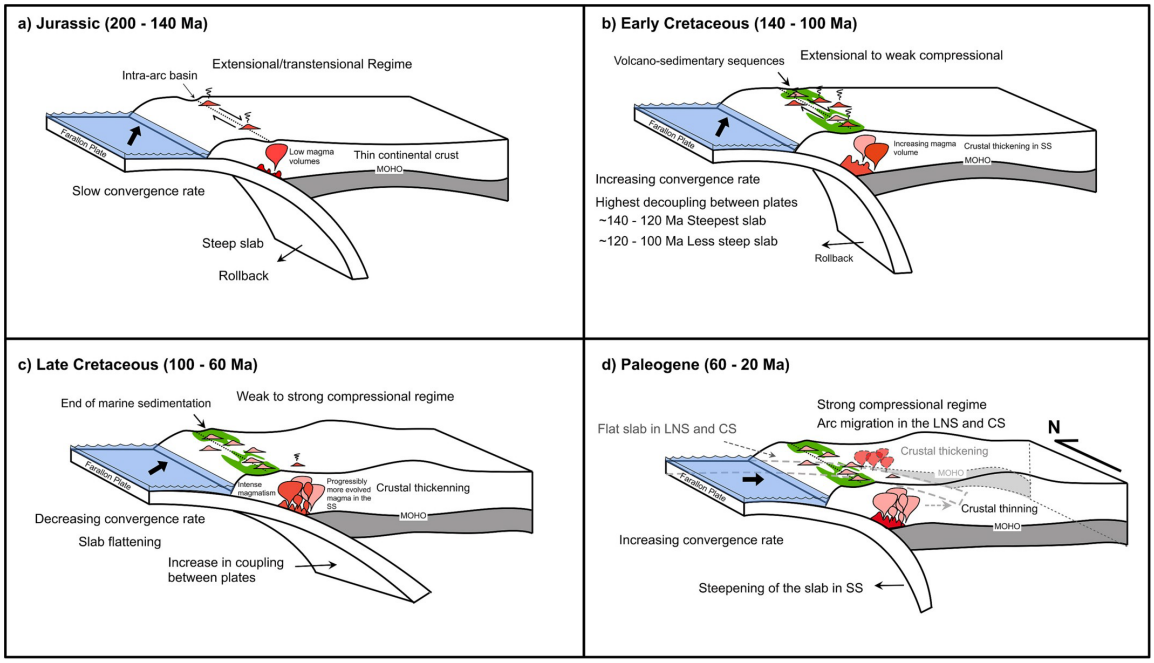

Figure 33. Tectonomagmatic evolution of western Peru. **(a)** Jurassic stage (~200–140 Ma): transtensional to extensional regime controlled by the absolute motion of the upper plate, slow convergence rate and reduced magmatism. **(b)** Early Cretaceous stage (~140–100 Ma): transition from an extensional to a weak compressional, the onset of the Andean orogeny with increasing magmatism, and marked by marine transgressions. **(c)** Late Cretaceous stage (~100–60 Ma) represent the transition from weak compressional to a strong compressional setting with decreasing convergence rates, slab flattening, increasing plate coupling, and intense magmatism. **(d)** Paleogene stage (60–20 Ma) characterized by increasing convergence rates, strong compressional regime, low magmatism and contrasting behavior between northern (flat slab, crustal thinning) and southern (steepening slab, crustal thickening) Peru.

The Jurassic-Early Cretaceous stage (~200 to 140 Ma) from Late Jurassic to Berriasian has been associated with a transtensional to extensional regime (Kay et al., 1999; Ramos, 1999) in the arc controlled by the absolute motion of the upper plate when Gondwana moved to the east, the Farallon plate convergence direction towards the N, with decoupling in the plates, and the trench rollback produced extension in the upper

plate (Daly, 1989; Ramos, 1999; Ramos and Alemán, 2000). The period of extension in the back arc at the same time is related to the break-up of Gondwana and to the Tethyan rifting. The extension is attributed to a global change in plate kinematics (Ramos and Alemán, 2000; Ramos, 2010) characterized by large-scale marine transgressions and scarce juvenile arc magmatism in intra-arc basins up to 9 km thick along the continental margin (Romero et al., 2013; Sempere et al., 2002). In northern Peru, the activity of the continental volcanic arc ceased by the end of Kimmeridgian times (~150 to 140 Ma ago, Aspden et al., 1987; Mourier, 1988; Litherland, 1994). In the back-arc areas of central Peru, scattered lava flows interbedded in Early Liassic marine sediments display alkaline chemistry, indicating that an extensional tectonic regime still prevailed in the back-arc (Regan, 1985; Romeuf et al., 1997). At the same time in southern Peru abundant arc magmatism, a rapidly evolving tectonic regime, subaerial back-arc sedimentation and local marine fore-arc deposits prevailed (Jaillard et al., 2000). These features are attributed to a steeply dipping slab, a slow oblique convergence rate, and a thin continental crust.

The Early Cretaceous stage (~140 to 100 Ma) marks the onset of the Andean orogeny characterized by the transition from an extensional to a weak contractional setting due to a complete reorganization of the paleographic pattern and tectonic evolution of the Andean margin (Ramos and Alemán, 2000). The deformed and eroded magmatic arc is then overlain by unconformable Valanginian (?) to Albian fluvio-marine deposits and the creation of a N-S trending pull-apart basin (Villagomez et al., 1996). This unconformity suggests the occurrence of a significant latest Jurassic-Early Cretaceous tectonic event (Litherland, 1994). Volcanic arc activity in central Peru

continued during part of the Berriasian times. In central and southern Peru, scarce outcrops of volcanic rocks in the coastal and western areas suggest that volcanic arc activity continued at least locally until Aptian times (Bellido Bravo, 1969; Vidal C et al., 1990). During the early Albian a multistage, extensional to transtensional subduction setting is characterized by (1) a calc-alkaline volcanic arc marked by a marine transgression culminating in the late Albian or early Cenomanian. (2) The intense volcanic activity in the magmatic arc and the beginning of upper-crustal magmatic intrusions. (3) Early Cretaceous plutons intruded folded Jurassic to Early Cretaceous volcaniclastics, indicating a contractional phase in the Early Cretaceous. In northern Peru, the NW trending magmatic arc in the Late Tithonian represents evidence for a drastic change in the convergence direction towards NE. During this phase, a change from a slow to fast convergence rate occurs (2–15 cm/yr) (Jaillard and Soler, 1996; Soler and Bonhomme, 1990).

A Late Cretaceous stage is characterized by the transition from a weak to strong contractional setting starting at ~100 Ma. This is marked by local folding and faulting, the end of marine sedimentation, and intense magmatic activity (Soler and Bonhomme, 1990). The contractional setting led to the emplacement of the bulk of the PCB between about ~100 Ma and 60 Ma (Hildebrand and Whalen, 2014; Mukasa, 1986; Pitcher et al., 1985). The change from marine sedimentation of the Jurassic and Early Cretaceous to continental sedimentation in the Late Cretaceous documents uplift, which is thought to be caused by contraction. The early Coniacian was characterized by a strong contractional tectonic regime, a progressive change of slab dip from ±45° to ±30°, and changes in convergence rates from slow to rapid to slow again (65–55 Ma: 5–7 cm/yr; 50–37 Ma:

>10 cm/yr; 36–25 Ma: ~5 cm/yr). Crust continues to thicken due to tectonic shortening, causing extensive folding and reverse faulting (Dalmayrac et al., 1977; Pfiffner and Gonzalez, 2013). This phase is marked by shallowing subduction angle with variable changes in convergence rate (Mégard, 1984; Pardo-Casas and Molnar, 1987; Ramos and Alemán, 2000; Soler and Bonhomme, 1990). During this phase, large volumes of volcanic and plutonic rocks were emplaced all along the Peruvian margin (Jaillard et al., 2000).

The final stage starts in the Paleogene and is characterized by a strong contractional regime, a relatively flat slab dip of 30° for north and central Peru, but steeper subduction at ~40° in southern Peru. At ~24 Ma the convergence rate is rapid again (>10 cm/yr). A change in convergence direction from N to NE occurred in the Paleocene with a fast pulse in the Eocene between 55 and 40 Ma (Sdrolias and Müller, 2006). The major Late Eocene shortening phase is marked by a significant eastward shift of the magmatic front and migration of the arc (Jaillard and Soler, 1996). The magmatic belt records no changes in subduction parameters until the end of the magmatic activity in central Peru at ~3 Ma.

High rates of tectonic erosion of the overriding plate and the end of volcanism in central Peru have been linked to a low subduction angle related to the subduction of the Nazca ridge (Gutscher, 2002). In the Andes, the variation in the angle of subduction between the different segments is attributed to changes in slab buoyancy. Flattening due to the effect of the collision of aseismic ridges or steepening caused by the displacement towards the south of the collision zone (Ramos and Folguera, 2005).

The link between magmatism and tectonic settings and subduction parameters in the Andes have been discussed by several authors. For example, Bussell and Pitcher (1985) concluded that periods of rapid convergence coincided with enhanced PCB magmatic activity and suggested a relationship between the time of magmatic pulses and the concurrent relative plate motion between the South American and Nazca plates. However, other authors have found that the magmatic pulses are not always directly linked to contractional deformation events and that the emplacement of the PCB took place during slow convergence (Jaillard and Soler, 1996; Soler and Bonhomme, 1990). More recently, Jaillard et al. (2000), Pfiffner and Gonzalez (2013), and Kirsch et al. (2016) presented evidence that the PCB magmatic pulses are not directly linked to contractional deformation events nor known subduction parameters.

The PCB Basement

A study of tectonic events affecting the continental margin of Peru suggests a strong influence from the Precambrian Arequipa and Paracas terranes that collided with the Amazonian craton (Carlotto et al., 2009; Mišković et al., 2009; Ramos, 2009; Ramos, 2018), as well as subsequent contrasting Paleozoic evolution (**Figure 32**).

The Arequipa allochthonous terrane was first recognized by Dalmayrac et al. (1977, 1980). Seismological studies of Dorbath (1996) together with the gravimetric, geochemical, and isotopic analyses of Mamani-Huisa (2006) and Mamani et al. (2008, 2010) outlined the extent of this cratonic block. A consensus finds that the Arequipa Massif, as part of the Arequipa terrane with a protolith age of ~2000 Ma, was first accreted in the late Mesoproterozoic during the amalgamation of the Rodinia

supercontinent (Loewy et al., 2004; Reimann et al., 2010). During the Ordovician it was reactivated, when a back-arc basin formed along the old Mesoproterozoic suture (Díaz-Martínez et al., 2001; Sempere et al., 2008). This weak suture zone accompanied the emplacement of Late Paleozoic and Oligocene-Early Miocene granites during extensional regimes, and even controlled the crustal delamination at late Cenozoic times (Beck and Zandt, 2002; Jiménez and López-Velásquez, 2008).

In central Peru, the story is different for the 1158 Ma parautochthonous Paracas terrane (Keppie and Ortega-Gutiérrez, 2010). The Paracas block collided during Early Ordovician against Gondwana at ~465 Ma and reactivated during Eopaleozoic extension that reopened the old suture to form oceanic crust between Amazonia and Paracas (Ramos, 2008). The subduction of this oceanic crust developed a magmatic arc which is preserved in the Eastern Cordillera of Peru. The presence of a cratonic block underlying the Western Cordillera and adjacent offshore was demonstrated by the studies of Romero Fernández et al. (2011), who confirmed a Precambrian basement underlying the Paracas terrane. Romero et al. (2013) and Ramos (2018) suggested that large parts of this basement have been eroded away by subduction erosion. During most of the Jurassic an extensional regime dominated the western margin of Peru and developed rift basins in the hanging-wall of the terrane sutures. The Peruvian Late Cretaceous orogeny produced the emplacement of the Coastal batholith, the beginning of deformation along the coast, and the first foreland basins.

The Arequipa and Paracas terranes are the most studied areas of the pre-PCB basement. In contrast, the Tahuin basement in the northwest region lacks geophysical, geochemical, and geochronological studies leading to disagreement about its tectonic

evolution. This block was considered by Feininger (1987) and Mpodozis and Ramos (1989) as an allochthonous Paleozoic terrane accreted during Cretaceous times, based on the comparison with the Paleozoic sequences exposed in southern Ecuador and on paleomagnetic data. Another interpretation, based on the U/Pb and Ar–Ar dating of metamorphic rocks, suggests that the Tahuín terrane collided against the Gondwana margin during the Alleghanian orogeny, possibly as a part of Laurentia, and it was left on the Gondwana margin after being detached from Laurentia (Cardona et al., 2005 ; Ramos, 2009). Other authors interpreted the Tahuín terrane as an autochthonous part of Gondwana (Bellido et al., 2009; Timoteo et al., 2012). New studies by Witt et al. (2017) in the Tahuin terrane indicate that this block collided against the Gondwana margin in the Early Permian after the docking of the Paracas terrane.

An understanding of the nature and evolution of the pre-PCB basement is still controversial, in spite of contributions from previous researchers. Therefore, one objective of this paper is to provide new data to identify magma sources, the role played by the different types of basement, and their direct relationship with the mechanisms of compositional diversity for the central and southern segments.

Segmentation and Superunits of the PCB

The south-to-north and west-to-east chemical variation of the PCB encouraged Cobbing and Pitcher (1983) to group the intrusive units within segments using the concept of "superunit". As a result, five distinct segments were proposed on the basis of compositional differences and named, from south to north: Toquepala (18–16.5° S), Arequipa (16.5–12° S), Lima (12–9° S), Trujillo (9–6.5° S), and Piura (6.5–4° S)

(Cobbing and Pitcher, 1972; Taylor, 1973; Regan, 1976; Cobbing et al., 1977; Cobbing and Pitcher, 1983).

The superunit concept was intended to identify distinct periods of magmatic activity characterized by distinct histories. This concept was used to infer a close genetic connection between all plutons within a superunit, which has some regional support from the detailed geochemical studies. However, this grouping system relied on poorly dated units resulting in disagreements about names of units (e.g., Instituto Geológico Minero y Metalúrgico Bulletins; Tosdal et al., 1981; Kaneoka and Guevara, 1984; Ellison et al., 1989; Mukasa, 1986, Mukasa, 1986; Clark et al., 1990; Quang et al., 2005). Also, dating from the various segments of the batholith demonstrated that plutons within individual proposed superunits were not always contemporaneous (Martínez Ardila et al., 2019a, 2019b; Moore and Agar, 1985; Mukasa, 1986). Despite the problems associated with the concept of superunits, this classification system continues to be used today to facilitate comparisons.

Recently, Ccallo Morocco et al. (2021) suggested reducing the previously proposed 5 PCB segments to only three: Piura (4–6° S), Lima (6–14.5° S), and Arequipa (14.5–18° S) and two transition zones between segments: Trujillo-Chiclayo (6–8.5° S) and Chaparra-Caraveli (14.5–16° S). The boundaries between PCB segments coincide with ancient fault zones where rifting during the Permo-Triassic and the Jurassic controlled basin formation, magmatism, and mineralization (Carlotto et al., 2009). For example, the boundary between the Piura and Trujillo segments is the Huancabamba deflection, a major oroclinal bend (Mitouard et al., 1990; Mourier, 1988). The boundary between the Trujillo and Lima segments is defined by NW-SE faults of the Contaya shear

zone (Carlotto et al., 2009; Zelasco, 2011). The boundary between Lima and Arequipa segments is defined by the NW-SE Iquipi fault system.

Synthesis of Datasets

Geochronology Data

The available geochronological data for the PCB were obtained from K–Ar isochron ages on hornblende and biotite (Clark et al., 1990; Litherland, 1994; Martínez Valladares and Cervantes Gárate, 2003; Moore, 1984; Stewart et al., 1974), Rb–Sr whole rock isochron ages (Beckinsale et al., 1985; Sanchez-Fernandez, 1982), U–Pb whole rock (bulk zircon) ages (Mukasa, 1986), and U–Pb zircon ages (Ccallo Morocco et al., 2021; Martínez Ardila et al., 2019a, 2019b and Santos et al., 2016). These methods all have limitations: (1) K–Ar ages are often cooling and/or reheating ages and don't necessarily provide information on original pluton crystallization times; (2) Rb–Sr ages may represent mixed isochrons of different minerals derived from different magmas; (3) Rb–Sr ages are greatly affected by hydrothermal processes; and (4) many of the early U–Pb zircon ages were whole-rock, multi-grain zircon ages that average different zircon populations from a single sample.

The available geochronological data from igneous units (Supplementary Data) supports the idea that the PCB was constructed by several magmatic pulses during the north-eastward migration of the arc from ~200 to 20 Ma (**Figure 34**). In addition, Martínez Ardila et al. (2019a, 2019b) and Voos et al. (2021) used U–Pb zircon ages to document three flare-ups (**Figure 34 (a)**) for the central transitional segment over 80 My: (1) ~136–126 Ma, (2) ~120–80 Ma, and (3) ~70–56 Ma, younging towards the northeast.

These ages were compared to ages found in the north segment, 100–95, 95–90, 90–70, and 70–50 Ma (Bussell and Pitcher, 1985; Myers, 1975), and suggested a synchrony of the described younger flare-ups along the two arc segments (Martínez Ardila et al., 2019a, 2019b).

Synthesis and New Ages

To supplement the available geochronological data for the PCB, we present 29 new U–Pb single zircon ages from plutonic samples obtained at the University of Arizona Laserchron Center. Measured 20 μm beam spots included cores and rims when textural complexity was identified in the zircons. Most of the U-Th/Pb isotopic measurements were performed by Element 2 single-collector laser ablation-inductively coupled plasma mass spectrometry (LA-ICP-MS) followed the procedure outlined by Gehrels et al. (2008) and Johnston et al. (2009). Final ages reported and discussed throughout this paper are concordia ages calculated using the Isoplot Excel® macro of Ludwig (2003). Ages given in the text and figures are quoted at a 2σ confidence level. All geochronological data are included in supplementary material, and errors are reported at ±2σ (see the Supplementary Data).

Petrology and Geochemistry

Previously recognized along-arc chemical trends from south to central Peru include decreasing K_2O (Cobbing, 1985) and Sr_i values (Beckinsale et al., 1985; Boily et al., 1989; Winter, 2008) and increasing $^{206}Pb/^{204}Pb$ isotope ratios (Mukasa, 1984). For example, it is suggested that in the southern segment the rise of magmas through thicker

Precambrian and Paleozoic basement of the Arequipa terrane (Couch et al., 1981; Jones, 1981) results in higher crustal contamination indicated by more evolved Sr_i and Pb isotope data (Beckinsale et al., 1985; Boily et al., 1989 and Mukasa, 1986). The central segment is characterized by a larger proportion of gabbro, with most gabbro plutons occurring along the western flank, and by a diversity of more siliceous rocks including quartz diorite, tonalite, granite, and monzogranite (Regan, 1985), all with primitive isotope ratios (Beckinsale et al., 1985; Boily et al., 1989; Martínez Ardila et al., 2019a, 2019b; Mukasa, 1986). More limited contamination in the central segment has been explained as the result of magmas interacting with a different type of basement, in this case the Mesoproterozoic Paracas terrane (Mamani et al., 2010; Petford and Atherton, 1995).

Across-strike petrological changes have also been described for the south and central segments. The high Pb-isotope ratios indicate that subducted sediments were incorporated into the mantle sources (Couch et al., 1981; Martínez Ardila et al., 2019a, 2019b and Mukasa, 1986). Martínez Ardila et al. (2019a, 2019b) suggested that the across-arc chemical variation in the Ica-Pisco plutons of the central segment resulted from three magma sources consisting of the mantle reservoir, subducted sediments, and old continental crust, with different degrees of contamination by subducted sediments at the mantle source and crustal assimilation during magma transport and emplacement. These geochemical variations from older western to younger eastern plutons show an initial decrease in the mantle component, a general increase in the isotopically evolved component, and an initial increase and later decrease in the volcanic and plutonic host rock components.

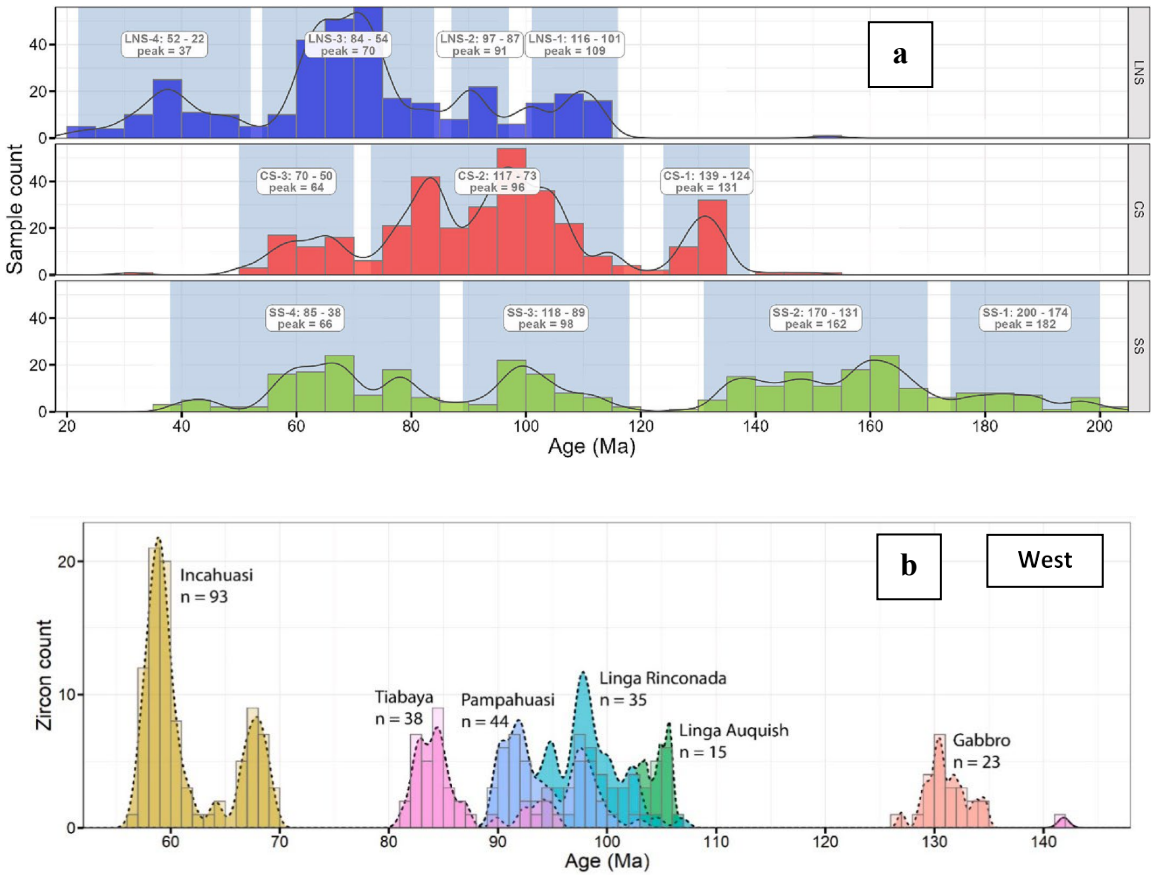

Figure 34 **(a)** Igneous bedrock age spectra histogram and kernel density estimation depicting flare-ups across the Lower North Segment (LNS), Central Transitional Segment (CS), and South Segment (SS). The sample ages are a combination of measured U–Pb ages and geochemistry samples that have K–Ar, Rb–Sr, Ar–Ar, and estimated ages. Age data are smoothed by randomizing around a ± 10 Ma range to reduce spikes in estimated ages. Where no measured age is available for a geochemistry sample, the age is estimated from the geological unit it was taken from. Note that vertical height has not significance for magma volumes. **(b)** Igneous bedrock U–Pb age spectra of 248 individual zircons from 9 samples collected from the Peruvian Coastal Batholith near Ica, adapted from Martínez et al. (2019).

Synthesis of Geochemical Data

Our geochemical dataset (see the Supplementary Data) comes from integrating new with published data. The INGEMMET database that became available in 2021 (http://metadatos.ingemmet.gob.pe:8080/geonetwork/srv/eng/catalog.search#/home) is

complemented with the most recent dataset published by Martínez Ardila et al. (2019a, 2019b), plus new geochemical data. We present new whole-rock geochemical data of major and trace elements from >1000 samples, and Sr, Nd, and Pb isotope ratios from 87 samples of the PCB (see the Supplementary Data) in **Figures 35-39**. New whole rock samples were analyzed for major element chemistry at the ALS laboratories using a Thermo Jarrell Ash Enviro II simultaneous and sequential ICP with a detection limit from 0.001 to 0.01% for major elements, from 0.002 to 0.05 ppm for REE, and from 0.01 to 20 ppm for other trace elements. Two instrumentation techniques were used by ALS Laboratories to obtain the chemical data: ICM90A using sodium peroxide fusion analyzed via ICP-MS for trace elements, and ICP95A using lithium metaborate fusion analyzed via ICP atomic emission spectroscopy (AES) for major and some trace elements. The isotopic ratios of $^{87}Sr/^{86}Sr$ and $^{143}Nd/^{144}Nd$ and the trace element concentrations of Rb, Sr, Sm, and Nd were measured by thermal ionization mass spectrometry in the Geochronology and Thermochronology Lab of the University of Arizona and were performed on a VG Sector TIMS instrument using the techniques described by Ducea (1998) and Otamendi et al. (2009). The common isotopes of lead were analyzed on separate batches of dissolved samples. Lead was extracted using an anion exchange procedure modified after Chen and Wasserburg (1981).

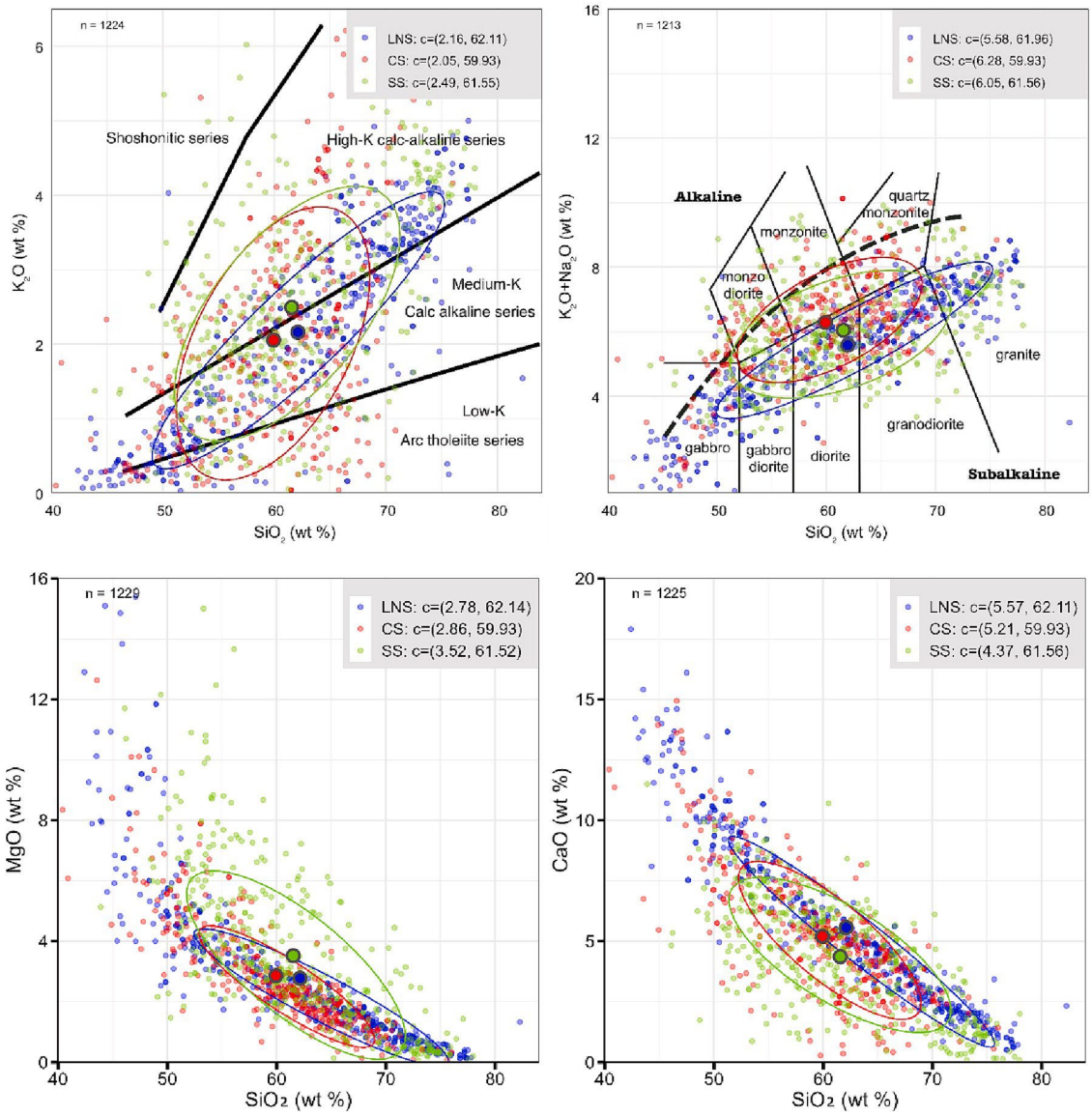

Figure 35. Harker diagrams of selected major oxides for the PCB segments using our suggested boundaries: South Segment (SS), Central Transitional Segment (CS), and Lower Northern Segment (LNS). Datasets includes plutonic and associated volcanic rocks. Statistical analyses were run on the compiled datasets to calculate the mean for identifying trends and evaluate the boundaries for each segment (Supplementary Data 1). The ovals are used in the plots to emphasize the different trends of the plutons.

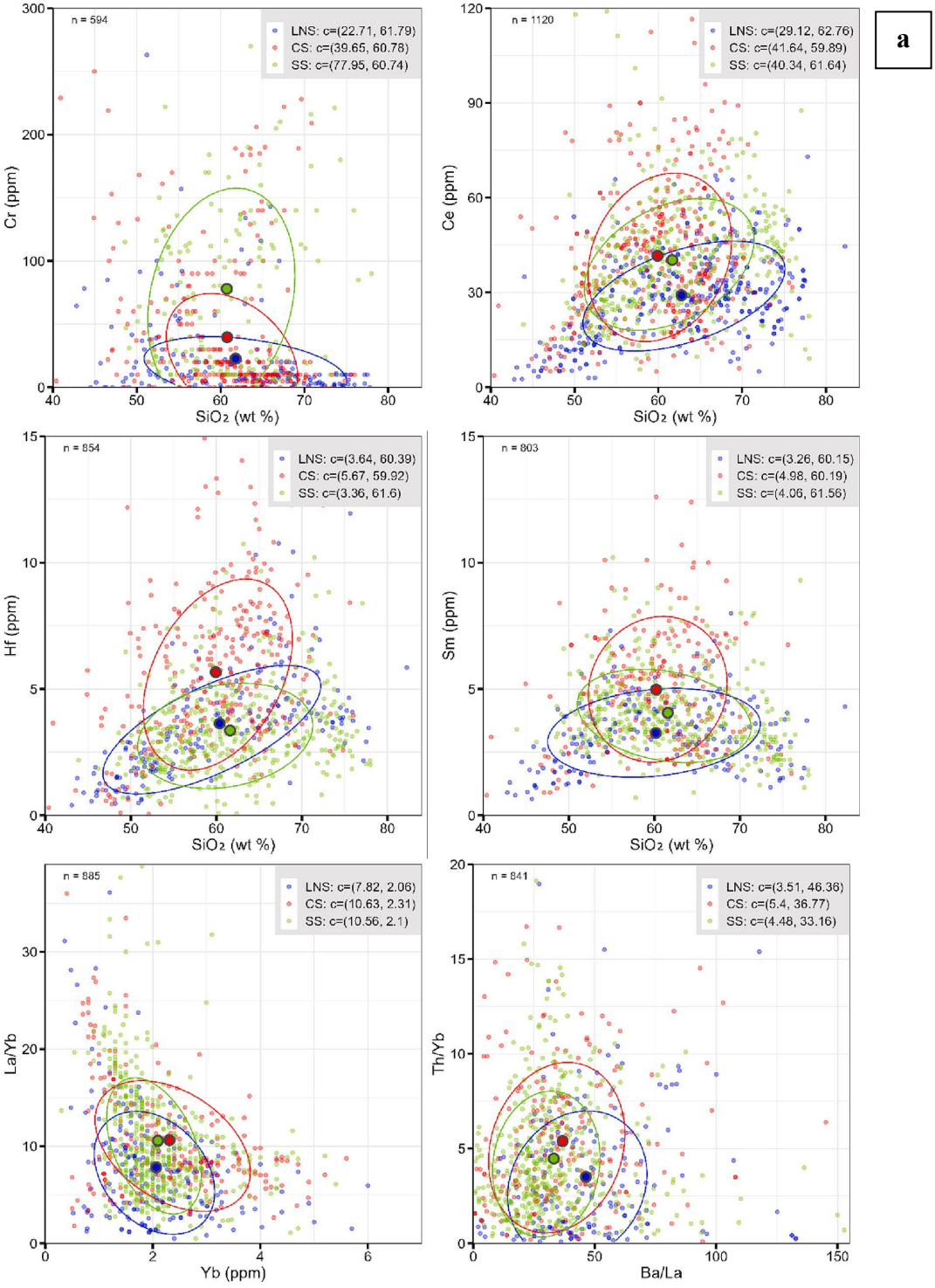

Figure 36. **(a)** Along-arc Harker diagrams trace elements for the PCB using our suggested boundaries: South Segment (SS), Central Transitional Segment (CS), and Lower Northern Segment (LNS). Statistical analyses were run on the compiled datasets to calculate the mean for identifying trends and evaluate the boundaries for each segment (Supplementary Data). **(b)** Along-arc REE multielemental. Primitive mantle (P-mantle) normalization data are from Sun and McDonough (1989).

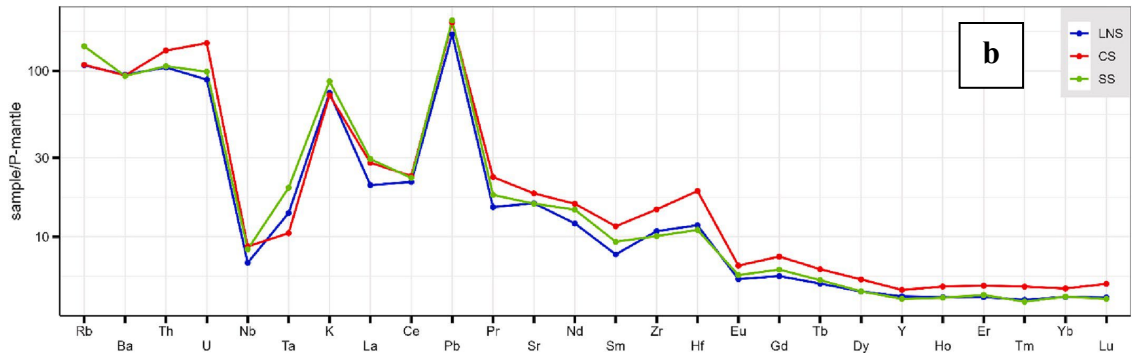

Figure 36. (continued).

We use quartz $\delta^{18}O$ values to estimate the primary oxygen isotopic composition in our analysis. Oxygen isotopes were analyzed using the laser fluorination method of Sharp (1990) and a ThermoFinnigan DeltaPlus XP mass spectrometer at IIRMES, California State University, Long Beach. Quartz is the major rock forming mineral in intermediate to felsic igneous rocks that is most resistant to subsolidus isotopic exchange as the result of hydrothermal processes (Gregory et al., 1989). The 65 samples chosen for this study contain rock-forming mineral assemblages that meet the criteria of $^{18}O/^{16}O$ equilibrium using the method of Javoy et al. (1970).

Spatial and Temporal Variations

Previous investigations focused on the geochemical trends of the Lima and Arequipa segments (**Figure 32**). For this reason, less information is available for the Piura, Trujillo, and Toquepala segments, so this limits our ability to compare all the PCB segments and requires a different approach to synthesize the PCB data.

Statistical analyses were run on the compiled datasets to calculate the mean for identifying trends and evaluate the boundaries for each segment. Limited age and chemical

data for the upper northern PCB (4–8° S) makes it difficult to identify temporal and chemical trends and is not included in this study. Our suggested along-arc segments are lower northern (LNS at 8–12.5° S), central transitional (CS at 12.5–15° S), and southern (SS at 15–18.4° S), and across arc zones are west-to-east distance. For these divisions of the PCB, we will study different flare-ups based on U–Pb zircon ages (200–20 Ma). The suggested new boundaries are based on the mean of chemical proxies and abrupt changes in the distribution of samples. In a first approach, **Figure 34 (a)** displays the geochronological data used to define the flare-ups and **Figures 35** through **39** display the chemical data using our suggested boundaries.

Figures 35 through **39** summarize the variation of geochemical parameters along- and across-arc in the PCB. The PCB chemical signature is predominantly metaluminous with calc-alkaline affinities. The chemical differences along-arc segments are recognized by changes in the following proxies: K_2O, CaO, MgO, Cr, Ce, Hf, Sm, and La/Yb elements, and Sr_i, $\delta^{18}O$, and Pb isotopes. The chemical changes can be grouped in two categories: (1) elements that decrease from the SS to the LNS, K_2O (2.5 to 2.13 wt%), MgO (3.51 to 2.78 wt%), Ce (40.42 to 29.12 ppm), La/Yb (10.58 to 7.84), Sr_i (0.758 to 0.704), and $\delta^{18}O$ (8.85 to 8.38); and (2) elements that increase from the SS to the LNS, CaO (4.36 to 5.57 wt%), and εNd (-0.87 to 2.53). The changes identified reveal that the SS is significantly different from the LNS. In addition, we conclude that the CS between 12.5° S and 15° S is a transitional boundary between the LNS and SS, because it exhibits gradual changes for most of the chemical proxy values. The CS is distinguished by having the highest values of Hf (5.64 ppm), Sm (4.98 ppm), Th/Yb (5.39), and $^{207}Pb/^{204}Pb$ and $^{206}Pb/^{204}Pb$ isotopes (15.64 and 18.68 respectively) in the PCB. In general, from S to N there is a decrease of K_2O, MgO, Cr, Ce, La/Yb, Sr_i, and $\delta^{18}O$ and an increase of CaO and εNd (**Table 4**). Quartz $\delta^{18}O$ values from

the northern segment range from +7.1‰ to +9.7‰ (n = 24), with an average of 8.38‰ (**Figure 37 (b)**). These values are consistent with whole rock $\delta^{18}O$ values (between +5.7‰ and + 7.6‰, n = 11) reported by Beckinsale et al. (1985) from the 65 Ma Cañas/Sayan plutonic complex at Rio Huaral in the LNS. The CS exhibits slightly higher average quartz $\delta^{18}O$ values (+8.68‰, this study and Gonzalez et al., 2020) than the LNS with a range of +7.3‰ to +9.7‰ (n = 24). SS rocks have a bimodal distribution of oxygen isotope values that are age dependent (**Figure 40**). Plutons older than 120 Ma have quartz $\delta^{18}O$ values that average + 10.0‰ (n = 8) and a range of +8.4‰ to +12.0‰. In contrast, plutons younger than 120 Ma have lower and more homogeneous quartz $\delta^{18}O$ values (+7.7‰ to +8.5‰, n = 9) that average + 8.1‰.

The across-arc, west-east trends of the PCB were defined using perpendicular distance of samples from the Andean foothills. The western zone is <30 km from the beginning of foothills; the central zone is between 30 and 60 km; and the eastern zone is >60 km. Again, the chemical changes can be grouped in two categories: (1) elements and isotopes that decrease from W to E, CaO (5.85 to 4.3 wt%), MgO (3.83 to 2.53 wt%), Cr (48.05 to 41.04 ppm), εNd (1.55 to 0.61), and $^{206}Pb/^{204}Pb$ (18.68 to 18.37); and (2) elements and isotopes that increase from W to E, K_2O (1.78 to 2.69 wt%), Ce (33 to 46.6 ppm), Hf (4.18 to 4.51 ppm), Sm (4.09 to 4.45 ppm), La/Yb (7.89 to 12.51), Th/Yb (3.56 to 5.06), $\delta^{18}O$ (8.46 to 8.99), Sr_i (0.7047 to 0.7057). The central zone exhibits gradual changes for most of the chemical proxies, but lower values of MgO (2.16 wt%), Cr (33.58 ppm), and Hf (3.81 ppm). A general trend from W to E is the decrease in CaO, MgO, εNd, and $^{206}Pb/^{204}Pb$, and an increase of K_2O, Ce, Hf, La/Yb, Sr_i, and $\delta^{18}O$ (**Table 5**).

Primitive mantle-normalized multielement patterns along- and across-arc segments of the PCB (**Figures 36 (b)** and **39 (d)**) observe strong negative anomalies for Nb and positive for K and Pb, enrichment in large-ion lithophile elements (LILEs), light rare earth elements (LREE), and depletion in heavy rare earth elements (HREE). Slightly LILE enriched patterns are observed for the SS and CS with respect to the LNS. These segments show an enrichment of LILEs (e.g., Rb, K, Sr, Pb, Eu) and high- field strength elements (HFSEs) (e. g., La, Th, U, Hf, Nb) compared to the LNS. Across-arc trends for the C and E zones are slightly more enriched in large-ion lithophile elements (LILEs) (e.g., Rb, Ba, Th, K), but more depleted in heavy rare earth elements (HREE) (e.g., Ho, Er, Tm, Yb) than the W zone.

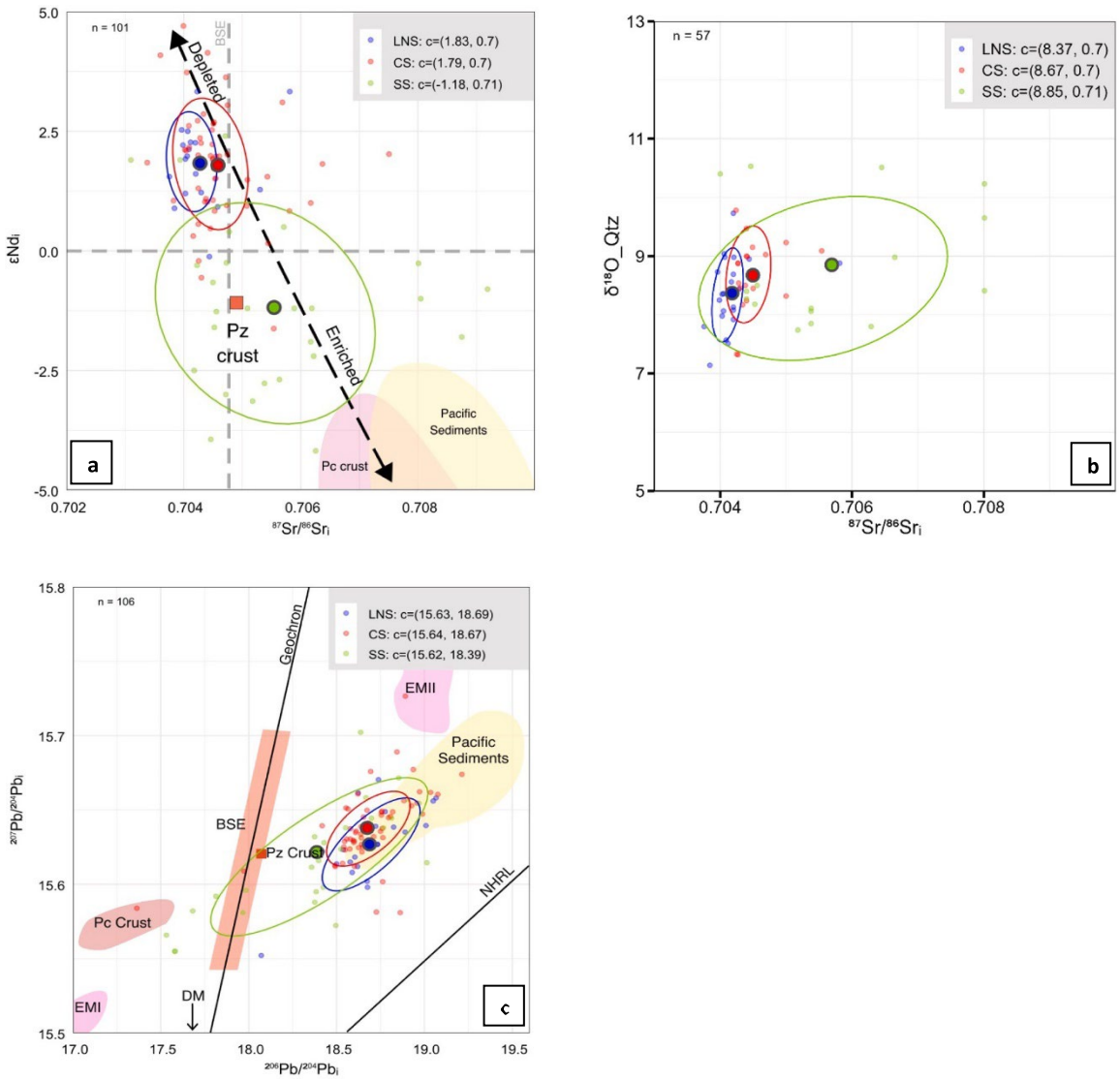

Figure 37. Isotopes along the arc **(a)** Isotope ratios of Nd and Sr. The data show a slight increase of Sr_i towards younger and more evolved plutons. Paleozoic (Pz) and Precambrian (Pc). **(b)** $\delta^{18}O$ for quartz. Note the slight increasing trend from LNS towards the CTS and SS. **(c)** Magma sources and variation of $^{207}Pb/^{204}Pb_i$ versus $^{206}Pb/^{204}Pb_i$. For comparison, five fields are included: depleted mantle (DM), Pacific sediments and Precambrian and Paleozoic crust. The line labeled NHRL (Northern Hemisphere Regression line) denotes the approximate lower limit of mid-ocean ridge basalt (MORB) Pb isotopic signatures. Pacific Sediment data is from Reynolds and Dasch (1971) and Chow and Pattersonc (1962); Precambrian crust data from Mukasa (1986); mantle reservoir data from Zindler and Hart (1986), and our data.

Age Spectra for the PCB

The measured bedrock U–Pb crystallization ages from mafic and felsic compositions for the PCB yield the flare-ups depicted in **Figure 34 (a)** for ages between 200 and 20 Ma for the three segments (Supplementary Data). Four flare-ups were identified in the PCB lower north segment (LNS-1, LNS-2, LNS-3, LNS-4), three in the central transitional segment (CS-1, CS-2, CS-3) and four in the south segment (SS-1, SS-2, SS-3, SS-4). Our results reveal a general trend of northward and eastward younging ages. The spatiotemporal trend shows magmatism migrating from S to N, with an Early Jurassic flare-up (~200–174 Ma) identified in the SS and a late Paleogene flare-up (~52–22 Ma) identified in the LNS. This study reveals along-arc variation during periods of increased magmatic activity, where flare-ups are temporally offset between neighboring segments. Older flare-ups started first in the SS. This S to N trend represents a W to E migration of the magmatic arc as well (**Table 5**).

West to East Arc Migration for Plutons Near Pisco

U–Pb zircon ages for the PCB shown in **Figure 32** show that arc magmatism migrated from west to east. Specifically, we have studied this west to east migration in the Pisco area.

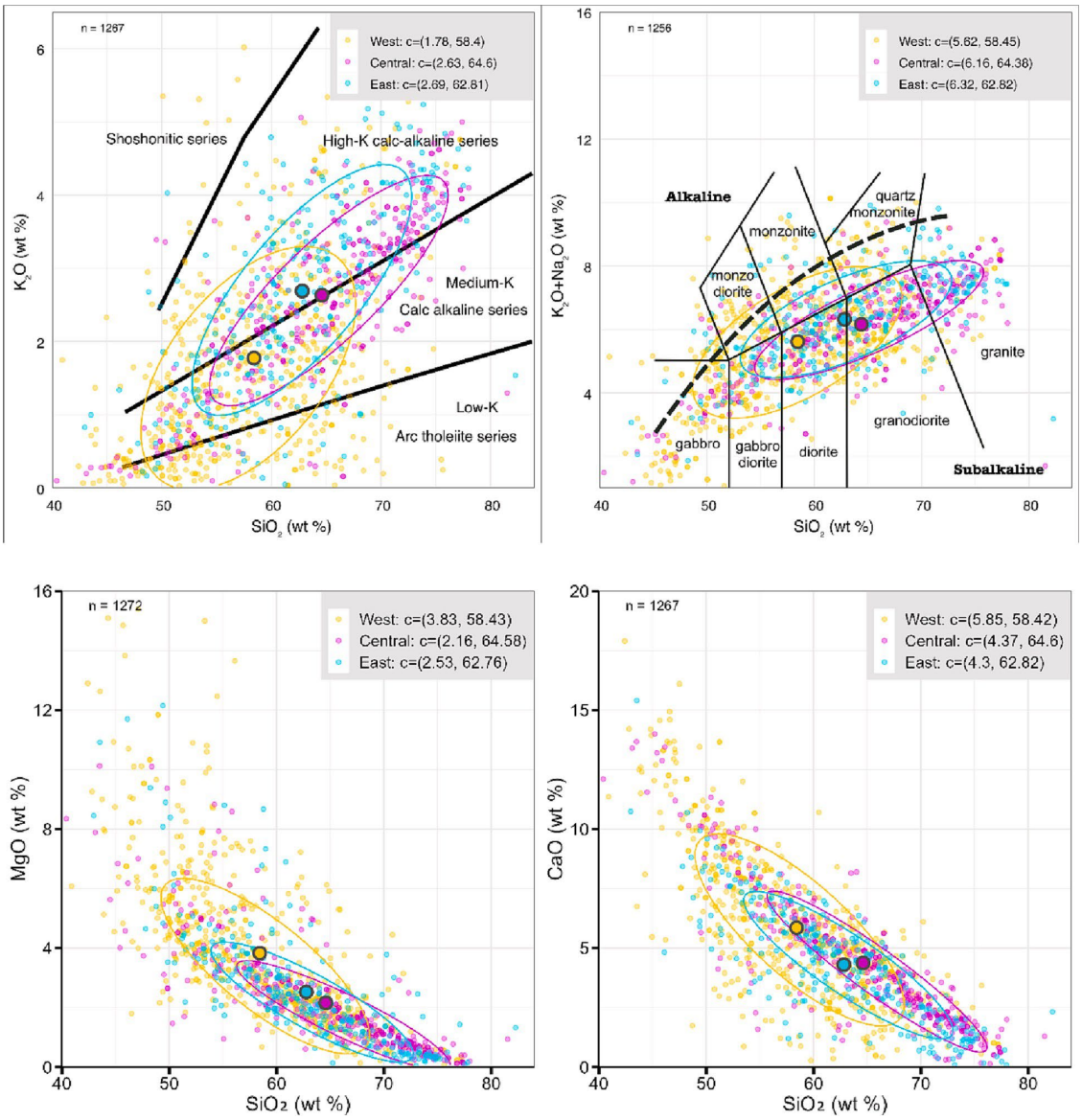

Figure 38. Harker diagrams of selected trace elements for the PCB across-arc segments using our suggested boundaries: West, Central, and East. Datasets include plutonic and associated volcanic rocks. Statistical analyses were run on the compiled datasets to calculate the mean for identifying trends (Supplementary Data 1).

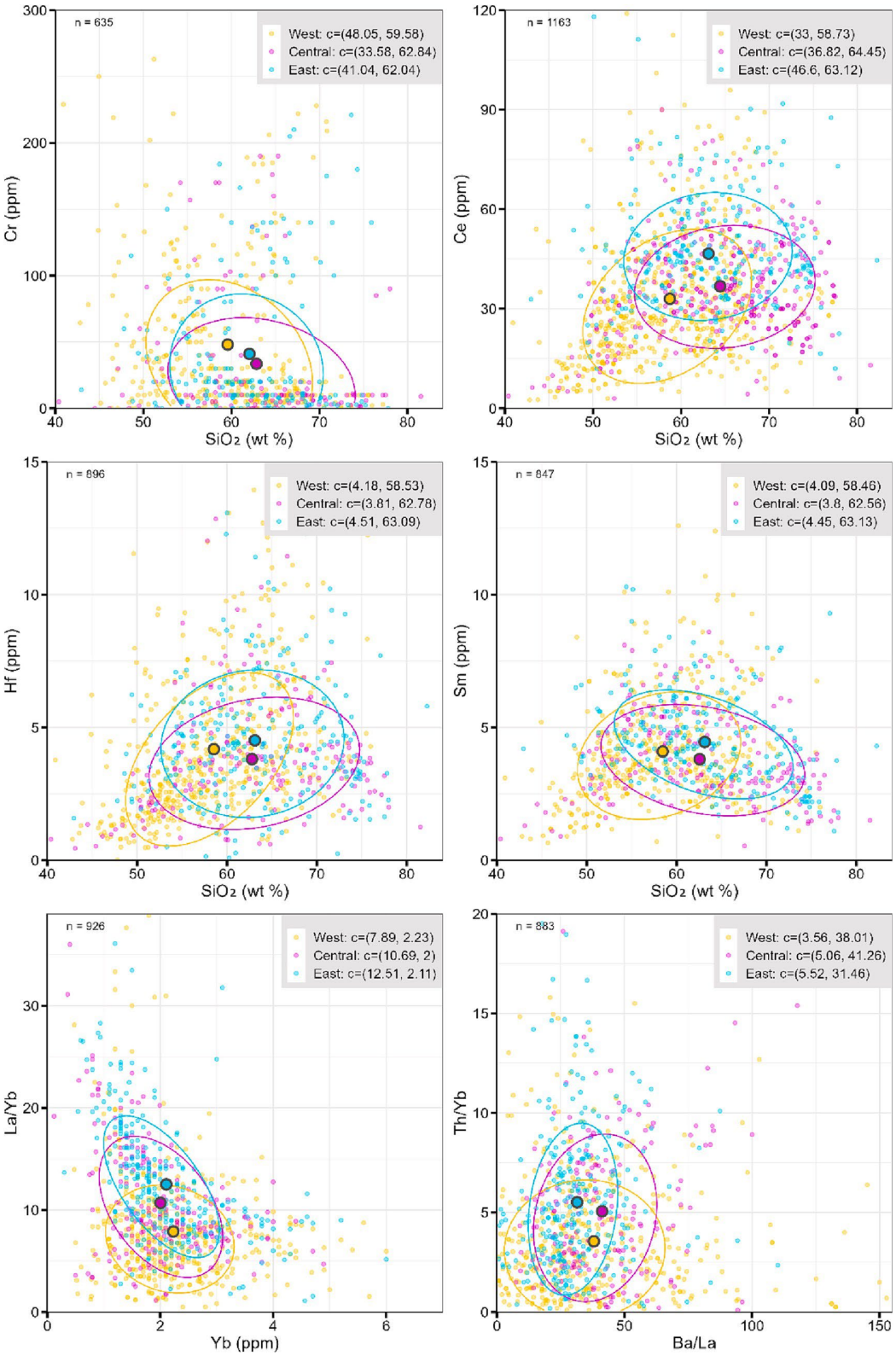

Figure 38. (continued).

U–Pb zircon ages published by Martínez Ardila et al. (2019a, 2019b) displayed the W to E migration of the magmatic arc in the CS of the PCB. **Figure 34 (b)** displays U–Pb zircon ages plotted as the 248 individual zircons that make up 9 igneous bedrock samples averaging about 25 zircons each. The order of crystallization for major units of the Ica-Pisco plutons started in the W with gabbro-diorite plutons in the Early Cretaceous (131.0 Ma), followed by Linga Auquish (104.8 Ma), Linga Rinconada (98.3 Ma), Pampahuasi (97.8 and 91.4 Ma), Tiabaya (85.3 and 84.4 Ma) and finally in the E with Incahuasi (68 and 58 Ma) in the Early Paleogene.

Moho Depth Calculations for Crustal Thickness

Present-day crustal thickness for the Central Andes decreases from 60 to 65 km in the SS and CS at about 8–12° S to 40–45 km in the LNS at about 12–7° S (James, 1971; Schmitz, 1994; Dorbath, 1996; Swenson et al., 2000). Present-day crustal thickness increases from west to east in the LNS and CS from ~20 km up to 45 km, and in the SS from 40 km up to 60 km (Schellart, 2017). Crustal thickness is hard to estimate for past geological times; however, it appears that the Central Andean crust underwent significant thinning up until 90 Ma (Sempere et al., 2002), slowly started thickening after 90 Ma, and experienced a significant thickening after 30 Ma in association with tectonic shortening (e.g., Ganne et al., 2017; Garzione et al., 2008; Gregory-Wodzicki, 2000; Isacks, 1988; Mamani et al., 2010).

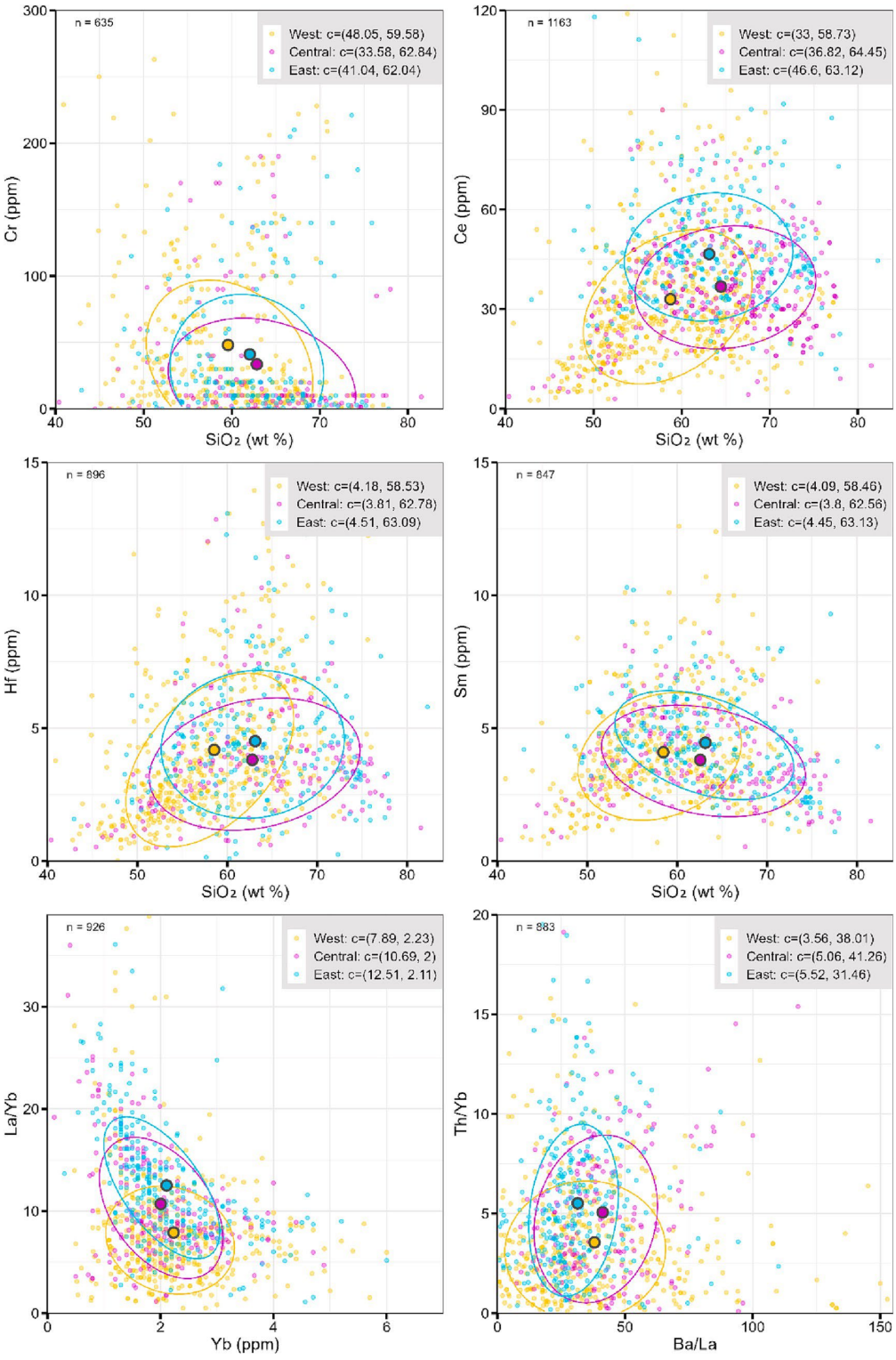

Figure 38. (continued).

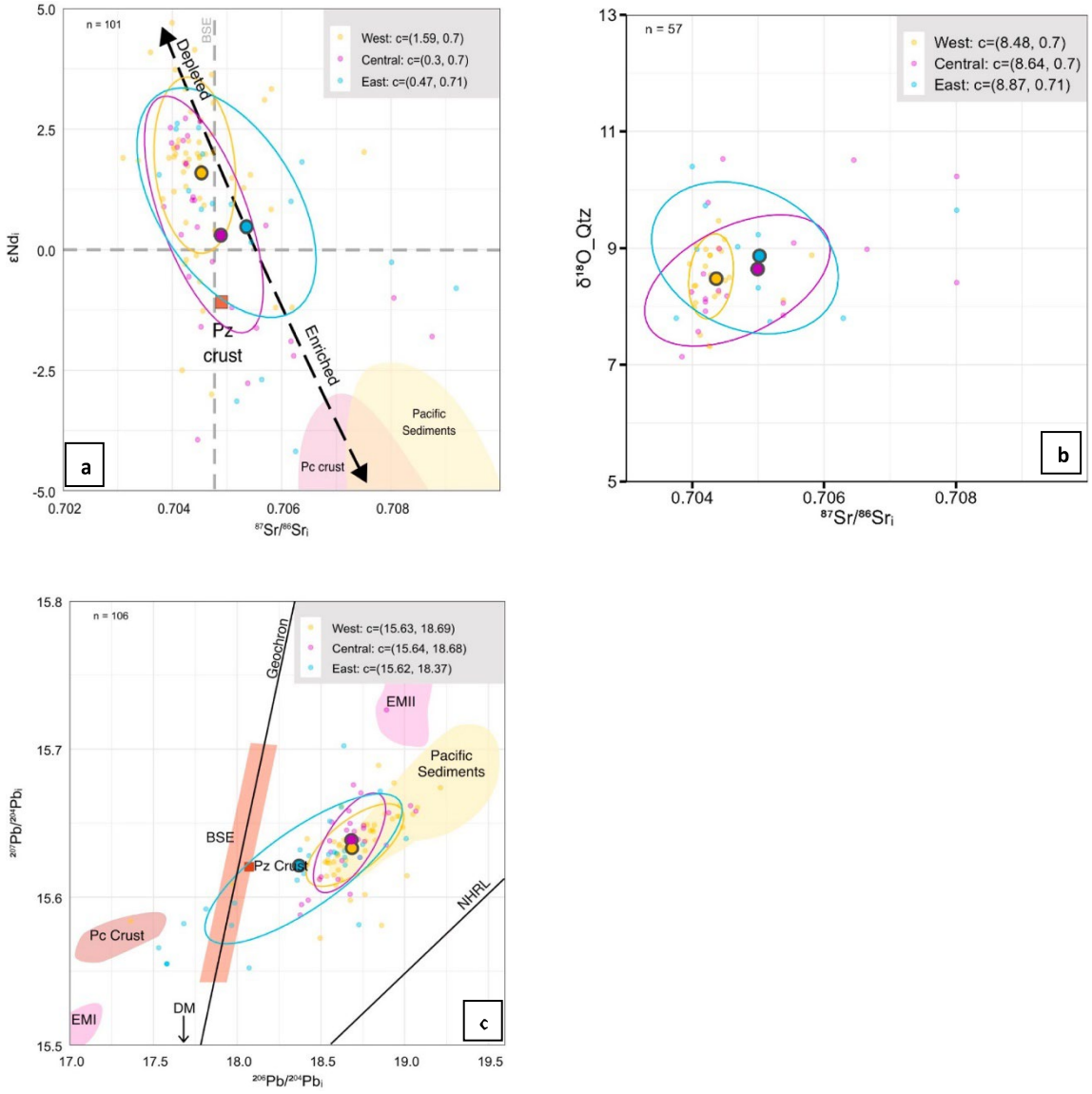

Figure 39. Isotopes across the arc **(a)** Isotope ratios of Nd and Sr. The data show a slight increase of Sr_i towards younger and more evolved plutons. Paleozoic (Pz) and Precambrian (Pc). **(b)** $\delta^{18}O$ for quartz. Note the slight increasing trend from LNS towards the CTS and SS. **(c)** Magma sources and variation of $^{207}Pb/^{204}Pb_i$ versus $^{206}Pb/^{204}Pb_i$. For comparison, five fields are included: depleted mantle (DM), Pacific sediments and Precambrian and Paleozoic crust. The line labeled NHRL (Northern Hemisphere Regresion line) denotes the approximate lower limit of mid-ocean ridge basalt (MORB) Pb isotopic signatures. Pacific Sediment data is from Reynolds and Dasch (1971) and Chow and Pattersonc (1962); Precambrian crust data from Mukasa (1986); mantle reservoir data from Zindler and Hart (1986), and our data. **(d)** Across-arc REE multielemental. Primitive mantle (P-mantle) normalization data are from Sun and McDonough (1989).

To qualitatively determine changes in crustal thickness from the Jurassic (~200 Ma) to Pleistocene (~1 Ma) in the Central Andes, Mamani et al. (2010) identified changes in Dy/Yb and Sm/Yb ratios. Lavas younger than 30 Ma have high Dy/Yb and Sm/Yb ratios; rocks older than 30 Ma display lower $^{87}Sr/^{86}Sr$, Dy/Yb, and Sm/Yb ratios; and rocks older than 91 Ma have even lower $^{87}Sr/^{86}Sr$, Dy/Yb, and Sm/Yb ratios. This suggests that major crustal thickening began in the mid-Oligocene at about 30 Ma and that crustal thickness has continued to increase until the present.

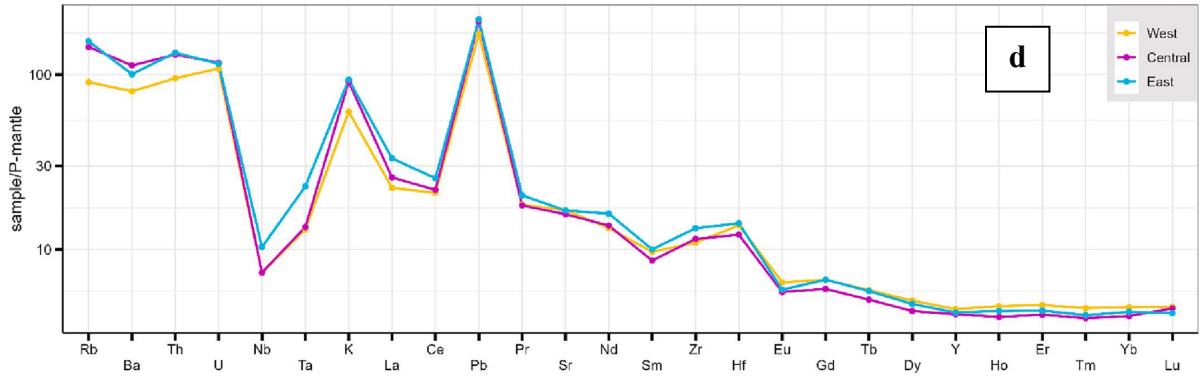

Figure 39. (continued).

Table 4. Chemical trends along arc segments.

Chemical Proxy	Trend from S to N
K_2O, MgO, Ce, Cr, La/Yb, Sri, $\delta^{18}O$	SS > CS > LNS
CaO, εNd	SS < CS < LNS
Hf, Sm, Th/Yb, and Pb isotopes	Low-High-Low

To estimate crustal thickness for the three segments of the PCB (Supplementary Data), Moho depth estimates were obtained from multiple whole rock chemical proxies following the method outlined by Luffi and Ducea (2022) and using age bins defined by major episodic flare-ups of magmatism for each segment (see **Figure 34**). Our approach has limitations because the geochronological and geochemical data do not have a one-to-

one correspondence, i.e., each geochemical data set does not necessarily have an associated U–Pb age. Thus, the geochemistry used for the Moho calculations for each flare-up are not exactly the same flare-ups defined by our geochronological dataset. Recognizing this limitation, our calculations have estimated crustal thickness evolution from south to north as follows: (1) the Southern PCB thickens from 34 km at ~200 Ma to 43 km at ~89 Ma and then thins to 39 km at ~60 Ma; (2) the Central PCB has less dramatic changes, starting with constant thickness at 36 km at ~139–73 Ma and then thickening to 43 km at ~60 Ma; (3) the lower Northern PCB shows a constant thickness of 29 km at ~116–87 Ma and then thickening from 34.5 km at ~84 Ma to 42.5 km at ~22 Ma. In summary, crust for the LNS and CS was thinner in the middle Cretaceous and thickened during the late Cretaceous and into the Early Cenozoic (**Figure 40**). The SS was different because a thinning episode started in the late-Cretaceous and continued until the late-Eocene (~85–38 Ma).

Assimilation and Fractional Crystallization (AFC)

Elemental and isotopic variation in igneous rocks can be modeled using crustal contamination or assimilation and fractional crystallization (AFC) calculations (DePaolo, 1981). Previous AFC modeling of the PCB includes the work by Boily et al. (1989) on the SS and Martínez Ardila et al. (2019a, 2019b) on the CS. Boily et al. (1989) proposed an AFC model requiring first a lower Precambrian crust and then a middle upper Precambrian crust to explain the geochemical diversity of the plutonic rocks. Martínez Ardila et al. (2019a, 2019b) suggested that magmas in the central transitional segment are made up of 70% mantle, 20% subducted oceanic sediments, and assimilation of 10%

lower crust (Precambrian and Paleozoic) and upper crust (Mesozoic volcanic and plutonic units).

To address the causes of the geochemical variation along the PCB, we did AFC modeling of the potential crustal contributions for each of the arc segments using Sr elemental and isotopic compositions (**Figure 41**). The first step is selection of the input parameters for the end members and the bulk partition coefficient (D). The end members for each segment are the parental mantle melt composition (C_0) and the potential assimilants (C_a): Pacific sediments, Precambrian and Paleozoic basement, and altered oceanic crust (AOC). The most primitive sample in the dataset are used to approximate C_0 (e.g., Keskin, 2013; Stracke et al., 2003). For C_a, three values were considered to estimate a likely maximum amount of crust assimilated: (1) the respective composition of the crustal basement in each segment from our geochemical dataset, (2) chemical and isotope data of Pacific sediments from Chow and Patterson (1962) and Reynolds and Dasch (1971), and (3) values for AOC from Ishikawa and Tera (1999). The Sr bulk partition coefficient (D) used in the modeling is from Rollinson (1993) and the GERM Kd database for basalts (https://earthref.org/GERM/).

The modeled curves used different values of r which is the ratio of mass assimilation rate to fractional crystallization rate. The input parameters determine the position and shape of the modeled curves, so the parameters are varied for the three datasets until a reasonable fit to the data occurs (**Figure 41**). The most representative AFC fits for the Sr data for each segment are explained below.

South Segment: Parental mantle magmas assimilated up to ~20–25% of Precambrian crust during fractional crystallization at the emplacement level. Possibly

minor contamination from Paleozoic crust and Pacific sediments in the source region could also take place. In **Figure 41 (a)** it is observed that the assimilation is lower during the 118–89 Ma episode and increases with the younger 85–38 Ma flare-up.

Central Transitional Segment: In CS parental mantle magmas interacted with three types of assimilants: (1) Pacific sediments with ~5–10% assimilation in the source region, (2) basement with ~10–15% assimilation of altered oceanic crust, and (3) minor Precambrian and Paleozoic crustal assimilation during fractional crystallization. The assimilation of isotopically evolved materials increased through time reaching a maximum at 70–50 Ma (**Figure 41 (b)**).

Lower North Segment: The model curves for the LNS indicated that contamination of parental magmas in this segment resulted from a less evolved end member characterized by low Sr and Sr_i values (**Figure 41 (c)**). This suggests that the ~20–30% assimilation observed in the LNS is derived from AOC and took place during fractional crystallization. Our AFC modeling cannot identify assimilation of continental crust or Pacific sediments observed in the other segments or changes in the amount of assimilation through time.

Discussion

Modern Overview of the PCB

Construction of the PCB began in the Early Jurassic when a magmatic arc developed along the western margin of Gondwana in an attenuated crust within an extensional tectonic setting that changed to strongly contractional in the Late Cretaceous

(Jaillard and Soler, 1996; Matthews et al., 2012; Pardo-Casas and Molnar, 1987; Ramos, 2018; Soler and Bonhomme, 1990).

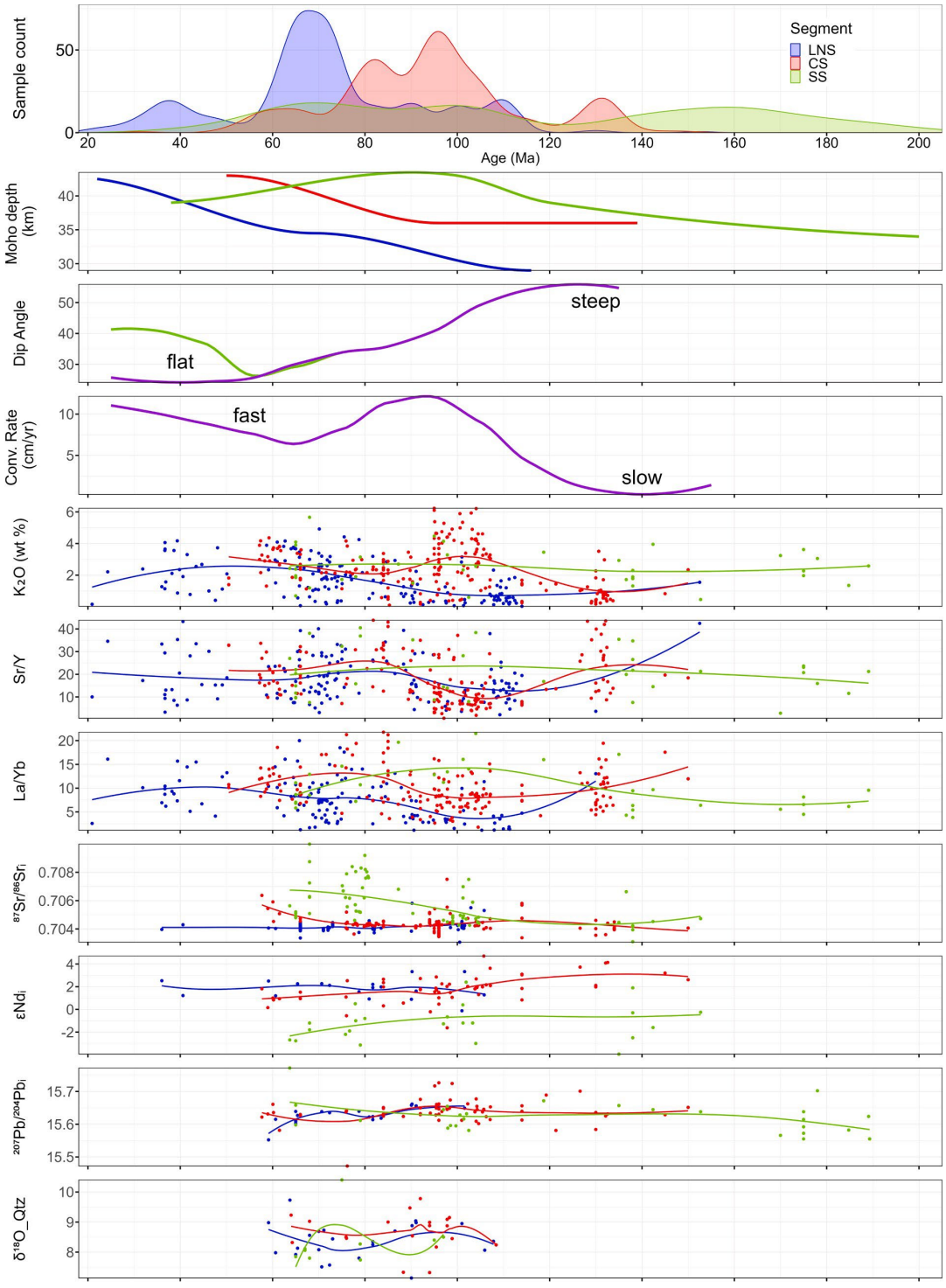

Figure 40. Age histogram and whole-rock petrogenetic indicators. The geochemical data are used to estimate crustal thickness. All geochemical parameters are plotted according to the outcrop age. Data source includes our new age and chemical data and compiled whole rock data (Supplementary Data). South Segment (SS), Central Transitional Segment (CS), and Lower Northern Segment (LNS).

Table 5. Chemical trends across arc segments.

Chemical Proxy	Trend from W to E
K_2O, Ce, Hf, Sm, La/Yb, Th/Yb, Sr_i	W < C < E
Ca, MgO, εNd, $^{206}Pb/^{204}Pb$	W > C > E
Cr	High-Low-High
$^{207}Pb/^{204}Pb$	Low-High-Low

Table 6. Summary of the parameters for each flare-up, including the range, duration, peak and Moho depth.

Flare-up	Range (Ma)	Duration	Peak	Moho Depth
SS-1	200–174	26	182	34
SS-2	170–131	39	162	39
SS-3	118–89	29	98	43
SS-4	85–38	47	66	39
CS-1	139–124	15	131	36
CS-2	117–73	44	96	36
CS-3	70–50	20	64	43
LNS-1	116–101	15	109	29
LNS-2	97–87	10	91	29
LNS-3	84–54	30	70	34.5
LNS-4	52–22	30	37	42.5

Plutons were emplaced through two different basements. The SS arc magmas were emplaced in older ~1900 Ma continental crust of the Arequipa terrane and the CS and LNS magmas in the younger ~1200 Ma continental crust of the Paracas terrane where an intra-arc Cretaceous basin developed by attenuation of preexisting crust (Ramos and Alemán, 2000). The boundary between the CS and SS coincides with the suture zone between the Arequipa and Paracas terrains. Therefore, there is a strong link between the chemical changes along-arc in the PCB and the type of basement where the plutons are emplaced (Dalmayrac et al., 1977; Mamani et al., 2010).

The geochemical and geochronological data presented in this study display along-strike and across-strike variations in basement types and/or crustal thickness, magma

sources, magmatic differentiation processes, and amounts of crustal assimilation through time and space for the PCB. Uranium-lead zircon age patterns for the PCB display along-arc variation in the timing of increased magmatic activity, where the oldest flare-up started in the southern segment and flare-ups progressing north are temporally offset (not continuous) between neighboring segments. We defined 4 flare-ups for the SS from ~200 to 38 Ma, 3 flare-ups for the CS from ~139 to 50 Ma, and 3 flare-ups for the LNS from ~116 to 22 Ma. We will discuss possible causes for the spatial and temporal chemical trends in the PCB segments by integrating: (1) patterns of episodic magmatism and linked chemical data, (2) tectonic setting and subduction parameters that characterized magmatic episodes, (3) calculations of Moho depths, and (4) estimates of mantle and crustal contributions through time and space.

South Segment: In the SS the magmatic arc was emplaced in the Arequipa terrane where the tectonic setting changed from extension in the Jurassic to contraction in the Cretaceous to extension again in the Paleogene. Four magmatic episodes are defined at 200–174 Ma, 170–131 Ma, 118–89 Ma, and 85–38 Ma. The first three flare-ups started with a continental crust of ~34 km that thickened to 43 km by the end of the 118–89 Ma flare-up, possibly associated with the emplacement of plutons and the beginning of a contractional regime. The arc in this segment records high values for K_2O, La/Yb, and Sr_i (**Figure 35**). These values indicate a magma source consisting of ~70% mantle affected by ~25–30% continental crustal contamination from the old Arequipa Precambrian and Paleozoic basement rocks **(Figure 41 (b)**).

Central Transitional Segment: In this CS the magmatic arc was emplaced in the northern end of the Arequipa terrane and the southern end of the Paracas terrane. The

transition lies near the Abancay-Andahuaylas shear zone (SZAA), a structure that has been suggested as the boundary between the two terranes (Ccallo Morocco et al., 2021; Mamani et al., 2010; Ramos, 2018). This is supported by the observed gradual chemical changes across this structure. Three magmatic episodes are observed at 134–124 Ma, 117–73 Ma, and 70–50 Ma. The first two flare-ups occurred primarily during extension with minimal change in crustal thickness. The final 70–50 Ma magmatic episode occurred at the beginning of a contractional regime as the continental crust thickened from ~36 km to 43 km. The high values of Ce, Hf, and Sm plus the REE whole rock geochemistry indicate more fractionated magmas. The La/Yb ratio is similar to that for the SS rocks and might indicate a deep magma source, suggesting a greater possibility for assimilation during magma ascent. Sr and Nd isotopes are primitive and indicate a significant contribution from mantle melting (**Figures 40** and **41c**). Whereas Pb isotopes suggest assimilation of 15–20% oceanic crust combined with melting/fluids from 5 to 10% subducted Pacific Ocean sediments and minor assimilation from Precambrian and Paleozoic basement during magma ascent and emplacement. Geochemical variations from older to younger plutons show a decrease in the mantle component.

Lower North Segment: In the LNS the magmatic arc was emplaced in the Paracas terrane. Four magmatic episodes are observed at 116–101 Ma, 97–87 Ma, 84–54 Ma, and 54–22 Ma. The first two flare-ups occurred in thin ~29 km crust during a continuous contractional setting, high convergence rates, and therefore coupling between plates. The crust eventually thickened to 42 km by the end of the 52–22 Ma flare-up. The arc in this segment records low values for K_2O, La/Yb, Sr_i, and Pb isotopes. These values indicate magmas coming from a shallower magma source and the contamination of ~70% mantle

magmas by ~20–30% assimilation of altered oceanic crust with minor involvement of continental crust. In the LNS the chemical proxies show various spatiotemporal patterns seemingly unrelated to assumed changes in the subduction parameters and tectonic settings throughout the magmatic episodes.

Across-arc Petrological Variations

The values of K_2O (1.78 to 2.69 wt%), Ce (33 to 46.6 ppm), Hf (4.18 to 4.51 ppm), La/Yb (7.89 to 12.51), Sr_i (0.7047 to 0.7057), and $\delta^{18}O$ (8.46 to 8.99) increase towards the east suggesting a more evolved signature of the arc there (**Figures 38** and **39**). The La/Yb ratio and REE whole rock geochemistry indicate that the youngest inboard plutons have a deeper magma source, suggesting a thicker lower crust with greater possibility for assimilation during magma ascent. The arc migrated to the east through time during which magma chemistries experienced an increase in K_2O, La/Yb ratio, $\delta^{18}O$, Sr_i, and Pb isotopes. An increase in assimilation as the arc migrates to the east can be predicted by crustal thickening, but this may not be the only explanation for the observed petrological variations. Instead, these isotopically evolved signatures can be linked to partial melting of the mantle that occurs farther away from the trench in response to slab flattening and may reflect incorporation of continental lithospheric mantle in the melt region (Chapman et al., 2017).

Causes of Compositional Diversity

Flare-ups, Magma Sources, and Assimilation

The along-arc trend in the PCB from south to north is towards less evolved Sr, Nd, and Pb isotopes. This can be explained by a combination of four factors: (1) interaction of arc magmas with two different basement types, i.e., the Arequipa continental crust or the Paracas attenuated continental crust covered by mafic pillow lavas and pyroclastic rocks interfingered with marine sediments (Mamani et al., 2008; Ramos, 2010, Ramos, 2018), (2) variation of crustal assimilation at emplacement levels associated with changes in crustal thickness (Cobbing and Pitcher, 1972), (3) a changing amount of subducted sediment assimilated at the magma source, and (4) the nature of the mantle reservoir (Martínez Ardila et al., 2019a, 2019b; Mukasa, 1986).

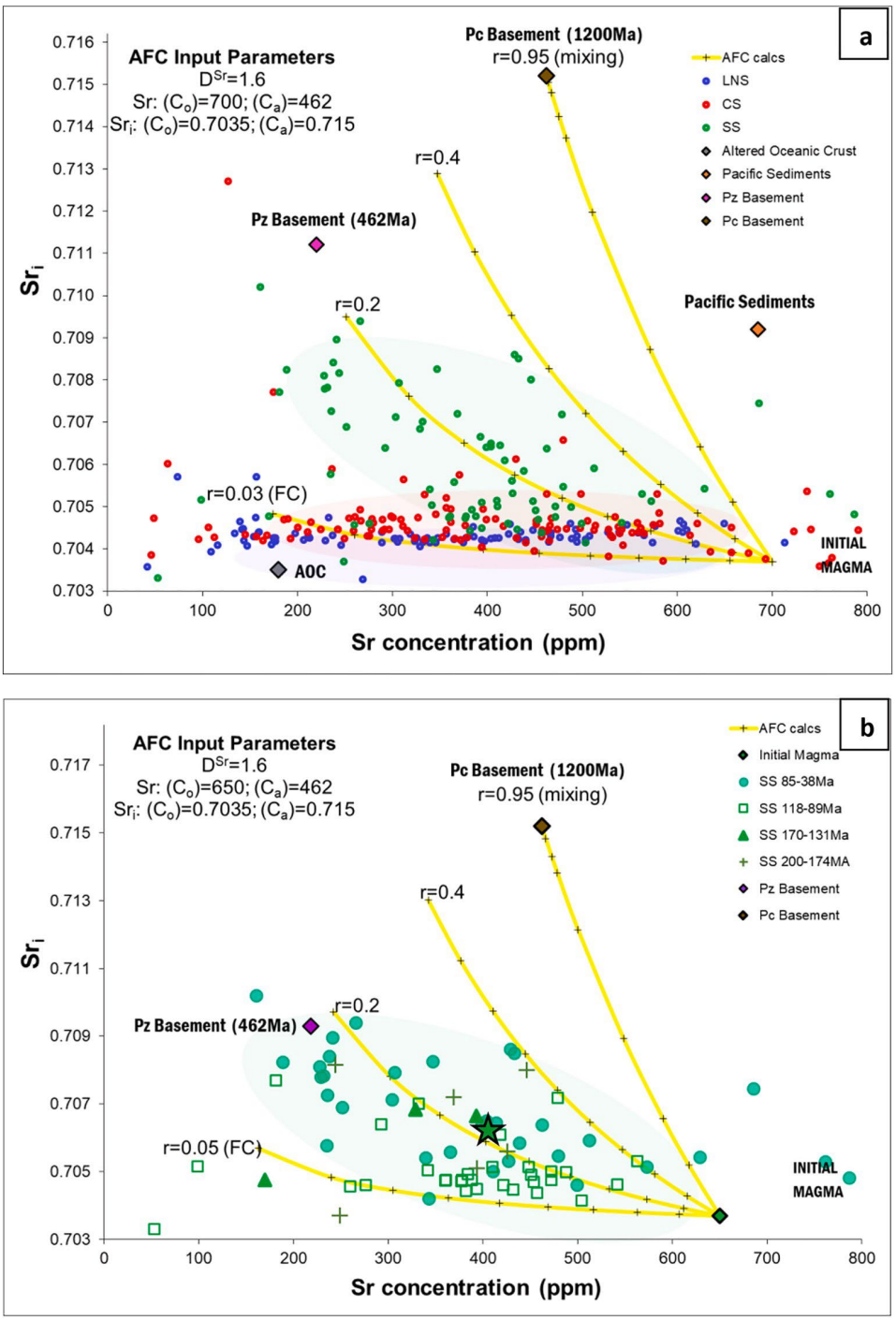

Figure 41. AFC modeling for Sr_i vs. Sr plot. The initial magma composition uses a Sr_i and Sr values suggested for parental mantle (Gale et al., 2003; Faure, 2009). Color fields represent the distribution of the samples, and the star symbol indicates their respective averages. **(a)** Higher assimilation of Pc crust in the SS. The maximum amounts of crust assimilated to form the arcs are: **(b)** 25% Pc with minor Pz crust for the SS; (c) 10–15% for AOC (Altered Oceanic Crust) and 10% Pacific sediments for CS, and **(c)** an average of 30% AOC for LNS.

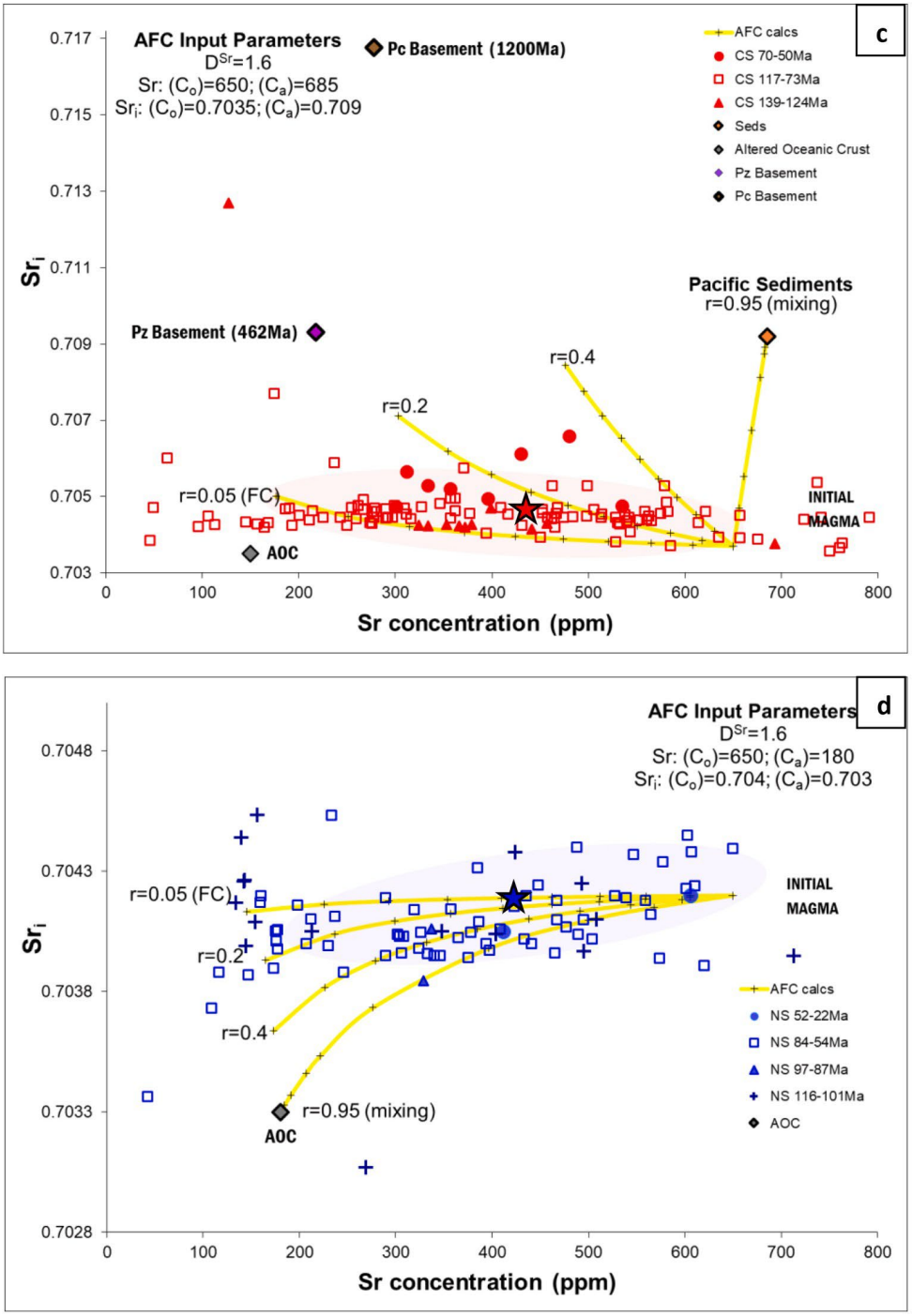

Figure 41. (continued).

The geochemical evidence suggests that granitoids in the SS of the PCB have been modified by magmas rising through the Arequipa terrane assimilating Precambrian

and Paleozoic basement (Beckinsale et al., 1985; Boily et al., 1989). More limited crustal contamination was previously suggested for the CS and LNS, but this is questionable. The primitive composition associated with the Paracas terrane means that a less evolved crustal isotope signature could have still been assimilated in significant amounts. The high Pb isotope ratios observed especially in the CS supports the interpretation that both basement and subducted Pacific sediments were assimilated into the mantle magmas that formed the plutons of the CS (Couch et al., 1981; Martínez Ardila et al., 2019a, 2019b; Mukasa, 1986).

Quartz $\delta^{18}O$ values of +7.1‰ to +12.0‰ cover the entire range of values produced by variable mixtures of (1) melt derived from the mantle where quartz $\delta^{18}O \sim$ +7‰; (e.g., Eiler, 2001; Zheng, 1993) and (2) melts of material that experienced at least one cycle of surficial weathering (e.g., Taylor Jr. and Sheppard, 1986) or low temperature alteration on the seafloor (e.g., Hanson et al., 1993; Holk et al., 2008) resulting in quartz $\delta^{18}O$ values > + 12.0‰. This ambiguity can be resolved by using a radiogenic isotope tracer such as Sr in conjunction with $\delta^{18}O$ values (e.g., James, 1982; Kistler et al., 2014; Lackey et al., 2008), which can distinguish between older and younger assimilants and whether assimilation is due to source or crustal contamination. Our data clearly indicate crustal contamination **(Figure 37 (b))**, as $\delta^{18}O$ values rise at a greater rate than $^{87}Sr/^{86}Sr_i$ values. Most plutons lie on a trend between a depleted mantle primary magma source with low $\delta^{18}O$ and $^{87}Sr/^{86}Sr_i$ and a young weathered/altered assimilant with high $\delta^{18}O$ and low initial $^{87}Sr/^{86}Sr$, consistent with altered oceanic crust or volcano-clastic sediments deposited in the Huarmey-Cañete Basin. The exceptions are the >120 Ma plutons from the SS and a few plutons from the CS, which display variable $\delta^{18}O$ values and more

evolved $^{87}Sr/^{86}Sr_i$ values indicating the incorporation of an older assimilant, such as Precambrian basement rocks of the Arequipa Terrane. The Sr, Nd, and Pb isotopes and $\delta^{18}O$, as well as AFC modeling, indicate that the relative contributions from mantle and crust differ for different arc segments. They also show that the PCB magmas have experienced fractional crystallization with < 20–30% crustal assimilation, implying that the great majority of these magmas are mantle-derived. Thus, since the greatest volumetric change during flare-ups is an increase in mantle magmas, the flare-ups must result largely from episodic mantle processes; crustal melting was not required for triggering the flare-up and only played a secondary role in modifying melt compositions.

Crustal Thickness

Previous studies of Central Andean magmatism have concluded that the thickened crust has strongly affected Andean arc magmas through crustal contamination (e.g., DeCelles et al., 2009; Kay et al., 1994, 1999; Kay et al., 1999; Wörner et al., 2000). The same has been assumed for the PCB, i.e., the composition of the PCB was strongly affected by magmas intruded into and traversing a thick continental crust (Beckinsale et al., 1985; Boily et al., 1989). If correct, an increase in Sr/Y, La/Yb, and Sr_i is explained as the result of crustal thickening and linked with arc magma production (Haederle and Atherton, 2002; Mamani et al., 2010). However, the compositional changes identified in the PCB are not expected to be the same through time because the thickness of the crust has changed as well (see **Table 6** and **Figure 40**).

Magma addition to the arc displays a non-steady-state pattern of temporal and spatial scales, and available estimates of magma addition are insufficient to explain all of the

observed crustal thickness changes (Trumbull et al., 2006; Wörner et al., 2000). Besides crustal thickness, alternative mechanisms to change chemical compositions have been proposed, such as "source contamination" by subduction erosion of the forearc (Clift and Hartley, 2007; Kay et al., 2005; Stern et al., 1981), or the influence of enriched subcontinental mantle lithosphere in the source region (Rogers and Hawkesworth, 1989). If partial melting occurs further away from the trench as the arc migrates, it can incorporate higher amounts of lithospheric mantle and the resulting magmas will show a more evolved chemical signature (Chapman et al., 2021). In that case, these chemical changes may reflect not only changes in crustal thickness but also lateral migration of the arc resulting in magma passing through crust with different chemical properties and an increase in lithospheric mantle input (Kirsch et al., 2016; Paterson et al., 2016).

The Role of Tectonism

In the past, links between tectonic processes and magma compositions have been suggested for the PCB (Mamani et al., 2010). Five aspects of tectonics can be considered when evaluating such relationships between tectonics and magmatism in arcs: (1) motions of subducting plates, (2) tectonic styles in arcs, (3) crustal thicknesses. (4) relations between individual plutons and regional deformation (e.g., faults, folding), and (5) tectonic triggers for magma flare-ups. We have not presented the appropriate data to discuss (4) and will not discuss this aspect further.

An examination of **Figure 40** shows no correlations between subduction parameters and arc flare-ups or geochemistry in the PCB, a result that is typical for arcs elsewhere (Chapman et al., 2021; Kirsch et al., 2016; Paterson and Ducea, 2015).

Tectonic regimes in the PCB have clearly changed through time from a dominantly regional extensional regime from Early Jurassic to Early Cretaceous (190–120 Ma) to a contractional regime in Late Cretaceous during which large sections of the forearc were removed by subduction erosion (120 to 80 Ma) and significant mountain building began (80–70 Ma). In spite of these widespread changes, data in **Figure 40** indicate that different arc segments responded to these shifting tectonic regimes in different ways including crustal thicknesses and arc geochemistry. In general, our spatiotemporal reconstructions in **Figure 40** reveal no clear (consistent) coupling between PCB segments nor between tectonic regimes and magma geochemistry. Instead our dataset reinforces the idea of complexity in the arc requiring interactions between multiple causes to yield the final arc signatures.

Triggers of arc flare-ups have been a topic of much recent interest in the geologic community (DeCelles et al., 2009; Kirsch et al., 2016; Martínez Ardila et al., 2019a, 2019b; Paterson and Ducea, 2015). In previous studies including our own, attempts to determine triggers for magmatic flare-ups largely focused on determining if they were external (lower plate) or internal (upper plate) with the latter also being divided between potential crustal or mantle processes. We now recognize that a complex interplay likely occurs between all of these, with external processes controlling fairly instantaneous boundary conditions for arc behavior, while upper plate processes are influenced by long composite histories of continental margins. In other words, the characteristics of the mantle and overlying crustal columns, upon which the external boundary conditions are superposed, has evolved over 10s to 100s of millions of years. As noted in many other studies of flare-ups in arcs (Chapman et al., 2021; Kirsch et al., 2016; Martínez Ardila et al., 2019a, 2019b), we see no correlations between external plate motion features and flare-ups (**Figure 40**). But this is likely because

the signal of changing boundary conditions is filtered in complex ways by responses of a very heterogenous mantle/crustal arc column.

In the PCB the spatial and temporal variability of arc flare-ups, mantle and basement types, tectonic regimes, crustal thicknesses and igneous geochemistry imply that an equivalent temporal-spatial variability is needed for flare-up triggers. For example, not every flare-up is associated with thick crust and lulls are not necessarily associated with thin crust. And geochemical data do not show consistent patterns during flare-up initiations, nor in flare-ups in different arc segments. To us, this suggested "variability of triggers" implies a variability in how different processes interacted. Even so, much of our geochemical data and modeling point towards the importance of mantle sources to produce the greatest volume of magmatism during flare-ups suggesting that episodic mantle processes likely play the dominate role in triggering flare-ups.

Episodic mantle processes (both external and internal) are thus a ripe target for future studies of arc flare-up triggers. For example, plate motion (such as convergence rate) might influence the behavior of the mantle (England and Katz, 2010; Turner and Langmuir, 2015). Higher convergence rates can produce more hydration of the mantle wedge (e.g., Cagnioncle et al., 2007; Plank et al., 2009), and/or increase the temperature of the mantle wedge corner (England and Katz, 2010; England and Wilkins, 2004; Turner and Langmuir, 2015) resulting in an increase in mantle melting.

Missing Datasets: Ages to Define Flare-ups and Spatial and Temporal Trends

In order to correlate magma composition with the evolution of crust for the PCB, the sequence of magmatic events and associated geochemical signatures must be constrained by

absolute ages. In the past, timing of magmatism in the PCB was somewhat poorly understood due to heavy dependence on whole-rock Rb–Sr and K–Ar geochronology, both of which can yield questionable crystallization ages due to low closure temperatures and isotopic disturbances by subsequent thermal episodes (Dodson, 1973). This is a particularly acute problem in Peru where ~150 My of uninterrupted subduction occurs during the Andean orogenic cycle (Benavides Cáceres, 1999). More ages and chemical data are still needed for the upper northern segment, since we were not able to fully characterize it: our restricted dataset for this segment allowed us to only examine the most southern part of the northern section.

Timing of PCB emplacement also needs to consider whether the Jurassic magmatism is due to back-arc volcanism or a different subduction-related process and why it is volumetrically restricted.

Finally, we recognize that the ideas presented in this paper should be re-evaluated as larger and more precise geochronological, geochemical, and plate kinematic datasets become available in the future.

Conclusions

This paper presented a complete compilation and analysis of all available geochronological, geochemical, and plate kinematic datasets for the PCB, including our new data, to clarify the temporal and spatial record of magmatic events and provide a more rigorous interpretation of the causes of arc magmatism and its chemical diversity. Below, we summarize five major contributions of our work.

(1) The magmatic episodes in the PCB are now better characterized using zircon geochronology coupled with whole-rock geochemical analyses. The PCB shows a clear non-steady-state pattern of magmatism at variable temporal and spatial scales, including between arc segments (**Figures 32** and **34**). Some flare-ups are discrete, but others are synchronous for hundreds of kilometers along-arc and exhibit a periodicity of 30–40 My. We find no evidence to support a continuous and volumetrically constant pattern of magmatism in the PCB, as previously used to support the "superunit" concept.

(2) Arc magma chemistry varies in both space and time, including between arc segments (**Figures 35**–**38** and **Figure 40**). The identified chemical diversity both along- and across-arc are the result of changing upper plate mantle input (transitioning from depleted to lithospheric mantle), types of upper plate basement (i.e., Paracas and Arequipa terranes), varying types and degrees of assimilated material from Pacific sediments, changing crustal thickness, arc migration, and the extent of magma fractionation.

(3) We find no convincing correlations between arc chemistry and plate motion phenomena such as convergence rate and dip angle. However, upper plate tectonic phenomena, such as styles of tectonics (extension, contraction, transpression) and/or crustal thickness may show weak relationships to geochemical signals, although it is typically hard to fully separate different tectonic effects from other parameters such as mantle and basement type.

(4) In previous studies, including our own, attempts to determine triggers for magmatic flare-ups largely focused on determining if they were external (lower plate) or

internal (upper plate) with the latter also being divided into crustal or mantle processes. We now recognize that a complex interplay likely occurs between all of these with external processes controlling fairly instantaneous boundary conditions for arc behavior while upper plate processes are influenced by lengthy composite histories of continental margins. Even so we see no correlations between plate motion features and flare-ups (**Figure 40**). The spatial and temporal variability of arc flare-ups, mantle and basement types, tectonic regimes, crustal thicknesses and igneous geochemistry in the PCB signals an equivalent variability in flare-up triggers. However much of our geochemical data and modeling point towards the importance of mantle sources to produce the greatest volume of magmatism indicating that episodic mantle processes likely play the dominant role in triggering flare-ups.

(5) Possibly the most important result is the documentation of the incredible heterogeneity of both tectonic and magmatic arc be-havior over short spatial lengths. Therefore, the causes also have to be heterogeneous over these length scales. Most data presented in **Figure 40** points to both along and across arc complexity, including from one segment to the next and from one flare-up to the next. This complexity must reflect a dynamic interaction between lower plate driven boundary conditions on upper plate long term evolution of mantle, crustal basement and evolving magma systems.

Declaration of Competing Interest

The authors declare that they have no known competing financial interests or personal relationships that could have appeared to influence the work reported in this paper.

Acknowledgements

The authors acknowledge financial support for this study from Loma Linda University and the Geoscience Research Institute (Projects GRI2014-BC01 and GRI2015-AM10). We thank Orlando Poma for his valuable assistance during fieldwork. We thank the lab scientists at the Arizona LaserChron Center for help while using their geochronology lab.

We are especially grateful to the Bendezu Family for their kindness and hospitality during our visits to Peru. We also would like to thank the editor Greg Shellnutt and reviewers Victor Ramos and Francisco Pereira for their useful comments that helped improve the quality of the manuscript. Martínez-Ardila thanks Felipe Pichinual for data synthesis and drafting help, Luiz Pereira and Alex Voos for helping with data compilation.

Supplementary data

Supplementary data to this article can be found online at https://doi.org/10.1016/j.lithos.2023.107298.

References

Agar, R., 1978. The Peruvian Coastal Batholith: Its Monzonitic Rocks and their Related Mineralization. The Geology of the Rio Pisco, a Sector of the Arequipa Segment of the Coastal Batholith [Doctor of Philosophy]. University of Liverpool (293 p).

Arndt, N.T., Goldstein, S.L., 1989. An open boundary between lower continental crust and mantle: its role in crust formation and crustal recycling. Tectonophysics 161 (3–4), 201–212.

Aspden, J.A., McCourt, W.J., Brook, M., 1987. Geometrical control of subduction-related magmatism: the Mesozoic and Cenozoic plutonic history of Western Colombia. J. Geol. Soc. 144 (6), 893–905.

Atherton, M., Aguirre, 1992. Thermal and geotectonic setting of cretaceous volcanic rocks near Ica, Peru, in relation to Andean crustal thinning. J. S. Am. Earth Sci. 5 (1), 47–69.

Atherton, M., Pitcher, W., Warden, V., 1983. The Mesozoic marginal basin of Central Peru. Nature 305 (5932), 303–306.

Atherton, M., Warden, V., Sanderson, L., 1985. The Mesozoic marginal basin of Central Peru: A geochemical study of within-plate-edge volcanism. In: Pitcher, W.S., et al. (Eds.), Magmatism at a Plate Edge: The Peruvian Andes. John Wiley, New York, pp. 47–58.

Attia, S., Cottle, J.M., Paterson, S.R., 2020. Erupted zircon record of continental crust formation during mantle driven arc flare-ups. Geology 48 (5), 446–451.

Bahlburg, H., Carlotto, V., Cárdenas, J., 2006. Evidence of early to Middle Ordovician arc volcanism in the Cordillera oriental and Altiplano of southern Peru, Ollantaytambo Formation Umachiri beds. J. S. Am. Earth Sci. 22 (1–2), 52–65.

Beck, S.L., Zandt, G., 2002. The nature of orogenic crust in the Central Andes: Journal of Geophysical Research: Solid. Earth 107 (B10) (p. ESE 7-1-ESE 7-16).

Beckinsale, R.D., Sanchez-Fernandez, A.W., Brook, M., Cobbing, E.J., Taylor, W.P., Moore, N.D., 1985. Rb-Sr whole-rock isochrons and K-Ar age determinations for the Coastal Batholith of Peru. In: Pitcher, W.S., et al. (Eds.), Magmatism at a Plate Edge: The Peruvian Andes. John Wiley, New York, pp. 177–202.

Bellido Bravo, E., 1969. Sinopsis de la Geología del Perú. Boletin Servicio Geologico Minero del Perú 22, 54.

Bellido, F., Valverde, P., Jaimes, F., Carlotto, V., Díaz-Martínez, E., 2009. Datación y caracterización geoquímica de los granitoides peralumínicos de los cerros de Amotape y de los Macizos de Illescas y Paita (Noroeste de Perú). Boletín Sociedad Geológica del Perú 103, 197–213.

Benavides Cáceres, V., 1999. Orogenic evolution of the Peruvian Andes: the Andean cycle. In: Skinner, B. (Ed.), Geology and mineral deposits of Central Andes, 7. Society of Economic Geology Special Publication, pp. 61–107.

Boily, M., Brooks, C., Ludden, J.N., 1989. Chemical and isotopic evolution of the Coastal Batholith of southern Peru. J. Geophys. Res. 94 (89), 12483–12489.
Bussell, M.A., Pitcher, W.S., 1985. The structural controls of batholith emplacement. In: Pitcher, W.S., et al. (Eds.), Magmatism at a Plate Edge: The Peruvian Andes. John Wiley, New York, pp. 167–176.

Bussell, M.A., Pitcher, W.S., Wilson, P.A., 1976. Ring complexes of the Peruvian Coastal Batholith: a long-standing subvolcanic regime. Can. J. Earth Sci. 13 (8), 1020–1030.

Cagnioncle, A.M., Parmentier, E., Elkins-Tanton, L.T., 2007. Effect of solid flow above a subducting slab on water distribution and melting at convergent plate boundaries. J. Geophys. Res. Solid Earth 112 (B09402). https://doi.org/10.1029/ 2007JB004934.

Cao, W., Paterson, S., Saleeby, J., Zalunardo, S., 2016. Bulk arc strain, crustal thickening, magma emplacement, and mass balances in the Mesozoic Sierra Nevada arc. J. Struct. Geol. 84, 14–30.

Cardona, A., Cordani, U.G., Nutran, A., Zimmermann, U., Sanchez, A.W., 2005. Tectonic setting and geochronology of Pre-Llanvirnian metamorphic rocks of the Marañon Complex (E. Peru): from rifting to collision to form the Rheic ocean: Gondwana 12 “geological and biological, heritage of Gondwana”.

Carlotto, V., Quispe, J., Acosta, H., Rodríguez, R., Romero, D., Cerpa, L., Mamani, M., Díaz-Martínez, E., Navarro, P., Jaimes, F., 2009. Dominios geotectónicos y metalogénesis del Perú. Boletín de la Sociedad Geológica del Perú 103 (1), 1–89.

Casquet, C., Fanning, C.M., Galindo, C., Pankhurst, R.J., Rapela, C.W., Torres, P., 2010. The Arequipa Massif of Peru: New SHRIMP and isotope constraints on a Paleoproterozoic inlier in the Grenvillian orogen. J. S. Am. Earth Sci. 29 (1), 128–142.

Castro, A., Rodriguez, C., Fernández, C., Aragón, E., Pereira, M.F., Molina, J.F., 2021. Secular variations of magma source compositions in the North Patagonian batholith from the Jurassic to Tertiary: was mélange melting involved? Geosphere 17 (3), 766–785.

Castro, A., Vogt, K., Gerya, T., 2013. Generation of new continental crust by sublithospheric silicic-magma relamination in arcs: a test of Taylor's andesite model. Gondwana Res. 23 (4), 1554–1566.

Castroviejo Bolibar, R., Rodrigues, J.F., Carrascal, R., Chirif, H., Acosta, J., Uribe, R., 2009. Mineralogía del Macizo Ultramáfico de Tapo (Cordillera Oriental Andina, Perú): Revista de la Sociedad Española de Mineralogía, Macla, 11, pp. 55–56.

Ccallo Morocco, W.E., López Aguilar, Y.P., Guo, W., Liu, J., Chen, S., Duan, Z., 2021. Características litogeoquímicas y petrográficas en los bordes norte y sur del segmento Lima-Batolito de la Costa, comparada con el sureste de China. Instituto Geológico Minero y Metalúrgico del Perú "INGEMMET" D (35), 10–12.

Chapman, J., Ducea, M., Kapp, P., Gehrels, G., DeCelles, P., 2017. Spatial and temporal radiogenic isotopic trends of magmatism in Cordilleran orogens. Gondwana Res. 48, 189–204.

Chapman, J.B., Shields, J.E., Ducea, M.N., Paterson, S.R., Attia, S., Ardill, K.E., 2021. The causes of continental arc flare ups and drivers of episodic magmatic activity in Cordilleran orogenic systems. Lithos 398. https://doi.org/10.1016/j. lithos.2021.106307.

Chen, J.H., Wasserburg, G.J., 1981. Isotopic determination of uranium in picomole and subpicomole quantities. Anal. Chem. 53 (13), 2060–2067.

Chin, E.J., Lee, C.-T.A., Blichert-Toft, J., 2015. Growth of upper plate lithosphere controls tempo of arc magmatism: Constraints from Al-diffusion kinetics and coupled Lu-Hf and Sm-Nd chronology. Geochem. Perspect. Lett. 1, 20–32.

Chow, T.J., Patterson, C., 1962. The occurrence and significance of lead isotopes in pelagic sediments. Geochim. Cosmochim. Acta 26 (2), 263–308.

Clark, A.H., Farrar, E., Kontak, D.J., Langridge, R.J., Arenas, F., France, L.J., McBride, S. L., Woodman, P.L., Wasteneys, H.A., Sandeman, H.A., 1990. Geologic and geochronologic constraints on the metallogenic evolution of the Andes of southeastern Peru. Econ. Geol. 85 (7), 1520–1583.

Clift, P.D., Hartley, A.J., 2007. Slow rates of subduction erosion and coastal underplating along the Andean margin of Chile and Peru. Geology 35 (6), 503–506.

Cobbing, E., 1978. The Andean geosyncline in Peru, and its distinction from Alpine geosynclines. J. Geol. Soc. 135 (2), 207–218.

Cobbing, E.J., 1985. The Central Andes: Peru and Bolivia: the Ocean Basins and margins: volume 7A. Pacific Ocean 219–264.

Cobbing, E.J., Ozard, J.M., Snelling, N.J., 1977. Reconnaissance geochronology of the crystalline basement rocks of the Coastal Cordillera of southern Peru. Geol. Soc. Am. Bull. 88 (2), 241–246.

Cobbing, E.J., Pitcher, W.S., 1972. The Coastal Batholith of Central Peru. J. Geol. Soc. 128 (5), 421–454.

Cobbing, E.J., Pitcher, W.S., 1983. Andean plutonism in Peru and its relationship to volcanism and metallogenesis at a segmented plate edge. Geol. Soc. Am. Mem. 159, 277–291.

Couch, R., Whiltsett, R.M., Huehn, B., Briceno-Guarupe, L., 1981. Structures of the continental margin of Peru and Chile. In: Kulm, L.D., Dymond, J., Dasch, E.J., Hussong, D.M., Geological Society of America Memoirs (Eds.), Nazca Plate: Crustal Formation and Andean Convergence, 154, pp. 703–726.

Dalmayrac, B., Lancelot, J., Leyreloup, A., 1977. Two-billion-year granulites in the late Precambrian metamorphic basement along the southern Peruvian coast. Science 198 (4312), 49–51.

Daly, M.C., 1989. Correlations between Nazca/Farallon plate kinematics and forearc basin evolution in Ecuador. Tectonics 8 (4), 769–790.

De Haller, A., Corfu, F., Fontboté, L., Schaltegger, U., Barra, F., Chiaradia, M., Frank, M., Alvarado, J.Z., 2006. Geology, geochronology, and Hf and Pb isotope data of the Raúl-Condestable iron oxide-copper-gold deposit, central coast of Peru. Econ. Geol. 101 (2), 281–310.

DePaolo, D.J., 1981. Trace element and isotopic effects of combined wallrock assimilation and fractional crystallization. Earth Planet. Sci. Lett. 53 (2), 189–202.

de Silva, S.L., Riggs, N.R., Barth, A.P., 2015. Quickening the Pulse: Fractal Tempos in Continental Arc Magmatism. Elements 11 (2), 113–118.

de Silva, S.L., Gosnold, W.D., 2007. Episodic construction of batholiths: Insights from the spatiotemporal development of an ignimbrite flare-up. J. Volcanol. Geotherm. Res. 167 (1–4), 320–335.

DeCelles, P.G., Ducea, M.N., Kapp, P., Zandt, G., 2009. Cyclicity in Cordilleran orogenic systems. Nat. Geosci. 2 (4), 251–257.

DeCelles, P.G., Zandt, G., Beck, S.L., Currie, C.A., Ducea, M.N., Kapp, P., Gehrels, G.E., Carrapa, B., Quade, J., Schoenbohm, L.M., 2015. Cyclical Orogenic Processes in the Cenozoic central Andes, 212. Geological Society of America Memoirs, pp. 459–490.

Díaz-Martínez, E., Acosta, H., Cárdenas, J., Carlotto, V., Rodríguez, R., 2001. Paleozoic diamictites in the Peruvian Altiplano: evidence and tectonic implications. J. S. Am. Earth Sci. 14, 587–592.

Dodson, M.H., 1973. Closure temperature in cooling geochronological and petrological systems. Contrib. Mineral. Petrol. 40 (3), 259–274.

Dorbath, C., 1996. Velocity structure of the Andes of Central Peru from locally recorded earthquakes. Geophys. Res. Lett. 23 (2), 205–208.

Ducea, M., 1998. A Petrologic Investigation of Deep-Crustal and Upper-Mantle Xenoliths from the Sierra Nevada, California: Constraints on Lithospheric Composition beneath Continental Arcs and the Origin of Cordilleran Batholiths [PhD Dissertation]. California Institute of Technology (364 p).

Ducea, M.N., 2001. The California arc: Thick granitic batholiths, eclogitic residues, lithospheric-scale thrusting, and magmatic flare-ups. GSA Today 11, 4–10.

Dunbar, R.B., Marty, R.C., Baker, P.A., 1990. Cenozoic marine sedimentation in the Sechura and Pisco basins, Peru. Palaeogeogr. Palaeoclimatol. Palaeoecol. 77 (3–4), 235–261.

Eiler, J.M., 2001. Oxygen isotope variations of basaltic lavas and upper mantle rocks. Rev. Mineral. Geochem. 43 (1), 319–364.

Ellison, R., Klinck, B., Hawkins, M., 1989. Deformation events in the Andean orogenic cycle in the Altiplano and Western Cordillera, southern Peru. J. S. Am. Earth Sci. 2 (3), 263–276.

England, P.C., Katz, R.F., 2010. Melting above the anhydrous solidus controls the location of volcanic arcs. Nature 467 (7316), 700–703.

England, P., Wilkins, C., 2004. A simple analytical approximation to the temperature structure in subduction zones. Geophys. J. Int. 159 (3), 1138–1154.

Espurt, N., Funiciello, F., Martinod, J., Guillaume, B., Regard, V., Faccenna, C., Brusset, S., 2008. Flat subduction dynamics and deformation of the south American plate: Insights from analog modeling. Tectonics 27 (3). https://doi.org/10.1029/2007TC002175.

Fanlo, I., Gervilla, F., Castroviejo, R., Rodrigues, J.F., Pereira, E., Acosta, J., Uribe, R., 2009. Metamorphism of chromitites in the Tapo ultramafic massif, Eastern Cordillera, Peru. In: Proceedings 10th Biennial SGA Meeting, Townsville, Australia, pp. 161–163.

Feininger, T., 1987. Allochthonous terranes in the Andes of Ecuador and northwestern Peru. Can. J. Earth Sci. 24, 266–278.

Ganne, J., Schellart, W., Rosenbaum, G., Feng, X., De Andrade, V., 2017. Probing crustal thickness evolution and geodynamic processes in the past from magma records: an integrated approach. Geol. Soc. Am. Spec. Pap. 526, 1–25.

Garzione, C.N., Hoke, G.D., Libarkin, J.C., Withers, S., MacFadden, B., Eiler, J., Ghosh, P., Mulch, A., 2008. Rise of the Andes. Science 320 (5881), 1304–1307.

Gehrels, G.E., Valencia, V.A., Ruiz, J., 2008. Enhanced precision, accuracy, efficiency, and spatial resolution of U-Pb ages by laser ablation–multicollector–inductively coupled plasma–mass spectrometry. Geochem. Geophys. Geosyst. 9 (3) https://doi.org/10.1029/2007GC001805.

Gonzalez, L., Clausen, B., Holk, G., Poma, O., 2020. Using Stable Isotopes to better understand the Petrologic and Hydrothermal Evolution of cretaceous Linga Complex of the Peruvian Coastal Batholith, near Ica. Boletín de la Sociedad Geológica del Perú 113, 12–25.

Gregory, R.T., Criss, R.E., Taylor Jr., H.P., 1989. Oxygen isotope exchange kinetics of mineral pairs in closed and open systems: applications to problems of hydrothermal alteration of igneous rocks and Precambrian iron formations. Chem. Geol. 75 (1–2), 1–42.

Gregory-Wodzicki, K.M., 2000. Uplift history of the Central and Northern Andes: a review: GSA. Bulletin 112 (7), 1091–1105.

Gutscher, M.-A., 2002. Andean subduction styles and their effect on thermal structure and interplate coupling. J. S. Am. Earth Sci. 15, 3–10.

Haederle, M., Atherton, M.P., 2002. Shape and Intrusion Style of the Coastal Batholith, vol. v. 345. Tectonophysics, Peru, pp. 17–28.

Hanson, R.B., Sorensen, S.S., Barton, M.D., Fiske, R.S., 1993. Long-term evolution of fluid–rock interactions in magmatic arcs: evidence from the Ritter Range pendant, Sierra Nevada, California, and numerical modeling. J. Petrol. 34 (1), 23–62.

Harrison, J.V., 1960. Geología de los alrededores de Baños en el Occidente del Peru Central. Boletin de la Sociedad Geologica del Perú 35, 63–77.

Henrique-Pinto, R., Basei, M.A.S., Santos, P.R.D., Saad, A., Milani, E., Cingolani, C., Frugis, G.L., 2021. Paleozoic Paraná Basin transition from collisional retro-foreland to pericratonic syneclise: Implications on the geodynamic model of Gondwana proto-Andean margin. J. S. Am. Earth Sci. 111 https://doi.org/10.1016/j.jsames.2021.103511.

Hildebrand, R.S., Whalen, J.B., 2014. Arc and Slab-Failure Magmatism in Cordilleran Batholiths I – The Cretaceous Coastal Batholith of Peru and its Role in South American Orogenesis and Hemispheric Subduction Flip. Geosci. Can. 41 (3), 255–282. https://doi.org/10.12789/geocanj.2014.41.047.

Hildreth, W., Moorbath, S., 1988. Crustal contributions to arc magmatism in the Andes of Central Chile. Contrib. Mineral. Petrol. 98 (4), 455–489.

Holk, G.J., Taylor, B.E., Galley, A.G., 2008. Oxygen isotope mapping of the Archean Sturgeon Lake caldera complex and VMS-related hydrothermal system, Northwestern Ontario, Canada. Mineral. Deposita 43, 623–640.

Hughes, G.R., Mahood, G.A., 2008. Tectonic controls on the nature of large silicic calderas in volcanic arcs. Geology 36 (8), 627–630.

Isacks, B.L., 1988. Uplift of the central Andean plateau and bending of the Bolivian orocline. J. Geophys. Res. Solid Earth 93 (B4), 3211–3231.

Ishikawa, T., Tera, F., 1999. Two isotopically distinct fluid components involved in the Mariana arc: evidence from Nb/B ratios and B, Sr, Nd, and Pb isotope systematics. Geology 27 (1), 83–86.

Jaillard, E., Hérail, G., Monfret, T., Díaz-Martínez, E., Baby, P., Lavenu, A., Dumont, J.F., 2000. Tectonic evolution of the Andes of Ecuador, Peru, Bolivia and northernmost Chile. In: Cordani, U.G., Milani, E.J., Thomaz Filho, A., Campos, D.A. (Eds.), Tectonic evolution of South America, pp. 481–559. Rio de Janeiro, Brazil.

Jaillard, E., Soler, P., 1996. Cretaceous to early Paleogene tectonic evolution of the northern Central Andes (0–18° S) and its relations to geodynamics. Tectonophysics 259 (1–3), 41–53.

James, D.E., 1971. Plate tectonic model for the evolution of the Central Andes. Geol. Soc. Am. Bull. 82 (12), 3325–3346.

James, D.E., 1982. A combined O, Sr, Nd, and Pb isotopic and trace element study of crustal contamination in central Andean lavas, I. Local geochemical variations. Earth Planet. Sci. Lett. 57 (1), 47–62.

Javoy, M., Fourcade, S., Allegre, C.J., 1970. Graphical method for examination of $^{18}O/^{16}O$ fractionations in silicate rocks. Earth Planet. Sci. Lett. 10, 12–16.

Jenks, W.F., Harris, E.G., 1953. Plutonics near Arequipa as a petrologic sample of the coastal batholith of Peru. Boletín de la Sociedad Geológica del Perú 26, 79–94.

Jiménez, N., López-Velásquez, S., 2008. Magmatism in the Huarina belt, Bolivia, and its geotectonic implications. Tectonophysics 459 (1), 85–106.

Johnston, S., Gehrels, G., Valencia, V., Ruiz, J., 2009. Small-volume U–Pb zircon geochronology by laser ablation-multicollector-ICP-MS. Chem. Geol. 259 (3–4), 218–229.

Jones, P.R., 1981. Crustal structures of the Peru continental margin and adjacent Nazca plate, 9° S latitude. In: Kulm, L.D., Dymond, J., Dasch, E.J., Hussong, D.M. (Eds.), Nazca plate: Crustal formation and Andean convergence, 154. Geological Society of America Memoir, pp. 423–443.

Kaneoka, I., Guevara, C., 1984. K-Ar age determinations of late Tertiary and Quaternary Andean volcanic rocks, southern Peru. Geochem. J. 18 (5), 233–239.

Kay, S.M., Coira, B., Viramonte, J., 1994. Young mafic back arc volcanic rocks as indicators of continental lithospheric delamination beneath the argentine Puna plateau, Central Andes: Journal of Geophysical Research: Solid. Earth 99 (B12), 24323–24339.

Kay, S.M., Godoy, E., Kurtz, A., 2005. Episodic arc migration, crustal thickening, subduction erosion, and magmatism in the south-Central Andes. Geol. Soc. Am. Bull. 117 (1–2), 67–88.

Kay, S.M., Mpodozis, C., Coira, B., 1999. Neogene magmatism, tectonism, and mineral deposits of the Central Andes (22° S to 33° S), in B. Skinner, ed. Geology and mineral deposits of Central Andes. Soc. Econ. Geol. 7, 27–59.

Keppie, J.D., Ortega-Gutiérrez, F.J., 2010. 1.3–0.9 Ga Oaxaquia (Mexico): Remnant of an arc/backarc on the northern margin of Amazonia. J. S. Am. Earth Sci. 29 (1), 21–27.

Keskin, M., 2013. AFC-Modeler: a Microsoft Excel Workbook Program for Modelling Assimilation combined with Fractional Crystallization (AFC) Process in Magmatic Systems by using Equations of DePaolo (1981). Turk. J. Earth Sci. 22 (2), 304–319.

Kirsch, M., Paterson, S.R., Wobbe, F., Martinez-Ardila, A.M., Clausen, B.L., Alasino, P.H., 2016. Temporal histories of Cordilleran continental arcs: testing models for magmatic episodicity. Am. Mineral. 101 (10), 2133–2154.

Kistler, R.W., Wooden, J.L., Premo, W.R., Morton, D.M., 2014. Pb-Sr-Nd-O isotopic characterization of Mesozoic rocks throughout the northern end of the Peninsular Ranges Batholith: Isotopic evidence for the magmatic evolution of oceanic arc-continental margin accretion during the late cretaceous of southern California. In: Morton, D.M., Miller, F.K. (Eds.), Peninsular Ranges Batholith, Baja California and Southern California, vol. 211. Geological Society of America Memoir, pp. 263–316.

Lackey, J.S., Valley, J.W., Chen, J.H., Stockli, D.F., 2008. Dynamic magma systems, crustal recycling, and alteration in the Central Sierra Nevada Batholith: the oxygen isotope record. J. Petrol. 49, 1397–1426.

Lipman, P.W., 2007. Incremental assembly and prolonged consolidation of Cordilleran magma chambers: evidence from the Southern Rocky Mountain volcanic field. Geosphere 3 (1), 42.

Litherland, M., 1994. The metamorphic belts of Ecuador. Overseas Mem Br Geol Surv v. 11, 1–147.

Loewy, S.L., Connelly, J.N., Dalziel, I.W.D., 2004. An orphaned basement block: the Arequipa-Antofalla Basement of the central Andean margin of South America. Geol. Soc. Am. Bull. 116 (1–2), 171–187.

Ludwig, K., 2003. User's Manual for Isoplot 3.00. A Geochronological Toolkit for Microsoft Excel, vol. 4. Berkeley Geochronology Center Special Publication.

Luffi, P., Ducea, M., 2022. Chemical mohometry: Assessing crustal thickness of ancient orogens using geochemical and isotopic data. Rev. Geophys. v. 60, no. 2 https://doi.org/10.1029/2021RG000753.

Mamani-Huisa, M.-I., 2006. Variations in Magma Composition in Time and Space along the Central Andes (13° S - 28° S): Göttingen Univ (Dissertation, 125p).

Mamani, M., Tassara, A., Wörner, G., 2008. Composition and structural control of crustal domains in the Central Andes. Geochem. Geophys. Geosyst. 9 (3), Q03006. https://doi.org/10.1029/2007GC001925.

Mamani, M., Wörner, G., Sempere, T., 2010. Geochemical variations in igneous rocks of the Central Andean orocline (13° S to 18° S): Tracing crustal thickening and magma generation through time and space. Geol. Soc. Am. Bull. 122 (1–2), 162–182.

Martínez Ardila, A.M., Clausen, B.L., Memeti, V., Paterson, S.R., 2019a. Source contamination, crustal assimilation, and magmatic recycling during three flare-up events in the cretaceous Peruvian Coastal Batholith: an example from the Ica-Pisco plutons. J. S. Am. Earth Sci. 95 https://doi.org/10.1016/j.jsames.2019.102300.

Martínez Ardila, A.M., Paterson, S.R., Memeti, V., Parada, M.A., Molina, P.G., 2019b. Mantle driven cretaceous flare-ups in Cordilleran arcs. Lithos 326, 19–27.

Martínez Valladares, W., Cervantes Gárate, J., 2003. Rocas ígneas en el sur del Perú: nuevos datos geocronométricos, geoquímicos y estructurales entre los paralelos 16° y 18° 30' Latitud Sur. Boletín D 26, 140.

Matthews, K.J., Seton, M., Müller, R.D., 2012. A global-scale plate reorganization event at 105-100 Ma. Earth Planet. Sci. Lett. 355, 283–298.

Mégard, F., 1984. The Andean orogenic period and its major structures in central and northern Peru. J. Geol. Soc. 141 (5), 893–900.

Mišković, A., Spikings, R. A., Chew, D. M., Košler, J., Ulianov, A., and Schaltegger, U., 2009, Tectonomagmatic evolution of Western Amazonia: Geochemical characterization and zircon U-Pb geochronologic constraints from the Peruvian Eastern Cordilleran granitoids. Geol. Soc. Am. Bull. 121 (9–10), 1298–1324.

Mitouard, P., Kissel, C., Laj, C., 1990. Post-Oligocene rotations in southern Ecuador and northern Peru and the formation of the Huancabamba deflection in the Andean Cordillera. Earth Planet. Sci. Lett. 98 (3–4), 329–339.

Moore, N.D., 1979. The geology and geochronology of the Arequipa segment of the Coastal Batholith of Peru. University of Liverpool, dissertation, p. 549.

Moore, N., Agar, R., 1985. Variations along a batholith: The Arequipa segment of the Coastal Batholith of Peru. In: Pitcher, W.S., et al. (Eds.), Magmatism at a Plate Edge: The Peruvian Andes. John Wiley, New York, pp. 108–118.

Moore, N.D., 1984. Potassium-Argon ages from the Arequipa Segment of the Coastal Batholith of Peru and their correlation with regional tectonic events. J. Geol. Soc. 141 (3), 511–519.

Mourier, T., 1988. La transition entre Andes marginales et Andes cordilleraines á ophiolites: évolution sédimentaire, magmatique et structurale du relais de Huancabamba (3 á 8 Lat: S; Nord Pérou-Sud Equateur): Paris, 11.

Mpodozis, C., Ramos, V.A., 1989. The Andes of Chile and Argentina. In: Ericksen, G.E., et al. (Eds.), Geology of the Andes and its Relation to Hydrocarbon and Mineral Resources: Houston, Texas, Circum-Pacific Council for Energy and Mineral Resources Earth Science Series, pp. 59–90 vol. v. 11, ch. 5.

Mukasa, S.B., 1984. Comparative Pb Isotope Systematics and Zircon U-Pb Geochronology for the Coastal, San Nicolas and Cordillera Blanca Batholiths, Peru. University of California, Santa Barbara dissertation (387 p).

Mukasa, S.B., 1986. Common Pb isotopic compositions of the Lima, Arequipa and Toquepala segments in the Coastal batholith, Peru: Implications for magmagenesis. Geochim. Cosmochim. Acta 50, 771–782.

Myers, J.S., 1975. Cauldron Subsidence and Fluidization: Mechanisms of Intrusion of the Coastal Batholith of Peru into its own Volcanic Ejecta. Geol. Soc. Am. Bull. 86 (9), 1209–1220.

Noble, D.C., McKee, E.H., Megard, F., 1978. Eocene uplift and unroofing of the coastal batholith near Lima, central Peru. J. Geol. 86 (3), 403–405.

Otamendi, J.E., Ducea, M.N., Tibaldi, A.M., Bergantz, G.W., de la Rosa, J.D., Vujovich, G. I., 2009. Generation of Tonalitic and Dioritic Magmas by coupled Partial Melting of Gabbroic and Metasedimentary Rocks within the Deep Crust of the Famatinian Magmatic Arc, Argentina. J. Petrol. 50 (5), 841–873.

Pardo-Casas, F., Molnar, P., 1987. Relative motion of the Nazca (Farallon) and South American Plates since late cretaceous time. Tectonics 6 (3), 233–248.

Paterson, S.R., Memeti, V., Mundil, R., Žák, J., 2016. Repeated, multiscale, magmatic erosion and recycling in an upper-crustal pluton: Implications for magma chamber dynamics and magma volume estimates. Am. Mineral. 101, 23.

Paterson, S.R., Ducea, M.N., 2015. Arc magmatic tempos: gathering the evidence. Elements 11 (2), 91–98.

Petford, N., Atherton, M.P., 1995. Crustal segmentation and the isotopic significance of the Abancay Deflection: Northern Central Andes (9-20° S): Andean. Geology 22 (2), 235–243.

Pfiffner, O., Gonzalez, L., 2013. Mesozoic–Cenozoic Evolution of the Western Margin of South America: Case Study of the Peruvian Andes. Geosciences 3 (2), 262.

Pitcher, W.S., Atherton, M.P., Cobbing, E.J., Beckinsale, R.D., 1985. Magmatism at a Plate Edge: The Peruvian Andes. Wiley.

Plank, T., Cooper, L.B., Manning, C.E., 2009. Emerging geothermometers for estimating slab surface temperatures. Nat. Geosci. 2 (9), 611–615.

Polliand, M., Schaltegger, U., Frank, M., Fontbote, L., 2005. Formation of intra-arc volcanosedimentary basins in the western flank of the central Peruvian Andes during Late Cretaceous oblique subduction: field evidence and constraints from U–Pb ages and Hf isotopes. Int. J. Earth Sci. 94, 231–242.

Quang, C.X., Clark, A.H., Lee, W., Hawkes, N., 2005. Response of supergene processes to episodic Cenozoic uplift, pediment erosion, and ignimbrite eruption in the porphyry copper province of southern Peru. Econ. Geol. 100 (1), 87–114.

Ramos, V., Alemán, A., 2000. Tectonic evolution of the Andes. In: Cordani, U.G.,

Milani, E.J., Filho, A. Thomaz, Campos, D.A. (Eds.), Tectonic evolution of South America: 31st International Geological Congress, Río de Janeiro, pp. 635–685.

Ramos, V.A., 1999. Plate tectonic setting of the Andean Cordillera. Episodes J. Int. Geosci. 22 (3), 183–190.

Ramos, V.A., 2008. Patagonia: a Paleozoic continent adrift? J. South Am. Earth Sci. 26 (3), 235–251.

Ramos, V.A., 2009. Anatomy and global context of the Andes: Main geologic features and the Andean orogenic cycle. In: Kay, S.M., Ramos, V.A., Dickinson, W.R. (Eds.), Backbone of the Americas: Shallow Subduction, Plateau Uplift, and Ridge and Terrane Collision: Geological Society of American Memoir, vol. 204, pp. 31–65.

Ramos, V.A., 2010. The tectonic regime along the Andes: Present-day and Mesozoic regimes. Geol. J. 45 (1), 2–25.

Ramos, V.A., 2018. Tectonic evolution of the Central Andes: From terrane accretion to crustal delamination. In: Zamora, G., McClay, K.M., Ramos, V.A. (Eds.), Petroleum Basins and Hydrocarbon Potential of the Andes of Peru and Bolivia: AAPG Memoir, vol. 117, pp. 1–34.

Ramos, V.A., Folguera, A., 2005. Tectonic evolution of the Andes of Neuquén: constraints derived from the magmatic arc and foreland deformation. Geol. Soc. London Spec. Publ. 252 (1), 15–35.

Regan, P.F., 1976. The Genesis and Emplacement of Mafic Plutonic Rocks of the Coastal Andean Batholith, Lima Province, Peru. University of Liverpool dissertation (186p).

Regan, P.F., 1985. The early basic intrusions. In: Pitcher, W.S., et al. (Eds.), Magmatism at a Plate Edge: The Peruvian Andes. John Wiley, New York, pp. 72–89.

Reimann, C.R., Bahlburg, H., Kooijman, E., Berndt, J., Gerdes, A., Carlotto, V., López, S., 2010. Geodynamic evolution of the early Paleozoic Western Gondwana margin 14°–17° S reflected by the detritus of the Devonian and Ordovician basins of southern Peru and northern Bolivia. Gondwana Res. 18 (2–3), 370–384.

Reynolds, P.H., Dasch, E.J., 1971. Lead isotopes in marine manganese nodules and the ore-lead growth curve. J. Geophys. Res. 76 (21), 5124–5129.

Rodrigues, J., Acosta, J., Castroviejo, R., Quispe, J., Romero, D., Uribe, R., Campian, M., 2010. Geología y estructura de las ultramafitas de Tapo y Acobamba (Tarma, Perú). Removilización tectónica Andina de un segmento ofiolítico Pre-Andino: XV Congreso Peruano de Geologia. In: Resumenes Extendidos. Sociedad Geologica del Peru, Pub Esp., no. 9, pp. 79–82.

Rodríguez Morante, I., Huanacuni Mamani, D., 2011. Síntesis geoeconómica de la región Piura: Instituto Geológico Minero y Metalúrgico del Perú "INGEMMET", pp. 79–82.
Rogers, G., Hawkesworth, C.J., 1989. A geochemical traverse across the North Chilean Andes: evidence for crust generation from the mantle wedge. Earth Planet. Sci. Lett. 91 (3–4), 271–285.

Rollinson, H., 1993. Using Geochemical Data. Longman, London (352p).

Romero, D., Valencia, K., Alarcón, P., Peña, D., Ramos, V.A., 2013. The offshore basement of Perú: evidence for different igneous and metamorphic domains in the forearc. J. S. Am. Earth Sci. 42, 47–60.

Romero Fernández, D., Valencia, K., Alarcón, P., Ramos, V., 2011. Geología de la costa pacífica del Perú central entre Chiclayo y Paracas (7 214 sur). In: Proceedings Memorias 14th Congreso Latinoamericano de Geología and 13th Congreso Colombiano de Geología, Medellín, pp. 110–111.

Romeuf, N., Münch, P., Soler, P., Jaillard, E., Pik, R., Aguirre, L., 1997. Mise en évidence de deux lignées magmatiques dans le volcanisme du Jurassique inférieur de la zone subandine équatorienne: Comptes Rendus-Academie des Sciences Paris serie 2 Sciences de la Terre et des Planetes Fascicule A, v. 324, pp. 361–368.

Sanchez-Fernandez, A.W., 1982. Edades Rb-Sr en los segmentos Arequipa-Toquepala del Batolito de la costa del Peru, Quinto Congreso Latinoamericano de Geologia: Argentina, pp. 487–504.

Santos, A., Weimin, G., Tassinari, C., Soberon, D., Ccallo, W., 2016. Geocronología U-Pb sobre zircones en la contrastación de la evolución espacial-temporal del magmatismo y la metalogenia del Batolito de la Costa “segmento Arequipa”. In: Proceedings XVIII Congreso Peruano de Geológía, pp. 1–7.

Schellart, W.P., 2017. Andean mountain building and magmatic arc migration driven by subduction-induced whole mantle flow. Nat. Commun. 8 (1), 2010.

Schmitz, M., 1994. A balanced model of the southern Central Andes. Tectonics 13 (2), 484–492.

Schwartz, J.J., Klepeis, K.A., Sadorski, J.F., Stowell, H.H., Tulloch, A.J., Coble, M.A., 2017. The tempo of continental arc construction in the Mesozoic median Batholith, Fiordland, New Zealand. Lithosphere 9 (3), 343–365.

Sdrolias, M., Müller, R.D., 2006. Controls on back-arc basin formation. Geochem. Geophys. Geosyst. v. 7, no. 4 https://doi.org/10.1029/2005GC001090.

Sébrier, M., Mercier, J.L., Macharé, J., Bonnot, D., Cabrera, J., Blanc, J.L., 1988. The state of stress in an overriding plate situated above a flat slab: the Andes of Central Peru. Tectonics 7 (4), 895–928.

Sempere, T., Carlier, G., Soler, P., Fornari, M., Carlotto, V.C., Jacay, J., Arispe, O., Néraudeau, D., Cárdenas, J., Rosas, S., Jiménez, N., 2002. Late Permian–Middle Jurassic lithospheric thinning in Peru and Bolivia, and its bearing on Andean-age tectonics. Tectonophysics 345 (1–4), 153–181.

Sempere, T., Folguera, A., Gerbault, M., 2008. New insights into Andean evolution: an introduction to contributions from the 6th ISAG symposium (Barcelona, 2005). Tectonophysics 459 (1). https://doi.org/10.1016/j.tecto.2008.03.011.

Shackleton, R., Ries, A., Coward, M., Cobbold, P.R., 1979. Structure, metamorphism and geochronology of the Arequipa Massif of coastal Peru. J. Geol. Soc. 136 (2), 195–214.

Sharp, Z.D., 1990. A laser-based microanalytical method for the in-situ determination of oxygen isotope ratios of silicates and oxides. Geochim. Cosmochim. Acta 54, 1353–1357.

Soler, P., Bonhomme, M.G., 1990. Relation of magmatic activity to plate dynamics in Central Peru from late cretaceous to present. In: Kay, S.M., Rapela, C.W. (Eds.), Plutonism from Antarctica to Alaska: Geological Society of America Special Paper, 241, pp. 173–192.

Stern, T.W., Bateman, P.C., Morgan, B.A., Newell, M.F., Peck, D.L., 1981. Isotopic U-Pb Ages of Zircon from the Granitoids of the Central Sierra Nevada, California. USGS Professional Paper, 1185.

Stewart, J., Garcia, W., 1968. Geológia de los cuadrangulos de Mollendo y La Joya. Boletin del Servicio Geológico Minero del Perú 19 (19), 1–93.

Stewart, J.W., Evernden, J.F., Snelling, N.J., 1974. Age determinations from Andean Peru: a reconnaissance survey. Geol. Soc. Am. Bull. 85 (7), 1107–1116.

Stracke, A., et al., 2003. Recycling oceanic crust: Quantitative constraints. Geochem. Geophys. Geosyst. 4 (3), 14–33.

Swenson, J.L., Beck, S.L., Zandt, G., 2000. Crustal structure of the Altiplano from broadband regional waveform modeling: implications for the composition of thick continental crust. J. Geophys. Res. Solid Earth 105 (B1), 607–621.

Taylor Jr., H.P., Sheppard, S.M.F., 1986. Igneous rocks: I. Processes of isotopic fractionation and isotope systematics. In: Valley, J.W., Taylor Jr., H.P., O'Neil, J.R. (Eds.), Stable Isotopes in High Temperature Geological Processes. Reviews in Mineralogy, 16, pp. 227–272.

Taylor, W.P., 1973. The Geochemistry and Mineralogy of Cañas and Puscao Plutons, Lima Province. Peru. University of Liverpool dissertation (196p).

Timoteo, D., Romero, D., Valencia, K.J.L., 2012. Posible existencia de la Faja Alleghanide? en el Noroeste del Perú: Recientes dataciones Ar/Ar y U-Pb, e implicancias en un Sistema Petrolero de la Cuenca Talara: Sociedad Geológica del Perú, 16th Congreso Peruano de Geológía.

Tosdal, R., Farrar, E., Clark, A.H., 1981. K-Ar geochronology of the late Cenozoic volcanic rocks of the Cordillera Occidental, southernmost Peru. J. Volcanol. Geotherm. Res. 10 (1–3), 157–173.

Trumbull, R.B., Riller, U., Oncken, O., Scheuber, E., Munier, K., Hongn, F.D., 2006. The time-space distribution of Cenozoic volcanism in the South-Central Andes: a new data compilation and some tectonic implications. Andes Active Subduction Orogeny 29–43. https://doi.org/10.1007/978-3-540-48684-8_2.

Turner, S.J., Langmuir, C.H., 2015. The global chemical systematics of arc front stratovolcanoes: evaluating the role of crustal processes. Earth Planet. Sci. Lett. 422, 182–193.

Vidal C, C.E., Injoque-Espinoza, J., Sidder, G.B., Mukasa, S.B., 1990. Amphibolitic Cu-Fe skarn deposits in the central coast of Peru. Econ. Geol. 85 (7), 1447–1461.

Villagomez, R., Jaillard, E., Bulot, L., Rivadeneira, M., Vera, R., 1996. The Aptian-late Albian marine transgression in the oriente basin of Ecuador. In: International Symposium on Andean Geodynamics, 3rd, St. Malo, France, 1996, Proceedings, pp. 521–524.

Voos, A., Martinez-Ardila, A.M., Clausen, B.L., 2021. Zircon ages reveal unexpected older flare-up in the Peruvian Coastal Batholith. GSA Cordilleran Online Section 53.

Willner, A.P., Tassinari, C.C., Rodrigues, J.F., Acosta, J., Castroviejo, R., Rivera, M., 2014. Contrasting Ordovician high-and low-pressure metamorphism related to a microcontinent-arc collision in the Eastern Cordillera of Perú (Tarma province). J. S. Am. Earth Sci. 54, 71–81.

Winter, L.S., 2008. The Genesis of “Giant” Copper-Zinc-Gold-Silver Volcanogenic Massive Sulphide Deposits at Tambogrande, Perú : Age, Tectonic Setting, Paleomorphology, Lithogeochemistry, and Radiogenic Isotopes [Doctor of Philosophy - PhD: University of British Columbia] (274 p).

Wipf, M.A., 2006. Evolution of the Western Cordillera and Coastal Margin of Peru: Evidence from Low-Temperature Thermochronology and Geomorphology. PhD thesis. Swiss Fed. Inst. of Technol, Zürich, Switzerland, pp. 14–18.

Wise, J., 2002. Examples of syntectonic emplacement instead of passive pluton emplacement in the Coastal Batholith of Peru and implications for late Creataceous Nazca plate motions. Boletin de la Sociedad Geológica del Peru 94, 99–106.

Witt, C., Rivadeneira, M., Poujol, M., Barba, D., Beida, D., Beseme, G., Montenegro, G., 2017. Tracking ancient magmatism and Cenozoic topographic growth within the Northern Andes forearc: Constraints from detrital U-Pb zircon ages. Geol. Soc. Am. Bull. 129 (3–4), 415–428.

Wörner, G., Lezaun, J., Beck, A., Heber, V., Lucassen, F., Zinngrebe, E., Rössling, R., Wilke, H.G., 2000. Precambrian and early Paleozoic evolution of the Andean basement at Belen (northern Chile) and Cerro Uyarani (western Bolivia Altiplano). J. S. Am. Earth Sci. 13 (8), 717–737.

Zelasco, L.D.N., 2011. Tectonic Evolution of the Contaya Arch Ucyali Basin, Peru. MS Thesis. Graduate Studies of Texas A&M University, p. 57.

Zellmer, G.F., 2008. Some first-order observations on magma transfer from mantle wedge to upper crust at volcanic arcs: Geological Society. Lond. Special Publ. 304 (1), 15–31.

Zheng, Y.F., 1993. Calculation of oxygen isotope fractionation in hydroxyl-bearing silicates. Earth Planet. Sci. Lett. 120 (3–4), 247–263.

CHAPTER 5

CONCLUSIONS

> "Everyone who is seriously involved in the pursuit of science becomes convinced that a spirit is manifest in the laws of the Universe – a spirit vastly superior to that of man, and one in the face of which we with our modest powers must feel humble."
>
> ~ Albert Einstein

This research project has focused on providing insight into the ongoing discussion of what mechanisms are ultimately responsible for driving magmatism in continental arcs and was inspired by Paterson and Ducea (2015) and Kirsch et al. (2016). The Peruvian segment of the American Cordillera was selected as an ideal location to address this issue. It is a region with a long history of subduction magmatism, with a relatively good (and growing) geochronology and geochemistry dataset being available.

Arc Tempos Geochronology Analysis

The first part of the project involved assembling all available geochronology data, adding more data through fieldwork, and visualizing the temporal magmatic history using age spectra. With the aid of GIS and data analysis tools, parameters gathered from age spectra could be used to consider estimates on mantle magma addition volumes. This also required paleo-crust thickness data which was obtained through a very recent and innovative technique called mohometry (Luffi and Ducea, 2022). Finally, estimated mantle magma addition volume per unit area was needed to complete the requirements for magma volume estimates. This was provided by the recent work of Ratschbacher et al. (2019) that carefully

analyzed a number of tilted arc sections and took into consideration the various complicating factors before arriving at a specific quantity.

Overall results for flare-ups and lulls in the three segments of the Peruvian Coastal Batholith and the Eastern Cordillera show similar mantle magma additions to the arc crust for each, at 1070k km^3 and 1148k km^3 for the PCB and EC respectively, assuming a mantle/crust ratio of 80/20. Spatiotemporal patterns were considered for each flare-up for the lower north, central and south segments of the Peruvian Coastal Batholith and the Eastern Cordillera. An online interactive application was created to allow the spatiotemporal data relating to flare-ups to be explored interactively.

Arc Geochemistry Analysis

The second part of the project addresses the main question of the driving mechanism for continental arc flare-ups. This involved assembling a geochemical dataset from existing data augmented with new geochemical data from fieldwork performed for this project. Although much previous geochemical data was available, most did not have measured ages. To be useful in analyzing geochemical changes during flare-ups and lulls, geochemical data need to have well constrained ages, so a great amount of these had to be removed. Since it could be shown that ages obtained through K-Ar, Ar-Ar and Rb-Sr methods did not change age spectra much as compared to only using the more reliable U-Pb data, these data were added, increasing available geochemistry sample data by ~40% to over 1000 samples.

The first geochemistry analysis compared flare-ups to lulls using a narrowly defined range for flare-ups for the three segments of the Peruvian Coastal Batholith (lower north, central and south). Secondly, the rising parts of flare-ups was compared to falling parts. In

each case, weak support was found for upper plate arc internal feedback models, suggesting other factors are involved. Large scale tectonics related to the lower plate are potential driving mechanisms for flare-ups and lulls as can be seen by similar patterns during the Cretaceous and Paleogene for the Peruvian Coastal Batholith. Scale is an important consideration, with different processes possibly operating at different scales.

Future Work

This type of analysis has great potential to elucidate the mechanisms driving continental arc magmatism, however obtaining meaningful results depends greatly on having access to a good amount of high-quality data at sufficient temporal and spatial resolution. Although data for the Peruvian arc are relatively good, the analysis done in this project was still data constrained, especially when looking at smaller areas and time periods, which is necessary to understand processes operating at smaller scales. Using the techniques outlined here on another arc segment that has more such data available such as the Sierra Nevada or Peninsular Ranges batholiths would be a worthwhile project. As more data become available in Peru and elsewhere, further refinements of these techniques, such as involving additional geochemical variables in time series analysis, can be expected to reveal more intricate details regarding the driving mechanisms behind Earth's dynamically evolving continental arc systems.

Personal Reflections on this Project

This project has been very enriching to work on in many ways. Fieldwork in the high Eastern Cordillera mountains around Cusco and beyond remains one of the main highlights.

Running multiple U-Pb radiometric dating sessions in Arizona was valuable and enjoyable in various ways, such as opportunities to learn a lot on each visit and being able to work alongside experts in the field. Working with large amounts of data, figuring out how data should be stored, managed and configured to facilitate analysis by software was an interesting educational experience. By far the most time-consuming part of the project was developing the R code necessary to implement the data analysis and plots. A programmatical approach was selected because it offers almost unlimited flexibility to implement ideas. However, this flexibility comes at the cost of learning and implementation difficulty. An added bonus however is the capacity to run analyses and plot generation in batch mode, being able to tweak parameters and cope with data changes easily, as long as this capability was built into the code. A notable trade-off was on the decision between expending more effort on setting up a block of code to make analyses run with minimal effort (relatively automatically) or expend less initial time on the code but require more effort when running analyses. In some cases the initial coding effort was justified and in others it was not.

References

Kirsch, M., Paterson, S. R., Wobbe, F., Martínez, A. M., Clausen, B. L., and Alasino, P. H., 2016, Temporal histories of Cordilleran continental arcs: Testing models for magmatic episodicity: American Mineralogist, v. 101, no. 10, p. 2133-2154.

Luffi, P., and Ducea, M., 2022, Chemical Mohometry: Assessing Crustal Thickness of Ancient Orogens Using Geochemical and Isotopic Data: Reviews of Geophysics, v. 60, no. 2.

Paterson, S. R., and Ducea, M. N., 2015, Arc magmatic tempos: gathering the evidence: Elements, v. 11, no. 2, p. 91-98.

Ratschbacher, B. C., Paterson, S. R., and Fischer, T. P., 2019, Spatial and depth-dependent variations in magma volume addition and addition rates to continental arcs: Application to global CO2 fluxes since 750 Ma: Geochemistry, Geophysics, Geosystems, v. 20, no. 6, p. 2997-3018.

APPENDIX A

ZIRCON SEPARATION AND IMAGING

Zircon Separation: Arizona LaserChron Center

Zircon crystals were extracted from samples at the Arizona LaserChron Center (www.laserchron.org) by traditional methods of crushing and grinding, followed by separation with a Wilfley table, heavy liquids, and a Frantz magnetic separator. Samples were processed such that all zircons were retained in the final heavy mineral fraction. For detrital analyses, a large split of grains (generally thousands of grains) was incorporated into a 1" epoxy mount together with fragments or loose grains of Sri Lanka, FC-1, and R33 zircon crystals that were used as primary standards. For igneous samples, ~50 high-quality grains were selected and mounted with standards, generally with four samples per mount. The mounts were sanded down to a depth of ~20 microns, polished, imaged, and cleaned prior to isotopic analysis.

Zircon Separation: California State University, Fullerton

The following steps were followed to separate zircons for igneous bedrock and detrital zircon samples.

1. Crushing – the sample was run through a Braun Chipmunk VD67 jaw crusher to produce millimeter-size rock chips.
2. Pulverizing – a Bico Braun Disc Pulverizer, Model UA reduced the rock chips to sand-sized particles.

3. Washing and decanting – the very small-sized fraction was removed by washing and decanting and samples were dried using a Thermo Scientific Precision drying oven and Infrared heat lamp and reflector.
4. Hand magnetic separation – a Magnetic Separator Pickup Tool separated (ferromagnetic) iron magnetite minerals from other minerals.
5. Frantz separation – a Frantz Isodynamic Separator separated minerals that are slightly attractive magnetically (paramagnetic) from minerals that are slightly repulsive magnetically (diamagnetic), with zircons being diamagnetic.
6. Heavy liquid separation – lithium heteropolytungstate (LST) was used to separate lighter fraction minerals (quartz, feldspar) from heavier fraction minerals (apatite, zircon). The heavy liquid was reclaimed by rinsing the sample and filters and evaporating the water using a stirring hotplate.
7. Final frantzing – the heavy fraction was run through the Frantz separator again to remove any remaining paramagnetic minerals.
8. Microscope – final identification of zircons to separate from other minerals, e.g., apatite. A portable ultraviolet lamp was used to distinguish zircons from apatite.

Imaging: Arizona LaserChron Center

Images were made at the Arizona LaserChron SEM facility (www.geoarizonasem.org) with a Hitachi 3400N SEM equipped with a Gatan CL2 detector system and an Oxford EDS/EBSD system. BSE imaging provides image contrast as a function of elemental composition, as well as surface topography. The production efficiency for backscattered electrons is proportional to the sample material's mean

atomic number, which results in image contrast as a function of composition, i.e., higher atomic number material appears brighter than low atomic number material in a backscattered electron image. CL imaging collects cathodoluminescence emitted from the material, which is used to examine internal structures of semiconductors, rocks, ceramics, glass etc. in order to get information on the composition, growth and quality of the material.

APPENDIX B

GEOCHRONOLOGY ANALYSIS METHODS

U-Pb Geochronology Analysis of Igneous Bedrock and Detrital Zircons

Earlier geochronologic analyses of zircon grains were performed on the older multicollector inductively coupled plasma-mass spectrometer (GVI Isoprobe) coupled to a 193 nm Excimer laser ablation system (New Wave Instruments and Lambda Physik), also known as the Nu instrument, at the Arizona LaserChron Center (ALC, 2022). This setup was equipped with channeltron and Faraday collectors configured and operated as described in Gehrels et al. (2008).

All subsequent geochronologic analyses of zircon grains (the vast majority) were analyzed using a Photon Machines Analyte G2 excimer laser equipped with HelEx ablation cell using a spot diameter of between 10 and 30 microns at the Arizona LaserChron Center (ALC, 2022). The ablated material is carried in helium into the plasma source of an Element2 HR ICP-MS, which sequences rapidly through U, Th, Pb, and other isotopes, for example Hg. Signal intensities are measured with an SEM (secondary electron multiplier) that operates in pulse counting mode for signals less than 50K cps, in both pulse-counting and analog mode for signals between 50K and 5M cps, and in analog mode above 5M cps. In a recent modification to improve efficiency by operating only in the pulse counting mode, ^{238}U ions are calculated from ^{235}U. The calibration between pulse-counting and analog signals is determined line-by-line for signals between 50K and 5M cps, and is applied to >5M cps signals. Four intensities are determined and averaged for each isotope, with dwell times of 0.0052 sec for ^{202}Pb,

0.0075 sec for ^{204}Pb, 0.0202 sec for ^{206}Pb, 0.0284 sec for ^{207}Pb, 0.0026 sec for ^{208}Pb, 0.0026 sec for ^{232}U, and 0.0104 sec for ^{238}U.

The laser can be set to several different energy and dwell modes. With the laser set to an energy density of ~5 J/cm^2, a repetition rate of 8 Hz, and an ablation time of 10 seconds, ablation pits are ~12 microns in depth. Sensitivity with these settings is approximately ~5000 cps/ppm. Each analysis consists of 5 sec on peaks with the laser off (for backgrounds), 10 sec with the laser firing (for peak intensities), and a 20 second delay to purge the previous sample and save files.

Data Reduction

Following analysis, data reduction was performed with a LaserChron Center in-house Python decoding routine and an Excel spreadsheet (E2agecalc) (more recently this has been switched to a MatLab® application) that:

1. Decodes .dat files with measured intensities from the Thermo software (routine written by John Hartman, University of Arizona)
2. Imports intensities and a sample name for each analysis
3. Calculates average intensities for each isotope (based on the sum of all counts while the laser is firing)
4. Subtracts ^{204}Hg from the ^{204}Pb signal to yield ^{204}Pb intensity (using natural ^{202}Hg/^{204}Hg of 4.3). This Hg correction is not significant for most analyses because Hg backgrounds are low (generally ~150 cps at mass ^{204}Pb).
5. Performs a common Pb correction based on the measured ^{206}Pb/^{204}Pb and the assumed composition of common Pb based on Stacey and Kramers (1975)

6. Calculates measured 206/238, 206/207, and 208/232 ratios
7. Compares measured and known ratios for the three standards to determine fractionation factors for $^{206}Pb/^{238}U$, $^{206}Pb/^{207}Pb$, and $^{208}Pb/^{232}U$. These correction factors are generally <5% for $^{206}Pb/^{238}U$, <2% for $^{206}Pb/^{207}Pb$, and <20% for $^{208}Pb/^{232}U$.
8. Determines an overdispersion factor if the standard analyses show greater dispersion than expected from measurement uncertainties
9. Uses a sliding-window average to apply fractionation factors to unknowns (generally averaging 8 standard analyses)
10. Calculates fractionation-corrected $^{206}Pb/^{238}U$, $^{206}Pb/^{207}Pb$, and $^{208}Pb/^{232}U$ ratios and ages for unknowns
11. Propagates measurement uncertainties for $^{206}Pb/^{238}U$ and $^{208}Pb/^{232}U$ that are based on the scatter about a regression of measured values. Uncertainties for $^{206}Pb/^{207}Pb$ and $^{206}Pb/^{204}Pb$ are based on the standard deviation of measured values since these ratios generally do not change during an analysis. The sum of this uncertainty and any over-dispersion factor is reported as the internal (or measurement) uncertainty for each analysis. These uncertainties are reported at the 1-sigma level.
12. Calculates the down-hole slope of $^{206}Pb/^{238}U$ to highlight analyses in which $^{206}Pb/^{238}U$ is compromised due to heterogeneity in age (e.g., crossing an age boundary) or intersection of a fracture or inclusion.
13. Calculates concentrations of U and Th for unknowns based on the measured intensity and known concentrations of FC-1.

14. Calculates the external (systematic) uncertainties for $^{206}Pb/^{238}U$, $^{206}Pb/^{207}Pb$, and $^{208}Pb/^{232}U$, which include contributions from (a) the scatter of standard analyses, (b) uncertainties in the ages of the standards, (c) uncertainties in the composition of common Pb, and (4) uncertainties in the decay constants for ^{235}U and ^{238}U.
15. Determines a "Best Age" for each analysis, which is generally the $^{206}Pb/^{238}U$ age for <1400 Ma ages and the $^{206}Pb/^{207}Pb$ age for >1400 Ma ages.
16. Provides preliminary filters that highlight analyses with >20% discordance, >5% reverse discordance, or >10% internal (measurement) uncertainty.
17. Corrects $^{206}Pb/^{238}U$ ages for U-Th disequilibrium. This has a significant impact only on very young (~<2 Ma) ages.
18. Calculates the radiation dosage that the analyzed portion of each zircon has experienced, assuming a value of 2.3 for the Th/U of the magma. This is plotted against $^{206}Pb/^{238}U$ age to help identify Pb loss.
19. Creates a publication-ready data table with concentrations, isotope ratios, and ages for unknowns.

For detrital zircon analyses, the ages are shown on Pb*/U concordia diagrams and relative age-probability diagrams using the routines in Isoplot (Ludwig, 2008). The age-probability diagrams show each age and its uncertainty (for measurement error only) as a normal distribution and sum all ages from a sample into a single curve. Composite age probability plots are made from an in-house Excel program that normalizes each curve according to the number of constituent analyses, such that each curve contains the same area, and then stacks the probability curves.

For igneous bedrock analyses, the ages are shown on Pb*/U concordia diagrams and weighted mean diagrams using the routines in Isoplot (Ludwig, 2008). The weighted mean diagrams show the weighted mean (weighting according to the square of the internal uncertainties), the uncertainty of the weighted mean, the external (systematic) uncertainty that corresponds to the ages used, the final uncertainty of the age (determined by quadratic addition of the weighted mean and external uncertainties), and the MSWD of the data set.

Notes:

1. Analyses with >10% uncertainty (1-sigma) in $^{206}Pb/^{238}U$ age are not included.
2. Analyses with >10% uncertainty (1-sigma) in $^{206}Pb/^{207}Pb$ age are not included, unless $^{206}Pb/^{238}U$ age is <500 Ma.
3. Best age is determined from $^{206}Pb/^{238}U$ age for analyses with $^{206}Pb/^{238}U$ age <1400 Ma and from $^{206}Pb/^{207}Pb$ age for analyses with $^{206}Pb/^{238}U$ age > 1400 Ma.
4. Concordance is based on $^{206}Pb/^{238}U$ age / $^{206}Pb/^{207}Pb$ age. Value is not reported for $^{206}Pb/^{238}U$ ages <500 Ma because of large uncertainty in $^{206}Pb/^{207}Pb$ age.
5. Analyses with $^{206}Pb/^{238}U$ age > 500 Ma and with >20% discordance (<80% concordance) are not included.
6. Analyses with $^{206}Pb/^{238}U$ age > 500 Ma and with >5% reverse discordance (<105% concordance) are not included.
7. All uncertainties are reported at the 1-sigma level, and include only measurement errors.
8. Systematic errors are as follows (at 2-sigma level): [sample #: 2.5% ($^{206}Pb/^{238}U$) & 1.4% ($^{206}Pb/^{207}Pb$)] These values are reported on cells U1 and W1 of NUagecalc.

9. Analyses conducted by LA-MC-ICP-MS, as described by Gehrels et al. (2008).
10. U concentration and U/Th are calibrated relative to Sri Lanka (SR) zircon standard and are accurate to ~20%.
11. Common Pb correction is from measured ^{204}Pb with common Pb composition interpreted from Stacey and Kramers (1975).
12. Common Pb composition assigned uncertainties of 1.5 for $^{206}Pb/^{204}Pb$, 0.3 for $^{207}Pb/^{204}Pb$, and 2.0 for $^{208}Pb/^{204}Pb$.
13. U/Pb and $^{206}Pb/^{207}Pb$ fractionation is calibrated relative to fragments of a large Sri Lanka zircon of 563.5 ± 3.2 Ma (2-sigma).
14. U decay constants and composition as follows: $^{235}U = 9.8485 \times 10^{-10}$, $^{238}U = 1.55125 \times 10^{-10}$, $^{238}U/^{235}U = 137.88$.
15. Weighted mean and concordia plots determined with Isoplot (Ludwig, 2008)

References

ALC, 2022, Arizona LaserChron Center, U-Pb anlytical methods: https://www.laserchron.org.

Gehrels, G. E., Valencia, V. A., and Ruiz, J., 2008, Enhanced precision, accuracy, efficiency, and spatial resolution of U-Pb ages by laser ablation–multicollector–inductively coupled plasma–mass spectrometry: Geochemistry, Geophysics, Geosystems, v. 9, no. 3.

Ludwig, K., 2008, Isoplot 3.7: Berkeley Geochronology Center Special Publication 4.

Stacey, J. T., and Kramers, J., 1975, Approximation of terrestrial lead isotope evolution by a two-stage model: Earth and Planetary Science Letters, v. 26, no. 2, p. 207-221.

APPENDIX C

SUPPORTING FIGURES

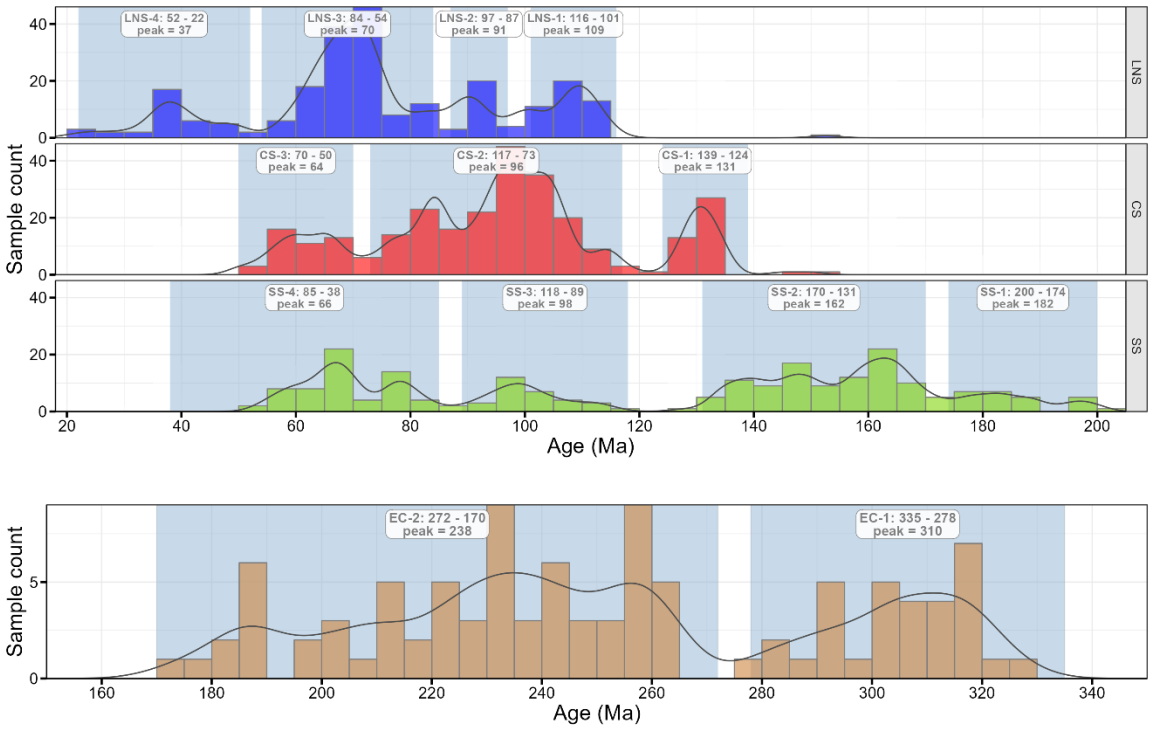

Figure 42. Bedrock sample age spectra for the three PCB segments and the EC, including only samples dated using zircon U-Pb geochronology (n = 867). Flare-up parameters are indicated. This figure can be compared to **Figures 10** and **20** that include ages using K-Ar, Ar-Ar and Rb-Sr dating methods.

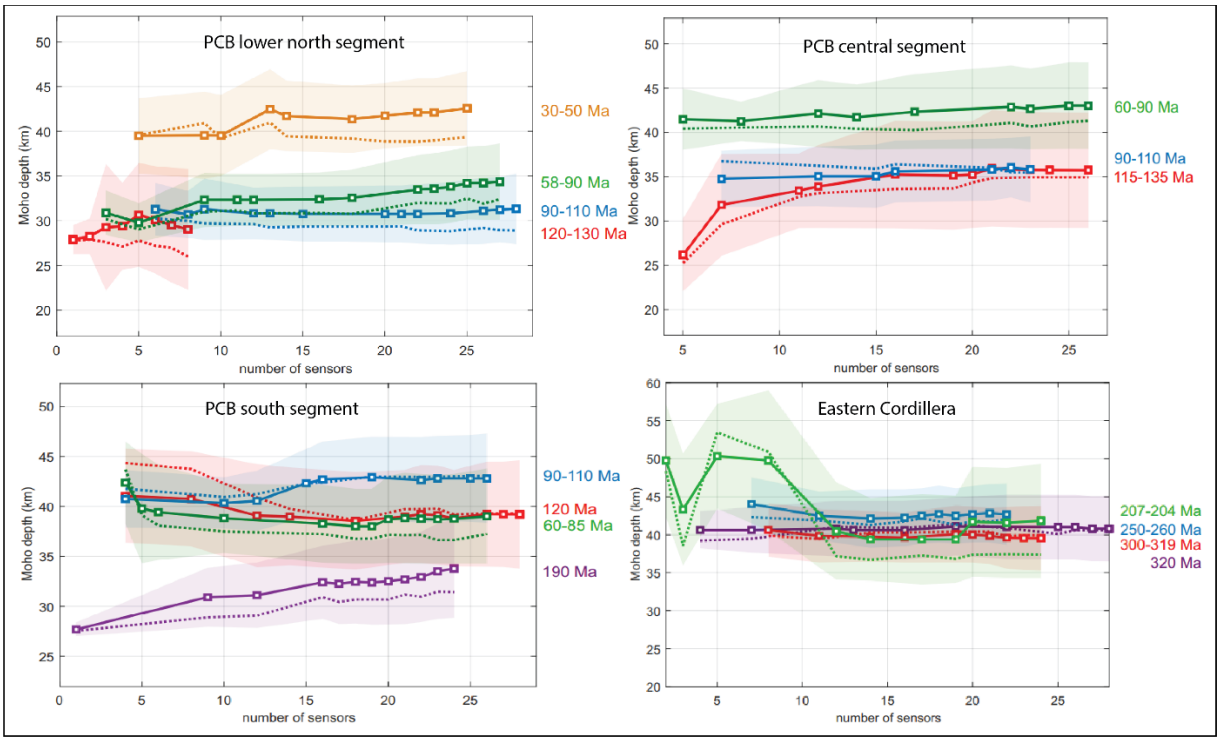

Figure 43. Mohometer calculations showing paleo-crustal thickness estimates for the three PCB segments and the EC using the approach of Luffi and Ducea (2022), corresponding to flare-ups as determined from the geochemical data. Number of sensors refers to the number of geochemical crustal thickness proxies used in each case. Paleo-crustal thickness values associated with each flare-up were determined as: LNS1 = 29; LNS2 = 31.5; LNS3 = 34.5; LNS4 = 42.5; CS1 = 36; CS2 = 36; CS3 = 43; SS1 = 34; SS2 = 39; SS3 = 43; SS4 = 39; EC1 = 43; EC2 = 39.

APPENDIX D

ADDITIONAL AND UNCONVENTIONAL IDEAS

Arc and Slab-Failure Magmatism

In the standard model of Cordilleran arc magmatism, arcs oscillate between compression and extension due to factors like slab dip, convergence rate or obliqueness. Hildebrand (2014) developed an alternative and more controversial model of Peruvian arc magmatism from work on several Cordilleran batholiths of North America. He proposes that magmatism occurs in two phases during terrane collision: an early arc phase and a subsequent phase of slab failure magmatism – a post-deformational phase representing a period of exhumation and erosion related to thickening of the crust during the collision. Slab failure magmatism occurs due to competing buoyancies between the oceanic and continental slabs. This results in the lower plate ultimately breaking by viscous necking at its weakest point, and sinking into the mantle, allowing asthenosphere to well up through the tear and melt adiabatically and then interact with the crust in the collision zone. Resulting magmas form linear arrays above tears in the descending slab as they flow through the breach in the slab.

Hildebrand and Whalen (2014) apply this model to the Peruvian Andes, proposing a westward dipping subduction zone beneath an ocean lying between the South American continent and the then off-shore Arequipa terrane. When this ocean closed in the Late Cretaceous, the Arequipa terrane collided with South America creating the Marañon fold and thrust belt. After magmatism shut down at 82 Ma, numerous along arc-strike dike swarms formed at 73 – 71 Ma, attesting to arc-parallel extension which they interpret to be the result of slab failure of the west-dipping South American lithosphere during the

Arequipa terrane collision. They suggest the PCB as a whole contains two periods of slab failure magmatism with a period of arc magmatism in between: 105 – 101 Ma and ~77 – 62 Ma. They attribute variations in magmatism as being due to complex plate interactions related to the Arequipa terrane leading to three periods of subduction, with two collisions, and two periods of slab-failure magmatism.

Mantle Plumes

The existence of hotspots was first proposed by Wilson (1963) to explain the linear chain configuration of the Hawaiian islands, and as evidence for fixed mantle plumes under moving crustal plates. Morgan (1972) saw hotspots as being the surface expressions of deep plumes in the earth's mantle. In the mantle plume hypothesis, the earth is seen as a massive heat engine driven by the heat from the initial formation of the earth, gravitational compression and radioactive decay as well as the release of heat of crystallization at the inner/outer core boundary. Plumes are predicted to arise as a result of mantle convection transporting heat away from the core to the earth's surface and dissipated mainly but not exclusively by oceanic crust formation at mid-ocean ridges (Larson, 1991b). The large thermal gradient at the core-mantle boundary (D" layer) is a key factor driving mantle convection. The existence of mantle plumes has become the focus of controversy and heated debate, possibly due to the excessive use of the plume hypothesis by over enthusiastic adopters without a lot of supporting evidence (Davies, 2005). Plume skeptics support their arguments mainly from early difficulties in imaging the plumes, and from the work of Anderson (1994), who maintains mantle plumes are not compatible with the geophysical makeup of the mantle, and suggests the plate tectonic

model better accounts for the observed evidence. Of course, plumes and plate tectonics are not mutually exclusive. New evidence seems to increasingly support the plume hypothesis, especially from seismic tomography which has produced detailed images of plumes below hotspots like Yellowstone (Davies, 2005; Kerr, 2013). Seismic tomography has also revealed two very large bodies of low seismic velocity in the mantle, termed superplumes (Romanowicz and Gung, 2002).

Plumes and Exceptionally Voluminous Cretaceous Magmatism

The Cretaceous to Early Cenozoic is a period of exceptionally voluminous magmatic activity (e.g. Cao et al., 2017; Ducea et al., 2015; Kirsch et al., 2016; Morton et al., 2014; Paterson et al., 2017; Paterson and Ducea, 2015). The mid-Cretaceous geological record has been characterized as having a pulse in seafloor spreading, eustatic sea level rise, hydrocarbon production, and an extended period of normal magnetic polarity (Larson and PITMAN III, 1972; Seton et al., 2009). A core/mantle-derived superplume has been suggested as a possible explanation for these anomalies. Another possibly related suggestion is that the massive plate tectonic reorganization associated with continental breakup during this interval could generate the same effects. We examine these ideas briefly here.

The Mid-Cretaceous Superplume Hypothesis

Larson (1991b) introduced the idea of a mid-Cretaceous superplume by correlating pulses of geologic events. In this study, a quantitative calculation of Earth's ocean-crustal budget over the past 150 My found that oceanic crustal production

increased by 50% to 75% in the mid-Cretaceous. Evidence was based on magnetic lineation mapping, magnetic reversal stratigraphic calibration and ocean-crustal dating. The Ontong Java and Kerguelen Large Igneous Province (LIP) plateaus of the western Pacific were also included as other significant components of oceanic crust formed during the Cretaceous. A long Cretaceous interval (41 My) of normal magnetic polarity, the Cretaceous Normal Superchron (CNS) was found to range from the early Aptian to the Santonian/Campanian boundary. The results of this study are displayed in **Figure 44**. There is a clear pulse in world total ocean crust production between 120 and 80 Ma and this comes mainly from the Pacific. The mid-Cretaceous increase is sudden and peaked soon after its onset, after which it decreased. Emplacement rates of oceanic LIP plateaus increase and decrease in a similar manner.

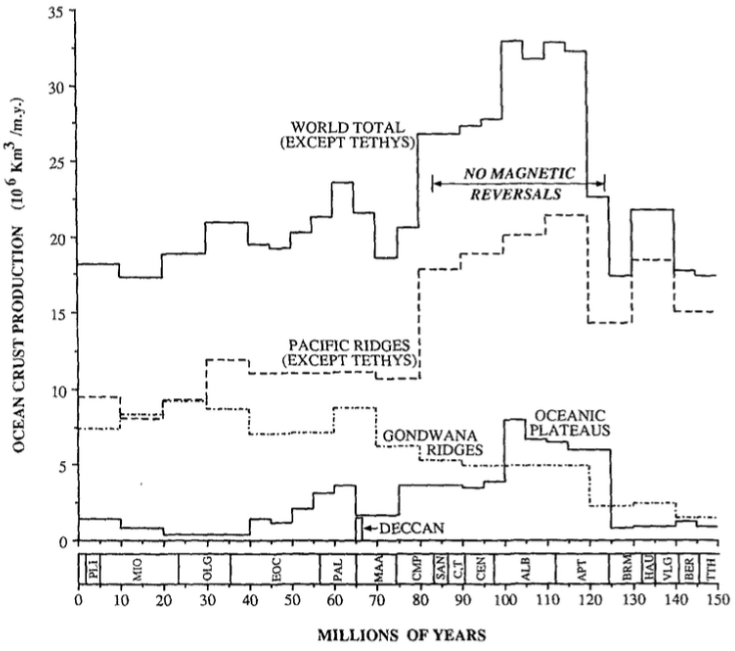

Figure 44. World oceanic crust production for past 150 My. From Larson (1991b).

Larson (1991b) argued that present-day variation in spreading rates depends on the availability of long subducting slabs that could drive rapid spreading and this could also explain faster spreading rates in the Cretaceous. However, the geologic record for the rim of the Pacific basin does not indicate faster subduction speeds, arguing that the pulse in oceanic spreading rates is not subduction related. Moreover, the Pacific oceanic plateaus show a record of forming from an abnormally high amount of mantle melting, requiring higher temperatures and implying a deeper source in the mantle. The increase in oceanic plateau LIP and total ocean floor production correlates well with the CNS in the mid-Cretaceous. This strong correlation suggests that the heat source for the pulse comes from near the core/mantle boundary and extraction of this heat increased convection in the outer core and altered the frequency of magnetic reversals, effectively locking the magnetic field into a long period of uniform polarity. After 41 My, the preexisting temperatures were reestablished, and magnetic reversals proceeded again.

The evidence leads to the hypothesis that a superplume arose from just above the core/mantle boundary at about 125 Ma as a result of whole mantle convection, and erupted below the Pacific basin. A "superswell" has been imaged below the present-day Pacific that is suggested to be the nearly exhausted remnant of this superplume. This mid-Cretaceous superplume is predicted to have had minimum dimensions of 6000 × 10000 km^2 with the present day Pacific superswell being close to its center.

Consequences of the Mid-Cretaceous Superplume

If the increased rate of Pacific sea floor spreading coinciding with the CNS is the result of a mantle superplume beneath the Pacific Ocean, are there any other anomalies

evident in the geological record? In addition are there any other periods where the same situation has existed? It is significant that the largest and second largest LIPs on earth in terms of volume were emplaced during this period, the Ontong Java (> 40 million km^3) and Kerguelen (> 15 million km^3) oceanic plateaus (Coffin and Eldholm, 1994).

Larson (1991b) has also addressed these questions. The extraordinary pulse of heat from the deep mantle drove one or more superplumes that erupted beneath the Cretaceous Pacific basin to create the huge LIPs in the present day Pacific. This effect also spread to other oceans. The large pulse in ocean crust production would likely have been accompanied by a substantial increase in outgassing of volatile material from the mantle. This would have had significant consequences for the Earth, such as an increase in global temperature and higher production of organic material.

An extreme increase in CO_2 (6 – 8 times present-day levels) would create a super greenhouse effect, raising the mid-Cretaceous temperatures. This extra CO_2 could have come from outgassing during the big increase in basalt during LIP emplacement and increased mid-ocean ridge activity as well as from increased volcanic activity behind subduction zones as the increased rate of seafloor spreading sped up subduction.

Black shales have been interpreted to indicate times of large increases in organic production and poor basin ventilation (anoxic conditions). Therefore an increase in nutrients and carbon supplied by higher rates of ocean crust production could result in black shales. Periods of prominent black shale deposition have been correlated worldwide. Over the last 150 Ma, a notable pulse in black shale production began in the Aptian, correlating with the start of increased ocean-floor production and declining when ocean-floor production tapers off around 80 Ma.

World oil production is not uniformly distributed throughout geological time – around 60% was generated from 112 to 88 Ma (Irving et al., 1974). The peak in oil generation in **Figure 45** correlates with the increase in ocean-crust production. Increased ocean-crust production could contribute to the pulse in oil generation by increasing the supply of carbon, sulphur and phosphorus and possibly nitrogen from the mantle. This would increase the nutrient supply, resulting in large plankton blooms that thrived in the warm mid-Cretaceous oceans that resulted from the super greenhouse effect.

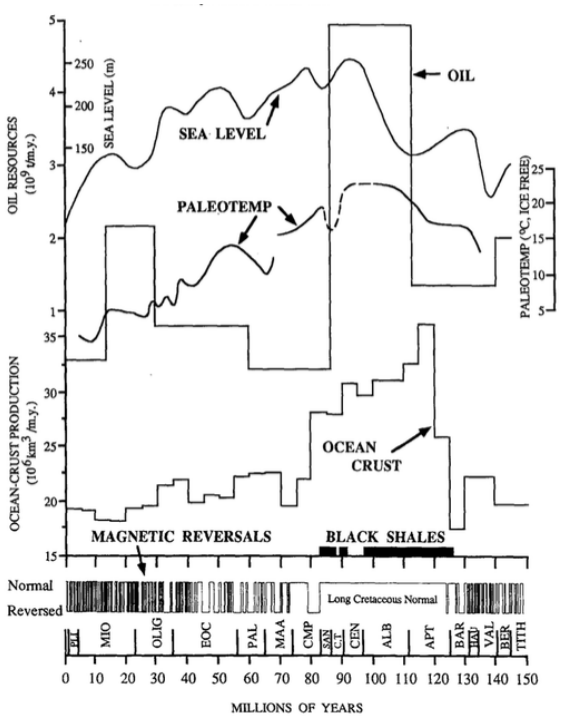

Figure 45. World ocean-crust production, magnetic reversal stratigraphy, high latitude sea-surface paleotemperatures, eustatic sea level, black shale deposition and world oil resources. From (Larson, 1991b).

The mid-Cretaceous is also characterized by a transgression and a super high-stand in world sea level. This would have had the effect of greatly increasing the

continental shelf area, providing a large area for organic material deposition. Increased ocean-floor production alone does not account for the global sea level rise, since the sea level started rising in the Jurassic before the increase in ocean-crust production. However, it does seem that the pulse in ocean-crust production is an important contributor to the observed increases in black shale, oil and eustatic sea level rise (Larson, 1991b).

Other Superplume Episodes

Is the mid-Cretaceous superplume a unique event in the geological record, or are there other similar episodes of global changes induced by an abnormal release of heat from the core/mantle boundary? Larson (1991a) notes that while the Pennsylvanian and Permian are almost entirely reversely magnetized, this period was characterized by a long fairly continuous glaciation that began in the Ordovician as Gondwanaland drifted over the South Pole. It is speculated that even a superplume could not prevent glaciation of such a large landmass over the pole.

Interestingly, there is a large anomaly in coal production during the Pennsylvanian-Permian reversed polarity interval, similar to the increased oil production during the mid-Cretaceous normal polarity interval. Carboniferous coal produced during this interval makes up about 50% of world coal resources. Since world coal reserves are believed to be far greater than oil and gas reserves combined, this is significant. This interval corresponds to the Absaroka sequence, with the transgression beginning at roughly the same time as the reversed polarity interval. The larger trend in the late Paleozoic is one of a falling eustatic sea level while in the Jurassic-Cretaceous it is a rising trend. These opposing larger trends could explain the formation of coal in the

Pennsylvanian-Permian and oil in the Cretaceous. To summarize, the Cretaceous with large areas of flooded continental platforms would have been ideal for marine plankton deposition and oil production. The Pennsylvanian-Permian period had the larger trend of falling sea level superimposed on the Absaroka transgression, leading to swampy continental areas favoring the deposition of peat and formation of coal. The Pennsylvanian-Permian reversed polarity interval was characterized by sequence stratigraphy and climate with coal production anomalies, comparable to events in the mid-Cretaceous. This suggests this period was also a time of superplume activity.

Looking earlier than this, in the Early Paleozoic, there are also long intervals of reversed polarity in the Late Devonian, Middle Ordovician and Late Cambrian, possibly corresponding to the Kaskaskia, Tippecanoe and Sauk sequences. There is the problem though, that magnetic stratigraphy from these earlier periods is sparse and has a large error margin. Also, most of the world's coal, oil and gas are found within the last two constant polarity intervals, so little remains to correlate with the earlier constant-polarity periods.

There may have been more abundant and intense superplumes in Earth's early history. More heat generated from a higher concentration of radioactive isotopes and a larger outer core would have contributed to this (Larson, 1991b). Using data on maximum dike widths and flood basalt surface area, Abbott and Isley (2002) found that the largest Precambrian superplumes erupted at least 10 times more lava than the largest Phanerozoic superplumes, with the possibility of enough superplumes to completely resurface the Earth.

Opposition to the Cretaceous Superplume Hypothesis

Although there seems to be good geological evidence to support the Cretaceous superplume, there is opposition to this idea. Heller et al. (1996) argued that the Cretaceous increase in sea level was not due to a pulse in rapid seafloor spreading, but rather was due to changes in area of ocean basins during the continental breakup and amalgamation cycle. They indicate that geochemistry proxies of mid-Cretaceous seawater don't correlate with the seafloor spreading. However, Seton et al. (2009) found that global average seafloor spreading rates were indeed highest during the Cretaceous, and the subsequent drop in sea levels was driven by a combination of decreasing seafloor spreading rates and aging ocean basins.

Don Anderson, as already noted, does not accept the mantle plumes hypothesis. Anderson (1994) attributes the pulse of Pacific oceanic crust formation in the Cretaceous to effects related to the breakup of Pangea and a rapid expansionary change in the Pacific plate. He makes the case that tomography reveals the upper mantle of the Pacific Ocean to be hot and this facilitated the rapid expansion during supercontinent breakup. A band of cool mantle separated the Pacific basin from the supercontinent, resulting in subduction in this region. Larson (1991b) pointed out the timing coincidence between the CNS and Pacific spreading rates, but he can be criticized for ignoring the coincidence of major plate tectonic effects during this time. Anderson (1994) argues that upper mantle conditions and past history such as continental insulation and subduction control lateral mantle temperature variations and magmatism more than core-mantle conditions. In other words, passive mantle upwellings controlled by lithospheric conditions is more plausible than superplumes.

References

Abbott, D. H., and Isley, A. E., 2002, The intensity, occurrence, and duration of superplume events and eras over geological time: Journal of Geodynamics, v. 34, no. 2, p. 265-307.

Anderson, D. L., 1994, Superplumes or supercontinents?: Geology, v. 22, no. 1, p. 39-42.

Cao, W., Lee, C.-T. A., and Lackey, J. S., 2017, Episodic nature of continental arc activity since 750 Ma: A global compilation: Earth and Planetary Science Letters, v. 461, p. 85-95.

Coffin, M. F., and Eldholm, O., 1994, Large igneous provinces: crustal structure, dimensions, and external consequences: Reviews of Geophysics, v. 32, no. 1, p. 1-36.

Davies, G. F., 2005, A case for mantle plumes: Chinese Science Bulletin, v. 50, no. 15, p. 1541-1554.

Ducea, M. N., Paterson, S. R., and DeCelles, P. G., 2015, High-volume magmatic events in subduction systems: Elements, v. 11, no. 2, p. 99-104.

Heller, P. L., Anderson, D. L., and Angevine, C. L., 1996, Is the middle Cretaceous pulse of rapid sea-floor spreading real or necessary?: Geology, v. 24, no. 6, p. 491-494.

Hildebrand, R., 2014, Geology, mantle tomography, and inclination corrected paleogeographic trajectories support westward subduction during Cretaceous orogenesis in the North American Cordillera: Geoscience Canada: Journal of the Geological Association of Canada/Geoscience Canada: journal de l'Association Géologique du Canada, v. 41, no. 2, p. 207-224.

Hildebrand, R., and Whalen, J., 2014, Arc and Slab-Failure Magmatism in Cordilleran Batholiths I: The Cretaceous Coastal Batholith of Peru and its Role in South American Orogenesis and Hemispheric Subduction Flip: Geoscience Canada: Journal of the Geological Association of Canada/Geoscience Canada: journal de l'Association Géologique du Canada, v. 41, no. 3, p. 255-282.

Irving, E., North, F., and Couillard, R., 1974, Oil, climate, and tectonics: Canadian Journal of Earth Sciences, v. 11, no. 1, p. 1-17.

Kerr, R. A., 2013, Solid-Earth science. Geophysical exploration linking deep Earth and backyard geology: Science, v. 340, no. 6138, p. 1283-1285.

Kirsch, M., Paterson, S. R., Wobbe, F., Martínez, A. M., Clausen, B. L., and Alasino, P. H., 2016, Temporal histories of Cordilleran continental arcs: Testing models for magmatic episodicity: American Mineralogist, v. 101, no. 10, p. 2133-2154.

Larson, R. L., 1991a, Geological consequences of superplumes: Geology, v. 19, no. 10, p. 963-966.

Larson, R. L., 1991b, Latest pulse of Earth: Evidence for a mid-Cretaceous superplume: Geology, v. 19, no. 6, p. 547-550.

Larson, R. L., and PITMAN III, W. C., 1972, World-wide correlation of Mesozoic magnetic anomalies, and its implications: Geological Society of America Bulletin, v. 83, no. 12, p. 3645-3662.

Luffi, P., and Ducea, M., 2022, Chemical Mohometry: Assessing Crustal Thickness of Ancient Orogens Using Geochemical and Isotopic Data: Reviews of Geophysics, v. 60, no. 2.

Morgan, W. J., 1972, Deep mantle convection plumes and plate motions: AAPG Bulletin, v. 56, no. 2, p. 203-213.

Morton, D. M., Miller, F. K., Kistler, R. W., Premo, W. R., Lee, C.-T. A., Langenheim, V. E., Wooden, J. L., Snee, L. W., Clausen, B. L., and Cossette, P., 2014, Framework and petrogenesis of the northern Peninsular Ranges batholith, southern California: Geological Society of America Memoir, v. 211, p. 61-143.

Paterson, S., Clausen, B., Memeti, V., and Schwartz, J. J., 2017, Arc magmatism, tectonism, and tempos in Mesozoic arc crustal sections of the Peninsular and Transverse Ranges, southern California, USA, Field Excursions in Southern California: Field Guides to the 2016 GSA Cordilleran Section Meeting, Volume 45, Geological Society of America, p. 81.

Paterson, S. R., and Ducea, M. N., 2015, Arc magmatic tempos: gathering the evidence: Elements, v. 11, no. 2, p. 91-98.

Romanowicz, B., and Gung, Y., 2002, Superplumes from the core-mantle boundary to the lithosphere: Implications for heat flux: Science, v. 296, no. 5567, p. 513-516.

Seton, M., Gaina, C., Müller, R., and Heine, C., 2009, Mid-Cretaceous seafloor spreading pulse: Fact or fiction?: Geology, v. 37, no. 8, p. 687-690.

Wilson, J. T., 1963, A possible origin of the Hawaiian Islands: Canadian Journal of Physics, v. 41, no. 6, p. 863-870.

APPENDIX E

SAMPLES COLLECTED

Table 7. List of samples personally collected during fieldwork.

Sample #	Long	Lat	Location	Rock	Age (est.)	Type	Weight (Kg)	Map Unit
17319A	-72.0241	-13.5075	Cusco	Sandstone	100	DZ	0.45	KsP-c
17319C	-72.1227	-13.3741	Maras	Sandstone	100	DZ	0.60	Ki-c
17319Ia	-72.0853	-13.2488	Urubamba	Andesite	250	bedrock	1.15	PEI-c
17319Ib	-72.0853	-13.2488	Urubamba	Monzogranite	250	bedrock	0.65	PET-mgr,gr
17320C	-72.3886	-13.1881	Chilca	Granite	250	bedrock	1.80	PET-mgr,gr
17320D	-72.2208	-13.2668	Urubamba	Andesite	250	bedrock	1.50	PEI-c
17320E	-72.2016	-13.2811	Urubamba	Quartzite	100	DZ	0.60	Ki-c
17322A	-71.7036	-13.5500	Huambuto	Sandstone	250	DZ	0.40	PEI-c
17322B	-71.6994	-13.5433	Huambuto	Andesite	250	bedrock	1.20	PEI-c
17322C	-71.6415	-13.4087	Paccpapata	Shale/slate	375	DZ	0.20	SD-ms
17322D	-71.6571	-13.4904	Huancarani	Siltstone	375	DZ	0.40	SD-ms
17323A	-70.9799	-13.5888	Marcapata	Schist	475	DZ	0.42	O-ms
17323B	-70.9256	-13.5776	Ccocha	Tonalite	250	bedrock	1.90	PET-mgr,gr
17323C	-70.8949	-13.4840	Mamabamba	Gneiss	525	DZ	0.40	D-gr
17323D	-70.8848	-13.3543	Choquellusca	Ortho-gneiss	250	DZ	0.95	PET-mgr,gr
17323E	-70.5085	-13.1873	San Lorenzo	Quartzite	100	DZ	0.60	Ki-c
17323F	-70.4774	-13.6674	Chacaneque	Tonalite	250	bedrock	1.30	PET-mgr,gr
17323G	-70.4872	-13.8188	Ollachea	Nepheline syenite	175	bedrock	2.70	Jim-sie
17323H	-70.5157	-13.8708	Macusani	Andesite porphyry	250	bedrock	1.80	PEI-c
17324B	-70.1359	-14.0405	Ajoyani	Monzogranite	250	bedrock	2.20	PET-mgr,gr
17324E	-70.2407	-15.0563	Santiago de Pupuja	Tonalite	20	bedrock	1.25	PN-tn,gd
17324F	-70.3740	-15.0464	Pucara	Granodiorite		bedrock	1.40	N-gd,tn
17326A	-70.5983	-14.8879	Ayaviri	Tonalite		bedrock	0.35	Nm-c
17326B	-70.9691	-14.4977	Santa Rosa	granodiorite/diorite	50	bedrock	20	PN-tn,gd

Table 7. (continued).

Sample #	Long	Lat	Location	Rock	Age (est.)	Type	Weight (Kg)	Map Unit
17326D	-71.1596	-14.4517	Marangani	Sandstone	250	DZ	0.15	CpPE-m
17326E	-71.2317	-14.2602	Sicuani	Sandstone	300	DZ	0.50	Cm-c
17327A	-72.2957	-13.1999	Ollantaytambo	Shale/slate	525	DZ	0.25	Eo-ms
17327B	-72.3932	-13.0716	Ollantaytambo	Shale/slate	475	DZ	0.20	O-ms
17327D	-72.5811	-13.1542	Machu Picchu	Granite/granodiorite	300	bedrock	1.90	PET-mgr,gr
17327E	-72.5808	-13.1511	Machu Picchu	Granite/granodiorite	300	bedrock	1.70	PET-mgr,gr
17328A	-72.2237	-13.4944	Compone	Tonalite	25	bedrock	1.10	PN-vs
17328C	-72.3630	-13.4421	Ancahuasi	Tonalite	50	bedrock	1.80	PN-tn,gd
17328D	-72.5462	-13.5531	Mollepata	Sandstone	100	DZ	0.55	Kis-m
17329A	-72.9948	-13.6633	Abancay	Sandstone	100	DZ	0.60	KsP-c
17329C	-72.9555	-13.7015	Abancay	Tonalite	20	bedrock	2.10	PN-tn,gd
17329E	-72.9205	-13.6844	Abancay	Granodiorite	250	bedrock	1.75	PET-tn,gd
17330A	-71.9841	-13.5095	Sacsayhuaman	Diorite	65	bedrock	1.80	KP-tn,gd,di
18619A	-70.4741	-14.0050	N of Macusani	volcanic tuff	20	bedrock	0.24	Np-ya
18619B	-70.4845	-13.9456	N of Macusani	andesite porphyry	275	bedrock	0.26	Mitu Grp
18622A	-71.9719	-13.3233	Sacred Valley	hypabyssal volcanics	275	bedrock	1.42	Mitu Grp
18624A	-72.9719	-13.3233	Machu Picchu	granite	275	bedrock	1.19	
18625A	-71.9786	-13.5125	Cusco	diorite	28	bedrock	1.94	Sacsayhuaman
18627A	-73.6789	-13.5158	3km N of Uripa	granite	275	bedrock	1.82	Pi-gr
18627C	-73.8893	-13.4033	W of Uripa	biotite tuff	20	bedrock	0.54	N-ja
18627D	-74.0659	-13.3766	E of Ayacucho	granite	275	bedrock	1.46	P-que
18628A	-74.3287	-13.3014	W of Ayacucho	granite	275	bedrock	1.66	Pm-que
18628B	-74.4420	-13.3383	W of Ayacucho	tuff	20	bedrock	1.66	Np-po1
18701A	-75.6628	-14.4633	Ocucaje	granite	420	bedrock	1.47	P-pgr, San Nicolas
18703A	-73.6469	-14.0440	Paico	granite	1000	bedrock	2.56	

APPENDIX F

GEOCHRONOLOGY DATA

Table 8. List of samples used in geochronology analysis.

Sample #	Long	Lat	Location	Rock	Age	# spots	Map Unit
15810A	-71.6205	-16.4565	Arequipa Laderas	tonalite	178.0	36	KTi-tol
15810E	-71.7101	-16.5423	Arequipa La Joya	granodiorite	65.0	33	KTi-gr / KTi-gd_
15811A	-71.5984	-16.4596	Arequipa	tonalite	79.0	33	Tiabaya KTi-gd
15811C	-71.4196	-16.5851	Yarabamba	granodiorite	63.7	23	Tiabaya KTi-gd
170320C	-72.3886	-13.1881	Chilca	granite	455.0	32	PET-mgr,gr
170323B	-70.9256	-13.5776	Ccocha	tonalite	228.7	35	PET-mgr,gr
170323G	-70.4872	-13.8188	Ollachea	nepheline syenite	179.1	31	Jim-sie
170323H	-70.5157	-13.8708	Macusani	andesite porphyry	189.0	31	PEI-c
170324F	-70.3740	-15.0464	Pucara	granodiorite	16.0	31	N-gd,tn
170327E	-72.5808	-13.1511	Machu Picchu	monzogranite	302.8	33	PET-mgr,gr
170329C	-72.9555	-13.7015	Abancay	tonalite	238.6	35	PN-tn,gd
170329E	-72.9205	-13.6844	Abancay	granodiorite	222.5	34	PET-tn,gd
170330A	-71.9841	-13.5095	Sacsayhuaman	diorite	26.0	34	KP-tn,gd,di
18622A	-71.9719	-13.3233	Sacred Valley	hypabyssal volcanics	308.9	42	Mitu Grp
18627A	-73.6789	-13.5158	3km N of Uripa	granite	230.0	21	Pi-gr
18628A	-74.3287	-13.3014	W of Ayacucho	granite	243.9	30	Pm-que
18701A	-75.6628	-14.4633	Ocucaje	granite	462.4	27	P-pgr, San Nicolas
18703A	-73.6469	-14.044	Paico	granite	1132.0	44	
A11-118A	-72.0241	-13.5075	Pisco	sandstone	DZ	168	
170319A	-72.0241	-13.5075	Cusco	sandstone	DZ	210	KsP-c, Saegarara Fm
170323E	-70.5085	-13.1873	San Lorenzo	quartzite	DZ	108	Ki-c, Oriente Grp

Table 9. U-Pb geochronology analysis data for sample 15810A, ordered by best age.

		Isotope ratios									Apparent ages (Ma)							
Analysis	U	$^{206}Pb/^{204}Pb$	U/Th	$^{206}Pb/^{207}Pb$	±	$^{207}Pb/^{235}U$	±	$^{206}Pb/^{238}U$	±	error	$^{206}Pb/^{238}U$	±	$^{207}Pb/^{235}U$	±	$^{206}Pb/^{207}Pb$	±	Best age	±
	(ppm)				(%)		(%)		(%)	corr.		(Ma)		(Ma)		(Ma)	(Ma)	(Ma)
Spot 63	1844	104965	1.1	20.0273	0.7	0.1817	1.5	0.0264	1.3	0.88	168.0	2.2	169.5	2.3	190.8	16.3	168.0	2.2
Spot 62 c	1788	53340	1.0	20.0979	1.0	0.1821	1.6	0.0266	1.3	0.80	168.9	2.2	169.9	2.6	182.6	23.0	168.9	2.2
Spot 41	573	6909	2.0	16.6113	2.5	0.2212	2.9	0.0267	1.5	0.50	169.6	2.4	202.9	5.4	609.8	55.1	169.6	2.4
Spot 68	596	9551	1.5	20.0937	1.2	0.1843	1.7	0.0269	1.2	0.71	170.9	2.0	171.8	2.6	183.1	27.3	170.9	2.0
Spot 37	1286	45946	1.0	20.2282	0.8	0.1871	2.1	0.0275	1.9	0.92	174.6	3.3	174.1	3.3	167.5	19.1	174.6	3.3
Spot 61	1308	38369	1.2	20.1137	0.6	0.1886	1.7	0.0275	1.5	0.93	175.0	2.7	175.4	2.7	180.8	14.5	175.0	2.7
Spot 65	876	200285	1.5	19.9076	0.8	0.1916	1.5	0.0277	1.2	0.83	176.0	2.1	178.0	2.4	204.8	19.4	176.0	2.1
Spot 57	1074	39849	1.3	20.0648	0.8	0.1901	1.4	0.0277	1.2	0.84	176.0	2.1	176.7	2.3	186.4	18.3	176.0	2.1
Spot 70	1589	30700	1.7	19.9167	0.8	0.1916	1.5	0.0277	1.3	0.83	176.1	2.2	178.0	2.5	203.6	19.5	176.1	2.2
Spot 64	946	368745	1.3	19.7886	0.9	0.1934	1.5	0.0278	1.2	0.80	176.6	2.0	179.5	2.4	218.6	20.5	176.6	2.0
Spot 40	1212	50129	1.1	19.9761	0.8	0.1917	1.5	0.0278	1.3	0.84	176.7	2.2	178.1	2.4	196.7	18.6	176.7	2.2
Spot 49 c	759	35005	1.3	20.2802	0.9	0.1889	1.9	0.0278	1.7	0.89	176.7	3.0	175.7	3.1	161.5	20.5	176.7	3.0
Spot 50	1024	34522	1.1	19.9281	0.9	0.1930	1.6	0.0279	1.4	0.85	177.5	2.4	179.2	2.6	202.3	19.9	177.5	2.4
Spot 45	1015	35447	1.6	19.9675	0.8	0.1927	1.5	0.0279	1.3	0.84	177.5	2.2	179.0	2.5	197.8	19.2	177.5	2.2
Spot 60	1033	30476	1.2	19.9941	0.8	0.1932	1.3	0.0280	1.0	0.80	178.2	1.8	179.3	2.2	194.7	18.4	178.2	1.8
Spot 47	1025	101238	1.1	19.6306	0.7	0.1969	1.3	0.0280	1.0	0.81	178.3	1.8	182.5	2.1	237.2	17.1	178.3	1.8
Spot 59	709	845479	1.8	19.9256	0.9	0.1955	1.5	0.0283	1.2	0.80	179.7	2.2	181.3	2.6	202.7	21.3	179.7	2.2
Spot 52	558	15160	1.4	19.8943	1.1	0.1961	1.5	0.0283	1.0	0.66	179.9	1.8	181.8	2.5	206.3	26.2	179.9	1.8
Spot 55	625	16756	1.8	19.8893	1.0	0.1961	1.6	0.0283	1.3	0.80	179.9	2.3	181.9	2.7	206.9	22.5	179.9	2.3

Table 9. Sample 15810A (continued).

		Isotope ratios									Apparent ages (Ma)							
Analysis	U (ppm)	$^{206}Pb/^{204}Pb$	U/Th	$^{206}Pb/^{207}Pb$	± (%)	$^{207}Pb/^{235}U$	± (%)	$^{206}Pb/^{238}U$	± (%)	error corr.	$^{206}Pb/^{238}U$	± (Ma)	$^{207}Pb/^{235}U$	± (Ma)	$^{206}Pb/^{207}Pb$	± (Ma)	Best age (Ma)	± (Ma)
Spot 51	675	20569	1.8	19.9784	0.9	0.1961	1.7	0.0284	1.4	0.84	180.7	2.6	181.8	2.9	196.5	21.9	180.7	2.6
Spot 66	307	34460	1.6	20.0069	1.2	0.1969	1.8	0.0286	1.3	0.72	181.7	2.3	182.5	2.9	193.2	28.2	181.7	2.3
Spot 36	600	36369	1.2	19.8012	0.9	0.2001	1.5	0.0288	1.3	0.82	182.7	2.3	185.2	2.6	217.1	20.2	182.7	2.3
Spot 48	497	17747	1.5	20.1769	1.0	0.1970	1.8	0.0288	1.5	0.84	183.3	2.7	182.6	3.0	173.4	22.8	183.3	2.7
Spot 67	893	36383	1.1	20.1626	0.8	0.1975	1.4	0.0289	1.1	0.82	183.6	2.0	183.0	2.3	175.1	18.3	183.6	2.0
Spot 69	695	15432	1.1	20.1214	0.9	0.1989	1.3	0.0290	0.9	0.72	184.5	1.7	184.2	2.2	179.9	21.2	184.5	1.7
Spot 56	629	8840	1.1	20.2080	0.8	0.1983	1.4	0.0291	1.2	0.83	184.8	2.2	183.7	2.4	169.9	18.4	184.8	2.2
Spot 58	815	27064	1.6	20.1298	0.8	0.1993	1.5	0.0291	1.3	0.85	185.0	2.4	184.5	2.6	178.9	18.4	185.0	2.4
Spot 46	848	34946	1.0	20.0239	0.6	0.2009	1.1	0.0292	1.0	0.85	185.5	1.8	185.9	1.9	191.2	13.7	185.5	1.8
Spot 42 c	681	39092	1.5	19.9780	0.8	0.2016	1.6	0.0292	1.4	0.87	185.7	2.6	186.5	2.7	196.5	18.4	185.7	2.6
Spot 54	532	8065	1.2	20.4548	0.8	0.1980	1.5	0.0294	1.3	0.84	186.7	2.3	183.5	2.5	141.5	18.9	186.7	2.3
Spot 43	616	10035	1.4	20.4692	0.9	0.1982	1.9	0.0294	1.7	0.89	187.1	3.1	183.6	3.2	139.8	20.5	187.1	3.1
Spot 44	469	30274	1.5	20.0910	1.0	0.2029	1.7	0.0296	1.4	0.81	187.9	2.6	187.6	3.0	183.4	23.4	187.9	2.6
Spot 38	531	190445	1.5	19.8725	1.0	0.2088	1.4	0.0301	1.0	0.71	191.2	1.9	192.5	2.5	208.8	23.0	191.2	1.9
Spot 53	277	208779	1.6	19.9870	0.7	0.2078	1.4	0.0301	1.2	0.86	191.4	2.3	191.7	2.4	195.5	16.3	191.4	2.3
Spot 39	606	25777	1.3	20.0872	1.0	0.2071	1.5	0.0302	1.2	0.77	191.7	2.2	191.1	2.6	183.8	22.2	191.7	2.2

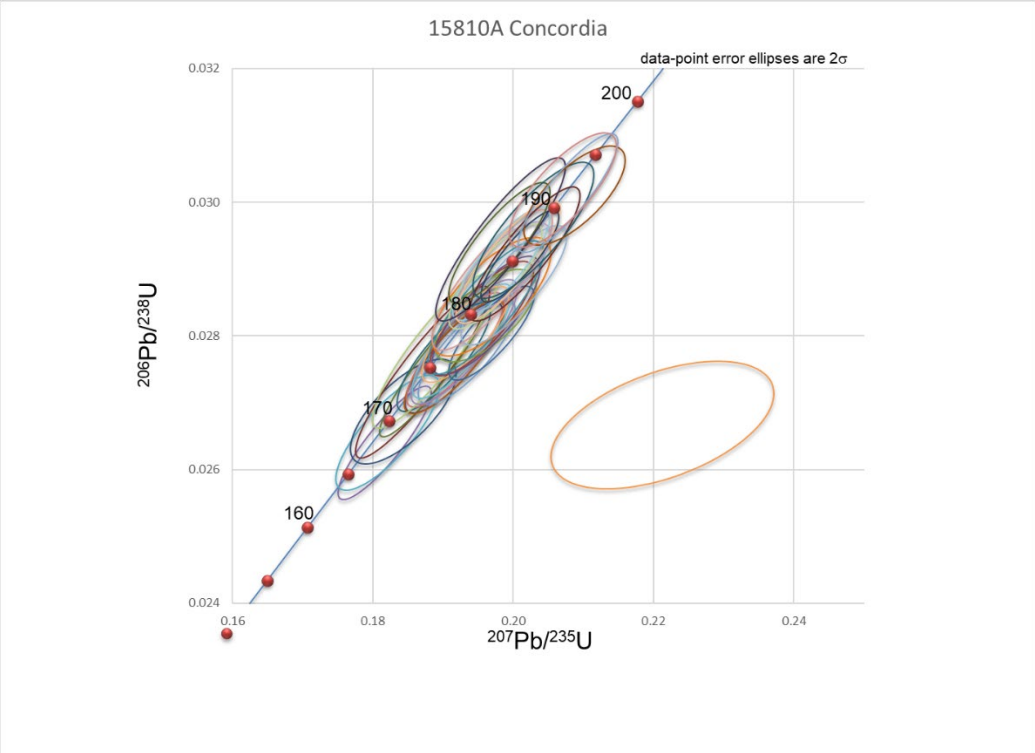

Figure 47. Concordia plot for sample 15810A

Figure 46. CL image for sample 15810A

Table 10. U-Pb geochronology analysis data for sample 15810E, ordered by best age.

		Isotope ratios									Apparent ages (Ma)							
Analysis	U (ppm)	$^{206}Pb/^{204}Pb$	U/Th	$^{206}Pb/^{207}Pb$	± (%)	$^{207}Pb/^{235}U$	± (%)	$^{206}Pb/^{238}U$	± (%)	error corr.	$^{206}Pb/^{238}U$	± (Ma)	$^{207}Pb/^{235}U$	± (Ma)	$^{206}Pb/^{207}Pb$	± (Ma)	Best age (Ma)	± (Ma)
Spot 52	318	61454	1.1	21.5944	1.5	0.0628	1.9	0.0098	1.1	0.59	63.1	0.7	61.8	1.1	12.6	36.8	63.1	0.7
Spot 54	252	9867	1.1	21.4138	1.6	0.0640	2.3	0.0099	1.6	0.70	63.7	1.0	62.9	1.4	32.8	39.3	63.7	1.0
Spot 67	86	4093	1.7	23.0144	2.4	0.0596	2.7	0.0099	1.3	0.49	63.8	0.8	58.7	1.5	NA	NA	63.8	0.8
Spot 48	145	43264	1.3	21.0078	1.4	0.0655	2.3	0.0100	1.8	0.80	64.0	1.2	64.4	1.4	78.5	32.7	64.0	1.2
Spot 70	102	2890	1.4	23.5317	3.1	0.0587	3.5	0.0100	1.6	0.46	64.2	1.0	57.9	2.0	NA	NA	64.2	1.0
Spot 37	247	11725	1.1	21.5616	1.3	0.0640	2.0	0.0100	1.5	0.77	64.2	1.0	63.0	1.2	16.3	30.2	64.2	1.0
Spot 36	214	19777	2.2	21.4314	1.3	0.0645	2.1	0.0100	1.6	0.78	64.3	1.0	63.5	1.3	30.8	31.2	64.3	1.0
Spot 66	107	21834	1.4	21.3471	1.8	0.0649	2.5	0.0100	1.8	0.69	64.5	1.1	63.8	1.6	40.3	43.9	64.5	1.1
Spot 41	144	91389	1.2	21.4191	1.7	0.0647	2.2	0.0101	1.4	0.64	64.5	0.9	63.6	1.4	32.2	41.4	64.5	0.9
Spot 45	105	4529	1.8	22.3492	4.2	0.0620	4.5	0.0101	1.5	0.34	64.5	1.0	61.1	2.7	NA	NA	64.5	1.0
Spot 53	68	1345	2.1	27.3555	11.0	0.0510	11.1	0.0101	1.4	0.13	64.9	0.9	50.5	5.5	NA	NA	64.9	0.9
Spot 69	99	9433	1.2	22.0414	2.6	0.0634	3.0	0.0101	1.5	0.50	65.1	1.0	62.4	1.8	NA	NA	65.1	1.0
Spot 58	71	6616	1.8	22.9890	2.4	0.0608	2.9	0.0101	1.6	0.55	65.1	1.0	60.0	1.7	NA	NA	65.1	1.0
Spot 60	96	12592	1.1	20.6778	2.2	0.0677	2.6	0.0102	1.2	0.48	65.1	0.8	66.5	1.7	115.9	53.0	65.1	0.8
Spot 49	224	18343	1.8	21.1594	1.4	0.0664	1.9	0.0102	1.4	0.71	65.4	0.9	65.3	1.2	61.3	32.2	65.4	0.9
Spot 39	102	40159	1.4	20.8383	2.0	0.0676	2.2	0.0102	1.0	0.47	65.5	0.7	66.4	1.4	97.7	46.3	65.5	0.7

Table 10. Sample 15810E (continued).

Analysis	U (ppm)	$^{206}Pb/^{204}Pb$	U/Th	$^{206}Pb/^{207}Pb$	± (%)	$^{207}Pb/^{235}U$	± (%)	$^{206}Pb/^{238}U$	± (%)	error corr.	$^{206}Pb/^{238}U$	± (Ma)	$^{207}Pb/^{235}U$	± (Ma)	$^{206}Pb/^{207}Pb$	± (Ma)	Best age (Ma)	± (Ma)
					Isotope ratios									Apparent ages (Ma)				
Spot 59	104	6198	2.4	23.1144	2.6	0.0610	3.2	0.0102	1.8	0.58	65.6	1.2	60.2	1.9	NA	NA	65.6	1.2
Spot 68	122	6246	1.1	23.2244	2.2	0.0609	2.8	0.0103	1.6	0.59	65.8	1.1	60.1	1.6	NA	NA	65.8	1.1
Spot 64	160	60539	1.3	21.2495	1.7	0.0667	2.4	0.0103	1.8	0.72	65.9	1.2	65.5	1.6	51.2	40.6	65.9	1.2
Spot 56	123	6292	1.7	17.5236	3.3	0.0809	3.5	0.0103	1.3	0.36	66.0	0.8	79.0	2.7	493.1	72.6	66.0	0.8
Spot 51	74	6474	1.9	20.4018	3.2	0.0696	3.6	0.0103	1.5	0.41	66.1	1.0	68.3	2.4	147.5	76.1	66.1	1.0
Spot 46	123	6230	0.9	21.2846	2.0	0.0667	2.4	0.0103	1.3	0.55	66.1	0.9	65.6	1.5	47.3	48.1	66.1	0.9
Spot 40	113	29202	1.2	22.0931	2.0	0.0645	2.7	0.0103	1.8	0.69	66.3	1.2	63.4	1.7	NA	NA	66.3	1.2
Spot 44	74	11519	2.3	20.1086	2.4	0.0710	2.8	0.0104	1.3	0.48	66.5	0.9	69.7	1.9	181.4	56.8	66.5	0.9
Spot 50	104	6618	1.3	20.6875	2.2	0.0691	2.5	0.0104	1.2	0.48	66.5	0.8	67.9	1.7	114.8	52.5	66.5	0.8
Spot 47	163	10979	1.5	20.4649	1.5	0.0701	2.0	0.0104	1.4	0.66	66.7	0.9	68.8	1.4	140.3	36.0	66.7	0.9
Spot 55	124	5457	2.2	22.6180	2.4	0.0635	3.0	0.0104	1.9	0.61	66.8	1.2	62.5	1.8	NA	NA	66.8	1.2
Spot 62	52	1714	2.0	25.7549	7.9	0.0569	8.0	0.0106	1.6	0.20	68.2	1.1	56.2	4.4	NA	NA	68.2	1.1
Spot 61	59	2369	1.6	21.4844	7.3	0.0690	7.6	0.0108	2.3	0.30	68.9	1.6	67.7	5.0	24.9	174.6	68.9	1.6
Spot 65	64	4110	1.9	17.9852	4.2	0.0824	4.9	0.0108	2.5	0.51	68.9	1.7	80.4	3.8	435.5	94.3	68.9	1.7
Spot 57	132	95974	2.1	16.1303	4.3	0.0921	4.6	0.0108	1.6	0.36	69.2	1.1	89.5	4.0	673.0	92.4	69.2	1.1
Spot 63	85	44003	1.9	14.6516	3.9	0.1019	4.3	0.0108	1.6	0.38	69.5	1.1	98.5	4.0	875.3	81.7	69.5	1.1
Spot 38	110	3908	1.9	10.2611	12.2	0.1455	12.4	0.0108	2.0	0.16	69.5	1.4	138.0	16.0	1575.2	229.4	69.5	1.4

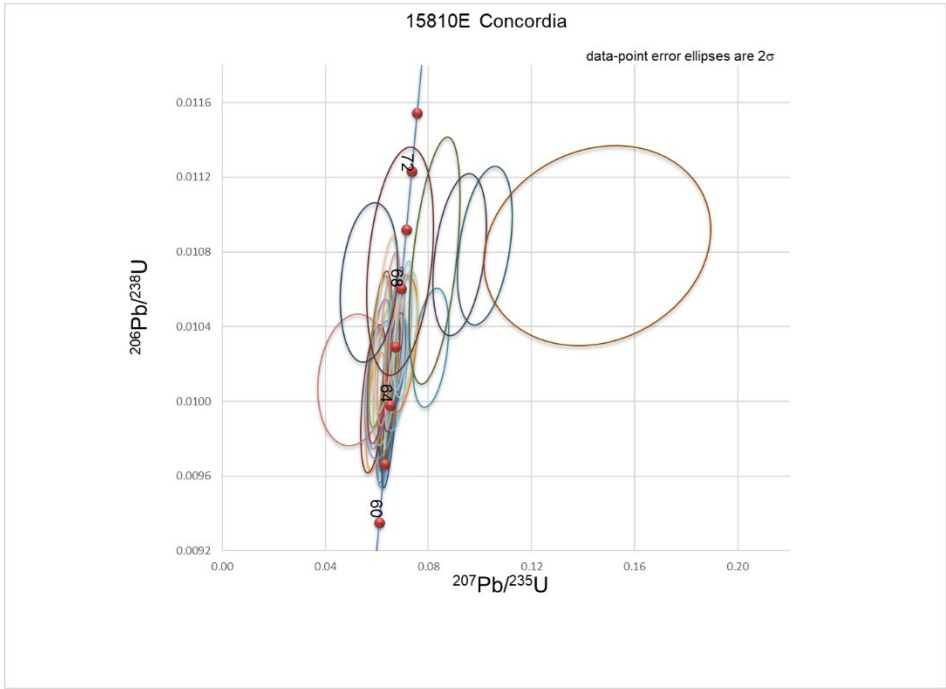

Figure 48. Concordia plot for sample 15810E

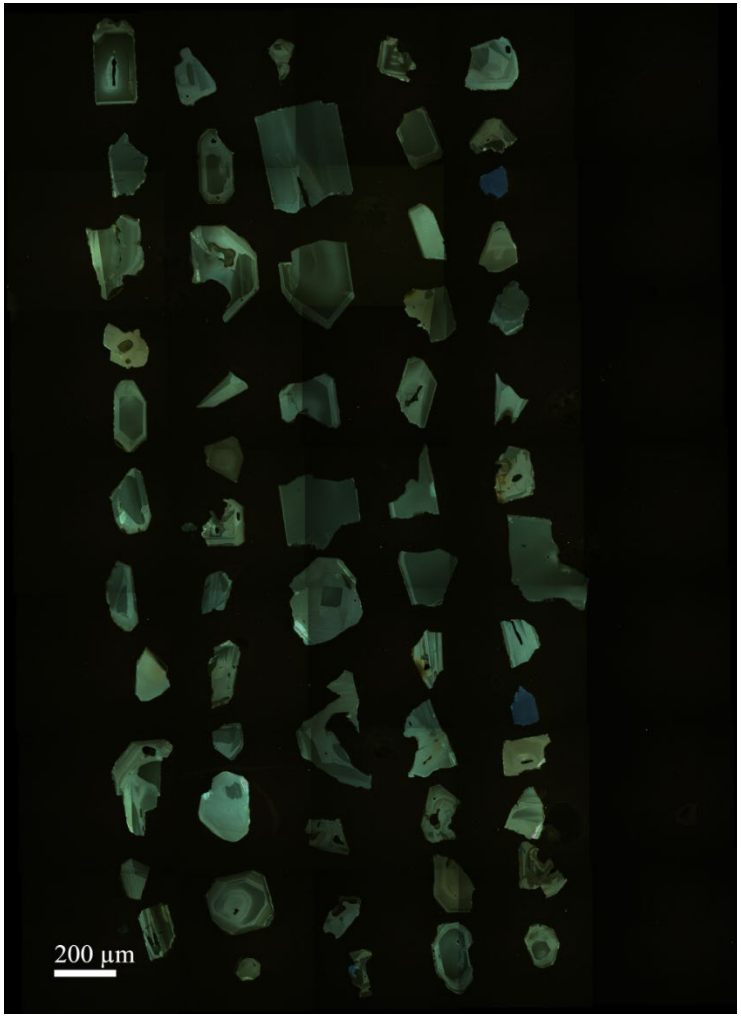

Figure 49. CL image for sample 15810E

Table 11. U-Pb geochronology analysis data for sample 15811A, ordered by best age.

		Isotope ratios									Apparent ages (Ma)							
Analysis	U (ppm)	$^{206}Pb/^{204}Pb$	U/Th	$^{206}Pb/^{207}Pb$	± (%)	$^{207}Pb/^{235}U$	± (%)	$^{206}Pb/^{238}U$	± (%)	error corr.	$^{206}Pb/^{238}U$	± (Ma)	$^{207}Pb/^{235}U$	± (Ma)	$^{206}Pb/^{207}Pb$	± (Ma)	Best age (Ma)	± (Ma)
Spot 16	290	61487	1.5	21.3082	1.4	0.0770	1.9	0.0119	1.3	0.70	76.3	1.0	75.3	1.4	44.7	32.4	76.3	1.0
Spot 23	316	19819	1.2	20.9073	1.3	0.0784	1.7	0.0119	1.1	0.65	76.3	0.8	76.7	1.2	89.8	29.7	76.3	0.8
Spot 1	504	88810	0.8	20.5029	1.4	0.0801	2.0	0.0119	1.3	0.68	76.4	1.0	78.2	1.5	135.9	33.6	76.4	1.0
Spot 18	368	15320	1.2	21.0994	1.7	0.0778	2.1	0.0119	1.2	0.60	76.4	0.9	76.1	1.5	68.1	40.0	76.4	0.9
Spot 31	228	8160	1.6	22.0563	1.4	0.0748	1.9	0.0120	1.3	0.67	76.7	1.0	73.2	1.4	NA	NA	76.7	1.0
Spot 29	475	28043	1.0	21.3961	1.1	0.0772	1.5	0.0120	1.0	0.67	76.8	0.8	75.5	1.1	34.8	26.6	76.8	0.8
Spot 26	181	195688	1.2	21.0983	1.5	0.0784	2.1	0.0120	1.5	0.73	76.9	1.2	76.6	1.6	68.2	34.7	76.9	1.2
Spot 5	307	23310	1.1	21.0975	1.1	0.0786	1.7	0.0120	1.2	0.74	77.1	0.9	76.8	1.2	68.3	26.4	77.1	0.9
Spot 35	179	5916	1.6	22.5830	1.5	0.0737	2.0	0.0121	1.4	0.68	77.4	1.1	72.2	1.4	NA	NA	77.4	1.1
Spot 12	209	18583	1.2	19.6610	2.3	0.0848	2.6	0.0121	1.1	0.44	77.5	0.9	82.6	2.1	233.6	53.7	77.5	0.9
Spot 25	293	23390	1.5	21.3179	1.5	0.0786	2.1	0.0122	1.5	0.72	77.9	1.2	76.8	1.6	43.6	34.9	77.9	1.2
Spot 11	348	54713	1.3	20.2708	1.1	0.0827	1.5	0.0122	1.0	0.65	77.9	0.7	80.7	1.2	162.6	26.5	77.9	0.7
Spot 9	208	15445	1.3	21.3442	1.7	0.0787	2.1	0.0122	1.2	0.59	78.1	1.0	76.9	1.5	40.6	39.9	78.1	1.0
Spot 32	132	3977	1.4	21.8507	1.4	0.0771	1.7	0.0122	0.9	0.55	78.4	0.7	75.4	1.2	NA	NA	78.4	0.7
Spot 8	230	35375	1.4	21.4038	1.1	0.0788	1.6	0.0122	1.2	0.74	78.4	0.9	77.0	1.2	33.9	26.6	78.4	0.9
Spot 34	146	6676	1.8	19.4216	2.2	0.0869	2.6	0.0122	1.3	0.50	78.4	1.0	84.6	2.1	261.8	51.2	78.4	1.0

Table 11. 15811A (continued).

		Isotope ratios									Apparent ages (Ma)							
Analysis	U (ppm)	$^{206}Pb/^{204}Pb$	U/Th	$^{206}Pb/^{207}Pb$	± (%)	$^{207}Pb/^{235}U$	± (%)	$^{206}Pb/^{238}U$	± (%)	error corr.	$^{206}Pb/^{238}U$	± (Ma)	$^{207}Pb/^{235}U$	± (Ma)	$^{206}Pb/^{207}Pb$	± (Ma)	Best age (Ma)	± (Ma)
Spot 15	368	19918	1.0	21.0704	1.2	0.0805	1.7	0.0123	1.2	0.69	78.8	0.9	78.6	1.3	71.4	28.6	78.8	0.9
Spot 22	197	19217	2.0	21.1755	1.4	0.0801	2.1	0.0123	1.5	0.74	78.9	1.2	78.3	1.6	59.6	33.2	78.9	1.2
Spot 33	306	26936	1.0	20.9199	1.3	0.0812	1.8	0.0123	1.2	0.67	79.0	0.9	79.3	1.4	88.4	31.9	79.0	0.9
Spot 21	222	52669	1.6	19.8830	2.2	0.0860	2.7	0.0124	1.5	0.56	79.5	1.2	83.8	2.2	207.6	52.0	79.5	1.2
Spot 4	159	19306	1.3	17.7115	2.4	0.0979	2.8	0.0126	1.5	0.53	80.6	1.2	94.8	2.6	469.5	53.2	80.6	1.2
Spot 20	858	102376	2.9	21.3942	1.0	0.0810	1.5	0.0126	1.1	0.73	80.6	0.9	79.1	1.1	35.0	23.8	80.6	0.9
Spot 30	322	48790	2.1	21.0190	1.4	0.0828	2.1	0.0126	1.6	0.76	80.8	1.3	80.7	1.6	77.2	32.2	80.8	1.3
Spot 27	340	47366	1.2	18.0793	2.1	0.0971	2.8	0.0127	1.8	0.66	81.6	1.5	94.1	2.5	423.9	46.9	81.6	1.5
Spot 24	464	7560	0.9	17.8460	2.5	0.0984	2.9	0.0127	1.4	0.48	81.6	1.1	95.3	2.6	452.8	56.4	81.6	1.1
Spot 13	241	14128	1.1	21.4517	1.4	0.0831	1.9	0.0129	1.3	0.66	82.8	1.0	81.0	1.5	28.6	34.6	82.8	1.0
Spot 14	189	32544	1.9	21.2168	1.2	0.0844	1.7	0.0130	1.2	0.72	83.3	1.0	82.3	1.3	54.9	28.0	83.3	1.0
Spot 3	536	63230	1.9	20.4216	0.9	0.0887	1.5	0.0131	1.2	0.79	84.2	1.0	86.3	1.3	145.2	22.0	84.2	1.0
Spot 19	244	14984	2.0	21.1773	1.6	0.0855	2.0	0.0131	1.2	0.59	84.2	1.0	83.3	1.6	59.4	38.8	84.2	1.0
Spot 2	246	8944	1.2	16.0787	2.6	0.1149	2.9	0.0134	1.2	0.42	85.9	1.0	110.5	3.0	679.8	55.3	85.9	1.0
Spot 17	266	54857	1.4	20.5086	1.2	0.0938	2.1	0.0140	1.6	0.80	89.3	1.5	91.0	1.8	135.3	28.7	89.3	1.5
Spot 10	303	14755	1.5	14.0100	2.9	0.1374	3.2	0.0140	1.4	0.43	89.4	1.2	130.7	4.0	967.4	59.5	89.4	1.2
Spot 7	144	44500	1.7	21.5560	2.1	0.0907	4.8	0.0142	4.3	0.90	90.8	3.9	88.1	4.0	16.9	50.1	90.8	3.9

.

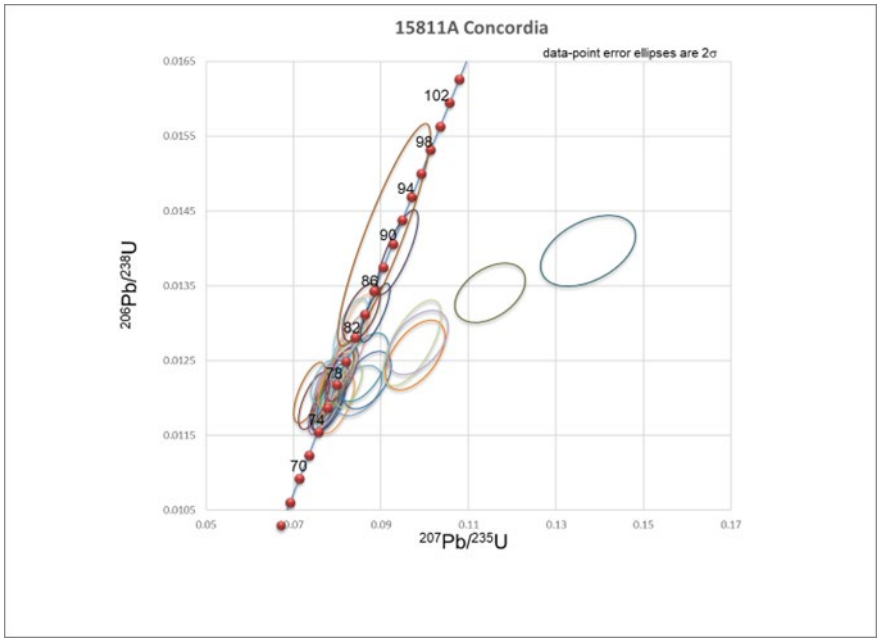

Figure 50. Concordia plot for sample 15811A

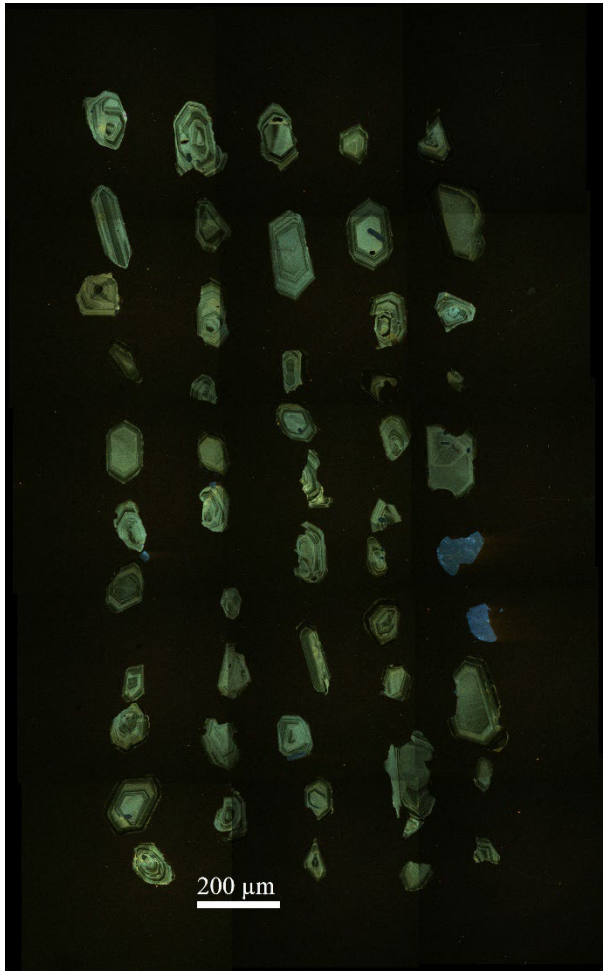

Figure 51. CL image for sample 15811A

Table 12. U-Pb geochronology analysis data for sample 15811C, ordered by best age.

		Isotope ratios									Apparent ages (Ma)							
Analysis	U (ppm)	$^{206}Pb/^{204}Pb$	U/Th	$^{206}Pb/^{207}Pb$	± (%)	$^{207}Pb/^{235}U$	± (%)	$^{206}Pb/^{238}U$	± (%)	error corr.	$^{206}Pb/^{238}U$	± (Ma)	$^{207}Pb/^{235}U$	± (Ma)	$^{206}Pb/^{207}Pb$	± (Ma)	Best age (Ma)	± (Ma)
Spot 28	988	59957	0.8	20.9116	1.1	0.0630	1.8	0.0096	1.4	0.78	61.3	0.8	62.0	1.1	89.4	25.9	61.3	0.8
Spot 14	430	33817	0.9	20.9151	1.6	0.0635	2.4	0.0096	1.8	0.75	61.8	1.1	62.5	1.5	89.0	37.4	61.8	1.1
Spot 24	5589	1831	1.4	7.9975	10.8	0.1663	11.3	0.0096	3.3	0.29	61.9	2.0	156.2	16.3	2028.6	191.3	61.9	2.0
Spot 2	737	16702	0.9	21.6450	1.1	0.0615	1.6	0.0097	1.2	0.73	62.0	0.7	60.6	0.9	7.0	26.3	62.0	0.7
Spot 13	433	8588	0.8	21.3695	1.7	0.0626	2.3	0.0097	1.5	0.66	62.3	0.9	61.7	1.4	37.8	41.2	62.3	0.9
Spot 19	1169	83264	1.1	18.8896	2.4	0.0710	2.7	0.0097	1.3	0.49	62.4	0.8	69.6	1.8	325.2	54.1	62.4	0.8
Spot 21	1379	22042	0.9	21.2724	1.2	0.0631	1.8	0.0097	1.3	0.74	62.4	0.8	62.1	1.1	48.6	29.4	62.4	0.8
Spot 5	235	2904	0.9	23.4693	1.9	0.0573	2.2	0.0098	1.2	0.53	62.6	0.7	56.5	1.2	NA	NA	62.6	0.7
Spot 18	519	44235	1.0	20.8013	1.3	0.0647	1.8	0.0098	1.2	0.68	62.6	0.8	63.6	1.1	101.9	30.8	62.6	0.8
Spot 25	323	35018	0.9	21.1227	1.5	0.0639	2.3	0.0098	1.7	0.74	62.8	1.1	62.9	1.4	65.5	36.7	62.8	1.1
Spot 1	838	15169	0.9	21.7055	1.3	0.0622	1.8	0.0098	1.3	0.70	62.9	0.8	61.3	1.1	NA	NA	62.9	0.8
Spot 23	2675	140620	0.9	20.1408	0.9	0.0671	1.3	0.0098	1.0	0.74	62.9	0.6	65.9	0.9	177.6	21.0	62.9	0.6
Spot 12	654	42210	0.7	21.0083	1.1	0.0652	1.3	0.0099	0.8	0.62	63.7	0.5	64.1	0.8	78.4	25.1	63.7	0.5
Spot 27	382	80833	1.1	20.1140	1.9	0.0683	2.3	0.0100	1.2	0.51	64.0	0.7	67.1	1.5	180.7	45.1	64.0	0.7
Spot 16	2908	1930	1.6	8.9150	10.9	0.1568	11.9	0.0101	4.9	0.41	65.0	3.2	147.9	16.4	1834.1	198.1	65.0	3.2
Spot 10	292	27812	1.0	21.0268	1.7	0.0666	2.1	0.0102	1.3	0.60	65.2	0.8	65.5	1.3	76.3	39.9	65.2	0.8
Spot 3	200	63336	1.1	21.3340	2.0	0.0660	2.3	0.0102	1.2	0.53	65.5	0.8	64.9	1.5	41.8	46.7	65.5	0.8
Spot 26	456	98717	0.9	20.8416	1.2	0.0684	1.7	0.0103	1.2	0.73	66.3	0.8	67.2	1.1	97.3	27.5	66.3	0.8
Spot 17	145	15275	1.7	20.8060	2.5	0.0688	2.9	0.0104	1.4	0.49	66.6	0.9	67.6	1.9	101.3	60.1	66.6	0.9
Spot 6	363	12589	1.1	18.7260	3.8	0.0769	4.0	0.0105	1.4	0.34	67.0	0.9	75.2	2.9	344.9	85.5	67.0	0.9
Spot 11	421	41899	1.1	21.4454	1.3	0.0677	1.8	0.0105	1.2	0.69	67.6	0.8	66.5	1.2	29.3	31.3	67.6	0.8
Spot 22	293	2808	0.8	9.4708	3.3	0.1576	3.5	0.0108	1.3	0.38	69.4	0.9	148.6	4.9	1723.8	59.8	69.4	0.9
Spot 4	274	943	2.0	4.7245	13.2	0.3507	13.8	0.0120	4.1	0.30	77.0	3.2	305.3	36.5	2917.6	214.9	77.0	3.2

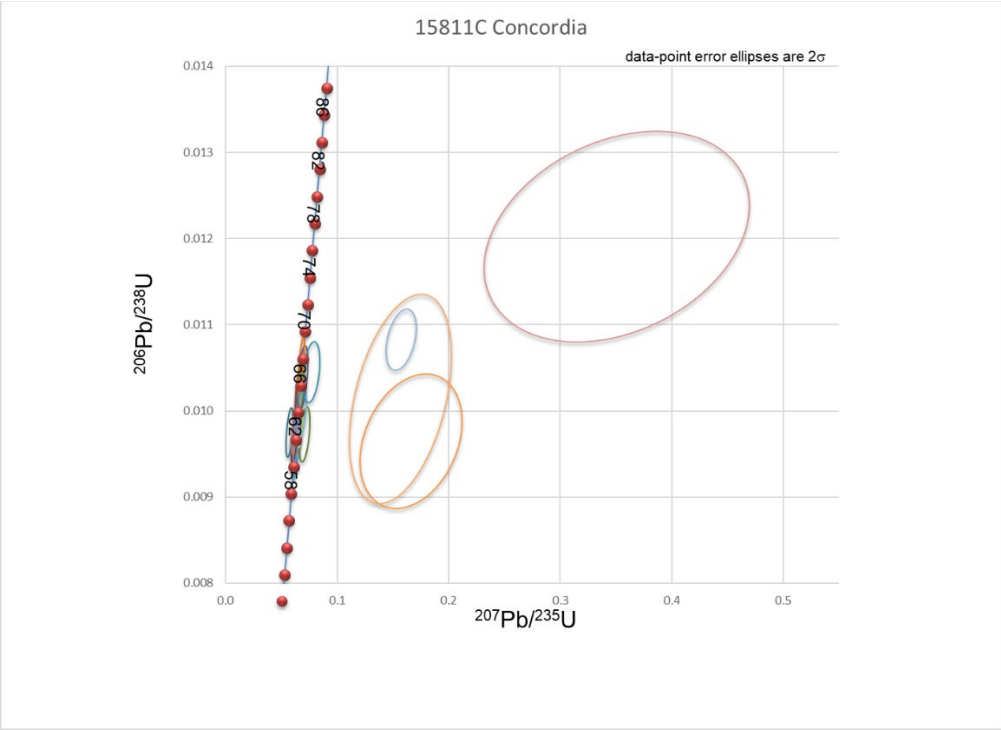

Figure 52. Concordia plot for sample 15811C

Table 13. U-Pb geochronology analysis data for sample 17320C, ordered by best age.

				Isotope ratios							Apparent ages (Ma)							
Analysis	U (ppm)	$^{206}Pb/^{204}Pb$	U/Th	$^{206}Pb/^{207}Pb$	± (%)	$^{207}Pb/^{235}U$	± (%)	$^{206}Pb/^{238}U$	± (%)	error corr.	$^{206}Pb/^{238}U$	± (Ma)	$^{207}Pb/^{235}U$	± (Ma)	$^{206}Pb/^{207}Pb$	± (Ma)	Best age (Ma)	± (Ma)
Spot 5	2162	12092	2.7	17.0492	1.2	0.4190	1.9	0.0518	1.4	0.77	325.8	4.6	355.3	5.6	553.3	25.7	325.8	4.6
Spot 18	1444	99411	2.1	17.9019	0.8	0.4014	1.4	0.0521	1.2	0.83	327.6	3.8	342.6	4.1	445.8	17.4	327.6	3.8
Spot 34	2490	54083	4.1	17.0305	0.8	0.4842	2.0	0.0598	1.9	0.93	374.6	6.9	401.0	6.7	555.7	16.5	374.6	6.9
Spot 20	1855	203484	3.4	17.0139	0.9	0.4980	1.5	0.0615	1.3	0.82	384.6	4.7	410.3	5.2	557.8	19.1	384.6	4.7
Spot 19	908	11337	1.6	17.4382	0.9	0.5308	1.5	0.0672	1.2	0.82	419.0	4.9	432.3	5.2	503.9	18.7	419.0	4.9
Spot 13	1581	54485	2.2	17.9364	1.0	0.5266	1.5	0.0685	1.2	0.78	427.3	5.0	429.5	5.4	441.5	21.7	427.3	5.0
Spot 10	1276	38399	3.1	17.5913	1.0	0.5571	1.5	0.0711	1.1	0.76	442.9	4.8	449.7	5.4	484.6	21.5	442.9	4.8
Spot 1	1244	46073	2.8	17.9648	0.7	0.5498	1.4	0.0717	1.2	0.85	446.2	5.2	444.9	5.1	438.0	16.5	446.2	5.2
Spot 32	1379	161690	2.9	17.7590	0.8	0.5641	1.6	0.0727	1.4	0.88	452.3	6.1	454.2	5.8	463.6	17.0	452.3	6.1
Spot 2	505	22695	1.4	16.9988	0.8	0.5935	1.3	0.0732	1.1	0.80	455.4	4.6	473.1	5.0	559.8	17.4	455.4	4.6
Spot 27	485	76493	2.7	17.2110	0.7	0.5865	1.6	0.0732	1.4	0.89	455.7	6.2	468.6	5.9	532.7	15.5	455.7	6.2
Spot 17	637	195444	1.2	17.6229	0.7	0.5730	1.6	0.0733	1.5	0.89	455.8	6.4	460.0	6.0	480.6	16.2	455.8	6.4
Spot 3	1079	223454	2.9	17.9208	0.9	0.5670	1.4	0.0737	1.0	0.73	458.6	4.4	456.1	5.1	443.5	21.0	458.6	4.4
Spot 31	1056	9552	4.2	16.8936	0.8	0.6017	1.3	0.0738	1.1	0.79	458.7	4.7	478.3	5.1	573.3	17.6	458.7	4.7
Spot 30	953	114515	3.9	17.7480	0.8	0.5747	1.3	0.0740	1.0	0.80	460.3	4.7	461.1	4.8	465.0	17.3	460.3	4.7
Spot 25	1584	89277	3.8	17.5693	0.9	0.5810	1.5	0.0741	1.2	0.82	460.6	5.5	465.1	5.6	487.3	19.0	460.6	5.5
Spot 12	1200	149740	2.7	17.9353	0.7	0.5696	1.3	0.0741	1.1	0.83	461.0	4.9	457.8	4.8	441.7	16.2	461.0	4.9
Spot 8	345	87721	1.9	17.2420	0.8	0.5937	1.5	0.0743	1.2	0.84	461.8	5.5	473.2	5.6	528.7	17.3	461.8	5.5

Table 13. Sample 17320C (continued).

					Isotope ratios							Apparent ages (Ma)						
Analysis	U (ppm)	$^{206}Pb/^{204}Pb$	U/Th	$^{206}Pb/^{207}Pb$	± (%)	$^{207}Pb/^{235}U$	± (%)	$^{206}Pb/^{238}U$	± (%)	error corr.	$^{206}Pb/^{238}U$	± (Ma)	$^{207}Pb/^{235}U$	± (Ma)	$^{206}Pb/^{207}Pb$	± (Ma)	Best age (Ma)	± (Ma)
Spot 15	813	235035	2.1	17.3634	0.9	0.5896	1.5	0.0743	1.3	0.81	461.9	5.6	470.6	5.8	513.3	20.0	461.9	5.6
Spot 28	620	31778	2.1	17.7665	0.7	0.5767	1.3	0.0743	1.1	0.83	462.2	4.9	462.3	4.9	462.7	16.4	462.2	4.9
Spot 21	626	200633	3.2	17.5464	0.9	0.5848	1.4	0.0745	1.0	0.75	462.9	4.7	467.5	5.2	490.2	20.1	462.9	4.7
Spot 24	183	13802	1.3	17.7204	1.0	0.5854	1.4	0.0753	1.0	0.73	467.8	4.7	468.0	5.4	468.4	22.0	467.8	4.7
Spot 26	457	39249	2.0	16.8525	1.0	0.6176	1.6	0.0755	1.3	0.80	469.3	5.7	488.3	6.1	578.6	20.8	469.3	5.7
Spot 7	309	179518	1.8	17.5449	0.9	0.5953	1.6	0.0758	1.3	0.80	470.9	5.7	474.3	5.9	490.4	20.6	470.9	5.7
Spot 33	467	32811	0.8	17.6365	0.8	0.5943	1.5	0.0761	1.2	0.85	472.5	5.6	473.6	5.5	478.9	17.0	472.5	5.6
Spot 11	562	11413	0.9	17.0473	0.7	0.6211	1.4	0.0768	1.2	0.87	477.1	5.4	490.5	5.3	553.6	14.8	477.1	5.4
Spot 14	57	8748	0.9	13.6127	1.5	1.7712	1.8	0.1749	1.0	0.58	1039.3	10.0	1035.0	11.7	1025.8	29.9	1025.8	29.9
Spot 4	199	43306	1.6	12.5824	0.8	2.0941	1.1	0.1912	0.8	0.70	1127.8	8.2	1146.9	7.7	1183.2	15.7	1183.2	15.7
Spot 16	95	32145	2.4	12.5162	0.7	2.1885	1.2	0.1987	1.0	0.81	1168.6	10.7	1177.4	8.7	1193.6	14.6	1193.6	14.6
Spot 35	217	97015	1.7	12.2899	0.9	2.3227	1.5	0.2071	1.1	0.79	1213.5	12.7	1219.3	10.4	1229.5	17.7	1229.5	17.7
Spot 22	134	33804	2.7	12.2761	0.8	2.3394	1.4	0.2084	1.1	0.83	1220.2	12.7	1224.3	9.8	1231.7	15.1	1231.7	15.1
Spot 23	232	80379	1.7	8.7604	0.7	5.1880	1.6	0.3298	1.5	0.90	1837.3	23.7	1850.7	14.0	1865.7	13.1	1865.7	13.1

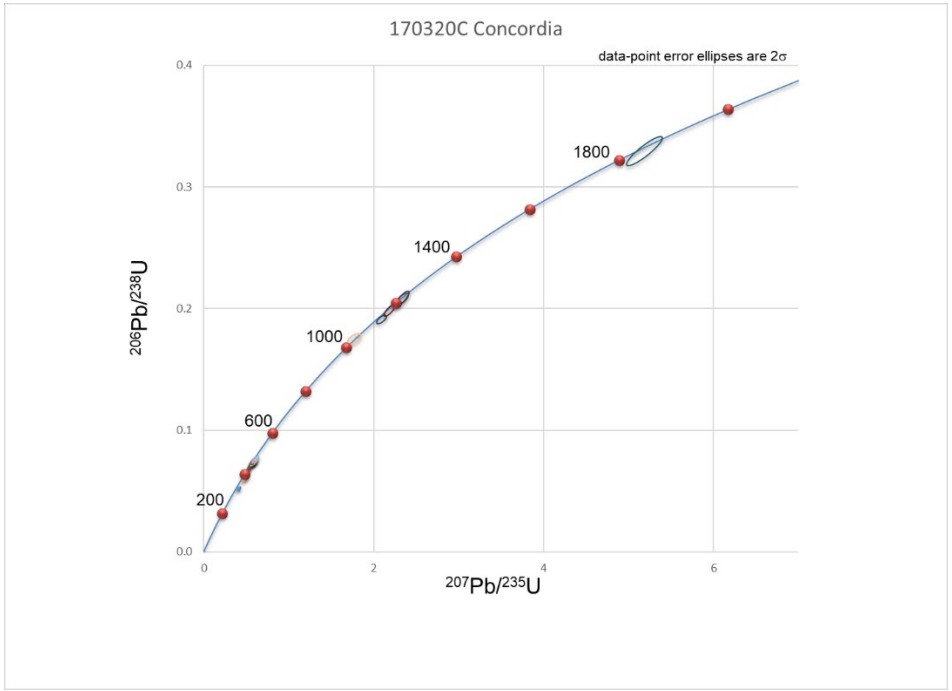

Figure 54. Concordia plot for sample 17320C

Figure 53. CL image for sample 17320C

Table 14. U-Pb geochronology analysis data for sample 17323B, ordered by best age.

		Isotope ratios									Apparent ages (Ma)							
Analysis	U (ppm)	$^{206}Pb/^{204}Pb$	U/Th	$^{206}Pb/^{207}Pb$	± (%)	$^{207}Pb/^{235}U$	± (%)	$^{206}Pb/^{238}U$	± (%)	error corr.	$^{206}Pb/^{238}U$	± (Ma)	$^{207}Pb/^{235}U$	± (Ma)	$^{206}Pb/^{207}Pb$	± (Ma)	Best age (Ma)	± (Ma)
Spot 36	4325	3675856	88.7	19.7099	0.8	0.2314	1.6	0.0331	1.4	0.87	209.9	3.0	211.4	3.1	227.9	18.5	209.9	3.0
Spot 37 c	3654	1118001	5.5	19.7612	0.9	0.2400	1.8	0.0344	1.6	0.88	218.1	3.4	218.4	3.6	221.9	20.2	218.1	3.4
Spot 66	3754	698474	0.7	20.0409	1.0	0.2397	1.7	0.0349	1.4	0.80	220.9	2.9	218.2	3.3	189.2	23.9	220.9	2.9
Spot 54	3750	128724	18.5	20.0799	1.0	0.2397	1.8	0.0349	1.5	0.84	221.3	3.4	218.2	3.6	184.7	23.4	221.3	3.4
Spot 40	3563	649610	3.0	19.9909	0.9	0.2418	1.8	0.0351	1.5	0.87	222.2	3.4	219.9	3.5	195.1	20.0	222.2	3.4
Spot 55	2859	503935	1.7	19.9676	0.8	0.2423	1.7	0.0351	1.5	0.88	222.5	3.4	220.3	3.5	197.7	19.1	222.5	3.4
Spot 44	2967	251293	4.7	19.9061	1.1	0.2437	2.0	0.0352	1.7	0.85	223.0	3.8	221.4	4.0	204.9	25.0	223.0	3.8
Spot 69	1868	1035031	1.6	19.6145	1.2	0.2480	1.9	0.0353	1.5	0.77	223.6	3.3	224.9	3.9	239.1	28.4	223.6	3.3
Spot 67	714	441779	2.3	19.3975	0.8	0.2515	1.7	0.0354	1.5	0.88	224.3	3.4	227.8	3.5	264.6	19.1	224.3	3.4
Spot 68	781	218348	1.5	19.1540	1.1	0.2558	1.7	0.0355	1.3	0.78	225.2	2.9	231.2	3.5	293.5	24.4	225.2	2.9
Spot 59	2105	153246	15.1	19.7038	0.9	0.2489	1.6	0.0356	1.3	0.82	225.4	2.9	225.7	3.2	228.5	20.9	225.4	2.9
Spot 70	2687	878926	1.1	19.8514	0.8	0.2480	1.5	0.0357	1.3	0.84	226.3	2.8	224.9	3.1	211.3	19.3	226.3	2.8
Spot 61	922	174485	25.1	19.2654	0.8	0.2576	1.6	0.0360	1.4	0.87	228.1	3.1	232.7	3.3	280.3	18.1	228.1	3.1
Spot 65	264	372361	1.4	19.5753	1.1	0.2536	1.7	0.0360	1.3	0.79	228.1	3.0	229.5	3.5	243.6	24.3	228.1	3.0
Spot 49	267	12763	1.3	19.9905	1.1	0.2484	1.7	0.0360	1.3	0.75	228.2	2.9	225.3	3.5	195.1	26.4	228.2	2.9
Spot 50	431	180551	1.6	19.4234	1.0	0.2557	1.7	0.0360	1.4	0.82	228.2	3.1	231.2	3.5	261.6	22.2	228.2	3.1
Spot 43	1306	338701	1.0	19.5830	0.7	0.2545	1.6	0.0362	1.4	0.89	229.0	3.2	230.2	3.3	242.8	16.7	229.0	3.2
Spot 39	204	23205	1.5	19.9518	1.4	0.2502	1.9	0.0362	1.3	0.68	229.3	3.0	226.7	3.9	199.6	33.0	229.3	3.0
Spot 45	1032	129345	1.5	19.8359	0.8	0.2526	1.6	0.0364	1.3	0.84	230.2	3.0	228.7	3.2	213.1	19.5	230.2	3.0

Table 14. Sample 17323B (continued).

		Isotope ratios									Apparent ages (Ma)							
Analysis	U (ppm)	$^{206}Pb/^{204}Pb$	U/Th	$^{206}Pb/^{207}Pb$	± (%)	$^{207}Pb/^{235}U$	± (%)	$^{206}Pb/^{238}U$	± (%)	error corr.	$^{206}Pb/^{238}U$	± (Ma)	$^{207}Pb/^{235}U$	± (Ma)	$^{206}Pb/^{207}Pb$	± (Ma)	Best age (Ma)	± (Ma)
Spot 51	332	21799	1.2	19.9705	1.1	0.2511	1.7	0.0364	1.3	0.75	230.3	2.8	227.4	3.4	197.4	25.7	230.3	2.8
Spot 56	1761	133656	2.7	19.8786	0.9	0.2527	1.9	0.0364	1.6	0.87	230.7	3.7	228.7	3.8	208.1	21.1	230.7	3.7
Spot 58	777	68834	1.4	19.6904	1.0	0.2555	1.6	0.0365	1.3	0.81	231.1	3.0	231.0	3.4	230.1	22.3	231.1	3.0
Spot 41	852	140937	1.7	19.4437	0.8	0.2588	1.5	0.0365	1.3	0.85	231.1	3.0	233.7	3.2	259.1	18.6	231.1	3.0
Spot 42	873	87048	1.7	19.3761	1.0	0.2601	1.9	0.0366	1.5	0.83	231.5	3.5	234.8	3.9	267.1	23.8	231.5	3.5
Spot 57	282	16496	1.2	19.9317	1.2	0.2535	1.8	0.0367	1.3	0.72	232.1	2.9	229.4	3.7	201.9	28.6	232.1	2.9
Spot 62	2792	189718	1.1	20.3713	0.9	0.2484	1.4	0.0367	1.1	0.79	232.5	2.5	225.3	2.8	151.0	20.2	232.5	2.5
Spot 53	1384	200494	1.4	19.7250	0.7	0.2571	1.4	0.0368	1.2	0.87	232.9	2.7	232.3	2.8	226.1	15.5	232.9	2.7
Spot 47	1429	92376	5.5	19.7866	0.8	0.2569	1.6	0.0369	1.4	0.87	233.5	3.3	232.2	3.4	218.9	18.8	233.5	3.3
Spot 48	849	39187	2.0	20.0854	0.8	0.2533	1.5	0.0369	1.2	0.84	233.7	2.8	229.3	3.0	184.0	18.7	233.7	2.8
Spot 38	916	149930	5.9	19.4783	0.8	0.2615	1.5	0.0370	1.3	0.84	233.9	2.9	235.8	3.1	255.1	18.6	233.9	2.9
Spot 64	443	139690	1.2	19.7052	0.9	0.2586	1.7	0.0370	1.4	0.85	234.1	3.3	233.5	3.5	228.4	20.2	234.1	3.3
Spot 60	741	879062	3.6	19.6295	0.9	0.2660	1.7	0.0379	1.5	0.85	239.8	3.5	239.5	3.7	237.3	21.5	239.8	3.5
Spot 46	162	20096	0.5	19.5424	1.5	0.2673	2.2	0.0379	1.6	0.74	239.8	3.8	240.5	4.7	247.5	34.2	239.8	3.8
Spot 52	1227	102951	2.1	19.8046	0.9	0.2744	1.4	0.0394	1.1	0.79	249.3	2.8	246.2	3.1	216.7	20.4	249.3	2.8
Spot 63	262	48928	5.4	19.3801	1.4	0.3123	1.8	0.0439	1.2	0.66	277.0	3.3	276.0	4.4	266.7	31.9	277.0	3.3

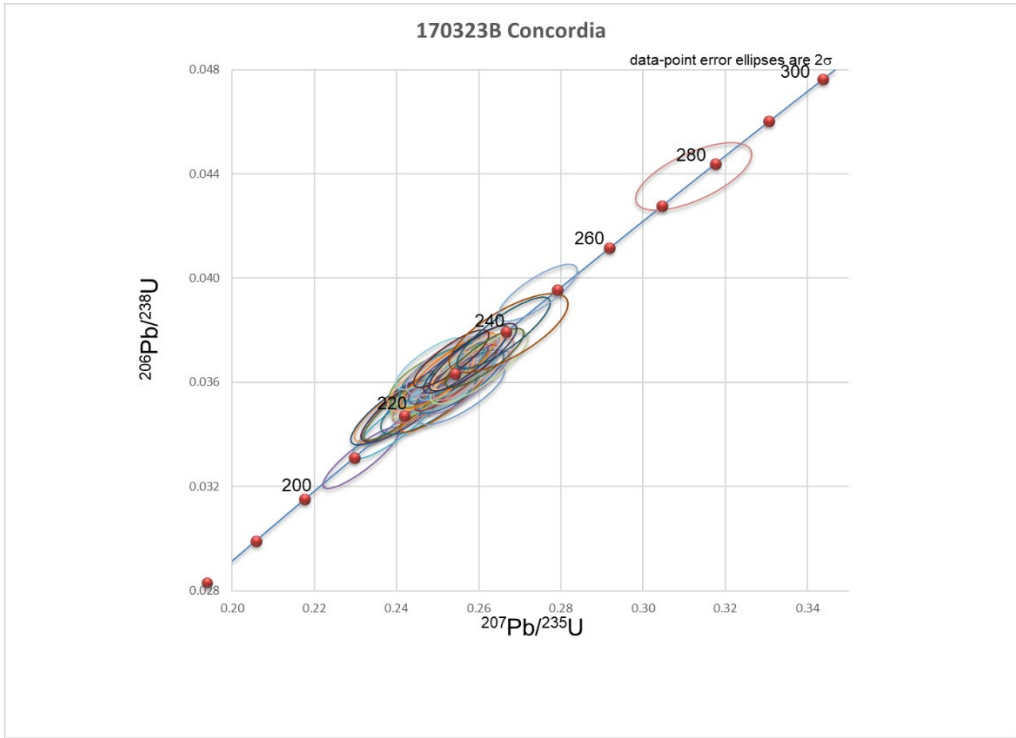

Figure 55. Concordia plot for sample 17323B

Table 15. U-Pb geochronology analysis data for sample 17323G, ordered by best age.

		Isotope ratios									Apparent ages (Ma)							
Analysis	U (ppm)	$^{206}Pb/^{204}Pb$	U/Th	$^{206}Pb/^{207}Pb$	± (%)	$^{207}Pb/^{235}U$	± (%)	$^{206}Pb/^{238}U$	± (%)	error corr.	$^{206}Pb/^{238}U$	± (Ma)	$^{207}Pb/^{235}U$	± (Ma)	$^{206}Pb/^{207}Pb$	± (Ma)	Best age (Ma)	± (Ma)
Spot 35	3291	438658	3.1	20.3296	0.8	0.1767	1.7	0.0261	1.5	0.89	165.8	2.5	165.2	2.6	155.9	18.1	165.8	2.5
Spot 14	269	119105	0.4	20.3016	1.0	0.1833	1.7	0.0270	1.4	0.83	171.7	2.5	170.9	2.7	159.1	22.8	171.7	2.5
Spot 33	153	97316	0.5	17.6400	1.6	0.2115	2.0	0.0271	1.2	0.60	172.2	2.0	194.8	3.5	478.5	35.2	172.2	2.0
Spot 27	194	12176	0.3	18.3613	1.6	0.2040	1.9	0.0272	1.0	0.54	172.8	1.8	188.5	3.3	389.2	36.2	172.8	1.8
Spot 20	399	177987	0.4	20.0253	1.0	0.1877	1.7	0.0273	1.3	0.79	173.4	2.3	174.6	2.7	191.1	23.8	173.4	2.3
Spot 34	120	10044	0.4	20.9381	1.5	0.1796	2.0	0.0273	1.4	0.68	173.5	2.4	167.7	3.2	86.4	35.5	173.5	2.4
Spot 22	135	7688	0.3	17.7062	1.8	0.2133	2.5	0.0274	1.7	0.67	174.3	2.9	196.3	4.5	470.2	40.9	174.3	2.9
Spot 2	270	22502	0.4	16.4127	3.2	0.2327	3.5	0.0277	1.3	0.36	176.2	2.2	212.5	6.7	635.8	69.5	176.2	2.2
Spot 30	202	27758	0.3	20.1677	1.5	0.1897	1.9	0.0278	1.1	0.60	176.5	2.0	176.4	3.1	174.5	35.6	176.5	2.0
Spot 24	130	19119	0.4	15.4044	2.7	0.2486	3.0	0.0278	1.2	0.40	176.7	2.1	225.4	6.0	770.7	57.2	176.7	2.1
Spot 13	204	15941	0.4	17.2897	1.4	0.2219	1.6	0.0278	0.7	0.48	177.0	1.3	203.5	2.9	522.6	30.0	177.0	1.3
Spot 18	231	32048	0.4	16.9085	1.5	0.2276	1.9	0.0279	1.2	0.63	177.5	2.1	208.2	3.7	571.4	33.0	177.5	2.1
Spot 17	196	18059	0.5	20.3415	1.6	0.1895	2.1	0.0280	1.4	0.64	177.8	2.4	176.2	3.5	154.5	38.6	177.8	2.4
Spot 11	137	33936	0.5	15.3104	2.4	0.2548	2.6	0.0283	1.0	0.37	179.9	1.7	230.5	5.3	783.6	50.2	179.9	1.7
Spot 32	77	4586	0.5	10.8289	7.1	0.3624	7.2	0.0285	1.2	0.16	181.0	2.1	314.0	19.4	1473.7	134.3	181.0	2.1
Spot 25	140	5300	0.3	14.5096	3.0	0.2710	3.3	0.0285	1.3	0.39	181.4	2.3	243.5	7.1	895.5	62.5	181.4	2.3
Spot 4	72	10607	0.2	16.4367	2.8	0.2404	3.1	0.0287	1.3	0.42	182.2	2.3	218.7	6.0	632.7	60.0	182.2	2.3
Spot 10	136	3234	0.3	11.7193	4.4	0.3381	4.5	0.0288	0.8	0.17	182.7	1.4	295.7	11.5	1322.2	85.4	182.7	1.4
Spot 26	133	7426	0.2	14.7171	1.9	0.2706	2.2	0.0289	1.2	0.53	183.6	2.1	243.2	4.7	866.1	38.5	183.6	2.1

Table 15. Sample 17323G (continued).

Analysis	U (ppm)	$^{206}Pb/^{204}Pb$	U/Th	$^{206}Pb/^{207}Pb$	± (%)	$^{207}Pb/^{235}U$	± (%)	$^{206}Pb/^{238}U$	± (%)	error corr.	$^{206}Pb/^{238}U$	± (Ma)	$^{207}Pb/^{235}U$	± (Ma)	$^{206}Pb/^{207}Pb$	± (Ma)	Best age (Ma)	± (Ma)
					Isotope ratios						Apparent ages (Ma)							
Spot 1	541	5068	1.3	12.0372	5.2	0.3367	5.7	0.0294	2.1	0.38	186.8	3.9	294.7	14.5	1270.1	102.2	186.8	3.9
Spot 12	198	281834	0.1	16.5441	3.3	0.2486	3.5	0.0298	1.1	0.32	189.6	2.1	225.5	7.0	618.6	70.6	189.6	2.1
Spot 28	419	8381016	1.6	18.6508	1.9	0.2230	2.6	0.0302	1.7	0.68	191.7	3.3	204.4	4.7	354.0	42.2	191.7	3.3
Spot 19	141	62102	0.7	15.5093	2.0	0.2694	3.0	0.0303	2.2	0.73	192.5	4.2	242.2	6.4	756.4	42.7	192.5	4.2
Spot 8	128	3351	0.3	9.5174	3.9	0.4399	4.0	0.0304	1.0	0.25	192.9	1.9	370.2	12.5	1714.7	71.6	192.9	1.9
Spot 21	94	1493	0.7	5.8773	13.3	0.7169	13.8	0.0306	3.5	0.25	194.1	6.6	548.8	58.4	2558.3	223.8	194.1	6.6
Spot 7	69	4807	0.9	18.4386	3.1	0.2771	3.3	0.0371	1.3	0.38	234.7	2.9	248.3	7.3	379.8	69.3	234.7	2.9
Spot 15	82	4193	1.1	12.8829	3.6	0.4991	3.8	0.0467	1.3	0.33	293.9	3.6	411.1	12.8	1136.4	71.2	293.9	3.6
Spot 9	132	50981	0.4	15.0442	3.8	0.4618	6.6	0.0504	5.4	0.82	317.0	16.7	385.5	21.3	820.4	80.3	317.0	16.7
Spot 31	323	13215	2.2	16.9768	1.8	0.4162	3.7	0.0513	3.3	0.87	322.3	10.2	353.4	11.1	562.6	39.4	322.3	10.2
Spot 29	383	77226	1.1	14.2401	1.3	1.2575	2.7	0.1299	2.4	0.88	787.4	17.8	826.8	15.4	934.0	26.7	787.4	17.8
Spot 23	246	423035	1.7	9.1804	1.0	4.1226	3.7	0.2746	3.5	0.96	1564.2	48.9	1658.8	29.9	1780.7	18.4	1780.7	18.4

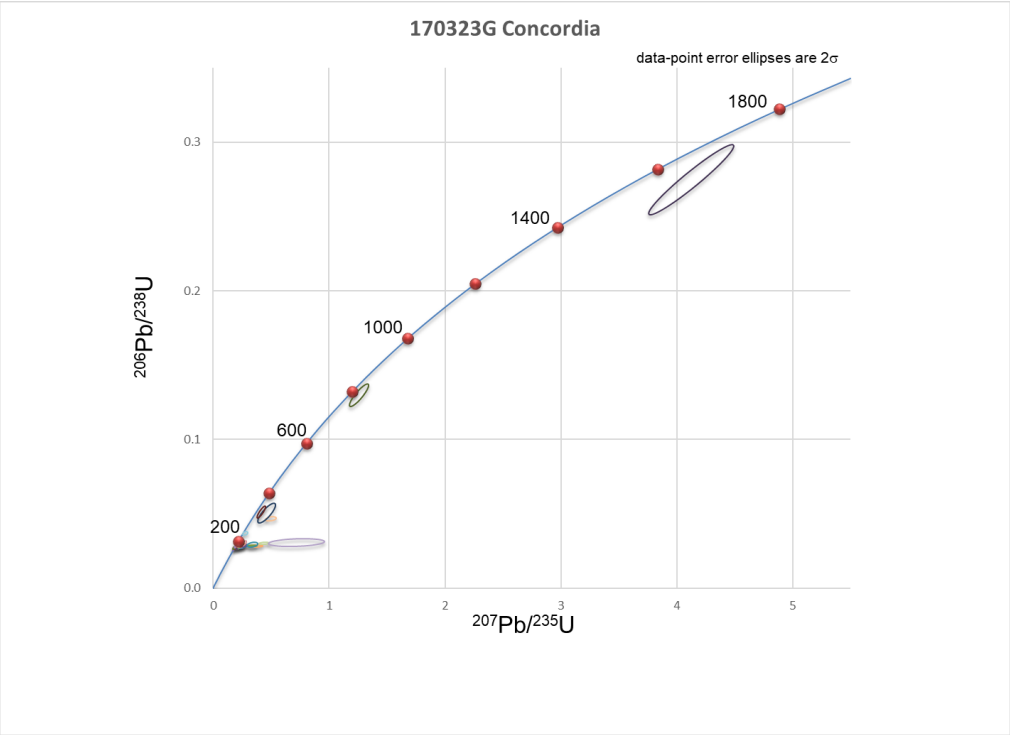

Figure 56. Concordia plot for sample 17323G

Table 16. U-Pb geochronology analysis data for sample 17323H, ordered by best age.

		Isotope ratios									Apparent ages (Ma)							
Analysis	U (ppm)	$^{206}Pb/^{204}Pb$	U/Th	$^{206}Pb/^{207}Pb$	± (%)	$^{207}Pb/^{235}U$	± (%)	$^{206}Pb/^{238}U$	± (%)	error corr.	$^{206}Pb/^{238}U$	± (Ma)	$^{207}Pb/^{235}U$	± (Ma)	$^{206}Pb/^{207}Pb$	± (Ma)	Best age (Ma)	± (Ma)
Spot 30	296	11582	4.3	21.3986	1.6	0.0781	2.4	0.0121	1.8	0.76	77.7	1.4	76.3	1.8	34.5	37.3	77.7	1.4
Spot 36	1001	76383	0.9	20.3804	0.9	0.0831	1.7	0.0123	1.5	0.85	78.8	1.2	81.1	1.4	150.0	21.3	78.8	1.2
Spot 23	68	2086	1.6	24.0111	5.8	0.0788	6.0	0.0137	1.5	0.25	87.9	1.3	77.0	4.4	NA	NA	87.9	1.3
Spot 13	566	11670	3.8	21.0724	1.7	0.1018	2.3	0.0156	1.6	0.68	99.6	1.5	98.5	2.2	71.2	40.1	99.6	1.5
Spot 37r	409	12936	4.1	21.1039	1.2	0.1050	1.9	0.0161	1.4	0.75	102.8	1.5	101.4	1.8	67.6	29.6	102.8	1.5
Spot 35c	467	44291	3.6	20.8231	1.1	0.1088	1.7	0.0164	1.2	0.74	105.2	1.3	104.9	1.7	99.4	26.5	105.2	1.3
Spot 9	105	2939	0.9	23.5000	3.1	0.1070	3.5	0.0182	1.5	0.44	116.6	1.8	103.2	3.4	NA	NA	116.6	1.8
Spot 26r	191	43881	1.8	19.8604	1.5	0.1697	1.7	0.0245	0.9	0.53	155.8	1.4	159.2	2.6	210.2	34.1	155.8	1.4
Spot 19c	253	5547	1.1	21.0960	1.2	0.1634	1.9	0.0250	1.4	0.75	159.2	2.2	153.7	2.7	68.5	29.6	159.2	2.2
Spot 28	925	73398	2.1	19.6037	2.3	0.2050	2.9	0.0292	1.8	0.63	185.3	3.3	189.4	5.0	240.3	52.5	185.3	3.3
Spot 22	152	4629	2.0	20.9858	1.3	0.1934	1.7	0.0294	1.2	0.68	187.1	2.2	179.5	2.8	80.9	30.0	187.1	2.2
Spot 29c	876	48712	1.3	20.2669	0.8	0.2015	1.5	0.0296	1.3	0.86	188.2	2.4	186.4	2.5	163.1	18.1	188.2	2.4
Spot 14r	195	6497	2.5	20.5568	1.5	0.1987	1.8	0.0296	1.1	0.61	188.2	2.1	184.0	3.1	129.8	34.6	188.2	2.1
Spot 25r	539	157556	2.0	19.2285	1.2	0.2129	1.8	0.0297	1.4	0.75	188.7	2.6	196.0	3.3	284.7	27.7	188.7	2.6
Spot 10	544	65069	2.0	20.2857	0.8	0.2022	1.8	0.0298	1.6	0.89	189.0	3.0	187.0	3.1	160.9	19.1	189.0	3.0
Spot 15	463	21618	2.4	20.3022	1.2	0.2023	1.8	0.0298	1.4	0.76	189.3	2.6	187.0	3.1	159.0	27.4	189.3	2.6
Spot 16c	692	40733	1.6	20.2440	1.0	0.2029	1.8	0.0298	1.5	0.83	189.4	2.8	187.6	3.1	165.7	23.2	189.4	2.8
Spot 18c	591	35936	2.9	20.0431	1.0	0.2053	1.8	0.0299	1.6	0.85	189.7	2.9	189.6	3.2	188.9	22.8	189.7	2.9

Table 16. Sample 17323H (continued).

Analysis	U (ppm)	$^{206}Pb/^{204}Pb$	U/Th	$^{206}Pb/^{207}Pb$	± (%)	$^{207}Pb/^{235}U$	± (%)	$^{206}Pb/^{238}U$	± (%)	error corr.	$^{206}Pb/^{238}U$	± (Ma)	$^{207}Pb/^{235}U$	± (Ma)	$^{206}Pb/^{207}Pb$	± (Ma)	Best age (Ma)	± (Ma)
					Isotope ratios							Apparent ages (Ma)						
Spot 20r	853	167560	3.7	19.9324	0.8	0.2065	1.6	0.0299	1.4	0.86	189.7	2.6	190.6	2.8	201.9	19.1	189.7	2.6
Spot 7r1	577	87922	2.0	20.0525	0.8	0.2054	1.7	0.0299	1.4	0.86	189.8	2.7	189.7	2.9	187.9	19.5	189.8	2.7
Spot 33	832	861830	2.2	20.0926	0.8	0.2055	1.7	0.0300	1.4	0.87	190.3	2.7	189.8	2.9	183.2	18.9	190.3	2.7
Spot 4	1091	58323	3.0	19.9629	0.7	0.2069	1.6	0.0300	1.4	0.88	190.4	2.6	191.0	2.7	198.3	17.2	190.4	2.6
Spot 5	322	29867	2.4	20.4957	1.2	0.2023	1.9	0.0301	1.5	0.79	191.1	2.8	187.1	3.2	136.8	27.1	191.1	2.8
Spot 34	518	138698	1.9	20.0083	0.9	0.2074	1.7	0.0301	1.4	0.84	191.2	2.7	191.3	2.9	193.0	21.0	191.2	2.7
Spot 17r	209	65065	5.6	20.0302	1.7	0.2076	2.1	0.0302	1.3	0.60	191.6	2.4	191.5	3.7	190.5	39.0	191.6	2.4
Spot 21r	1025	43414	2.6	20.1708	1.0	0.2071	1.9	0.0303	1.7	0.86	192.5	3.2	191.1	3.4	174.1	23.1	192.5	3.2
Spot 27	628	110137	2.2	19.9349	0.7	0.2097	1.6	0.0303	1.5	0.90	192.6	2.8	193.3	2.8	201.6	16.1	192.6	2.8
Spot 0c	1154	151344	3.3	19.9230	1.0	0.2115	1.7	0.0306	1.4	0.81	194.2	2.6	194.8	3.0	203.0	22.5	194.2	2.6
Spot 8	781	46243	2.0	20.1953	1.0	0.2091	1.8	0.0306	1.5	0.84	194.5	3.0	192.8	3.2	171.3	23.1	194.5	3.0
Spot 31	527	18236	1.2	20.2752	1.0	0.2262	2.2	0.0333	1.9	0.88	211.0	4.0	207.0	4.1	162.1	24.0	211.0	4.0
Spot 1	9	434	0.3	3.7313	1.9	1.7849	2.3	0.0483	1.3	0.56	304.2	3.8	1040.0	14.7	3293.7	29.5	304.2	3.8
Spot 39	149	35430	1.4	13.4650	0.7	1.8492	1.4	0.1807	1.1	0.83	1070.6	11.2	1063.1	8.9	1047.9	15.1	1047.9	15.1
Spot 11r	111	386045	1.4	13.4499	0.7	1.8293	1.4	0.1785	1.1	0.84	1058.9	11.2	1056.0	9.0	1050.1	15.0	1050.1	15.0
Spot 12c	76	17203	0.8	13.0047	1.2	1.9003	1.7	0.1793	1.2	0.71	1063.2	11.6	1081.2	11.2	1117.6	23.7	1117.6	23.7
Spot 3	136	59404	2.2	11.3627	0.8	2.8550	1.3	0.2354	1.1	0.80	1362.6	13.0	1370.1	10.0	1381.8	15.5	1381.8	15.5
Spot 38	213	144691	3.9	11.2533	0.8	2.8626	1.3	0.2337	1.1	0.81	1354.0	13.4	1372.1	10.1	1400.4	15.0	1400.4	15.0
Spot 2	66	43581	1.8	9.4713	0.9	4.4292	1.5	0.3044	1.2	0.80	1713.0	17.8	1717.8	12.2	1723.7	16.1	1723.7	16.1
Spot 32	899	187940	8.9	9.2244	0.7	4.1222	1.5	0.2759	1.3	0.88	1570.7	18.7	1658.7	12.4	1772.0	13.0	1772.0	13.0

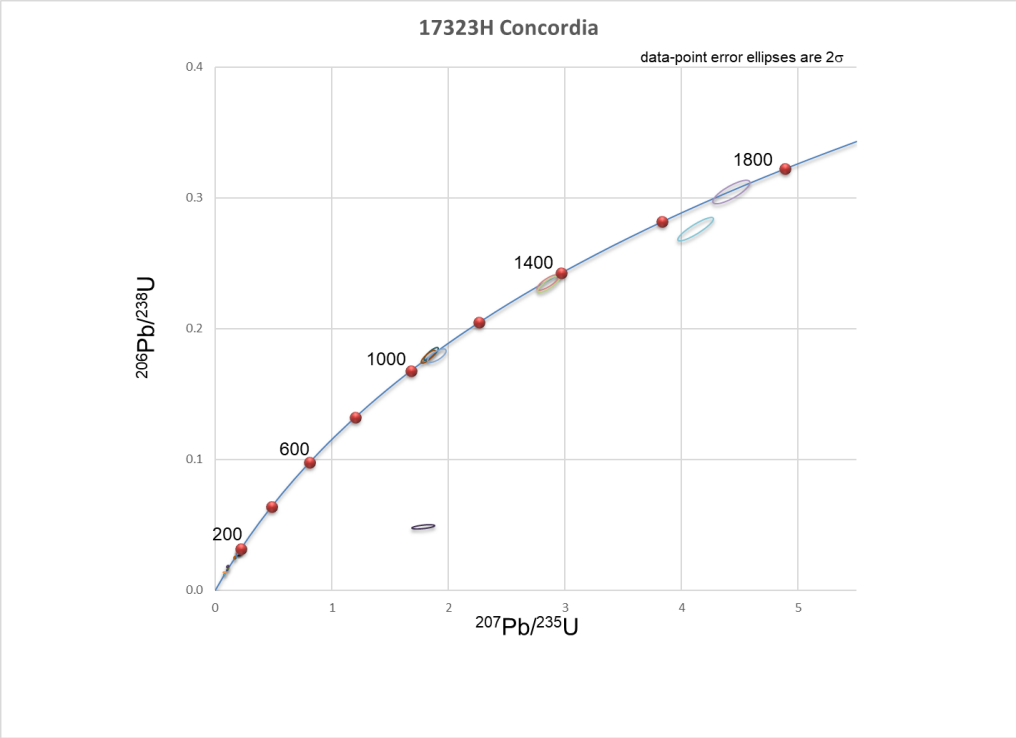

Figure 57. Concordia plot for sample 17323H

Table 17. U-Pb geochronology analysis data for sample 17324F, ordered by best age.

				Isotope ratios							Apparent ages (Ma)							
Analysis	U	$^{206}Pb/^{204}Pb$	U/Th	$^{206}Pb/^{207}Pb$	±	$^{207}Pb/^{235}U$	±	$^{206}Pb/^{238}U$	±	error	$^{206}Pb/^{238}U$	±	$^{207}Pb/^{235}U$	±	$^{206}Pb/^{207}Pb$	±	Best age	±
	(ppm)				(%)		(%)		(%)	corr.		(Ma)		(Ma)		(Ma)	(Ma)	(Ma)
Spot 21	5678	142978	27.6	21.4168	1.2	0.0137	1.7	0.0021	1.2	0.68	13.7	0.2	13.8	0.2	32.5	29.9	13.7	0.2
Spot 29	3019	25703	39.4	20.3760	1.1	0.0151	1.7	0.0022	1.3	0.75	14.4	0.2	15.2	0.3	150.5	26.5	14.4	0.2
Spot 24	592	2243	3.7	23.7211	3.2	0.0136	3.5	0.0023	1.3	0.38	15.0	0.2	13.7	0.5	NA	NA	15.0	0.2
Spot 18	396	2955	8.0	21.0033	4.0	0.0161	4.3	0.0025	1.7	0.39	15.8	0.3	16.2	0.7	79.0	94.4	15.8	0.3
Spot 1	246	3451	3.3	17.1507	5.1	0.0197	5.3	0.0025	1.5	0.28	15.8	0.2	19.8	1.0	540.3	111.6	15.8	0.2
Spot 17	255	38853	4.0	19.5781	3.9	0.0173	4.1	0.0025	1.4	0.35	15.8	0.2	17.4	0.7	243.3	89.0	15.8	0.2
Spot 27	50	918	1.2	20.3443	10.6	0.0166	11.1	0.0025	3.2	0.28	15.8	0.5	16.7	1.8	154.1	250.0	15.8	0.5
Spot 31	89	963	1.3	32.3533	10.8	0.0106	11.0	0.0025	2.1	0.19	16.0	0.3	10.7	1.2	NA	NA	16.0	0.3
Spot 25	240	2293	0.7	23.5304	8.5	0.0146	8.7	0.0025	1.8	0.21	16.0	0.3	14.7	1.3	NA	NA	16.0	0.3
Spot 12	1105	140789	2.6	21.5328	1.9	0.0161	2.4	0.0025	1.4	0.60	16.2	0.2	16.3	0.4	19.5	45.8	16.2	0.2
Spot 23	451	5261	1.9	21.6894	2.9	0.0160	3.5	0.0025	1.9	0.55	16.3	0.3	16.2	0.6	2.1	70.3	16.3	0.3
Spot 30	244	2443	2.2	17.5370	6.7	0.0200	6.9	0.0025	1.5	0.22	16.4	0.2	20.1	1.4	491.5	147.7	16.4	0.2
Spot 16	353	56602	2.8	19.6217	3.4	0.0183	3.7	0.0026	1.5	0.42	16.8	0.3	18.4	0.7	238.2	77.6	16.8	0.3
Spot 4	161	1309	1.1	20.7643	8.3	0.0174	8.6	0.0026	2.0	0.23	16.9	0.3	17.5	1.5	106.1	197.1	16.9	0.3
Spot 13	405	1685	2.0	27.2723	4.9	0.0135	5.4	0.0027	2.2	0.41	17.3	0.4	13.7	0.7	NA	NA	17.3	0.4
Spot 15	280	9441	3.9	21.8342	3.1	0.0169	3.5	0.0027	1.5	0.44	17.3	0.3	17.1	0.6	NA	NA	17.3	0.3
Spot 20 c	281	8556	0.8	19.3257	2.8	0.0202	3.5	0.0028	2.1	0.60	18.2	0.4	20.3	0.7	273.1	63.5	18.2	0.4

Table 17. Sample 17324F (continued).

Analysis	U (ppm)	$^{206}Pb/^{204}Pb$	U/Th	$^{206}Pb/^{207}Pb$	± (%)	$^{207}Pb/^{235}U$	± (%)	$^{206}Pb/^{238}U$	± (%)	error corr.	$^{206}Pb/^{238}U$	± (Ma)	$^{207}Pb/^{235}U$	± (Ma)	$^{206}Pb/^{207}Pb$	± (Ma)	Best age (Ma)	± (Ma)
					Isotope ratios													
													Apparent ages (Ma)					
Spot 11	36	1034	1.5	2.5239	7.8	0.2032	8.8	0.0037	4.2	0.48	23.9	1.0	187.9	15.1	3894.1	117.0	23.9	1.0
Spot 14	40	15049	2.5	14.6231	1.6	0.5660	2.4	0.0601	1.8	0.75	375.9	6.5	455.4	8.7	879.3	32.3	375.9	6.5
Spot 35	133	30111	1.4	17.6074	1.1	0.5514	1.6	0.0704	1.1	0.72	438.9	4.8	445.9	5.7	482.6	23.9	438.9	4.8
Spot 10	409	123246	2.9	17.8529	0.8	0.5533	1.7	0.0717	1.5	0.89	446.2	6.4	447.1	6.0	451.9	16.8	446.2	6.4
Spot 33	256	60391	11.2	17.4905	1.0	0.5711	1.6	0.0725	1.2	0.75	451.1	5.1	458.8	5.8	497.3	22.9	451.1	5.1
Spot 5	225	120239	5.3	17.7730	1.0	0.5716	1.5	0.0737	1.1	0.75	458.5	4.9	459.1	5.4	461.9	21.4	458.5	4.9
Spot 34	479	48372	2.8	17.6977	0.8	0.5765	1.5	0.0740	1.3	0.84	460.4	5.7	462.2	5.7	471.3	18.4	460.4	5.7
Spot 19	415	142480	24.2	17.6033	1.0	0.5807	1.8	0.0742	1.5	0.84	461.2	6.8	464.9	6.8	483.1	21.9	461.2	6.8
Spot 26	284	669936	12.9	17.5275	1.1	0.5841	1.8	0.0743	1.5	0.80	461.9	6.5	467.1	6.8	492.6	24.2	461.9	6.5
Spot 28	253	58316	3.2	17.7107	0.8	0.5803	1.5	0.0746	1.3	0.85	463.6	5.7	464.6	5.6	469.6	17.5	463.6	5.7
Spot 2	110	26169	3.2	17.5877	1.2	0.5846	1.9	0.0746	1.5	0.78	463.9	6.7	467.4	7.2	485.0	26.2	463.9	6.7
Spot 7	666	98339	13.1	17.5921	0.9	0.6033	1.8	0.0770	1.5	0.87	478.2	7.1	479.3	6.8	484.5	18.9	478.2	7.1
Spot 32	212	41918	11.1	17.6847	1.1	0.6022	1.8	0.0773	1.4	0.80	479.8	6.6	478.6	6.8	472.9	23.7	479.8	6.6

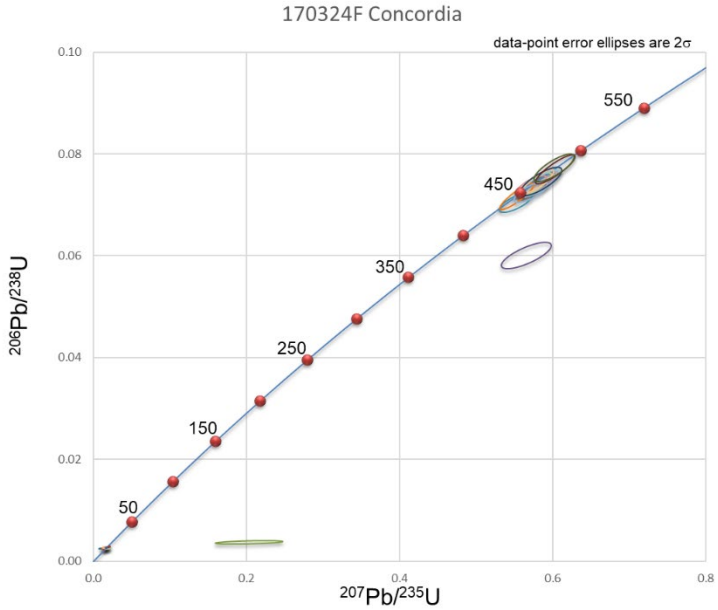

Figure 59. Concordia plot for sample 17324F

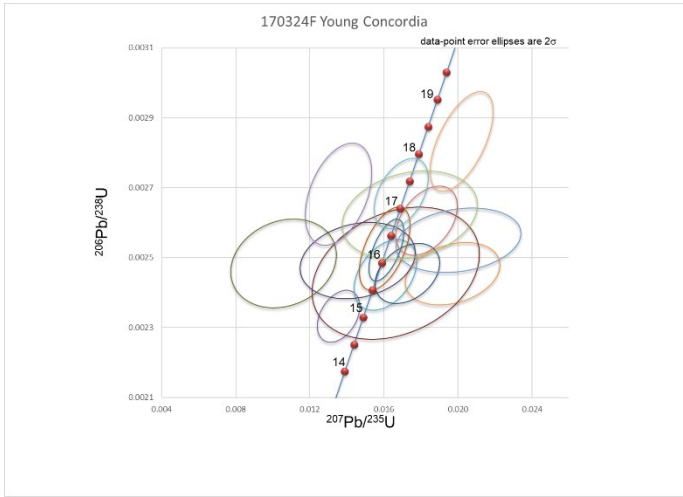

Figure 58. Young Concordia plot for sample 17324F

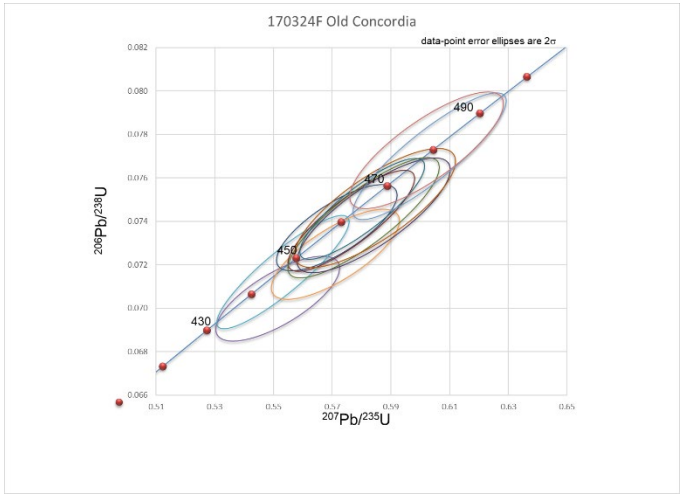

Figure 60. Old Concordia plot for sample 17324F

Table 18. U-Pb geochronology analysis data for sample 17327E, ordered by best age.

		Isotope ratios									Apparent ages (Ma)							
Analysis	U (ppm)	$^{206}Pb/^{204}Pb$	U/Th	$^{206}Pb/^{207}Pb$	± (%)	$^{207}Pb/^{235}U$	± (%)	$^{206}Pb/^{238}U$	± (%)	error corr.	$^{206}Pb/^{238}U$	± (Ma)	$^{207}Pb/^{235}U$	± (Ma)	$^{206}Pb/^{207}Pb$	± (Ma)	Best age (Ma)	± (Ma)
Spot 40	1929	179354	2.6	18.7725	1.0	0.3278	2.0	0.0447	1.7	0.86	281.6	4.7	287.9	4.9	339.3	22.8	281.6	4.7
Spot 46	2752	114115	2.6	18.6706	1.3	0.3362	2.7	0.0456	2.4	0.88	287.2	6.7	294.3	6.9	351.6	28.7	287.2	6.7
Spot 57	1712	565027	3.4	19.0355	1.0	0.3323	2.1	0.0459	1.9	0.87	289.3	5.3	291.3	5.4	307.7	23.7	289.3	5.3
Spot 67	1541	159898	3.2	19.4133	0.8	0.3343	1.6	0.0471	1.4	0.88	296.6	4.1	292.8	4.1	262.8	17.4	296.6	4.1
Spot 47	659	98572	2.0	18.6073	1.1	0.3494	2.1	0.0472	1.8	0.86	297.2	5.2	304.3	5.5	359.3	23.8	297.2	5.2
Spot 68	862	1611671	4.0	18.8851	1.0	0.3445	2.3	0.0472	2.1	0.91	297.4	6.0	300.6	5.9	325.8	21.7	297.4	6.0
Spot 53	690	101135	2.7	18.8936	0.8	0.3453	1.8	0.0473	1.6	0.89	298.1	4.6	301.1	4.6	324.7	17.9	298.1	4.6
Spot 59	1364	92368	3.5	19.0344	0.8	0.3432	1.7	0.0474	1.4	0.86	298.5	4.1	299.6	4.3	307.8	19.3	298.5	4.1
Spot 37	961	75057	2.9	18.7940	0.8	0.3477	1.5	0.0474	1.3	0.85	298.6	3.7	303.0	3.9	336.7	17.8	298.6	3.7
Spot 39	2957	133426	1.4	19.5124	1.1	0.3356	2.2	0.0475	2.0	0.88	299.3	5.8	293.9	5.7	251.1	24.4	299.3	5.8
Spot 41	1761	165751	2.3	19.3043	1.0	0.3395	1.9	0.0476	1.6	0.85	299.5	4.8	296.8	4.9	275.7	23.2	299.5	4.8
Spot 56	1173	91247	2.2	18.5057	1.3	0.3557	2.3	0.0478	1.8	0.81	300.8	5.4	309.0	6.1	371.6	29.8	300.8	5.4
Spot 48	1003	94923	2.3	19.1958	0.7	0.3429	1.6	0.0478	1.5	0.90	300.8	4.3	299.4	4.2	288.6	15.9	300.8	4.3
Spot 50	628	36533	1.8	19.2439	1.1	0.3422	1.7	0.0478	1.3	0.77	300.9	3.7	298.8	4.3	282.9	24.1	300.9	3.7
Spot 45	1316	70269	3.0	19.0675	0.9	0.3462	1.5	0.0479	1.2	0.80	301.6	3.5	301.9	3.9	303.9	20.7	301.6	3.5
Spot 61	1727	1026774	2.0	19.2951	1.1	0.3425	2.2	0.0479	1.9	0.86	301.9	5.5	299.1	5.6	276.8	25.2	301.9	5.5
Spot 62	699	74424	2.2	18.7752	1.0	0.3524	1.6	0.0480	1.2	0.79	302.3	3.6	306.5	4.1	339.0	21.8	302.3	3.6
Spot 60	1203	2403156	2.1	19.2314	0.8	0.3447	1.6	0.0481	1.3	0.84	302.8	3.9	300.7	4.1	284.3	19.4	302.8	3.9

Table 18. Sample 17327E (continued).

Analysis	U (ppm)	$^{206}Pb/^{204}Pb$	U/Th	$^{206}Pb/^{207}Pb$	± (%)	$^{207}Pb/^{235}U$	± (%)	$^{206}Pb/^{238}U$	± (%)	error corr.	$^{206}Pb/^{238}U$	± (Ma)	$^{207}Pb/^{235}U$	± (Ma)	$^{206}Pb/^{207}Pb$	± (Ma)	Best age (Ma)	± (Ma)
					Isotope ratios						Apparent ages (Ma)							
Spot 44	1161	106950	1.5	19.0969	0.7	0.3474	1.3	0.0481	1.1	0.85	303.1	3.3	302.7	3.5	300.4	16.2	303.1	3.3
Spot 70	1024	106773	3.4	18.9978	0.8	0.3506	1.8	0.0483	1.6	0.90	304.3	4.7	305.2	4.6	312.2	17.6	304.3	4.7
Spot 55	1141	791922	2.2	19.1555	0.7	0.3482	1.4	0.0484	1.2	0.85	304.6	3.4	303.4	3.6	293.4	16.3	304.6	3.4
Spot 52	1326	127094	3.3	19.1028	0.9	0.3492	1.9	0.0484	1.6	0.89	304.7	4.9	304.1	4.9	299.7	19.5	304.7	4.9
Spot 58	207	44483	0.8	19.0969	1.0	0.3493	1.7	0.0484	1.3	0.79	304.7	3.9	304.2	4.4	300.4	23.2	304.7	3.9
Spot 63	1277	258113	3.3	19.0136	0.9	0.3511	1.9	0.0484	1.7	0.88	304.9	4.9	305.5	4.9	310.3	19.9	304.9	4.9
Spot 49	1534	344961	1.6	19.0779	0.8	0.3500	1.3	0.0485	1.1	0.82	305.0	3.3	304.7	3.5	302.7	17.5	305.0	3.3
Spot 69	690	98362	3.7	18.9602	0.9	0.3538	1.7	0.0487	1.5	0.87	306.4	4.4	307.6	4.6	316.7	19.6	306.4	4.4
Spot 64	922	105024	2.0	19.0340	1.0	0.3528	1.7	0.0487	1.4	0.82	306.7	4.1	306.8	4.5	307.9	22.0	306.7	4.1
Spot 38	998	80785	2.1	19.0053	0.8	0.3534	1.5	0.0487	1.3	0.86	306.7	3.9	307.3	4.0	311.3	17.6	306.7	3.9
Spot 36	1243	247304	2.9	19.2108	0.7	0.3511	1.4	0.0489	1.3	0.88	308.1	3.8	305.6	3.8	286.8	15.6	308.1	3.8
Spot 51	397	55717	2.0	18.9267	1.0	0.3585	2.1	0.0492	1.8	0.88	309.8	5.6	311.1	5.6	320.8	22.8	309.8	5.6
Spot 43	1580	118985	4.1	19.3295	1.2	0.3523	2.0	0.0494	1.6	0.81	310.9	4.8	306.4	5.2	272.7	26.6	310.9	4.8
Spot 66	503	46401	4.1	18.3811	1.0	0.3749	1.7	0.0500	1.4	0.82	314.5	4.2	323.3	4.6	386.8	21.5	314.5	4.2
Spot 42	837	196199	2.9	19.3218	0.9	0.3583	1.6	0.0502	1.3	0.83	315.9	4.2	310.9	4.3	273.6	20.6	315.9	4.2

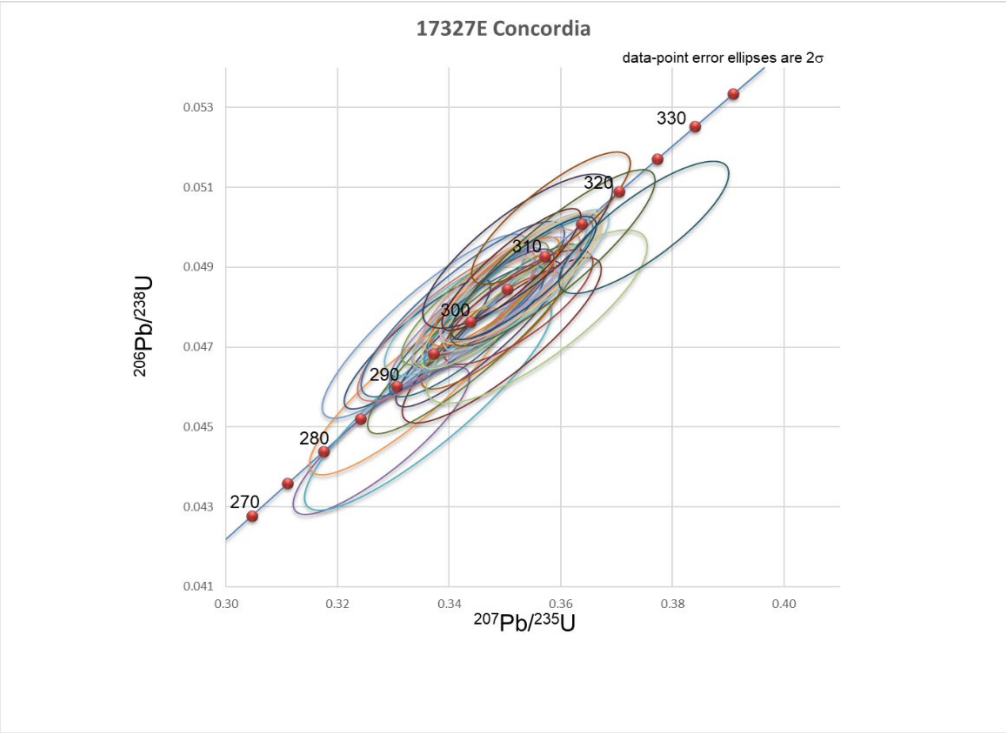

Figure 61. Concordia plot for sample 17327E

Table 19. U-Pb geochronology analysis data for sample 17329C, ordered by best age.

		Isotope ratios									Apparent ages (Ma)							
Analysis	U (ppm)	$^{206}Pb/^{204}Pb$	U/Th	$^{206}Pb/^{207}Pb$	± (%)	$^{207}Pb/^{235}U$	± (%)	$^{206}Pb/^{238}U$	± (%)	error corr.	$^{206}Pb/^{238}U$	± (Ma)	$^{207}Pb/^{235}U$	± (Ma)	$^{206}Pb/^{207}Pb$	± (Ma)	Best age (Ma)	± (Ma)
Spot 43	633	1414575	3.2	19.0996	0.9	0.2521	1.9	0.0349	1.7	0.88	221.4	3.7	228.3	3.9	300.1	20.6	221.4	3.7
Spot 65	395	686999	2.0	19.0397	0.9	0.2559	1.8	0.0353	1.5	0.85	223.9	3.3	231.3	3.6	307.2	21.0	223.9	3.3
Spot 61	662	40267	1.2	18.5560	1.2	0.2683	1.7	0.0361	1.3	0.72	228.8	2.8	241.3	3.7	365.5	27.1	228.8	2.8
Spot 64	1034	75378	1.2	18.9806	1.0	0.2659	1.6	0.0366	1.2	0.77	231.8	2.8	239.4	3.4	314.3	23.5	231.8	2.8
Spot 39	1261	117319	1.0	19.5692	0.9	0.2592	1.6	0.0368	1.3	0.82	233.0	3.0	234.0	3.3	244.4	20.6	233.0	3.0
Spot 46	414	261820	1.1	19.4926	0.9	0.2604	1.6	0.0368	1.3	0.81	233.1	2.9	235.0	3.3	253.4	21.3	233.1	2.9
Spot 38	541	30485	1.2	18.3912	1.1	0.2766	1.5	0.0369	1.0	0.69	233.6	2.4	247.9	3.3	385.6	24.6	233.6	2.4
Spot 47	435	35417	2.0	19.3639	0.9	0.2643	1.4	0.0371	1.1	0.76	235.0	2.4	238.1	2.9	268.6	20.5	235.0	2.4
Spot 37	406	31637	1.4	17.4066	1.6	0.2954	2.2	0.0373	1.6	0.69	236.1	3.6	262.8	5.2	507.9	35.7	236.1	3.6
Spot 56	416	69566	1.6	19.1246	1.2	0.2689	2.3	0.0373	1.9	0.85	236.1	4.5	241.8	4.9	297.1	27.1	236.1	4.5
Spot 63	296	33614	1.3	19.6171	1.3	0.2622	1.8	0.0373	1.3	0.69	236.2	2.9	236.4	3.9	238.7	30.4	236.2	2.9
Spot 66	643	69460	1.1	19.4368	1.1	0.2651	1.5	0.0374	1.1	0.72	236.6	2.6	238.8	3.3	260.0	24.7	236.6	2.6
Spot 49	527	51440	1.2	19.2138	1.0	0.2686	1.3	0.0374	0.8	0.63	237.0	1.9	241.5	2.8	286.4	23.1	237.0	1.9
Spot 60	571	43373	2.1	19.3382	1.0	0.2674	1.9	0.0375	1.6	0.85	237.5	3.8	240.6	4.1	271.6	23.3	237.5	3.8
Spot 44	182	36627	2.3	18.9531	1.2	0.2730	1.9	0.0375	1.4	0.75	237.5	3.2	245.1	4.1	317.6	28.2	237.5	3.2
Spot 69	565	102471	1.0	19.4503	0.8	0.2662	1.5	0.0376	1.3	0.85	237.7	3.0	239.6	3.3	258.4	18.6	237.7	3.0
Spot 51	354	134767	1.9	18.9994	1.1	0.2725	1.8	0.0376	1.4	0.78	237.7	3.3	244.7	3.9	312.1	25.6	237.7	3.3
Spot 67	299	20748	1.2	17.2769	2.0	0.3000	2.4	0.0376	1.3	0.55	238.0	3.0	266.4	5.6	524.3	43.8	238.0	3.0

Table 19. 17329C (continued).

					Isotope ratios						Apparent ages (Ma)							
Analysis	U	$^{206}Pb/^{204}Pb$	U/Th	$^{206}Pb/^{207}Pb$	±	$^{207}Pb/^{235}U$	±	$^{206}Pb/^{238}U$	±	error	$^{206}Pb/^{238}U$	±	$^{207}Pb/^{235}U$	±	$^{206}Pb/^{207}Pb$	±	Best age	±
	(ppm)				(%)		(%)		(%)	corr.		(Ma)		(Ma)		(Ma)	(Ma)	(Ma)
Spot 53	673	75726	4.9	19.3944	0.9	0.2685	1.2	0.0378	0.8	0.69	239.1	2.0	241.5	2.6	265.0	20.2	239.1	2.0
Spot 41	666	77736	4.6	19.2107	1.0	0.2726	1.6	0.0380	1.3	0.79	240.4	3.0	244.8	3.5	286.8	22.3	240.4	3.0
Spot 42	461	113358	2.5	19.3906	1.1	0.2703	1.8	0.0380	1.4	0.78	240.6	3.2	243.0	3.8	265.5	25.5	240.6	3.2
Spot 57	350	27966	1.1	19.2278	1.1	0.2729	1.8	0.0381	1.5	0.81	240.9	3.5	245.0	3.9	284.8	24.2	240.9	3.5
Spot 70	159	5019	2.2	16.1248	1.9	0.3255	2.2	0.0381	1.2	0.52	240.9	2.7	286.1	5.5	673.7	40.2	240.9	2.7
Spot 59	276	24286	1.4	19.7822	1.2	0.2670	1.8	0.0383	1.3	0.74	242.4	3.2	240.3	3.8	219.4	27.9	242.4	3.2
Spot 54	598	98526	2.1	19.1883	1.0	0.2763	1.7	0.0385	1.4	0.82	243.3	3.2	247.7	3.7	289.5	21.9	243.3	3.2
Spot 48	766	9536	1.6	15.0493	2.4	0.3531	2.7	0.0386	1.3	0.46	243.9	3.0	307.1	7.2	819.6	50.3	243.9	3.0
Spot 58	548	21484	1.9	19.0607	1.1	0.2790	1.8	0.0386	1.4	0.78	244.1	3.4	249.9	4.1	304.7	26.0	244.1	3.4
Spot 40	869	21144	0.8	17.2819	1.5	0.3080	2.0	0.0386	1.3	0.65	244.3	3.2	272.7	4.9	523.6	33.9	244.3	3.2
Spot 45	325	8241	1.4	16.2181	1.9	0.3283	2.3	0.0386	1.3	0.58	244.3	3.2	288.2	5.8	661.4	40.2	244.3	3.2
Spot 52	876	135977	1.5	19.5194	0.7	0.2743	1.3	0.0388	1.1	0.82	245.7	2.5	246.1	2.8	250.2	16.7	245.7	2.5
Spot 55	665	28406	1.6	16.5935	1.3	0.3231	1.9	0.0389	1.3	0.70	246.0	3.2	284.2	4.6	612.1	28.8	246.0	3.2
Spot 50	515	488789	1.0	17.5968	1.3	0.3074	1.9	0.0392	1.4	0.75	248.1	3.5	272.1	4.6	483.9	28.1	248.1	3.5
Spot 68	432	6441	1.6	12.6607	2.3	0.4479	2.5	0.0411	1.1	0.45	259.9	2.9	375.8	8.0	1170.9	45.0	259.9	2.9
Spot 62	337	60943	2.7	13.8200	0.9	1.5420	1.9	0.1546	1.6	0.87	926.9	14.0	947.3	11.5	995.1	18.6	995.1	18.6

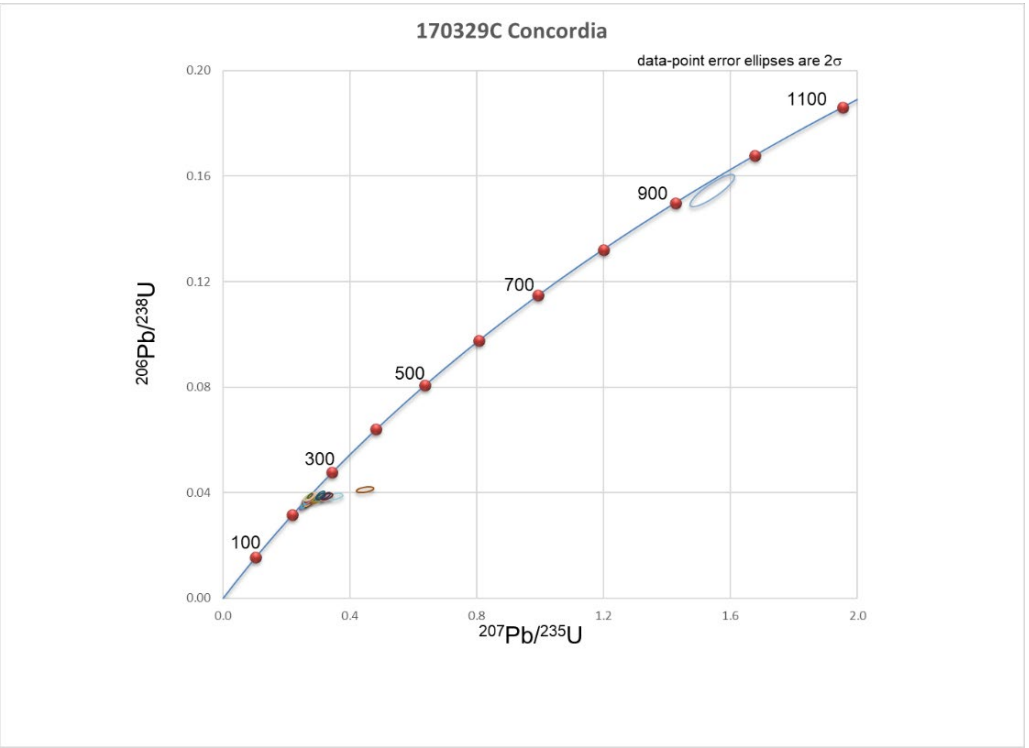

Figure 62. Concordia plot for sample 17329C

Table 20. U-Pb geochronology analysis data for sample 17329E, ordered by best age.

					Isotope ratios						Apparent ages (Ma)							
Analysis	U (ppm)	$^{206}Pb/^{204}Pb$	U/Th	$^{206}Pb/^{207}Pb$	± (%)	$^{207}Pb/^{235}U$	± (%)	$^{206}Pb/^{238}U$	± (%)	error corr.	$^{206}Pb/^{238}U$	± (Ma)	$^{207}Pb/^{235}U$	± (Ma)	$^{206}Pb/^{207}Pb$	± (Ma)	Best age (Ma)	± (Ma)
Spot 4	584	18597	31.9	19.4509	0.7	0.2402	1.4	0.0339	1.2	0.86	214.9	2.6	218.6	2.8	258.3	16.7	214.9	2.6
Spot 7	68	5454	1.8	20.0127	1.7	0.2360	2.0	0.0343	1.1	0.56	217.2	2.4	215.2	3.9	192.5	38.9	217.2	2.4
Spot 2	117	4602	2.9	20.5045	1.7	0.2317	2.2	0.0345	1.3	0.62	218.5	2.9	211.6	4.1	135.8	39.9	218.5	2.9
Spot 13	256	48217	2.7	19.5939	1.1	0.2431	1.8	0.0346	1.4	0.80	219.0	3.1	220.9	3.6	241.5	25.0	219.0	3.1
Spot 3	85	18323	3.4	18.9910	1.4	0.2509	2.1	0.0346	1.6	0.73	219.1	3.3	227.3	4.3	313.0	32.9	219.1	3.3
Spot 28	307	9306	3.2	19.7672	1.2	0.2410	1.7	0.0346	1.2	0.69	219.1	2.5	219.3	3.3	221.1	27.7	219.1	2.5
Spot 22	559	1503306	4.4	19.4746	0.8	0.2449	1.2	0.0346	0.9	0.75	219.3	2.0	222.4	2.4	255.5	18.6	219.3	2.0
Spot 18	156	11273	1.8	19.5454	1.8	0.2449	2.2	0.0347	1.3	0.58	220.1	2.7	222.5	4.4	247.2	41.3	220.1	2.7
Spot 5	156	17551	1.5	19.5710	1.2	0.2451	1.7	0.0348	1.2	0.70	220.5	2.7	222.6	3.5	244.2	28.6	220.5	2.7
Spot 15	200	41057	1.6	19.2331	1.1	0.2498	1.7	0.0349	1.3	0.78	220.9	2.9	226.4	3.5	284.1	24.6	220.9	2.9
Spot 32	402	727558	4.0	19.1008	0.8	0.2516	1.3	0.0349	1.0	0.81	221.0	2.2	227.9	2.6	299.9	17.2	221.0	2.2
Spot 25	87	6866	2.2	20.0812	1.5	0.2395	2.0	0.0349	1.4	0.67	221.1	3.0	218.0	4.0	184.5	35.2	221.1	3.0
Spot 20	268	132763	4.4	19.6249	0.7	0.2451	1.5	0.0349	1.3	0.87	221.1	2.8	222.6	2.9	237.8	16.5	221.1	2.8
Spot 23	345	19436	2.0	19.4525	1.0	0.2473	1.7	0.0349	1.4	0.80	221.1	3.0	224.4	3.4	258.1	23.8	221.1	3.0
Spot 1	133	31739	2.4	19.6076	0.9	0.2459	1.4	0.0350	1.0	0.75	221.6	2.2	223.2	2.7	239.9	20.5	221.6	2.2
Spot 27	54	4460	2.5	20.5624	3.3	0.2350	3.6	0.0351	1.4	0.40	222.2	3.1	214.3	6.9	129.1	77.0	222.2	3.1
Spot 8	100	24411	3.2	19.2430	1.2	0.2512	1.8	0.0351	1.3	0.74	222.2	2.9	227.6	3.7	283.0	28.2	222.2	2.9
Spot 14	103	7062	2.1	19.8022	1.4	0.2444	1.7	0.0351	1.0	0.60	222.5	2.2	222.0	3.4	217.0	31.5	222.5	2.2
Spot 31	104	25505	2.2	19.4683	1.2	0.2488	1.7	0.0351	1.2	0.72	222.7	2.7	225.6	3.5	256.3	27.3	222.7	2.7

Table 20. Sample 17329E (continued).

Analysis	U (ppm)	$^{206}Pb/^{204}Pb$	U/Th	$^{206}Pb/^{207}Pb$	± (%)	$^{207}Pb/^{235}U$	± (%)	$^{206}Pb/^{238}U$	± (%)	error corr.	$^{206}Pb/^{238}U$	± (Ma)	$^{207}Pb/^{235}U$	± (Ma)	$^{206}Pb/^{207}Pb$	± (Ma)	Best age (Ma)	± (Ma)
					Isotope ratios							Apparent ages (Ma)						
Spot 11	67	7968	1.9	19.7713	1.5	0.2453	2.0	0.0352	1.3	0.65	223.0	2.9	222.8	4.0	220.6	35.5	223.0	2.9
Spot 19	156	19639	1.6	19.5157	1.1	0.2499	1.4	0.0354	1.0	0.66	224.2	2.1	226.5	2.9	250.7	24.7	224.2	2.1
Spot 9	107	12932	1.7	19.6860	1.6	0.2477	2.0	0.0354	1.1	0.58	224.2	2.5	224.7	3.9	230.6	36.9	224.2	2.5
Spot 16	139	21866	2.8	19.4662	1.0	0.2509	1.4	0.0354	1.1	0.75	224.5	2.4	227.3	2.9	256.5	21.9	224.5	2.4
Spot 26	244	87777	1.7	19.1678	1.0	0.2550	1.5	0.0355	1.1	0.73	224.7	2.5	230.6	3.2	291.9	23.9	224.7	2.5
Spot 12	89	4127	1.9	20.3997	1.8	0.2400	2.1	0.0355	1.0	0.49	225.1	2.3	218.5	4.1	147.8	42.8	225.1	2.3
Spot 29	92	7965	2.3	19.5946	1.6	0.2500	1.8	0.0355	0.9	0.50	225.1	2.0	226.5	3.7	241.4	36.3	225.1	2.0
Spot 35	166	21752	2.8	19.3060	1.3	0.2540	1.6	0.0356	1.0	0.63	225.4	2.3	229.9	3.3	275.5	28.9	225.4	2.3
Spot 34	70	23400	1.8	19.6001	1.6	0.2511	2.1	0.0357	1.4	0.65	226.2	3.0	227.5	4.2	240.7	36.4	226.2	3.0
Spot 24	55	39528	3.0	19.1957	1.5	0.2565	2.2	0.0357	1.5	0.70	226.3	3.3	231.8	4.5	288.6	35.3	226.3	3.3
Spot 6	95	8643	2.1	19.3332	1.6	0.2552	2.2	0.0358	1.5	0.68	226.7	3.3	230.8	4.5	272.2	36.4	226.7	3.3
Spot 17	95	23278	1.8	19.5208	1.6	0.2534	2.3	0.0359	1.5	0.68	227.3	3.4	229.3	4.6	250.1	37.9	227.3	3.4
Spot 33	123	4110	1.5	11.6118	4.4	0.4280	4.6	0.0361	1.4	0.30	228.4	3.1	361.8	14.0	1340.0	85.0	228.4	3.1
Spot 30	44	2863	2.6	20.7943	2.5	0.2419	2.8	0.0365	1.2	0.42	231.1	2.6	220.0	5.5	102.7	60.1	231.1	2.6
Spot 10	110	29356	2.6	19.0660	1.4	0.2644	2.0	0.0366	1.4	0.71	231.6	3.2	238.2	4.3	304.0	32.2	231.6	3.2

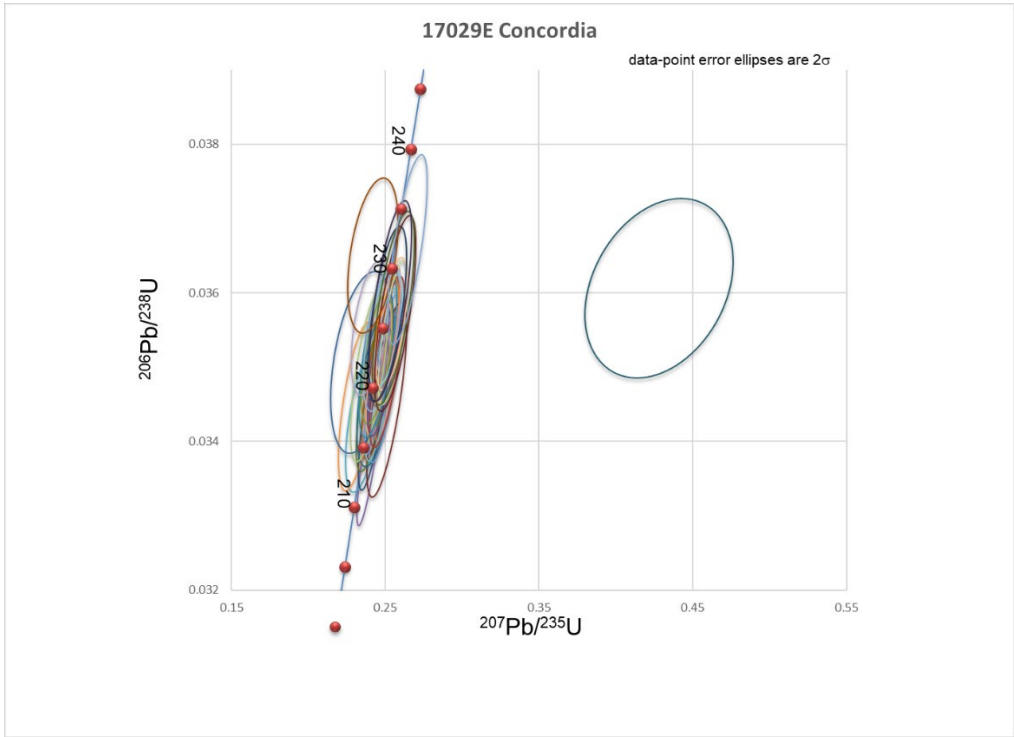

Figure 63. Concordia plot for sample 17329E

Table 21. U-Pb geochronology analysis data for sample 17330A, ordered by best age.

		Isotope ratios									Apparent ages (Ma)							
Analysis	U (ppm)	$^{206}Pb/^{204}Pb$	U/Th	$^{206}Pb/^{207}Pb$	± (%)	$^{207}Pb/^{235}U$	± (%)	$^{206}Pb/^{238}U$	± (%)	error corr.	$^{206}Pb/^{238}U$	± (Ma)	$^{207}Pb/^{235}U$	± (Ma)	$^{206}Pb/^{207}Pb$	± (Ma)	Best age (Ma)	± (Ma)
Spot 20	5104	20623	0.6	20.6690	0.9	0.0193	1.8	0.0029	1.6	0.88	18.6	0.3	19.4	0.3	116.9	20.6	18.6	0.3
Spot 22	5104	29890	0.6	21.2135	0.7	0.0200	1.4	0.0031	1.2	0.87	19.8	0.2	20.1	0.3	55.3	16.7	19.8	0.2
Spot 3	5104	39314	0.6	21.1557	0.9	0.0221	1.7	0.0034	1.4	0.83	21.9	0.3	22.2	0.4	61.8	21.8	21.9	0.3
Spot 13	5104	13466	0.6	21.2432	0.7	0.0225	1.5	0.0035	1.4	0.89	22.3	0.3	22.6	0.3	51.9	16.7	22.3	0.3
Spot 29	5104	8150	0.6	21.0263	1.0	0.0232	1.7	0.0035	1.4	0.83	22.8	0.3	23.3	0.4	76.4	22.8	22.8	0.3
Spot 30	5104	25752	0.6	21.5528	0.7	0.0230	1.4	0.0036	1.2	0.87	23.1	0.3	23.1	0.3	17.3	16.8	23.1	0.3
Spot 15	5104	24591	0.6	21.0834	0.9	0.0241	1.6	0.0037	1.3	0.84	23.7	0.3	24.2	0.4	69.9	20.3	23.7	0.3
Spot 11	5104	2623	0.6	16.4931	2.4	0.0318	2.8	0.0038	1.4	0.51	24.5	0.4	31.8	0.9	625.2	52.5	24.5	0.4
Spot 9	5104	27848	0.6	20.5842	0.8	0.0262	1.8	0.0039	1.6	0.89	25.2	0.4	26.3	0.5	126.7	19.4	25.2	0.4
Spot 10	5104	9216	0.6	20.4383	1.0	0.0265	2.2	0.0039	2.0	0.90	25.3	0.5	26.6	0.6	143.4	22.5	25.3	0.5
Spot 12	5104	532710	0.6	21.2666	0.8	0.0257	1.9	0.0040	1.7	0.91	25.5	0.4	25.8	0.5	49.3	19.3	25.5	0.4
Spot 23	5342	12360	0.6	19.3457	1.0	0.0283	1.9	0.0040	1.6	0.86	25.6	0.4	28.4	0.5	270.8	22.3	25.6	0.4
Spot 8	5104	5197	0.6	19.9746	0.7	0.0276	1.2	0.0040	1.0	0.84	25.7	0.3	27.6	0.3	196.9	15.5	25.7	0.3
Spot 21	5138	166068	1.0	21.1779	0.8	0.0267	1.8	0.0041	1.6	0.89	26.4	0.4	26.8	0.5	59.3	19.5	26.4	0.4
Spot 1	4455	14725	0.7	21.8275	0.8	0.0261	1.4	0.0041	1.2	0.82	26.6	0.3	26.2	0.4	NA	NA	26.6	0.3
Spot 6	4294	94309	0.8	21.1324	0.6	0.0280	1.7	0.0043	1.6	0.93	27.6	0.4	28.0	0.5	64.4	15.3	27.6	0.4
Spot 7	4461	16602	0.5	20.2994	1.2	0.0295	1.7	0.0044	1.2	0.71	28.0	0.3	29.6	0.5	159.3	27.8	28.0	0.3

Table 21. Sample 17330A (continued).

Analysis	U (ppm)	$^{206}Pb/^{204}Pb$	U/Th	$^{206}Pb/^{207}Pb$	± (%)	$^{207}Pb/^{235}U$	± (%)	$^{206}Pb/^{238}U$	± (%)	error corr.	$^{206}Pb/^{238}U$	± (Ma)	$^{207}Pb/^{235}U$	± (Ma)	$^{206}Pb/^{207}Pb$	± (Ma)	Best age (Ma)	± (Ma)
					Isotope ratios													
												Apparent ages (Ma)						
Spot 31	4274	14783	0.5	20.4337	1.0	0.0295	1.3	0.0044	0.9	0.65	28.1	0.2	29.5	0.4	143.9	24.0	28.1	0.2
Spot 5	3652	6785	0.7	21.0141	0.9	0.0291	1.6	0.0044	1.3	0.81	28.5	0.4	29.1	0.5	77.7	22.0	28.5	0.4
Spot 4	3752	5727	0.4	20.8031	1.1	0.0294	2.0	0.0044	1.6	0.82	28.5	0.5	29.4	0.6	101.7	27.0	28.5	0.5
Spot 2	2478	6550	0.4	16.5311	3.9	0.0401	4.1	0.0048	1.1	0.28	31.0	0.4	40.0	1.6	620.3	85.0	31.0	0.4
Spot 18	14	2433	2.1	22.9220	4.4	0.1304	7.5	0.0217	6.0	0.80	138.3	8.2	124.5	8.7	NA	NA	138.3	8.2
Spot 17	5104	124746	3.2	18.5386	0.7	0.1718	3.2	0.0231	3.1	0.97	147.3	4.5	161.0	4.7	367.6	16.6	147.3	4.5
Spot 19	3476	43725	4.2	19.0755	0.9	0.2942	1.8	0.0407	1.5	0.86	257.3	3.9	261.9	4.1	302.9	20.4	257.3	3.9
Spot 25	116	4436	2.1	20.8288	3.8	0.2833	4.1	0.0428	1.5	0.38	270.3	4.1	253.3	9.1	98.7	89.2	270.3	4.1
Spot 24	78	4133	2.1	20.7656	3.7	0.2951	4.0	0.0445	1.5	0.39	280.5	4.2	262.6	9.2	105.9	86.8	280.5	4.2
Spot 16	2531	137412	1.2	19.7018	0.7	0.3147	1.4	0.0450	1.3	0.89	283.7	3.5	277.8	3.4	228.8	15.1	283.7	3.5
Spot 34	1183	91044	3.5	18.7173	0.9	0.3357	1.4	0.0456	1.1	0.77	287.4	3.1	293.9	3.6	346.0	20.3	287.4	3.1
Spot 26	413	4660	0.9	17.7548	2.6	0.3601	3.1	0.0464	1.7	0.56	292.3	4.9	312.3	8.4	464.2	57.2	292.3	4.9
Spot 35	1456	55842	3.1	19.4767	0.7	0.3331	1.6	0.0471	1.5	0.90	296.5	4.3	291.9	4.1	255.3	16.6	296.5	4.3
Spot 28	776	84777	3.7	18.4047	0.9	0.3668	1.5	0.0490	1.1	0.77	308.3	3.4	317.3	4.0	383.9	21.1	308.3	3.4
Spot 33	1209	205564	4.0	19.2838	0.9	0.3534	1.5	0.0494	1.2	0.82	311.1	3.8	307.3	4.0	278.1	19.7	311.1	3.8
Spot 27	143	2597	0.5	17.6314	1.2	0.4025	1.5	0.0515	1.0	0.63	323.7	3.0	343.4	4.4	479.6	26.1	323.7	3.0

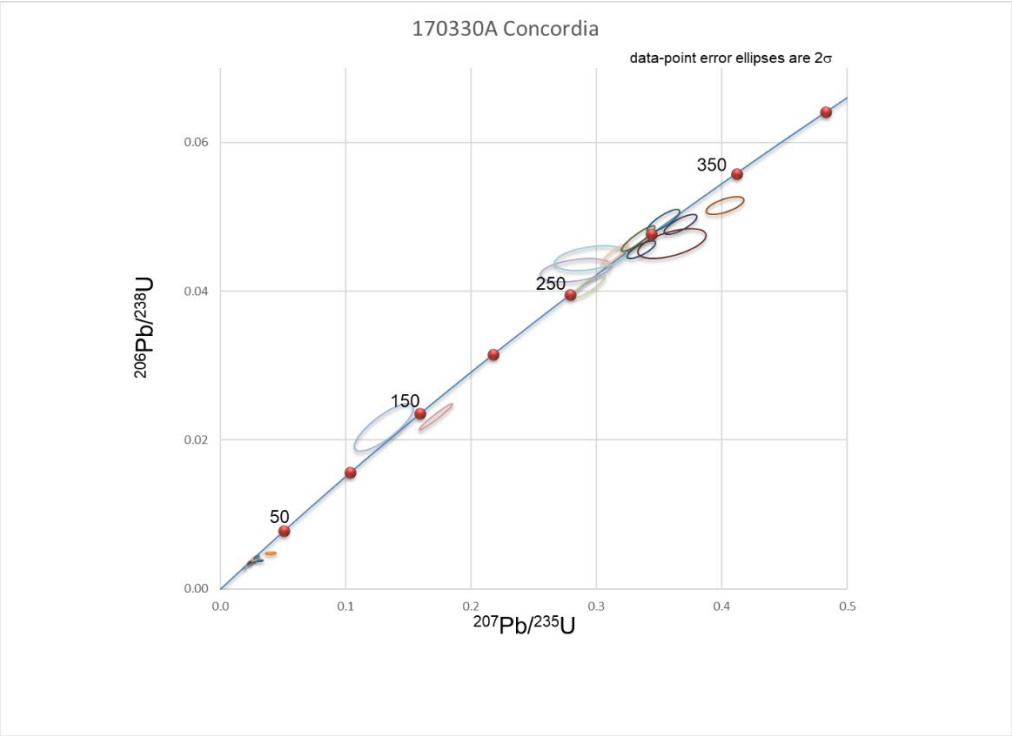

Figure 64. Concordia plot for sample 17330A

Table 22. U-Pb geochronology analysis data for sample 18622A, ordered by best age.

		Isotope ratios									Apparent ages (Ma)							
Analysis	U (ppm)	$^{206}Pb/^{204}Pb$	U/Th	$^{206}Pb/^{207}Pb$	± (%)	$^{207}Pb/^{235}U$	± (%)	$^{206}Pb/^{238}U$	± (%)	error corr.	$^{206}Pb/^{238}U$	± (Ma)	$^{207}Pb/^{235}U$	± (Ma)	$^{206}Pb/^{207}Pb$	± (Ma)	Best age (Ma)	± (Ma)
Spot 6 c	57	13383	0.8	13.6019	1.0	1.7926	1.5	0.1769	1.1	0.75	1050.1	10.8	1042.8	9.7	1027.4	20.0	1027.4	20.0
Spot 26	71	21611	0.8	13.5470	0.9	1.8494	1.4	0.1818	1.1	0.80	1076.7	11.4	1063.2	9.4	1035.6	17.2	1035.6	17.2
Spot 44	42	18842	1.0	13.5246	0.9	1.8647	1.3	0.1830	0.9	0.69	1083.3	8.9	1068.7	8.5	1038.9	18.7	1038.9	18.7
Spot 47	70	63154	0.8	13.5086	1.1	1.8754	1.5	0.1838	1.0	0.70	1087.8	10.4	1072.5	9.8	1041.3	21.3	1041.3	21.3
Spot 28	83	38103	1.3	13.5050	0.6	1.8533	1.3	0.1816	1.1	0.87	1075.8	11.3	1064.6	8.6	1041.8	12.8	1041.8	12.8
Spot 38 c	44	10526	0.9	13.5030	0.8	1.8519	1.3	0.1814	1.0	0.76	1074.9	9.7	1064.1	8.4	1042.1	16.7	1042.1	16.7
Spot 9 c	56	13969	0.7	13.4711	1.0	1.8365	1.6	0.1795	1.2	0.78	1064.3	12.1	1058.6	10.4	1047.0	20.2	1047.0	20.2
Spot 49	100	11516	1.5	13.4631	0.8	1.8563	1.3	0.1813	1.1	0.82	1074.3	10.7	1065.7	8.7	1048.1	15.4	1048.1	15.4
Spot 43 c	68	30775	0.7	13.4623	0.9	1.8272	1.6	0.1785	1.3	0.82	1058.7	12.6	1055.3	10.3	1048.3	18.1	1048.3	18.1
Spot 3	96	15625	0.9	13.4575	0.9	1.8533	1.5	0.1810	1.2	0.81	1072.3	12.2	1064.6	10.0	1049.0	17.9	1049.0	17.9
Spot 29	54	14781	1.0	13.4522	1.2	1.9071	1.6	0.1861	1.1	0.67	1100.5	11.0	1083.6	10.9	1049.8	24.5	1049.8	24.5
Spot 35	58	39224	0.7	13.4260	0.9	1.8417	1.3	0.1794	1.0	0.72	1063.7	9.4	1060.5	8.8	1053.7	18.7	1053.7	18.7
Spot 5	57	21300	0.9	13.4028	0.8	1.8699	1.4	0.1818	1.1	0.81	1077.0	11.2	1070.5	9.3	1057.2	16.8	1057.2	16.8
Spot 19	174	109948	0.7	13.3832	0.6	1.8964	1.3	0.1842	1.2	0.88	1089.6	11.6	1079.8	8.7	1060.1	12.6	1060.1	12.6
Spot 4	41	31832	1.1	13.3712	0.9	1.8377	1.4	0.1783	1.0	0.72	1057.6	9.6	1059.0	9.0	1061.9	19.0	1061.9	19.0
Spot 0	119	78852	1.4	13.3509	0.7	1.8717	1.2	0.1813	1.0	0.80	1074.2	9.9	1071.1	8.2	1065.0	15.0	1065.0	15.0
Spot 31	120	40543	1.3	13.3420	0.9	1.8618	1.4	0.1802	1.0	0.76	1068.3	10.3	1067.6	9.1	1066.3	18.0	1066.3	18.0
Spot 40 r	123	25483	1.2	13.3195	0.7	1.9155	1.4	0.1851	1.2	0.84	1094.9	11.6	1086.5	9.1	1069.7	14.7	1069.7	14.7
Spot 12 r	52	95739	1.2	13.3167	0.9	1.8362	1.3	0.1774	0.9	0.72	1052.8	9.1	1058.5	8.5	1070.2	18.0	1070.2	18.0
Spot 46 r	141	323872	1.0	13.2941	0.8	1.8060	1.1	0.1742	0.8	0.71	1035.2	7.3	1047.6	7.1	1073.6	15.4	1073.6	15.4

Table 22. Sample 18622A (continued).

Analysis	U (ppm)	$^{206}Pb/^{204}Pb$	U/Th	$^{206}Pb/^{207}Pb$	± (%)	$^{207}Pb/^{235}U$	± (%)	$^{206}Pb/^{238}U$	± (%)	error corr.	$^{206}Pb/^{238}U$	± (Ma)	$^{207}Pb/^{235}U$	± (Ma)	$^{206}Pb/^{207}Pb$	± (Ma)	Best age (Ma)	± (Ma)
					Isotope ratios							Apparent ages (Ma)						
Spot 39 c	181	92072	1.6	13.2854	1.0	1.8610	2.3	0.1794	2.1	0.89	1063.7	20.3	1067.3	15.2	1074.9	20.7	1074.9	20.7
Spot 34	68	30121	1.1	13.2422	0.8	1.8356	1.5	0.1764	1.3	0.85	1047.1	12.1	1058.3	9.7	1081.4	15.4	1081.4	15.4
Spot 23	136	44749	1.2	13.2415	0.7	1.8564	1.3	0.1784	1.0	0.81	1058.0	10.0	1065.7	8.3	1081.5	14.7	1081.5	14.7
Spot 13 r	139	27095	1.7	13.2023	0.9	1.8831	1.3	0.1804	0.9	0.71	1069.1	8.9	1075.2	8.4	1087.5	17.9	1087.5	17.9
Spot 11	81	75130	1.1	13.1970	0.6	1.8868	1.4	0.1807	1.2	0.89	1070.7	12.2	1076.5	9.3	1088.2	13.0	1088.2	13.0
Spot 30	235	976072	4.5	13.1607	0.8	1.9265	1.5	0.1840	1.3	0.84	1088.6	12.9	1090.3	10.3	1093.8	16.8	1093.8	16.8
Spot 20 r	159	245177	1.3	13.1577	0.8	1.9187	1.5	0.1832	1.2	0.84	1084.3	12.4	1087.6	9.9	1094.2	16.4	1094.2	16.4
Spot 27	80	62099	1.1	13.1393	0.9	1.8764	1.3	0.1789	0.9	0.71	1060.9	8.7	1072.8	8.4	1097.0	17.9	1097.0	17.9
Spot 21 r	129	51727	1.3	13.1385	0.6	1.8887	1.1	0.1801	1.0	0.84	1067.3	9.4	1077.1	7.6	1097.1	12.4	1097.1	12.4
Spot 16 r	77	28509	1.2	13.1300	1.0	1.8753	1.4	0.1787	1.0	0.72	1059.6	10.0	1072.4	9.4	1098.4	19.5	1098.4	19.5
Spot 48	322	77804	1.5	13.1277	0.9	1.8134	1.7	0.1727	1.4	0.84	1027.1	13.7	1050.3	11.2	1098.8	18.4	1098.8	18.4
Spot 17 r	109	23450	1.4	13.1239	0.7	1.9114	1.4	0.1820	1.2	0.88	1078.0	12.3	1085.1	9.4	1099.4	13.7	1099.4	13.7
Spot 10 c	79	151471	0.8	13.0908	0.9	1.8826	1.5	0.1788	1.1	0.78	1060.5	11.1	1075.0	9.6	1104.5	18.1	1104.5	18.1
Spot 33	123	69351	1.3	13.0823	0.8	1.8789	1.5	0.1784	1.2	0.84	1058.0	12.2	1073.7	9.9	1105.7	16.2	1105.7	16.2
Spot 15 c	158	47023	1.0	13.0558	0.6	1.9020	1.2	0.1802	1.0	0.86	1067.9	10.1	1081.8	8.0	1109.8	12.5	1109.8	12.5
Spot 7	118	63198	1.3	12.9871	0.9	1.9117	1.5	0.1801	1.2	0.81	1067.7	11.8	1085.2	9.9	1120.3	17.2	1120.3	17.2
Spot 45 r	137	60142	1.2	12.9350	0.7	1.8188	1.2	0.1707	1.0	0.82	1016.0	9.6	1052.2	8.1	1128.3	14.0	1128.3	14.0
Spot 36	71	33413	0.8	12.8340	0.9	1.9242	1.4	0.1792	1.1	0.78	1062.5	10.5	1089.5	9.2	1143.9	17.2	1143.9	17.2
Spot 1 c	57	23313	1.0	12.8222	1.0	1.9480	1.4	0.1812	1.0	0.68	1073.7	9.5	1097.8	9.5	1145.8	20.8	1145.8	20.8
Spot 18	401	35393	0.9	12.6282	0.8	1.8434	1.7	0.1689	1.5	0.87	1006.1	13.7	1061.1	11.0	1176.0	16.1	1176.0	16.1
Spot 32	110	19112	0.9	12.6034	0.9	1.8550	1.4	0.1696	1.1	0.80	1010.1	10.6	1065.2	9.4	1179.9	17.0	1179.9	17.0
Spot 22	137	163040	1.0	12.4117	0.8	1.8886	1.3	0.1701	1.0	0.79	1012.6	9.7	1077.1	8.7	1210.1	15.8	1210.1	15.8

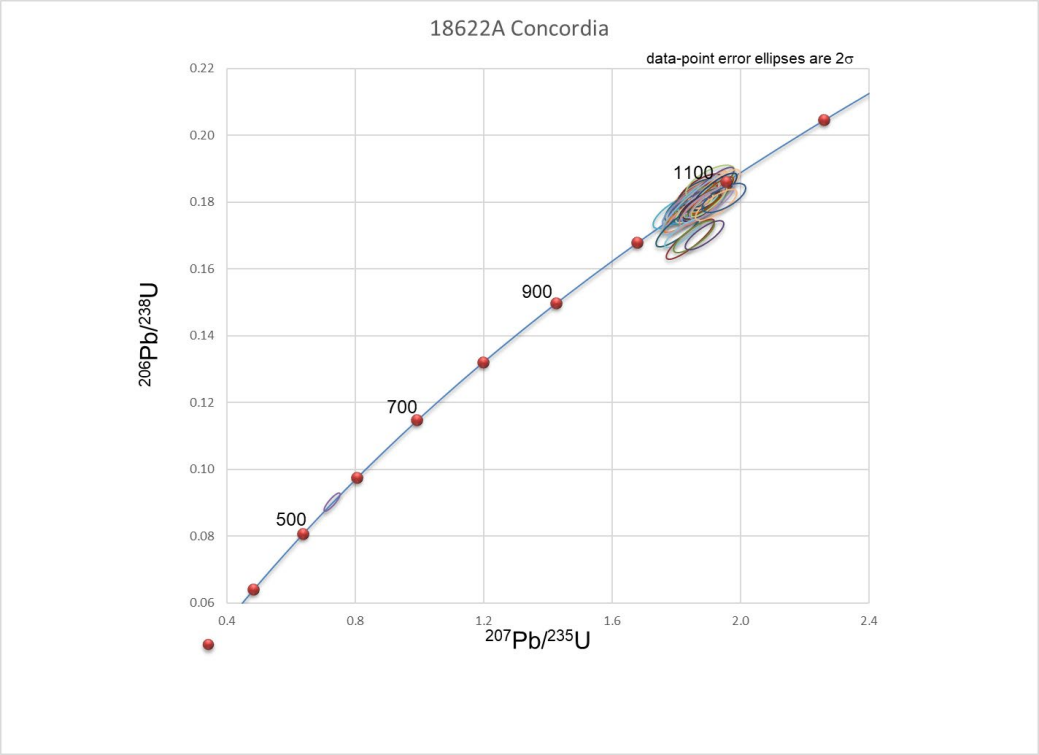

Figure 66. Concordia plot for sample 18622A

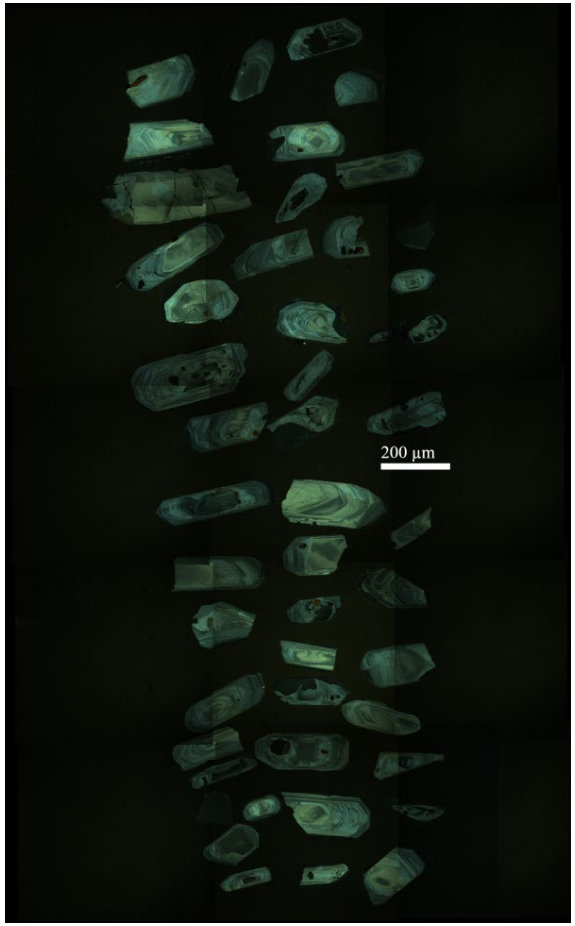

Figure 65. CL image for sample 18622A

Table 23. U-Pb geochronology analysis data for sample 18627A, ordered by best age.

				Isotope ratios							Apparent ages (Ma)							
Analysis	U	$^{206}Pb/^{204}Pb$	U/Th	$^{206}Pb/^{207}Pb$	±	$^{207}Pb/^{235}U$	±	$^{206}Pb/^{238}U$	±	error	$^{206}Pb/^{238}U$	±	$^{207}Pb/^{235}U$	±	$^{206}Pb/^{207}Pb$	±	Best age	±
	(ppm)				(%)		(%)		(%)	corr.		(Ma)		(Ma)		(Ma)	(Ma)	(Ma)
Spot 19	1163	30408	4.0	18.5705	0.8	0.2738	1.5	0.0369	1.2	0.84	233.5	2.8	245.7	3.2	363.7	18.2	233.5	2.8
Spot 5	1370	3472	3.7	12.6927	1.1	0.4157	1.8	0.0383	1.5	0.81	242.2	3.5	353.0	5.4	1165.9	21.3	242.2	3.5
Spot 23	758	7929	2.1	15.4435	2.3	0.3448	2.6	0.0386	1.3	0.49	244.4	3.1	300.8	6.9	765.4	48.6	244.4	3.1
Spot 13	1700	2342	3.3	10.7190	0.8	0.5017	1.9	0.0390	1.7	0.90	246.7	4.1	412.8	6.4	1493.0	15.8	246.7	4.1
Spot 0	929	3043	5.0	12.2814	4.9	0.4413	5.1	0.0393	1.5	0.28	248.7	3.5	371.2	15.8	1230.9	95.9	248.7	3.5
Spot 4	725	1627	5.0	9.0305	1.2	0.6111	1.9	0.0400	1.5	0.77	253.1	3.7	484.3	7.4	1810.7	22.5	253.1	3.7
Spot 2	704	3368	4.4	12.2058	1.8	0.4535	2.2	0.0402	1.2	0.57	253.8	3.1	379.7	6.9	1243.0	35.3	253.8	3.1
Spot 3	785	908	3.1	6.4216	1.2	0.9028	1.9	0.0421	1.5	0.78	265.6	3.8	653.2	9.1	2409.0	20.2	265.6	3.8
Spot 20	1249	833	2.8	5.5880	1.8	1.0731	2.3	0.0435	1.4	0.62	274.6	3.8	740.3	11.9	2642.5	29.4	274.6	3.8
Spot 9	1423	771	3.4	5.4812	1.1	1.0977	1.7	0.0437	1.3	0.76	275.4	3.5	752.2	9.3	2674.5	18.9	275.4	3.5
Spot 10	1086	640	2.2	4.7050	0.7	1.3693	1.5	0.0467	1.3	0.86	294.5	3.7	875.9	8.7	2924.3	12.1	294.5	3.7
Spot 15	1345	572	2.2	4.4589	2.5	1.4497	3.0	0.0469	1.7	0.55	295.5	4.8	909.7	18.3	3010.9	40.8	295.5	4.8
Spot 24	692	451	3.2	3.4292	3.4	2.1410	3.9	0.0533	2.0	0.51	334.6	6.5	1162.2	27.0	3425.5	52.3	334.6	6.5
Spot 16	144	15946	2.4	17.1520	1.2	0.7114	1.7	0.0885	1.2	0.71	546.9	6.2	545.6	7.0	540.2	25.6	546.9	6.2
Spot 6 r	146	133990	2.8	12.7828	0.8	2.2204	1.5	0.2059	1.3	0.85	1207.2	13.9	1187.5	10.3	1151.8	15.2	1151.8	15.2
Spot 21	55	11920	2.3	12.7709	1.4	2.0964	1.9	0.1943	1.3	0.68	1144.4	13.9	1147.6	13.4	1153.7	28.2	1153.7	28.2
Spot 8	39	24438	2.0	12.7329	1.2	2.0907	1.7	0.1932	1.3	0.74	1138.5	13.3	1145.8	11.8	1159.6	23.1	1159.6	23.1
Spot 17 c	69	50654	1.8	12.6800	0.9	2.1112	1.5	0.1942	1.2	0.81	1144.3	12.5	1152.5	10.1	1167.8	16.9	1167.8	16.9
Spot 14 c	106	24460	1.8	12.6136	0.9	2.1710	1.5	0.1987	1.2	0.80	1168.3	12.6	1171.8	10.2	1178.3	17.5	1178.3	17.5
Spot 12	78	32206	1.9	12.5192	1.0	2.2239	1.6	0.2020	1.3	0.80	1186.1	13.9	1188.6	11.2	1193.1	19.0	1193.1	19.0
Spot 22 r	224	14758	4.8	12.1868	1.0	2.1206	1.6	0.1875	1.2	0.79	1107.9	12.7	1155.5	10.9	1246.0	18.9	1246.0	18.9

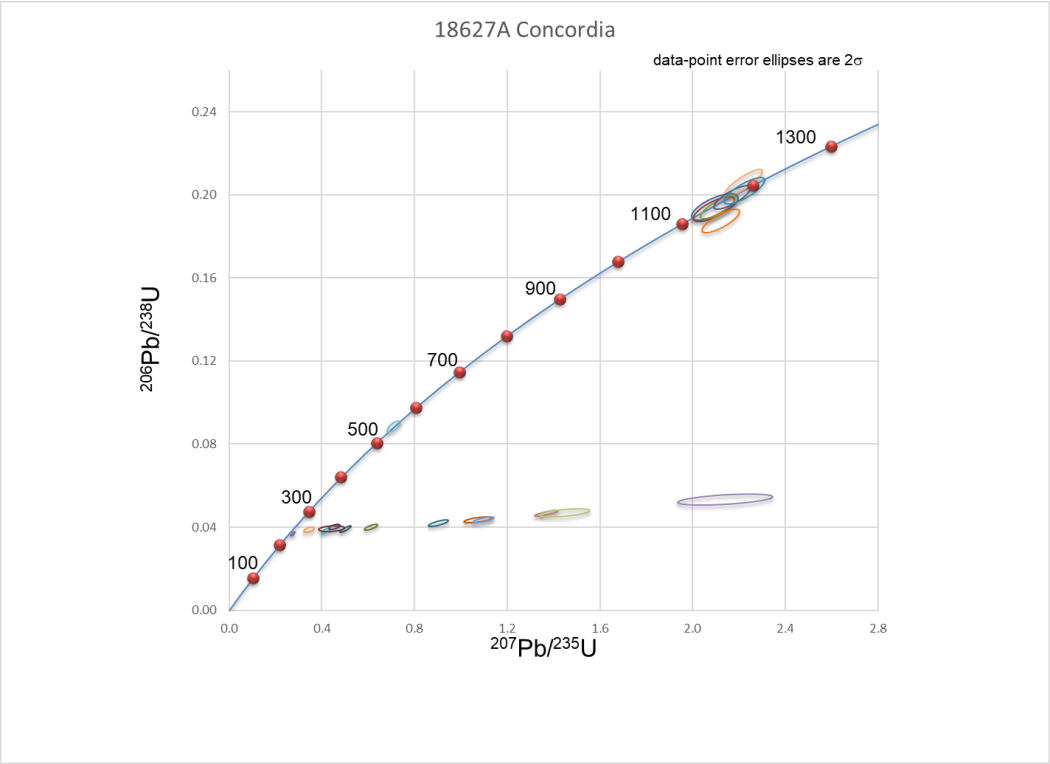

Figure 67. Concordia plot for sample 18627A

Table 24. U-Pb geochronology analysis data for sample 18628A, ordered by best age.

				Isotope ratios							Apparent ages (Ma)							
Analysis	U	$^{206}Pb/^{204}Pb$	U/Th	$^{206}Pb/^{207}Pb$	±	$^{207}Pb/^{235}U$	±	$^{206}Pb/^{238}U$	±	error	$^{206}Pb/^{238}U$	±	$^{207}Pb/^{235}U$	±	$^{206}Pb/^{207}Pb$	±	Best age	±
	(ppm)				(%)		(%)		(%)	corr.		(Ma)		(Ma)		(Ma)	(Ma)	(Ma)
Spot 19	135	30284	1.6	19.4453	1.3	0.2666	1.7	0.0376	1.1	0.66	238.0	2.6	239.9	3.6	259.0	29.1	238.0	2.6
Spot 25 r	121	20846	2.3	19.4759	1.3	0.2670	1.6	0.0377	1.0	0.60	238.7	2.2	240.3	3.4	255.3	29.8	238.7	2.2
Spot 16 r	93	3286	2.3	21.3329	1.8	0.2440	2.1	0.0378	1.1	0.52	239.0	2.6	221.7	4.2	41.8	43.5	239.0	2.6
Spot 23	132	5495	1.6	20.4380	3.1	0.2564	3.3	0.0380	1.1	0.32	240.6	2.5	231.8	6.8	143.4	72.7	240.6	2.5
Spot 29	77	17887	2.1	19.9560	2.0	0.2639	2.3	0.0382	1.1	0.49	241.7	2.7	237.8	4.8	199.1	45.9	241.7	2.7
Spot 7 r	108	12612	2.4	19.3194	1.6	0.2734	2.2	0.0383	1.4	0.65	242.4	3.4	245.4	4.7	273.9	37.3	242.4	3.4
Spot 13 r	144	9941	2.3	19.5221	1.3	0.2706	2.0	0.0383	1.4	0.74	242.5	3.4	243.2	4.2	249.9	30.3	242.5	3.4
Spot 27	136	42894	1.7	18.9839	1.3	0.2784	1.7	0.0383	1.1	0.64	242.6	2.5	249.4	3.7	313.9	28.9	242.6	2.5
Spot 9 c	109	11481	1.8	19.8728	1.9	0.2661	2.4	0.0384	1.3	0.57	242.7	3.2	239.5	5.0	208.8	45.0	242.7	3.2
Spot 151	78	37657	2.2	19.5183	1.5	0.2716	1.9	0.0385	1.2	0.65	243.3	2.9	244.0	4.1	250.3	33.4	243.3	2.9
Spot 22 c	134	10283	1.6	18.8764	1.7	0.2814	2.0	0.0385	1.1	0.54	243.8	2.5	251.7	4.4	326.8	37.7	243.8	2.5
Spot 150	143	50472	1.5	19.1275	1.3	0.2780	1.5	0.0386	0.9	0.57	244.0	2.1	249.1	3.4	296.7	28.9	244.0	2.1
Spot 8	143	8463	1.6	19.9456	1.1	0.2667	1.5	0.0386	1.0	0.65	244.1	2.3	240.0	3.2	200.3	26.0	244.1	2.3
Spot 14	87	244819	2.2	18.7831	1.9	0.2832	2.2	0.0386	1.2	0.52	244.1	2.8	253.2	5.0	338.0	43.2	244.1	2.8
Spot 149	97	4140	1.8	20.7289	1.5	0.2567	1.9	0.0386	1.2	0.62	244.2	2.8	232.0	3.9	110.1	35.2	244.2	2.8
Spot 28	153	32384	1.6	19.5985	1.3	0.2715	1.8	0.0386	1.3	0.72	244.2	3.1	243.9	3.9	240.9	29.2	244.2	3.1
Spot 30	104	27240	2.0	19.9536	1.5	0.2668	1.9	0.0386	1.2	0.63	244.3	2.9	240.1	4.1	199.4	34.2	244.3	2.9
Spot 3 c	185	24127	1.6	19.8692	1.2	0.2683	1.6	0.0387	1.0	0.66	244.7	2.5	241.4	3.4	209.2	27.6	244.7	2.5
Spot 11	126	6049	2.0	20.0004	1.8	0.2669	2.1	0.0387	1.1	0.52	245.0	2.7	240.2	4.5	194.0	42.1	245.0	2.7

Table 24. Sample 18628A (continued).

Analysis	U	$^{206}Pb/^{204}Pb$	U/Th	$^{206}Pb/^{207}Pb$	±	$^{207}Pb/^{235}U$	±	$^{206}Pb/^{238}U$	±	error	$^{206}Pb/^{238}U$	±	$^{207}Pb/^{235}U$	±	$^{206}Pb/^{207}Pb$	±	Best age	±
	(ppm)				(%)		(%)		(%)	corr.		(Ma)		(Ma)		(Ma)	(Ma)	(Ma)
Spot 21	95	7658	2.1	19.0304	2.0	0.2811	2.3	0.0388	1.2	0.53	245.5	3.0	251.5	5.2	308.3	45.1	245.5	3.0
Spot 147	110	11512	2.1	19.8107	1.3	0.2702	1.6	0.0388	1.0	0.63	245.6	2.5	242.8	3.5	216.0	29.5	245.6	2.5
Spot 24	135	20336	1.6	19.5985	1.1	0.2740	1.6	0.0390	1.2	0.73	246.4	2.8	245.9	3.4	240.9	24.7	246.4	2.8
Spot 15 r	50	60611	1.8	19.2538	1.8	0.2789	2.4	0.0390	1.6	0.66	246.4	3.7	249.8	5.2	281.7	40.6	246.4	3.7
Spot 2 c	133	18939	1.6	19.7281	1.4	0.2725	1.8	0.0390	1.1	0.60	246.7	2.6	244.7	3.9	225.7	33.1	246.7	2.6
Spot 5	182	18912	1.6	19.4776	1.1	0.2770	1.7	0.0392	1.3	0.76	247.6	3.1	248.3	3.7	255.2	25.3	247.6	3.1
Spot 20	139	10332	1.6	20.3184	1.4	0.2672	1.8	0.0394	1.1	0.64	249.1	2.8	240.4	3.8	157.1	31.9	249.1	2.8
Spot 1 r	96	19938	2.4	20.0472	1.4	0.2709	1.8	0.0394	1.1	0.63	249.1	2.7	243.4	3.8	188.5	32.1	249.1	2.7
Spot 6 c	93	14184	1.8	19.7561	1.3	0.2754	1.8	0.0395	1.3	0.70	249.6	3.1	247.0	4.0	222.4	30.5	249.6	3.1
Spot 148	133	42491	1.6	19.7849	1.4	0.2793	1.8	0.0401	1.0	0.59	253.4	2.6	250.1	3.9	219.1	33.1	253.4	2.6
Spot 10 c	81	21359	2.4	19.3173	1.4	0.2861	1.7	0.0401	1.0	0.60	253.4	2.5	255.5	3.8	274.1	31.2	253.4	2.5

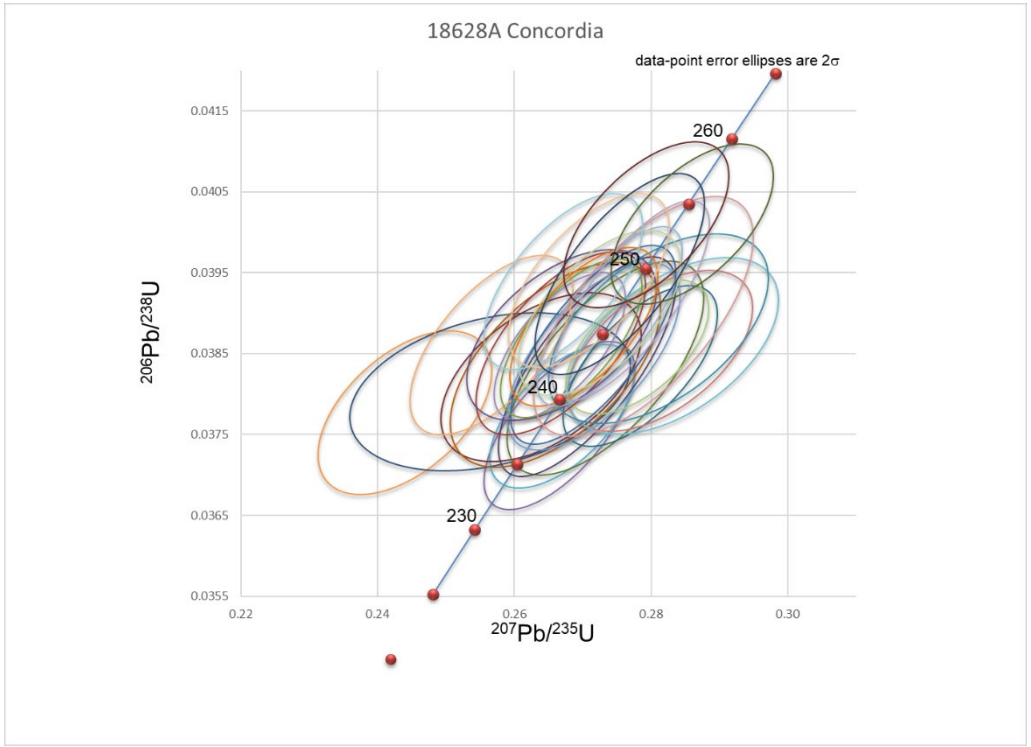

Figure 69. Concordia plot for sample 18628A

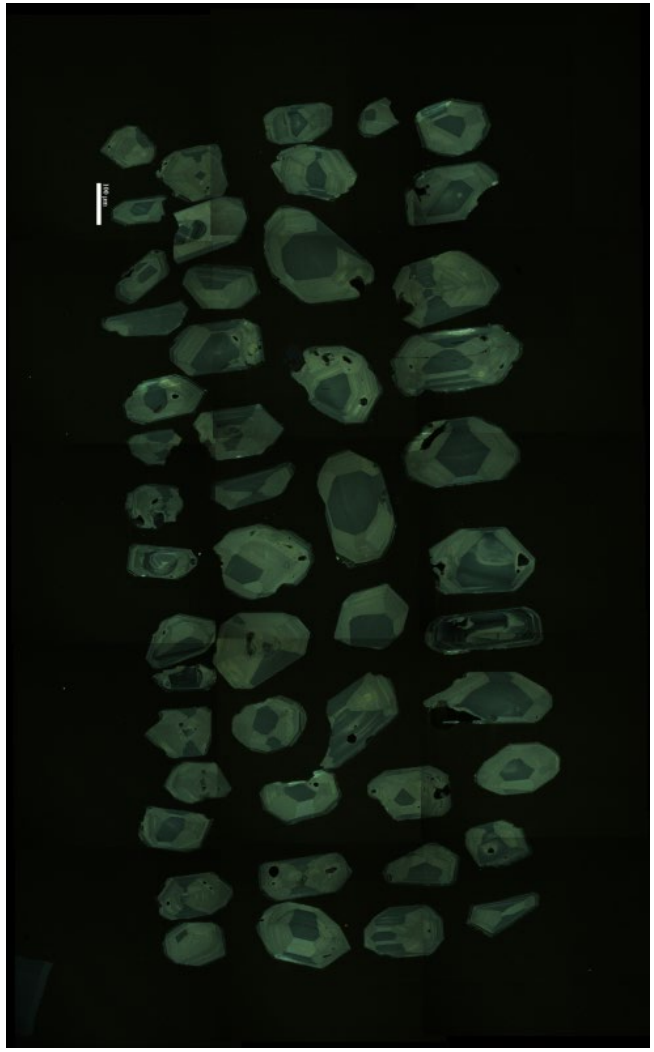

Figure 68. CL image for sample 18628A

Table 25. U-Pb geochronology analysis data for sample 18701A, ordered by best age.

		Isotope ratios									Apparent ages (Ma)							
Analysis	U (ppm)	$^{206}Pb/^{204}Pb$	U/Th	$^{206}Pb/^{207}Pb$	± (%)	$^{207}Pb/^{235}U$	± (%)	$^{206}Pb/^{238}U$	± (%)	error corr.	$^{206}Pb/^{238}U$	± (Ma)	$^{207}Pb/^{235}U$	± (Ma)	$^{206}Pb/^{207}Pb$	± (Ma)	Best age (Ma)	± (Ma)
Spot 0	150	10973	3.1	18.5530	1.0	0.4898	1.5	0.0659	1.1	0.76	411.6	4.4	404.7	4.9	365.9	21.5	411.6	4.4
Spot 5	75	11504	1.0	18.1767	1.2	0.5439	1.6	0.0717	1.1	0.69	446.6	4.9	441.0	5.8	411.9	26.1	446.6	4.9
Spot 39	191	18677	1.3	17.8392	1.1	0.5593	1.8	0.0724	1.4	0.79	450.6	6.1	451.1	6.5	453.7	24.2	450.6	6.1
Spot 31	160	15892	1.4	17.9310	1.2	0.5572	1.7	0.0725	1.2	0.72	451.2	5.3	449.7	6.2	442.2	26.3	451.2	5.3
Spot 43	113	17086	1.0	17.7282	1.4	0.5642	1.9	0.0726	1.4	0.72	451.7	6.1	454.3	7.1	467.5	30.0	451.7	6.1
Spot 38	131	83482	1.8	17.6935	1.0	0.5691	1.5	0.0731	1.1	0.75	454.6	4.8	457.5	5.4	471.8	21.5	454.6	4.8
Spot 45	181	14425	1.0	18.3084	1.2	0.5500	1.7	0.0731	1.3	0.72	454.6	5.5	445.0	6.3	395.7	27.0	454.6	5.5
Spot 34	131	58028	1.0	17.5982	1.0	0.5730	1.6	0.0732	1.3	0.79	455.2	5.6	460.0	6.0	483.8	21.9	455.2	5.6
Spot 42	209	70524	1.1	17.6322	0.8	0.5741	1.5	0.0734	1.2	0.82	456.9	5.3	460.6	5.4	479.5	18.4	456.9	5.3
Spot 26	145	70467	1.1	17.8554	1.0	0.5678	1.5	0.0736	1.0	0.70	457.6	4.5	456.6	5.4	451.6	23.3	457.6	4.5
Spot 21	393	100642	1.5	17.5229	0.7	0.5798	1.6	0.0737	1.5	0.91	458.5	6.5	464.4	6.0	493.2	14.6	458.5	6.5
Spot 3	121	114345	1.4	17.6534	1.2	0.5758	1.7	0.0738	1.2	0.71	458.7	5.3	461.8	6.3	476.8	26.2	458.7	5.3
Spot 33	286	86710	1.1	17.8017	0.9	0.5713	2.0	0.0738	1.8	0.88	459.0	7.8	458.9	7.4	458.3	20.9	459.0	7.8
Spot 44	161	24133	1.3	17.9630	1.0	0.5662	1.5	0.0738	1.1	0.74	459.0	4.9	455.6	5.5	438.2	22.3	459.0	4.9
Spot 14r	261	45250	1.7	17.6462	1.0	0.5765	1.7	0.0738	1.3	0.79	459.1	5.9	462.2	6.2	477.7	23.0	459.1	5.9
Spot 24	203	22858	1.2	17.9713	0.9	0.5664	1.5	0.0739	1.1	0.78	459.3	5.1	455.7	5.4	437.2	20.2	459.3	5.1
Spot 40	132	16255	1.1	18.1198	1.0	0.5618	1.7	0.0739	1.4	0.81	459.4	6.0	452.7	6.1	418.9	22.2	459.4	6.0
Spot 19	188	27182	1.4	17.4905	1.1	0.5830	1.9	0.0740	1.6	0.82	460.1	7.0	466.4	7.1	497.3	24.0	460.1	7.0
Spot 46	154	37751	1.2	17.6147	1.0	0.5789	1.6	0.0740	1.3	0.79	460.1	5.7	463.7	6.0	481.7	22.0	460.1	5.7
Spot 48c	210	46175	0.9	17.7066	0.9	0.5770	1.6	0.0741	1.3	0.80	461.0	5.6	462.5	5.9	470.2	21.0	461.0	5.6
Spot 28	375	697593	1.6	17.8339	0.8	0.5730	1.9	0.0742	1.7	0.89	461.1	7.5	460.0	6.9	454.3	18.7	461.1	7.5
Spot 12	111	34790	1.4	17.4880	1.0	0.5847	1.5	0.0742	1.1	0.75	461.3	4.9	467.4	5.5	497.6	21.4	461.3	4.9

Table 25. Sample 18701A (continued).

		Isotope ratios									Apparent ages (Ma)							
Analysis	U (ppm)	$^{206}Pb/^{204}Pb$	U/Th	$^{206}Pb/^{207}Pb$	± (%)	$^{207}Pb/^{235}U$	± (%)	$^{206}Pb/^{238}U$	± (%)	error corr.	$^{206}Pb/^{238}U$	± (Ma)	$^{207}Pb/^{235}U$	± (Ma)	$^{206}Pb/^{207}Pb$	± (Ma)	Best age (Ma)	± (Ma)
Spot 29	126	41719	1.0	17.5359	1.0	0.5836	1.6	0.0743	1.2	0.77	461.7	5.4	466.8	5.9	491.6	22.3	461.7	5.4
Spot 13c	197	413475	1.9	17.6629	1.0	0.5821	1.5	0.0746	1.1	0.75	463.8	5.0	465.8	5.6	475.6	21.7	463.8	5.0
Spot 18r	439	1077754	2.1	17.7974	1.0	0.5783	1.8	0.0747	1.5	0.85	464.3	6.8	463.4	6.7	458.8	21.1	464.3	6.8
Spot 27	141	12919	1.3	17.7761	1.0	0.5795	1.5	0.0747	1.1	0.74	464.7	5.1	464.2	5.8	461.5	23.0	464.7	5.1
Spot 8	389	235389	1.0	17.3147	0.9	0.5958	1.9	0.0749	1.7	0.88	465.4	7.6	474.6	7.3	519.5	19.9	465.4	7.6
Spot 41	182	53342	1.2	17.6625	1.0	0.5847	1.5	0.0749	1.1	0.74	465.8	4.9	467.5	5.5	475.7	21.9	465.8	4.9
Spot 25	205	187728	1.2	17.6912	1.0	0.5840	1.5	0.0750	1.2	0.78	466.0	5.3	467.0	5.7	472.1	21.2	466.0	5.3
Spot 16	120	17709	1.3	17.7330	1.3	0.5835	1.7	0.0751	1.1	0.63	466.7	4.8	466.7	6.3	466.9	29.2	466.7	4.8
Spot 6r5	401	73352	1.7	17.9354	0.9	0.5773	2.0	0.0751	1.8	0.90	467.0	8.1	462.7	7.4	441.7	19.1	467.0	8.1
Spot 17	177	12170	1.3	18.1784	1.0	0.5699	1.6	0.0752	1.2	0.77	467.2	5.6	457.9	5.9	411.7	22.8	467.2	5.6
Spot 23r	70	35855	1.7	17.4621	1.2	0.5942	1.7	0.0753	1.2	0.70	467.9	5.4	473.6	6.5	500.9	26.7	467.9	5.4
Spot 11c	118	68000	2.4	17.8036	1.1	0.5836	1.4	0.0754	0.9	0.63	468.6	4.0	466.8	5.2	458.1	24.1	468.6	4.0
Spot 32	170	17045	1.1	17.8851	0.9	0.5819	1.7	0.0755	1.4	0.82	469.3	6.1	465.7	6.2	447.9	21.0	469.3	6.1
Spot 2	105	22787	1.7	18.0609	1.2	0.5798	1.5	0.0760	1.0	0.64	472.1	4.4	464.3	5.6	426.1	26.0	472.1	4.4
Spot 47	207	50521	1.0	17.7338	1.1	0.5921	1.7	0.0762	1.3	0.76	473.4	5.8	472.2	6.4	466.8	24.5	473.4	5.8
Spot 20r	232	13260	1.8	18.0476	0.9	0.5821	1.8	0.0762	1.5	0.84	473.6	6.8	465.8	6.6	427.8	21.2	473.6	6.8
Spot 4	96	15164	1.8	17.8968	1.3	0.5873	1.7	0.0763	1.1	0.66	473.8	5.0	469.1	6.3	446.5	28.2	473.8	5.0
Spot 7	72	9078	1.4	18.2747	1.3	0.5787	1.6	0.0767	1.0	0.64	476.6	4.8	463.6	6.1	399.8	28.2	476.6	4.8
Spot 35	121	17399	1.5	18.2468	1.4	0.5802	1.6	0.0768	0.7	0.48	477.1	3.4	464.6	5.8	403.2	30.5	477.1	3.4
Spot 9	450	55190	1.4	17.8220	0.9	0.5943	1.7	0.0769	1.5	0.86	477.3	6.9	473.6	6.6	455.8	19.9	477.3	6.9
Spot 22	122	22368	1.7	17.7789	1.3	0.5965	1.8	0.0770	1.2	0.66	477.9	5.4	475.0	6.7	461.1	29.1	477.9	5.4
Spot 1r2	105	97646	1.6	17.7366	1.1	0.5987	1.6	0.0771	1.2	0.72	478.5	5.4	476.4	6.2	466.4	25.0	478.5	5.4
Spot 37	139	19015	1.4	17.7324	1.0	0.5992	1.5	0.0771	1.2	0.75	478.8	5.4	476.7	5.9	466.9	22.5	478.8	5.4
Spot 15c	368	75232	1.3	17.5897	1.0	0.6055	2.0	0.0773	1.7	0.87	479.9	7.9	480.7	7.5	484.8	21.3	479.9	7.9
Spot 36	132	84075	1.6	16.9739	1.2	0.6303	2.0	0.0776	1.5	0.79	481.9	7.2	496.3	7.7	562.9	26.3	481.9	7.2
Spot 49	50	3007	1.8	16.5233	4.0	0.6484	4.2	0.0777	1.2	0.28	482.6	5.4	507.5	16.7	621.3	86.8	482.6	5.4
Spot 10c	121	33959	1.5	8.8457	0.8	5.1434	1.6	0.3301	1.4	0.87	1839.0	21.9	1843.3	13.4	1848.2	14.0	1848.2	14.0

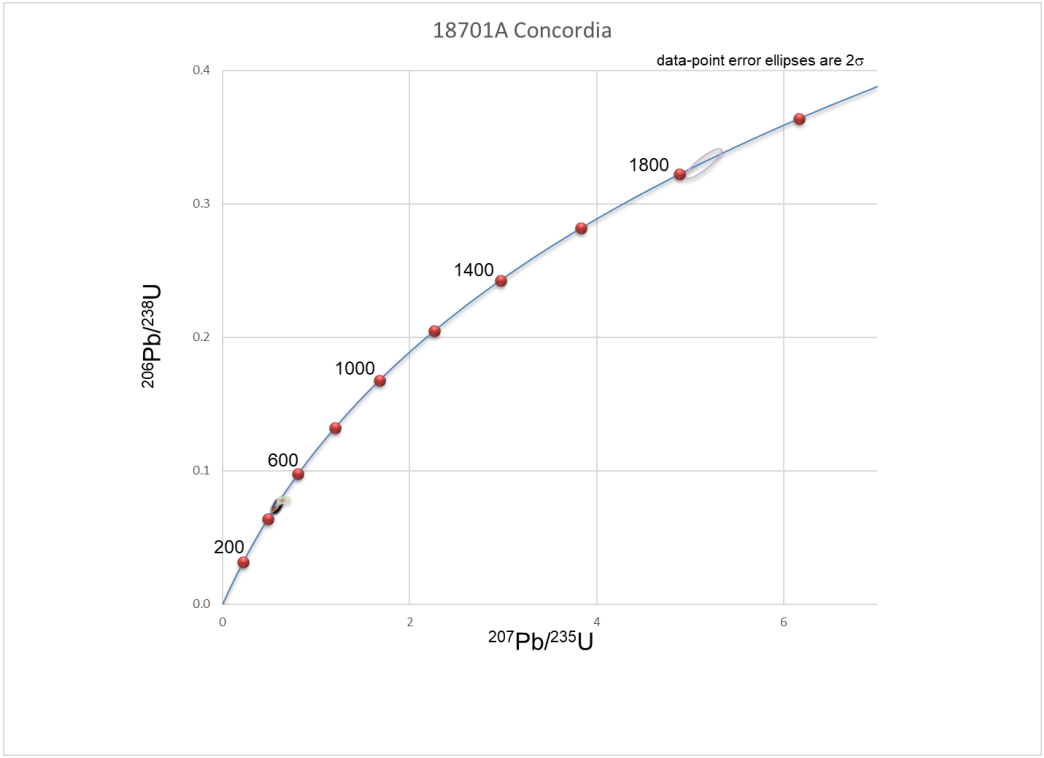

Figure 70. Concordia plot for sample 18701A

Figure 71. CL image for sample 18701A

Table 26. U-Pb geochronology analysis data for sample 18703A, ordered by best age.

		Isotope ratios									Apparent ages (Ma)							
Analysis	U (ppm)	$^{206}Pb/^{204}Pb$	U/Th	$^{206}Pb/^{207}Pb$	± (%)	$^{207}Pb/^{235}U$	± (%)	$^{206}Pb/^{238}U$	± (%)	error corr.	$^{206}Pb/^{238}U$	± (Ma)	$^{207}Pb/^{235}U$	± (Ma)	$^{206}Pb/^{207}Pb$	± (Ma)	Best age (Ma)	± (Ma)
Spot 47	102	39913	4.7	13.8051	1.0	1.6827	1.5	0.1685	1.1	0.75	1004.1	10.5	1002.0	9.7	997.3	20.6	997.3	20.6
Spot 21 r	137	53696	3.4	13.6445	0.8	1.6578	1.3	0.1641	1.0	0.76	979.7	8.7	992.5	8.0	1021.1	16.7	1021.1	16.7
Spot 23	100	49962	2.7	13.5698	0.9	1.7022	1.4	0.1676	1.1	0.77	998.9	10.3	1009.4	9.2	1032.2	18.4	1032.2	18.4
Spot 0 r	129	22878	2.4	13.5246	1.0	1.7788	1.4	0.1746	0.9	0.68	1037.2	8.9	1037.8	8.8	1038.9	20.1	1038.9	20.1
Spot 6 c	344	180055	8.3	13.3233	0.6	1.8249	1.6	0.1764	1.4	0.92	1047.4	13.8	1054.5	10.2	1069.2	12.0	1069.2	12.0
Spot 13 c	36	43359	2.6	13.3108	1.2	1.8662	1.7	0.1802	1.2	0.68	1068.3	11.4	1069.2	11.2	1071.0	24.9	1071.0	24.9
Spot 29 r	171	70676	4.0	13.2627	0.8	1.9677	1.4	0.1894	1.2	0.81	1117.9	12.0	1104.5	9.6	1078.3	16.7	1078.3	16.7
Spot 27 r	124	62226	2.3	13.2590	0.7	1.8356	1.2	0.1766	1.0	0.82	1048.4	9.9	1058.3	8.2	1078.9	14.4	1078.9	14.4
Spot 39 c	428	1240232	9.5	13.2560	0.7	1.8216	1.4	0.1752	1.2	0.86	1040.8	11.6	1053.3	9.2	1079.3	14.1	1079.3	14.1
Spot 10	22	6472	2.0	13.1893	1.8	1.9629	2.2	0.1878	1.3	0.59	1109.7	13.3	1102.9	14.9	1089.4	35.9	1089.4	35.9
Spot 36	79	16289	1.7	13.1819	0.8	1.9397	1.5	0.1855	1.3	0.86	1097.1	13.3	1094.9	10.3	1090.5	15.8	1090.5	15.8
Spot 38 r	240	238132	4.0	13.1776	0.6	1.8976	1.3	0.1814	1.1	0.89	1074.9	11.1	1080.3	8.3	1091.2	11.3	1091.2	11.3
Spot 14	257	60883	6.0	13.1770	0.8	1.8340	1.3	0.1753	1.1	0.80	1041.5	10.2	1057.7	8.6	1091.3	15.7	1091.3	15.7
Spot 19 r	166	74469	3.8	13.1138	0.8	1.9852	1.4	0.1889	1.2	0.81	1115.4	12.0	1110.5	9.7	1100.9	16.7	1100.9	16.7
Spot 48	90	50621	1.8	13.0711	0.8	2.0151	1.4	0.1911	1.2	0.82	1127.4	12.2	1120.6	9.8	1107.4	16.5	1107.4	16.5
Spot 11 c	469	72927	2.5	12.9992	0.6	1.8118	1.5	0.1709	1.4	0.91	1017.0	12.8	1049.7	9.9	1118.5	12.7	1118.5	12.7
Spot 20 c	56	43095	1.7	12.9717	0.9	1.9286	1.4	0.1815	1.1	0.79	1075.3	10.9	1091.0	9.3	1122.7	17.0	1122.7	17.0
Spot 5	53	36541	1.9	12.9520	0.9	2.0386	1.3	0.1916	1.0	0.73	1130.0	9.9	1128.5	8.9	1125.7	17.7	1125.7	17.7
Spot 22	77	12992	1.7	12.9437	0.9	2.1391	1.4	0.2009	1.1	0.78	1180.2	11.5	1161.5	9.5	1127.0	17.3	1127.0	17.3

Table 26. Sample 18703A (continued).

		Isotope ratios									Apparent ages (Ma)							
Analysis	U (ppm)	$^{206}Pb/^{204}Pb$	U/Th	$^{206}Pb/^{207}Pb$	± (%)	$^{207}Pb/^{235}U$	± (%)	$^{206}Pb/^{238}U$	± (%)	error corr.	$^{206}Pb/^{238}U$	± (Ma)	$^{207}Pb/^{235}U$	± (Ma)	$^{206}Pb/^{207}Pb$	± (Ma)	Best age (Ma)	± (Ma)
Spot 24	44	100446	1.4	12.9415	1.0	2.1021	1.5	0.1974	1.1	0.74	1161.3	12.1	1149.5	10.6	1127.3	20.7	1127.3	20.7
Spot 30 c	156	53425	7.3	12.9345	0.9	1.9142	1.8	0.1796	1.6	0.87	1065.1	15.4	1086.0	12.0	1128.4	17.6	1128.4	17.6
Spot 31 c	44	18705	1.8	12.9225	0.9	2.0754	1.6	0.1946	1.3	0.82	1146.2	13.7	1140.7	10.9	1130.2	18.4	1130.2	18.4
Spot 25	116	26976	1.5	12.9092	0.9	2.0263	1.4	0.1898	1.1	0.77	1120.3	10.9	1124.4	9.4	1132.3	17.5	1132.3	17.5
Spot 40	58	43199	1.7	12.9066	0.8	2.0566	1.3	0.1926	1.1	0.80	1135.4	11.1	1134.5	9.0	1132.7	15.6	1132.7	15.6
Spot 16	101	73624	2.4	12.8798	0.8	1.8017	1.4	0.1684	1.2	0.85	1003.2	11.2	1046.1	9.3	1136.8	15.2	1136.8	15.2
Spot 32	68	75775	1.6	12.8554	0.8	2.0477	1.4	0.1910	1.2	0.82	1126.8	12.1	1131.5	9.7	1140.6	16.2	1140.6	16.2
Spot 8 c	83	24070	1.3	12.8452	0.7	2.0589	1.1	0.1919	0.9	0.76	1131.6	8.9	1135.2	7.7	1142.2	14.6	1142.2	14.6
Spot 37	30	30069	1.8	12.8410	1.3	2.0866	1.9	0.1944	1.4	0.74	1145.2	14.8	1144.4	13.0	1142.8	25.1	1142.8	25.1
Spot 2	121	29455	1.9	12.7755	0.8	2.0621	1.5	0.1911	1.2	0.85	1127.6	12.9	1136.3	10.0	1153.0	15.1	1153.0	15.1
Spot 26	85	95094	1.2	12.7636	1.1	2.0936	1.6	0.1939	1.2	0.76	1142.4	12.8	1146.7	11.2	1154.8	21.1	1154.8	21.1
Spot 18 c	85	40345	1.5	12.7512	0.6	2.0660	1.2	0.1911	1.1	0.87	1127.6	10.9	1137.6	8.3	1156.8	11.8	1156.8	11.8
Spot 34	106	43587	1.4	12.7181	0.7	2.0603	1.3	0.1901	1.1	0.84	1122.1	11.3	1135.7	9.0	1161.9	14.4	1161.9	14.4
Spot 17	19	40776	2.3	12.7029	1.1	2.0194	1.8	0.1861	1.5	0.81	1100.4	15.0	1122.0	12.5	1164.3	21.6	1164.3	21.6
Spot 42 r	310	635877	6.1	12.6958	0.7	2.1282	1.4	0.1960	1.2	0.88	1154.0	12.8	1158.0	9.5	1165.4	13.0	1165.4	13.0
Spot 46	200	86843	5.1	12.6938	0.8	2.0981	1.4	0.1932	1.2	0.84	1138.9	12.1	1148.2	9.5	1165.7	15.1	1165.7	15.1
Spot 9 r	69	28994	2.4	12.6937	1.0	2.2237	1.8	0.2048	1.5	0.84	1201.1	16.6	1188.5	12.6	1165.7	19.5	1165.7	19.5
Spot 35	82	80101	1.4	12.6463	0.9	2.1404	1.3	0.1964	0.9	0.73	1156.0	9.7	1162.0	8.7	1173.2	17.0	1173.2	17.0
Spot 15	77	153461	1.9	12.5818	0.9	2.2006	1.3	0.2009	1.0	0.71	1180.1	10.4	1181.2	9.4	1183.3	18.6	1183.3	18.6
Spot 1 r	465	776742	2.6	12.5551	0.7	2.0810	1.6	0.1896	1.4	0.89	1119.0	14.9	1142.5	11.1	1187.5	14.2	1187.5	14.2
Spot 12	88	18360	1.3	12.3821	1.1	2.1480	1.5	0.1930	1.0	0.67	1137.5	10.5	1164.4	10.4	1214.8	21.8	1214.8	21.8
Spot 45	342	24285	2.1	12.2105	1.1	2.0790	1.9	0.1842	1.5	0.81	1089.8	15.5	1141.9	13.1	1242.2	22.0	1242.2	22.0
Spot 49 r	91	31649	1.7	12.1951	1.1	2.0880	1.4	0.1848	1.0	0.66	1092.9	9.6	1144.9	9.9	1244.7	21.2	1244.7	21.2
Spot 44	111	9481	0.6	11.5060	0.9	1.0790	4.6	0.0901	4.5	0.98	556.0	23.9	743.1	24.1	1357.7	16.6	1357.7	16.6
Spot 4 c	488	9552	1.6	11.3217	0.7	2.3494	1.5	0.1930	1.3	0.89	1137.6	13.5	1227.4	10.4	1388.7	12.5	1388.7	12.5

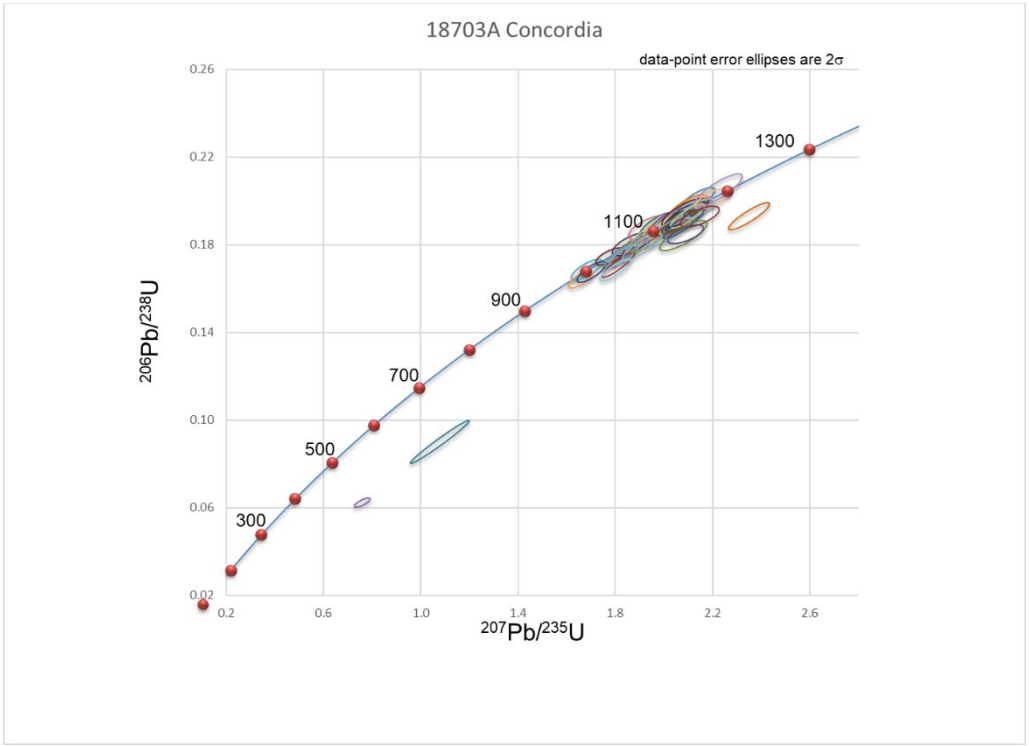

Figure 72. Concordia plot for sample 18703A

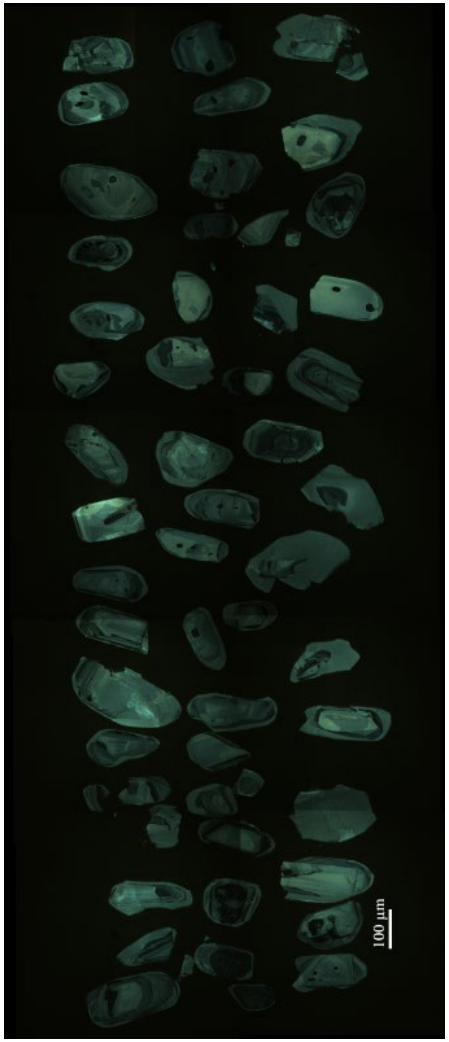

Figure 73. CL image for sample 18703A

Table 27. U-Pb DZ geochronology analysis data for sample A11-118A, ordered by best age.

		Isotope ratios									Apparent ages (Ma)							
Analysis	U (ppm)	$^{206}Pb/^{204}Pb$	U/Th	$^{206}Pb/^{207}Pb$	± (%)	$^{207}Pb/^{235}U$	± (%)	$^{206}Pb/^{238}U$	± (%)	error corr.	$^{206}Pb/^{238}U$	± (Ma)	$^{207}Pb/^{235}U$	± (Ma)	$^{206}Pb/^{207}Pb$	± (Ma)	Best age (Ma)	± (Ma)
#118	129	60	0.9	3.2620	8.1	0.0316	8.7	0.0007	3.4	0.38	4.8	0.2	31.6	2.7	3503.7	124.9	4.8	0.2
#161	122	60	0.8	3.6166	74.8	0.0288	74.9	0.0008	3.4	0.05	4.9	0.2	28.8	21.3	3343.3	NA	4.9	0.2
#109	119	60	0.9	3.2214	53.5	0.0331	53.6	0.0008	3.2	0.06	5.0	0.2	33.1	17.5	3523.0	NA	5.0	0.2
#140	369	60	1.1	3.2264	54.0	0.0332	54.0	0.0008	2.0	0.04	5.0	0.1	33.2	17.6	3520.6	NA	5.0	0.1
#147	252	60	0.6	3.4818	7.8	0.0310	8.3	0.0008	2.7	0.33	5.0	0.1	31.0	2.5	3402.5	122.1	5.0	0.1
#51	200	60	1.0	3.2589	5.5	0.0344	6.0	0.0008	2.4	0.40	5.2	0.1	34.4	2.0	3505.1	85.0	5.2	0.1
#19	184	60	0.6	4.8294	94.5	0.0233	94.6	0.0008	3.1	0.03	5.3	0.2	23.4	21.9	2882.7	NA	5.3	0.2
#193	468	255	0.8	94.6499	229.5	0.0015	229.5	0.0010	1.7	0.01	6.5	0.1	1.5	3.4	NA	NA	6.5	0.1
#178	384	327	0.6	67.2038	8.5	0.0021	8.7	0.0010	2.1	0.24	6.5	0.1	2.1	0.2	NA	NA	6.5	0.1
#43	716	5874	0.5	22.1289	3.8	0.0064	4.4	0.0010	2.3	0.51	6.6	0.2	6.5	0.3	NA	NA	6.6	0.2
#204	325	255	1.1	67.5027	86.7	0.0021	86.7	0.0010	2.0	0.02	6.7	0.1	2.2	1.9	NA	NA	6.7	0.1
#56	611	382	0.5	27.4484	55.2	0.0053	55.2	0.0011	1.8	0.03	6.8	0.1	5.3	2.9	NA	NA	6.8	0.1
#169	653	685	0.5	31.2091	7.5	0.0046	7.6	0.0011	1.5	0.20	6.8	0.1	4.7	0.4	NA	NA	6.8	0.1
#93	383	524	0.5	34.8554	51.3	0.0042	51.3	0.0011	2.5	0.05	6.8	0.2	4.2	2.2	NA	NA	6.8	0.2
#157	131	332	0.9	49.9618	13.4	0.0029	13.7	0.0011	2.9	0.21	6.8	0.2	3.0	0.4	NA	NA	6.8	0.2
#39	326	260	0.4	15.7103	18.2	0.0093	18.4	0.0011	2.4	0.13	6.8	0.2	9.4	1.7	730.1	389.3	6.8	0.2
#111	472	881	0.8	29.1798	6.0	0.0050	6.2	0.0011	1.8	0.28	6.9	0.1	5.1	0.3	NA	NA	6.9	0.1
#58	621	967	0.6	25.7491	6.1	0.0057	6.4	0.0011	2.1	0.32	6.9	0.1	5.8	0.4	NA	NA	6.9	0.1
#54	402	469	1.0	55.1119	39.4	0.0027	39.4	0.0011	2.1	0.05	6.9	0.1	2.7	1.1	NA	NA	6.9	0.1
#130	843	2953	0.6	22.7858	6.0	0.0065	6.2	0.0011	1.5	0.25	6.9	0.1	6.5	0.4	NA	NA	6.9	0.1
#55	419	1016	1.0	24.2147	5.7	0.0061	6.0	0.0011	2.0	0.33	6.9	0.1	6.2	0.4	NA	NA	6.9	0.1
#1	306	400	0.7	65.3328	27.4	0.0023	27.5	0.0011	2.8	0.10	6.9	0.2	2.3	0.6	NA	NA	6.9	0.2
#125	477	314	0.2	38.8883	23.1	0.0038	23.2	0.0011	1.6	0.07	6.9	0.1	3.9	0.9	NA	NA	6.9	0.1
#46	505	951	0.6	29.2841	23.7	0.0051	23.7	0.0011	1.7	0.07	7.0	0.1	5.2	1.2	NA	NA	7.0	0.1
#151	206	518	0.7	13.8854	16.5	0.0108	17.0	0.0011	3.8	0.22	7.0	0.3	10.9	1.8	986.4	338.9	7.0	0.3
#11	387	670	0.6	17.4685	20.8	0.0086	21.0	0.0011	2.3	0.11	7.0	0.2	8.7	1.8	501.0	463.1	7.0	0.2
#207	281	1029	0.6	9.4838	15.9	0.0160	16.1	0.0011	2.4	0.15	7.1	0.2	16.1	2.6	1722.0	293.7	7.1	0.2

Table 27. Sample A11-118A (continued).

				Isotope ratios							Apparent ages (Ma)							
Analysis	U (ppm)	$^{206}Pb/^{204}Pb$	U/Th	$^{206}Pb/^{207}Pb$	± (%)	$^{207}Pb/^{235}U$	± (%)	$^{206}Pb/^{238}U$	± (%)	error corr.	$^{206}Pb/^{238}U$	± (Ma)	$^{207}Pb/^{235}U$	± (Ma)	$^{206}Pb/^{207}Pb$	± (Ma)	Best age (Ma)	± (Ma)
#159	435	675	1.0	28.3279	8.1	0.0054	8.3	0.0011	1.7	0.20	7.1	0.1	5.4	0.4	NA	NA	7.1	0.1
#192	366	847	0.6	27.7273	12.4	0.0055	12.6	0.0011	2.3	0.19	7.1	0.2	5.6	0.7	NA	NA	7.1	0.2
#74	233	6423	0.6	11.9481	10.0	0.0128	10.3	0.0011	2.5	0.24	7.1	0.2	12.9	1.3	1285.5	195.0	7.1	0.2
#97	451	1196	0.6	26.9154	17.5	0.0058	17.7	0.0011	2.8	0.16	7.3	0.2	5.9	1.0	NA	NA	7.3	0.2
#81	284	2482	0.6	7.3718	13.5	0.0213	14.0	0.0011	3.9	0.27	7.4	0.3	21.4	3.0	2172.4	236.5	7.4	0.3
#106	192	1031	0.9	14.6847	14.3	0.0110	14.7	0.0012	3.5	0.24	7.6	0.3	11.1	1.6	871.5	297.9	7.6	0.3
#139	1055	856	0.2	8.0555	10.6	0.0201	11.0	0.0012	2.9	0.26	7.6	0.2	20.2	2.2	2016.5	189.2	7.6	0.2
#40	619	2388	1.1	21.3429	8.0	0.0078	8.3	0.0012	2.0	0.24	7.8	0.2	7.9	0.7	41.8	192.7	7.8	0.2
#183	379	711	0.5	9.3166	6.9	0.0179	7.3	0.0012	2.1	0.29	7.8	0.2	18.1	1.3	1754.7	127.3	7.8	0.2
#172	450	833	1.0	8.0213	18.1	0.0212	18.4	0.0012	3.3	0.18	7.9	0.3	21.3	3.9	2024.1	322.8	7.9	0.3
#30	738	518	0.4	6.3015	3.8	0.0270	4.2	0.0012	1.9	0.45	8.0	0.2	27.1	1.1	2441.8	63.9	8.0	0.2
#20	407	634	0.5	7.1396	19.6	0.0242	19.8	0.0013	2.7	0.14	8.1	0.2	24.3	4.7	2228.0	343.1	8.1	0.2
#122	779	2219	0.9	23.2427	4.0	0.0083	4.2	0.0014	1.3	0.32	9.0	0.1	8.4	0.3	NA	NA	9.0	0.1
#176	323	391	0.9	3.9524	42.9	0.0514	43.1	0.0015	3.9	0.09	9.5	0.4	50.9	21.4	3203.7	719.3	9.5	0.4
#78	430	3546	0.6	21.2434	5.0	0.0097	5.3	0.0015	1.7	0.32	9.6	0.2	9.8	0.5	53.0	119.0	9.6	0.2
#6	134	8292	0.6	4.0894	4.9	0.0517	6.8	0.0015	4.8	0.70	9.9	0.5	51.2	3.4	3149.7	77.7	9.9	0.5
#116	1154	11384	1.1	20.4385	3.1	0.0110	3.6	0.0016	1.8	0.51	10.5	0.2	11.1	0.4	144.3	72.0	10.5	0.2
#63	580	8383	0.6	17.1645	5.2	0.0136	5.6	0.0017	1.9	0.34	10.9	0.2	13.7	0.8	539.5	114.9	10.9	0.2
#146	217	4228	0.8	15.4723	6.6	0.0154	6.9	0.0017	2.0	0.29	11.1	0.2	15.5	1.1	762.4	138.5	11.1	0.2
#18	938	1687	1.0	24.6748	2.1	0.0138	2.5	0.0025	1.4	0.54	15.9	0.2	13.9	0.3	NA	NA	15.9	0.2
#105	646	4491	1.4	14.7834	4.3	0.0249	4.5	0.0027	1.5	0.34	17.2	0.3	25.0	1.1	857.6	89.0	17.2	0.3
#156	886	34502	1.1	21.1141	2.7	0.0183	3.1	0.0028	1.5	0.49	18.0	0.3	18.4	0.6	67.5	64.4	18.0	0.3
#23	871	5513	1.3	22.7910	2.7	0.0179	3.0	0.0030	1.4	0.46	19.0	0.3	18.0	0.5	NA	NA	19.0	0.3
#108	1614	20350	1.1	20.5854	2.2	0.0199	2.5	0.0030	1.1	0.44	19.1	0.2	20.0	0.5	127.5	51.8	19.1	0.2
#137	375	1459	0.8	22.7783	8.0	0.0185	8.2	0.0031	1.7	0.20	19.7	0.3	18.6	1.5	NA	NA	19.7	0.3
#179	872	3342	0.5	22.9907	3.1	0.0188	3.3	0.0031	1.2	0.35	20.1	0.2	18.9	0.6	NA	NA	20.1	0.2
#79	509	2136	1.0	22.2016	4.8	0.0194	5.0	0.0031	1.4	0.28	20.2	0.3	19.5	1.0	NA	NA	20.2	0.3

Table 27. Sample A11-118A (continued).

		Isotope ratios									Apparent ages (Ma)							
Analysis	U (ppm)	$^{206}Pb/^{204}Pb$	U/Th	$^{206}Pb/^{207}Pb$	± (%)	$^{207}Pb/^{235}U$	± (%)	$^{206}Pb/^{238}U$	± (%)	error corr.	$^{206}Pb/^{238}U$	± (Ma)	$^{207}Pb/^{235}U$	± (Ma)	$^{206}Pb/^{207}Pb$	± (Ma)	Best age (Ma)	± (Ma)
#83	507	1986	0.8	23.9614	3.0	0.0181	3.1	0.0031	1.0	0.33	20.2	0.2	18.2	0.6	NA	NA	20.2	0.2
#150	343	2054	0.7	23.3838	3.7	0.0186	4.0	0.0032	1.6	0.39	20.3	0.3	18.7	0.7	NA	NA	20.3	0.3
#197	468	1931	1.0	23.6726	3.5	0.0184	3.8	0.0032	1.3	0.36	20.4	0.3	18.5	0.7	NA	NA	20.4	0.3
#168	683	1751	0.5	25.3383	6.4	0.0172	6.5	0.0032	1.4	0.21	20.4	0.3	17.4	1.1	NA	NA	20.4	0.3
#50	562	2665	1.0	24.4173	2.8	0.0179	3.1	0.0032	1.3	0.41	20.4	0.3	18.0	0.6	NA	NA	20.4	0.3
#196	1701	19968	0.6	21.0064	1.9	0.0208	2.3	0.0032	1.3	0.57	20.4	0.3	20.9	0.5	79.6	45.0	20.4	0.3
#90	505	1963	0.9	23.4787	5.8	0.0188	6.0	0.0032	1.4	0.24	20.6	0.3	18.9	1.1	NA	NA	20.6	0.3
#174	762	37866	0.5	20.9578	2.8	0.0211	3.2	0.0032	1.6	0.50	20.6	0.3	21.2	0.7	85.2	66.5	20.6	0.3
#94	458	2042	1.2	24.8985	5.7	0.0177	5.8	0.0032	1.3	0.22	20.6	0.3	17.9	1.0	NA	NA	20.6	0.3
#3	709	1747	1.0	25.8409	8.9	0.0171	9.1	0.0032	1.7	0.19	20.7	0.4	17.2	1.5	NA	NA	20.7	0.4
#64	1085	12013	0.7	20.7371	2.4	0.0214	2.6	0.0032	1.0	0.40	20.7	0.2	21.5	0.6	110.2	56.1	20.7	0.2
#173	330	2524	0.8	19.9518	4.6	0.0223	4.7	0.0032	1.3	0.27	20.8	0.3	22.4	1.1	200.6	106.1	20.8	0.3
#98	307	9840	1.2	19.3760	3.6	0.0231	3.9	0.0032	1.5	0.40	20.9	0.3	23.2	0.9	268.2	81.6	20.9	0.3
#71	298	2676	0.8	23.0919	7.1	0.0194	7.4	0.0033	1.8	0.24	20.9	0.4	19.5	1.4	NA	NA	20.9	0.4
#149	341	24254	0.9	19.5832	2.7	0.0229	3.0	0.0033	1.3	0.42	20.9	0.3	23.0	0.7	243.7	62.6	20.9	0.3
#148	198	776	1.5	31.9266	5.9	0.0141	6.2	0.0033	1.9	0.31	21.0	0.4	14.2	0.9	NA	NA	21.0	0.4
#154	232	627	1.2	41.6878	51.0	0.0108	51.1	0.0033	2.0	0.04	21.0	0.4	10.9	5.5	NA	NA	21.0	0.4
#88	590	14134	1.0	21.6501	2.5	0.0208	2.7	0.0033	1.1	0.42	21.0	0.2	20.9	0.6	7.5	59.0	21.0	0.2
#89	452	21703	1.0	20.7678	3.4	0.0217	3.8	0.0033	1.6	0.43	21.0	0.3	21.8	0.8	106.7	80.4	21.0	0.3
#113	572	2440	0.9	23.6928	2.5	0.0190	2.8	0.0033	1.3	0.47	21.0	0.3	19.1	0.5	NA	NA	21.0	0.3
#219	1589	50217	0.4	13.3437	6.8	0.0340	7.1	0.0033	2.2	0.31	21.2	0.5	34.0	2.4	1067.0	136.3	21.2	0.5
#36	275	13472	0.7	19.9694	3.9	0.0228	4.1	0.0033	1.3	0.32	21.2	0.3	22.9	0.9	198.5	90.9	21.2	0.3
#198	363	17379	1.1	19.8395	3.0	0.0229	3.4	0.0033	1.6	0.47	21.3	0.3	23.0	0.8	213.7	69.1	21.3	0.3
#72	449	6556	1.1	12.1636	8.0	0.0376	8.1	0.0033	1.5	0.19	21.4	0.3	37.5	3.0	1250.6	156.4	21.4	0.3
#129	275	25150	1.3	22.2625	3.4	0.0207	3.7	0.0033	1.5	0.41	21.5	0.3	20.8	0.8	NA	NA	21.5	0.3
#4	1228	6225	0.3	20.4706	3.6	0.0226	3.8	0.0034	1.4	0.36	21.6	0.3	22.7	0.9	140.6	83.7	21.6	0.3
#153	397	2013	1.1	23.1649	2.8	0.0200	3.1	0.0034	1.4	0.44	21.7	0.3	20.1	0.6	NA	NA	21.7	0.3

Table 27. Sample A11-118A (continued).

		Isotope ratios									Apparent ages (Ma)							
Analysis	U (ppm)	$^{206}Pb/^{204}Pb$	U/Th	$^{206}Pb/^{207}Pb$	± (%)	$^{207}Pb/^{235}U$	± (%)	$^{206}Pb/^{238}U$	± (%)	error corr.	$^{206}Pb/^{238}U$	± (Ma)	$^{207}Pb/^{235}U$	± (Ma)	$^{206}Pb/^{207}Pb$	± (Ma)	Best age (Ma)	± (Ma)
#8	567	1283	1.1	22.9788	7.5	0.0203	7.6	0.0034	1.4	0.19	21.8	0.3	20.4	1.5	NA	NA	21.8	0.3
#32	271	783	0.6	32.3999	15.3	0.0144	15.4	0.0034	1.4	0.09	21.8	0.3	14.5	2.2	NA	NA	21.8	0.3
#45	288	2443	1.2	23.3206	6.1	0.0201	6.4	0.0034	1.7	0.27	21.9	0.4	20.2	1.3	NA	NA	21.9	0.4
#143	231	621	1.3	39.3327	10.9	0.0119	10.9	0.0034	1.3	0.12	21.9	0.3	12.0	1.3	NA	NA	21.9	0.3
#25	1882	85097	1.0	20.6189	1.6	0.0229	2.0	0.0034	1.1	0.57	22.0	0.2	23.0	0.4	123.7	37.9	22.0	0.2
#38	428	2291	1.2	22.0619	3.4	0.0214	3.7	0.0034	1.5	0.41	22.0	0.3	21.5	0.8	NA	NA	22.0	0.3
#162	299	7089	1.2	11.6118	10.5	0.0409	10.6	0.0034	1.7	0.16	22.2	0.4	40.7	4.3	1340.8	203.8	22.2	0.4
#65	1340	3378	1.7	22.2805	3.1	0.0214	3.3	0.0035	1.1	0.32	22.3	0.2	21.5	0.7	NA	NA	22.3	0.2
#155	1420	8495	1.4	20.4618	2.0	0.0234	2.3	0.0035	1.1	0.48	22.4	0.2	23.5	0.5	141.7	46.5	22.4	0.2
#132	291	1979	1.4	22.4942	9.0	0.0213	9.2	0.0035	1.8	0.20	22.4	0.4	21.4	2.0	NA	NA	22.4	0.4
#37	442	1878	1.5	24.3725	8.0	0.0197	8.1	0.0035	1.5	0.19	22.4	0.3	19.8	1.6	NA	NA	22.4	0.3
#27	2620	19876	2.2	20.5038	1.3	0.0234	1.7	0.0035	1.1	0.65	22.4	0.2	23.5	0.4	136.8	29.8	22.4	0.2
#141	244	3542	1.0	21.3912	4.6	0.0231	5.0	0.0036	2.0	0.39	23.1	0.5	23.2	1.1	36.4	109.3	23.1	0.5
#99	1173	3101	0.7	18.5060	2.8	0.0268	3.5	0.0036	2.1	0.60	23.2	0.5	26.9	0.9	372.5	63.3	23.2	0.5
#103	534	4085	1.0	20.4431	3.8	0.0252	4.1	0.0037	1.7	0.41	24.0	0.4	25.2	1.0	143.8	88.2	24.0	0.4
#101	2354	921	0.4	4.9112	14.6	0.1106	15.1	0.0039	4.0	0.26	25.4	1.0	106.6	15.3	2855.4	238.5	25.4	1.0
#10	292	1255	1.0	18.4720	6.8	0.0297	7.0	0.0040	1.7	0.24	25.7	0.4	29.8	2.1	376.7	153.1	25.7	0.4
#29	694	3841	0.6	22.8592	2.6	0.0246	3.2	0.0041	1.8	0.56	26.2	0.5	24.6	0.8	NA	NA	26.2	0.5
#186	574	2908	0.7	23.7449	2.6	0.0239	3.0	0.0041	1.4	0.47	26.5	0.4	24.0	0.7	NA	NA	26.5	0.4
#134	374	5899	0.7	6.0622	13.6	0.0943	13.8	0.0041	2.7	0.19	26.7	0.7	91.5	12.1	2507.1	229.2	26.7	0.7
#87	846	31173	1.5	20.8235	1.5	0.0303	1.8	0.0046	1.0	0.55	29.5	0.3	30.3	0.6	100.4	36.5	29.5	0.3
#167	2412	24827	0.6	20.8245	1.6	0.0304	2.1	0.0046	1.3	0.65	29.6	0.4	30.4	0.6	100.3	37.4	29.6	0.4
#206	1239	27256	1.3	20.8760	2.0	0.0313	2.4	0.0047	1.3	0.54	30.5	0.4	31.3	0.7	94.4	48.2	30.5	0.4
#82	321	747	0.9	2.7638	6.6	0.4616	6.8	0.0093	1.8	0.26	59.4	1.1	385.4	21.8	3757.5	99.9	59.4	1.1
#123	1663	22558	0.5	20.3409	1.7	0.0801	2.0	0.0118	1.1	0.52	75.8	0.8	78.3	1.5	155.6	40.4	75.8	0.8
#75	569	21979	1.4	21.1554	1.4	0.0774	1.7	0.0119	1.0	0.56	76.2	0.7	75.7	1.3	62.8	33.9	76.2	0.7
#114	753	8167	0.9	20.5466	2.2	0.0818	2.5	0.0122	1.2	0.50	78.2	1.0	79.9	1.9	132.0	51.4	78.2	1.0
#210	271	25075	1.5	21.0111	2.3	0.0802	2.6	0.0122	1.2	0.46	78.3	0.9	78.3	1.9	79.1	53.9	78.3	0.9

Table 27. Sample A11-118A (continued).

				Isotope ratios							Apparent ages (Ma)							
Analysis	U (ppm)	$^{206}Pb/^{204}Pb$	U/Th	$^{206}Pb/^{207}Pb$	± (%)	$^{207}Pb/^{235}U$	± (%)	$^{206}Pb/^{238}U$	± (%)	error corr.	$^{206}Pb/^{238}U$	± (Ma)	$^{207}Pb/^{235}U$	± (Ma)	$^{206}Pb/^{207}Pb$	± (Ma)	Best age (Ma)	± (Ma)
#47	788	14503	0.8	20.9251	1.5	0.0815	2.0	0.0124	1.3	0.65	79.2	1.0	79.5	1.5	88.9	35.3	79.2	1.0
#22	1287	8705	0.6	21.1760	1.2	0.0835	1.6	0.0128	1.1	0.70	82.2	0.9	81.4	1.3	60.5	28.0	82.2	0.9
#203	300	4856	0.9	22.2360	2.4	0.0800	2.7	0.0129	1.3	0.47	82.7	1.0	78.1	2.0	NA	NA	82.7	1.0
#110	557	656088	1.2	20.4428	1.4	0.0879	1.8	0.0130	1.2	0.65	83.5	1.0	85.5	1.5	143.8	32.0	83.5	1.0
#53	2404	24046	2.3	18.9523	2.4	0.0948	2.6	0.0130	1.1	0.43	83.5	0.9	92.0	2.3	318.6	54.3	83.5	0.9
#59	345	20841	1.1	19.6171	2.3	0.0919	2.6	0.0131	1.3	0.49	83.8	1.1	89.3	2.2	239.7	52.9	83.8	1.1
#91	443	5155	1.1	22.1290	2.1	0.0825	2.5	0.0132	1.4	0.55	84.8	1.2	80.5	2.0	NA	NA	84.8	1.2
#44	231	5549	1.3	21.4029	2.6	0.0871	2.8	0.0135	1.2	0.41	86.6	1.0	84.8	2.3	35.1	61.6	86.6	1.0
#24	653	51029	1.5	20.7659	1.4	0.0898	2.0	0.0135	1.4	0.72	86.6	1.2	87.3	1.6	107.0	32.1	86.6	1.2
#131	592	6449	1.4	22.1852	1.5	0.0903	1.8	0.0145	0.9	0.51	93.0	0.8	87.8	1.5	NA	NA	93.0	0.8
#9	398	5839	2.5	21.2715	2.0	0.0963	2.5	0.0149	1.5	0.59	95.2	1.4	93.4	2.2	49.8	48.3	95.2	1.4
#128	518	3157	2.2	22.1625	1.6	0.0926	1.9	0.0149	1.1	0.58	95.3	1.1	89.9	1.7	NA	NA	95.3	1.1
#136	587	9848	1.3	20.6536	1.3	0.0994	1.9	0.0149	1.3	0.69	95.3	1.2	96.2	1.7	119.7	31.4	95.3	1.2
#127	361	18065	2.1	20.4959	1.7	0.1006	2.1	0.0150	1.2	0.58	95.7	1.1	97.3	1.9	137.8	39.5	95.7	1.1
#191	516	36444	2.3	20.5556	1.1	0.1005	1.4	0.0150	1.0	0.69	95.9	0.9	97.2	1.3	130.9	24.8	95.9	0.9
#133	782	67968	1.7	20.8792	1.2	0.1004	1.8	0.0152	1.3	0.72	97.3	1.2	97.1	1.6	94.1	28.7	97.3	1.2
#100	299	299816	1.3	20.3164	2.2	0.1036	2.5	0.0153	1.1	0.43	97.7	1.0	100.1	2.4	158.4	52.5	97.7	1.0
#201	478	106313	1.6	20.0481	1.5	0.1068	1.8	0.0155	1.0	0.57	99.4	1.0	103.1	1.8	189.4	34.8	99.4	1.0
#112	784	38732	1.3	20.7357	1.0	0.1074	1.8	0.0162	1.5	0.83	103.4	1.5	103.6	1.8	110.3	23.2	103.4	1.5
#138	697	11790	0.7	21.2481	1.3	0.1137	1.7	0.0175	1.1	0.62	112.1	1.2	109.4	1.8	52.4	31.9	112.1	1.2
#187	640	106222	1.1	20.2821	1.4	0.1206	1.7	0.0177	1.0	0.58	113.4	1.1	115.6	1.9	162.3	33.1	113.4	1.1
#104	70	1720	1.3	23.5568	3.4	0.1155	3.7	0.0197	1.5	0.41	126.0	1.9	111.0	3.9	NA	NA	126.0	1.9
#184	260	4131	1.1	22.2621	1.8	0.1242	2.1	0.0201	1.1	0.52	128.1	1.3	118.9	2.3	NA	NA	128.1	1.3
#163	296	16812	0.8	18.6486	3.0	0.1579	3.2	0.0214	1.2	0.37	136.3	1.6	148.9	4.4	355.2	66.8	136.3	1.6
#60	516	15346	0.6	20.6957	1.5	0.1424	1.9	0.0214	1.1	0.59	136.4	1.5	135.2	2.4	114.9	35.9	136.4	1.5
#185	791	60618	1.6	18.8242	1.1	0.1616	2.4	0.0221	2.2	0.90	140.8	3.0	152.1	3.4	334.0	24.0	140.8	3.0
#119	744	25957	1.4	20.3663	1.1	0.1562	1.5	0.0231	1.0	0.68	147.1	1.5	147.3	2.0	152.6	25.5	147.1	1.5

Table 27. Sample A11-118A (continued).

				Isotope ratios							Apparent ages (Ma)							
Analysis	U (ppm)	$^{206}Pb/^{204}Pb$	U/Th	$^{206}Pb/^{207}Pb$	± (%)	$^{207}Pb/^{235}U$	± (%)	$^{206}Pb/^{238}U$	± (%)	error corr.	$^{206}Pb/^{238}U$	± (Ma)	$^{207}Pb/^{235}U$	± (Ma)	$^{206}Pb/^{207}Pb$	± (Ma)	Best age (Ma)	± (Ma)
#145	332	9619	1.3	18.1581	2.0	0.1780	2.4	0.0235	1.2	0.50	149.5	1.7	166.4	3.6	415.1	45.6	149.5	1.7
#189	213	11906	1.3	20.6723	2.2	0.1600	2.4	0.0240	1.1	0.46	152.9	1.7	150.7	3.4	117.6	50.8	152.9	1.7
#115	1172	38166	0.9	19.7748	0.9	0.1842	1.3	0.0264	0.9	0.73	168.2	1.6	171.7	2.0	221.2	20.0	168.2	1.6
#208	644	71250	0.7	19.9567	1.1	0.1828	1.8	0.0265	1.5	0.81	168.4	2.4	170.5	2.8	200.0	24.7	168.4	2.4
#61	917	85370	0.9	20.1084	1.0	0.1832	1.4	0.0267	0.9	0.67	170.1	1.6	170.8	2.2	182.4	24.4	170.1	1.6
#102	2285	351545	0.9	20.1334	0.9	0.1864	1.3	0.0272	1.0	0.75	173.2	1.7	173.5	2.1	179.5	20.7	173.2	1.7
#182	194	7146	1.4	20.9915	2.7	0.1852	2.9	0.0282	1.1	0.38	179.3	1.9	172.5	4.6	81.3	63.8	179.3	1.9
#62	76	4952	0.6	19.0950	3.8	0.2833	4.0	0.0393	1.2	0.31	248.2	3.0	253.3	9.0	301.6	86.9	248.2	3.0
#124	177	6221	1.7	19.0844	1.6	0.2892	2.2	0.0400	1.6	0.71	253.1	3.9	257.9	5.1	302.8	35.9	253.1	3.9
#57	886	29878	1.0	19.4101	0.9	0.2931	1.6	0.0413	1.3	0.82	260.8	3.3	261.0	3.7	264.2	21.0	260.8	3.3
#77	343	33042	1.2	18.9128	1.1	0.3142	1.5	0.0431	1.1	0.72	272.1	2.9	277.4	3.7	323.4	24.2	272.1	2.9
#85	2323	207817	3.0	18.4545	0.7	0.4155	1.1	0.0556	0.9	0.81	349.0	3.1	352.8	3.3	378.8	14.8	349.0	3.1
#177	314	13179	1.3	14.8884	2.1	0.5505	2.3	0.0595	1.1	0.49	372.4	4.1	445.3	8.5	843.0	42.7	372.4	4.1
#49	297	18335	0.6	16.2058	2.1	0.5356	2.6	0.0630	1.5	0.57	393.7	5.6	435.5	9.2	664.0	45.8	393.7	5.6
#194	625	98882	1.9	17.0847	0.9	0.5955	1.5	0.0738	1.2	0.78	459.1	5.1	474.4	5.6	549.7	20.4	459.1	5.1
#202	418	118143	0.8	17.8002	1.1	0.5716	1.5	0.0738	1.0	0.67	459.1	4.4	459.0	5.4	459.4	24.2	459.1	4.4
#14	320	20529	1.1	17.7752	1.0	0.5728	1.6	0.0739	1.2	0.76	459.5	5.3	459.8	5.8	462.6	22.7	459.5	5.3
#120	297	134091	1.0	17.5793	1.0	0.5894	1.6	0.0752	1.2	0.79	467.3	5.6	470.5	6.0	487.1	21.6	467.3	5.6
#171	721	43763	0.7	17.8262	0.7	0.5823	1.1	0.0753	0.9	0.77	468.1	4.0	466.0	4.3	456.2	16.3	468.1	4.0
#164	815	141107	11.1	16.8843	0.8	0.7783	1.4	0.0953	1.1	0.83	587.1	6.4	584.5	6.1	575.4	16.8	587.1	6.4
#181	398	65361	1.4	14.3073	1.0	1.2862	2.8	0.1335	2.7	0.94	807.9	20.2	839.6	16.2	925.2	20.5	807.9	20.2
#69	412	51601	2.9	14.2245	0.8	1.4487	1.8	0.1495	1.6	0.90	898.3	13.6	909.4	10.8	937.2	15.9	937.2	15.9
#48	255	41669	4.9	13.8182	0.8	1.6925	1.2	0.1697	0.9	0.74	1010.4	8.2	1005.7	7.6	996.3	16.2	996.3	16.2
#220	185	1575983	1.6	13.7312	0.9	1.6915	1.3	0.1685	1.0	0.73	1004.0	8.9	1005.3	8.4	1009.1	18.0	1009.1	18.0
#205	360	101583	2.4	12.6027	0.8	2.1755	1.5	0.1989	1.2	0.83	1169.6	12.8	1173.2	10.1	1180.9	16.2	1180.9	16.2
#180	511	268926	1.6	12.1416	0.9	2.2850	1.2	0.2013	0.9	0.72	1182.3	9.5	1207.7	8.6	1254.1	16.7	1254.1	16.7
#76	124	92434	1.4	11.6913	1.0	2.6827	1.8	0.2276	1.5	0.83	1321.8	17.6	1323.7	13.2	1327.6	19.5	1327.6	19.5

Table 27. Sample A11-118A (continued).

Analysis	U (ppm)	$^{206}Pb/^{204}Pb$	U/Th	$^{206}Pb/^{207}Pb$	± (%)	$^{207}Pb/^{235}U$	± (%)	$^{206}Pb/^{238}U$	± (%)	error corr.	$^{206}Pb/^{238}U$	± (Ma)	$^{207}Pb/^{235}U$	± (Ma)	$^{206}Pb/^{207}Pb$	± (Ma)	Best age (Ma)	± (Ma)
					Isotope ratios							Apparent ages (Ma)						
#7	519	83478	1.9	10.5424	0.9	2.8192	1.4	0.2157	1.0	0.74	1258.9	11.7	1360.7	10.4	1525.2	17.6	1525.2	17.6
#165	366	192878	1.0	10.2583	1.2	3.2796	1.6	0.2441	1.1	0.69	1408.0	14.1	1476.2	12.6	1576.5	21.9	1576.5	21.9
#15	301	328872	0.5	8.7590	1.0	5.2239	1.4	0.3320	1.0	0.73	1848.1	16.7	1856.5	12.1	1866.8	17.4	1866.8	17.4
#107	187	42067	1.8	7.4189	0.7	7.4670	1.3	0.4020	1.0	0.81	2178.0	18.7	2169.0	11.2	2161.3	12.8	2161.3	12.8
#42	678	191406	1.2	5.4723	0.7	12.8602	1.3	0.5106	1.1	0.82	2659.3	22.9	2669.5	12.1	2677.9	12.1	2677.9	12.1

.

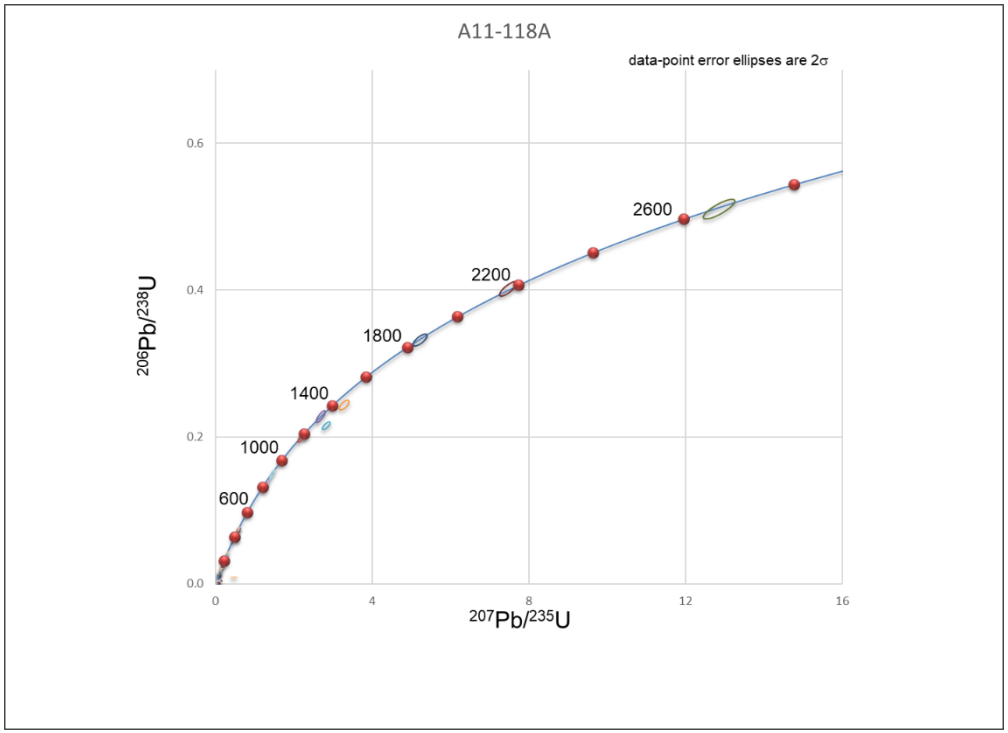

Figure 74. Concordia plot for sample A11-118A

Table 28. U-Pb DZ geochronology analysis data for sample 170319A, ordered by best age.

		Isotope ratios									Apparent ages (Ma)							
Analysis	U (ppm)	$^{206}Pb/^{204}Pb$	U/Th	$^{206}Pb/^{207}Pb$	± (%)	$^{207}Pb/^{235}U$	± (%)	$^{206}Pb/^{238}U$	± (%)	error corr.	$^{206}Pb/^{238}U$	± (Ma)	$^{207}Pb/^{235}U$	± (Ma)	$^{206}Pb/^{207}Pb$	± (Ma)	Best age (Ma)	± (Ma)
#52	172	1280	0.7	26.1500	15.5	0.0395	15.5	0.0075	1.1	0.07	48.1	0.5	39.3	6.0	NA	NA	48.1	0.5
#189	82	4097	0.7	17.9256	3.1	0.0591	3.5	0.0077	1.6	0.45	49.3	0.8	58.3	2.0	443.8	68.9	49.3	0.8
#198	127	25653	0.8	19.7334	3.6	0.0537	3.8	0.0077	1.1	0.29	49.3	0.5	53.1	2.0	226.1	84.3	49.3	0.5
#144	163	3225	1.0	21.9506	2.3	0.0506	2.6	0.0081	1.2	0.48	51.8	0.6	50.1	1.3	NA	NA	51.8	0.6
#168	29	1486	1.2	22.9559	4.9	0.0488	5.3	0.0081	2.1	0.38	52.2	1.1	48.4	2.5	NA	NA	52.2	1.1
#93	327	28985	0.6	21.0430	1.7	0.0592	2.1	0.0090	1.2	0.57	58.0	0.7	58.4	1.2	75.5	40.2	58.0	0.7
#164	104	8049	1.3	21.6512	3.0	0.0592	3.2	0.0093	1.3	0.41	59.7	0.8	58.4	1.8	7.4	71.2	59.7	0.8
#2	164	6666	1.0	20.7981	2.8	0.0628	3.0	0.0095	1.1	0.37	60.8	0.7	61.8	1.8	103.3	66.7	60.8	0.7
#81	462	74238	0.9	20.5618	1.4	0.0654	2.0	0.0098	1.4	0.72	62.6	0.9	64.3	1.3	130.2	33.0	62.6	0.9
#72	203	4547	1.0	20.5656	2.7	0.0665	2.9	0.0099	1.0	0.36	63.6	0.6	65.4	1.8	129.8	62.8	63.6	0.6
#217	321	4493	1.0	22.2181	1.9	0.0627	2.3	0.0101	1.2	0.52	64.8	0.8	61.7	1.4	NA	NA	64.8	0.8
#161	187	1491	1.3	23.2006	2.3	0.0602	2.7	0.0101	1.4	0.53	65.0	0.9	59.4	1.6	NA	NA	65.0	0.9
#99	357	3790	5.1	23.0879	2.0	0.0616	2.5	0.0103	1.4	0.58	66.1	0.9	60.7	1.5	NA	NA	66.1	0.9
#58	135	954	1.3	28.7295	2.4	0.0499	2.7	0.0104	1.2	0.45	66.7	0.8	49.4	1.3	NA	NA	66.7	0.8
#65	269	2875	1.1	23.7540	2.7	0.0624	3.0	0.0108	1.2	0.39	69.0	0.8	61.5	1.8	NA	NA	69.0	0.8
#146	1058	76572	1.2	20.7100	0.9	0.0726	1.4	0.0109	1.1	0.76	69.9	0.8	71.2	1.0	113.3	22.0	69.9	0.8
#113	73	1260	1.6	25.9740	6.8	0.0587	7.0	0.0111	1.8	0.26	70.9	1.3	57.9	4.0	NA	NA	70.9	1.3
#9	208	2264	3.1	23.8028	2.3	0.0648	2.7	0.0112	1.4	0.51	71.8	1.0	63.8	1.7	NA	NA	71.8	1.0
#82	193	2746	0.7	23.8274	1.9	0.0658	2.2	0.0114	1.0	0.47	72.9	0.8	64.7	1.4	NA	NA	72.9	0.8
#36	317	4650	0.5	21.8876	1.6	0.0730	1.9	0.0116	1.2	0.60	74.3	0.9	71.5	1.3	NA	NA	74.3	0.9
#160	41	15195	2.2	19.9167	3.4	0.0806	3.7	0.0116	1.5	0.41	74.7	1.1	78.7	2.8	204.7	78.7	74.7	1.1
#203	367	93448	0.8	20.3532	1.7	0.0792	2.1	0.0117	1.2	0.57	75.0	0.9	77.4	1.5	154.1	40.2	75.0	0.9
#170	221	15947	1.3	20.9956	1.8	0.0772	2.2	0.0118	1.3	0.58	75.4	0.9	75.6	1.6	80.9	42.1	75.4	0.9
#214	242	15279	0.9	20.2450	1.8	0.0804	2.3	0.0118	1.4	0.61	75.7	1.1	78.5	1.7	166.6	42.4	75.7	1.1
#63	96	5530	1.0	19.2614	2.4	0.0849	2.8	0.0119	1.4	0.51	76.1	1.1	82.8	2.2	281.8	55.7	76.1	1.1
#205	67	1510	1.8	17.6184	4.5	0.0940	4.7	0.0120	1.5	0.32	77.0	1.2	91.3	4.1	482.2	98.5	77.0	1.2
#187	318	6121	1.2	20.4875	2.5	0.0810	2.7	0.0120	1.1	0.41	77.2	0.8	79.1	2.1	138.7	57.8	77.2	0.8

Table 28. Sample 170319A (continued).

		Isotope ratios									Apparent ages (Ma)							
Analysis	U (ppm)	$^{206}Pb/^{204}Pb$	U/Th	$^{206}Pb/^{207}Pb$	± (%)	$^{207}Pb/^{235}U$	± (%)	$^{206}Pb/^{238}U$	± (%)	error corr.	$^{206}Pb/^{238}U$	± (Ma)	$^{207}Pb/^{235}U$	± (Ma)	$^{206}Pb/^{207}Pb$	± (Ma)	Best age (Ma)	± (Ma)
#169	76	1070	1.1	29.0612	10.3	0.0579	10.4	0.0122	1.3	0.12	78.2	1.0	57.1	5.8	NA	NA	78.2	1.0
#165	356	19899	0.6	20.6072	1.4	0.0817	1.8	0.0122	1.2	0.66	78.3	0.9	79.7	1.4	125.0	32.3	78.3	0.9
#49	211	3618	0.6	21.4611	4.5	0.0788	4.7	0.0123	1.3	0.28	78.6	1.0	77.0	3.5	28.6	107.6	78.6	1.0
#46	177	10290	2.7	20.9408	1.8	0.0810	2.0	0.0123	1.0	0.51	78.8	0.8	79.0	1.5	87.1	41.6	78.8	0.8
#166	389	8842	0.6	17.7058	2.9	0.0958	3.4	0.0123	1.7	0.51	78.8	1.4	92.9	3.0	471.2	64.8	78.8	1.4
#105	106	2924	1.5	23.1642	3.1	0.0737	3.3	0.0124	1.3	0.39	79.3	1.0	72.2	2.3	NA	NA	79.3	1.0
#45	447	6950	0.6	21.7183	1.4	0.0791	2.1	0.0125	1.5	0.72	79.9	1.2	77.3	1.5	NA	NA	79.9	1.2
#194	130	2458	1.1	22.5597	3.6	0.0768	3.9	0.0126	1.4	0.37	80.6	1.2	75.2	2.8	NA	NA	80.6	1.2
#42	479	60187	0.5	20.7162	1.2	0.0839	1.7	0.0126	1.2	0.72	80.8	1.0	81.8	1.3	112.6	28.2	80.8	1.0
#75	653	287991	1.1	20.6989	1.2	0.0841	1.6	0.0126	1.0	0.65	80.9	0.8	82.0	1.3	114.5	29.0	80.9	0.8
#177	3436	47821	0.7	20.8590	1.0	0.0840	1.6	0.0127	1.2	0.78	81.5	1.0	81.9	1.2	96.3	23.5	81.5	1.0
#208	79	1014	1.6	29.8739	10.7	0.0591	10.8	0.0128	1.3	0.12	82.0	1.1	58.3	6.1	NA	NA	82.0	1.1
#116	124	3096	0.8	21.5665	5.2	0.0820	5.3	0.0128	1.0	0.19	82.2	0.8	80.0	4.0	16.8	123.9	82.2	0.8
#23	377	3421	1.4	21.6349	1.5	0.0834	1.9	0.0131	1.2	0.62	83.9	1.0	81.3	1.5	9.2	36.6	83.9	1.0
#184	157	2752	2.3	21.9122	3.4	0.0839	3.6	0.0133	1.2	0.32	85.4	1.0	81.8	2.8	NA	NA	85.4	1.0
#136	260	6450	1.8	20.3132	1.7	0.0913	2.4	0.0135	1.6	0.68	86.1	1.4	88.7	2.0	158.7	40.3	86.1	1.4
#86	144	3213	0.9	22.3795	3.1	0.0839	3.4	0.0136	1.5	0.43	87.2	1.3	81.8	2.7	NA	NA	87.2	1.3
#179	243	10031	2.1	20.2347	1.6	0.0942	1.9	0.0138	1.1	0.57	88.5	1.0	91.4	1.7	167.8	36.9	88.5	1.0
#156	414	14794	3.7	20.9033	1.6	0.0915	1.9	0.0139	1.1	0.55	88.8	0.9	88.9	1.6	91.3	38.2	88.8	0.9
#204	545	19114	0.9	20.3390	1.3	0.0941	1.9	0.0139	1.3	0.69	88.9	1.1	91.3	1.6	155.8	31.6	88.9	1.1
#95	247	6797	1.8	18.1896	1.9	0.1071	2.3	0.0141	1.3	0.57	90.5	1.2	103.3	2.3	411.2	42.2	90.5	1.2
#210	276	8337	1.7	20.8070	2.5	0.0983	2.7	0.0148	1.1	0.39	94.9	1.0	95.2	2.5	102.2	59.5	94.9	1.0
#55	194	12389	1.2	20.5326	1.9	0.1024	2.1	0.0153	1.0	0.49	97.6	1.0	99.0	2.0	133.6	44.0	97.6	1.0
#141	96	2275	1.3	23.0525	2.7	0.1058	2.9	0.0177	1.1	0.38	113.1	1.2	102.1	2.8	NA	NA	113.1	1.2
#149	338	18647	0.7	19.8320	1.2	0.1301	1.6	0.0187	1.0	0.65	119.6	1.2	124.2	1.8	214.6	27.6	119.6	1.2
#109	376	75656	2.0	20.2208	1.2	0.1334	1.6	0.0196	1.1	0.66	125.0	1.3	127.2	2.0	169.4	28.9	125.0	1.3
#74	160	7840	0.8	15.8831	4.4	0.1742	4.5	0.0201	1.2	0.26	128.2	1.5	163.1	6.8	706.9	93.3	128.2	1.5

Table 28. Sample 170319A (continued).

		Isotope ratios									Apparent ages (Ma)							
Analysis	U (ppm)	$^{206}Pb/^{204}Pb$	U/Th	$^{206}Pb/^{207}Pb$	± (%)	$^{207}Pb/^{235}U$	± (%)	$^{206}Pb/^{238}U$	± (%)	error corr.	$^{206}Pb/^{238}U$	± (Ma)	$^{207}Pb/^{235}U$	± (Ma)	$^{206}Pb/^{207}Pb$	± (Ma)	Best age (Ma)	± (Ma)
#134	227	94144	0.6	20.1076	2.2	0.1447	2.6	0.0211	1.4	0.55	134.7	1.9	137.2	3.3	182.5	50.1	134.7	1.9
#173	93	3148	1.0	21.9506	2.2	0.1331	2.6	0.0212	1.3	0.49	135.2	1.7	126.9	3.1	NA	NA	135.2	1.7
#191	271	6991	1.0	17.2334	2.8	0.1737	3.1	0.0217	1.2	0.40	138.5	1.7	162.6	4.6	530.8	61.3	138.5	1.7
#18	244	5845	1.4	20.9307	1.9	0.1449	2.4	0.0220	1.4	0.60	140.4	2.0	137.4	3.0	88.2	44.8	140.4	2.0
#196	362	13368	1.4	20.8999	1.6	0.1479	1.8	0.0224	1.0	0.54	143.0	1.4	140.1	2.4	91.7	36.9	143.0	1.4
#163	383	55551054	1.2	16.1179	2.5	0.2043	2.9	0.0239	1.6	0.54	152.2	2.4	188.8	5.0	675.6	52.5	152.2	2.4
#218	125	21490	0.7	20.6062	1.5	0.1641	1.7	0.0245	0.9	0.53	156.2	1.4	154.3	2.5	125.1	34.3	156.2	1.4
#54	513	128963	0.9	19.5250	1.0	0.2847	1.8	0.0403	1.6	0.84	254.9	3.9	254.4	4.2	250.6	23.0	254.9	3.9
#89	83	48073	0.7	18.7004	1.4	0.2992	1.8	0.0406	1.1	0.61	256.6	2.8	265.8	4.3	349.0	32.8	256.6	2.8
#51	194	6455	1.0	19.9131	1.7	0.2957	2.1	0.0427	1.3	0.59	269.7	3.3	263.0	5.0	205.1	40.0	269.7	3.3
#118	64	20639	8.8	18.7784	1.7	0.3194	2.0	0.0435	1.1	0.53	274.6	2.9	281.5	5.0	339.6	38.6	274.6	2.9
#66	93	2704	0.9	21.0328	1.8	0.3053	2.1	0.0466	1.1	0.51	293.6	3.1	270.5	5.0	76.7	43.0	293.6	3.1
#7	418	27917	1.0	19.3077	1.2	0.3403	1.8	0.0477	1.3	0.72	300.2	3.8	297.4	4.6	276.3	28.2	300.2	3.8
#200	195	29170	1.0	18.8267	1.5	0.3517	1.8	0.0480	1.0	0.56	302.5	3.0	306.0	4.8	333.8	33.8	302.5	3.0
#88	476	24751	1.6	18.1838	2.1	0.4163	2.9	0.0549	2.0	0.70	344.7	6.8	353.4	8.7	412.0	46.4	344.7	6.8
#188	85	21616	1.0	17.9283	1.8	0.4509	2.2	0.0587	1.3	0.60	367.5	4.7	377.9	6.9	443.5	39.0	367.5	4.7
#32	149	36538	0.6	17.9491	1.1	0.5298	1.7	0.0690	1.2	0.73	430.1	5.0	431.7	5.8	440.9	25.1	430.1	5.0
#213	370	54020	0.4	17.3533	1.1	0.5551	2.2	0.0699	1.9	0.87	435.5	8.1	448.4	8.1	515.5	24.4	435.5	8.1
#104	148	73837	1.3	17.5265	1.3	0.5926	1.7	0.0754	1.2	0.68	468.4	5.3	472.6	6.5	493.7	28.0	468.4	5.3
#53	82	9727	0.9	17.6174	1.6	0.5930	1.9	0.0758	1.1	0.55	471.0	4.8	472.8	7.4	482.3	36.0	471.0	4.8
#101	189	28972	0.9	17.3798	1.0	0.6376	1.5	0.0804	1.1	0.72	498.6	5.2	500.8	6.0	512.2	23.0	498.6	5.2
#122	260	27168	0.9	17.5640	0.8	0.6347	1.2	0.0809	0.8	0.73	501.4	4.1	499.0	4.6	489.0	17.4	501.4	4.1
#83	137	16586	1.3	17.4177	1.3	0.6517	1.6	0.0824	1.0	0.61	510.2	4.8	509.5	6.4	507.4	28.0	510.2	4.8
#120	65	9603	0.8	17.4967	1.8	0.6604	2.4	0.0838	1.5	0.64	519.0	7.5	514.9	9.5	497.5	40.0	519.0	7.5
#171	77	23614	1.3	16.9413	1.2	0.6922	1.7	0.0851	1.2	0.71	526.4	6.1	534.1	7.0	568.1	25.6	526.4	6.1
#108	150	73861	1.3	16.9009	1.0	0.6966	1.6	0.0854	1.2	0.76	528.4	6.1	536.8	6.6	573.3	22.5	528.4	6.1
#152	100	657608	0.6	16.9930	1.2	0.6957	2.5	0.0858	2.2	0.88	530.6	11.3	536.2	10.5	561.5	26.0	530.6	11.3

Table 28. Sample 170319A (continued).

				Isotope ratios							Apparent ages (Ma)							
Analysis	U (ppm)	$^{206}Pb/^{204}Pb$	U/Th	$^{206}Pb/^{207}Pb$	± (%)	$^{207}Pb/^{235}U$	± (%)	$^{206}Pb/^{238}U$	± (%)	error corr.	$^{206}Pb/^{238}U$	± (Ma)	$^{207}Pb/^{235}U$	± (Ma)	$^{206}Pb/^{207}Pb$	± (Ma)	Best age (Ma)	± (Ma)
#67	142	65116	1.9	17.1100	1.0	0.6920	1.5	0.0859	1.2	0.78	531.3	6.0	534.0	6.3	546.5	21.0	531.3	6.0
#216	393	101100	2.4	17.0106	0.9	0.7120	1.4	0.0879	1.0	0.75	543.0	5.4	545.9	5.9	559.2	20.0	543.0	5.4
#193	102	33747	6.3	16.6212	1.3	0.7297	1.6	0.0880	0.9	0.58	543.7	4.9	556.4	6.9	609.5	28.6	543.7	4.9
#25	113	18377	1.0	17.1193	1.0	0.7096	1.4	0.0881	1.0	0.72	544.5	5.1	544.5	5.8	545.3	20.9	544.5	5.1
#159	160	37265	1.1	16.9106	1.0	0.7207	1.5	0.0884	1.1	0.77	546.2	5.9	551.1	6.3	572.0	20.7	546.2	5.9
#26	134	28213	1.1	17.1429	1.2	0.7158	1.7	0.0890	1.2	0.73	549.8	6.5	548.2	7.1	542.3	25.3	549.8	6.5
#69	97	16577	0.4	16.9353	1.4	0.7250	1.7	0.0891	0.9	0.57	550.1	4.9	553.6	7.1	568.9	29.7	550.1	4.9
#128	411	50176	3.3	16.9370	1.0	0.7277	1.5	0.0894	1.1	0.75	552.1	5.9	555.2	6.4	568.7	21.4	552.1	5.9
#207	146	360444	0.5	16.7416	0.9	0.7404	1.4	0.0899	1.1	0.77	555.2	5.8	562.7	6.1	593.9	19.8	555.2	5.8
#103	68	10096	0.3	16.6811	1.2	0.7442	1.7	0.0901	1.1	0.68	556.0	6.1	564.9	7.3	601.7	26.9	556.0	6.1
#139	294	68988	1.4	17.2299	1.0	0.7223	1.3	0.0903	0.9	0.66	557.3	4.7	552.0	5.7	531.2	22.0	557.3	4.7
#167	179	10412	2.0	16.8534	1.4	0.7403	1.7	0.0905	0.9	0.53	558.7	4.8	562.6	7.2	579.4	30.8	558.7	4.8
#135	52	73921	0.9	16.3370	1.1	0.7674	1.7	0.0910	1.3	0.77	561.3	7.1	578.3	7.6	646.7	23.4	561.3	7.1
#117	71	56529	0.8	16.8051	1.2	0.7592	1.5	0.0926	0.9	0.61	570.7	5.0	573.6	6.5	585.7	25.5	570.7	5.0
#219	77	5906	1.1	17.0338	1.1	0.7646	1.4	0.0945	0.9	0.65	582.1	5.2	576.7	6.3	556.3	23.7	582.1	5.2
#3	462	47104	1.2	16.8130	0.9	0.7756	1.5	0.0946	1.2	0.82	582.8	6.8	583.0	6.7	584.6	18.9	582.8	6.8
#125	60	18519	1.0	16.6819	1.3	0.7872	1.7	0.0953	1.1	0.65	586.7	6.0	589.6	7.4	601.6	27.3	586.7	6.0
#190	53	9502	0.8	16.7561	1.8	0.7843	2.1	0.0954	1.2	0.55	587.2	6.6	588.0	9.6	592.0	39.0	587.2	6.6
#121	205	191807	2.8	16.6210	1.2	0.7944	1.5	0.0958	1.0	0.65	589.7	5.5	593.6	6.8	609.5	25.0	589.7	5.5
#157	539	158666	1.2	16.6562	1.0	0.7949	1.5	0.0961	1.1	0.73	591.3	6.2	594.0	6.8	604.9	22.6	591.3	6.2
#155	258	76159	1.7	16.4759	0.8	0.8146	1.2	0.0974	1.0	0.79	599.0	5.6	605.0	5.6	628.4	16.2	599.0	5.6
#5	150	44210	2.0	16.7656	1.1	0.8139	1.7	0.0990	1.3	0.75	608.6	7.4	604.6	7.8	590.7	24.6	608.6	7.4
#31	138	8418	1.0	16.7049	1.2	0.8336	1.5	0.1010	1.0	0.62	620.5	5.6	615.6	7.1	598.6	26.3	620.5	5.6
#148	91	16968	0.9	16.4704	0.9	0.8497	1.2	0.1015	0.8	0.65	623.5	4.7	624.5	5.7	629.1	19.9	623.5	4.7
#85	304	39647	1.1	16.5929	0.9	0.8437	1.7	0.1016	1.4	0.84	623.7	8.3	621.2	7.7	613.1	19.2	623.7	8.3
#37	187	47398	0.2	16.0865	1.1	0.8884	1.6	0.1037	1.1	0.70	636.0	6.6	645.5	7.4	679.7	23.8	636.0	6.6
#84	40	27490	1.0	15.8298	1.8	0.9064	2.3	0.1041	1.5	0.65	638.4	9.1	655.1	11.2	714.0	37.5	638.4	9.1

Table 28. Sample 170319A (continued).

		Isotope ratios									Apparent ages (Ma)							
Analysis	U (ppm)	$^{206}Pb/^{204}Pb$	U/Th	$^{206}Pb/^{207}Pb$	± (%)	$^{207}Pb/^{235}U$	± (%)	$^{206}Pb/^{238}U$	± (%)	error corr.	$^{206}Pb/^{238}U$	± (Ma)	$^{207}Pb/^{235}U$	± (Ma)	$^{206}Pb/^{207}Pb$	± (Ma)	Best age (Ma)	± (Ma)
#57	262	209461	3.2	16.1454	0.8	0.8994	1.2	0.1054	0.9	0.78	645.8	5.8	651.4	5.8	672.0	16.4	645.8	5.8
#199	128	44821	0.5	16.0952	0.8	0.9032	1.2	0.1055	0.9	0.75	646.4	5.4	653.4	5.6	678.6	16.5	646.4	5.4
#39	328	98427	1.5	16.0733	0.7	0.9255	1.3	0.1079	1.0	0.81	660.7	6.5	665.3	6.2	681.5	15.9	660.7	6.5
#62	700	5678189	54.1	16.0299	0.8	0.9378	1.6	0.1091	1.4	0.88	667.4	9.2	671.7	8.1	687.3	16.9	667.4	9.2
#182	85	33308	0.8	15.9431	1.0	0.9625	1.4	0.1113	1.1	0.74	680.5	6.9	684.6	7.2	698.9	20.7	680.5	6.9
#174	24	33325	2.9	15.7900	2.0	1.0049	2.2	0.1151	0.9	0.43	702.5	6.2	706.3	11.0	719.3	41.5	702.5	6.2
#68	207	96727	1.1	15.8679	1.0	1.0092	1.3	0.1162	0.8	0.63	708.6	5.3	708.5	6.4	708.9	20.9	708.6	5.3
#43	306	186024	6.1	15.0841	1.1	1.0637	1.7	0.1164	1.3	0.77	709.9	9.0	735.6	9.1	815.7	23.4	709.9	9.0
#4	237	263365	2.9	14.8183	1.0	1.1041	1.8	0.1187	1.4	0.81	723.1	9.9	755.3	9.4	852.7	21.3	723.1	9.9
#147	41	8852	0.5	15.0666	1.8	1.1958	2.1	0.1307	1.0	0.48	792.0	7.4	798.6	11.5	818.1	38.2	792.0	7.4
#34	232	95080	0.9	14.6690	0.8	1.2498	1.2	0.1330	0.9	0.75	805.1	6.8	823.3	6.7	873.8	16.1	805.1	6.8
#21	34	100971	1.5	14.4954	1.4	1.4001	1.9	0.1473	1.4	0.70	885.6	11.2	889.0	11.4	898.3	28.4	885.6	11.2
#211	76	21139	1.7	14.3129	1.1	1.4611	1.5	0.1517	0.9	0.64	910.7	8.0	914.5	9.0	924.5	23.6	924.5	23.6
#209	134	60539	2.2	14.2521	1.2	1.4073	1.7	0.1455	1.1	0.69	875.9	9.4	892.0	9.9	933.2	25.0	933.2	25.0
#143	42	7598	1.0	14.1235	1.1	1.5773	1.5	0.1616	1.0	0.67	965.9	9.2	961.3	9.5	951.8	23.1	951.8	23.1
#19	85	28941	0.9	14.0734	0.7	1.3987	1.3	0.1428	1.1	0.83	860.6	8.9	888.4	7.9	959.0	15.2	959.0	15.2
#111	171	35050	1.3	14.0663	1.2	1.5781	1.4	0.1611	0.8	0.58	962.7	7.6	961.6	9.0	960.1	24.1	960.1	24.1
#78	44	31319	1.0	14.0400	1.3	1.4765	1.6	0.1504	1.0	0.62	903.3	8.3	920.8	9.7	963.9	25.7	963.9	25.7
#98	41	9113	1.0	14.0103	1.3	1.6248	1.7	0.1652	1.2	0.67	985.5	10.7	979.9	10.9	968.2	26.1	968.2	26.1
#73	168	22250	0.8	13.8618	0.9	1.6292	1.4	0.1639	1.1	0.76	978.2	9.5	981.5	8.7	989.9	18.3	989.9	18.3
#195	82	15832	0.9	13.8087	1.1	1.6147	1.5	0.1618	1.0	0.64	966.7	8.6	975.9	9.3	997.7	23.1	997.7	23.1
#140	218	2135011	2.1	13.7774	1.1	1.4615	1.6	0.1461	1.2	0.75	879.1	10.2	914.6	9.9	1002.3	21.8	1002.3	21.8
#132	334	97894	1.8	13.7644	0.7	1.6498	1.2	0.1648	0.9	0.76	983.2	8.0	989.5	7.3	1004.2	15.2	1004.2	15.2
#130	84	32263	0.9	13.7509	1.1	1.6272	1.4	0.1624	1.0	0.66	969.8	8.6	980.8	9.1	1006.2	21.9	1006.2	21.9
#24	111	18151	1.6	13.7067	0.9	1.6610	1.5	0.1652	1.3	0.81	985.5	11.4	993.7	9.8	1012.7	18.3	1012.7	18.3
#126	573	874672	3.8	13.6588	0.8	1.6677	1.2	0.1653	1.0	0.77	986.1	8.7	996.3	7.8	1019.8	15.7	1019.8	15.7
#124	117	41852	1.9	13.6164	1.0	1.6826	1.4	0.1662	1.0	0.69	991.3	9.1	1002.0	9.2	1026.1	21.1	1026.1	21.1

Table 28. Sample 170319A (continued).

		Isotope ratios									Apparent ages (Ma)							
Analysis	U (ppm)	$^{206}Pb/^{204}Pb$	U/Th	$^{206}Pb/^{207}Pb$	± (%)	$^{207}Pb/^{235}U$	± (%)	$^{206}Pb/^{238}U$	± (%)	error corr.	$^{206}Pb/^{238}U$	± (Ma)	$^{207}Pb/^{235}U$	± (Ma)	$^{206}Pb/^{207}Pb$	± (Ma)	Best age (Ma)	± (Ma)
#22	104	19914	2.1	13.6148	1.1	1.7597	1.7	0.1738	1.2	0.74	1033.2	11.8	1030.7	10.8	1026.4	22.9	1026.4	22.9
#212	145	47275	1.7	13.5988	0.8	1.6636	1.2	0.1641	0.9	0.73	979.8	8.2	994.7	7.8	1028.7	17.2	1028.7	17.2
#176	418	149361	1.2	13.5396	1.0	1.7460	1.7	0.1715	1.4	0.82	1020.5	13.2	1025.7	11.0	1037.5	19.8	1037.5	19.8
#16	18	10531	0.3	13.5247	1.6	1.7723	1.9	0.1739	1.0	0.52	1033.7	9.3	1035.4	12.1	1039.8	32.2	1039.8	32.2
#70	151	83498	2.7	13.5085	0.9	1.6915	1.4	0.1658	1.0	0.76	988.9	9.4	1005.3	8.6	1042.2	17.9	1042.2	17.9
#35	168	48606	1.6	13.4982	0.7	1.7740	1.2	0.1737	1.0	0.79	1032.7	9.3	1036.0	7.9	1043.7	15.0	1043.7	15.0
#64	193	83205	0.9	13.4790	0.9	1.7094	1.4	0.1672	1.1	0.77	996.6	10.2	1012.1	9.2	1046.6	18.6	1046.6	18.6
#106	47	73586	1.5	13.4556	0.9	1.7426	1.4	0.1701	1.0	0.75	1012.9	9.6	1024.4	8.9	1050.1	18.5	1050.1	18.5
#158	167	106448	1.4	13.4457	0.8	1.8280	1.1	0.1783	0.7	0.65	1057.9	7.1	1055.6	7.3	1051.6	17.1	1051.6	17.1
#41	124	32119	1.3	13.4121	0.8	1.8978	1.2	0.1847	0.9	0.73	1092.5	8.8	1080.3	7.9	1056.7	16.4	1056.7	16.4
#107	116	1802723	1.2	13.3925	0.9	1.8480	1.4	0.1796	1.1	0.77	1064.7	10.7	1062.7	9.4	1059.6	18.4	1059.6	18.4
#123	87	30146	1.3	13.3870	0.9	1.7540	1.4	0.1704	1.0	0.72	1014.2	9.3	1028.6	8.9	1060.4	19.1	1060.4	19.1
#48	122	22761	1.6	13.3845	1.1	1.8975	1.5	0.1843	1.1	0.72	1090.3	11.1	1080.2	10.2	1060.8	21.3	1060.8	21.3
#60	78	26483	2.0	13.3661	1.1	1.8249	1.7	0.1770	1.2	0.73	1050.5	11.7	1054.4	10.9	1063.6	23.0	1063.6	23.0
#59	97	122095	1.8	13.3279	1.2	1.8220	1.6	0.1762	1.1	0.65	1046.1	10.4	1053.4	10.8	1069.3	25.1	1069.3	25.1
#186	22	10148	1.2	13.3226	1.8	1.7783	2.0	0.1719	1.0	0.47	1022.6	9.1	1037.6	13.2	1070.1	36.1	1070.1	36.1
#50	92	22572	0.7	13.3005	1.0	1.8871	1.6	0.1821	1.3	0.80	1078.5	13.0	1076.6	10.9	1073.5	19.9	1073.5	19.9
#79	80	30389	2.2	13.2630	1.0	1.9635	1.4	0.1890	1.0	0.68	1115.7	9.9	1103.1	9.5	1079.1	20.7	1079.1	20.7
#100	54	320371	0.9	13.2077	1.0	1.8417	1.5	0.1765	1.1	0.75	1047.8	11.1	1060.5	10.0	1087.5	20.1	1087.5	20.1
#20	38	22624	1.1	13.1995	1.2	1.8777	1.5	0.1798	1.0	0.64	1066.0	9.7	1073.2	10.2	1088.8	23.5	1088.8	23.5
#33	63	34021	1.8	13.1549	0.9	1.8361	1.4	0.1753	1.0	0.74	1041.0	9.8	1058.5	9.0	1095.5	18.2	1095.5	18.2
#110	59	65131	2.2	13.1410	1.1	1.9147	1.4	0.1826	0.9	0.66	1081.0	9.3	1086.2	9.4	1097.6	21.2	1097.6	21.2
#178	249	89140	3.0	12.9629	0.9	2.0229	1.4	0.1903	1.0	0.73	1122.8	10.3	1123.2	9.3	1124.9	18.5	1124.9	18.5
#10	71	63276	0.5	12.9436	1.1	1.9889	1.5	0.1868	1.1	0.72	1104.0	11.4	1111.8	10.5	1127.9	21.2	1127.9	21.2
#183	361	48480	1.5	12.8852	0.8	1.7370	1.5	0.1624	1.2	0.82	970.1	10.8	1022.4	9.5	1136.9	16.8	1136.9	16.8

Table 28. Sample 170319A (continued).

		Isotope ratios									Apparent ages (Ma)							
Analysis	U	$^{206}Pb/^{204}Pb$	U/Th	$^{206}Pb/^{207}Pb$	±	$^{207}Pb/^{235}U$	±	$^{206}Pb/^{238}U$	±	error	$^{206}Pb/^{238}U$	±	$^{207}Pb/^{235}U$	±	$^{206}Pb/^{207}Pb$	±	Best age	±
	(ppm)				(%)		(%)		(%)	corr.		(Ma)		(Ma)		(Ma)	(Ma)	(Ma)
#119	242	99314	2.3	12.8742	0.8	2.0688	1.3	0.1933	1.0	0.79	1139.0	10.8	1138.6	8.9	1138.6	15.9	1138.6	15.9
#142	83	34510	2.0	12.8273	1.0	2.1193	1.4	0.1973	1.0	0.69	1160.5	10.1	1155.1	9.5	1145.8	19.7	1145.8	19.7
#28	46	44284	0.4	12.8151	1.1	1.9986	1.7	0.1858	1.2	0.75	1098.8	12.6	1115.0	11.3	1147.7	22.0	1147.7	22.0
#44	169	39466	1.4	12.7700	1.1	2.1134	1.5	0.1958	0.9	0.64	1152.8	9.8	1153.2	10.0	1154.7	22.2	1154.7	22.2
#175	22	16340	0.9	12.7405	1.4	2.0726	1.8	0.1916	1.1	0.61	1130.0	11.1	1139.8	12.1	1159.3	27.9	1159.3	27.9
#47	97	52329	0.8	12.6734	1.2	2.1037	1.4	0.1934	0.8	0.56	1140.0	8.1	1150.0	9.6	1169.7	22.9	1169.7	22.9
#180	177	70701	2.4	12.6154	0.8	2.1726	1.3	0.1989	1.0	0.77	1169.2	10.5	1172.3	8.8	1178.9	16.0	1178.9	16.0
#40	124	27121	1.2	12.6070	0.9	2.2579	1.4	0.2065	1.0	0.75	1210.3	11.4	1199.2	9.6	1180.2	17.8	1180.2	17.8
#71	321	140344	1.5	12.5979	0.8	2.2045	1.3	0.2015	0.9	0.76	1183.4	10.3	1182.5	8.8	1181.6	16.2	1181.6	16.2
#8	141	70924	2.6	12.5622	0.9	2.1618	1.6	0.1970	1.3	0.81	1159.4	13.4	1168.8	10.9	1187.2	18.4	1187.2	18.4
#87	25	13653	0.5	12.5504	1.4	2.0469	2.0	0.1864	1.4	0.72	1101.8	14.6	1131.3	13.7	1189.1	27.5	1189.1	27.5
#11	67	30011	1.9	12.5486	1.0	2.1885	1.5	0.1993	1.1	0.74	1171.4	11.7	1177.4	10.3	1189.3	19.6	1189.3	19.6
#12	123	479696	1.9	12.5475	1.0	2.2014	1.5	0.2004	1.1	0.74	1177.6	11.8	1181.5	10.4	1189.5	19.7	1189.5	19.7
#129	917	70878	1.2	12.5222	0.9	1.7651	3.1	0.1604	3.0	0.96	958.9	26.5	1032.7	20.1	1193.5	16.9	1193.5	16.9
#215	99	830704	2.1	12.5212	0.9	2.2267	1.5	0.2023	1.2	0.80	1187.7	12.6	1189.5	10.2	1193.7	17.4	1193.7	17.4
#90	59	36472	1.9	12.4578	1.3	2.3466	2.2	0.2121	1.8	0.80	1240.1	20.1	1226.5	15.8	1203.6	26.2	1203.6	26.2
#185	109	31577	1.6	12.4168	1.1	2.2280	1.6	0.2007	1.2	0.72	1179.2	12.8	1189.9	11.5	1210.1	22.5	1210.1	22.5
#151	128	69609	2.3	12.3985	1.1	2.1380	1.5	0.1923	1.1	0.71	1134.0	11.3	1161.2	10.6	1213.1	21.1	1213.1	21.1
#13	564	136202	5.5	12.3263	1.0	2.2609	1.7	0.2022	1.4	0.83	1187.2	15.7	1200.2	12.3	1224.5	19.2	1224.5	19.2
#145	247	26143	1.4	12.2833	1.4	2.1794	1.9	0.1942	1.3	0.67	1144.3	13.1	1174.5	13.1	1231.4	27.6	1231.4	27.6
#96	75	22580	0.7	11.9031	1.0	2.6215	1.4	0.2264	1.0	0.70	1315.6	11.4	1306.7	10.1	1292.8	19.2	1292.8	19.2
#61	183	60285	1.8	11.6934	1.0	2.7521	1.4	0.2335	0.9	0.66	1352.8	11.1	1342.7	10.2	1327.3	19.8	1327.3	19.8
#38	154	99904	1.7	11.6412	1.0	2.7847	1.3	0.2352	0.9	0.66	1361.8	10.7	1351.4	9.9	1335.9	19.3	1335.9	19.3
#172	53	13230	1.2	11.3565	1.2	2.9362	1.6	0.2419	1.0	0.64	1396.8	12.5	1391.3	11.8	1383.7	23.1	1383.7	23.1
#154	20	10388	0.6	11.1010	1.4	2.8150	1.9	0.2267	1.4	0.71	1317.4	16.3	1359.5	14.4	1427.2	25.9	1427.2	25.9
#220	539	676330	2.0	11.0823	0.9	2.8571	1.4	0.2297	1.0	0.77	1333.2	12.5	1370.7	10.2	1430.5	16.6	1430.5	16.6
#153	98	47137	2.3	10.7050	0.9	3.4264	1.4	0.2661	1.0	0.74	1521.2	13.9	1510.5	11.0	1496.3	17.8	1496.3	17.8

Table 28. Sample 170319A (continued).

		Isotope ratios									Apparent ages (Ma)							
Analysis	U (ppm)	$^{206}Pb/^{204}Pb$	U/Th	$^{206}Pb/^{207}Pb$	± (%)	$^{207}Pb/^{235}U$	± (%)	$^{206}Pb/^{238}U$	± (%)	error corr.	$^{206}Pb/^{238}U$	± (Ma)	$^{207}Pb/^{235}U$	± (Ma)	$^{206}Pb/^{207}Pb$	± (Ma)	Best age (Ma)	± (Ma)
#97	148	94926	1.1	10.3138	0.9	3.6759	1.3	0.2751	0.9	0.69	1566.6	12.0	1566.1	10.0	1566.4	17.1	1566.4	17.1
#206	105	459728	0.7	10.0250	0.9	3.5963	1.6	0.2616	1.4	0.84	1498.0	18.1	1548.7	12.9	1619.4	16.5	1619.4	16.5
#29	36	23449	1.1	9.9972	1.7	3.6712	2.1	0.2663	1.2	0.58	1522.0	16.8	1565.1	17.1	1624.6	32.4	1624.6	32.4
#201	238	72051	1.8	9.7605	1.2	3.6123	1.8	0.2558	1.4	0.76	1468.4	17.9	1552.2	14.2	1669.0	21.4	1669.0	21.4
#76	66	7735	2.9	9.6220	2.0	3.7849	2.5	0.2642	1.5	0.58	1511.5	19.6	1589.5	20.1	1695.4	37.6	1695.4	37.6
#150	186	4350	2.2	9.5247	4.7	3.4926	4.9	0.2414	1.3	0.26	1393.8	16.2	1525.5	38.8	1714.1	87.3	1714.1	87.3
#133	108	94852	0.9	9.3265	0.9	4.5905	1.3	0.3106	0.9	0.70	1743.9	13.5	1747.5	10.5	1752.7	16.5	1752.7	16.5
#15	119	77079	1.4	9.2991	0.8	4.5553	1.1	0.3074	0.7	0.70	1727.7	11.2	1741.1	8.9	1758.1	14.0	1758.1	14.0
#91	276	77270	0.8	9.1612	0.9	4.7899	1.6	0.3184	1.3	0.81	1781.9	20.0	1783.1	13.3	1785.4	16.9	1785.4	16.9
#6	182	62297	1.2	9.1496	0.9	4.7080	1.4	0.3126	1.0	0.72	1753.3	15.1	1768.7	11.4	1787.7	17.1	1787.7	17.1
#80	399	308233	5.2	8.8909	1.3	5.0632	2.6	0.3266	2.3	0.88	1822.0	36.8	1830.0	22.3	1839.8	22.7	1839.8	22.7
#92	256	84657	6.5	8.8571	0.9	5.1318	1.5	0.3298	1.2	0.80	1837.4	19.2	1841.4	12.7	1846.7	16.1	1846.7	16.1
#17	139	207026	0.9	8.8232	1.1	5.1907	1.4	0.3323	0.9	0.64	1849.6	14.4	1851.1	11.9	1853.6	19.4	1853.6	19.4
#112	119	141544	0.7	8.8182	0.8	5.5092	1.3	0.3525	1.1	0.78	1946.5	17.8	1902.0	11.6	1854.6	15.1	1854.6	15.1
#115	108	279579	0.4	8.3263	1.0	6.0056	1.4	0.3628	1.0	0.71	1995.5	17.1	1976.7	12.3	1957.7	17.9	1957.7	17.9
#30	188	61421	0.6	8.1610	0.8	6.0720	1.2	0.3596	0.9	0.71	1980.1	14.7	1986.2	10.5	1993.4	15.0	1993.4	15.0
#127	284	184258	0.4	8.1440	0.8	5.7990	1.4	0.3427	1.1	0.79	1899.5	17.7	1946.3	11.9	1997.1	15.0	1997.1	15.0
#14	263	69429	3.1	7.9331	0.9	5.5754	1.5	0.3209	1.2	0.78	1794.2	18.3	1912.3	12.9	2043.6	16.7	2043.6	16.7
#131	68	136717	1.1	7.7592	1.0	6.6946	1.6	0.3769	1.2	0.76	2061.8	21.7	2071.9	14.3	2082.7	18.3	2082.7	18.3
#137	129	233738	0.8	7.5933	0.9	6.1954	1.4	0.3413	1.1	0.79	1893.1	17.8	2003.8	12.1	2120.7	15.0	2120.7	15.0
#192	86	84656	2.2	7.4204	0.8	7.2007	1.2	0.3877	0.9	0.74	2112.1	16.5	2136.6	11.0	2160.9	14.4	2160.9	14.4
#114	89	80008	0.8	5.6077	0.7	11.7971	1.4	0.4800	1.1	0.84	2527.3	23.9	2588.4	12.8	2637.4	12.3	2637.4	12.3
#162	100	104292	1.4	4.5287	1.2	17.0065	1.7	0.5588	1.3	0.75	2861.8	30.0	2935.2	16.7	2986.6	18.6	2986.6	18.6

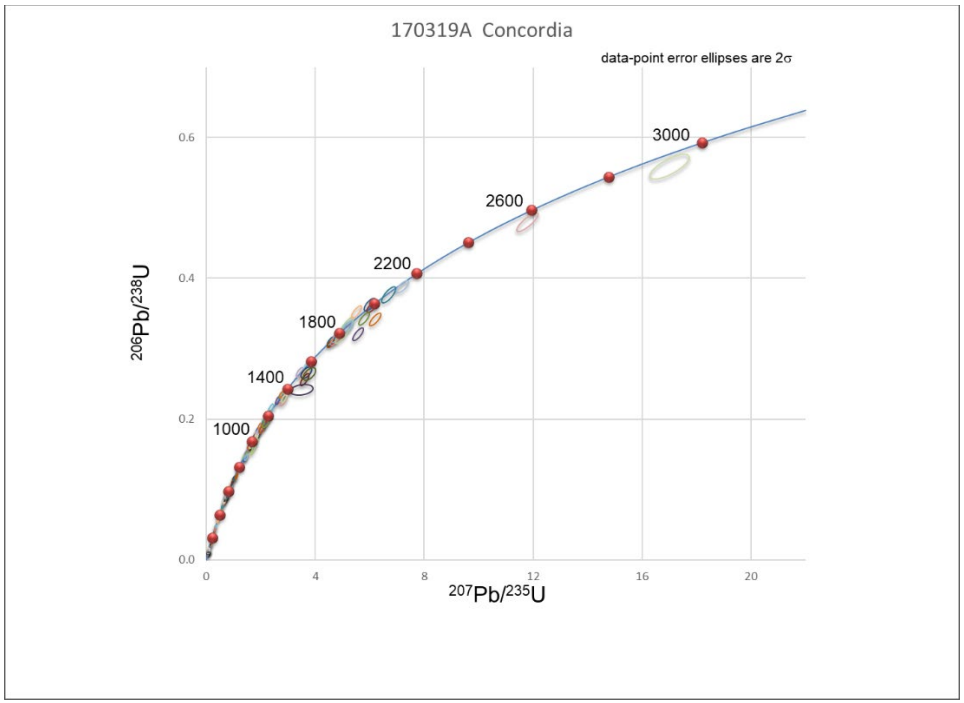

Figure 75. Concordia plot for sample 170319A

Table 29. U-Pb DZ geochronology analysis data for sample 170323E, ordered by best age.

		Isotope ratios									Apparent ages (Ma)							
Analysis	U (ppm)	$^{206}Pb/^{204}Pb$	U/Th	$^{206}Pb/^{207}Pb$	± (%)	$^{207}Pb/^{235}U$	± (%)	$^{206}Pb/^{238}U$	± (%)	error corr.	$^{206}Pb/^{238}U$	± (Ma)	$^{207}Pb/^{235}U$	± (Ma)	$^{206}Pb/^{207}Pb$	± (Ma)	Best age (Ma)	± (Ma)
#166	1822	21193	0.5	22.0873	2.0	0.0087	2.4	0.0014	1.3	0.56	8.9	0.1	8.7	0.2	NA	NA	8.9	0.1
#44	251	1034	1.6	30.3129	18.5	0.0416	18.6	0.0092	1.3	0.07	58.8	0.8	41.4	7.5	NA	NA	58.8	0.8
#209	233	1315	1.5	21.5223	4.8	0.0650	5.0	0.0101	1.4	0.28	65.1	0.9	63.9	3.1	21.8	115.6	65.1	0.9
#39	399	46447	2.0	19.7325	2.9	0.0903	3.1	0.0129	1.1	0.37	82.8	0.9	87.8	2.6	226.2	66.7	82.8	0.9
#220	3504	78873	0.7	20.0832	1.1	0.1142	1.7	0.0166	1.3	0.77	106.4	1.4	109.8	1.7	185.3	25.1	106.4	1.4
#57	2466	2953	2.1	8.6599	2.8	0.6199	4.2	0.0390	3.1	0.74	246.3	7.5	489.8	16.2	1887.3	50.4	246.3	7.5
#150	566	23262	1.5	19.7720	1.2	0.2821	1.8	0.0405	1.3	0.72	255.7	3.2	252.3	3.9	221.6	28.2	255.7	3.2
#115	1269	34289	1.0	18.0762	0.9	0.3177	1.5	0.0417	1.2	0.80	263.2	3.1	280.1	3.7	425.2	20.2	263.2	3.1
#140	1376	77533	0.9	19.3013	0.9	0.3022	1.3	0.0423	1.0	0.77	267.2	2.7	268.1	3.2	277.1	19.6	267.2	2.7
#54	1724	4618	3.7	12.7858	1.1	0.4818	1.5	0.0447	1.0	0.65	281.9	2.7	399.3	5.0	1152.2	22.8	281.9	2.7
#206	1471	3700	1.2	9.1587	1.0	0.7676	3.4	0.0510	3.3	0.95	320.7	10.2	578.4	15.1	1785.8	18.6	320.7	10.2
#24	48	13091	0.9	17.1958	1.8	0.7178	2.2	0.0896	1.2	0.54	552.9	6.3	549.4	9.2	535.6	40.0	552.9	6.3
#23	405	58186	2.9	17.0256	0.8	0.7648	1.8	0.0945	1.6	0.88	582.0	8.7	576.8	7.8	557.3	18.4	582.0	8.7
#112	298	87775	1.0	16.5089	0.7	0.8003	2.8	0.0959	2.7	0.96	590.1	15.0	597.0	12.5	624.1	16.0	590.1	15.0
#1	50	125548	0.9	16.6133	1.7	0.7969	2.1	0.0961	1.3	0.62	591.3	7.4	595.1	9.5	610.5	35.8	591.3	7.4
#156	394	14921	1.1	16.4863	0.9	0.8428	1.6	0.1008	1.4	0.84	619.2	8.2	620.7	7.7	627.1	19.2	619.2	8.2
#98	535	66976	1.0	16.4175	0.9	0.8659	1.4	0.1031	1.0	0.75	632.8	6.2	633.3	6.5	636.1	19.5	632.8	6.2
#141	77	77693	2.1	16.1015	1.1	0.9438	1.6	0.1103	1.1	0.69	674.3	7.0	674.9	7.8	677.8	24.5	674.3	7.0
#27	352	250574	2.3	15.4157	0.9	1.0341	1.3	0.1157	1.0	0.75	705.6	6.6	721.0	6.8	770.1	18.1	705.6	6.6
#210	1123	72357	2.5	15.4102	1.0	1.0423	1.4	0.1165	1.0	0.71	710.6	6.6	725.1	7.2	770.8	20.6	710.6	6.6
#103	190	38205	3.0	15.8455	0.9	1.0331	1.5	0.1188	1.2	0.79	723.5	7.9	720.5	7.5	711.9	19.0	723.5	7.9
#175	245	25580	1.2	15.1173	1.0	1.1789	1.4	0.1293	1.0	0.70	783.9	7.2	790.8	7.7	811.1	20.8	783.9	7.2
#82	66	9698	2.1	13.9704	1.2	1.6195	1.8	0.1642	1.3	0.73	979.9	12.1	977.8	11.4	974.0	25.2	974.0	25.2
#123	263	39856	1.6	13.6381	0.8	1.6243	1.5	0.1607	1.3	0.86	960.9	11.3	979.7	9.3	1022.9	15.5	1022.9	15.5
#7	46	9470	4.1	13.6345	1.6	1.7253	2.0	0.1707	1.1	0.56	1015.9	10.5	1018.0	12.8	1023.4	33.3	1023.4	33.3
#52	445	330379	2.7	13.6075	0.9	1.7283	1.4	0.1706	1.1	0.77	1015.7	10.1	1019.1	8.9	1027.4	17.9	1027.4	17.9
#95	187	75272	3.9	13.3924	0.8	1.7582	1.4	0.1709	1.1	0.80	1016.8	10.3	1030.2	8.9	1059.6	16.7	1059.6	16.7

Table 29. Sample 170323E (continued).

		Isotope ratios									Apparent ages (Ma)							
Analysis	U (ppm)	$^{206}Pb/^{204}Pb$	U/Th	$^{206}Pb/^{207}Pb$	± (%)	$^{207}Pb/^{235}U$	± (%)	$^{206}Pb/^{238}U$	± (%)	error corr.	$^{206}Pb/^{238}U$	± (Ma)	$^{207}Pb/^{235}U$	± (Ma)	$^{206}Pb/^{207}Pb$	± (Ma)	Best age (Ma)	± (Ma)
#144	59	24482	1.9	13.3209	1.1	1.9083	1.5	0.1844	1.0	0.69	1091.2	10.5	1084.0	10.1	1070.4	22.1	1070.4	22.1
#12	544	77579	2.0	13.3193	0.7	1.6195	1.6	0.1565	1.5	0.90	937.4	12.9	977.8	10.4	1070.6	14.5	1070.6	14.5
#19	18	2634	2.7	13.1879	3.5	1.9413	3.7	0.1858	1.1	0.28	1098.4	10.6	1095.4	24.8	1090.5	71.0	1090.5	71.0
#73	278	28580	2.1	13.1545	0.9	1.8928	1.3	0.1807	1.0	0.76	1070.6	9.9	1078.6	8.8	1095.6	17.3	1095.6	17.3
#22	251	11705	1.1	13.0599	1.1	1.9481	1.7	0.1846	1.3	0.75	1092.1	12.7	1097.8	11.3	1110.0	22.2	1110.0	22.2
#111	95	19306	3.6	12.7351	1.1	2.1519	1.6	0.1988	1.2	0.72	1169.1	12.4	1165.7	11.2	1160.1	22.5	1160.1	22.5
#129	243	42328	2.4	12.6304	0.9	2.1453	1.4	0.1966	1.0	0.73	1157.0	10.8	1163.5	9.6	1176.5	18.7	1176.5	18.7
#147	625	155454	4.7	12.6260	0.8	2.1976	1.3	0.2013	1.0	0.80	1182.4	11.3	1180.3	9.1	1177.2	15.5	1177.2	15.5
#167	174	235976	13.1	12.4446	0.8	2.2557	1.2	0.2037	0.9	0.74	1195.1	10.0	1198.6	8.7	1205.7	16.5	1205.7	16.5
#30	207	1254000	1.4	12.3987	0.7	2.3246	1.2	0.2091	1.0	0.81	1224.2	11.1	1219.8	8.7	1213.0	14.2	1213.0	14.2
#87	233	22624	1.9	12.3606	0.8	2.2537	1.3	0.2021	1.1	0.81	1186.7	11.6	1197.9	9.3	1219.1	15.3	1219.1	15.3
#211	271	30482	3.2	12.3480	0.9	2.3290	1.2	0.2087	0.8	0.69	1221.7	9.3	1221.2	8.6	1221.1	17.3	1221.1	17.3
#93	255	61736	2.5	12.3375	0.7	2.3060	1.2	0.2064	0.9	0.79	1209.8	10.0	1214.1	8.2	1222.7	13.9	1222.7	13.9
#85	185	52295	2.7	12.2970	0.7	2.3527	1.1	0.2099	0.9	0.81	1228.4	10.2	1228.4	8.0	1229.2	12.8	1229.2	12.8
#89	141	14134	3.6	12.2772	1.1	2.3720	1.8	0.2113	1.4	0.79	1235.8	15.7	1234.2	12.5	1232.4	21.0	1232.4	21.0
#153	515	65788	1.5	11.9722	1.1	2.4861	1.7	0.2160	1.3	0.77	1260.5	15.3	1268.0	12.6	1281.5	21.7	1281.5	21.7
#194	317	62408	1.0	11.8395	0.8	2.5758	1.2	0.2213	0.9	0.74	1288.6	10.7	1293.8	9.1	1303.2	16.3	1303.2	16.3
#83	142	176662	1.5	11.7628	0.9	2.6309	1.3	0.2245	0.9	0.70	1305.9	10.9	1309.3	9.6	1315.8	18.0	1315.8	18.0
#67	250	223200	2.7	11.7418	1.0	2.6278	1.4	0.2239	0.9	0.70	1302.3	11.2	1308.4	10.1	1319.3	19.0	1319.3	19.0
#69	361	77316	1.6	11.7366	0.9	2.7240	1.6	0.2320	1.3	0.81	1344.8	15.4	1335.0	11.7	1320.2	18.1	1320.2	18.1
#72	98	32290	4.5	11.7062	1.0	2.6084	1.4	0.2216	1.0	0.69	1290.1	11.3	1303.0	10.3	1325.2	19.7	1325.2	19.7
#43	236	34764	2.3	11.6814	1.1	2.7312	1.4	0.2315	1.0	0.67	1342.3	11.7	1337.0	10.7	1329.3	20.7	1329.3	20.7
#68	485	127012	1.4	11.6566	0.8	2.6947	1.4	0.2279	1.1	0.81	1323.6	13.2	1327.0	10.1	1333.4	15.6	1333.4	15.6
#46	223	37641	1.0	11.6447	1.1	2.7018	1.7	0.2283	1.3	0.75	1325.5	15.3	1328.9	12.6	1335.4	21.8	1335.4	21.8
#6	104	14302	1.6	11.6364	1.0	2.6817	1.5	0.2264	1.1	0.74	1315.7	12.9	1323.4	10.8	1336.8	18.9	1336.8	18.9
#125	432	81603	1.6	11.6142	0.7	2.7249	1.2	0.2296	1.0	0.82	1332.6	12.2	1335.3	9.2	1340.4	13.7	1340.4	13.7
#161	182	60208	1.7	11.5697	1.0	2.6216	1.4	0.2201	1.0	0.71	1282.3	11.3	1306.7	10.1	1347.9	18.6	1347.9	18.6

Table 29. Sample 170323E (continued).

				Isotope ratios							Apparent ages (Ma)							
Analysis	U	$^{206}Pb/^{204}Pb$	U/Th	$^{206}Pb/^{207}Pb$	±	$^{207}Pb/^{235}U$	±	$^{206}Pb/^{238}U$	±	error	$^{206}Pb/^{238}U$	±	$^{207}Pb/^{235}U$	±	$^{206}Pb/^{207}Pb$	±	Best age	±
	(ppm)				(%)		(%)		(%)	corr.		(Ma)		(Ma)		(Ma)	(Ma)	(Ma)
#48	152	24495	2.0	11.5549	0.8	2.8775	1.3	0.2413	1.0	0.75	1393.2	12.1	1376.0	9.7	1350.3	16.4	1350.3	16.4
#94	227	28279	1.2	11.5532	0.9	2.5456	1.8	0.2134	1.5	0.85	1246.9	17.1	1285.2	12.9	1350.6	17.9	1350.6	17.9
#102	164	162636	2.7	11.5476	0.9	2.7833	1.4	0.2332	1.0	0.75	1351.3	12.5	1351.1	10.3	1351.5	17.7	1351.5	17.7
#121	311	412267	1.1	11.5444	0.8	2.3789	1.4	0.1993	1.2	0.82	1171.4	12.4	1236.3	10.1	1352.1	15.7	1352.1	15.7
#8	154	23477	2.2	11.5395	0.7	2.7145	1.3	0.2273	1.1	0.83	1320.2	12.8	1332.4	9.6	1352.9	13.7	1352.9	13.7
#139	246	52303	3.2	11.5373	1.0	2.5270	1.4	0.2115	0.9	0.68	1237.0	10.4	1279.8	9.9	1353.3	19.2	1353.3	19.2
#9	145	17034	2.5	11.5364	0.9	2.6095	2.1	0.2184	1.9	0.90	1273.6	22.0	1303.3	15.6	1353.4	18.1	1353.4	18.1
#92	237	89857	2.8	11.5170	0.9	2.8168	1.3	0.2354	1.0	0.76	1362.7	12.5	1360.0	10.1	1356.7	17.0	1356.7	17.0
#47	159	33394	1.9	11.4995	1.2	2.8546	1.5	0.2382	1.0	0.63	1377.2	11.9	1370.0	11.5	1359.6	22.9	1359.6	22.9
#213	543	805967	9.5	11.4979	0.9	2.7940	1.3	0.2331	0.9	0.74	1350.7	11.4	1353.9	9.5	1359.9	16.7	1359.9	16.7
#53	382	118183	2.1	11.4849	0.8	2.7755	2.2	0.2313	2.1	0.94	1341.2	24.9	1349.0	16.3	1362.0	14.5	1362.0	14.5
#136	383	65132	1.1	11.4368	0.6	2.6610	1.4	0.2208	1.3	0.91	1286.2	15.0	1317.7	10.5	1370.1	11.6	1370.1	11.6
#20	357	72995	1.2	11.4358	0.8	2.8129	1.4	0.2334	1.1	0.81	1352.3	13.8	1359.0	10.5	1370.3	15.6	1370.3	15.6
#169	167	80397	2.3	11.4292	1.1	2.8661	1.5	0.2377	1.0	0.70	1374.6	13.0	1373.0	11.2	1371.4	20.5	1371.4	20.5
#205	471	199207	2.9	11.4292	0.8	2.8152	1.2	0.2335	0.8	0.71	1352.6	10.0	1359.6	8.7	1371.4	15.9	1371.4	15.9
#134	359	202910	2.6	11.3752	0.8	2.6989	1.6	0.2228	1.3	0.85	1296.4	15.6	1328.1	11.6	1380.5	15.7	1380.5	15.7
#208	67	63970	0.9	11.3673	1.0	2.8225	1.6	0.2328	1.3	0.80	1349.1	15.2	1361.5	11.8	1381.8	18.3	1381.8	18.3
#75	127	22231	0.6	11.3663	1.0	2.8097	1.5	0.2317	1.1	0.74	1343.5	13.1	1358.1	11.0	1382.0	19.1	1382.0	19.1
#110	214	164435	1.6	11.3587	0.7	2.9357	1.4	0.2420	1.2	0.86	1396.8	15.3	1391.2	10.8	1383.3	14.0	1383.3	14.0
#193	55	66990	1.8	11.3310	1.3	2.6529	2.3	0.2181	1.9	0.83	1271.9	22.1	1315.5	16.9	1388.0	24.4	1388.0	24.4
#157	202	26203	2.1	11.2839	1.0	2.8912	1.5	0.2367	1.1	0.74	1369.6	13.4	1379.6	11.1	1396.0	19.0	1396.0	19.0
#158	287	68924	1.6	11.2736	0.8	2.8444	1.4	0.2327	1.2	0.83	1348.5	14.5	1367.3	10.8	1397.7	15.3	1397.7	15.3
#207	580	2204206	1.0	11.2168	0.9	2.9453	1.4	0.2397	1.1	0.79	1385.2	14.1	1393.6	10.9	1407.4	17.0	1407.4	17.0
#215	112	18871	4.0	11.2137	1.1	2.9588	1.6	0.2407	1.3	0.76	1390.6	15.7	1397.1	12.4	1407.9	20.3	1407.9	20.3
#163	202	60888	2.5	11.2112	1.0	2.7558	1.4	0.2242	1.0	0.73	1303.9	12.4	1343.7	10.7	1408.4	18.8	1408.4	18.8
#122	153	68122	2.0	11.0817	0.9	2.8460	1.3	0.2288	1.0	0.76	1328.4	11.9	1367.8	9.8	1430.6	16.3	1430.6	16.3
#65	309	24019	1.1	11.0465	1.0	2.5674	1.5	0.2058	1.1	0.74	1206.3	12.3	1291.4	11.1	1436.6	19.7	1436.6	19.7

Table 29. Sample 170323E (continued).

					Isotope ratios							Apparent ages (Ma)							
Analysis	U	$^{206}Pb/^{204}Pb$	U/Th	$^{206}Pb/^{207}Pb$	±	$^{207}Pb/^{235}U$	±	$^{206}Pb/^{238}U$	±	error	$^{206}Pb/^{238}U$	±	$^{207}Pb/^{235}U$	±	$^{206}Pb/^{207}Pb$	±	Best age	±
	(ppm)				(%)		(%)		(%)	corr.		(Ma)		(Ma)		(Ma)	(Ma)	(Ma)
#219	423	11341	1.1	11.0055	1.0	2.5487	1.6	0.2035	1.2	0.76	1194.2	13.0	1286.1	11.5	1443.7	19.4	1443.7	19.4
#70	193	30358	1.4	10.9147	0.9	2.9106	1.4	0.2305	1.1	0.75	1337.2	12.9	1384.7	10.7	1459.5	17.8	1459.5	17.8
#34	243	35816	3.2	10.7820	0.8	3.3430	1.3	0.2615	1.0	0.78	1497.6	13.2	1491.1	9.8	1482.7	14.8	1482.7	14.8
#90	192	59508	2.0	10.6754	0.9	3.3356	1.4	0.2584	1.1	0.79	1481.5	14.6	1489.4	11.0	1501.5	16.5	1501.5	16.5
#2	68	14691	0.7	10.4680	2.3	3.1270	2.5	0.2375	0.9	0.38	1373.7	11.5	1439.4	18.9	1538.5	42.8	1538.5	42.8
#178	212	46373	9.7	10.2092	0.6	3.7231	1.3	0.2758	1.2	0.90	1570.1	16.4	1576.3	10.4	1585.5	10.4	1585.5	10.4
#145	209	63731	5.9	10.1628	0.9	3.8401	1.4	0.2832	1.0	0.72	1607.3	13.9	1601.2	10.9	1594.0	17.5	1594.0	17.5
#132	286	26461	3.1	10.1016	0.8	3.7055	1.4	0.2716	1.1	0.80	1548.9	14.9	1572.6	10.8	1605.2	15.1	1605.2	15.1
#201	407	63474	2.0	9.8189	1.0	4.1901	1.8	0.2985	1.5	0.82	1684.0	22.2	1672.1	15.0	1658.0	19.4	1658.0	19.4
#149	305	55146	0.8	9.3006	0.9	4.6653	1.4	0.3148	1.1	0.78	1764.4	17.3	1761.0	12.1	1757.8	16.6	1757.8	16.6
#21	177	66100	1.7	9.2171	1.0	4.6060	1.5	0.3080	1.1	0.72	1731.1	16.3	1750.4	12.4	1774.3	18.9	1774.3	18.9
#49	154	202092	1.4	9.1127	1.0	4.7699	1.4	0.3154	0.9	0.66	1767.2	14.0	1779.6	11.5	1795.0	18.6	1795.0	18.6
#152	509	18834	1.5	9.0561	0.8	3.9199	1.4	0.2576	1.1	0.80	1477.4	15.0	1617.8	11.4	1806.4	15.3	1806.4	15.3
#190	72	20952	0.8	9.0394	0.8	4.9226	1.3	0.3229	1.0	0.77	1803.7	15.9	1806.1	11.0	1809.7	15.1	1809.7	15.1
#40	42	78151	1.2	8.8560	1.2	5.2956	1.5	0.3403	1.0	0.65	1888.0	16.5	1868.2	13.2	1846.9	21.2	1846.9	21.2
#212	360	206662	3.8	8.7854	0.8	5.1168	1.5	0.3262	1.2	0.82	1819.8	19.2	1838.9	12.5	1861.4	15.2	1861.4	15.2
#131	209	213502	1.6	8.7744	1.0	5.3114	1.4	0.3382	1.0	0.70	1877.8	16.3	1870.7	12.2	1863.6	18.5	1863.6	18.5
#217	149	68577	1.5	8.7473	0.8	5.2421	1.3	0.3327	1.0	0.79	1851.5	16.6	1859.5	11.1	1869.2	14.4	1869.2	14.4
#11	179	62670	2.0	8.6339	0.8	5.4054	1.2	0.3386	1.0	0.78	1880.1	15.8	1885.7	10.7	1892.7	14.2	1892.7	14.2
#26	655	234543	1.9	8.3063	0.6	5.8707	1.1	0.3538	0.9	0.82	1952.8	15.7	1956.9	9.8	1962.0	11.6	1962.0	11.6
#162	343	46927	3.2	8.2087	0.8	4.6943	1.7	0.2796	1.5	0.88	1589.3	21.1	1766.2	14.2	1983.1	14.5	1983.1	14.5
#16	189	30202	2.3	7.6369	0.8	5.6294	2.1	0.3119	1.9	0.91	1750.3	29.0	1920.6	17.9	2110.6	14.9	2110.6	14.9
#101	50	41029	0.8	7.2467	1.0	7.6864	1.5	0.4042	1.1	0.75	2188.2	20.5	2195.0	13.2	2202.2	16.9	2202.2	16.9
#61	99	7806	2.1	5.5923	1.3	11.1131	1.6	0.4509	1.0	0.59	2399.4	19.1	2532.7	15.0	2641.9	21.6	2641.9	21.6
#71	208	72571	1.6	5.4471	0.9	12.9905	2.0	0.5134	1.8	0.88	2671.2	38.6	2679.0	18.9	2685.5	15.7	2685.5	15.7

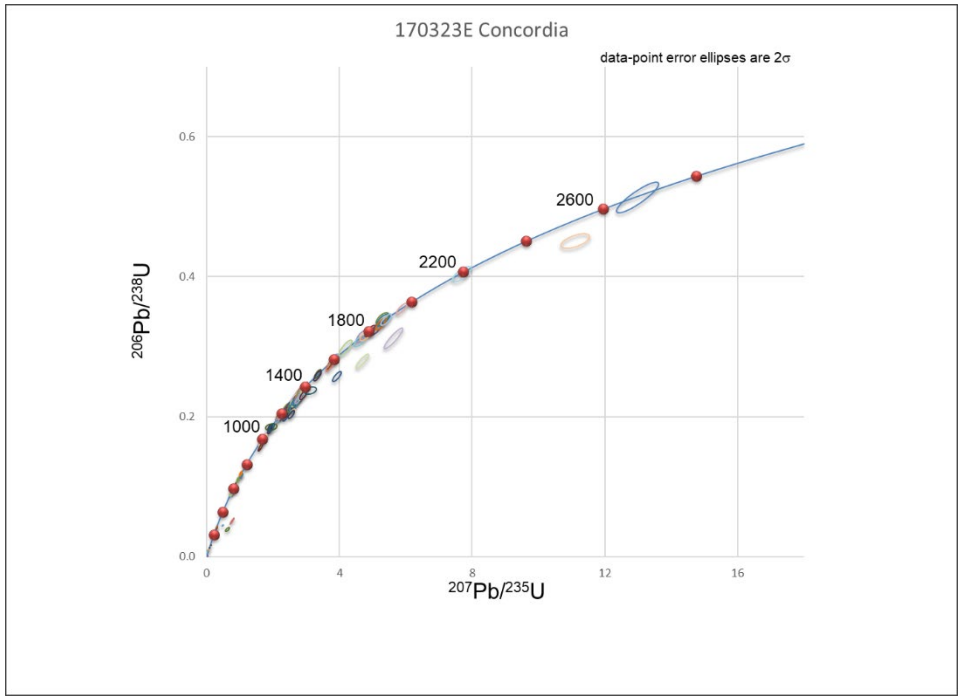

Figure 76. Concordia plot for sample 170323E

APPENDIX G

ISOTOPE DATA

Table 30. List of samples from PCB and EC arc-related igneous rocks used in isotope analysis.

Sample	Latitude	Longitude	Location	Rock type	Age (Ma)	Map Unit
15810A	-71.62051	-16.45656	Arequipa, Laderas	tonalite	178.0	KTi-tol
15811C	-71.41962	-16.58515	Arequipa	granodiorite	63.7	KTi-gd Tiabaya
170320C	-72.3886	-13.1881	Chilca	granite	455.0	PET-mgr,gr
170323B	-70.9256	-13.5776	Ccocha	gonalite	228.7	PET-mgr,gr
170323G	-70.4872	-13.8188	Ollachea	nepheline syenite	179.1	Jim-sie
170323H	-70.5157	-13.8708	Macusani	andesite porphyry	189.0	PEI-c
170324F	-70.374	-15.0464	Pucara	granodiorite	16.0	N-gd,tn
170327E	-72.5808	-13.1511	Machu Picchu	monzogranite	302.8	PET-mgr,gr
170329C	-72.9555	-13.7015	Abancay	tonalite	238.6	PN-tn,gd
170329E	-72.9205	-13.6844	Abancay	granodiorite	222.5	PET-tn,gd
18622A	-71.9719	-13.3233	Sacred Valley	hypabyssal volcanics	308.9	Mitu Grp
18628A	-74.3287	-13.3014	W of Ayacucho	granite	243.9	Pm-que
18701A	-75.6628	-14.4633	Ocucaje	granite	462.4	P-pgr, San Nicolas
18703A	-73.6469	-14.044	Paico	granite	1132.0	
18709A	-74.72142	-14.77444	Nazca	granodiorite	100.0	Tiabaya
18712C	-73.75681	-15.58253	Chala	gabbro	100.0	K-tgd-t Tiabaya

Table 31. Whole rock Sm-Nd isotopic compositions of selected samples from plutonic and volcanic units in the PCB and EC.

Sample	Sm/Nd	$^{147}Sm/^{144}Nd$	Sm (ppm)	Nd (ppm)	$^{143}Nd/^{144}Nd(0)$	std err (%)	Ndi	εNd(t)	ε(Nd)0	TCHUR
15810A	0.172474	0.104270	3.278175	19.00675	0.512517	0.001	0.512396	-0.25972	-2.37	0.20
15811C	0.218092	0.131847	2.957245	13.55960	0.512473	0.001	0.512418	-2.69154	-3.22	0.39
17320C	0.197150	0.119179	4.518169	22.91744	0.512218	0.001	0.511863	-3.68870	-8.19	0.83
17323B	0.232618	0.140624	1.942912	8.35238	0.512341	0.001	0.512131	-4.15736	-5.79	0.81
17323G	0.167742	0.101415	6.976093	41.58835	0.512783	0.001	0.512664	5.00972	2.82	-0.23
17323H	0.155698	0.094134	10.139670	65.12395	0.512780	0.001	0.512664	5.24754	2.78	-0.21
17324F	0.130571	0.078933	3.909441	29.94116	0.512289	0.001	0.512281	-6.56731	-6.80	0.45
17327E	0.193734	0.117120	5.342231	27.57513	0.512441	0.001	0.512209	-0.76503	-3.83	0.38
17329C	0.188932	0.114225	1.783519	9.44002	0.512742	0.001	0.512564	4.54481	2.02	-0.19
17329E	0.161725	0.097772	3.658125	22.61948	0.512566	0.001	0.512424	1.40719	-1.41	0.11
18622A	0.187164	0.113149	5.499050	29.38094	0.512447	0.001	0.512218	-0.42853	-3.73	0.35
18628A	0.218936	0.132361	7.020204	32.06511	0.512586	0.001	0.512375	0.99102	-1.02	0.12
18701A	0.161836	0.097826	5.305465	32.78288	0.511967	0.001	0.511671	-7.25480	-13.08	1.04
18703A	0.213052	0.128791	10.675530	50.10750	0.512153	0.001	0.511196	0.38920	-9.46	1.09
18709A	0.391476	0.236678	9.802905	25.04086	0.512680	0.001	0.512525	0.31034	0.82	0.16
18712C	0.227527	0.137546	4.657796	20.47143	0.512317	0.001	0.512227	-5.50767	-6.26	0.83

Table 32. Whole rock Rb-Sr and Pb isotopic compositions of selected samples from plutonic and volcanic units in the PCB and EC.

Sample	Rb	Sr	$^{87}Sr/^{86}Sr$ (0)	$^{87}Sr/^{86}Sr$(i)	$^{87}Rb/^{86}Sr$	Rb/Sr	std err%	$^{208}Pb/^{206}$	$^{207}Pb/^{206}Pb$	$^{206}Pb/^{204}Pb$	$^{207}Pb/^{204}Pb$	$^{208}Pb/^{204}Pb$
15810A	63.4	254.8	0.710	0.708	0.715	0.249	0.001	2.120	0.843	18.64	15.70	39.50
15811C	72.6	438.9	0.706	0.706	0.476	0.165	0.001	2.101	0.844	18.69	15.77	39.25
17320C	147.8	209.9	0.723	0.709	2.027	0.704	0.001	2.007	0.803	19.78	15.88	39.70
17323B	10.4	407.5	0.705	0.705	0.073	0.026	0.001	2.083	0.841	18.70	15.73	38.95
17323G	128.8	210.1	0.709	0.704	1.762	0.613	0.001	2.027	0.810	19.81	16.03	40.15
17323H	179.4	95.7	0.716	0.701	5.394	1.874	0.001	1.990	0.786	20.26	15.93	40.32
17324F	140.2	322.7	0.708	0.708	1.249	0.434	0.001	2.110	0.860	18.21	15.67	38.43
17327E	168.2	189.6	0.717	0.706	2.554	0.887	0.001	2.041	0.813	20.00	16.26	40.83
17329C	33.1	157.6	0.708	0.705	0.603	0.210	0.001	2.076	0.840	18.89	15.88	39.21
17329E	32.0	675.3	0.705	0.705	0.136	0.047	0.001	2.049	0.833	18.86	15.71	38.65
18622A	148.2	21.8	0.749	0.660	19.662	6.811	0.001	2.037	0.774	20.36	15.76	41.48
18628A	103.1	222.2	0.710	0.705	1.335	0.464	0.001	2.067	0.834	18.77	15.66	38.80
18701A	136.3	217.9	0.721	0.709	1.801	0.625	0.001	2.125	0.844	18.56	15.66	39.45
18703A	117.6	53.3	0.783	0.677	6.384	2.204	0.001	2.144	0.878	17.76	15.59	38.08
18709A	47.5	539.6	0.705	0.704	0.253	0.088	0.001	2.057	0.828	18.92	15.67	38.92
18712C	56.6	329.0	0.708	0.707	0.495	0.172	0.001	2.067	0.835	18.78	15.69	38.83

APPENDIX H

GEOCHEMICAL DATA

Table 33. List of samples used in geochemical analysis.

Sample #	Long	Lat	Location	Rock	Age	Map Unit
11828I	-75.02568	-14.07509	Rio Grande	monzonite	64.3	K-mt-I Incahausi
15805B	-77.48187	-11.07911	Huaral	tonalite	91.1	KTi-t-sr Santa Rosa
15805Da	-77.30866	-11.10967	Huaral	gabbro	84.4	KTi-gb
15805Db	-77.30866	-11.10967	Huaral		68.0	KTi-a-s_ Sayán
15805E	-77.26955	-11.14182	Huaral		65.0	KTi-a-c
15805G	-77.30197	-11.15795	Huaral		71.1	
15805J	-77.31313	-11.46112	Rio Huaral			Ki-c Casma volc
15806B	-77.75457	-10.50878	Barranca		105.0	
15806C	-77.74517	-10.48674	Rio Forteleza		70.6	KTi-Ap Puscao
15806E	-77.67071	-10.37575	Rio Forteleza	granodiorite	65.4	Kti-gd-src Santa Rosa
15806F	-77.55432	-10.19259	Rio Forteleza	diorite	40.6	KTi-di-p Paccho
15806K	-77.48613	-10.15378	Rio Forteleza	granite	64.0	Ki-sg-sj San Jeronimo
15810A	-71.62051	-16.45656	Arequipa		178.0	
15810E	-71.71012	-16.54234	Arequipa	granodiorite	65.0	KTi-gd
15811A	-71.5984	-16.4596	Arequipa	tonalite	79.0	Tiabaya KTi-gd
15811C	-71.4196	-16.5851	Yarabamba	granodiorite	63.7	Tiabaya KTi-gd
17320C	-72.3886	-13.1881	Chilca	monzogranite/granite	455.0	PET-mgr,gr
17323B	-70.9256	-13.5776	Ccocha	monzogranite/granite	228.7	PET-mgr,gr
17323G	-70.4872	-13.8188	Ollachea	nepheline syenite	179.1	Jim-sie
17323H	-70.5157	-13.8708	Macusani	andesite porphyry	189.0	PEI-c
17324F	-70.3740	-15.0464	Pucara	granodiorite/tonalite	16.0	N-gd,tn

Table 33. (continued).

Sample #	Long	Lat	Location	Rock	Age	Map Unit
17327E	-72.5808	-13.1511	Machu Picchu	monzogranite	302.8	PET-mgr,gr
17329C	-72.9555	-13.7015	Abancay	tonalite	238.6	PN-tn,gd
17329E	-72.9205	-13.6844	Abancay	granodiorite	222.5	PET-tn,gd
17330A	-71.9841	-13.5095	Sacsayhuaman	diorite	26.0	KP-tn,gd,di
18627A	-73.6789	-13.5158	3km N of Uripa	granite	230.0	Pi-gr
18628A	-74.3287	-13.3014	W of Ayacucho	granite	243.9	Pm-que
18701A	-75.6628	-14.4633	Ocucaje	granite	462.4	P-pgr San Nicolas
18703A	-73.6469	-14.044	Paico	granite	1132.0	
18709A	-74.72142	-14.77444	Nazca	granite	84.0	
18710A	-74.89516	-14.9643	Nazca Copara	granite	99.0	KS-gd-l
18710C	-74.83145	-14.97139		volcanic	120.0	Ks-bu
18710E	-74.85875	-14.56744	Nazca Chirimoyo	granite	75.9	
18711A	-74.59435	-15.35897	Acari El Molino	monzonite	97.8	
18711B	-74.59103	-15.35139	Acari El Molino	tonalite	95.0	Kti-toca Calapampa
18711D	-74.52242	-15.19025	Acari	tonalite	152.7	KTi-csr Santa Rita complex
18712A	-73.87572	-15.75042	Chala	monzonite	142.3	K-m-l Linga
18712C	-73.75681	-15.58253	Chala	tonalite	136.5	K-tgd-t Tiabaya
18712D	-73.71275	-15.56172	Chala	gabbro	75.0	K-gb
18713A	-74.42375	-15.45782	Chala	monzonite	97.0	K-m-l_ Linga
18713D	-74.27765	-15.27598	Yauca	granodiorite	135.0	K-tgd-t Tiabaya
18715A	-76.21101	-13.03652	Rio Canete	tonalite	90.0	K-tgd-t Tiabaya
18715B	-76.19553	-13.02828	Rio Canete	tonalite	90.3	K-tgd-i Incahuasi
18715D	-75.9809	-12.83712	Rio Canete	granodiorite	29.2	Catahuasi
18715E	-75.94917	-12.84264	Rio Canete	andesite		Tantara
18715H	-75.96725	-12.64746	Rio Canete	monzogranite		Catahuasi
18716A	-76.48568	-12.74512	Asia	granite	94.2	K-gbdi-p Patap

Table 33. (continued).

Sample #	Long	Lat	Location	Rock	Age	Map Unit
18716C	-76.46722	-12.72718	Asia	granodiorite	95.4	K-gd-t Tiabaya
18716E	-76.34284	-12.61934	Lunahuana Coayllo	monozodiorite	75.0	K-mzdi-tgd-co Cochahuasi
18716F	-76.41785	-12.70732	Asia	monzogranite	301.2	K-mgr-l Linga
18716G	-76.3981	-12.72774	Asia	granodiorite	98.8	K-gd-j Jecuan
18717B	-76.869	-12.2028	Lurin_Picapiedra		101.0	Ks-a-at Atocongo Jecuan
18717D	-76.6757	-12.1176	Rio Lurin	tonalite	72.3	Ks-tgd-t
18717E	-76.7136	-12.1185	Rio Lurin	diorite	90.0	Ks-di-pt_Patap
18717F	-76.75	-12.1343	Lurin Cieneguilla	granodiorite	60.0	Ks-tgd-sr Santa Rosa
18717I	-76.8175	-12.1154	Rio Lurin	tonalite	81.7	Ks-tdi-sr Santa Rosa
18718C	-76.6397	-11.8552	Chosica Santa Eulalia	granodiorite	60.0	Ks-sr/tgd Santa Rosa
18718D	-76.6311	-11.8157	Chosica Santa Eulalia	diorite	36.4	Ks-pa tdi Paccho

Table 34. Major element data for PCB and EC igneous units analyzed using fused bead acid digestion and inductively coupled plasma atomic emission spectroscopy (ICP-AES). Loss on ignition (LOI) by furnace or thermogravimetric analysis (TGA).

	SiO_2	Al_2O_3	Fe_2O_3	CaO	MgO	Na_2O	K_2O	Cr_2O3	TiO_2	MnO	P_2O_5	SrO	BaO	LOI
Method	ME_ICP06	ME_ICP06	ME_ICP06	ME_ICP06	ME_ICP06	ME_ICP06	ME_ICP06	ME_ICP06	ME_ICP06	ME_ICP06	ME_ICP06	ME_ICP06	ME_ICP06	ME_ICP06
Detection limit	0.01	0.01	0.01	0.01	0.01	0.01	0.01	0.01	0.01	0.01	0.01	0.01	0.01	0.01
Units	%	%	%	%	%	%	%	%	%	%	%	%	%	%
11828I	56.1	16.65	8.07	7.11	4.08	2.96	1.86	0.01	0.79	0.13	0.16	0.04	0.05	0.64
15805B	66.5	15.35	5.63	4.45	1.67	3.72	2.24	<0.002	0.48	0.12	0.16	0.04	0.11	0.71
15805Da	52.9	16.5	7.6	10.05	5.03	3.27	0.63	0.011	0.58	0.16	0.09	0.05	0.03	1.52
15805Db	77.5	12.25	1.7	1.59	0.4	3.75	3	<0.002	0.15	0.03	0.04	0.01	0.09	0.49
15805E	77.2	12.1	1.88	1.28	0.4	3.44	3.67	0.002	0.15	0.06	0.04	0.02	0.12	0.62
15805G	57	18.4	6.61	6.56	2.14	3.94	1.81	<0.002	0.66	0.13	0.24	0.05	0.06	0.62
15805J	51.6	16.1	11.35	9.53	3.79	1.04	0.03	<0.002	1.04	0.16	0.17	0.05	<0.01	4.19
15806B	60.4	16.5	7.43	6.1	2.82	3.24	2.32	<0.002	0.57	0.14	0.13	0.04	0.08	1.05
15806C	64.4	16.1	6.87	4.84	1.58	4.16	1.73	0.004	0.41	0.14	0.16	0.05	0.08	1.01
15806E	75	12.85	3.97	1.9	0.4	3.88	2.56	<0.002	0.2	0.05	0.04	0.02	0.12	0.42
15806F	61.9	16.1	6.09	4.95	2.29	3.78	1.91	0.003	0.66	0.1	0.16	0.07	0.14	2.75
15806K	74.8	13.8	1.48	1.64	0.26	4.27	3.67	0.002	0.16	0.05	0.04	0.01	0.08	1.09
15810A	68.1	15.35	4.4	2.13	1.56	4.46	2.95	<0.002	0.25	0.11	0.09	0.03	0.06	1.17
15810B	52.2	15.1	11.95	7.58	5.08	2.38	1.35	0.003	0.91	0.2	0.19	0.03	0.03	2.51
15810E	73.1	14.05	3.04	1.82	0.74	3.28	3.9	<0.002	0.21	0.07	0.07	0.02	0.05	1.27
15811A	63	16.2	6	5.21	2.06	3.09	3.14	<0.002	0.4	0.13	0.18	0.06	0.12	1
15811C	59.9	16.6	7.97	4.5	2.38	3.24	3.95	<0.002	0.9	0.12	0.2	0.05	0.11	1.1

Table 34. (continued).

Method	SiO_2 ME_ICP06	Al_2O_3 ME_ICP06	Fe_2O_3 ME_ICP06	CaO ME_ICP06	MgO ME_ICP06	Na_2O ME_ICP06	K_2O ME_ICP06	Cr_2O3 ME_ICP06	TiO_2 ME_ICP06	MnO ME_ICP06	P_2O_5 ME_ICP06	SrO ME_ICP06	BaO ME_ICP06	LOI ME_ICP06
Detection limit	0.01	0.01	0.01	0.01	0.01	0.01	0.01	0.01	0.01	0.01	0.01	0.01	0.01	0.01
Units	%	%	%	%	%	%	%	%	%	%	%	%	%	%
15826A	48.1	19.75	9.01	10.65	5.9	2.8	0.24	0.009	0.69	0.14	0.06	0.1	0.01	1.19
17315A	75.5	12.95	2.78	1.33	0.58	5.41	0.39	<0.002	0.18	0.02	0.03	0.02	0.03	1.22
17315D	52.3	18.5	9.56	9.53	5.22	2.34	0.46	<0.002	0.58	0.17	0.06	0.03	0.02	0.94
17315F	59.1	18.1	5.44	6.25	1.74	4.2	1.51	<0.002	0.4	0.13	0.23	0.11	0.08	2.86
17316G	50.9	19.4	8.53	8.87	4.56	3.91	0.84	0.004	0.91	0.15	0.21	0.09	0.05	1.26
17320C	55.7	17.45	8.62	6.27	3.38	4.03	2.33	0.002	0.83	0.07	0.16	0.05	0.05	2.31
17323B	47.4	18.35	10.75	9.15	9.33	2.51	0.48	0.018	0.61	0.15	0.04	0.05	0.02	0.8
17323G	54.4	19.4	5.76	1.91	0.72	9.3	5.38	<0.002	0.67	0.15	0.22	0.02	0.04	2.6
17323H	55	16.7	7.6	3.04	1.55	2.89	7.59	<0.002	1.08	0.14	0.31	0.01	0.02	4.8
17324F	70.6	14.9	3.33	1.49	0.59	3.67	4.7	<0.002	0.4	0.03	0.08	0.04	0.15	1.11
17327E	71.1	13.75	2.91	1.56	0.65	3.74	4.12	<0.002	0.32	0.07	0.07	0.02	0.09	0.86
17329C	61.1	18.5	4.75	1.69	1	7.74	1.5	<0.002	0.39	0.06	0.27	0.02	0.06	1.97
17329E	60.1	17.35	6.14	5.06	2.28	4.02	1.74	0.002	0.59	0.08	0.11	0.08	0.06	1.24
18715A	65.5	16.3	5.22	5.02	1.61	3.87	1.77	<0.002	0.46	0.16	0.16	0.06	0.14	0.74
18709A	57	17.6	7.65	7.33	3.3	3.23	1.67	<0.002	0.63	0.12	0.16	0.07	0.05	1.23
18710A	57.8	17	1.76	8.41	3.01	7.37	0.41	<0.002	0.71	0.03	0.08	0.04	0.01	2.48
18710C	56.9	17.8	2.57	7.92	5.43	5.57	1.49	0.002	0.55	0.11	<0.01	0.09	0.06	2.01
18710E	76	13.35	1.7	1.43	0.33	3.59	4.16	<0.002	0.15	0.03	0.02	0.01	0.07	0.51
18711A	56.6	16.5	8.82	6.11	3.13	3.58	3.28	0.003	0.85	0.15	0.38	0.05	0.1	0.32
18711B	60.4	15.95	6.95	4.06	1.83	3.59	4.47	<0.002	0.75	0.12	0.27	0.03	0.12	0.49

Table 34. (continued).

Method	SiO_2 ME_ICP06	Al_2O_3 ME_ICP06	Fe_2O_3 ME_ICP06	CaO ME_ICP06	MgO ME_ICP06	Na_2O ME_ICP06	K_2O ME_ICP06	Cr_2O3 ME_ICP06	TiO_2 ME_ICP06	MnO ME_ICP06	P_2O_5 ME_ICP06	SrO ME_ICP06	BaO ME_ICP06	LOI ME_ICP06
Detection limit	0.01	0.01	0.01	0.01	0.01	0.01	0.01	0.01	0.01	0.01	0.01	0.01	0.01	0.01
Units	%	%	%	%	%	%	%	%	%	%	%	%	%	%
18711D	54.8	19.05	5.8	9.19	3.44	5.24	0.46	<0.002	1.07	0.08	0.38	0.06	0.03	1.01
18712A	74	14.05	2.31	1.53	0.38	3.58	3.95	<0.002	0.18	0.04	0.05	0.02	0.09	1.12
18712C	61.1	17	6.33	5.95	2.84	2.38	1.72	0.005	0.62	0.11	0.13	0.04	0.04	1.9
18712D	61.8	16.55	5.59	5.3	2.52	3.02	1.73	<0.002	0.48	0.1	0.15	0.05	0.04	1.72
18713A	61.8	16.5	7.1	4.72	2.05	3.3	4.14	<0.002	0.63	0.12	0.2	0.05	0.13	0.86
18713D	68.4	15.25	3.82	4.09	1.4	2.87	2.93	<0.002	0.32	0.09	0.1	0.05	0.08	0.84
18715B	60.4	17.55	6.9	5.83	2.11	4.12	1.45	0.002	0.54	0.16	0.18	0.06	0.07	1.5
18715D	60.9	16.25	6.44	4.78	2.59	4.45	2.59	0.006	0.88	0.1	0.25	0.06	0.07	1.21
18715E	50.6	19.25	9.17	8.81	4.53	3.73	1	0.004	1.12	0.12	0.22	0.09	0.03	1.11
18715H	75	13.5	1.43	0.57	0.17	4.24	4.76	<0.002	0.18	0.04	0.03	<0.01	0.09	0.52
18716A	46.7	13.3	13	11.45	10.1	1.64	0.4	0.015	0.69	0.22	0.07	0.03	0.02	1.26
18716C	66.2	16.6	5.22	4.37	0.92	4.48	1.59	<0.002	0.45	0.07	0.12	0.03	0.08	0.73
18716F	47.2	18.3	10.75	12.8	8.24	1.62	0.29	0.016	0.64	0.18	0.12	0.05	0.02	0.29
18717B	74.5	13	2.85	1.87	0.43	3.87	3.15	<0.002	0.19	0.04	0.04	0.01	0.1	0.59
18717D	67.8	15.45	4.4	3.9	1.68	3.82	2.83	0.002	0.46	0.08	0.11	0.04	0.08	0.86
18717E	57.9	16.65	8.67	6.84	3.41	3.82	1.33	0.005	0.79	0.21	0.22	0.04	0.08	1.16
18717F	68.2	16.75	3.23	3.78	1.03	5.58	1.51	0.002	0.34	0.06	0.13	0.12	0.09	0.62
18717I	52.4	18.1	7.49	8.73	5.18	3.96	0.85	0.014	0.99	0.12	0.35	0.14	0.04	1.72
18718C	71.8	14.4	3.02	2.42	0.87	3.43	4.16	<0.002	0.32	0.06	0.08	0.04	0.08	0.84
18718D	66.8	15.2	4.81	3.19	1.23	3.73	4.06	0.002	0.51	0.05	0.13	0.03	0.09	1.25

Table 35. Trace element data for PCB and EC igneous units arranged alphabetically from Ba to Nd analyzed using fused bead acid digestion and inductively coupled plasma mass spectroscopy (ICP-MS).

	Ba	Ce	Cr	Cs	Dy	Er	Eu	Ga	Gd	Hf	Ho	La	Lu	Nb	Nd
Method	ME-MS81	ME-MS81	ME-MS81	ME-MS81	ME-MS81	ME-MS81	ME-MS81	ME-MS81	ME-MS81	ME-MS81	ME-MS81	ME-MS81	ME-MS81	ME-MS81	ME-MS81
Detection limit	0.5	0.1	10	0.01	0.05	0.03	0.02	0.1	0.05	0.1	0.01	0.1	0.01	0.1	0.1
Units	ppm	ppm	ppm	ppm	ppm	ppm	ppm	ppm	ppm	ppm	ppm	ppm	ppm	ppm	ppm
11828I	486	41.2	80	7.66	4.55	2.8	1.19	19.7	4.51	4.6	0.86	19.3	0.36	5.9	22.2
15805B	999	41.2	10	7.27	3.96	2.59	0.94	16.3	4.16	4.5	0.84	20.2	0.44	4.8	19.7
15805Da	313	16.7	90	1.75	2.42	1.4	0.69	16.3	2.49	1.6	0.5	9.6	0.22	1.9	7.9
15805Db	779	33.7	10	2.37	1.98	1.59	0.34	12.3	1.92	2.7	0.45	18.2	0.28	6.1	11.4
15805E	1115	22	10	4.41	1.61	1.12	0.29	12.2	1.35	2.5	0.33	13.2	0.24	4.8	7.4
15805G	530	40	10	2.55	4.7	2.66	1.07	19.9	4.94	3.8	0.92	18.8	0.41	5	21.7
15805J	25.8	25	10	0.19	4.52	2.87	1.45	22.1	4.56	2	0.89	12.7	0.36	2.1	15.7
15806B	695	29.2	10	3.01	4.82	3.2	0.79	16.7	4.37	3.9	0.89	12	0.42	4.2	16.1
15806C	711	26.9	30	1.7	2.93	1.72	0.76	18.1	2.91	3.4	0.53	12.6	0.26	4.2	13.6
15806E	1105	24.6	10	1.56	1.16	0.68	0.53	14.1	1.3	2.4	0.25	13.5	0.15	3.5	8.7
15806F	1265	64.2	20	0.87	2.83	1.31	1.13	19.9	3.81	3.9	0.49	43.3	0.17	7.1	23.9
15806K	743	36.8	10	2.22	2.71	1.76	0.36	14.1	2.44	3.5	0.55	16.4	0.27	6.1	14.9
15810A	461	39.3	10	0.65	2.11	1.31	0.77	13.7	2.38	2.5	0.42	20.2	0.21	2.3	18.1
15810B	243	32.4	20	2.87	4.12	2.49	0.9	15.5	4.29	3.6	0.81	13.9	0.32	2.6	19.9
15810E	458	54.2	10	2.72	3.64	2.38	0.8	16.4	4.08	3.8	0.72	26.7	0.36	14	23.6
15811A	1020	32.1	10	2.77	2.36	1.43	0.9	15.7	2.87	2.8	0.48	15.1	0.2	3.2	17.7
15811C	830	73.5	10	18.05	3.87	2.39	1.04	17.5	4.63	12.4	0.8	34.4	0.36	8.2	33.9

Table 35. (continued).

Method	Ba ME-MS81	Ce ME-MS81	Cr ME-MS81	Cs ME-MS81	Dy ME-MS81	Er ME-MS81	Eu ME-MS81	Ga ME-MS81	Gd ME-MS81	Hf ME-MS81	Ho ME-MS81	La ME-MS81	Lu ME-MS81	Nb ME-MS81	Nd ME-MS81
Detection limit	0.5	0.1	10	0.01	0.05	0.03	0.02	0.1	0.05	0.1	0.01	0.1	0.01	0.1	0.1
Units	ppm	ppm	ppm	ppm	ppm	ppm	ppm	ppm	ppm	ppm	ppm	ppm	ppm	ppm	ppm
15826A	122	10.7	70	0.19	1.59	0.9	0.86	22.2	1.88	0.5	0.31	4.9	0.09	0.5	7.8
17315A	309	52.9	10	0.17	3.56	2.28	0.67	13.8	3.52	4.3	0.69	30	0.4	2.5	20.9
17315D	230	13.6	10	1.05	3.4	2.4	0.67	17.6	2.86	2.1	0.71	5.7	0.37	0.9	10.2
17315F	765	24.1	<10	3.09	1.91	1.19	0.85	20.8	2.22	2.2	0.34	11.7	0.17	2	12.8
17316G	447	18.9	30	1.14	1.96	1.16	1.03	21.4	2.26	0.7	0.41	9	0.14	2	12
17320C	397	19.9	10	2.41	2.52	1.56	0.84	17.9	2.67	3.1	0.49	9.3	0.2	2.9	13
17323B	146.5	12.1	120	0.35	1.48	0.88	0.71	13.8	1.65	0.9	0.3	5.9	0.12	3.6	6.5
17323G	386	148.5	<10	3.84	6.65	3.68	1.79	29.1	6.99	15.7	1.25	84.7	0.59	213	50.6
17323H	194	216	<10	15.25	17.85	10	3.28	45.2	16.6	33.8	3.78	109	1.58	273	78.8
17324F	1300	77.1	10	2.04	1	0.41	0.93	27.1	2.09	7.1	0.14	45.5	0.05	8.6	30.9
17327E	850	61.9	10	4.54	3.59	2.2	0.93	19	3.77	5	0.7	31.3	0.33	19.2	24.7
17329C	586	26.7	10	1.75	2.28	1.31	0.87	22.2	2.15	3.5	0.4	12.9	0.23	14.1	13.8
17329E	437	8.2	10	1.47	1.24	0.64	0.57	17.6	1.35	2.1	0.22	3.5	0.09	2.4	6.1
18709A	414	49.1	10	3.33	3.63	2.08	1.2	18.9	3.95	3.4	0.65	23.3	0.29	4.6	24
18710A	92.5	25.3	<10	2.22	4.15	2.73	0.92	17.8	4	4.3	0.9	8.1	0.41	3.5	17.4
18710C	523	13.7	20	2.02	2.14	1.48	0.42	18.1	2.07	1.9	0.51	6.4	0.26	0.9	8.1
18710E	639	31.7	10	2.75	1.37	1	0.32	13.6	1.37	3.8	0.3	18.7	0.2	3.5	10.6
18711A	870	78.4	30	9.57	5.34	3.34	1.36	19.8	7.13	3.2	1.13	36.8	0.43	8.8	42.4
18711B	1010	91.4	10	19.05	5.91	3.7	1.19	19.1	7.1	8	1.18	44.5	0.48	10.4	44.8
18711D	234	41.2	10	0.96	4.85	2.64	2.07	19.8	5.81	3.6	0.99	16.3	0.41	5.3	28.1

Table 35. (continued).

Method	Ba ME-MS81	Ce ME-MS81	Cr ME-MS81	Cs ME-MS81	Dy ME-MS81	Er ME-MS81	Eu ME-MS81	Ga ME-MS81	Gd ME-MS81	Hf ME-MS81	Ho ME-MS81	La ME-MS81	Lu ME-MS81	Nb ME-MS81	Nd ME-MS81
Detection limit	0.5	0.1	10	0.01	0.05	0.03	0.02	0.1	0.05	0.1	0.01	0.1	0.01	0.1	0.1
Units	ppm	ppm	ppm	ppm	ppm	ppm	ppm	ppm	ppm	ppm	ppm	ppm	ppm	ppm	ppm
18712A	732	28.6	10	2.25	2	1.35	0.44	12.9	1.72	3.7	0.4	15.2	0.25	5.5	12.5
18712C	323	17.6	40	6.67	2.78	1.71	0.79	16.5	2.87	3.6	0.58	7.1	0.25	6.2	11.9
18712D	287	29	10	3.87	1.95	1.27	0.75	16.5	2.17	2.7	0.39	15.5	0.16	3.8	14.5
18713A	1125	64.2	10	8.51	4.58	2.92	1.06	18.3	5.53	5.1	0.84	30.3	0.39	7.7	33
18713D	660	47.2	10	3.58	1.91	1.41	0.77	15.3	1.91	2.9	0.37	24.3	0.22	6.6	17.7
18715A	1130	27.8	10	1.91	3.02	1.6	1.03	18.3	2.98	3.7	0.51	12.8	0.28	3.6	16.8
18715B	624	37.6	10	6.06	6.47	4.28	1.08	21.6	5.78	4.2	1.3	18.2	0.69	7.6	18.9
18715D	676	49.7	40	3.17	4.28	2.15	1.22	21.3	5.07	4.9	0.78	20.7	0.25	11.4	28.2
18715E	295	20.5	30	7.11	2.12	1.24	1.04	23.4	2.68	1	0.46	9	0.14	3.2	12.9
18715H	783	47.3	10	4.06	2.55	1.65	0.57	17.6	2.6	6.3	0.46	24.4	0.28	13	19.3
18716A	174.5	13.4	100	0.75	2.34	1.39	0.65	14.1	2.27	1.1	0.43	5.2	0.17	2	8.2
18716C	738	35.5	10	3.16	4.14	3.12	1.33	18.7	4.11	7.3	0.9	17.7	0.49	2.2	16.5
18716E	874	51.6	<10	1.11	8.24	5.26	1.89	20.9	8.29	5.2	1.67	23	0.78	5.3	30.6
18716F	196.5	15.2	110	0.24	2.17	1.25	0.78	16.5	2.57	1.2	0.47	7	0.18	1	9.1
18716G	1800	29.9	10	0.54	4.59	2.91	0.73	17.1	4.36	6.7	0.93	12.4	0.47	5.7	17.6
18717B	875	34.2	10	7.31	2.84	1.93	0.38	13.9	2.38	3.8	0.55	20.1	0.32	4.5	12.7
18717D	766	50.1	20	2.69	2.87	1.81	0.75	18	2.96	5.3	0.51	26.5	0.26	6.4	20.3
18717E	768	36.3	40	1.85	3.76	2.57	1.19	20.5	4.03	3	0.74	18.2	0.34	4.5	18.6
18717F	852	25.8	20	0.95	0.92	0.6	0.56	21.6	1.38	3.2	0.16	13.5	0.09	2.4	11.5
18717I	387	27.1	100	1.06	2.67	1.39	1.29	24.2	3.4	1.9	0.46	11	0.12	3.1	18.6
18718C	760	55.4	10	5	2.95	1.64	0.62	16.4	3.28	5.2	0.52	28	0.26	8.3	21.2
18718D	795	67	10	4.91	5.27	3.01	0.9	18.7	5.44	8	1.04	32.3	0.44	10.5	29.7

Table 36. Trace element data for PCB and EC igneous units arranged alphabetically from Pr to Zr, analyzed using fused bead, acid digestion and inductively coupled plasma mass spectroscopy (ICP-MS).

	Pr	Rb	Sm	Sn	Sr	Ta	Tb	Th	Tm	U	V	W	Y	Yb	Zr
Method	ME-MS81	ME-MS81	ME-MS81	ME-MS81	ME-MS81	ME-MS81	ME-MS81	ME-MS81	ME-MS81	ME-MS81	ME-MS81	ME-MS81	ME-MS81	ME-MS81	ME-MS81
Detection limit	0.02	0.2	0.03	1	0.1	0.1	0.01	0.5	0.01	0.05	5	1	0.1	0.03	2
Units	ppm	ppm	ppm	ppm	ppm	ppm	ppm	ppm	ppm	ppm	ppm	ppm	ppm	ppm	ppm
11828I	5.13	80	5.21	2	357	0.6	0.66	8.25	0.39	2.17	209	2	23.6	2.51	154
15805B	5.07	94.8	4.26	1	337	0.6	0.57	10.85	0.35	1.77	73	2	23.2	2.77	158
15805Da	2.04	10.3	2.1	1	435	0.2	0.37	3.01	0.19	1.04	228	1	12.7	1.17	57
15805Db	3.52	97	1.87	1	159	0.7	0.27	13.65	0.24	3.24	8	1	13.1	1.79	83
15805E	2.33	117.5	1.47	1	160	0.6	0.23	11.5	0.16	2.75	11	2	9.5	1.23	83
15805G	5.16	52.2	4.58	1	465	0.5	0.74	6.19	0.39	1.45	124	1	24.4	2.49	131
15805J	3.88	1	4.24	2	475	0.2	0.7	2.36	0.34	0.94	380	5	24.4	2.68	72
15806B	3.94	58.4	4.12	1	348	0.5	0.69	7.7	0.44	1.66	167	1	26.7	2.92	129
15806C	3.59	45.6	2.9	1	467	0.4	0.42	3.85	0.25	1.02	70	1	16.6	1.79	121
15806E	2.58	63.5	1.48	1	207	0.4	0.19	7.21	0.11	1.3	14	1	6.9	0.86	85
15806F	6.94	39.1	4.19	1	606	0.6	0.46	4.32	0.19	1.85	106	1	14	1.2	149
15806K	4.49	108.5	2.72	2	151	0.7	0.41	14.1	0.26	2.95	6	2	16.4	1.99	110
15810A	4.58	50.7	3.26	1	206	0.2	0.34	10.95	0.18	1.63	47	1	11.3	1.39	82
15810B	4.42	37.7	4.86	1	249	0.2	0.64	3.98	0.34	0.62	251	1	21.5	2.26	112
15810E	6.21	145.5	4.49	3	206	1.5	0.59	14.5	0.31	1.85	30	1	21.5	2.4	119
15811A	4.11	103	3.62	1	450	0.3	0.38	8.9	0.2	2.18	113	1	12.2	1.41	100
15811C	8.55	135	6.16	2	320	0.6	0.65	15.9	0.33	4.46	121	4	21.3	2.3	438

Table 36. (continued).

Method	Pr ME-MS81	Rb ME-MS81	Sm ME-MS81	Sn ME-MS81	Sr ME-MS81	Ta ME-MS81	Tb ME-MS81	Th ME-MS81	Tm ME-MS81	U ME-MS81	V ME-MS81	W ME-MS81	Y ME-MS81	Yb ME-MS81	Zr ME-MS81
Detection limit	0.02	0.2	0.03	1	0.1	0.1	0.01	0.5	0.01	0.05	5	1	0.1	0.03	2
Units	ppm	ppm	ppm	ppm	ppm	ppm	ppm	ppm	ppm	ppm	ppm	ppm	ppm	ppm	ppm
15826A	1.63	3	1.79	4	843	0.1	0.26	0.47	0.13	0.16	292	<1	7.6	0.81	19
17315A	5.66	8.4	4.06	3	157	0.3	0.55	9.99	0.32	3.68	14	2	20.5	2.64	150
17315D	2.01	11.2	2.93	1	240	0.2	0.46	1.03	0.31	0.44	228	1	20.2	2.32	63
17315F	3.15	40	2.62	1	987	0.2	0.31	2.2	0.16	0.71	60	1	10.7	1.13	72
17320C	2.92	64.4	3.16	2	379	0.2	0.4	6.26	0.19	1.28	198	1	13.7	1.5	104
17323B	1.45	8.4	1.51	1	317	0.3	0.24	1	0.1	0.24	73	<1	7.4	0.86	28
17323G	14.85	129	9.05	6	205	12.1	1	28.7	0.52	9.11	16	2	34.6	3.81	830
17323H	22.7	200	14.6	14	99.8	15.9	2.89	35	1.57	14.15	<5	8	94.7	10.7	1790
17324F	8.7	139	3.84	2	306	0.7	0.2	14	0.05	2.03	28	1	4.4	0.36	245
17327E	6.73	171	4.34	3	177	1.5	0.59	12.5	0.31	4.37	29	1	20.2	2.15	169
17329C	3.42	42.4	2.72	1	175	1	0.33	5.03	0.21	1.49	47	1	12.2	1.39	127
17329E	1.17	28.1	1.61	1	523	0.2	0.21	0.69	0.07	0.77	89	1	5.8	0.51	70
17316G	2.6	24.5	2.82	<1	737	0.2	0.35	0.53	0.16	0.33	208	1	10.2	0.89	20
18709A	5.89	53.6	4.9	2	559	0.3	0.54	10.6	0.29	2.85	209	1	18.2	2.06	118
18710A	3.85	6.8	3.77	1	299	0.3	0.63	7.29	0.37	1.72	192	<1	24.2	2.67	138
18710C	1.78	36	1.85	1	710	0.1	0.33	1.59	0.23	0.32	135	4	13.1	1.52	64
18710E	3.15	136	1.66	1	141	0.5	0.2	18.1	0.14	3.33	22	1	9	1.31	110
18711A	10.1	152.5	8.59	2	409	0.6	0.93	18.65	0.47	5.48	200	3	29.3	2.74	91
18711B	11.15	226	9	4	276	0.8	0.95	35.8	0.45	8.27	105	3	31.6	3.47	280
18711D	5.79	9.3	6.23	1	530	0.3	0.78	3.08	0.34	0.82	159	1	24.9	2.55	149
18712A	3.34	117.5	2.3	1	170	0.4	0.27	11.6	0.2	3.01	15	1	11.7	1.57	126

Table 36. (continued).

Method	Pr ME-MS81	Rb ME-MS81	Sm ME-MS81	Sn ME-MS81	Sr ME-MS81	Ta ME-MS81	Tb ME-MS81	Th ME-MS81	Tm ME-MS81	U ME-MS81	V ME-MS81	W ME-MS81	Y ME-MS81	Yb ME-MS81	Zr ME-MS81
Detection limit	0.02	0.2	0.03	1	0.1	0.1	0.01	0.5	0.01	0.05	5	1	0.1	0.03	2
Units	ppm	ppm	ppm	ppm	ppm	ppm	ppm	ppm	ppm	ppm	ppm	ppm	ppm	ppm	ppm
18712C	2.76	64.3	3.3	2	301	0.4	0.4	1.25	0.26	0.99	104	1	15.1	1.65	123
18712D	3.4	70	2.93	1	343	0.3	0.29	3.38	0.16	0.7	109	47	10.6	1.06	85
18713A	7.98	160.5	6.78	3	361	0.5	0.78	14.75	0.39	4.09	123	1	25	2.7	172
18713D	4.92	96.2	2.97	1	393	0.8	0.3	16.35	0.17	3.88	74	1	11.1	1.42	79
18715A	3.65	44.7	3.73	1	474	0.4	0.46	3.43	0.25	1.23	59	1	15.1	1.69	120
18715B	4.84	76	4.82	2	498	1	0.9	4.48	0.62	3.57	97	1	39.9	4.68	141
18715D	6.83	74.2	6.11	2	521	0.8	0.74	8.85	0.28	3.04	120	3	21	1.85	174
18715E	2.87	72.3	2.63	1	783	0.2	0.35	0.58	0.16	0.42	239	4	11.5	1.05	36
18715H	5.24	218	3.42	2	55.5	1.2	0.38	23	0.23	5.03	8	6	14.5	1.64	174
18716A	1.86	9.9	2	1	278	0.2	0.36	1.04	0.16	0.27	393	1	12.7	1.29	35
18716C	4.3	44	4.04	2	311	0.2	0.62	6.29	0.39	2.08	47	2	26.5	3.36	266
18716E	7.2	32.4	7.22	1	311	0.4	1.25	5.99	0.71	1.72	64	1	43.8	4.89	194
18716F	2.16	3	2.34	1	434	0.1	0.35	1.34	0.17	0.34	279	1	11.2	1.13	43
18716G	4.27	82.4	3.99	1	190.5	0.5	0.7	20.9	0.43	4.88	45	1	26.8	3.27	221
18717B	3.64	152.5	2.6	1	139.5	0.7	0.41	18.35	0.28	3.15	29	4	17.2	2.02	117
18717D	5.66	88.8	3.52	1	386	0.7	0.43	15.55	0.24	2.82	77	1	15.5	1.77	194
18717E	4.74	50.7	4.1	1	329	0.4	0.59	7.3	0.34	1.74	175	1	21	2.46	107
18717F	3.09	32.1	1.81	1	1020	0.3	0.18	2.8	0.07	0.99	54	1	5.4	0.48	116
18717I	3.98	23.6	3.91	1	1205	0.2	0.48	1.28	0.18	0.44	192	1	12.6	1.08	56
18718C	5.92	175	3.63	1	338	0.9	0.47	33	0.23	9.8	41	2	15.9	1.74	165
18718D	8.04	155	6.11	3	268	0.9	0.83	20	0.42	5.65	67	3	28.6	3.1	288

Table 37. Trace element base metals data for PCB and EC igneous units arranged alphabetically from Ag to Zn, analyzed using four acid digestion followed by ICP-AES measurement.

	Ag	As	Cd	Co	Cu	Li	Mo	Ni	Pb	Sc	Tl	Zn
Method	ME-4ACD81	ME-4ACD81	ME-4ACD81	ME-4ACD81	ME-4ACD81	ME-4ACD81	ME-4ACD81	ME-4ACD81	ME-4ACD81	ME-4ACD81	ME-4ACD81	ME-4ACD81
Detection limit	0.02	0.2	0.03	1	0.1	0.1	0.01	0.5	0.01	0.05	5	1
Units	ppm	ppm	ppm	ppm	ppm	ppm	ppm	ppm	ppm	ppm	ppm	ppm
11828I	<0.5	7	<0.5	21	56	20	1	21	14	22	<10	78
15805B	<0.5	<5	<0.5	10	9	20	<1	4	11	9	<10	47
15805Da	<0.5	<5	<0.5	24	22	20	1	12	6	35	<10	65
15805Db	<0.5	<5	<0.5	2	13	10	<1	1	7	3	<10	13
15805E	<0.5	<5	<0.5	1	3	30	1	2	10	3	<10	15
15805G	<0.5	<5	<0.5	12	40	10	1	3	11	13	<10	80
15805J	<0.5	<5	<0.5	20	21	10	1	4	7	31	<10	56
15806B	<0.5	6	<0.5	17	50	10	1	4	9	18	<10	71
15806C	<0.5	5	<0.5	9	18	20	1	8	6	7	<10	71
15806E	<0.5	<5	<0.5	3	8	10	<1	3	16	2	<10	42
15806F	<0.5	<5	<0.5	12	18	20	10	8	28	8	<10	90
15806K	<0.5	7	<0.5	1	3	10	<1	<1	20	3	<10	36
15810A	<0.5	<5	<0.5	6	8	10	1	2	9	7	<10	48
15810B	<0.5	12	<0.5	41	862	10	1	21	26	38	<10	149
15810E	<0.5	<5	<0.5	3	9	20	<1	4	19	5	<10	21
15811A	<0.5	<5	<0.5	12	17	20	<1	6	11	10	<10	51

Table 37. (continued).

Method	Ag ME-4ACD81	As ME-4ACD81	Cd ME-4ACD81	Co ME-4ACD81	Cu ME-4ACD81	Li ME-4ACD81	Mo ME-4ACD81	Ni ME-4ACD81	Pb ME-4ACD81	Sc ME-4ACD81	Tl ME-4ACD81	Zn ME-4ACD81
Detection limit	0.02	0.2	0.03	1	0.1	0.1	0.01	0.5	0.01	0.05	5	1
Units	ppm	ppm	ppm	ppm	ppm	ppm	ppm	ppm	ppm	ppm	ppm	ppm
15811C	<0.5	8	<0.5	16	133	40	1	9	28	13	<10	80
15826A	<0.5	<5	<0.5	29	19	<10	<1	33	<2	19	<10	70
17315A	0.8	<5	<0.5	8	439	<10	1	2	4	4	<10	27
17315D	<0.5	6	<0.5	34	91	10	1	11	6	25	<10	83
17315F	<0.5	10	<0.5	8	7	40	<1	<1	10	4	<10	68
17316G	<0.5	5	0.7	23	64	10	<1	17	7	17	<10	98
17320C	<0.5	14	<0.5	19	78	10	<1	11	5	19	<10	31
17323B	<0.5	<5	<0.5	52	48	20	<1	147	4	16	<10	73
17323G	<0.5	14	<0.5	6	8	70	9	2	28	2	<10	99
17323H	<0.5	<5	<0.5	3	1	30	3	4	6	2	<10	9
17324F	<0.5	6	<0.5	3	4	40	2	4	26	2	<10	81
17327E	<0.5	<5	<0.5	4	4	30	1	4	19	6	<10	40
17329C	<0.5	<5	<0.5	5	177	20	1	2	13	3	<10	52
17329E	<0.5	<5	<0.5	17	57	20	<1	20	10	8	<10	71
18709A	<0.5	<5	<0.5	15	70	10	<1	8	8	18	<10	50
18710A	<0.5	<5	<0.5	3	21	10	1	4	<2	16	<10	10
18710C	<0.5	5	<0.5	6	4	20	<1	6	<2	16	<10	33
18710E	<0.5	<5	<0.5	1	5	10	<1	1	13	2	<10	9
18711A	<0.5	7	<0.5	21	157	20	3	13	17	21	<10	86

Table 37. (continued).

Method	Ag ME-4ACD81	As ME-4ACD81	Cd ME-4ACD81	Co ME-4ACD81	Cu ME-4ACD81	Li ME-4ACD81	Mo ME-4ACD81	Ni ME-4ACD81	Pb ME-4ACD81	Sc ME-4ACD81	Tl ME-4ACD81	Zn ME-4ACD81
Detection limit	0.02	0.2	0.03	1	0.1	0.1	0.01	0.5	0.01	0.05	5	1
Units	ppm	ppm	ppm	ppm	ppm	ppm	ppm	ppm	ppm	ppm	ppm	ppm
18711B	<0.5	8	<0.5	14	150	30	1	4	23	15	<10	73
18711D	<0.5	<5	<0.5	14	18	<10	<1	6	<2	18	<10	19
18712A	<0.5	<5	<0.5	1	16	10	4	1	10	3	<10	140
18713A	<0.5	<5	<0.5	14	90	20	3	5	12	14	<10	59
18713D	<0.5	<5	<0.5	7	4	20	<1	2	21	9	<10	49
18715A	<0.5	<5	<0.5	8	5	10	<1	3	23	7	<10	92
18715B	<0.5	7	<0.5	13	4	10	1	4	9	12	<10	80
18715D	<0.5	7	<0.5	15	41	20	1	18	8	13	<10	75
18715E	<0.5	<5	<0.5	24	9	20	<1	13	8	17	<10	73
18715H	<0.5	<5	<0.5	<1	3	20	1	<1	14	2	<10	30
18716A	<0.5	<5	0.6	54	101	10	<1	32	11	51	<10	102
18716C	<0.5	<5	<0.5	6	26	10	1	3	7	9	<10	45
18716E	<0.5	<5	<0.5	15	16	10	<1	2	4	17	<10	53
18716F	<0.5	<5	<0.5	41	12	<10	<1	46	3	36	<10	71
18716G	<0.5	<5	0.5	4	6	<10	1	3	5	8	<10	22
18717B	<0.5	<5	<0.5	2	9	10	1	2	6	4	<10	19
18717D	<0.5	<5	<0.5	9	8	20	<1	8	8	8	<10	42

Table 37. (continued).

Method	Ag ME-4ACD81	As ME-4ACD81	Cd ME-4ACD81	Co ME-4ACD81	Cu ME-4ACD81	Li ME-4ACD81	Mo ME-4ACD81	Ni ME-4ACD81	Pb ME-4ACD81	Sc ME-4ACD81	Tl ME-4ACD81	Zn ME-4ACD81
Detection limit	0.02	0.2	0.03	1	0.1	0.1	0.01	0.5	0.01	0.05	5	1
Units	ppm	ppm	ppm	ppm	ppm	ppm	ppm	ppm	ppm	ppm	ppm	ppm
18717E	<0.5	<5	<0.5	19	13	10	<1	13	3	15	<10	91
18717F	<0.5	<5	<0.5	6	6	20	<1	8	3	3	<10	39
18717I	<0.5	<5	<0.5	25	16	10	<1	55	7	15	<10	76
18712C	<0.5	<5	<0.5	11	10	40	<1	5	13	17	<10	71
18712D	<0.5	<5	<0.5	12	29	10	<1	4	23	12	<10	53
18718C	<0.5	5	<0.5	5	244	10	4	4	9	5	<10	44
18718D	<0.5	6	<0.5	6	13	30	1	5	15	9	<10	41

APPENDIX I

R CODE MODULES USED FOR DATA ANALYSIS AND PLOTTING

Packages Used

```
update.packages()
sessionInfo()
library(installr)
library(readxl)
library(pillar)
library(tidyverse)
library(openxlsx)
library(devtools)
library(ggplot2)
library(ggthemes)
library(rbokeh)
library(dplyr)
library(plyr)
library(magrittr)
library(hrbrthemes)
library(tidyr)
library(viridis)
library(Cairo) #exporting antialiased
library(WriteXLS)
library(Rmisc)
library(r2symbols)
library(forcats)
library(httr)
library(grid)
```

```
library(patchwork)
library(tidyr)
library(gghighlight)
library(ggtext)
library(ggalt)
library(SciViews)
library(DescTools)
library(gridExtra)
library(cowplot)
library(ggpubr)
library(arcgisbinding)
library(sp)
library(svglite)
library(lemon)
library(janitor)
library(reshape2)
library(signal)
```


Read in Data From Excel File

```
setwd ("R:\\Projects\\Geochem\\PhD\\Publications\\")
options(warn=-1) # turn off warning messages
col_dataTypes = c("guess","guess","guess","guess","guess", "guess","guess","guess","guess","guess"
,"guess","guess","guess","numeric","guess", "guess","guess","guess","numeric", "numeric", "numeric
","numeric","numeric","numeric","numeric","numeric","numeric","numeric","numeric","numeric","numer
ic","numeric","numeric","numeric","numeric","numeric","numeric","numeric","numeric","numeric","num
eric","numeric","numeric","numeric","numeric","numeric","numeric","numeric","numeric","numeric","n
umeric","numeric","numeric","numeric","numeric","numeric","numeric","numeric","numeric","numeric",
```

```
"numeric","numeric","numeric","numeric","numeric","numeric","numeric","numeric","numeric","numeric
","numeric","numeric","numeric","numeric","numeric","numeric","numeric","numeric","numeric","numer
ic","numeric","numeric","numeric","numeric","numeric","numeric","numeric","numeric","numeric","num
eric","numeric","numeric","numeric","numeric","numeric","numeric","numeric","numeric","numeric","n
umeric","numeric","numeric","numeric","numeric","numeric","numeric","numeric","numeric","numeric",
"numeric","numeric","numeric","numeric","numeric","numeric","numeric","numeric","numeric","numeric
","numeric","numeric","numeric","numeric","numeric","numeric","numeric","numeric","numeric","numer
ic","guess","guess","guess","guess","guess","guess","guess","guess","guess","guess")
PeruData = read_excel("PeruAllData_3-27-2023.xlsx", sheet = 1, col_types = col_dataTypes)
FlareupData = read_excel("R:\\Projects\\Geochem\\PhD\\Publications\\Moho flareups.xlsx",
                         sheet = 1)
setwd ("R:\\Projects\\Geochem\\PhD\\Publications\\Peru PhD\\Figures")
```


R-ArcGIS Bridge Applied to Smoothing GIS Geological Unit Data

```
#to smooth geological unit data ages in geodatabase
arc.check_product()
PCB_Object = arc.open(path = 'R:\\Projects\\Geochem\\PhD\\Publications\\Lithos\\PCB\\PCB.gdb\\
                      Peru_data_XYTableToP_Project')
PCB_GIS <- arc.select(object = PCB_Object, fields = names(PCB_Object@fields))

igneousUnitsFlareupsObject = arc.open(path = 'R:\\Projects\\Geochem\\PhD\\Publications\\PeruGIS\\
                                      PeruGIS.gdb\\IgneousUnitsFlareupsPCB_EC')
igneousUnitsFlareups <- arc.select(object = igneousUnitsFlareupsObject,
                                   fields = names(igneousUnitsFlareupsObject@fields))

#smooth data using jitter function
for (i in 1:nrow(igneousUnitsFlareups))
```

```
{
if (igneousUnitsFlareups$Use[i] >= 4) {
    igneousUnitsFlareups$AgeJ[i] = jitter(igneousUnitsFlareups$Age[i], amount = 10)
}
  else
    igneousUnitsFlareups$AgeJ[i] = igneousUnitsFlareups$Age[i]
}
#write feature class to geodatabase
arc.write('R:\\Projects\\Geochem\\PhD\\Publications\\PeruGIS\\PeruGIS.gdb\\
          IgneousUnitsFlareupsPCB_EC_1', igneousUnitsFlareups, shape_info = arc.shapeinfo(igneousU
nitsFlareupsObject))
```


Label Formatting Function for All Plots

```
formatLabel <- function(var) {
  var = paste(var, " (ppm)", sep = "")
  var = gsub("_J", "", var)
  var = gsub("F", "", var)
  var = gsub("_", "/", var)
  var = gsub("A/NK", "A+NK", var)
  var = gsub("Tote", "Fe_tote", var)
  var = gsub("SiO2 \\(ppm\\)", "SiO2 (wt %)", var)
  var = gsub("K2O \\(ppm\\)", "K2O (wt %)", var)
  var = gsub("CaO \\(ppm\\)", "CaO (wt %)", var)
  var = gsub("Na2O \\(ppm\\)", "Na2O (wt %)", var)
  var = gsub("K/Na \\(ppm\\)", "K2O+Na2O (wt %)", var)
  var = gsub("A/NK \\(ppm\\)", "A+Na2O (wt %)", var)
  var = gsub("MnO \\(ppm\\)", "MnO (wt %)", var)
```

```
  var = gsub("MgO \\(ppm\\)", "MgO (wt %)", var)
  var = gsub("TiO2 \\(ppm\\)", "TiO2 (wt %)", var)
  var = gsub("Al2O3 \\(ppm\\)", "Al2O3 (wt %)", var)
  var = gsub("TotFe \\(ppm\\)", "TotFe (wt %)", var)
  var = gsub("Age \\(ppm\\)", "Age (Ma)", var)
  var = gsub("Sri \\(ppm\\)", "87Sr/86Sr_i", var)
  var = gsub("Sr/Y \\(ppm\\)", "Sr/Y", var)
  var = gsub("La/Yb \\(ppm\\)", "La/Yb", var)
  var = gsub("Rb/Sr \\(ppm\\)", "Rb/Sr", var)
  var = gsub("Th/Yb \\(ppm\\)", "Th/Yb", var)
  var = gsub("Ba/La \\(ppm\\)", "Ba/La", var)
  var = gsub("Nb/Yb \\(ppm\\)", "Nb/Yb", var)
  var = gsub("Sm/Yb \\(ppm\\)", "Sm/Yb", var)
  var = gsub("Y/Nb \\(ppm\\)", "Y/Nb", var)
  var = gsub("206Pb/204Pbi \\(ppm\\)", "206Pb/204Pb_i", var)
  var = gsub("207Pb/204Pbi \\(ppm\\)", "207Pb/204Pb_i", var)
  var = gsub("208Pb/204Pbi \\(ppm\\)", "208Pb/204Pb_i", var)
  var = gsub("eNd \\(ppm\\)", "εNd_i", var)
  var = gsub("eHf \\(ppm\\)", "εHf", var)
  var = gsub("d18O/Qtz \\(ppm\\)", "δ18O_Qtz", var)
  s = str_extract(var, "\\d+") # extract digits
  if (is.na(s)){     # no digits
    return(var)
  }
  if (str_length(s) > 1) {  #isotope
    var = chartr("0", "⁰", var)
    var = chartr("1", "¹", var)
    var = chartr("2", "²", var)
    var = chartr("3", "³", var)
    var = chartr("4", "⁴", var)
```

```
    var = chartr("5", "⁵", var)
    var = chartr("6", "⁶", var)
    var = chartr("7", "⁷", var)
    var = chartr("8", "⁸", var)
  } else {          # not isotope
    var = chartr("2", "₂", var)
    var = chartr("3", "₃", var)
  }
  return(var)
}
```


PCB Geochemistry Bivariate Plots by Segment

```
#estimated ages
PCB = PeruData %>%
  dplyr::filter(`Area_ID` == 'Peru', Analysis_Type == 'Whole Rock',
     Location_1 == 'PCB-North Segment' | Location_1 == 'PCB-Central Segment' |
     Location_1 == 'PCB-South Segment', Rock_Type1 == "Plutonic" | Rock_Type1 == "Volcanic" |

Rock_Type1 == "Igneous", Method_Age == "U-Pb" |
           Method_Age == "U-Pb infer" | Method_Age == "Rb-Sr" | Method_Age == "K-Ar" |
           Method_Age == "Ar-Ar" | Method_Age == "Estimate")

ord1=c('PCB-North Segment', 'PCB-Central Segment', 'PCB-South Segment')

PCB %<>%
  mutate(Rock_Type1 = as.factor(Rock_Type1))
PCB %<>%
```

```
  mutate(Location_1 = factor(Location_1, levels = ord1)) %<>%
  arrange(Location_1)

PCB$Age = as.numeric(PCB$Age)
PCB$Age_J = PCB$Age
#apply jitter to smooth data
PCB$Hf_J = jitter(PCB$Hf, amount = 0.5)
PCB$Sc_J = jitter(PCB$Sc, amount = 5)
PCB$Ta_J = jitter(PCB$Ta, amount = 0.1)
PCB$Tm_J = jitter(PCB$Tm, amount = 0.05)
PCB$U_J = jitter(PCB$U, amount = 0.5)
PCB$Tb_J = jitter(PCB$Tb, amount = 0.5)
PCB$MnO_J = jitter(PCB$MnO, amount = 0.5)
PCB$Nb_J = jitter(PCB$Nb, amount = 2)

#calculate total iron, isotopes and elemental ratios
PCB$TotFe = (PCB$Fe2O3 * 0.8998) + PCB$FeO
PCB$Sri = as.numeric(PCB$F87Sr_86Sri_est)
PCB$Rb_Sr = PCB$Rb/PCB$Sr
PCB$A_NK = (PCB$Al2O3/101.9613) / ((PCB$Na2O/61.9789) + (PCB$K2O/94.196))
PCB$Sr_Y = PCB$Sr/PCB$Y
PCB$F206Pb_204Pbi
PCB$K_Na = PCB$K2O + PCB$Na2O
PCB$La_Yb = PCB$La/PCB$Yb
PCB$Y_Nb = PCB$Y/PCB$Nb
PCB$Nb_Yb = PCB$Nb/PCB$Yb
PCB$Th_Yb = PCB$Th/PCB$Yb
PCB$Ba_La = PCB$Ba/PCB$La

p = data.frame(PCB$eNd, PCB$Location_1)
```

```
#plotting function
plotChem <- function(PCB, yvar, xvar, y1, y2, x1, x2, titl, fname) {
  #filter x and y variables based on parameters
  PCB = PCB %>%
    dplyr::filter(PCB[[yvar]] >= y1 & PCB[[yvar]] <= y2, PCB[[xvar]] >= x1 & PCB[[xvar]] <= x2)
     #format labels
     xvar1 = formatLabel(xvar)
     yvar1 = formatLabel(yvar)
     #aggregate based on PCB segment
     c.y = aggregate(PCB[[yvar]], by = list(Name=PCB$Location_1), FUN = mean, na.rm = TRUE)
     c.x = aggregate(PCB[[xvar]], by = list(Name=PCB$Location_1), FUN = mean, na.rm = TRUE)
     c = data.frame(x = c.x, y= c.y)
     r = ddply(PCB,"Location_1", function(x) cor(x[[yvar]],x[[xvar]], use = "complete.obs"))
     l = ddply(PCB,"Location_1", function(x) coefficients(lm(x[[yvar]] ~ x[[xvar]])))
     p1 = PCB %>%
          ggplot(aes(x = PCB[[xvar]], y = PCB[[yvar]], color = Location_1)) +
          geom_point(alpha = 0.4, aes()) +
          coord_cartesian(ylim=c(y1, y2)) +
          scale_x_continuous(name = xvar1, breaks = scales::pretty_breaks(n = 4),
                             limits = c(x1, x2), expand = c(0, 0)) +
          scale_y_continuous(name = yvar1, limits = c(y1, y2), expand = c(0, 0)) +
          theme_bw() +
          stat_ellipse(aes(), alpha = 1, show.legend = F, type = "t", linetype = 1,
                level = 0.68, geom = "path") +
          geom_point(data = c, aes(x=x.x, y=y.x), show.legend = F, size = 5, shape = 19,
              color = "grey30") +
          geom_point(data = c, aes(x=x.x, y=y.x, color = x.Name), show.legend = F, size = 3,
           shape = 19) +
          scale_color_manual(name="Segment",
                labels = c(paste("LNS: c=(", round(c.y$x[1], 2), ", ", round(c.x$x[1], 2), ")",
```

```
                    sep = ""), # comment out to use default colors if < 3 segments
                    paste("CS: c=(", round(c.y$x[2], 2), ", ", round(c.x$x[2], 2), ")", sep = ""),
                                paste("SS: c=(", round(c.y$x[3], 2), ", ", round(c.x$x[3], 2), ")",
                                sep = "")), values = c('blue', 'red', '#82D30C')) +
                  annotate(geom = "Text", x = -Inf, y = Inf, hjust = -0.5, vjust = 2,
                        label = paste(titl, "n = ", nrow(PCB), sep = "")) +
                  theme(legend.position = c(1, 1),
                        legend.title = element_blank(), #remove legend title
                        legend.justification = c("right", "top"),
                        legend.box.just = "right",
                        legend.box.margin = margin(0.5, 0.5, 0.1, 0.1),
                        legend.background = element_rect(fill = "grey90"),
                        text = element_text(size=16),
                        axis.text.x=element_text(size=14),
                        axis.text.y=element_text(size=14),
                        axis.title.x=element_text(size=16),
                        axis.title.y=element_text(size=16),
                        axis.ticks = element_line(size = 1, color="black"),
                        axis.ticks.length = unit(2, "mm"),
                        axis.line = element_line(size = 1/2, color = "black", linetype=1),
                        axis.text = element_text(angle = 0, color="black", size=4, face=1))
      #save as either .png or .svg (vector format)
      ggsave(fname, p1, device = "png",type = "cairo", dpi = 300, height = 6, width = 6) #6x14
      #ggsave(fname, p1, device = "svg", dpi = 300, height = 6, width = 6) #6x14
  return(p1)
}

#loop through all rows in plotlist parameter file, generating a plot for each row
plotData = read_excel("R:\\Projects\\Geochem\\PhD\\Publications\\plotlist.xlsx", sheet = 2)
setwd ("R:\\Projects\\Geochem\\PhD\\Publications\\Peru PhD\\Figures")
```

```
for (i in 1:nrow(plotData)) {
  print(i)
  print(paste(plotData$y[i], " vs ", plotData$x[i]))
  plotChem(PCB, plotData$y[i], plotData$x[i], plotData$y1[i], plotData$y2[i], plotData$x1[i],
   plotData$x2[i], "", paste(plotData$y[i], "_", plotData$x[i], ".png", sep = ""))
}
```

PCB Geochemistry E-W Plots

```
PCB = PeruData %>%
  dplyr::filter(`Area_ID` == 'Peru', Analysis_Type == 'Whole Rock',
         Location_1 == 'PCB-North Segment' | Location_1 == 'PCB-Central Segment' |
         Location_1 == 'PCB-South Segment',
         Rock_Type1 == "Plutonic" | Rock_Type1 == "Volcanic" | Rock_Type1 == "Igneous",
         Method_Age == "U-Pb" | Method_Age == "U-Pb infer" | Method_Age == "Rb-Sr" |
         Method_Age == "K-Ar" | Method_Age == "Ar-Ar" | Method_Age == "Estimate")

ord1=c('PCB-North Segment', 'PCB-Central Segment', 'PCB-South Segment')
ord1=c('West', 'Central', 'East')

PCB %<>%
  mutate(Rock_Type1 = as.factor(West_east))
PCB %<>%
  mutate(West_east = factor(West_east, levels = ord1)) %<>%
  arrange(West_east)
PCB$Lat

PCB$Sr_Y = PCB$Sr/PCB$Y
```

```
PCB$Age = as.numeric(PCB$Age)

#mild data smoothing
PCB$Age_J = jitter(PCB$Age, amount = 5)
PCB$Hf_J = jitter(PCB$Hf, amount = 0.5)
PCB$Sc_J = jitter(PCB$Sc, amount = 5)
PCB$Ta_J = jitter(PCB$Ta, amount = 0.1)
PCB$Tm_J = jitter(PCB$Tm, amount = 0.05)
PCB$U_J = jitter(PCB$U, amount = 0.5)
PCB$Tb_J = jitter(PCB$Tb, amount = 0.5)
PCB$MnO_J = jitter(PCB$MnO, amount = 0.5)
PCB$Nb_J = jitter(PCB$Nb, amount = 2)

#calculate elemental values and ratios
PCB$TotFe = (PCB$Fe2O3 * 0.8998) + PCB$FeO
PCB$Sri = as.numeric(PCB$F87Sr_86Sri_est)
PCB$Rb_Sr = PCB$Rb/PCB$Sr
PCB$A_NK = (PCB$Al2O3/101.9613) / ((PCB$Na2O/61.9789) + (PCB$K2O/94.196))
PCB$F206Pb_204Pbi
PCB$K_Na = PCB$K2O + PCB$Na2O
PCB$La_Yb = PCB$La/PCB$Yb
PCB$Y_Nb = PCB$Y/PCB$Nb
PCB$Nb_Yb = PCB$Nb/PCB$Yb
PCB$Th_Yb = PCB$Th/PCB$Yb
PCB$Ba_La = PCB$Ba/PCB$La

p = data.frame(PCB$eNd, PCB$Location_1)
```

Plotting Function

```
plotChem <- function(PCB, yvar, xvar, y1, y2, x1, x2, titl, fname) {
  PCB = PCB %>%
    dplyr::filter(PCB[[yvar]] >= y1 & PCB[[yvar]] <= y2, PCB[[xvar]] >= x1 & PCB[[xvar]] <= x2)
  xvar1 = formatLabel(xvar)
  yvar1 = formatLabel(yvar)
  c.y = aggregate(PCB[[yvar]], by = list(Name=PCB$West_east), FUN = mean, na.rm = TRUE)
  c.x = aggregate(PCB[[xvar]], by = list(Name=PCB$West_east), FUN = mean, na.rm = TRUE)
  c = data.frame(x = c.x, y= c.y)
  r = ddply(PCB,"West_east", function(x) cor(x[[yvar]],x[[xvar]], use = "complete.obs"))
  l = ddply(PCB,"West_east", function(x) coefficients(lm(x[[yvar]] ~ x[[xvar]])))
  p1 = PCB %>%
    ggplot(aes(x = PCB[[xvar]], y = PCB[[yvar]], color = West_east)) +
    geom_point(alpha = 0.4, aes()) +
    coord_cartesian(ylim=c(y1, y2)) +
    scale_x_continuous(name = xvar1, breaks = scales::pretty_breaks(n = 4), limits = c(x1, x2),
                       expand = c(0, 0)) +
    scale_y_continuous(name = yvar1, limits = c(y1, y2), expand = c(0, 0)) + theme_bw() +
    stat_ellipse(aes(), alpha = 1, show.legend = F, type = "t", linetype = 1, level = 0.68,
                 geom = "path") +
    geom_point(data = c, aes(x=x.x, y=y.x), show.legend = F, size = 5, shape = 19,
               color = "grey30") +
    geom_point(data = c, aes(x=x.x, y=y.x, color = x.Name), show.legend = F, size = 3, shape = 19)
+
    scale_color_manual(name="Segment", labels = c(paste("West: c=(", round(c.y$x[1], 2), ", ",
                                     round(c.x$x[1], 2), ")",
                                     sep = ""), # comment out to use default colors if < 3 segments
                                     paste("Central: c=(", round(c.y$x[2], 2), ", ",
                                           round(c.x$x[2], 2), ")", sep = ""),
```

```
                                        paste("East: c=(", round(c.y$x[3], 2), ", ",
                                        round(c.x$x[3], 2), ")",
                                        sep = "")), values = c('#FFC300', '#E00EF3', '#0EE7F3')) +
    annotate(geom = "Text", x = -Inf, y = Inf, hjust = -0.5, vjust = 2,
             label = paste(titl, "n = ", nrow(PCB), sep = "")) +
    theme(legend.position = c(1, 1),
          legend.title = element_blank(), # remove legend title
          legend.justification = c("right", "top"),
          legend.box.just = "right",
          legend.box.margin = margin(0.5, 0.5, 0.1, 0.1),
          legend.background = element_rect(fill = "grey90"),
          text = element_text(size=16),
          axis.text.x=element_text(size=14),
          axis.text.y=element_text(size=14),
          axis.title.x=element_text(size=16),
          axis.title.y=element_text(size=16),
          axis.ticks = element_line(size = 1, color="black"),
          axis.ticks.length = unit(2, "mm"),
          axis.line = element_line(size = 1/2, color = "black", linetype=1),
          axis.text = element_text(angle = 0, color="black", size=4, face=1))
  ggsave(fname, p1, device = "png", type = "cairo", dpi = 300, height = 6, width = 6) #6x14
  #ggsave(fname, p1, device = "svg", dpi = 300, height = 6, width = 6)
  return(p1)
}

#loop through all rows in plotlist parameter file, generating a plot for each row
plotData = read_excel("R:\\Projects\\Geochem\\PhD\\Publications\\plotlist.xlsx", sheet = 2)
setwd ("R:\\Projects\\Geochem\\PhD\\Publications\\Peru PhD\\Figures")
for (i in 1:nrow(plotData)) {
  print(i)
```

```
  print(paste(plotData$y[i], " vs ", plotData$x[i]))
  plotChem(PCB, plotData$y[i], plotData$x[i], plotData$y1[i], plotData$y2[i], plotData$x1[i],
           plotData$x2[i], "", paste(plotData$y[i], "_", plotData$x[i], "_W_E.png", sep = ""))
}
```

Stacked Plots - Plot Geochem by Time

```
ageStart = 18 #155 #18
ageEnd = 202 #420 #202
binWidth = 5 #10 #5

#read in flare-up parameters and tectonic data
FlareupData = read_excel("R:\\Projects\\Geochem\\PhD\\Publications\\Moho flareups.xlsx",
                         sheet = 1)
TectonicData = read_excel("R:\\Projects\\Geochem\\PhD\\Publications\\Moho flareups.xlsx",
                         sheet = 3)
setwd ("R:\\Projects\\Geochem\\PhD\\Publications\\Peru PhD\\Figures")

#extract relevant PCB chemical data from global PCB data PeruData
PCB = PeruData %>%
  dplyr::filter(`Area_ID` == 'Peru', Analysis_Type == 'Whole Rock',
        Location_1 == 'PCB-North Segment' | Location_1 == 'PCB-Central Segment' |
        Location_1 == 'PCB-South Segment' | Location_1 == 'EC',
        Rock_Type1 == "Plutonic" | Rock_Type1 == "Volcanic" |
          Rock_Type1 == "Igneous", Method_Age == "U-Pb" |
        Method_Age == "U-Pb infer" | Method_Age == "Rb-Sr" |
          Method_Age == "K-Ar" | Method_Age == "Ar-Ar")
```

```r
eHfData = PeruData %>%
  dplyr::filter(`Area_ID` == 'Peru', Analysis_Type == 'eHf' | Analysis_Type == 'Whole Rock',
         Method_Age == "U-Pb" | Method_Age == "U-Pb infer", !is.na(eHf))

PCB$Age_J = PCB$Age



#apply mild smoothing to noted sharp peaks
PCB %<>%
  mutate(Age_J = case_when(Age_J == 60 ~ jitter(Age_J, amount = 2),
                           Age_J == 78 ~ jitter(Age_J, amount = 5),
                           Age_J == 98 ~ jitter(Age_J, amount = 2),
                           Age_J == 100 ~ jitter(Age_J, amount = 2),
                           Age_J == 103 ~ jitter(Age_J, amount = 2),
                           Age_J == 105 ~ jitter(Age_J, amount = 2),
                           Age_J == 110 ~ jitter(Age_J, amount = 2),
                           Age_J == 131 ~ jitter(Age_J, amount = 2),
                           TRUE ~ Age_J))

#apply mild smoothing to sharp chemical data due to various analysis artifacts
PCB$Hf_J = jitter(PCB$Hf, amount = 0.5)
PCB$Sc_J = jitter(PCB$Sc, amount = 5)
PCB$Ta_J = jitter(PCB$Ta, amount = 0.1)
PCB$Tm_J = jitter(PCB$Tm, amount = 0.05)
PCB$U_J = jitter(PCB$U, amount = 0.5)
PCB$Tb_J = jitter(PCB$Tb, amount = 0.5)
PCB$MnO_J = jitter(PCB$MnO, amount = 0.5)
PCB$Nb_J = jitter(PCB$Nb, amount = 2)
```

```r
#calculate element ratios and other values
PCB$TotFe = (PCB$Fe2O3 * 0.8998) + PCB$FeO
PCB$Rb_Sr = PCB$Rb/PCB$Sr
PCB$A_NK = (PCB$Al2O3/101.9613) / ((PCB$Na2O/61.9789) + (PCB$K2O/94.196))
PCB$Sr_Y = PCB$Sr/PCB$Y
PCB$K_Na = PCB$K2O + PCB$Na2O
PCB$La_Yb = PCB$La/PCB$Yb
PCB$Y_Nb = PCB$Y/PCB$Nb
PCB$Nb_Yb = PCB$Nb/PCB$Yb
PCB$Th_Yb = PCB$Th/PCB$Yb
PCB$Ba_La = PCB$Ba/PCB$La
PCB$La_Yb = PCB$La/PCB$Yb
PCB$Sri = as.numeric(PCB$F87Sr_86Sri)
PCB$dO18_Qtz = as.numeric(PCB$d18O_Qtz)
PCB$Ce_Y = as.numeric(PCB$Ce/PCB$Y)
PCB$eNd = round(PCB$eNd, digits = 3)
PCB$Sm_Yb = round(PCB$Sm / PCB$Yb, digits = 1)

ord1=c('PCB-North Segment', 'PCB-Central Segment', 'PCB-South Segment', 'EC')
PCB %<>%
  mutate(Location_1 = factor(Location_1, levels = ord1)) %<>%
  arrange(Location_1)
PCB$Moho = NA
PCB$flareup = NA

#add moho and flareup data from parameter file to geochemistry dataframe
for (i in 1:nrow(PCB)) {
  for (j in 1:nrow(FlareupData)) {
    if (PCB$Location_1[i] == FlareupData$Segment[j]) {
      if (!is.na(PCB$Age_J[i])) {
```

```
        if ((PCB$Age_J[i] <= FlareupData$Start[j]) & (PCB$Age_J[i] >= FlareupData$End[j])) {
          PCB$Moho[i] = FlareupData$Moho[j]
          PCB$flareup[i] = FlareupData$Name[j]
        }
      }
    }
  }
}
#reorganize fields in dataframe
PCB <- PCB %>% relocate(Age_J, .before = Age)
PCB <- PCB %>% relocate(Moho, .before = Age_J)
PCB <- PCB %>% relocate(flareup, .before = Moho)

#histogram and density plot of age data for segments
plotAgeData <- function(ds, segment, flareupData, color, adj) {
  segData = ds %>%
    dplyr::filter(Location_1 == segment)
  p = ggplot() +
    #individual segments
    geom_rect(data = subset(FlareupData, Segment == segment), aes(xmin = Start,
                  xmax = End, ymin = -Inf, ymax = Inf), fill = "grey60", alpha = 0.2) +
    geom_histogram(data = segData, aes(x = Age_J), col = "grey50",
                   fill = color, binwidth = binWidth, boundary = 0,
                    position = "identity", closed = "left", size = 0.5, alpha = 0.3) +
    geom_density(data = segData, aes(x = Age_J, y=binWidth*..count..), adjust = adj,
                 col = color, position = "stack",
                 fill = "NA", linetype=2, lwd = 3, alpha = 1) + #0.25 for zoomed in plot
    theme_ipsum() +
    geom_label(data = subset(FlareupData, Segment == segment),
               aes(x= End + (Start - End)/2 - 0, y=Inf,
```

```
            label = paste(Name, ": ", Start, " - ", End, "\n", "peak = ", Peak, sep = "")),
            vjust = 1.2,
            lineheight = 0.7, color="grey30", label.r = unit(0.8, "lines"),
            label.padding = unit(0.6, "lines"),
            size=7 , angle=0, fontface="bold", alpha = 0.6) +
  annotate("text", x = Inf, y = Inf, hjust = 1.3, vjust = 5,
           label = paste("n = ", nrow(segData), sep = ""),
            size = 10, color = "black") +
  scale_x_continuous(name = "Age (Ma)", breaks = scales::pretty_breaks(n = 10),
                     limits = c(ageStart, ageEnd),
            expand = c(0, 0)) +
  scale_y_continuous(name = "Sample count", expand = expansion(mult = c(0, .05)),
                     breaks = scales::pretty_breaks(n = 2)) +
  theme_bw() +
  theme(legend.position = c(.9, .9),
        legend.title=element_text(size=26),
        legend.text=element_text(size=24),
        legend.justification = c("right", "top"),
        legend.box.just = "right",
        legend.box.margin = margin(0.5, 0.5, 0.1, 0.1),
        legend.background = element_rect(fill = "white"),
        text = element_text(size=18),
        strip.text = element_text(size = 12),
        strip.background = element_rect(fill = "grey90"),
        axis.text.x= element_text(size=24),
        axis.text.y=element_text(size=28),
        axis.title.x=element_text(size=24),
        axis.title.y=element_text(size=28),
        axis.ticks = element_line(size = 1, color="black"),
        axis.ticks.length = unit(2, "mm"),
```

```
          axis.line = element_line(size = 1/2, color = "black", linetype=1),
          axis.text = element_text( angle = 0, color="black", size=10, face=1))
  return(p)
}
```

Plot Moho Data

```
plotMoho <- function(FlareupData, segment, color) {
  p1 = ggplot() +
    # individual segments
    geom_smooth(formula = y ~ x, data = subset(FlareupData, Segment == segment),
                aes(x = Peak1, y = Moho), span = 1, method = "loess", col = color, size = 2,
alpha = 1, se = FALSE) +
    geom_rect(data = subset(FlareupData, Segment == segment),
         aes(xmin = Start, xmax = End, ymin = -Inf, ymax = Inf), fill = "grey60", alpha = 0.2) +
    scale_x_continuous(name = element_blank(),
         breaks = scales::pretty_breaks(n = 10), limits = c(ageStart, ageEnd), expand = c(0, 0)) +
    scale_y_continuous(name = "Moho depth \n(km)", expand = c(0, 0),
         breaks = scales::pretty_breaks(n = 3)) +
    theme_bw() +
    coord_cartesian(clip = "off") +
    theme(legend.position = "none",
        strip.text = element_text(size = 12), # for facet_wrap
        strip.background = element_rect(fill = "grey90"),
        axis.text.x=element_blank(),
        axis.text.y=element_text(size=24),
        axis.title.x=element_text(size=18),
        axis.title.y=element_text(size=26),
```

```
        axis.ticks = element_line(size = 1, color="black"),
        axis.ticks.length = unit(2, "mm"),
        axis.line = element_line(size = 1/2, color = "black", linetype=1))
  return(p1)
}
```

Plot Convergence Data

```
plotConvergence <- function(FlareupData, convergenceData, segment, color) {
  p1 = ggplot() +
    # individual segments
    geom_smooth(formula = y ~ x, data = convergenceData, aes(x = Mid, y = Convergence),
                span = 0.6, method = "loess", col = "purple", size = 2, alpha = 1, se = FALSE) +
    geom_rect(data = subset(FlareupData, Segment == segment), aes(xmin = Start, xmax = End,
                ymin = -Inf, ymax = Inf), fill = "grey60", alpha = 0.2) +
    annotate("text", x = 55, y = 9.9, label = "fast", size = 12, parse = TRUE) +
    annotate("text", x = 140, y = 2.4, label = "slow", size = 12, parse = TRUE) +
    scale_x_continuous(name = element_blank(), breaks = scales::pretty_breaks(n = 10),
                       limits = c(ageStart, ageEnd),
                       expand = c(0, 0)) +
    scale_y_continuous(name = "Conv. Rate \n(cm/yr)", expand = c(0, 0),
                       breaks = scales::pretty_breaks(n = 3)) +
    theme_bw() +
    coord_cartesian(clip = "off") +
    theme(legend.position = "none",
          strip.text = element_text(size = 12), # for facet_wrap
          strip.background = element_rect(fill = "grey90"),
          axis.text.x=element_blank(),
```

```
          axis.text.y=element_text(size=24),
          axis.title.x=element_text(size=18),
          axis.title.y=element_text(size=26),
          axis.ticks = element_line(size = 1, color="black"),
          axis.ticks.length = unit(2, "mm"),
          axis.line = element_line(size = 1/2, color = "black", linetype=1))
  return(p1)
}
```

Plot Dip Angle


```
plotDipAngle <- function(FlareupData, convergenceData, segment, color) {
  p1 = ggplot() +
    # individual segments
    geom_smooth(formula = y ~ x, data = convergenceData, aes(x = Mid, y = DipAngle),
                span = 0.6, method = "loess",
                col = "purple", size = 2, alpha = 1, se = FALSE) +
    geom_rect(data = subset(FlareupData, Segment == segment), aes(xmin = Start, xmax = End,
                                                                  ymin = -Inf, ymax = Inf),
              fill = "grey60", alpha = 0.2) +
    annotate("text", x = 40, y = 31, label = "flat", size = 12, parse = TRUE) +
    annotate("text", x = 130, y = 50, label = "steep", size = 12, parse = TRUE) +
    scale_x_continuous(name = element_blank(), breaks = scales::pretty_breaks(n = 10),
                       limits = c(ageStart, ageEnd),
                       expand = c(0, 0)) +
    scale_y_continuous(name = "Dip Angle", expand = c(0, 0),
                       breaks = scales::pretty_breaks(n = 3)) +
    theme_bw() +
```

```
    coord_cartesian(clip = "off") +
    theme(legend.position = "none",
          strip.text = element_text(size = 12), # for facet_wrap
          strip.background = element_rect(fill = "grey90"),
          axis.text.x=element_blank(),
          axis.text.y=element_text(size=24),
          axis.title.x=element_text(size=18),
          axis.title.y=element_text(size=26),
          axis.ticks = element_line(size = 1, color="black"),
          axis.ticks.length = unit(2, "mm"),
          axis.line = element_line(size = 1/2, color = "black", linetype=1))
  return(p1)
}
```


Plot eHf

```
plot_eHf <- function(eHfData, FlareupData, segment) {
  ds = subset(eHfData, Age <= (ageEnd - 20) & Age > ageStart & eHf < 7 & eHf > -7)
  p1 = ggplot() +
    # individual segments
    #geom_point(data = ds, aes(x = Age, y = ds$eHf), col = "purple", size = 2) +
    geom_smooth(formula = y ~ x, data = ds, aes(x = Age, y = eHf), span = 0.6,
                method = "loess", col = "purple",
                fill = "purple", size = 2, alpha = 0.3, se = F) +
    geom_rect(data = subset(FlareupData, Segment == segment),
              aes(xmin = Start, xmax = End, ymin = -Inf, ymax = Inf),
              fill = "grey60", alpha = 0.2) +
    annotate("text", x = Inf, y = Inf, hjust = 1.3, vjust = 2,
```

```
            label = paste("n = ", nrow(!is.na(ds)), sep = ""),
            size = 10, color = "black") +
    scale_x_continuous(name = element_blank(), breaks = scales::pretty_breaks(n = 10),
                       limits = c(ageStart, ageEnd),
                       expand = c(0, 0)) +
    scale_y_continuous(name = "εHf", expand = c(0, 0), breaks = scales::pretty_breaks(n = 3)) +
    theme_bw() +
    coord_cartesian(clip = "off") +
    theme(legend.position = "none",
          strip.text = element_text(size = 12), # for facet_wrap
          strip.background = element_rect(fill = "grey90"),
          axis.text.x=element_blank(),
          axis.text.y=element_text(size=24),
          axis.title.x=element_text(size=18),
          axis.title.y=element_text(size=26),
          axis.ticks = element_line(size = 1, color="black"),
          axis.ticks.length = unit(2, "mm"),
          axis.line = element_line(size = 1/2, color = "black", linetype=1))
  return(p1)
}
```


Read Flare-up Parameters

```
FlareupData_RF = read_excel("R:\\Projects\\Geochem\\PhD\\Publications\\Moho flareups.xlsx",
     sheet = 1)
FlareupData_FL = read_excel("R:\\Projects\\Geochem\\PhD\\Publications\\Moho flareups.xlsx",
     sheet = 2)
plotData = read_excel("R:\\Projects\\Geochem\\PhD\\Publications\\plotlist.xlsx", sheet = 5)
```

Plot Chemistry Data and Calculate Mean Values for Flare-ups and Lulls, Store in a Dataframe for Further Analysis

```
plotChemTime <- function(ds, FlareupData, segment, var1, color, y1, y2) {
  flareups = subset(FlareupData, Segment == segment)
  ds1 = ds %>%
    dplyr::filter(ds$Location_1 == segment, ds[[var1]] >= y1 & ds[[var1]] <= y2,
                  ds$Age_J <= flareups$Start[1], ds$Age_J >= flareups$End[nrow(flareups)])
  print(var1)
  ds1 = ds %>%
    dplyr::filter(ds$Location_1 == segment, ds[[var1]] >= y1 & ds[[var1]] <= y2,
                  ds$Age_J <= flareups$Start[1])
  #print(nrow(ds1))
  for (i in 1:nrow(flareups)) {
    FlareupInterval = subset(ds1, ds1$Age_J <= flareups$Start[i] & ds1$Age_J >= flareups$End[i])
    flareups$varMean[i] = mean(FlareupInterval[[var1]], na.rm=T)
    rising = subset(ds1, ds1$Age_J <= flareups$Start[i] & ds1$Age_J > flareups$Peak[i])
    falling = subset(ds1, ds1$Age_J <= flareups$Peak[i] & ds1$Age_J > flareups$End[i])
    flareup = subset(ds1, ds1$Age_J <= flareups$Start[i] & ds1$Age_J > flareups$End[i])
    if (i < nrow(flareups)) {
        lull = subset(ds1, ds1$Age_J <= flareups$End[i] & ds1$Age_J > flareups$Start[i+1])}
    else { lull = subset(ds1, ds1$Age_J <= flareups$End[i])}
    varNameRising = paste(segment, "_rising_", i, sep = "")
    varNameFalling = paste(segment, "_falling_", i, sep = "")
    varNameFlareup = paste(segment, "_flareup_", i, sep = "")
    varNameLull = paste(segment, "_lull_", i, sep = "")
    #switch between RF and FL style flareups
    if (flareup_lull == T) { #store in global plotdata and for use in plotting means
      plotData[[varNameFlareup]][which (plotData$y == var1)] <<- mean(flareup[[var1]], na.rm=T)
      flareups$mean1[i] = mean(flareup[[var1]], na.rm=T)
      plotData[[varNameLull]][which (plotData$y == var1)] <<- mean(lull[[var1]], na.rm=T)
```

```
    flareups$mean2[i] = mean(lull[[var1]], na.rm=T)
  } else if (rising_falling == T) {
    plotData[[varNameRising]][which (plotData$y == var1)] <<- mean(rising[[var1]], na.rm=T)
    flareups$mean1[i] = mean(rising[[var1]], na.rm=T)
    plotData[[varNameFalling]][which (plotData$y == var1)] <<- mean(falling[[var1]], na.rm=T)
    flareups$mean2[i] = mean(falling[[var1]], na.rm=T)
  }
}
LNS = ds %>%
  dplyr::filter(ds$Location_1 == "PCB-North Segment", ds[[var1]] >= y1 & ds[[var1]] <= y2)
CS = ds %>%
  dplyr::filter(ds$Location_1 == "PCB-Central Segment", ds[[var1]] >= y1 & ds[[var1]] <= y2)
SS = ds %>%
  dplyr::filter(ds$Location_1 == "PCB-South Segment", ds[[var1]] >= y1 & ds[[var1]] <= y2)
var1_f = formatLabel(var1)
p = ggplot() +
  #plotting individual segments
  geom_point(data = ds1, aes(x = Age_J, y = ds1[[var1]]), col = color, size = 2) +
  geom_smooth(formula = y ~ x, data = ds1, aes(x = Age_J, y = ds1[[var1]]),
              method = "loess", span = 0.5, se = T,
              level = 0.67, alpha = 0.3, linetype = 1, lwd = 2, col = color, fill = color) +
  #plotting FL
  geom_rect(data = subset(FlareupData, Segment == segment),
              aes(xmin = Start, xmax = End, ymin = -Inf, ymax = Inf),
              fill = "grey60", alpha = 0.2) +
  #plotting RF
  geom_rect(data = subset(FlareupData, Segment == segment), aes(xmin = Start, xmax = Peak, ymi
            n = -Inf, ymax = Inf), fill = "peru", alpha = 0.2) +
  geom_rect(data = subset(FlareupData, Segment == segment), aes(xmin = Peak, xmax = End,
```

```
                ymin = -Inf, ymax = Inf), fill = "darkolivegreen", alpha = 0.2) +
    #use for FL
    geom_point(data = flareups, aes(x=Peak, y=mean1), fill = "gold",
                show.legend = F, size = 9, shape = 24) +
    geom_point(data = flareups, aes(x=End-6, y=mean2), fill = "blue",
                show.legend = F, size = 9, shape = 24) +
    #use for RF
    geom_point(data = flareups, aes(x= Peak + (Start-Peak)/2, y=mean1), fill = "peru",
    show.legend = F, size = 9, shape = 24) +
    geom_point(data = flareups, aes(x= End + (Peak-End)/2, y=mean2), fill = "darkolivegreen",
    show.legend = F, size = 9, shape = 24) +
    annotate("text", x = Inf, y = Inf, hjust = 1.3, vjust = 2,
             label = paste("n = ", nrow(!is.na(ds1)), sep = ""), size = 10, color = "black") +
    scale_x_continuous(name = element_blank(), breaks = scales::pretty_breaks(n = 10),
                       limits = c(ageStart, ageEnd), expand = c(0, 0)) +
    scale_y_continuous(name = var1_f, expand = c(0, 0), breaks = scales::pretty_breaks(n = 3)) +
    theme_bw() +
    coord_cartesian(clip = "off") +
    theme(legend.position = "none",
          strip.text = element_text(size = 12), # for facet_wrap
          strip.background = element_rect(fill = "grey90"),
          axis.text.x=element_blank(),
          axis.text.y=element_text(size=24),
          axis.title.x=element_text(size=18),
          axis.title.y=element_text(size=26),
          axis.ticks = element_line(size = 1, color="black"),
          axis.ticks.length = unit(2, "mm"),
          axis.line = element_line(size = 1/2, color = "black", linetype=1))
  return(p)
}
```

Function for Organizing Time Series Panels - PCB

```
#general geochem
runTimeChemPCB <- function(segment, color, showSamples, adj, fname) {
  p = list()
  h = vector()
  p[[1]] = plotAgeData(PCB, segment, FlareupData, color, adj)
  p[[2]] = plotMoho(FlareupData, segment, color)
  #p[[3]] = plotExten_Compress(FlareupData, TectonicData, segment, color)
  p[[3]] = plotDipAngle(FlareupData, TectonicData, segment, color)
  p[[4]] = plotConvergence(FlareupData, TectonicData, segment, color)
  p[[5]] = plot_eHf(eHfData, FlareupData, segment)
  h[[1]] = 3
  h[[2]] = 2
  h[[3]] = 2
  h[[4]] = 2
  h[[5]] = 2
  # read in the list of geochemical variables to plot
  plotData = read_excel("R:\\Projects\\Geochem\\PhD\\Publications\\plotlist.xlsx", sheet = 5)
  for (i in 1:nrow(plotData)) {
    p[[i+5]] = plotChemTime(PCB, FlareupData, segment, plotData$y[i], color,
                            plotData$y1[i], plotData$y2[i])
    h[[i+5]] = 2
  }
  plot = ggarrange(plotlist = p, heights = h, ncol=1, align="v")
  ggsave(fname, plot, device = "png",type = "cairo", dpi = 300, height = 30, width = 22)
}
```

Function for Organizing Time Series Panels - EC

```
runTimeChemEC <- function(segment, color, showSamples, adj, fname) {
  p = list()
  h = vector()
  p[[1]] = plotAgeData(PCB, segment, FlareupData, color, adj)
  p[[2]] = plotMoho(FlareupData, segment, color)
  p[[3]] = plot_eHf(eHfData, FlareupData, segment)
  h[[1]] = 3
  h[[2]] = 2
  h[[3]] = 2
  plotData = read_excel("R:\\Projects\\Geochem\\PhD\\Publications\\plotlist.xlsx", sheet = 5)
  for (i in 1:nrow(plotData)) {
    p[[i+3]] = plotChemTime(PCB, FlareupData, segment, plotData$y[i], color,
                            plotData$y1[i], plotData$y2[i])
    h[[i+3]] = 2
  }
  plot = ggarrange(plotlist = p, heights = h, ncol=1, align="v")
  ggsave(fname, plot, device = "png",type = "cairo", dpi = 300, height = 30, width = 22)
}
```

Setup Data Parameters for PCB and EC Time Series Plots

```
setwd("R:\\Projects\\Geochem\\PhD\\Publications\\Peru PhD\\Figures")

#modify here to change segments being plotted
#3 segments of PCB
segments = c("PCB-North Segment", "PCB-Central Segment", "PCB-South Segment")
colors = c("blue", "red", "#82D30C")
```

```
adj = c(0.7, 0.6, 0.3)
ageStart = 18
ageEnd = 205
binWidth = 5
timePlotData = data.frame(segments, colors, adj)

FlareupData = FlareupData_FL
flareup_lull = T
rising_falling = F

#loop through the 3 segments for flare-ups and lulls
for (i in 1:nrow(timePlotData)) {
  print(i)
  print(paste(timePlotData$segments[i], " ", "Geochem"))
  runTimeChemPCB(timePlotData$segments[i], timePlotData$colors[i], T,
                 timePlotData$adj[i], paste("Geochem_time_FL_", timePlotData$segments[i],
                 ".png", sep = "")) #Sri = 0.702, 0.71, SiO2 = 40, 84, lat = -19, -2.5,
}

FlareupData = FlareupData_RF
rising_falling  = T
flareup_lull = F
#loop through the 3 segments for rising and falling
for (i in 1:nrow(timePlotData)) {
  print(i)
  print(paste(timePlotData$segments[i], " ", "Geochem"))
  runTimeChemPCB(timePlotData$segments[i], timePlotData$colors[i], T, timePlotData$adj[i],
                 paste("Geochem_time_RF_", timePlotData$segments[i], ".png", sep = ""))
}
```

```
#EC
segments = c("EC")
colors = c("peru")
adj = c(0.4)
ageStart = 150
ageEnd = 350
binWidth = 5
timePlotData = data.frame(segments, colors, adj)

FlareupData = FlareupData_FL
flareup_lull = T
rising_falling = F
runTimeChemEC(timePlotData$segments[1], timePlotData$colors[1], T, timePlotData$adj[1],
              paste("Geochem_time_FL_", timePlotData$segments[1], ".png", sep = ""))

FlareupData = FlareupData_RF
rising_falling  = T
flareup_lull = F
runTimeChemEC(timePlotData$segments[1], timePlotData$colors[1], T,
              timePlotData$adj[1], paste("Geochem_time_RF_", timePlotData$segments[1],
              ".png", sep = ""))
```


Analysis of the Results from Flare-up/Lull and Rising/Falling Comparison Data

```
#rename dataframe fields
plotData1 = plotData %>%
  dplyr::rename("NS-1_flareup" = "PCB-North Segment_flareup_1",
                "NS-1_lull" = "PCB-North Segment_lull_1",
```

```
"NS-2_flareup" = "PCB-North Segment_flareup_2",
"NS-2_lull" = "PCB-North Segment_lull_2",
"NS-3_flareup" = "PCB-North Segment_flareup_3",
"NS-3_lull" = "PCB-North Segment_lull_3",
"NS-4_flareup" = "PCB-North Segment_flareup_4",
"NS-4_lull" = "PCB-North Segment_lull_4",
"CS-1_flareup" = "PCB-Central Segment_flareup_1",
"CS-1_lull" = "PCB-Central Segment_lull_1",
"CS-2_flareup" = "PCB-Central Segment_flareup_2",
"CS-2_lull" = "PCB-Central Segment_lull_2",
"CS-3_flareup" = "PCB-Central Segment_flareup_3",
"CS-3_lull" = "PCB-Central Segment_lull_3",
"CS-4_flareup" = "PCB-Central Segment_flareup_4",
"CS-4_lull" = "PCB-Central Segment_lull_4",
"SS-1_flareup" = "PCB-South Segment_flareup_1",
"SS-1_lull" = "PCB-South Segment_lull_1",
"SS-2_flareup" = "PCB-South Segment_flareup_2",
"SS-2_lull" = "PCB-South Segment_lull_2",
"SS-3_flareup" = "PCB-South Segment_flareup_3",
"SS-3_lull" = "PCB-South Segment_lull_3",
"SS-4_flareup" = "PCB-South Segment_flareup_4",
"SS-4_lull" = "PCB-South Segment_lull_4",
"EC-1_flareup" = "EC_flareup_1",
"EC-1_lull" = "EC_lull_1",
"EC-2_flareup" = "EC_flareup_2",
"EC-2_lull" = "EC_lull_2",
"EC-3_flareup" = "EC_flareup_3",
"EC-3_lull" = "EC_lull_3",
"NS-1_rising" = "PCB-North Segment_rising_1",
"NS-1_falling" = "PCB-North Segment_falling_1",
```

```
                "NS-2_rising" = "PCB-North Segment_rising_2",
                "NS-2_falling" = "PCB-North Segment_falling_2",
                "NS-3_rising" = "PCB-North Segment_rising_3",
                "NS-3_falling" = "PCB-North Segment_falling_3",
                "NS-4_rising" = "PCB-North Segment_rising_4",
                "NS-4_falling" = "PCB-North Segment_falling_4",
                "CS-1_rising" = "PCB-Central Segment_rising_1",
                "CS-1_falling" = "PCB-Central Segment_falling_1",
                "CS-2_rising" = "PCB-Central Segment_rising_2",
                "CS-2_falling" = "PCB-Central Segment_falling_2",
                "CS-3_rising" = "PCB-Central Segment_rising_3",
                "CS-3_falling" = "PCB-Central Segment_falling_3",
                "SS-1_rising" = "PCB-South Segment_rising_1",
                "SS-1_falling" = "PCB-South Segment_falling_1",
                "SS-2_rising" = "PCB-South Segment_rising_2",
                "SS-2_falling" = "PCB-South Segment_falling_2",
                "SS-3_rising" = "PCB-South Segment_rising_3",
                "SS-3_falling" = "PCB-South Segment_falling_3",
                "SS-4_rising" = "PCB-South Segment_rising_4",
                "SS-4_falling" = "PCB-South Segment_falling_4",
                "EC-1_rising" = "EC_rising_1",
                "EC-1_falling" = "EC_falling_1",
                "EC-2_rising" = "EC_rising_2",
                "EC-2_falling" = "EC_falling_2")
```

```
setwd ("R:\\Projects\\Geochem\\PhD\\Publications\\Peru PhD\\Figures")
write.xlsx(plotData1, "FlareupResults.xlsx")

# Extract relevant fields
plotData1 = plotData1[ -c(2:3) ]

# Transpose matrix
plotDataT = t(plotData1)

# Set up row names
plotDataT %<>%
  row_to_names(row_number = 1)

# Output col names to check
colnames(plotDataT)

# Convert to dataframe
plotDataT = as.data.frame(plotDataT)

# Convert flareupCat to column
plotDataT %<>%
  rownames_to_column(var="flareupCat")

# Loop through columns and format as numeric data
for (i in 2:ncol(plotDataT)) {
  c = colnames(plotDataT)[i]
```

```
  plotDataT[[c]] = as.numeric(plotDataT[[c]])
}

# Assign name to first column
colnames(plotDataT)[1] ="flareupArea"

#create categorical variable to indicate flareup or lull, rising or falling
plotDataT %<>%
  mutate(flareupCategory = case_when(grepl("flareup", flareupArea) ~ "flareup",
                                     grepl("lull", flareupArea) ~ "lull",
                                     grepl("rising", flareupArea) ~ "rising",
                                     grepl("falling", flareupArea) ~ "falling",
                             TRUE ~ "none"))

# Setup tags for each combination of flare-up/lull and rising/falling
NS_FL = c("NS-1_flareup", "NS-2_flareup", "NS-3_flareup", "NS-4_flareup", "NS-1_lull",
          "NS-2_lull", "NS-3_lull", "NS-4_lull")
CS_FL = c("CS-1_flareup", "CS-2_flareup", "CS-3_flareup", "CS-4_flareup", "CS-1_lull",
          "CS-2_lull", "CS-3_lull", "CS-4_lull")
SS_FL = c("SS-1_flareup", "SS-2_flareup", "SS-3_flareup", "SS-4_flareup", "SS-1_lull",
          "SS-2_lull", "SS-3_lull", "SS-4_lull")
EC_FL = c("EC-1_flareup", "EC-2_flareup", "EC-3_flareup", "EC-1_lull", "EC-2_lull",
          "EC-3_lull")

NS_RF = c("NS-1_rising", "NS-2_rising", "NS-3_rising", "NS-4_rising", "NS-1_falling",
          "NS-2_falling", "NS-3_falling", "NS-4_falling")
CS_RF = c("CS-1_rising", "CS-2_rising", "CS-3_rising", "CS-4_rising", "CS-1_falling",
          "CS-2_falling", "CS-3_falling", "CS-4_falling")
SS_RF = c("SS-1_rising", "SS-2_rising", "SS-3_rising", "SS-4_rising", "SS-1_falling",
          "SS-2_falling", "SS-3_falling", "SS-4_falling")
EC_RF = c("EC-1_rising", "EC-2_rising", "EC-3_rising", "EC-1_falling", "EC-2_falling",
```

```
          "EC-3_falling")


# Create categorical variable to pair means by flareup
plotDataT$flareupNum =  substr(plotDataT$flareupArea, 1, 4)
plotDataT$flareupNum[plotDataT$flareupNum == "NS-1"] = "LNS-1"
plotDataT$flareupNum[plotDataT$flareupNum == "NS-2"] = "LNS-2"
plotDataT$flareupNum[plotDataT$flareupNum == "NS-3"] = "LNS-3"
plotDataT$flareupNum[plotDataT$flareupNum == "NS-4"] = "LNS-4"


# To pair the flareups and reorder
ord1=c('flareup', 'lull', 'rising', 'falling')
plotDataT1 = plotDataT %>%
  mutate(flareupCategory = factor(flareupCategory, levels = ord1)) %>%  arrange(flareupCategory)

# Create categorical variable to pair mean results by area
plotDataT1$flareupMeanArea =  substr(plotDataT1$flareupArea, 1, 2)
```


Function to Construct Mean Comparisons and Output as Bar Plots

```
plotResultsFlareupMeans <- function(plotDataT, area, yvar, range, color) {
  yvar1 = as.character(yvar)
  yvar2 = formatLabel(yvar)
  ds = subset(plotDataT, flareupArea %in% area)
  #output results as bar plot
  p1 = ggplot(data = ds, aes(x = flareupNum, y = ds[[yvar]],
                             fill = flareupCategory)) +
```

```
    geom_col(stat = "identity", position = position_dodge(), width = .8, alpha = 0.5) +
    geom_text(aes(label = round(ds[[yvar]], 4)), vjust = 1.2, size = 2,
              position = position_dodge(0.8)) +
    scale_x_discrete(name = element_blank(), expand = c(0, 0)) +
    scale_y_continuous(name = yvar2, expand = expansion(mult = range),
                       breaks = scales::pretty_breaks(n = 3)) +
    theme_bw() +
    scale_fill_manual(values = color) +
    theme(legend.position = "none",
        legend.title = element_blank(),
        legend.text = element_text(size=12),
        axis.text.x=element_text(size=8),
        axis.text.y=element_text(size=8),
        axis.title.x=element_text(size=8),
        axis.title.y=element_text(size=8),
        axis.ticks = element_line(size = 0.5, color="black"),
        axis.ticks.length = unit(1, "mm"),
        axis.line = element_line(size = 1/4, color = "black", linetype=1))
  return(p1)
}
```


Setup Parameters for Plotting

```
p = list()
h = vector()
# range coefficients for y axis - old values
rangeFL = list(c(-0.77, .02), c(-0.2, .05), c(0, .05), c(0, .05), c(-0.2, .05),
               c(-0.993, .001), c(0, .1))
```

```
rangeRF = list(c(-0.4, .05), c(0, .05), c(0, .05), c(0, .05), c(0, .05),
               c(-0.993, .001), c(0, .1))
#new tweaked values
rangeFL = list(c(-0.77, .02), c(-0.2, .05), c(-0.05, .05), c(-0.2, .05), c(-0.5, .05),
               c(-0.996, .0005), c(0.25, 0.05))
rangeRF = list(c(-0.77, .02), c(-0.2, .05), c(-0.05, .05), c(-0.3, .05), c(-0.5, .05),
               c(-0.996, .0005), c(0.25, 0.05))

#flareup lull - cycle through the segments by geochem variable
area = list(NS_FL, CS_FL, SS_FL, EC_FL)
for (i in 2:(ncol(plotDataT1)-3)) {
  yvar = as.name(colnames(plotDataT1)[i])
  print(yvar)
  for (j in 1:length(area)) {
    p[[j]] = plotResultsFlareupMeans(plotDataT1, area[[j]], yvar, rangeFL[[i-1]],
                                     c('red', 'steelblue'))
    h[[j]] = 2
  }
  # Arrange plots
  plot = ggarrange(plotlist = p, heights = h, ncol=1, align="v")
  # Construct file name using geochemical variable
  fname = paste("geochemResults_FL_1", yvar, ".png", sep = "")
  # Output plot
  ggsave(fname, plot, device = "png",type = "cairo", dpi = 300, height = 4, width = 3)
}

#rising falling - cycle through the segments by geochem variable
area = list(NS_RF, CS_RF, SS_RF, EC_RF)
for (i in 2:(ncol(plotDataT1)-3)) {
  yvar = as.name(colnames(plotDataT1)[i])
```

```
  print(yvar)
  for (j in 1:length(area)) {
    p[[j]] = plotResultsFlareupMeans(plotDataT1, area[[j]], yvar, rangeRF[[i-1]],
                                     c('peru', 'darkolivegreen'))
    h[[j]] = 2
  }
  # Arrange plots
  plot = ggarrange(plotlist = p, heights = h, ncol=1, align="v")
  # Construct file name using geochemical variable
  fname = paste("geochemResults_RF_1", yvar, ".png", sep = "")
  #output plot
  ggsave(fname, plot, device = "png",type = "cairo", dpi = 300, height = 4, width = 3)
}

# Order by segment
ord1=c('LNS', 'CS', 'SS', 'EC')
plotDataT1$flareupMeanArea[plotDataT1$flareupMeanArea == "NS"] = "LNS"
plotDataT1 = plotDataT1 %>%
  mutate(flareupMeanArea = factor(flareupMeanArea, levels = ord1)) %>%
  arrange(flareupMeanArea)
```


Function to Plot the Means for Each Segment

```
plotResultsAreaMeans <- function(plotDataT, area, yvar, rn, range, color) {
  yvar1 = as.character(yvar)
  yvar2 = formatLabel(yvar)
  print(rn)
  ds = subset(plotDataT, flareupArea %in% area)
```

```
  #output results as bar plot
  p1 = ggplot(data = ds, aes(x = flareupMeanArea, y = ds[[yvar]], fill = flareupCategory)) +
    geom_col(stat = "identity", position = position_dodge(), width = 0.8, alpha = 0.5) +
    geom_text(aes(label = round(ds[[yvar]], rn)), vjust = 1.4, size = 3,
              position = position_dodge(0.8)) +
    scale_x_discrete(name = element_blank(), expand = c(0, 0)) +
    scale_y_continuous(name = yvar2, expand = expansion(mult = range),
                       breaks = scales::pretty_breaks(n = 3)) +
    theme_bw() +
    scale_fill_manual(values = color) +
    theme(legend.position = "none",
          legend.title = element_blank(),
          legend.text = element_text(size=12),
          strip.text = element_text(size = 12),
          strip.background = element_rect(fill = "grey90"),
          axis.text.x=element_text(size=12),
          axis.text.y=element_text(size=12),
          axis.title.x=element_text(size=14),
          axis.title.y=element_text(size=13),
          axis.ticks = element_line(size = 1/2, color="black"),
          axis.ticks.length = unit(1, "mm"),
          axis.line = element_line(size = 1/4, color = "black", linetype=1))
  return(p1)
}
```

Calculate and Plot the Aggregated Means for Each Segment

```
# Initialize list of plots
p = list()

# Tags for different options
AREA_MEANS_FL = c("NS_flareup_mean", "CS_flareup_mean", "SS_flareup_mean",
                  "EC_flareup_mean", "NS_lull_mean", "CS_lull_mean", "SS_lull_mean",
                  "EC_lull_mean")
AREA_MEANS_RF = c("NS_rising_mean", "CS_rising_mean", "SS_rising_mean", "EC_rising_mean",
                  "NS_falling_mean", "CS_falling_mean", "SS_falling_mean", "EC_falling_mean")
#plot FL area means
plotDataT2 = plotDataT1 #plotDataT1[-c(9:11)]
plotDataT2 %<>% relocate(flareupArea, .after = last_col())

# Range values for geochmemical variables to an adjust bars to appropriate ranges
rangeFL = list(c(-0.77, .02), c(-0.2, .05), c(-0.05, .05), c(-0.2, .05), c(-0.5, .05),
               c(-0.996, .0005), c(0.25, 0.05))

# Cycle through each geochemical variable to plot comparison bars
for (i in 1:(ncol(plotDataT2)-4)) {
  rn = 1
  #print(i)
  yvar = as.name(colnames(plotDataT2)[i])
  if (paste(yvar) == "Sri") {
    rn = 4}
  print(yvar)
  #print(rn)
```

```
  p[[i]] = plotResultsAreaMeans(plotDataT2, AREA_MEANS_FL, yvar, rn,
                                rangeFL[[i]], c('red', 'steelblue'))
  h[[i]] = 2
}
plot = ggarrange(plotlist = p, heights = h, ncol=1, align="v")
fname = paste("geochemResultsAreaMeans_FL_", ".png", sep = "")
ggsave(fname, plot, device = "png",type = "cairo", dpi = 300, height = 10, width = 5)


rangeRF = list(c(-0.77, .02), c(-0.2, .05), c(-0.05, .05), c(-0.3, .05), c(-0.5, .05),
               c(-0.996, .0005), c(0.25, 0.05))
#plot RF area means
for (i in 1:(ncol(plotDataT2)-4)) {
  yvar = as.name(colnames(plotDataT2)[i])
  rn = 1
  yvar = as.name(colnames(plotDataT2)[i])
  if (paste(yvar) == "Sri") rn = 4
  print(yvar)
  p[[i]] = plotResultsAreaMeans(plotDataT2, AREA_MEANS_RF, yvar, rn, rangeRF[[i]],
                                c('peru', 'darkolivegreen'))
  h[[i]] = 2
}
plot = ggarrange(plotlist = p, heights = h, ncol=1, align="v")
fname = paste("geochemResultsAreaMeans_RF_", ".png", sep = "")
ggsave(fname, plot, device = "png",type = "cairo", dpi = 300, height = 10, width = 5)
```

Age Histogram Plots - 3 PCB Segments

```
BA = PeruData %>%
  filter(`Area_ID` == 'Peru', Analysis_Type == 'Whole Rock',
         Location_1 == "PCB-North Segment" | Location_1 == "PCB-Central Segment" |
           Location_1 == "PCB-South Segment",
         Rock_Type1 == "Plutonic" | Rock_Type1 == "Volcanic" | Rock_Type1 == "Igneous",
         Method_Age == "U-Pb" | Method_Age == "U-Pb infer",
  )
#including K-Ar, Ar-Ar, Sr-Rb
BA = PeruData %>%
  dplyr::filter(`Area_ID` == 'Peru', Analysis_Type == 'Whole Rock',
         Location_1 == "PCB-North Segment" | Location_1 == "PCB-Central Segment" |
           Location_1 == "PCB-South Segment",
         Rock_Type1 == "Plutonic" | Rock_Type1 == "Volcanic" | Rock_Type1 == "Igneous",
         Method_Age == "U-Pb" | Method_Age == "U-Pb infer" | Method_Age == "Rb-Sr" |
           Method_Age == "K-Ar" | Method_Age == "Ar-Ar",
  )

agedata = BA[, c("Location_1", "Age")]

ord1=c('PCB-North Segment', 'PCB-Central Segment', 'PCB-South Segment')
agedata %<>%
  mutate(Location_1 = factor(Location_1, levels = ord1)) %<>%
  arrange(Location_1)

FlareupData = read_excel("R:\\Projects\\Geochem\\PhD\\Publications\\Moho flareups.xlsx",
```

```
                          sheet = 1)
FlareupData$Location_1 = FlareupData$Segment
FlareupData = FlareupData %>%
  dplyr::filter(Location_1 %in% ord1)
FlareupData %<>%
  mutate(Location_1 = factor(Location_1, levels = ord1)) %<>%
  arrange(Location_1)

ageStart = 18
ageEnd = 205
binWidth = 5
nrows = nrow(dplyr::filter(agedata, Age < ageEnd))

seg_labels <- as_labeller(c(`0` = "LNS", `1` = "CS", `2` = "SS"))

labeli <- function(variable, value){
  names_li <- list("PCB-North Segment"="LNS", "PCB-Central Segment"="CS","PCB-South Segment"="SS")
  return(names_li[value])
}
agedata$Age_J = agedata$Age
agedata$Age_J = agedata$Age
agedata %<>%      #apply mild smoothing to sharp peaks
    mutate(Age_J = case_when(Age_J == 60 ~ jitter(Age_J, amount = 3),
                             Age_J == 98 ~ jitter(Age_J, amount = 3),
                             Age_J == 103 ~ jitter(Age_J, amount = 3),
                             Age_J == 105 ~ jitter(Age_J, amount = 3),
                             Age_J == 110 ~ jitter(Age_J, amount = 3),
                             Age_J == 131 ~ jitter(Age_J, amount = 3),
                                    TRUE ~ Age_J))

agedata$FlareupName = NA
```

```
p1 = agedata %>%
  ggplot() +
  scale_color_manual(name="Segment", labels = c('LNS', 'CS', 'SS'),
                     values = c('blue', 'red', '#82D30C')) +
  scale_fill_manual(name="Segment", labels = c('LNS', 'CS', 'SS'),
                    values = c('blue', 'red', '#82D30C')) +

  geom_rect(data = FlareupData, aes(xmin = Start, xmax = End, ymin = -Inf,
                                    ymax = Inf), fill = "steelblue", alpha = 0.3) +
  geom_histogram(data = agedata, aes(x = Age_J, fill = Location_1),
                 col = "grey50", binwidth = binWidth, boundary = 0,
                 position = "identity", closed = "left", size = 0.5, alpha = 0.6) +
  geom_density(data = agedata[agedata$Location_1=="PCB-North Segment",],
               aes(x = Age_J, y=binWidth*..count..), adjust = 0.5,
               col = "grey30", position = "stack", linetype=1, fill = "NA",
               lwd = 0.6, alpha = 1) + #0.25 for zoomed in plot
  geom_density(data = agedata[agedata$Location_1=="PCB-Central Segment",],
               aes(x = Age_J, y=binWidth*..count..), adjust = 0.5,
               col = "grey30", position = "stack", linetype=1, fill = "NA",
               lwd = 0.6, alpha = 1) + #0.25 for zoomed in plot
  geom_density(data = agedata[agedata$Location_1=="PCB-South Segment",],
               aes(x = Age_J, y=binWidth*..count..), adjust = 0.2,
               col = "grey30", position = "stack", linetype=1, fill = "NA",
               lwd = 0.6, alpha = 1) +
  theme_ipsum() +
  gghighlight(unhighlighted_params = list(agedata, colour = alpha("grey", 0),
                                          fill = alpha("white", 0))) +
  scale_x_continuous(name = "Age (Ma)", breaks = scales::pretty_breaks(n = 10),
                     limits = c(ageStart, ageEnd), expand = c(0, 0)) +
```

```
  scale_y_continuous(name = "Sample count", expand = c(0, 0),
                     breaks = scales::pretty_breaks(n = 2)) +
  theme_bw() +
  labs(fill = "Geologic period") +
  facet_wrap(~Location_1, scales = "free_y", ncol = 1, shrink = FALSE,
             strip.position = "right", labeller = labeli) +
  coord_capped_cart(bottom='both', left='both', xlim=c(18,205)) +
  geom_label(data=FlareupData, aes(x= End + (Start - End)/2 - 0, y=60,
                                   label = paste(Name, ": ", Start, " - ", z
                                                 End, "\n", "peak = ", Peak, sep = "")),
             lineheight = .8, color="grey50", label.r = unit(0.4, "lines"),
             label.padding = unit(0.2, "lines"), size=4 , angle=0,
             fontface="bold", alpha = 0.9) +
  coord_cartesian(clip = "off") +
  theme(legend.position = "none",
        text = element_text(size=18),
        strip.text = element_text(size = 12), # for facet_wrap
        strip.background = element_rect(fill = "grey90"),
        axis.text.x=element_text(size=15),
        axis.text.y=element_text(size=15),
        axis.title.x=element_text(size=20),
        axis.title.y=element_text(size=20),
        axis.ticks = element_line(size = 1, color="black"),
        axis.ticks.length = unit(2, "mm"),
        axis.line = element_line(size = 1/2, color = "black", linetype=1),
        axis.text = element_text( angle = 0, color="black", size=10, face=1)) #

ggsave("agehist_PCB.png", p1, device = "png", type = "cairo", dpi = 200,
       height = 6, width = 15)
```

Age Histogram Plots - EC

```
BA = PeruData %>%
  filter(`Area_ID` == 'Peru', Analysis_Type == 'Whole Rock',
         Location_1 == "EC",
         Rock_Type1 == "Plutonic" | Rock_Type1 == "Volcanic" | Rock_Type1 == "Igneous",
         Method_Age == "U-Pb" | Method_Age == "U-Pb infer",
  )

#including K-Ar, Ar-Ar, Sr-Rb
BA = PeruData %>%
  filter(`Area_ID` == 'Peru', Analysis_Type == 'Whole Rock',
         Location_1 == "EC",
         Rock_Type1 == "Plutonic" | Rock_Type1 == "Volcanic" | Rock_Type1 == "Igneous",
         Method_Age == "U-Pb" | Method_Age == "U-Pb infer" | Method_Age == "Rb-Sr" |
           Method_Age == "K-Ar" | Method_Age == "Ar-Ar",
  )

agedata = BA[, c("Location_1", "Age")]
ord1=c("EC")

FlareupData = read_excel("R:\\Projects\\Geochem\\PhD\\Publications\\Moho flareups.xlsx",
                  sheet = 1)
FlareupData$Location_1 = FlareupData$Segment
FlareupData = FlareupData %>%
  filter(Location_1 %in% ord1)
FlareupData %<>%
  mutate(Location_1 = factor(Location_1, levels = ord1)) %<>%
  arrange(Location_1)
```

```
ageStart = 150
ageEnd = 350
binWidth = 5
nrows = nrow(filter(agedata, Age < ageEnd))

seg_labels <- as_labeller(c(`0` = "EC"))
labeli <- function(variable, value){
  names_li <- list("EC")
  return(names_li[value])
}

agedata$Age_J = jitter(agedata$Age, amount = 5)
agedata %<>%      #apply mild smoothing to spikes
  mutate(Age_J = case_when(Age_J == 60 ~ jitter(Age_J, amount = 3),
                           Age_J == 98 ~ jitter(Age_J, amount = 3),
                           Age_J == 103 ~ jitter(Age_J, amount = 3),
                           Age_J == 105 ~ jitter(Age_J, amount = 3),
                           Age_J == 110 ~ jitter(Age_J, amount = 3),
                           Age_J == 131 ~ jitter(Age_J, amount = 3),
                           TRUE ~ Age_J))
agedata$FlareupName = NA

p1 = agedata %>%
  ggplot() +
  scale_color_manual(name="Segment", labels = c('EC'), values = c('peru')) +
  scale_fill_manual(name="Segment", labels = c('EC'), values = c('peru')) +
  geom_rect(data = FlareupData, aes(xmin = Start, xmax = End, ymin = -Inf, ymax = Inf),
            fill = "steelblue", alpha = 0.3) +
  geom_histogram(data = agedata, aes(x = Age_J, fill = Location_1),
                 col = "grey50", binwidth = binWidth, boundary = 0,
```

```
                position = "identity", closed = "left", size = 0.5, alpha = 0.6) +
geom_density(data = agedata[agedata$Location_1=="EC",],
             aes(x = Age_J, y=binWidth*..count..), adjust = 0.4,
             col = "grey30", position = "stack", linetype=1,
             fill = "NA", lwd = 0.6, alpha = 1) +
theme_ipsum() +
gghighlight(unhighlighted_params = list(agedata, colour = alpha("grey", 0.4),
                                        fill = alpha("white", 0.1))) +
scale_x_continuous(name = "Age (Ma)", breaks = scales::pretty_breaks(n = 10),
                   limits = c(ageStart, ageEnd), expand = c(0, 0)) +
scale_y_continuous(name = "Sample count", expand = c(0, 0),
                   breaks = scales::pretty_breaks(n = 2)) +
theme_bw() +
labs(fill = "Geologic period") +
geom_label(data=FlareupData, aes(x= End + (Start - End)/2 - 0, y=8,
                                 label = paste(Name, ": ", Start, " - ",
                                 End, "\n", "peak = ", Peak, sep = "")),
                                 lineheight = .8, color="grey50",
                                 label.r = unit(0.4, "lines"),
                                 label.padding = unit(0.2, "lines"), size=4.5 ,
                                 angle=0, fontface="bold", alpha = 0.9) +
coord_cartesian(clip = "off") +
theme(legend.position = "none",
      text = element_text(size=18),
      strip.text = element_text(size = 12),
      strip.background = element_rect(fill = "grey90"),
      axis.text.x=element_text(size=15),
      axis.text.y=element_text(size=15),
      axis.title.x=element_text(size=20),
      axis.title.y=element_text(size=20),
```

```
        axis.ticks = element_line(size = 1, color="black"),
        axis.ticks.length = unit(2, "mm"),
        axis.line = element_line(size = 1/2, color = "black", linetype=1),
        axis.text = element_text( angle = 0, color="black", size=10, face=1))

ggsave("agehist_EC.png", p1, device = "png", type = "cairo", dpi = 200, height = 3, width = 15)
```

Magma Volume Plots

```
#PCB
FlareupVolData = read_excel("R:\\Projects\\Geochem\\PhD\\Publications\\
                            Peru PhD\\Flareups_PCB_EC.xls", sheet = 1)
ageStart = 18
ageEnd = 205

#set break values for PCB - skip EC block below
breaks = c(15,20,25,30,35,40,45,50,55,60,65,70,75,80,85,90,95,100,105,110,115,120,125,130,135,140,
           145,150,155,160,165,170,175,180,185,190,195,200)
FlareupVolData = subset(FlareupVolData, Location1 == "PCB")

#EC
FlareupVolData = read_excel("R:\\Projects\\Geochem\\PhD\\Publications\\
                            Peru PhD\\Flareups_PCB_EC.xls", sheet = 1)
ageStart = 150
ageEnd = 350

#set break values for EC
breaks <- c(145,150,155,160,165,170,175,180,185,190,195,200,205,210,215,220,225,230,
```

```
            235,240,245,250,255,260,265,270,275,280,285,290,295,300,305,310,315,320,
            325,330,335,340,345,350)
FlareupVolData = subset(FlareupVolData, Location1 == "EC")

FlareupVolData_sorted = FlareupVolData[order(FlareupVolData$AgeJ),]
vol = FlareupVolData_sorted[, c("FlareUp", "AgeJ", "Unit_Vol_80_20", "Unit_Vol_50_50")]
#add age bins to each record
vol %<>% mutate(age_bin = cut(AgeJ, breaks=breaks, labels = F, ordered = TRUE,
                              include.lowest = T, right = FALSE, dig.lab = 10))
#remove null values
vol = vol[!is.na(vol$FlareUp), ]
#convert from m to km
vol$Unit_Vol_80_20 = vol$Unit_Vol_80_20/1000
vol$Unit_Vol_50_50 = vol$Unit_Vol_50_50/1000

#aggregate by age bins
vol_grp = vol %>%
  group_by(age_bin) %>%
  dplyr::summarize(Age = mean(AgeJ),
                   Sum_Vol_80_20 = sum(Unit_Vol_80_20),
                   Sum_Vol_50_50 = sum(Unit_Vol_50_50))

# find next higher integer divisable by 5 to use as x axis
input_array = vol_grp$Age
next_higher_divisible_by_5 <- integer(length(input_array))
for (i in 1:length(input_array)) {
  next_higher_divisible_by_5[i] = (input_array[i] %/% 5 + 1) * 5
}

vol_grp$age_bin = next_higher_divisible_by_5
```

```r
vol80_20 = sum(vol_grp$Sum_Vol_80_20)
vol50_50 = sum(vol_grp$Sum_Vol_50_50)

plot.new()

#plot bars and curves
p1 = vol_grp %>%
    ggplot(aes(x = age_bin, y = Sum_Vol_80_20), fill = age_bin) +
    geom_col(aes(x = age_bin, y = Sum_Vol_80_20), col = "black",
             fill = "#F1771D", stat='count', width = 5, linewidth = 0.1, alpha = 0.3) +
    geom_col(aes(x = age_bin, y = Sum_Vol_50_50), col = "black",
             fill = "#276FB7", stat='count', width = 5, linewidth = 0.1, alpha = 0.3) +
    geom_xspline(aes(x = age_bin, y = Sum_Vol_80_20), size=0.8,
                 spline_shape=0.4, col = "#F1771D") +
    geom_xspline(aes(x = age_bin, y = Sum_Vol_50_50), size=0.8,
                 spline_shape=0.4, col = "#276FB7") +
    coord_cartesian(ylim=c(0, max(vol_grp$Sum_Vol_80_20) +
                               max(vol_grp$Sum_Vol_80_20)/15)) +
    scale_x_continuous(name = "Age (Ma)", expand = c(0, 0),
                       breaks = scales::pretty_breaks(n = 10)) +
    scale_y_continuous(name = "MMA rate (1000 km³)", expand = c(0, 0),
                       breaks = scales::pretty_breaks(n = 5)) +
  theme_bw() +
    theme(legend.position = "none",
          legend.title = element_blank(), #remove legend title
          legend.justification = c("right", "top"),
          legend.box.just = "right",
          legend.box.margin = margin(0.5, 0.5, 0.1, 0.1),
          legend.background = element_rect(fill = "grey90"),
          text = element_text(size=12),
          axis.text.x=element_text(size=10),
```

```
          axis.text.y=element_text(size=10),
          axis.title.x=element_text(size=12),
          axis.title.y=element_text(size=12),
          axis.ticks = element_line(size = 0.5, color="black"),
          axis.ticks.length = unit(2, "mm"),
          axis.line = element_line(size = 1/2, color = "black", linetype=1),
          axis.text = element_text(angle = 0, color="black", size=4, face=1))

  ggsave("R:\\Projects\\Geochem\\PhD\\Publications\\Peru PhD\\figures\\
         flareup_vol_PCB.png", p1, device = "png", type = "cairo", dpi = 200,
         height = 3.2, width = 10)
```


REE Spider Plot

```
REEData = PeruData %>%
  filter(`Area_ID` == 'Peru', Analysis_Type == 'Whole Rock',
         Location_1 == 'PCB-North Segment' | Location_1 == 'PCB-Central Segment' | Location_1 == '
PCB-South Segment',
         Rock_Type1 == "Plutonic" | Rock_Type1 == "Volcanic" | Rock_Type1 == "Igneous") #, Rock_Ty
pe1 == "Plutonic")
         #Data_Source == "Clausen and Martinez" | Data_Source == "Clausen and Martinez_ September
2020" | Data_Source == "Clausen and Martinez_ March 2020" | Data_Source == "Clausen and Martínez")

#REEData = REEData %>%
#  filter(`Tb` <= 2.5)

labels = c('La', 'Ce', 'Pr', 'Nd', 'Sm', 'Eu', 'Gd', 'Tb', 'Dy', 'Ho', 'Er', 'Tm', 'Yb', 'Lu')
REE.cols = c('Location_1', labels)
```

```
#norm = c(0.31, 0.808,  0.122,  0.6,    0.195,  0.0735, 0.259,  0.0474, 0.322,  0.0718, 0.21,   0.
0324, 0.209, 0.0322) # Boynton 1984
norm = c(0.237, 0.613,  0.093,  0.457,  0.148,  0.056,  0.199,  0.036,  0.246,  0.055,  0.160,  0.
025,  0.161, 0.0322) # Sun & McDonough 1989 chondrite


REEData.raw = REEData[, REE.cols]
REEData = aggregate(REEData.raw[, REE.cols], by = list(Location_1=REEData.raw$Location_1), FUN = m
ean, na.rm = TRUE)
#means = colMeans(REEData[3:16], na.rm = TRUE)

REEData[, 3:16] = t(t(REEData[, 3:16]) / norm) #c(2, 1, 2, 2, 2, 2, 2, 2, 2, 2, 2, 2, 2, 1)
#REEData$Location_1 = REEData$Name


data.lf = REEData %>% dplyr::select(c(labels,"Location_1")) %>%
  pivot_longer(-Location_1,names_to="elements",values_to="val") %>%
  mutate(elements=factor(elements,levels=unique(labels)))

ord1=c('PCB-North Segment', 'PCB-Central Segment', 'PCB-South Segment')
data.lf %<>%
  mutate(Location_1 = factor(Location_1, levels = ord1)) %<>%
  arrange(Location_1)

plotSpider <- function(REE, elements, titl, fname) {
 p1 = REE %>%
    ggplot(mapping = aes(x = elements, y = val, color = Location_1)) + #shape = Rock_Type1,
    geom_line(aes(group = Location_1), size = 0.8) +
    geom_point(size = 1.5) +
    scale_x_discrete(name = "REE", labels=elements) +
    scale_y_continuous(name = "sample/chondrite",  limits = c(0, 100), breaks = scales::pretty_bre
```

```
aks(n = 2), expand = c(0, 0)) + theme_bw() + #theme_grey()
    scale_y_log10(name = "sample/chondrite") +
    theme_bw() +
    #stat_ellipse(aes(), alpha = 1, show.legend = F, type = "t", linetype = 1, level = 0.68, geom
= "path") +
    scale_color_manual(name="Segment", labels = c('North', 'Central', 'South'), values = c('blue',
'red', '#82D30C')) +
    annotate(geom = "Text", x = -Inf, y = Inf, hjust = -6, vjust = 2, label = paste(titl, sep = ""
)) + #label = expression("Greek text"^~ alpha * beta)
    theme(legend.position = c(1, 1),
          legend.title = element_blank(), # remove legend title
          legend.justification = c("right", "top"),
          legend.box.just = "right",
          legend.box.margin = margin(0.5, 0.5, 0.1, 0.1),
          legend.background = element_rect(fill = "grey90"),  #element_blank()
          text = element_text(size=12),
          axis.text.x=element_text(size=10),
          axis.text.y=element_text(size=10),
          axis.title.x=element_text(size=12),
          axis.title.y=element_text(size=12),
          axis.ticks = element_line(size = 1, color="black"),
          axis.ticks.length = unit(2, "mm"),
          axis.line = element_line(size = 1/2, color = "black", linetype=1),
          axis.text = element_text(angle = 0, color="black", size=4, face=1))
  ggsave(fname, p1, device = "png",type = "cairo", dpi = 300, height = 4, width = 12) #6x14
  return(p1)
}

plotSpider(data.lf, labels, "", "REESpider.png")
```

Multi-Element Plot - Segments

```
eleData = PeruData %>%
  dplyr::filter(`Area_ID` == 'Peru', Analysis_Type == 'Whole Rock',
         Location_1 == 'PCB-North Segment' | Location_1 == 'PCB-Central Segment' | Location_1 == '
PCB-South Segment',
         Rock_Type1 == "Plutonic" | Rock_Type1 == "Volcanic")

eleData$K = eleData$K2O * 8302

n1 = read_excel("R:\\Projects\\Geochem\\PhD\\Publications\\Peru PhD\\Chondrite and P-Mantle values
_spider REE plot.xlsx", sheet = 1) norm = as.numeric(as.vector(n1[2,]))

labels = colnames(n1)
element.cols = c('Location_1', labels)

elementData.raw = eleData[, element.cols]
elementData.ag = aggregate(elementData.raw[, element.cols],
by = list(Location_1=elementData.raw$Location_1), FUN = mean, na.rm = TRUE)
#means = colMeans(REEData[3:16], na.rm = TRUE)

elementData.ag[, 3:28] = t(t(elementData.ag[, 3:28]) / norm)

data.lf = elementData.ag %>% dplyr::select(c(labels,"Location_1")) %>%
  pivot_longer(-Location_1,names_to="elements",values_to="val") %>%
  mutate(elements=factor(elements,levels=unique(labels)))

ord1=c('PCB-North Segment', 'PCB-Central Segment', 'PCB-South Segment')
data.lf %<>%
  mutate(Location_1 = factor(Location_1, levels = ord1)) %<>%
```

```
  arrange(Location_1)

plotMultiElement <- function(elementData, ele, titl, fname) {
  p1 = elementData %>%
    ggplot(mapping = aes(x = elements, y = val, color = Location_1)) +
    geom_line(mapping = aes(group = Location_1), size = 0.8) +
    geom_point(size = 1.5) +
    scale_x_discrete(name = "", labels=elements, guide = guide_axis(n.dodge =2)) +
    scale_y_log10(name = "sample/P-mantle") +
    theme_bw() +
    scale_color_manual(name="Segment", labels = c('LNS', 'CS', 'SS'),
                       values = c('blue', 'red', '#82D30C')) +
    annotate(geom = "Text", x = -Inf, y = Inf, hjust = -6, vjust = 2,
             label = paste(titl, sep = "")) +
    theme(legend.position = c(1, 1),
          legend.title = element_blank(), # remove legend title
          legend.justification = c("right", "top"),
          legend.box.just = "right",
          legend.box.margin = margin(0.5, 0.5, 0.1, 0.1),
          legend.background = element_rect(fill = "grey90"),
          text = element_text(size=12),
          axis.text.x=element_text(size=10),
          axis.text.y=element_text(size=10),
          axis.title.x=element_text(size=12),
          axis.title.y=element_text(size=12),
          axis.ticks = element_line(size = 1, color="black"),
          axis.ticks.length = unit(2, "mm"),
          axis.line = element_line(size = 1/2, color = "black", linetype=1),
          axis.text = element_text(angle = 0, color="black", size=4, face=1))
  ggsave(fname, p1, device = "png",type = "cairo", dpi = 300, height = 4, width = 12)
```

```
return(p1)
}

plotMultiElement(data.lf, labels, "", "elementSpider.png")
```

Multi-Element Plot - W/E

```
eleData = PeruData %>%
  filter(`Area_ID` == 'Peru', Analysis_Type == 'Whole Rock',
         Location_1 == 'PCB-North Segment' | Location_1 == 'PCB-Central Segment' | Location_1 == '
PCB-South Segment',
         Rock_Type1 == "Plutonic" | Rock_Type1 == "Volcanic")

eleData$K = eleData$K2O * 8302

n1 = read_excel("R:\\Projects\\Geochem\\PhD\\Publications\\Peru PhD\\Chondrite and P-Mantle values
_spider REE plot.xlsx", sheet = 1)
norm = as.numeric(as.vector(n1[2,]))

labels = colnames(n1)
element.cols = c('West_east', labels)

elementData.raw = eleData[, element.cols]
elementData.ag = aggregate(elementData.raw[, element.cols],
by = list(West_east=elementData.raw$West_east), FUN = mean, na.rm = TRUE)

elementData.ag[, 3:28] = t(t(elementData.ag[, 3:28]) / norm)
```

```r
data.lf = elementData.ag %>% dplyr::select(c(labels,"West_east")) %>%
  pivot_longer(-West_east,names_to="elements",values_to="val") %>%
  mutate(elements=factor(elements,levels=unique(labels)))

ord1=c('West', 'Central', 'East')
data.lf %<>%
  mutate(West_east = factor(West_east, levels = ord1)) %<>%
  arrange(West_east)

plotMultiElement <- function(elementData, ele, titl, fname) {
  p1 = elementData %>%
    ggplot(mapping = aes(x = elements, y = val, color = West_east)) +
    geom_line(mapping = aes(group = West_east), size = 0.8) +
    geom_point(size = 1.5) +
    scale_x_discrete(name = "", labels=elements, guide = guide_axis(n.dodge =2)) +
    scale_y_log10(name = "sample/P-mantle") +
    theme_bw() +
    scale_color_manual(name="", labels = c('West', 'Central', 'East'),
                       values = c('#FFC300', '#E00EF3', '#0EE7F3')) +
    annotate(geom = "Text", x = -Inf, y = Inf, hjust = -6, vjust = 2,
             label = paste(titl, sep = "")) +
    theme(legend.position = c(1, 1),
          legend.title = element_blank(), # remove legend title
          legend.justification = c("right", "top"),
          legend.box.just = "right",
          legend.box.margin = margin(0.5, 0.5, 0.1, 0.1),
          legend.background = element_rect(fill = "grey90"),  #element_blank()
          text = element_text(size=12),
          axis.text.x=element_text(size=10),
          axis.text.y=element_text(size=10),
```

```
          axis.title.x=element_text(size=12),
          axis.title.y=element_text(size=12),
          axis.ticks = element_line(size = 1, color="black"),
          axis.ticks.length = unit(2, "mm"),
          axis.line = element_line(size = 1/2, color = "black", linetype=1),
          axis.text = element_text(angle = 0, color="black", size=4, face=1))
  ggsave(fname, p1, device = "png",type = "cairo", dpi = 300, height = 4, width = 12)
  return(p1)
}

plotMultiElement(data.lf, labels, "", "elementSpider_WE.png")
```